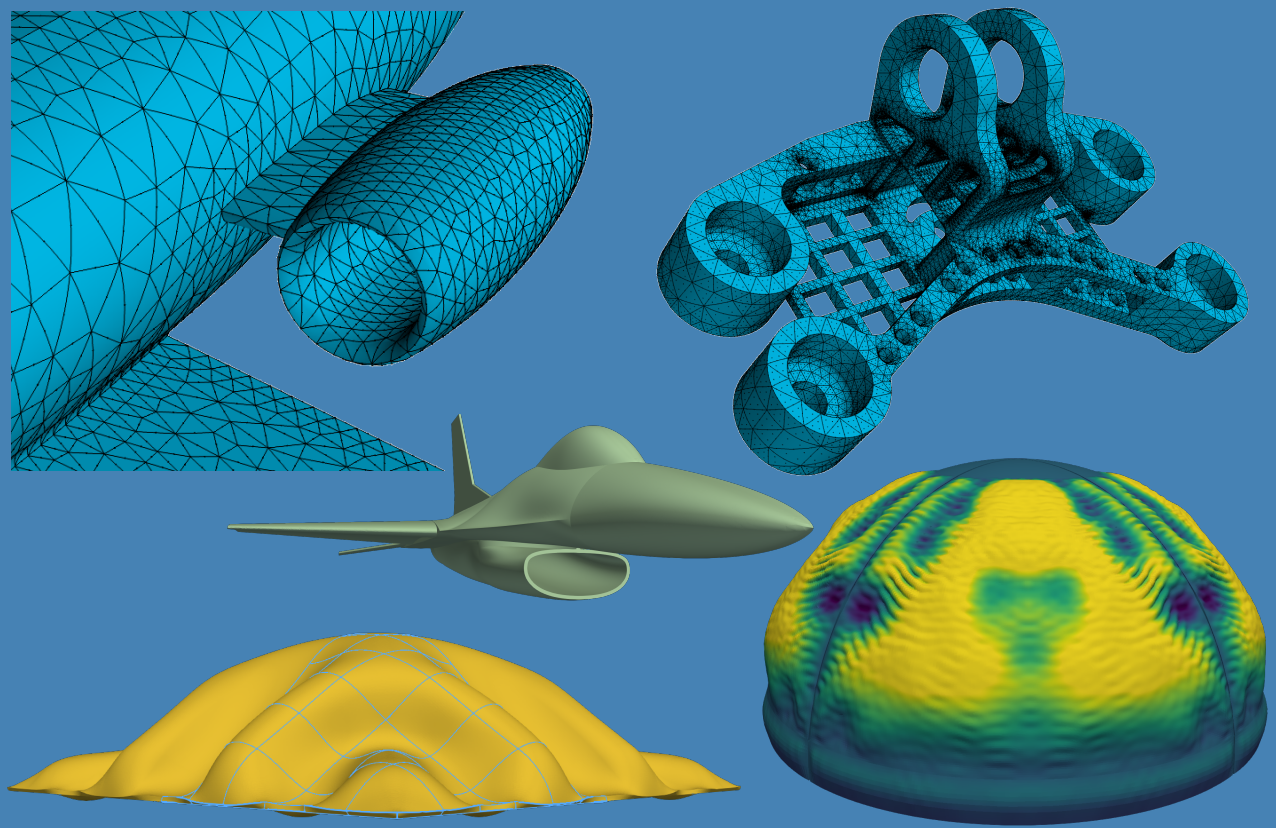


HIGH ORDER CURVILINEAR FINITE ELEMENTS FOR  
SMALL & LARGE DEFORMATION ELECTROMECHANICS:  
INTEGRATING CAD, MESH GENERATION & FINITE ELEMENT  
DESIGN FOR MULTIPHYSICS PROBLEMS



ROMAN POYA

ZIENKIEWICZ CENTRE FOR COMPUTATIONAL ENGINEERING  
SWANSEA UNIVERSITY

# **High order curvilinear finite elements for small and large deformation electromechanics: Integrating CAD, mesh generation and finite element design for multiphysics problems**

by

**Roman Poya**

Submitted to the College of Engineering in partial fulfilment of the  
requirements for the degree of

Doctor of Philosophy

at

Swansea University

21 May, 2018



**Swansea University**  
**Prifysgol Abertawe**



## DECLARATION

This work has not previously been accepted in substance for any degree and is not being concurrently submitted in candidature for any degree.

Signed ..... (candidate)  
Date .....

## STATEMENT 1

This thesis is the result of my own investigations, except where otherwise stated. When correction services have been used, the extent and nature of the correction is clearly marked in a footnote(s). Other sources are acknowledged by footnotes giving explicit references. A bibliography is appended.

Signed ..... (candidate)  
Date .....

## STATEMENT 2

I hereby give consent for my thesis, if accepted, to be available for photocopying and for inter-library loan, and for the title and summary to be made available to outside organisations.

Signed ..... (candidate)  
Date .....

*To my mother*

# Acknowledgement

I express my gratitude to my advisor Professor Antonio Javier Gil for his supervision, guidance and the ample opportunity he provided for me to carry out my doctoral research in Swansea. I would like to thank my second advisor Prof. Dr.-Ing. Wolfgang A. Wall from Technical University of Munich for allowing me to work in his research group “Lehrstuhl für Numerische Mechanik” in Germany, for a year. I thank Dr. Rogelio Ortigosa for his guidance and the entertaining discussions we had on myriad of topics concerning our research. Without his involvement and determination in the development of convex multi-variable electromechanics this thesis would not have been compiled, perhaps. A great deal of this work was carried out in collaboration with Dr. Ruben Sevilla on high order curvilinear mesh generation which eventually set the scene for the rest of the research on the development curvilinear finite elements, and for that, I am truly grateful to him. I am thankfull to Prof. Javier Bonet from Greenwich University for his occasional advisory and mentorship and Dr. Paul David Ledger for facilitating a consultancy research project for me from Siemens Magnet Technology (Siemens Healthcare™). I spent the last year of my PhD focussing on the development of an anisotropic mesh generator for the Airbus Defence and Space™, a rare opportunity given to me by Prof. Oubay Hassan, which I am genuinely grateful for. I thank all the folks in Swansea and Munich who I came across during the last four years in particular, Carla Schmutter, David Naumann, Scott Bagwell, Mar Giralt and Ceren Gürkan for their assistance whenever it was needed. I am grateful to my mother and my elder siblings Emal and Ajmal for always being supportive and ridiculously positive about my decisions, regardless of the outcome.

This PhD project was funded by the European Commission EACEA Agency, Framework Partnership Agreement 2013-0043 Erasmus Mundus Action 1b, as a part of the EM Joint Doctorate Simulation in Engineering and Entrepreneurship Development (SEED), and their financial support is gratefully acknowledged.

List of author's publications as a result of this work:

### Journal articles:

1. **R. Poya**, A. J. Gil, P. D. Ledger, "A computational framework for the analysis of linear piezoelectric beams using *hp*-FEM", *Computers and Structures* 152 (2015) 155-172. [<https://doi.org/10.1016/j.compstruc.2015.01.012>].
2. P. D. Ledger, A. J. Gil, **R. Poya**, M. Kruip, I. Wilkinson, S. Bagwell, "Solution of an industrially relevant coupled magneto-mechanical problem set on an axisymmetric domain", *Applied Mathematical Modelling* 40 (2016) 1959 - 1971. [<https://doi.org/10.1016/j.apm.2015.09.030>].
3. **R. Poya**, R. Sevilla, A. J. Gil, "A unified approach for a posteriori high-order curved mesh generation using solid mechanics", *Computational Mechanics* 58 (2016) 457-490. [<https://doi.org/10.1007/s00466-016-1302-2>].
4. **R. Poya**, A. J. Gil, R. Ortigosa, "A high performance data parallel tensor contraction framework: Application to coupled electro-mechanics", *Computer Physics Communications* 216 (2017) 35-52. [<https://doi.org/10.1016/j.cpc.2017.02.016>].
5. **R. Poya**, A. J. Gil, R. Ortigosa, R. Sevilla, J. Bonet, W. A. Wall, "A curvilinear high order finite element framework for electromechanics: from linearised electro-elasticity to massively deformable dielectric elastomers", *Computer Methods in Applied Mechanics and Engineering*, (2017), [<https://doi.org/10.1016/j.cma.2017.09.020>].
6. **R. Poya**, A. J. Gil, R. Ortigosa, R. Palma, "On a family of numerical models for couple stress based flexoelectricity of continua and beams", *Journal of the Mechanics and Physics of Solids*, (2018), Under Review.
7. R. Ortigosa, A. J. Gil, **R. Poya**, "Coupled BEM-FEM computational framework based on non-singular integrands and tensor cross product based formulation for the simulation of nonlinear electromechanics immersed in free space", *Computer Methods in Applied Mechanics and Engineering*, (2018), Under Review.
8. **R. Poya**, R. Ortigosa, A. J. Gil, "On the accurate numerical studies of dynamic wrinkling in soft dielectric elastomer films", *Soft Matter*, (2018), Submitted.

### Conference proceedings:

1. **R. Poya**, Antonio J. Gil, Javier Bonet, "A computational framework for linear elasticity coupled with nonlinear electro-magneto-static", *23rd UKACM (then UK-ACME) Conference on Computational Mechanics*, Swansea, UK, 8-10 April 2015.
2. **R. Poya**, A. J. Gil, J. Bonet, "Computational strategies for a new class of coupled models in electromechanics based on linear elasticity and non-linear electro-statics", *IMA Conference on Numerical Methods for Simulation*, Oxford, UK, 1-4 September 2015.
3. **R. Poya**, R. Sevilla, A. J. Gil, "A consistently linearised solid mechanics based mesh deformation technique for high order curved elements", *European Congress on Computational Methods in Applied Sciences and Engineering (ECCOMAS)*, Crete Island, Greece, 5-10 June 2016.
4. **R. Poya**, A. J. Gil and R. Ortigosa, "Development of monolithic and staggered schemes for coupled electromechanics with high order curvilinear finite elements". *Proceedings of the 7th International Conference on Computational Methods for Coupled Problems in Science and Engineering*, Rhodes Island, Greece, June 12-14, 2017.

5. A. J. Gil and R. Ortigosa, **R. Poya**, “A new framework for large strain electro-magneto-mechanics based on convex multi-variable strain energies: Conservation laws and hyperbolicity”. *Proceedings of the 7th International Conference on Computational Methods for Coupled Problems in Science and Engineering*, Rhodes Island, Greece, June 12-14, 2017.
6. R. Ortigosa, A. J. Gil, **R. Poya**, “A new framework for large strain electromechanics based on convex multi-variable strain energies”, *4th ECCOMAS Young Investigator Conference - YIC 2017*, 13-15 September 2017, Milan, Italy.

The work carried out resulted in heavy software development on many fronts. These were eventually divided into domain specific sub-packages once it became clear that they had found full-fledged applications by themselves and today all go through a rigorous testing, deployment, continuous integration and release cycle and are available under flexible open source licenses. A couple of these projects in particular **Fastor**, have found considerable appreciation from other research groups:

#### Software packages:

1. **PostMesh**: An a posteriori curvilinear surface and volume mesh generator for high order finite elements [<https://github.com/romeric/PostMesh>]
2. **FEAPB**: An intuitive user interface for hp-finite element analysis of three-dimensional piezoelectric beams [<https://github.com/romeric/feapb>]
3. **Fastor**: A light-weight high performance SIMD based tensor algebra framework in C++11/14/17 [<https://github.com/romeric/fastor>]
4. **Florence**: A Python based computational framework for integrated computer aided design, curvilinear mesh generation and finite and boundary element methods for linear and nonlinear analysis of solids and coupled electro-mechanical systems [<https://github.com/romeric/florence>]

# Abstract

The work presented in this thesis deals with three fundamental issues pertaining to the computational modelling of coupled electromechanical systems. Firstly, the problem of accurate geometrical representation is considered. An approach to accurately represent the geometry in standard high order finite elements is presented. To this end, the problem of generating curvilinear meshes which are required for high order finite element analysis is undertaken. As a matter of consequence, a curvilinear high order mesh generator for high order finite elements is developed using a metric controlled polyconvex mechanics analogy and using the finite element itself. The use of polyconvex elasticity to deform meshes with planar faces to curve faces seems to provide good quality high order volume meshes due to the fact that the fundamental distortion measures of deformation are already encoded in the definition of polyconvex elastic material model. The convergence properties of the finite element scheme on these meshes is shown to be dependent on these fundamental metrics, namely the edge distortion metric, face distortion metric and volume distortion metric. A series of  $h$  and  $p$  convergence studies have been carried out for Poisson type problems, elasticity problems and electro-elasticity problems on these meshes using different continuum mechanics analogies, different polyconvex and non-polyconvex material models with isotropic, anisotropic and boundary layer meshes. The scalability of the platform is shown through the generation of high order curved computational meshes with millions of nodes.

Putting the technique into practice, the second part of the thesis deals with the development of a curvilinear finite element technique for four classes of coupling in electromechanics. The first class is the large deformation - large electric field electromechanics, typically suitable for modelling massive deformations observed in Electro-Active Polymers (EAPs) and in particular Dielectric Elastomers (DEs). The recently developed convex multi-variable electro-elasticity is employed to model the large deformation characteristics of DEs and through exhaustive numerical simulations, massive deformations, instabilities in the form wrinkling, snap-through and pull-in instabilities are shown to be captured extremely well using the curvilinear high order displacement potential technique for convex multi-variable electro-elasticity.

The second class of electromechanics discussed is linearised electrostriction with nonlinear electrostatic response. The point of departure for modelling linearised electrostriction once again lies in the convex multi-variable energies which are consistently linearised and particularised for the case of small strains. A staggered scheme is developed to solve the nonlinear equations of electrostatics which is then coupled incrementally (non-iteratively) with the equations of elasticity providing significantly superior performance to the fully monolithic approach. Through numerical examples it is shown that the method is capable of capturing excessively large displacements as long as the strains remain small. Once again the curvilinear high order finite element scheme is utilised for this staggered approach.

The third class of electromechanics discussed is the most well established linear piezoelectricity. Due to the physical applications of this class in simplified settings and structurally reduced models a new variational and computational framework is introduced for the analysis of three dimensional linear piezoelectric beams using hp-finite elements. The framework is suitable for static, modal and dynamic scenarios; it is not restricted to either actuation or energy harvesting applications and, moreover, it can cope with any anisotropy or electric polarisation orientation. Derived from first principles, namely the fundamental equations of continuum piezoelectricity, a new set of beam balance equations is presented based on a Taylor series expansion for the displacement and electric potential across the cross section of the beam. The coupled nature of the piezoelectric phenomenon at a beam level arises via a series of mechanical (and electrical counterparts) stress and strain cross sectional area resultants. To benchmark the numerical algorithm, and in order to aid prospective researchers, a new closed-form solution is presented for the case of cantilever type systems subjected to end tip

mechanical/electrical loads. Finally, some numerical aspects of the  $hp$ -discretisation are investigated including the exponential convergence of the  $hp$ -refinements and the consideration of linear or quadratic electric potential expansions across the cross section of the beam.

Immediately following the linear piezoelectricity is the fourth class of electromechanics based on size dependent linear piezoelectricity or better known as flexoelectricity. Once again, an effort is made to develop a family of numerical models for the phenomenological linear flexoelectric theory for continua and their particularisation to the case of three-dimensional beams based on a skew-symmetric couple stress theory is presented. In contrast to the traditional flexoelectric models which assume coupling between electric polarisation and strain gradients, we postulate an electric enthalpy in terms of linear invariants of curvature and electric field. This is achieved by introducing the axial curvature vector as a strain gradient measure. The implication of this assumption is many-fold. Firstly, for isotropic (non-piezoelectric) materials it allows constructing flexoelectric energies without breaking material symmetry. Secondly, nonuniform distribution of volumetric part of strains (volumetric strain gradients) do not generate electric polarisation, as confirmed by experimental evidence to be the case for some important classes of flexoelectric materials. Thirdly, a state of plane strain generates out of plane deformation through strain gradient effects. Finally, extension and shear coupling modes cannot be characterised individually as they contribute to the generation of electric polarisation as a whole. Four distinct variational principles are presented for both continuum and beam models namely, a displacement-potential formulation, a penalty formulation, a Lagrange-multiplier formulation and an augmented Lagrangian formulation. The three latter formulations facilitate incorporation of strain gradient measures in to a standard finite element scheme while maintaining the  $C^0$  continuity. The efficacy of high order finite elements along with the computational efficiency of mixed finite elements are utilised to develop a series of low and high order mixed finite element schemes for couple stress based flexoelectricity. Numerical results of finite element discretisations for the three latter variational formulations are benchmarked against available closed form solutions in regards to electromechanical coupling efficiency. A detailed comparison of the developed couple stress based flexoelectric model with the standard strain gradient flexoelectric models is performed for the case of Barium Titanate where a myriad of simple analytical solutions are proposed in order to quantitatively describe the similarities and dissimilarities in effective electromechanical coupling under these two theories. It is observed that, if the same experimental flexoelectric constants are fitted in to both theories, the current couple stress theory in general, reports stronger electromechanical conversion efficiency. Finally, nanocompression of a complex flexoelectric conical pyramid for which analytical solution cannot be established is numerically studied at an unprecedented level of detail to pinpoint the robustness and advanced computational scalability of the framework.

The final and third part of the thesis deals with the high performance implementation of electromechanics using a generic domain-aware tensor contraction framework. In order to have a unified base for developing high performance kernels for all classes of electromechanics discussed, a new high performance tensor contraction framework for the numerical analysis of coupled electromechanics on streaming architectures is presented. In addition to explicit SIMD instructions and smart expression templates, the framework introduces domain specific constructs for the tensor cross product and its associated algebra. The two key ingredients of the presented expression template engine are as follows. First, the capability to mathematically transform complex chains of operations to simpler equivalent expressions, while potentially avoiding routes with higher levels of computational complexity and, second, to perform a compile time depth-first or breadth-first search to find the optimal contraction indices of a large tensor network in order to minimise the number of floating point operations. For optimisations of tensor contraction such as loop transformation, loop fusion and data locality optimisations, the framework relies heavily on compile time technologies rather than source-to-source translation or JIT techniques. Every aspect of the framework is examined through relevant performance benchmarks, including the impact of data parallelism on the performance of isomorphic and nonisomorphic tensor products, the FLOP and memory I/O optimality in

the evaluation of tensor networks, the compilation cost and memory footprint of the framework and the performance of tensor cross product kernels. The framework is then applied to finite element analysis of coupled electro-mechanical problems to assess the speed-ups achieved in kernel-based numerical integration of complex electro-elastic energy functionals. In this context, domain-aware expression templates combined with SIMD instructions are shown to provide a significant speed-up over the classical low-level style programming techniques.

# Contents

<b>1</b>	<b>Introductory Remarks</b>	<b>2</b>
1.1	Prelude . . . . .	2
1.2	State of the Art & Scope . . . . .	2
1.3	Accurate geometry representation in computational mechanics . . . . .	3
1.4	Novel computational techniques for different classes of electromechanics . . . . .	5
1.4.1	Class 1. Computational modelling of dielectric elastomers: State of the art	5
1.4.2	Class 2. Computational modelling of linearised electrostriction: State of the art . . . . .	6
1.4.3	Class 3. Computational modelling of linear piezoelectricity: State of the art . . . . .	7
1.4.4	Class 4. Computational modelling of linear flexoelectricity: State of the art . . . . .	9
1.5	High Performance Computation . . . . .	12
1.6	Structure of the thesis . . . . .	14
<b>2</b>	<b>Nonlinear Continuum Mechanics</b>	<b>2</b>
2.1	Introduction . . . . .	2
2.2	The classical approach to nonlinear elasticity . . . . .	3
2.2.1	Kinematics . . . . .	3
2.2.2	Governing equations of continuum mechanics . . . . .	4
2.2.3	The internal energy density in hyperelasticity . . . . .	4
2.2.4	Material characterisation in the reference configuration . . . . .	5
2.3	The objective representation in classical elasticity . . . . .	6
2.3.1	Kinematics . . . . .	6
2.3.2	The internal energy density in hyperelasticity . . . . .	6
2.3.3	Material characterisation in the reference configuration . . . . .	7
2.4	The tensor cross product based approach to polyconvex elasticity . . . . .	7
2.4.1	Kinematics . . . . .	7
2.4.2	The internal energy density in polyconvex hyperelasticity . . . . .	8
2.4.3	Material characterisation in the reference configuration . . . . .	9
2.5	The objective representation in polyconvex elasticity . . . . .	10
2.5.1	Objective kinematics . . . . .	10
2.5.2	The internal energy density in objective polyconvex hyperelasticity . . . . .	10
2.5.3	Material characterisation in the reference configuration . . . . .	11
2.6	Polyconvex nonlinear elasticity in spatial setting . . . . .	12
2.6.1	The Cauchy stress tensor and spatial tangent operator . . . . .	12
2.6.2	Governing equations of continuum mechanics in spatial setting . . . . .	12
2.7	The tensor cross product . . . . .	13
2.7.1	Definition for second order tensors and associated properties . . . . .	13
2.7.2	Definition of tensor cross product for some selected high order tensors .	14

<b>3 The Generation of High Order Curvilinear Meshes through Metric Controlled Polyconvex Nonlinear Elasticity</b>	<b>2</b>
3.1 Introduction . . . . .	2
3.2 Non-linear continuum mechanics for mesh deformation . . . . .	4
3.2.1 Kinematics . . . . .	4
3.2.2 The principle of virtual work in the material and spatial settings . . . . .	5
3.3 A consistent incrementally linearised solid mechanics approach . . . . .	6
3.4 Polyconvexity, non-polyconvexity and material characterisation for different formulations . . . . .	8
3.4.1 Material characterisation for the nonlinear hyperelastic case . . . . .	9
3.4.2 Material characterisation for the classical linear elastic case . . . . .	9
3.4.3 A modified Mooney-Rivlin model for mesh deformation . . . . .	10
3.4.4 A nearly incompressible polyconvex Mooney-Rivlin model . . . . .	10
3.4.5 A transversely isotropic non-polyconvex model . . . . .	11
3.5 Mesh quality (distortion) measures . . . . .	12
3.6 Projection techniques . . . . .	13
3.7 Multi-level mesh deformation technique . . . . .	15
3.8 Representative examples . . . . .	16
3.8.1 Mesh of a mechanical component . . . . .	18
3.8.2 Mesh around the SD7003 aerofoil . . . . .	26
3.8.3 Mesh around the NASA almond . . . . .	34
3.8.4 Meshes around full aircraft configurations . . . . .	39
3.8.5 Meshes around full racing car configuration . . . . .	41
3.8.6 Unstructured tetrahedral meshes of complex mechanical components . .	42
3.8.7 Structured and unstructured curved hexahedral meshes . . . . .	45
3.8.8 Unstructured prismatic and hybrid curved meshes . . . . .	46
3.9 Conclusions . . . . .	50
<b>4 Convex Multi-Variable Electromechanics</b>	<b>2</b>
4.1 Introduction . . . . .	2
4.2 Convex multi-variable electro-elasticity . . . . .	3
4.2.1 Kinematics . . . . .	3
4.2.2 Translational and rotational equilibrium . . . . .	3
4.2.3 Electrostatics: Gauss's and Faraday's laws . . . . .	4
4.2.4 The internal energy density in convex multi-variable electro-elasticity .	4
4.2.5 A simple convex multi-variable constitutive model . . . . .	6
4.3 Objective representation in convex multi-variable electro-elasticity . . . .	7
4.3.1 Kinematics . . . . .	7
4.3.2 The internal energy density in objective convex multi-variable electro-elasticity . . . . .	7
4.3.3 A simple objective convex multi-variable constitutive model . . . . .	10
4.4 Convex multi-variable electro-elasticity in spatial setting . . . . .	10
4.4.1 The Cauchy stress tensor, spatial electric field vector and tangent operator	10
4.4.2 Governing equations of continuum electromechanics in spatial setting .	11
4.5 Helmholtz-like energy density and Legendre transformation . . . . .	12
<b>5 Curvilinear Finite Elements for Large Deformations - Large Electric Fields Electromechanics</b>	<b>2</b>
5.1 Introduction . . . . .	2
5.2 Variational formulation . . . . .	4
5.2.1 Displacement-electric potential based variational formulation . . . . .	4
5.3 Numerical examples . . . . .	5
5.3.1 $h$ & $p$ convergence of the proposed high order framework . . . . .	6
5.3.2 Effect of accurate boundary representation in nonlinear electro-elasticity	10

5.3.3	Comparison of higher order displacement potential based formulation with 11 field mixed formulation for electro-elasticity . . . . .	14
5.3.4	Virtual prototyping of massive deformations and instabilities in dielectric elastomers through high performance numerical simulations . . . . .	21
5.4	Conclusions . . . . .	37
<b>6</b>	<b>Curvilinear Finite Elements for Small Deformations - Large Electric Fields Electromechanics</b>	<b>2</b>
6.1	Introduction . . . . .	2
6.2	Incrementally linearised electromechanics . . . . .	3
6.2.1	Symmetric linearised kinematics . . . . .	3
6.2.2	Variational Formulation . . . . .	4
6.2.3	The staggered approach to incrementally linearised electromechanics . . . . .	4
6.3	Numerical examples . . . . .	6
6.3.1	An electromechanical plate with multiple holes . . . . .	6
6.3.2	A simplified jelly fish undergoing voltage induced large displacement . . . . .	8
6.3.3	A self-rolling electromechanical actuator . . . . .	8
6.4	Conclusions . . . . .	11
<b>7</b>	<b>Linearised Electromechanics - Particularisation to Sensing and Energy Harvesting Piezoelectric Continua &amp; Beams</b>	<b>2</b>
7.1	Introduction . . . . .	2
7.2	Balance equations of electromechanics . . . . .	2
7.3	Kinematics and electrostatics of three-dimensional piezoelectric beams . . . . .	4
7.3.1	Kinematics . . . . .	4
7.3.2	Electrical Mapping . . . . .	5
7.4	Variational formulation . . . . .	6
7.5	Mechanical and electrical cross sectional balance equations . . . . .	9
7.5.1	Beam balance equations . . . . .	9
7.5.2	Internal area resultants . . . . .	10
7.6	Analytical solution of planar piezoelectric beams . . . . .	11
7.6.1	Linear electric potential distribution within the cross section . . . . .	13
7.6.2	Quadratic electric potential distribution within the cross section . . . . .	14
7.7	The Finite Element Discretisation . . . . .	16
7.8	Numerical examples . . . . .	17
7.8.1	The benchmark problem . . . . .	18
7.8.2	Shear actuator problem . . . . .	20
7.8.3	Ambient vibration energy harvester undergoing coupled bending-torsion . . . . .	23
7.8.4	Structural health assessment of a sophisticated multi-component actuation machine with multiple circular piezoelectric sensors - CAD driven high order curvilinear finite elements . . . . .	24
7.9	Conclusions . . . . .	28
<b>8</b>	<b>Linearised Electromechanics - Particularisation to Sensing and Energy Harvesting Flexoelectric Continua &amp; Beams</b>	<b>2</b>
8.1	Introduction . . . . .	2
8.2	Balance equations of electromechanics in micropolar continuum . . . . .	3
8.3	The skew-symmetric couple stress theory . . . . .	5
8.4	Variational formulations in couple stress based electromechanics of continua . . . . .	7
8.4.1	The displacement-potential variational formulation . . . . .	7
8.4.2	The penalty formulation . . . . .	9
8.4.3	The Lagrange multiplier formulation . . . . .	10
8.4.4	The augmented Lagrangian formulation . . . . .	11
8.5	Couple-stress flexoelectric theory for three-dimensional beams . . . . .	11

8.5.1	Kinematics of three-dimensional flexoelectric beams . . . . .	11
8.5.2	Electrical Mapping . . . . .	13
8.5.3	Displacement-potential variational formulation for flexoelectric beams . . . . .	14
8.5.4	Internal area resultants for displacement-potential formulation . . . . .	17
8.5.5	The penalty formulation for flexoelectric beams . . . . .	20
8.5.6	The Lagrange multiplier and augmented Lagrangian formulations for flexoelectric beams . . . . .	21
8.5.7	Governing equations of three-dimensional flexoelectric beams . . . . .	22
8.6	The finite element discretisation . . . . .	23
8.7	Numerical experiments . . . . .	25
8.7.1	A detailed comparison of couple stress based and strain gradient based flexoelectric models: vanishing volumetric strain gradients, the presence of reverse coupling modes and material characterisation for BaTiO <sub>3</sub> . . . . .	25
8.7.2	Benchmark example: Convergence studies and further quantification of curvature-induced electromechanical coupling efficiency . . . . .	31
8.7.3	Nanocompression of a flexoelectric conical pyramid . . . . .	34
8.8	Conclusion . . . . .	40
<b>9</b>	<b>Numerical Implementation of Coupled Electromechanics through a Data Parallel Tensor Contraction Framework</b>	<b>2</b>
9.1	Introduction . . . . .	2
9.2	Interface design principle for tensorial operations . . . . .	3
9.2.1	Data parallelism through SIMD vector types . . . . .	3
9.2.2	The abstract tensor class . . . . .	3
9.2.3	The tensor class . . . . .	3
9.2.4	Smart expression templates: Operation minimisation through mathematical transformation . . . . .	4
9.2.5	Smart expression templates: Operation minimisation through compile time depth-first constructive approach . . . . .	5
9.2.6	Data alignment and compile time construction of contraction loop nests	6
9.3	Benchmark examples . . . . .	8
9.3.1	Impact of SIMD vectorisation on the performance of tensor contraction of arbitrary order tensors . . . . .	9
9.3.2	The depth-first search approach and memory vs FLOPs tradeoff . . . . .	11
9.3.3	Compilation aspects of operation minimisation and further compile time tensor contraction optimisations . . . . .	14
9.4	Applications & Real-world experimentation: Kernel-based numerical integration of nonlinear materials . . . . .	17
9.4.1	Kernel-based data parallel code generation for electromechanics on curvilinear meshes . . . . .	22
9.5	Conclusions . . . . .	25
<b>10</b>	<b>Concluding Remarks &amp; Future Outlook</b>	<b>2</b>
10.1	Concluding Remarks . . . . .	2
10.2	Future Outlook . . . . .	4
<b>A</b>	<b>Coefficients of the closed-form solution for piezoelectric beam</b>	<b>2</b>
<b>B</b>	<b>Couple stress theories and constitutive laws for linear flexoelectricity</b>	<b>3</b>
B.1	The indeterminate couple stress theory and its relation to the classical Cosserat theory . . . . .	3
B.2	Constitutive equations for isotropic and anisotropic couple stress flexoelectric materials . . . . .	4

<b>C Boundary conditions, process design and rendering of curvilinear elements</b>	<b>6</b>
<b>D Computational terminologies, idioms and relationships in tensor networks' theory</b>	<b>9</b>
D.1 Computational aspects of tensor contraction . . . . .	9

# List of Figures

1.1	Generation of quality curvilinear meshes from CAD description a) A watertight CAD model for part of a turbine assembly, b) curvilinear tri-quadratic $q = 2$ fully unstructured hexahedral mesh of the component, c) A watertight CAD model of human head and d) $p = 3$ curvilinear unstructured tetrahedral mesh of the human head . . . . .	4
1.2	The four classes of electromechanical coupling studied in this work . . . . .	5
1.3	Buckling of a dielectric elastomer balloon under electric loading, showing large deformations and pre and post buckling states. Courtesy of [316] . . . . .	6
1.4	a) An example of electrostrictive and magnetostrictive coupling arising in Magnetic resonance imaging (MRI) [175, 14]; courtesy of Siemens Healthcare <sup>TM</sup> and, b) A shear mode drop-on-demand inkjet electrostrictive actuator; courtesy of Brünahl et. al. [36] . . . . .	6
1.5	Piezoresponse force microscopy experiment on fascia. a) sample topography, 5 $\mu\text{m}$ scan, (b) topography, zoom of (a), and (c) piezoresponse image [of the same area as in (b)] showing the orientation of the piezoelectric tensor. The piezoelectric response in fascia has either a positive (white) or negative (dark) value. Courtesy of Rivard et. al. [263] . . . . .	7
1.6	A graphical abstract of harvesting energy at the nano level. Electrospun PZT/PVP nanowires (second right from top), SEM micrographs of ZnO nanosheets (second left from bottom), (K,Na)NbO <sub>3</sub> nanorods grown hydrothermally on SrRuO <sub>3</sub> /SrTiO <sub>3</sub> substrate (top left-most and bottom right-most), and multiple circuit diagram and loading conditions. Courtesy of [35] . . . . .	10
1.7	a) An AVX-512 enabled 64 core Xeon Phi co-processors; courtesy of Intel <sup>TM</sup> and, b) A Tesla K80 Nvidia graphics processing card; courtesy of Nvidia <sup>TM</sup> . . . . .	13
1.8	Scope of this thesis . . . . .	14
2.1	Motion map of a body $V$ . . . . .	3
2.2	Motion map of a body $V$ and the kinematic measures $\{\mathbf{F}, \mathbf{H}, J\}$ . . . . .	8
3.1	An a posteriori mesh deformation technique based on continuum mechanics analogy . . . . .	3
3.2	Schematic representation of an a posteriori mesh deformation technique based on continuum mechanics analogy . . . . .	4
3.3	Deformation map of a linear mesh to curvilinear mesh and the related quality measures $\mathbf{F}$ , $\mathbf{H}$ and $J$ . . . . .	5
3.4	Schematic representation of an incrementally linearised solid mechanics approach. . . . .	7
3.5	Types of projection techniques used for placing high order nodes on to the actual CAD boundary . . . . .	14
3.6	Characteristics of different projection techniques . . . . .	15
3.7	Mixed projection strategy . . . . .	15
3.8	Multi-level projection and solid mechanics analogy for curves, followed by surfaces, followed by volumes . . . . .	17
3.9	Geometry of mechanical component. . . . .	18
3.10	Isotropic mesh of mechanical component. . . . .	18

3.11 Detailed view of the high-order isotropic meshes of mechanical component. . . . .	18
3.12 Minimum scaled Jacobian of the generated meshes as a function of the Poisson's ratio and the polynomial degree. . . . .	19
3.13 Minimum scaled Jacobian of the generated meshes as a function of the Poisson's ratio for $p=2$ using the ILE isotropic, CIL and non-linear approaches with different material models. . . . .	20
3.14 Minimum scaled Jacobian of the generated meshes as a function of the Poisson's ratio for $p=3$ using the ILE isotropic, CIL and non-linear approaches with different material models. . . . .	20
3.15 Minimum scaled Jacobian of the generated meshes as a function of the Poisson's ratio using the ILE isotropic, CIL and non-linear models with different material models and $p=4$ (a,b), $p=5$ (c,d) and $p=6$ (e,f) . . . . .	22
3.16 Mean value and standard deviation of the minimum scaled Jacobian of the generated meshes as a function of the Poisson's ratio for different materials and degrees of approximation. . . . .	23
3.17 Condition number of the system matrix as a function of the Poisson's ratio for $p=4$ using the ILE isotropic, CIL and non-linear approaches with different material models. . . . .	23
3.18 Minimum scaled Jacobian of the generated meshes as a function of the Poisson's ratio and the polynomial degree for isometric(a,b,c) and orthogonal(d,e,f) projection techniques. . . . .	24
3.19 Computational cost of various material models using three different formulations with $p=2$ (902 degrees of freedom) and $p=3$ (1,930 degrees of freedom). . . . .	25
3.20 Boundary layer mesh around an aerofoil. . . . .	26
3.21 Minimum scaled Jacobian of the generated meshes with $p=2$ as a function of the Poisson's ratio and the number of load increments. . . . .	27
3.22 Minimum scaled Jacobian of generated meshes with $p=2$ as a function of the Poisson's ratio and the number of load increments with a stretching of 100 in (a), (b) and (c) and with a stretching of 800 in (d), (e) and (f). . . . .	27
3.23 Minimum scaled Jacobian of the generated meshes with $p=4$ as a function of the Poisson's ratio and the number of load increments with a stretching of 50 in (a), (b) and (c) and with a stretching of 400 in (d), (e) and (f). . . . .	28
3.24 Minimum scaled Jacobian of the generated meshes with $p=6$ as a function of the Poisson's ratio and the number of load increments with a stretching of 100 in (a), (b) and (c) and with a stretching of 800 in (d), (e) and (f). . . . .	29
3.25 Ratio of the scaled Jacobian with 50 load increments over a single load increment (i.e. classical linear elasticity) for $\nu=0.495$ . The $x$ -label indicates the level of stretching. . . . .	30
3.26 Distribution of scaled Jacobian throughout the mesh for $p = 4$ and stretch level of 200. . . . .	30
3.27 Quality $Q_1$ of the generated meshes with $p=6$ as a function of the Poisson's ratio and the number of load increments with a stretching of 50 (a,b,c), 400 (d,e,f) and 1600 (g,h,i). . . . .	32
3.28 Different quality measures of the generated meshes with $p=2$ as a function of the Poisson's ratio for the mesh with a stretching of 25 and using five load increments. . . . .	33
3.29 Different quality measures of the generated meshes with $p=4$ as a function of the Poisson's ratio for the ILE isotropic approach and using five load increments. . . . .	33
3.30 Different quality measures of the generated meshes with $p=6$ as a function of the Poisson's ratio for the mesh with a stretching of 200 and using five load increments. . . . .	33
3.31 Computational cost of various material models using three different formulations and with different levels of stretching. . . . .	34

3.32 Approximation error in the $\mathcal{L}^2(\Omega)$ norm as a function of the square root of the number of degrees of freedom . . . . .	35
3.33 Isotropic mesh around the NASA almond. . . . .	35
3.34 Quality measure $Q_1$ of the generated meshes as a function of the Poisson's ratio and the polynomial degree. . . . .	36
3.35 Quality measure $Q_2$ of the generated meshes as a function of the Poisson's ratio and the polynomial degree. . . . .	36
3.36 Quality measure $Q_3$ of the generated meshes as a function of the Poisson's ratio and the polynomial degree. . . . .	37
3.37 Different quality measures of the generated meshes with $p=3$ as a function of the Poisson's ratio using 10 load increments. . . . .	37
3.38 Different quality measures of the generated meshes with $p=5$ as a function of the Poisson's ratio using 10 load increments. . . . .	38
3.39 Computational cost of various material models using three different formulations with $p=2$ (27,831 degrees of freedom) and $p=3$ (90,648 degrees of freedom). . . . .	38
3.40 Approximation error in the $\mathcal{L}^2(\Omega)$ norm as a function of the cubic root of the number of degrees of freedom. . . . .	39
3.41 Isotropic mesh around a Falcon aircraft. . . . .	40
3.42 Isotropic mesh around the DLR-F6 transport configuration. . . . .	41
3.43 Boundary layer mesh around the DLR-F6 transport configuration. . . . .	42
3.44 Isotropic mesh around the racing car. . . . .	43
3.45 Two views of the high-order curved mesh of mechanical valve . . . . .	44
3.46 Two views of the high-order curved mesh of a drill . . . . .	44
3.47 Two views of the high-order curved mesh of a complex mechanical component .	44
3.48 CAD geometry and two views of the high-order curved RAE2822 mesh . . . . .	45
3.49 Multiple views of the high-order curved hexahedral mesh of propeller. The colorbar for distortion measures is scaled in [0,1] with minimum values $Q_1 = 0.922$ , $Q_2 = 0.901$ and $Q_3 = 0.800$ . . . . .	46
3.50 Multiple views of the high-order unstructured curved hexahedral mesh of the car configuration . . . . .	47
3.51 CAD and high-order curved prismatic mesh of a mechanical component. The triangular surface mesh is generated without performing mesh enhancement (i.e. diagonal swapping) . . . . .	48
3.52 Two views of the high-order curved prismatic mesh of a inhomogenous plate .	48
3.53 Two views of the high-order curved hybrid (tetrahedral, prismatic and hexahedral) mesh of a mechanical component . . . . .	49
3.54 Multiple views of the high-order curved hex-dominant hand mesh . . . . .	49
3.55 Multiple views of the high-order curved quad-dominant hybrid mesh of a F16 fighter . . . . .	50
4.1 Motion map of a body $V$ and the kinematic measures $\{\mathbf{F}, \mathbf{H}, J\}$ . . . . .	3
4.2 Extension of polyconvexity to Convex Multi-Variable (CMV) electro-elasticity, showing internal energy and the associated work-conjugates . . . . .	7
4.3 Extension of frame invariant polyconvexity to objective Convex Multi-Variable (CMV) electro-elasticity, showing internal energy and the associated work-conjugates	10
5.1 The developed massively parallel open source computational framework for high order curvilinear finite elements for CMV electromechanics, its requirements and dependencies . . . . .	3
5.2 CAD geometry of the dielectric patch . . . . .	8
5.3 Illustration of computing the diameter (largest segment) in curvilinear meshes using sampling and tessellation strategy, for $p=2$ triangle and $q=3$ quadrilateral, $p=5$ tetrahedra and $q=2$ hexahedra . . . . .	9

5.4	Three representative curvilinear meshes used for convergence studies; a) medium tetrahedral mesh (9220 elements) b) fine tetrahedral mesh (26807 elements), and c) fine hexahedral mesh (5000 elements) . . . . .	9
5.5	$h$ convergence of $\mathcal{L}^2(V)$ norm of the error for different kinematic and kinetic variables, (a) & (b) $p = 2$ , (c) & (d) $p = 3$ , (e) & (f) $p = 4$ and (g) & (h) $p = 5$ . $R_\zeta$ indicates the rate of convergence of quantity $\zeta$ . . . . .	10
5.6	$p$ convergence of $\mathcal{L}^2(V)$ norm of the error for different kinematic and kinetic variables for mesh with 9220 elements. . . . .	11
5.7	CAD representation of plate with circular hole with dimensions $10 \times 20 \times 2 m^3$ . The circular hole with a radius of $5m$ is centred at $[0, 0, 0]^T$ . . . . .	12
5.8	Curvilinear meshes used for comparison a) $p = 3$ planar tetrahedra, b) $p = 3$ curvilinear tetrahedra, c) $p = 3$ planar hexahedra and, d) $p = 3$ curvilinear hexahedra . . . . .	12
5.9	Quadratic convergence of Newton-Raphson on curvilinear a ) tetrahedral mesh and, b) hexahedral mesh . . . . .	13
5.10	Evolution of voltage induced hydrostatic pressure in a plate with circular hole, a) planar $p = 5$ mesh, b) curved $p = 5$ mesh, c) planar $q = 5$ mesh and, d) curved $q = 5$ mesh . . . . .	14
5.11	Geometry of the patch for three different aspect ratios a) 10, b) 100 and, c) 1000 . . . . .	15
5.12	Description of the boundary conditions . . . . .	15
5.13	Voltage induced hydrostatic pressure $p_{hyd}$ for the medium mesh using a) $p = 2$ , b) $p = 3$ and, c) $p = 4$ . . . . .	19
5.14	Voltage induced large strain ( $H_{xz}$ ) for the coarse mesh using a) $p = 2$ , b) $p = 3$ and, c) $p = 4$ . . . . .	19
5.15	Voltage induced large strain ( $F_{zx}$ ) for the fine mesh using a) $p = 2$ , b) $p = 3$ and, c) $p = 4$ . . . . .	20
5.16	Voltage induced large strain ( $F_{zx}$ ) for the fine mesh using a) $q = 2$ , b) $q = 3$ and, c) $q = 4$ . . . . .	20
5.17	Voltage induced large strain ( $F_{zx}$ ) for the fine mesh using a) $q = 2$ , b) $q = 3$ and, c) $q = 4$ . . . . .	20
5.18	Geometry and a curved tetrahedral mesh of the dielectric shell-like cylindrical structure with $10m$ radius $0.333m$ thickness and $25m$ length, centred at $[0, 0, 0]^T$ . . . . .	21
5.19	Evolution of charge induced stresses in dielectric cylindrical structure with accumulated load factor $\Lambda$ being a) $\sigma_{yy}$ at $\Lambda = 0.678$ b) $\sigma_{yy}$ at $\Lambda = 0.785$ , c) $\sigma_{yy}$ at $\Lambda = 1.0$ d) $\sigma_{xy}$ at $\Lambda = 0.678$ e) $\sigma_{xy}$ at $\Lambda = 0.785$ , f) $\sigma_{xy}$ at $\Lambda = 1.0$ . . . . .	23
5.20	Non-dimensional quantity $\Phi/(H\sqrt{\frac{\mu_1}{\varepsilon_2}})$ quantifying electric voltage as a function of circumferential expansion, showing points of snap-through, pull-in instability and formation of coarse wrinkles in dielectric elastomer. $H$ stands for thickness and $\tilde{R} = 9.8333$ is the averaged radius accounting for thickness stretch . . . . .	24
5.21	Evolution of voltage induced strain $F_{xz}$ in dielectric cylindrical structure with accumulated load factor $\Lambda$ being a) $\Lambda = 0.538$ b) $\Lambda = 0.769$ , c) $\Lambda = 0.923$ and, d) $\Lambda = 1.0$ . . . . .	25
5.22	Evolution of voltage induced strain (co-factor of the deformation gradient) $H_{zy}$ in dielectric cylindrical structure with accumulated load factor $\Lambda$ being a) $\Lambda = 0.490$ b) $\Lambda = 0.686$ , c) $\Lambda = 0.784$ , d) $\Lambda = 0.882$ , e) $\Lambda = 0.941$ and, f) $\Lambda = 1.0$ . . . . .	25
5.23	Dielectric capsule centred at $[0, 0, 0]^T$ with an in-plane radius of $10m$ , thickness of $0.5m$ and a bulging factor of $2m$ a,b) CAD geometry and c) $q = 3$ structured hexahedral mesh . . . . .	26
5.24	Evolution of voltage induced hydrostatic pressure in dielectric capsule with the accumulated load factor $\Lambda$ being a) $\Lambda = 0.411$ , b) $\Lambda = 0.767$ , c) $\Lambda = 0.823$ , d) $\Lambda = 0.882$ , e) $\Lambda = 0.946$ and, f) $\Lambda = 1.0$ . . . . .	26
5.25	Geometries and meshes for the dielectric plates of size $100 \times 100 \times 1 m^3$ , a,b) without inclusions and, c,d) with inclusions . . . . .	27

5.26 Evolution of norm of displacements in dielectric plate with the accumulated load factor $\Lambda$ being a) $\Lambda = 0.482$ , b) $\Lambda = 0.602$ , c) $\Lambda = 0.843$ and, d) $\Lambda = 1.0$ . . . . .	28
5.27 Formation of folds in dielectric plate (at the final deformed configuration) captured on a $12 \times 12 \times 1$ hexahedral mesh with $q = 6$ polynomial interpolation . . . . .	28
5.28 Evolution of strains $F_{xz}$ in dielectric plate with inclusions with the accumulated load factor $\Lambda$ being a) $\Lambda = 0.482$ , b) $\Lambda = 0.602$ , c) $\Lambda = 0.843$ and, d) $\Lambda = 1.0$ . . . . .	28
5.29 Formation of folds in dielectric plate with inclusions (at the final deformed configuration) captured on an unstructured tetrahedral mesh with $p = 4$ polynomial interpolation . . . . .	29
5.30 A comparison of performance of high order curvilinear elements in capturing wrinkles . . . . .	29
5.31 Evolution of norm of displacements in dielectric plate under the application of surface charge . . . . .	29
5.32 Dielectric thin film with $100m$ radius and $1m$ thickness centred at $[0, 0, 0]^T$ , a) CAD geometry and, b) $q = 2$ mesh . . . . .	30
5.33 Evolution of voltage induced stress components $\sigma_{xz}$ (a,b,c,d,e,f) and $\sigma_{yz}$ (g,h,i,j,k,l) in dielectric film with the accumulated load factor $\Lambda$ being a,g) $\Lambda = 0.580$ , b,h) $\Lambda = 0.725$ , c,i) $\Lambda = 0.798$ , d,j) $\Lambda = 0.870$ , e,k) $\Lambda = 0.943$ and, f,l) $\Lambda = 1.0$ . . . . .	31
5.34 Evolution of voltage induced hydrostatic pressure in dielectric film with the accumulated load factor $\Lambda$ being a) $\Lambda = 0.221$ , b) $\Lambda = 0.332$ , c) $\Lambda = 0.443$ , d) $\Lambda = 0.554$ , e) $\Lambda = 0.665$ , f) $\Lambda = 0.887$ , g) $\Lambda = 0.943$ , h) $\Lambda = 0.971$ , and, i) $\Lambda = 1.0$ . . . . .	32
5.35 Evolution of voltage induced hydrostatic pressure in dielectric film with the accumulated load factor $\Lambda$ being (left to right - top to bottom) $\Lambda = 0.0$ , $\Lambda = 0.124$ , $\Lambda = 0.249$ , $\Lambda = 0.374$ , $\Lambda = 0.499$ , $\Lambda = 0.624$ , $\Lambda = 0.749$ , $\Lambda = 0.874$ , $\Lambda = 0.886$ , $\Lambda = 0.899$ , $\Lambda = 0.911$ , $\Lambda = 0.918$ , $\Lambda = 0.921$ , $\Lambda = 0.924$ , $\Lambda = 0.928$ , $\Lambda = 0.93$ , $\Lambda = 0.934$ , $\Lambda = 0.936$ , $\Lambda = 0.94$ , $\Lambda = 0.942$ , $\Lambda = 0.949$ , $\Lambda = 0.952$ , $\Lambda = 0.955$ , $\Lambda = 0.958$ , $\Lambda = 0.96$ , $\Lambda = 0.962$ , $\Lambda = 0.964$ , $\Lambda = 0.965$ , $\Lambda = 0.966$ , $\Lambda = 0.968$ , $\Lambda = 0.969$ , $\Lambda = 0.97$ , $\Lambda = 0.971$ , $\Lambda = 0.972$ , $\Lambda = 0.974$ , $\Lambda = 0.975$ , $\Lambda = 0.976$ , $\Lambda = 0.978$ , $\Lambda = 0.979$ , $\Lambda = 0.98$ , $\Lambda = 0.981$ , $\Lambda = 0.982$ , $\Lambda = 0.984$ , $\Lambda = 0.985$ , $\Lambda = 0.986$ , $\Lambda = 0.988$ , $\Lambda = 0.989$ , $\Lambda = 0.99$ , $\Lambda = 0.991$ , $\Lambda = 0.992$ , $\Lambda = 0.994$ , $\Lambda = 0.995$ , $\Lambda = 0.996$ , $\Lambda = 0.998$ , $\Lambda = 0.999$ and, $\Lambda = 1.0$ . . . . .	33
5.36 Dielectric arc with $10mm$ radius and $0.1mm$ thickness centred at $[0, 0, 0]^T$ , a) CAD geometry and, b) $q = 2$ mesh . . . . .	34
5.37 Evolution of voltage induced hydrostatic pressure in dielectric film with the accumulated load factor $\Lambda$ being a) $\Lambda = 0.489$ , b) $\Lambda = 0.653$ , c) $\Lambda = 0.734$ , d) $\Lambda = 0.857$ , e) $\Lambda = 0.938$ , and, f) $\Lambda = 1.0$ . . . . .	35
5.38 Evolution of voltage induced strain in dielectric film with the accumulated load factor $\Lambda$ being a) $\Lambda = 0.489$ , b) $\Lambda = 0.653$ , c) $\Lambda = 0.734$ , d) $\Lambda = 0.857$ , e) $\Lambda = 0.938$ , f) $\Lambda = 1.0$ , g) $\Lambda = 0.857$ , h) $\Lambda = 0.938$ , and, i) $\Lambda = 1.0$ . . . . .	36
5.39 Rear and front view of cap fixture mechanism for hemispherical dielectric film . . . . .	37
5.40 Close up of thick regions experiencing deeper formation of wrinkles . . . . .	38
5.41 Evolution of voltage induced strain $H_{zy}$ in dielectric film with the accumulated load factor $\Lambda$ being a) $\Lambda = 0.228$ , b) $\Lambda = 0.293$ , c) $\Lambda = 0.358$ , d) $\Lambda = 0.488$ , e) $\Lambda = 0.553$ , and, f) $\Lambda = 0.618$ , g) $\Lambda = 0.749$ , h) $\Lambda = 0.830$ , i) $\Lambda = 0.912$ , j) $\Lambda = 0.944$ , k) $\Lambda = 0.973$ , and, l) $\Lambda = 1.0$ . . . . .	39
6.1 Schematic representation of the staggered incrementally linearised scheme. . . . .	5
6.2 Electromechanical plate with holes a) CAD geometry and, b) $p = 4$ curvilinear mesh . . . . .	7
6.3 Convergence of the staggered scheme with respect to the monolithic solver as a function of increase in applied voltage quantified by $\mathcal{W}$ as defined in (6.10) . . . . .	8
6.4 Voltage induced strains $C_{xx}$ in electromechanical plate . . . . .	9
6.5 Geometry and mesh of the tetrahedral ellipsoidal jelly fish . . . . .	9

6.6	Voltage induced displacements $u_z$ in jelly fish at time steps a) 1, b) 20, c) 40, c) 60, d) 80, e) 100, f) 120, g) 120, h) 130, i) 140, j) 150, k) 160, l) 170, m) 180, n) 190, o) 200 . . . . .	10
6.7	Voltage induced strains $C_{xz}$ in electromechanical plate . . . . .	12
7.1	Decomposition of (a) Mechanical Boundary $\Gamma = \Gamma^\sigma \cup \Gamma^u$ and $\Gamma^\sigma \cap \Gamma^u = \emptyset$ and (b) Electrical Boundary $\Gamma = \Gamma^D \cup \Gamma^\psi$ and $\Gamma^D \cap \Gamma^\psi = \emptyset$ . . . . .	4
7.2	Motion of beam in $\mathbb{R}^3$ . The initial orthonormal triad $\{\mathbf{e}_1, \mathbf{e}_2, \mathbf{e}_3\}$ transforms to the orthonormal triad $\{\mathbf{c}_1, \mathbf{c}_2, \mathbf{c}_3\}$ . . . . .	4
7.3	Electrostatics of a three-dimensional piezoelectric beam . . . . .	6
7.4	Cantilever beam polarised along the length . . . . .	18
7.7	Convergence of the energy norm of the error under $p$ -refinement and with different numerical integration techniques. (a) Linear electric potential distribution. (b) Quadratic electric potential distribution. . . . .	19
7.5	Convergence of the error measured in the $L^2$ norm for the variables (a) $w$ ; (b) $\theta$ ; (c) $\phi$ ; (d) $\beta$ ; (e) $\gamma$ . . . . .	20
7.6	Convergence of the error measured in the $H^1$ norm for the variables (a) $w$ ; (b) $\theta$ ; (c) $\phi$ ; (d) $\beta$ ; (e) $\gamma$ . . . . .	21
7.8	Geometry of the shear actuator . . . . .	22
7.9	Transverse deflection obtained with various models (Shear factor $k_s = 5/6$ ). (a) Clamped-free; (b) Clamped-clamped; (c) Clamped-hinged; (d) Clamped-free with shear factor $k_s = 0.62$ . . . . .	22
7.10	bending and torsion mode of bending-torsion fibre . . . . .	23
7.11	Harmonic vibration with frequency $\omega_p = 10$ rad/sec . . . . .	24
7.12	Harvested power at various frequencies: (a) $\omega_P = 0.01$ rad/sec; (b) $\omega_P = 0.1$ rad/sec; (c) $\omega_P = 1$ rad/sec; (d) $\omega_P = 10$ rad/sec . . . . .	25
7.13	Measured total accumulated energies at each of the 17 piezoelectric sensors showing the (a) electrical energy, (b) strain energy, (c) vibration energy and, (d) total internal energy . . . . .	26
7.14	CAD model and $p = 4$ curvilinear mesh of the actuation machine. The CAD model (after rigorous clean-up) is composed of 1207 topological surfaces, 5897 intersection curves (subfigure (a)), and 11794 topological vertices. Subfigure (e) shows the location of one of the 17 circular piezoelectric sensor patches installed on the machine. Positioning of sensors on to the CAD requires a tight integration of geometrical design and finite elements in order to identify active and passive regions and impose the necessary boundary conditions which is straightforward in our developed framework . . . . .	27
7.15	Evolution of stress $\sigma_{xy}$ (Pa) in the machine as a result of continuous compressive pressure. <b>552M</b> further tetrahedral cells have been used to process an extremely smooth and detailed representation of the stress. Deformations are magnified by a factor of 5 . . . . .	29
8.1	Schematic representation of the governing equations of couple stress and the decomposition of the boundary of a couple stress continua into a) displacements and tractions, $\Gamma = \Gamma^\sigma \cup \Gamma^u$ and $\Gamma^\sigma \cap \Gamma^u = \emptyset$ , b) rotations and couples/moments $\Gamma = \Gamma^\mu \cup \Gamma^\omega$ and $\Gamma^\mu \cap \Gamma^\omega = \emptyset$ and, c) surface charge and electric flux, $\Gamma = \Gamma^D \cup \Gamma^\psi$ and $\Gamma^D \cap \Gamma^\psi = \emptyset$ . Note that, while the boundary conditions associated with the electrostatics of the system are independent in couple stress theory when the rotations are constrained and individual variations of the fields are not allowed, it is only possible to apply two tangential components of moments on a traction boundary $\Gamma^\sigma$ , and/or two tangential components of rotations on a displacement boundary $\Gamma^u$ [215, 154, 228]. Note that $\boldsymbol{\sigma}^t$ represents the non- symmetric stress tensor defined in section 8.3.) . . . . .	5

8.2 Motion of Beam in $\mathbb{R}^3$ . The initial orthonormal triad $\{\mathbf{e}_1, \mathbf{e}_2, \mathbf{e}_3\}$ transforms to the orthonormal triad $\{\mathbf{c}_1, \mathbf{c}_2, \mathbf{c}_3\}$ . . . . .	12
8.3 A schematic representation of electric polarisation in a centrosymmetric lattice beam, (a) undeformed state - no polarisation, (b) when uniformly strained, the atomic displacements of the centrosymmetric lattice will follow the elastic medium approximation resulting in no polarisation, (c) when strained non-uniformly, the atomic displacements no longer follow the elastic medium approximation and the symmetry restriction (symmetrical movement of ions) is broken resulting in electric polarisation opposite to the direction of applied strain, [338, 72].	14
8.4 A non-exhaustive list of the developed mixed finite elements for triangles: (a) P2-P2-P1 <sup>D</sup> -P1 <sup>D</sup> /P2-P2-P1 <sup>D</sup> , (b) P3-P3-P2 <sup>D</sup> -P2 <sup>D</sup> /P3-P3-P2 <sup>D</sup> , (c) P4-P4-P3 <sup>D</sup> -P3 <sup>D</sup> /P4-P4-P3 <sup>D</sup> ; quadrilaterals: (d) Q2-Q1 <sup>D</sup> -Q1 <sup>D</sup> /Q2-Q1 <sup>D</sup> , (e) Q3-Q3-Q2 <sup>D</sup> -Q2 <sup>D</sup> /Q3-Q3-Q2 <sup>D</sup> , (f) Q4-Q4-Q3 <sup>D</sup> -Q3 <sup>D</sup> /Q4-Q4-Q3 <sup>D</sup> ; tetrahedra: (g) P2-P2-P1 <sup>D</sup> -P1 <sup>D</sup> /P2-P2-P1 <sup>D</sup> , (h) P3-P3-P2 <sup>D</sup> -P2 <sup>D</sup> /P3-P3-P2 <sup>D</sup> , (i) P4-P4-P3 <sup>D</sup> -P3 <sup>D</sup> /P4-P4-P3 <sup>D</sup> and hexahedra: (j) Q2-Q2-Q1 <sup>D</sup> -Q1 <sup>D</sup> /Q2-Q2-Q1 <sup>D</sup> , (k) Q3-Q3-Q2 <sup>D</sup> -Q2 <sup>D</sup> /Q3-Q3-Q2 <sup>D</sup> , (l) Q4-Q4-Q3 <sup>D</sup> -Q3 <sup>D</sup> /Q4-Q4-Q3 <sup>D</sup> . The developed framework encompasses $P_n$ - $P_n$ - $P_{n-1}^D$ - $P_{n-1}^D$ , $P_n$ - $P_n$ - $P_{n-1}^D$ , $Q_n$ - $Q_n$ - $Q_{n-1}^D$ - $Q_{n-1}^D$ , $Q_n$ - $Q_n$ - $Q_{n-1}^D$ for any interpolation degree $n$ . . . . .	24
8.5 A non-exhaustive list of the developed mixed finite elements for one-dimensional beam elements: (a) P2-P2-P2-P2-P2-P1 <sup>D</sup> -P1 <sup>D</sup> -P1 <sup>D</sup> /P2-P2-P2-P2-P2-P1 <sup>D</sup> -P1 <sup>D</sup> , (b) P3-P3-P3-P3-P3-P2 <sup>D</sup> -P2 <sup>D</sup> -P2 <sup>D</sup> /P3-P3-P3-P3-P2 <sup>D</sup> -P2 <sup>D</sup> , (c) P4-P4-P4-P4-P4-P3 <sup>D</sup> -P3 <sup>D</sup> -P3 <sup>D</sup> /P4-P4-P4-P4-P4-P3 <sup>D</sup> -P3 <sup>D</sup> . The developed framework encompasses $P_n$ - $P_n$ - $P_n$ - $P_n$ - $P_n$ - $P_{n-1}^D$ - $P_{n-1}^D$ - $P_{n-1}^D$ - $P_{n-1}^D$ , $P_n$ - $P_n$ - $P_n$ - $P_n$ - $P_{n-1}^D$ - $P_{n-1}^D$ - $P_{n-1}^D$ - $P_{n-1}^D$ for any interpolation degree $n$ . . . . .	25
8.6 Indicatory surfaces of BaTiO <sub>3</sub> constitutive tensors namely, a) the elasticity tensor $\mathcal{C}$ , b) the dielectric tensor $\epsilon$ and, c) the piezoelectric tensor $e$ . . . . .	26
8.7 Indicatory surface of BaTiO <sub>3</sub> flexoelectric constitutive tensor under, a) standard strain gradient based flexoelectric theory (i.e. $\bar{f}$ ), b) couple stress based flexoelectric theory (i.e. $f$ ) . . . . .	27
8.8 Original and deformed shape of nanobeam . . . . .	28
8.9 Comparison of couple stress based and strain gradient based flexoelectric models for the case of (8.123), when material constants are fitted according to (8.122)	29
8.10 Original and deformed shape of nanobeam . . . . .	30
8.11 Comparison of couple stress based and strain gradient based flexoelectric models for the case of (8.124), when material constants are fitted according to (8.122)	31
8.12 Original and deformed shape of nanobeam . . . . .	31
8.13 Comparison of couple stress based and strain gradient based flexoelectric models for the case of (8.125), when material constants are fitted according to (8.122)	32
8.14 Cantilever beam chosen for convergence study of the developed finite element discretisation techniques . . . . .	33
8.15 Triangular and quadrilateral meshes (only aspect ratio 10 shown here) chosen for convergence study of the developed finite element discretisation techniques. Both meshes possess the same number of nodes . . . . .	33
8.16 Convergence of error in Electromechanical Coupling Efficiency (ECF) for different finite element discretisation techniques on triangular elements, a) aspect ratio 10, b) aspect ratio 25, c) aspect ratio 50, and quadrilateral elements, d) aspect ratio 10, e) aspect ratio 25, f) aspect ratio 50 . . . . .	34
8.17 Tetrahedral and hexahedral meshes (only aspect ratio 10 shown here) chosen for convergence study of the developed finite element discretisation techniques. Both meshes possess the same number of nodes . . . . .	34
8.18 Convergence of error in Electromechanical Coupling Efficiency (ECF) for different finite element discretisation techniques on tetrahedral and hexahedral elements for aspect ratio 10 . . . . .	35

8.19 Geometry and quartic ( $p = 4$ ) order curved mesh of the flexoelectric conical pyramid. The conical pyramid is being held by a plate-like support of size $100 \times 100\mu\text{m}^2$ and the total height of the pyramid is $130\mu\text{m}$ . The thickness of pyramid is $150\text{nm}$ throughout the structure. The circle in top conical frustum represents the region where the compressive load is applied . . . . .	36
8.20 Various representative results of the analysis on conical pyramid, a) convergence of the solution with mesh refinement, b) satisfaction of couple stress constraint, c) evolution of strain energy with and without consideration of flexoelectricity characterising evolution of normalised effective stiffness, d) evolution of electrical energy and, e) evolution of effective electromechanical coupling coefficient, f) evolution of normalised effective stiffness . . . . .	37
8.21 The final deformed conical pyramid configuration showing, a) electric potential $\psi$ , b) strain component $\varepsilon_{xy}$ and b) strain component $\varepsilon_{yz}$ . 355M cells have been used to process a detailed resolution of the results. Deformations (not magnitudes) are magnified by a factor of 10 for aesthetics and clarity . . . . .	38
8.22 The final deformed conical pyramid configuration showing, a,b) axial vorticity vector component $\omega_y$ and, c) axial curvature vector component $\chi_y$ . The curvature forms a spin around the deformed sink. 355M cells have been used to process a detailed resolution of the results. Deformations (not magnitudes) are magnified by a factor of 10 for aesthetics and clarity . . . . .	39
9.1 Loop transformation optimisation for the contraction loop nest of singleton $[\mathbf{D}]_{ijk} = [\mathbf{a}]_i [\mathbf{B}]_{jk}$ . . . . .	7
9.2 AVX vectorisation of the nonisomorphic tensor product of singleton $[\mathbf{C}]_{im} = [\mathbf{A}]_{ijkl} [\mathbf{B}]_{m j k l}$ on strides (cells represent tensor's dimensions not the register width). . . . .	7
9.3 Loop fusion for the evaluation of the network $[\mathbf{G}]_{jkl} = [\mathbf{A}]_{ijk} [\mathbf{B}]_{il} + \rho \text{tr}(\mathbf{I}) [\mathbf{c}]_k [\mathbf{D}]_{jl} + \sqrt{[\mathbf{E}]_{jkl}}$ . . . . .	8
9.4 Speed-ups achieved by SIMD vectorisation in performing outer product of tensors of single precision (SP) and double precision (DP) floating point over the scalar version with tensors of order (a) 2 ( $[\mathbf{A}]_{ij} [\mathbf{B}]_{kl}$ ), (b) 3 ( $[\mathbf{A}]_{ijk} [\mathbf{B}]_{lmn}$ ), (c) 4 ( $[\mathbf{A}]_{ijkl} [\mathbf{B}]_{mnop}$ ), (d) 5 ( $[\mathbf{A}]_{ijklm} [\mathbf{B}]_{nopqr}$ ), (e) 6 ( $[\mathbf{A}]_{ijklmn} [\mathbf{B}]_{opqrst}$ ) and, (f) 8 ( $[\mathbf{A}]_{ijklmno} [\mathbf{B}]_{pqrsstuwwxy}$ ). Since the order and dimension of the tensors in outer product are kept the same, a $4 \times 4$ for instance, essentially implies $[\mathbf{A}]_{4 \times 4} \otimes [\mathbf{B}]_{4 \times 4}$ . . . . .	10
9.5 Speed-ups achieved by SIMD vectorisation in performing tensor contraction on pairs of tensors of single precision (SP) and double precision (DP) floating point over the scalar version with (a) single index contraction ( $[\mathbf{A}]_{ijklm} [\mathbf{B}]_{njop}$ ) using SSE, (b) single index contraction ( $[\mathbf{A}]_{ijklm} [\mathbf{B}]_{njop}$ ) using AVX, (c) two index contraction ( $[\mathbf{A}]_{ijkl} [\mathbf{B}]_{ijm}$ ) using SSE, (d) two index contraction ( $[\mathbf{A}]_{ijkl} [\mathbf{B}]_{ijm}$ ) using AVX, (e) three index contraction ( $[\mathbf{A}]_{ijkl} [\mathbf{B}]_{ikjm}$ ) using SSE, (f) three index contraction ( $[\mathbf{A}]_{ijkl} [\mathbf{B}]_{ikjm}$ ) using AVX, (g) 8 index contraction ( $[\mathbf{A}]_{ijklmnopq} [\mathbf{B}]_{ijklmnopr}$ ) using SSE and, (h) 8 index contraction ( $[\mathbf{A}]_{ijklmnopq} [\mathbf{B}]_{ijklmnopr}$ ) using AVX. $x$ -labels represent the actual dimensions of the tensors. . . . .	11
9.6 Speed-up achieved for contraction of three tensor singletons ( $[\mathbf{A}]_{ijk} [\mathbf{B}]_{ijl} [\mathbf{C}]_{mnl}$ ) using by-pair contraction over single expression evaluation for tensor sizes that fit a) L1 cache (size of temporary created $16\text{KB}=0.5 \times \text{L1 cache}$ ), b) L2 cache (size of temporary created $128\text{KB}=0.5 \times \text{L2 cache}$ ), c) L3 cache (size of temporary created $10\text{MB}=0.5 \times \text{L3 cache}$ ) and, d) main memory (size of temporary created $80\text{MB}=4 \times \text{L3 cache}$ ). $x$ -labels indicate the number of FLOPs saved/reduced by utilising by-pair (FLOP optimal) contraction and numbers on top of bars show the corresponding speed-up. . . . .	13

9.7 Speed-up achieved for contraction of four tensor singletons ( $[A]_{ijk}[B]_{ijl}[C]_{mnk}[D]_{mno}$ ) using by-pair contraction over single expression evaluation for tensor sizes that fit a) L1 cache (size of temporary created 16KB=0.5×L1 cache), b) L2 cache (size of temporary created 128KB=0.5×L2 cache), c) L3 cache (size of temporary created 10MB=0.5×L3 cache) and, d) main memory (size of temporary created 80MB=4×L3 cache). $x$ -labels indicate the number of FLOPs saved/reduced by utilising by-pair (FLOP optimal) contraction and numbers on top of bars show the corresponding speed-up. . . . .	13
9.8 Compilation aspects of different optimisation levels for multi-index tensor contraction of singletons (Lower is better). a) compilation time (wall time), b) memory footprint, c) size of binaries generated, and d) eventual execution time (wall time). Contraction indices correspond to: (7 index) → $[A]_{ijklmno}[B]_{ijklmnop}$ (span $2^8 \times 8$ ), (6 index) → $[A]_{ijklmno}[B]_{ijklmnpr}$ (span $2^9 \times 9$ ), (5 index) → $[A]_{ijklmno}[B]_{ijklmprs}$ (span $2^{10} \times 10$ ), (4 index) → $[A]_{ijklmno}[B]_{ijklprst}$ (span $2^{11} \times 11$ ), (3 index) → $[A]_{ijklmno}[B]_{ijkprstu}$ (span $2^{12} \times 12$ ), (2 index) → $[A]_{ijklmno}[B]_{ijprstuv}$ (span $2^{13} \times 13$ ) and (1 index) → $[A]_{ijklmno}[B]_{iprstuvwxyz}$ (span $2^{14} \times 14$ ), respectively. Note that data for GCC 6.2.0 for 4 index contraction and lower is not available for optimisation level -DOPT=2, due to stall and excessive memory footprint. -DOPT is used as a shorter alias for -DCONTRACT_OPT. . . . .	15
9.9 Contribution percentile of different optimisations for numerical integration using Fastor; (a), (b), (c) for triangular mesh and (d), (e), (f) for tetrahedral mesh. . . . .	21
9.10 Meshes used for finite element benchmarks, a) A curved mechanical component [254] and b) Artificial hand used for simulating electrostriction [233]. . . . .	22
9.11 a) CAD geometry, b) curved tetrahedral mesh and, c) curved hexahedral mesh for electromechanical component with 1m thickness, 20m height ( $y$ -axis), 100m width ( $x$ -axis) and 500m length ( $z$ -axis) . . . . .	23
9.12 Speed-up achieved by compile time algorithmic transformation and data parallelism for numerical integration of work-conjugates and Hessian of convex multi-variable electro-elastic model (6.8) with high order curved tetrahedral and hexahedral meshes with compilers a,b) GCC, c,d) LLVM's Clang and, e,f) Intel's ICC . . . . .	24
9.13 Evolution of voltage induced hydrostatic pressure $p_{hyd}$ in electromechanical component with accumulated load factor $\Lambda$ being a) $\Lambda = 0.416$ b) $\Lambda = 0.806$ , c) $\Lambda = 0.889$ , d) $\Lambda = 0.944$ , e) $\Lambda = 0.972$ and, f) $\Lambda = 1.0$ . Note that in the figures shown, the electromechanical component is mirrored along the $z$ -axis . . . . .	25
C.1 Procedure to identify associativity between smooth and discrete topologies and reconstruct the smooth topology using curvilinear FEM . . . . .	7
C.2 Finding unit normals on a single curved mesh face . . . . .	8

# List of Tables

3.1	Computational requirement of different solid mechanics formulations for curved mesh generation . . . . .	8
5.1	Material properties for example 5.3.1 . . . . .	6
5.2	Distortion quality of high order curvilinear tetrahedral meshes . . . . .	8
5.3	Distortion quality of high curvilinear hexahedral mesh . . . . .	8
5.4	Material parameters for (5.13) with the vacuum permittivity $\epsilon_0 = 8.85418781 \times 10^{-12} (\text{N/V}^2)$ . . . . .	11
5.5	Distortion quality of high order curvilinear tetrahedral and hexahedral meshes . . . . .	11
5.6	Evolution of stresses at the circular tip of the plate for tetrahedral meshes . . . . .	13
5.7	Evolution of stresses at the circular tip of the plate for hexahedral meshes . . . . .	13
5.8	Distortion quality of high order curvilinear tetrahedral meshes . . . . .	15
5.9	Distortion quality of high order curvilinear hexahedral meshes . . . . .	15
5.10	Material parameters for (5.14) with the vacuum permittivity $\epsilon_0 = 8.85418781 \times 10^{-12} (\text{N/V}^2)$ . . . . .	16
5.11	Applied electric voltage as Dirichlet boundary condition for three aspect ratios . . . . .	16
5.12	Comparison of high order displacement potential and 11 field mixed formulations for different kinematic and kinetic measures, for aspect ratio 10 and Poisson's ratio 0.45 . . . . .	17
5.13	Comparison of high order displacement potential and 11 field mixed formulations for different kinematic and kinetic measures, for aspect ratio 10 and Poisson's ratio 0.499 . . . . .	17
5.14	Comparison of high order displacement potential and 11 field mixed formulations for different kinematic and kinetic measures, for aspect ratio 1000 and Poisson's ratio 0.45 . . . . .	18
5.15	Comparison of high order displacement potential and 11 field mixed formulations for different kinematic and kinetic measures, for aspect ratio 1000 and Poisson's ratio 0.499 . . . . .	18
5.16	Applied electric voltage as Dirichlet boundary condition for three aspect ratios . . . . .	19
5.17	Material parameters with the vacuum permittivity $\epsilon_0 = 8.85418781 \times 10^{-12} (\text{N/V}^2)$ . . . . .	22
6.1	Material parameters for (6.8) with the vacuum permittivity $\epsilon_0 = 8.85418781 \times 10^{-12} (\text{N/V}^2)$ . . . . .	7
7.1	Convergence of Numerical Scheme for Tip Values . . . . .	19
7.2	Point-wise % Error Incurred in Table 7.1 . . . . .	19
7.3	Natural frequencies of bending-torsion fibre ( $\text{Hz}$ ) . . . . .	23
8.1	Material constants for BaTiO <sub>3</sub> . . . . .	25
9.1	Compilation aspects & run time performance of -DCONTRRACT_OPT=1 normalised with respect to -DCONTRRACT_OPT=0 . . . . .	16
9.2	Compilation aspects & run time performance of -DCONTRRACT_OPT=2 normalised with respect to -DCONTRRACT_OPT=0 . . . . .	16

9.3	Compilation cost of operation minimisation <b>normalised</b> with respect to single expression evaluation for 3 tensor singleton . . . . .	17
9.4	Compilation cost of operation minimisation <b>normalised</b> with respect to single expression evaluation for 4 tensor singleton . . . . .	17
9.5	Compilation cost of operation minimisation <b>normalised</b> with respect to single expression evaluation for 5 tensor singleton . . . . .	18
9.6	Speed-ups achieved in numerical integration using Fastor over other implementations for the 2D triangular mesh . . . . .	20
9.7	Speed-ups achieved in numerical integration using Fastor over other implementations for the 3D tetrahedral mesh . . . . .	20
9.8	Degrees of freedom associated with each polynomial degree for tetrahedral and curvilinear meshes . . . . .	23
B.1	Constitutive equations for isotropic and anisotropic couple stress based linear flexoelectric materials . . . . .	4





# **Introductory Remarks, State of the Art and Scope**

# Chapter 1

## Introductory Remarks

### 1.1 Prelude

The industrial demand for real-world simulations of complex multi-physics problems poses a many-fold challenge to the field of computational mechanics. In particular, aligned with the theme of the work presented here, is computational modelling of coupled electro-mechanical systems. The many-fold nature of this challenge, pertaining to the modelling of real-world electro-mechanical devices, can be associated with the shortcomings and/or lack of robustness of mathematical models and computational tools to redress the underlying problems. As compared to the field of fluid dynamics and fluid-structure interaction, little research has gone into investigation of electromechanical couplings and in particular the different approaches that would be applicable for different electromechanical systems. As will be discussed in depth later, redressing these problems mandate revisiting the mathematical formulations, modernising the computational tools to harness the compute power of ever-growing microprocessor architectures and most importantly developing novel computational methodologies to tackle those aspects that had never been considered before. To set the scene, from a computational point of view, the pertaining problems can be categorised into three fields, namely

1. **Accurate geometrical representation** in computational modelling/numerical simulations.
2. Tailor-made **computational techniques** for different levels of coupling in electromechanics such as **one-way/two-way couplings, staggered schemes, monolithic approaches, coupling in structurally reduced models** and so on.
3. **High performance kernels** to solve the aforementioned problems within a reasonable time.

### 1.2 State of the Art & Scope

The thesis attempts to redress all the three aforementioned issues pertaining to the modelling of coupled and multi-physics problems, in particular, electromechanical coupling, by first starting with the problem of curvilinear mesh generation for high order accurate finite elements. This process, as will be discussed later, attempts to bridge the gap between finite elements and computer aided design (CAD) in a unique way making it possible to employ standard high order finite element techniques on curvilinear meshes. This is then accompanied by developing a comprehensive computational technique for four different classes of electromechanics, namely nonlinear convex multi-variable electroelasticity, geometrically linearised electrostriction, linear piezoelectricity and linear flexo (size-dependent piezo)-electricity. A high order curvilinear finite element method is developed to tackle the discretisation of the variational forms of the governing equations of all the aforementioned four classes of electromechanics. Finally, the efficiency in terms of computational implementation is considered and a high performant domain-aware tensor contraction framework is developed to implement the high order

curvilinear finite element formulations. The tensor contraction engine in particular, attempts to be cross-platform and applicable for CPUs and GPUs and streaming architectures alike. In the next few sections, we will discuss the state of the art pertaining to each of these three components of the thesis.

### 1.3 Accurate geometry representation in computational mechanics

In recent years, many computational methods have emerged to tackle numerical simulations with curvilinear geometries and been hoped to integrate CAD and finite element analysis and design. In particular, subdivision surfaces [50, 51], isogeometric analysis [129], T-Splines [20] and NURBS-enhanced finite element method [274], have gained considerable traction in the community. All the aforementioned techniques try to embed finite element analysis into standard computer aided design by exactly representing the geometry and augmenting or redesigning the finite element functional spaces. These techniques despite having revolutionised the computational analysis and design cycle, are still in infancy compared to the standard high order finite element method. One of the reasons hindering their progress is certainly in the generation of appropriate meshes necessary for numerical simulation due to the fact that some of the aforementioned techniques make it even harder to prepare computational meshes. In essence, they inevitably extend the issues of surface mesh generation to the enclosed volume.

The first part of this thesis aims to target the problem of curvilinear mesh generation. These curvilinear meshes can be either embedded into one of the aforementioned finite element technologies such as the NURBS-enhanced method [277] for exact CAD conforming geometrical representation or used as stand-alone meshes for standard finite element analysis leading to high order curvilinear finite element technique with *accurate* geometry representation. The curvilinear finite element framework discussed later on in this thesis is based on the latter approach.

The performance of high-order discretisation methods for the simulation of various problems in science and engineering has been the object of intensive research during the last two decades [285, 149, 123, 165]. These methods have the potential to offer an increased level of accuracy with a reduced number of degrees of freedom and, more importantly, a reduced computational cost [63, 275, 128].

The potential of high-order unstructured methods has been intensively studied by the computational fluid dynamics (CFD) community in the last decade due to their inherent ability to accurately predict the behaviour of complex high Reynolds number flows [185, 172, 320, 132]. It is also well known that low-order methods are highly dissipative and extremely refined meshes are required to properly resolve the propagation of vortices over long distances. The advantages of high-order methods have also attracted the attention of researchers working in wave propagation problems (e.g. acoustics and electromagnetics) due to their low dispersion and dissipation compared to low-order methods [122, 8, 184, 176, 276, 23]. In particular, the high-order discontinuous Galerkin method has become popular in this area due to its ability to propagate waves over long periods of time with a reduced computational cost compared to alternative low-order methods [53, 146, 45, 140, 159].

The use of curved elements is nowadays accepted to be crucial in order to fully exploit the advantages of high-order discretisation methods [76, 18, 186, 329, 164, 274, 303, 273], but until relatively recently, the challenge of automatically generating high-order curvilinear meshes has been an obstacle for the widespread application of high-order methods [317]. Methods to produce high-order curvilinear meshes are traditionally classified into *direct* methods and *a posteriori* methods [74, 75]. Direct methods build the curvilinear high-order mesh directly from the CAD boundary representation of the domain whereas *a posteriori* approaches rely on mature low-order mesh generation algorithms to produce an initial mesh that is subsequently curved using different techniques, such as local modification of geometric entities [74, 75, 281, 187, 280], solid mechanics analogies [242, 328] or optimisation [304, 100].

Within the category of a posteriori approaches, the solid mechanics analogy first proposed in [242] has become increasingly popular. The main idea is to consider the initial, low-order, mesh as the undeformed configuration of an elastic solid. High-order nodal distributions are then inserted into all of the elements and then the nodes over element edges/faces in contact with the curved parts of the boundary are projected onto the true CAD boundary. The displacement required to move the nodes onto the true boundary is interpreted as an essential boundary condition within the solid mechanics analogy. The solution of the elastic problem provides the desired curvilinear mesh as the deformed configuration, as shown in Figure 1.1.

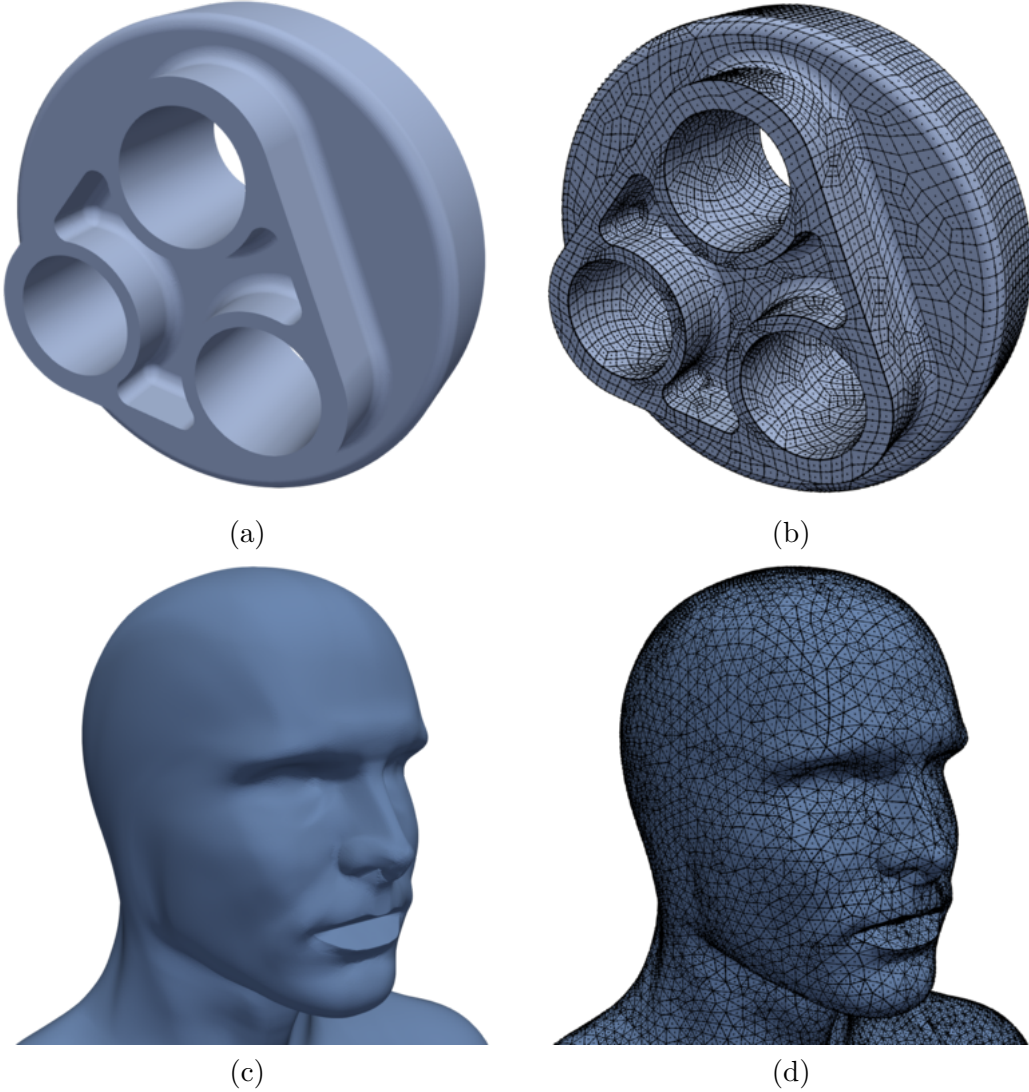


Figure 1.1: Generation of quality curvilinear meshes from CAD description a) A watertight CAD model for part of a turbine assembly, b) curvilinear tri-quadratic  $q = 2$  fully unstructured hexahedral mesh of the component, c) A watertight CAD model of human head and d)  $p = 3$  curvilinear unstructured tetrahedral mesh of the human head

The optimality of the standard finite element methods in terms of the  $h$  and  $p$  convergence properties is closely related to the fundamental quality measures quantifying the distortion of curvilinear meshes, namely, edge distortion, face distortion and volume distortion qualities. In this work, we employ a nonlinear polyconvex elasticity technique for generating curved meshes to control the quality of the generated meshes through these fundamental metrics. As will be discussed later, this technique for generating curvilinear meshes will become the driving force for our later developments on high order curvilinear finite elements for coupled electromechanics.

## 1.4 Novel computational techniques for different classes of electromechanics

The advancements in smart materials over the last few decades have shown a tremendous potential for the application electro-active, electrostrictive, piezoelectric and flexoelectric materials. Each of these material exhibit remarkable yet unique potential for different applications, such as unmanned aerial vehicle (UAV), self-charging batteries, artificial muscles, pattern forming, optics and retina adaptive displays and soft robotics, to name but a few. All of the these four classes of electromechanical material have been mathematically modelled in some shape or form by different researchers over the last few years. However, the capability of a material to exhibit the predicted experimental response is typically dictated by the level of sophistication of the underlying mathematical model and as a result there exist numerous models in the literature ranging from simplified models to high fidelity ones, some emphasising one characteristic and some neglecting selected features.

The objective of this thesis is to study the aforementioned four classes of electromechanics and develop new tailor-made computational technique for each of them. These four classes in particular are

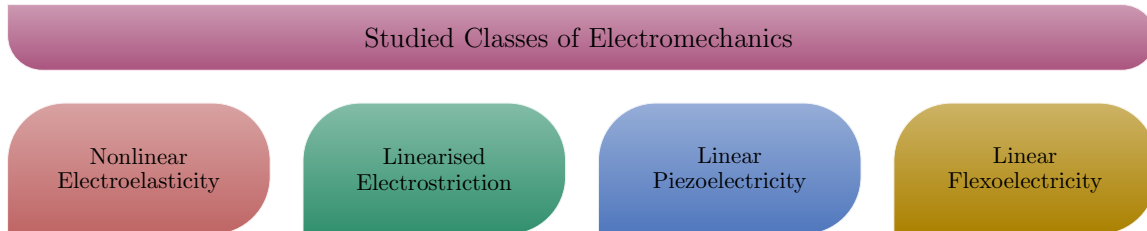


Figure 1.2: The four classes of electromechanical coupling studied in this work

In the upcoming sections we will discuss the state of the art in numerical modelling of each of these classes. In this process, we will also outline the contribution of the thesis and where it fits amongst the current state of research undertaken in the field.

### 1.4.1 Class 1. Computational modelling of dielectric elastomers: State of the art

Among the wide spectrum of smart materials, the first class of materials considered is the Electro-Active Materials (EAPs). This heterogeneous group can be subsequently classified into two main subgroups, namely Electronic Electro Active Polymers (EEAP) and Ionic Electro Active Polymers (IEAP). Within the first subgroup, Dielectric Elastomers (DEs) and electrostrictive relaxor ferroelectric polymers or simply Piezoelectric Polymers (PP), have become increasingly relevant. The second subgroup includes ionic gels, Ionic Polymer Metal Composites (IPMC) and carbon nanotubes [113].

Typically, experiments and computational modelling of DEs have focussed on the large deformation characteristics of these materials, due to the capability of DEs to undergo massive deformation. For instance, Figure 1.3 shows large deformation and buckling characteristics of a dielectric elastomer balloon. As a result, computational models in this regard are based on large strain large electric field electromechanical formulations [78, 37, 113]. Recently, Gil and Ortigosa [113, 233, 232] have shown that using the concept of convex multi-variable energies it is possible to numerically model these materials while guaranteeing material stability throughout the entire deformation and electric field regimes.

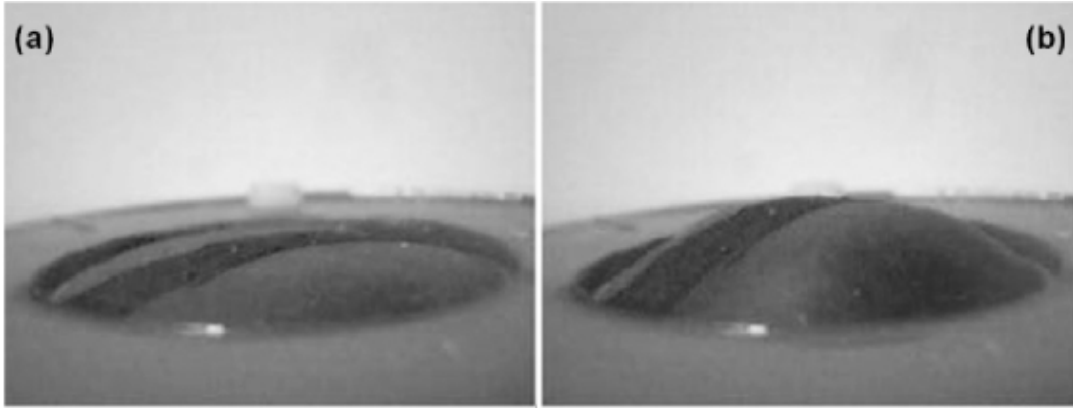


Figure 1.3: Buckling of a dielectric elastomer balloon under electric loading, showing large deformations and pre and post buckling states. Courtesy of [316]

From a computational implementation point of view, Vu and Steinmann [318, 319] have devised a finite element implementation of the dielectric elastomers using linear hexahedral finite elements based on a displacement potential formulation starting with the enthalpy energy. Gil and Ortigosa on the other hand have developed a mixed Hu-Washizu variational and computational framework for large deformation large electric field electromechanics based on an extended convex multi-variable kinematics set [233] by starting from the internal energy. In this thesis we follow the work of Gil and Ortigosa and describe the implementation of a high order displacement potential formulation for convex multi-variable electromechanics.

#### 1.4.2 Class 2. Computational modelling of linearised electrostriction: State of the art

In an important intermediate class of electromechanics, the large deformation characteristics of the system are neglected, whereas the nonlinearity still present in the material emanates from the electrostriction of the material through the Maxwell (for vacuum  $V_\infty$ ) or Minkowski (for material  $V$ ) stress tensors [89, 171, 241, 111]. A typical physical application of this approach is in the computational design of MRI scanners [175, 14], as shown in Figure 1.4.

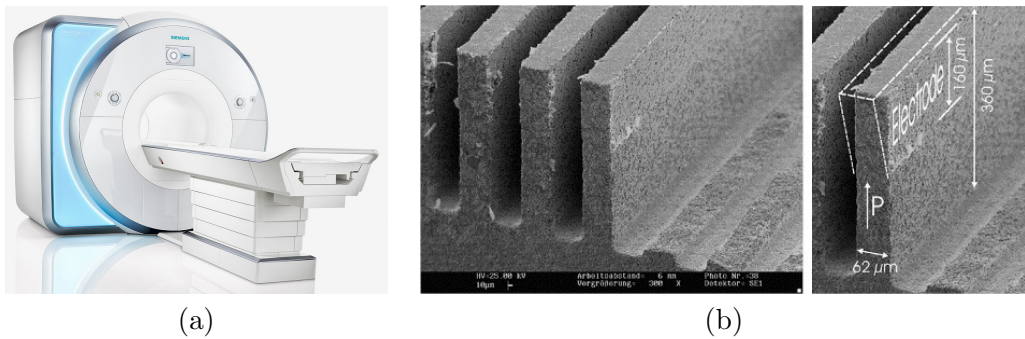


Figure 1.4: a) An example of electrostrictive and magnetostrictive coupling arising in Magnetic resonance imaging (MRI) [175, 14]; courtesy of Siemens Healthcare™ and, b) A shear mode drop-on-demand inkjet electrostrictive actuator; courtesy of Brünahl et. al. [36]

Theoretical aspects of these formulations were first introduced in Landau and Lifshitz [171]. The practical relevance of Maxwell stress tensor has led to a widespread utilisation of these formulations for exploiting electrostriction and magnetostriction. Unfortunately, electrostrictive models based on the utilisation of Minkowski stress tensor, in the generic case of anisotropy do not satisfy material frame indifference (i.e. objectivity or invariance of the energy with respect to rotations) of the electromechanical (total) stress tensor, due to the inherent non-symmetric nature of the Minkowski stress. Several authors in the past have used *ad-hoc* solutions, such

as symmetrisation of the total stress tensor, or consideration of the conservation of angular momentum in the formulation, as a remedy [241, 262]. Nevertheless, the extended electromechanical Hessian still remains non-symmetric, which dictates the development of specialised non-symmetric finite element frameworks. Recently, Bustamente [38] has shown that physically admissible energy functionals can be constructed by choosing suitable constitutive restrictions such that their linearisation yields objective Minkowski-type stresses.

In this thesis, a computational framework suitable for geometrically linearised large electric field electromechanics is presented based on the consistent linearisation of the convex multi-variable energies. A convex multi-variable strain energy description based on the works of Gil and Ortigosa [113, 233, 232] is chosen for modelling electrostriction. Following Bustamente [38], the thesis extends the framework developed by Gil and Ortigosa [113, 233] to the case of geometrically linearised electrostriction, to redress the aforementioned inconsistencies for the class of intermediate formulations. Importantly, all the aforementioned mathematical requirements are imposed at a large deformation level to arrive at a physically admissible energy functional. In this context, convex multi-variable energies typically expressed in terms of fundamental kinematic measures  $\{\mathbf{F}, \mathbf{H}, J\}$  are re-expressed in terms of a set of symmetric kinematics  $\{\mathbf{C}, \mathbf{G}, C\}$  to guarantee the objectivity of the energy functional. Linearisation with respect to geometrical fields is then performed by perturbing the energy in the vicinity of the reference configuration. Analogous to [254], this is achieved through a staggered scheme where the equations of electrostatics are solved in a nonlinear fashion whereas the linearised mechanical equations are updated incrementally.

#### 1.4.3 Class 3. Computational modelling of linear piezoelectricity: State of the art

The most common and well studied class of electromechanical materials are perhaps piezoelectric materials. Piezoelectric materials are exploited mainly for two major applications: actuation and sensing/energy harvesting. Energy harvesting implies induced electric polarisation as a result of mechanical straining (direct effect), whereas actuation implies induced mechanical straining as a result of electric polarisation (reverse effect) [92]. Certainly, these two phenomena can be viewed as unrelated, where different theoretical and numerical approaches can be employed. For instance, models of piezoelectric actuators have been devised with only mechanical degrees of freedom [334, 22, 9] and models of energy harvesters have been developed with more emphasis on electrical unknowns or, essentially, the final power output [92, 90, 80].

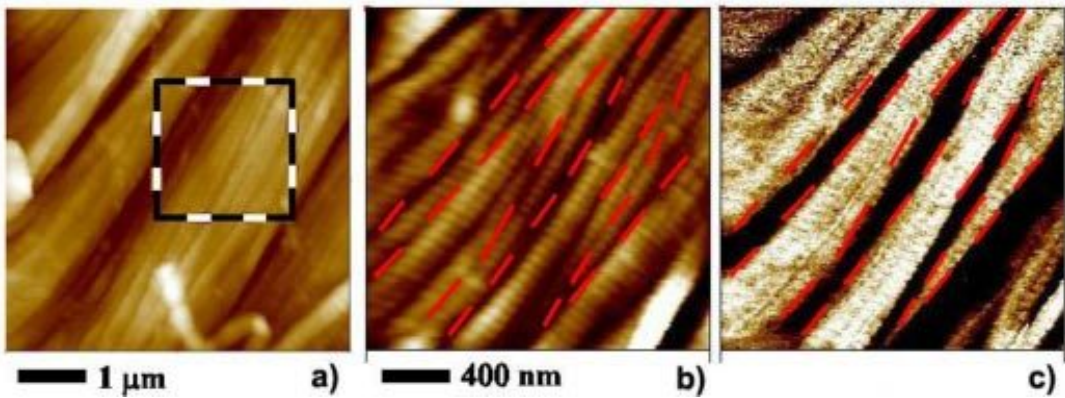


Figure 1.5: Piezoresponse force microscopy experiment on fascia. a) sample topography, 5  $\mu\text{m}$  scan, (b) topography, zoom of (a), and (c) piezoresponse image [of the same area as in (b)] showing the orientation of the piezoelectric tensor. The piezoelectric response in fascia has either a positive (white) or negative (dark) value. Courtesy of Rivard et. al. [263]

Some approaches can be found in the literature in the form of simplified single degree of freedom systems or two-dimensional beams, which are often referred to as lumped parameter

and distributed parameter models, respectively [92, 80, 307, 308, 2, 7]. In the lumped parameter model, the piezoelectric device is constructed via a mass-spring-damper system coupled with a capacitor and a resistor [264, 80, 297]. However, this simplified model lacks some important aspects of the coupled physical system, such as the consideration of high dynamic modes, an accurate distribution of the strain field and the effects of the former two into the overall electrical response [92]. The distributed parameter model, on the other hand, is based upon Euler-Bernoulli beam theory, neglecting rotation of the cross section with respect to the beam axis, possible shear deformation and rotational inertia [91, 90]. A review on the finite element modelling of piezoelectric beams is provided in [21] and a survey of energy harvesters with piezoelectric materials is reported in [13, 92].

One of the main simplifying assumptions in almost all of these approaches is that of vanishing electric field in certain directions, depending on the orientation of polarisation [80, 22, 307, 308, 9, 2]. In piezoelectric beam literature, these are normally referred to as different modes of coupling and are denoted by  $d_{ij}$ ,  $i, j = 1 \dots 6$  where  $d$  is the piezoelectric coupling parameter and the subscripts  $i$  and  $j$  indicate the poling direction and applied stress direction (in Voigt notation), respectively [157], with  $i = 3$  or  $j = 3$  representing the axial direction. In this setting, the two most common coupling mechanisms [334, 22, 9] are the  $d_{31}$  mode (shear actuation), which implies a coupling between the transverse electric field and axial strain and the  $d_{33}$  mode (extension actuation), which stands for coupling between the axial electric field and axial strain [80], with other coupling field mechanisms normally assumed to be zero.

On the mathematical modelling front, Benjeddou [22] attempts to build a unified two-dimensional (planar) beam finite element model for extension and shear actuation mechanisms. Tabesh [297] attempts to solve the problem of energy harvesting piezoelectric planar beams by employing Euler-Bernoulli theory with quadratic electric potential distribution across the height of the beam. As stated in [297, 249], a linear electric potential assumption is not sufficient to describe the electrostatics of the model as it violates Gauss's law, although many conventional models in the literature rely on this assumption [9, 80, 121].

Available literature on the numerical modelling of three-dimensional piezoelectric beams is scarce, specifically in the context of energy harvesting. Whilst a two-dimensional approach is sufficient for bending dominated energy harvesters, it is not satisfactory for capturing accurately piezoelectric (anisotropic) behaviour. Indeed, energy harvesters undergoing coupled bending-torsion [2] require a three-dimensional description. Moreover, there are actuators specifically designed to function in torsional modes such as helical springs [239, 39], for which two-dimensional descriptions cannot be used.

Wagner and co-workers [39, 153, 152] introduce a sophisticated three-dimensional beam finite element model with linear and nonlinear strain measures, including hysteresis, using a six field variational formulation and assuming a quadratic electric potential distribution across the cross sectional area. The work is restricted to static analysis only and requires a preprocessing stage to compute the warping patterns by solving a two-dimensional boundary value problem, using a separate finite element discretisation.

Another three-dimensional finite element formulation for piezoelectric beams is reported by Touratier [98]. Touratier's formulation is based on higher order shear deformation theory and trigonometric expansion of the displacement field, where for  $C^1$  continuity, a mixture of Hermite, quadratic and linear shape functions are utilised. A similar technique is also followed to incorporate the warping functions in the beam model. As a result, each beam finite element has three nodes along the length with 27 electrical degrees of freedom and 21 mechanical degrees of freedom. The work is restricted to static analysis and hence cannot be used for energy harvesting. Along the same lines, Koutsawa [160] attempts to solve the problem of static piezoelectric beams by using higher order displacement theories for beams.

In this thesis, by starting from the fundamental equations of continuum piezoelectricity, a unified static and dynamic computational framework is presented for three-dimensional piezoelectric beams, focussing on small strain theory (small electric fields). Mathematically, many of the well-established piezoelectric actuator models in the literature [9, 334, 22, 166] can be

regarded as special cases which sit within this unified formulation. The merit of approaching the problem in this fashion is that the strengths and limitations of the formulation can be easily identified for both actuators and energy harvesters applications, without placing a distinction upon one or the other. We present a simple three-dimensional finite element computational framework for linear piezoelectric beams, derived from first principles, in order to bridge the gap between existing simplified lumped or distributed parameter models [92, 80, 307, 308, 2, 264, 297] and the most sophisticated nonlinear warping beam models [39, 153, 152, 98, 160]. In the process, interesting new physical magnitudes, such as the coupled shear or the coupled bending/torsional moment introduced as a result of an electric displacement, will naturally arise.

The linearised kinematics of the beam follows the first order shear deformation theory of Timoshenko and the electric potential field is assumed to vary quadratically across the height and thickness of the beam section. The electric potential distribution is expanded in terms of the electric potential, its gradient and its Hessian, all being evaluated at the centre of mass of the cross section (i.e. second order Taylor expansion about the centre of mass). Following [126, 131], the postulated beam kinematics and electric field distribution are embedded into the variational form of the continuum piezoelectric problem. Standard beam integration across the cross sectional area can then be carried out to yield a set of partial differential equations (e.g. time and beam axis as independent variables) that are expressed in terms of stress and electric displacement beam resultants (e.g. shear force and moments). Crucially, a consistent use of anisotropic elastic, piezoelectric and dielectric constitutive tensors, enables strains and electric fields to be coupled in all three spatial directions, with no preference to a specific orientation.

Typically, piezoelectric materials are deposited either on one side (unimorph) or both sides (bimorph) of a substrate. The substrate is a non-electroactive platform which does not contribute to the electric output and merely serves as a mechanical supporting platform [92]. This can pose difficulties for integration of piezoelectric films with other microelectronic devices. Recently, there have been experimental reports on thick free-standing piezoelectric beams for energy harvesting [156, 155, 135, 158]. These are piezoelectric films which stand on their own, do not use a supporting platform and hence, offer the advantage of minimising the movement constraints on them, thereby maximising output power for energy harvesting [157]. Their thick electroactive layer make them a suitable candidate for models such as the one described in this thesis.

From the spatial discretisation standpoint, locking effects are eliminated through the use of higher order as well as hierarchical basis functions [295, 47, 111]. The resulting *hp*-finite element discretisation has eleven degrees of freedom per node<sup>1</sup> in three-dimensions and five degrees of freedom per node in two-dimensions, namely displacements, rotations, electric potential, gradient of electric potential and Hessian of electric potential. The computational framework is valid for static, modal and dynamic scenarios, the latter being of interest for energy harvesting. The set of resulting partial differential equations have also been solved analytically with the purpose of obtaining closed-form solutions, which, to the best of the authors' knowledge, are presented here for the first time and are suitable for the benchmarking of the finite element computational framework.

#### 1.4.4 Class 4. Computational modelling of linear flexoelectricity: State of the art

Modelling linear piezoelectricity for actuation and energy harvesting purposes using the classical continuum mechanics theory is now well established in the literature, [92, 80, 307, 308, 269, 250]. It is well known, that for a material to exhibit electric polarisation in the presence of mechanical strain (direct piezoelectric effect), it needs to have a noncentrosymmetric crystal structure, [325]. Recently, there has been a considerable research on producing piezoelectric effects from

---

<sup>1</sup>Strictly speaking, for hierarchical basis functions, the degrees of freedom are not associated with nodes but, instead, with polynomial coefficients.

centrosymmetric (non-piezoelectric) materials, for instance, from perovskite ferroelectrics [337, 338] and even graphene nano-shells and biological membranes, [79, 244, 200, 147, 201, 333, 73]. To generate polarisation in centrosymmetric materials, the inversion symmetry of the material needs to be broken and this becomes achievable through the application of non-uniform strains (strain gradients). Theoretical and experimental evidence of this size-dependent phenomenon which is also termed “flexoelectricity” has been reported in [298, 190, 191, 41, 193, 337, 279, 278, 107, 163] for other classes of centrosymmetric cubic and isotropic materials; see [298, 332] for a historical review. As discussed in [332] a crystalline material of any symmetry can be capable of producing electric polarisation under a nonuniform strain field or simply in the presence of strain gradient. The effective flexoelectric coefficients are certainly orders of magnitude smaller (in the range of  $\mu\text{C/m}$ , [190]) compared to their piezoelectric counterparts, however for nano-electromechanical systems where the device and material length scales are comparable, gradient of strain can have appreciable effects, [72, 141]. As depicted in Figure 1.6, Briscoe et. al. [35] has recently shown the potential of these material in nano energy harvesting from a purely experimentation point of view.

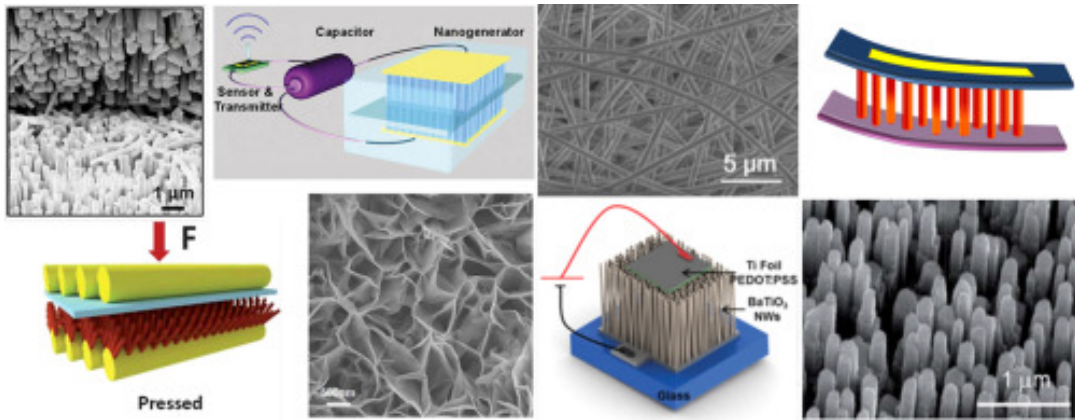


Figure 1.6: A graphical abstract of harvesting energy at the nano level. Electrospun PZT/PVP nanowires (second right from top), SEM micrographs of ZnO nanosheets (second left from bottom),  $(\text{K},\text{Na})\text{NbO}_3$  nanorods grown hydrothermally on  $\text{SrRuO}_3/\text{SrTiO}_3$  substrate (top left-most and bottom right-most), and multiple circuit diagram and loading conditions. Courtesy of [35]

From a generalised continuum mechanics point of view (c.f. [89] for related terminologies), flexoelectricity is considered as a higher order gradient theory where size effects are accounted for in a phenomenological sense. The study of higher order gradient theories and generalised continua dates back to the seminal work of [55] which was later revisited by [215, 211, 212, 213, 214], [305, 306, 83, 86, 85, 87, 88, 89, 82] among others. In general, the fundamental kinematic assumption of these theories is in considering every material particle in the continuum to be equipped with a substructure (micro-continuum). Different models of strain gradient theory assume different kinematics, [83, 305, 306, 170, 330]. The micropolar continuum is one particular member of this class in which every micro-continuum is treated as a rigid body equipped with a rotational field emanating from the microstructure and termed as micro-rotation “*triédre mobile*”, [55]. Since micro-rotations of discrete particles can not be considered continuous inside the matter, a different model of gradient theories called the couple stress theory considers macro-rotation “*triédre caché*” as a true continuum kinematical measure in order to study size effects, [215, 305, 154, 330, 237]. The couple stress model can be considered as a constrained theory of the micropolar continuum, [306, 225, 227].

Generalisation of standard continuum in the case of couple stress theory is based on the following concepts: i) the deformation of substructure is measured based on a field of proper orthogonal rotations in the configurational space of the continuum and, ii) an additional kinematic measure related to the gradient of this rotation (curvature) is included to the set of

thermodynamic state variables, [282, 290, 291, 224, 19]. Consequently, the work-conjugate to the curvature tensor, called the couple-stress enters the boundary value problem and in general the balance of angular momentum does not vanish.

State of the art flexoelectric models are however based on classical strain gradient theories of [212, 214, 86, 85, 306] where gradients of strain and electric field explicitly appear in the electric enthalpy of the system. As a result, a third order stress tensor (hyper stress) and a second order electric displacement tensor enter the boundary value problem, see [200, 201, 4, 3, 70]. In order to close this system, the Gauss's law needs to be modified to facilitate balance equation for the newly arisen high order tensorial quantities. For instance, the models used in [200, 195, 196, 279, 107, 4, 201, 199] are all based on this approach. Certainly, this is a deviation from the true solution of the Maxwell equations. Whether, micropolar, couple stress or in general, formulations based on curvature energy have an advantage over classical strain gradient theories, is yet to be established [44, 117].

Historically, flexoelectricity has been mainly studied in the context of beams. In fact, this is also reflected in the experimental set-ups for determining effective transverse flexoelectric coefficients (the bending piezoelectricity test), for example, in the works of [299, 97, 190, 191, 192, 193]. From the perspective of structural mechanics, amongst the many gradient theories, the couple stress theory has evolved as a competitive technique to model size effects in beams and plates [236, 237, 189, 258, 259, 288, 309]. The most successful implementation of couple stress theory for beams is based on the modified couple stress theory proposed by [330]. The modified couple stress theory assumes that the moment of couples vanishes and as a result the underlying curvature tensor is symmetric (and deviatoric) and work conjugate to a deviatoric couple stress. For isotropic materials, this scenario yields only one material length scale (since the spherical part of the curvature energy vanishes) which is a practically desirable feature in the analysis of micro and nanobeams. In [136] sense, this model corresponds to the *weakest* curvature energy allowable in linear Cosserat continuum.

Three competitive variants of the couple stress model can be considered to study flexoelectricity. The modified couple stress model of [330], the skew-symmetric couple stress model of [118] and the conformally invariant model of [109]. As it will be shown later, in the model of [330] the rotational kinematic measure namely, the symmetric deviatoric curvature tensor still contains diagonal terms that contribute to uniform contraction of the cross-section and torsional rigidity of the beam, although energetically (this curvature tensor is work-conjugate to the deviatoric couple stress) they are never activated. This effect has been mainly ignored in subsequent formulations of the modified couple stress theory for beam models, for instance in [236, 237, 189, 258, 259]. For classical beam models, it is certainly desirable to choose a kinematic measure that excludes cross-sectional terms. The skew-symmetric [118] and the conformal [109] couple stress models specifically preclude such terms in the curvature tensor and are more suited for the particularisation of couple stress to the case of beams. Among the two, the skew-symmetric couple stress model can be easily extended to the case of isotropic flexoelectricity, as the skew-symmetric nature of the curvature tensor (i.e. the axial curvature vector) makes it an ideal candidate for constructing linear invariants in conjunction with the electric field without breaking material symmetry.

For the case of beams, no particular assumption is made on the direction of anisotropy or electric polarisation and a consistent second order interpolation of the electric field across the cross section is utilised. Furthermore, as strain gradient theories in general lead to high continuity requirements in the choice of functional spaces (for a material of grade  $N$ ,  $C^N$  continuity is required [see [305]]) for finite element discretisation, by relying on mixed variational formulations this requirement is relaxed and standard  $C^0$  continuous interpolation functions are utilised for finite element discretisation, leading to an extremely efficient computational implementation.

## 1.5 High Performance Computation

The third part of this work deals with a high performance implementation of the computational methodologies developed for the four classes of electromechanics. The building block of this work has been the development a single domain-aware tensor contraction framework that is capable of transforming and mapping tensorial operations arising in high order finite element development of coupled electromechanics to low level machine instructions. Tensor contraction, which in its essence refers to operations involving natural pairing of tensors in finite dimensional vector spaces are archetypal of quantum and classical mechanics. It is well known that, efficient implementation of tensor contraction of tensor networks involving sum of multiple indices is a NP-hard problem [46, 260, 52, 54, 245, 93]. Current adopted methodologies typically rely either on graph optimisation techniques to find optimal contraction indices, such as depth-first [46, 54], breadth-first [119, 266] and cheapest-first constructive approaches [245, 93] or dynamic programming with memoisation [245], all well established in the field of quantum many-body physics and quantum chemistry. On the other hand, in the field of mechanics of continua, tensor contractions arise naturally, in the variational forms of the governing equations [230, 138, 173] and hence in their consistent linearisation. Finite element discretisation of these forms, then heavily rely on tensorial operations between the gradient of the chosen functional spaces and the work conjugates and Hessian of the internal energies [180, 11, 230].

A myriad of strategies can be applied to optimise tensor contractions that emerge from the discretisation of an underlying variational formulation. A noteworthy approach which is typically utilised by domain specific languages (DSLs) designed for automated finite element code generation, is the exploitation of the structure and topology of the tensors either by a careful study of the bilinear operator and the chosen functional spaces or by performing similar graph optimisation techniques in order to minimise the number of floating point operations [151, 230]. Such optimisation techniques have been applied successfully for instance in [150, 151, 181, 204, 256, 255] for various discretisation schemes such as continuous Galerkin, discontinuous Galerkin and various functional spaces such as  $H^1$ ,  $H(\text{div})$  and  $H(\text{curl})$  spaces, for elliptic as well as hyperbolic PDEs. As an automated finite element code generator, these approaches typically abstract away the numerical implementation from the mathematical formulation and have the potential to optimise the entire finite element assembly procedure.

The framework described in this work is not designed to act as an automated code generator for variational forms (form compiler). Instead, it is rather designed to serve as a generic tensor algebra library that facilitates an explicit mechanism for declaring tensorial operations, while potentially employing analogous optimisation techniques, where applicable. As a result, the implementation specificities of a given problem is left to the developer and not automated. However, the framework provides a high level API, to bring forth low level optimisations at the disposal of the user (say for explicit finite element programming) and as a result could be used as a standalone frontend software or an optimising backend for a form compiler.

Akin to the current framework are the specifically tailored numerical tensor algebra frameworks developed in C++. The foundation for implementation of a high performance tensor algebra framework was laid by the works of Veldhuizen et. al. [314, 58] and Landry [173] on **Blitz++** and **FTensor** libraries, respectively. Other notable examples of tensor algebra frameworks include **nDarray** [139], **LTensor** [179], **libtensor** [81] and **Eigen**'s third party tensor package [116]. Barring **Eigen** which is based on C++11 *variadic templates*, all of the aforementioned frameworks are C++03 compliant, which implies they are not truly multi-dimensional tensor libraries. In other words, these frameworks have support for tensors with up to a few spatial dimensions. In particular, **nDarray**, **FTensor** and **LTensor** support up to fourth order tensors, **libtensor** up to 6th order tensor and **Blitz++** up to 11th order tensors. Furthermore, none of the aforementioned frameworks implement domain-aware expression templates and optimisation algorithms, since they are designed as generic numerical tensor algebra libraries. On the other hand, such optimisation techniques are more suited to domain specific tensor contraction frameworks, examples of which include for instance, the **Tensor Contraction**

[Engine](#) [125, 183, 169], [TiledArray](#) [40] and [Cyclops Tensor Framework](#) [287, 286], which are designed for distributed and thread-parallel tensor operations for quantum mechanical computations. A few noteworthy differences between the current framework and the aforementioned tensor contraction libraries, specifically the Tensor Contraction Engine are as follows. a) the utilisation of compile time technologies for ahead-of-time evaluations using C++11 metaprogramming rather than source-to-source translation or JIT techniques, b) implementation of low-level optimisation techniques such as data parallelism and loop transformation (in C++) instead of relying on a low-level language optimising compiler (Fortran) c) the focus on small tensor networks rather than big, out-of-core tensors and finally d) the focus on continuum multi-physics simulations rather than quantum chemistry applications.

In this work, only dense data-parallel tensor arithmetics will be discussed, specifically due to the fact that for the applications of interest, neither a sparse representation would be beneficial nor the tensors are large enough to explore load balancing for thread level parallelism. A representative example of this is the computation of work-conjugates of a convex multi-variable energy functional on quadrature points. At this point, it is also worth mentioning that, from a finite element application point of view, the presented framework is designed for local computations and not for operations such as assembly of global finite element matrices, wherein more suitable storage-based data structures already exist [115].

The fundamental design principle that all tensor frameworks rely on is the concept of expression templates in C++ [313, 203, 173], which provides a powerful means for lazy or on-demand evaluation of arbitrary chained operators as well as delaying the evaluation of certain tensor algebraic operations. In contrast to the classical operator overloading technique, expression templates completely avoid the need for creation of intermediate temporaries. In [133, 134] novel expression templates are presented which go beyond the level 1 BLAS overloads whilst exploring other optimisation opportunities such as loop-tiling and data parallelism.

Recently, data parallel and stream computing have become a requisite for large scale simulations of scientific problems. Recent generations of CPUs and GPUs, require data-parallel codes for full efficiency. For instance, Figure 1.7 shows a Xeon Phi processor and a Tesla GPU both at their recent generation (as of 2017) and fundamentally designed for data parallel and stream computing. Data parallelism essentially implies that the same sequence of operations should be applied to multiple data sets synchronously. This reduces the need for instruction scheduling in favour of more arithmetic and logic units [162, 134]. On CPU architectures data parallelism is implemented via SIMD (Single Instruction Multiple Data) registers and instructions, wherein a single SIMD register can store multiple values and a single SIMD instruction can execute multiple operations on those values [322, 326, 188]. The FMA (Fused-Multiply-Add) instruction set is an archetypal example of data parallelism. There are typically two



Figure 1.7: a) An AVX-512 enabled 64 core Xeon Phi co-processors; courtesy of Intel<sup>TM</sup> and, b) A Tesla K80 Nvidia graphics processing card; courtesy of Nvidia<sup>TM</sup>

approaches to explicit vectorisation namely, the use of frameworks which are built as an extension to the language such as OpenMP [59, 231], Cilk Plus [96] and OpenCL [292] and the

use of SIMD vector types [94, 162, 116]. In this work, an explicit vectorisation approach using vector types is adopted.

In the high performance part of this thesis we will discuss the implementation aspects of a modern C++ based open-source data parallel tensor contraction framework named **Fastor**. The framework is based on statically sized arrays with a powerful in-built metaprogramming engine that allows it to perform sophisticated optimisations at compile time. In particular, its domain-aware or so-called smart expression template engine facilitates, a) transformation of chained operations to mathematically equivalent but highly efficient expressions, potentially avoiding the call to many level 3 type BLAS subroutines, b) compile time depth-first or breadth-first search to find the optimal contraction indices of complex tensor networks and, c) generation of customised kernels for operations on small tensors (of different order, size and data type) where typically the call to external libraries such as BLAS can be inefficient [162, 326, 120].

Overall, having a domain-aware framework for numerical implementation of electromechanics, makes it easier to map complex mathematical abstractions to the underlying microprocessor instructions with full-efficiency.

## 1.6 Structure of the thesis

The state of the art in curvilinear mesh generation and modelling of coupled electromechanics was presented in the last section with a brief overview of where the scope of the current thesis fits. In this section we will describe the layout of this thesis. It should be evident by now that, the thesis deals with three issues pertaining to computational modelling of electromechanical systems, namely accurate geometry representation, computational techniques for the four classes of electromechanics and subsequently a high performance implementation of these techniques using a tensor contraction framework. In its essence the scope of this thesis can be summarised as presented in Figure 1.8.



Figure 1.8: Scope of this thesis

The three colours in Figure 1.8 stand for the three parts of the thesis. These three parts and the subsequent chapters within are structured as follows:

### Part 1:

Part 1 of this work, deals with the generation of high order curvilinear meshes for finite element analysis. An a posteriori curvilinear mesh generator using polyconvex elasticity framework is described in this part. To this end, the thesis is divided into two chapters.

### **Chapter 2:**

In chapter 2, we start discussing the classical and modern approaches to nonlinear elasticity. The kinematics, governing equations and constitutive laws of elasticity are discussed in four different settings, namely the classical deformation gradient based nonlinear elasticity, the objective representation in classical elasticity, the tensor cross product based formulation for polyconvex nonlinear elasticity and the objective representation in polyconvex elasticity using the tensor cross product algebra. It is emphasised that the use of the tensor cross product simplifies the linearisation of polyconvex nonlinear elastic models significantly leading to new insights and facilitating an easy to implement finite element formulation. The updated Lagrangian form polyconvex elasticity is also presented in this section.

### **Chapter 3:**

In chapter 3, a unified approach for the a posteriori generation of arbitrary high-order curvilinear meshes via the polyconvex elasticity analogy is presented. The approach encompasses a variety of methodologies, ranging from the popular incremental linear elastic approach to very sophisticated non-linear elasticity. In addition, an intermediate consistent incrementally linearised approach is also presented and applied for the first time in this context. Utilising a consistent derivation from energy principles, a theoretical comparison of the various approaches is presented which enables a detailed discussion regarding the material characterisation (calibration) employed for the different solid mechanics formulations. Five independent quality measures are proposed and their relations with existing quality indicators, used in the context of a posteriori mesh generation, are discussed. Finally, a comprehensive range of numerical examples, both in two and three dimensions, including challenging geometries of interest to the solids, fluids, biomechanics and electromagnetics communities, are shown in order to illustrate and thoroughly compare the performance of the different methodologies. This comparison considers the influence of material parameters and number of load increments on the quality of the generated high-order mesh, overall computational cost and, crucially, the approximation properties of the resulting mesh when considering an isoparametric finite element formulation. Aspect of node sliding over the surface and untangling of complicated geometries is discussed by presenting a multi-level mesh deformation approach.

### **Part 2:**

Part 2 of this work, deals with the numerical modelling of electromechanics, in particular the four classes of electromechanics discussed earlier. To this end, this part of thesis is divided into 5 chapters.

### **Chapter 4:**

In chapter 4, we present the concept of convex multi-variable electro-elasticity. The extended kinematics set of convex multi-variable electro-elasticity, the governing equations and more importantly the convex multi-variable electromechanical internal energies are described in this chapter. A link is made between convex multi-variable electro-elasticity and polyconvex nonlinear elasticity, presenting the latter as direct extension and a superset of the former. The formulation for large strain large electric field electromechanics is discussed in terms of the fundamental kinematic and electrostatic measures and then later on presented in objective setting to facilitate its particularisation to the case of small strains. The equations of electromechanics are then also presented in an updated Lagrangian setting and the Helmholtz like energy is introduced for the later finite element implementation.

### **Chapter 5: Class 1:**

In chapter 5, we discuss the first class of electromechanics covered in this thesis, namely the large deformations large electric fields electromechanics and the convex multi-variable formulation for it. The variational form of the Helmholtz energy and its finite element implementation is discussed in this chapter, using a high order curvilinear finite element framework. The performance of high order curvilinear finite element framework is then analysed from the optimality and  $h$  and  $p$  convergence point of view and its performance with respect to the mixed Hu-Washizu variational principles is investigated under near incompressibility and shear locking scenarios. A suite of finite element studies is then carried out to exhibit the capability of this framework in capturing instabilities, snap-through and wrinkles in dielectric elastomeric films confirming experimental findings in this domain.

### **Chapter 6: Class 2:**

In chapter 6, we discuss the second class of electromechanics covered in this thesis, namely the small deformations large electric fields electromechanics. A staggered approach is devised to solve the small deformation electrostrictive materials in a significantly faster time compared to the fully coupled nonlinear electromechanics. The essence of the approach taken lies in guaranteeing the objectivity of the resulting work conjugates, by starting from the underlying convex multi-variable internal energy, whence avoiding the need for further symmetrisation of the resulting Maxwell and Minkowski-type stresses at small strain regime. In this context, the nonlinearity with respect to electrostatic counterparts such as electric displacements is still retained, hence resulting in a formulation similar but more competitive with the existing linearised electro-elasticity approaches. Through numerical studies it is shown that the staggered approach is also capable of tackling large displacement small strain problems.

### **Chapter 7: Class 3:**

In chapter 7, we discuss the third class of electromechanics covered in this thesis, namely the linear piezoelectricity. In this chapter, a new variational and computational framework is introduced for the analysis of three dimensional linear piezoelectric continua and beams using hp-finite elements is presented. Unlike existing publications on piezoelectric beams, the framework is very general and suitable for static, modal and dynamic scenarios; it is not restricted to either actuation or energy harvesting applications and, moreover, it can cope with any anisotropy or electric polarisation orientation. Derived from first principles, namely the fundamental equations of continuum piezoelectricity, a new set of beam balance equations is presented based on a Taylor series expansion for the displacement and electric potential across the cross section of the beam. The coupled nature of the piezoelectric phenomenon at a beam level arises via a series of mechanical (and electrical counterparts) stress and strain cross sectional area resultants. To benchmark the numerical algorithm, and in order to aid prospective researchers, a new closed-form solution is presented for the case of cantilever type systems subjected to end tip mechanical/electrical loads. To the best of the authors' knowledge, the analytical solution for this prototypical example has not been previously presented. Finally, some numerical aspects of the hp-discretisation are investigated including the exponential convergence of the hp-refinements and the consideration of linear or quadratic electric potential expansions across the cross section of the beam.

### **Chapter 8: Class 4:**

In chapter 8, we discuss the fourth class of electromechanics covered in this thesis, namely the linear flexoelectricity. In this chapter, a family of numerical models for the phenomenological linear flexoelectric theory for continua and their particularisation to the case of three-dimensional beams based on a skew-symmetric couple stress theory. In contrast to the traditional flexoelectric models based on standard strain gradient wherein coupling between electric

polarisation and strain gradients is assumed, we postulate an electric enthalpy in terms of linear invariants of curvature and electric field. This is achieved by introducing the axial curvature vector as a strain gradient measure. We have shown that the implication of this assumption is many-fold. Firstly, for isotropic (non-piezoelectric) materials it allows constructing flexoelectric energies without breaking material symmetry. Secondly, nonuniform distribution of volumetric part of strains (volumetric strain gradients) do not generate electric polarisation, as confirmed by experimental evidence to be the case for some important classes of flexoelectric materials. In this regard, the current flexoelectric model can be considered as a more restrictive case of strain gradient theories. Thirdly, a state of plane strain generates out of plane deformation through strain gradient effects. Finally, extension and shear coupling modes cannot be characterised individually as they contribute to the generation of electric polarisation as a whole. For the case of three-dimensional beams, we have shown that the skew-symmetric couple stress model in general, generate stresses spanned over the cross section rather than aligned with the longitudinal axis of the beam and as a result special care must be taken to integrate them over the cross section. Four distinct variational principles are presented for both continuum and beam models namely, a displacement-potential formulation, a penalty formulation, a Lagrange-multiplier formulation and an augmented Lagrangian formulation. The three latter formulations facilitate incorporation of strain gradient measures in to a standard finite element scheme while maintaining the  $C^0$  continuity. To this end, the efficacy of high order finite elements along with the computational efficiency of mixed finite elements have been utilised to develop a series of low and high order mixed finite element schemes for couple stress based flexoelectricity. Numerical results of finite element discretisations for the three latter variational formulations are first benchmarked against available closed form solutions in regards where good agreements was found between the reference and numerical results. Furthermore, a detailed comparison of the developed couple stress based flexoelectric model with the standard strain gradient flexoelectric models has been performed for the case of Barium Titanate where a myriad of simple analytical solutions have been proposed in order to quantitatively describe the similarities and dissimilarities in effective electromechanical coupling under these two theories. It is observed that, if the same experimental flexoelectric constants are fitted in to both theories, the current couple stress theory in general, reports stronger electromechanical conversion efficiency.

## Part 3:

Part 3 of this work, deals with the high performance implementation of the computational framework built for high order curvilinear finite elements for polyconvex elasticity and convex multi-variable electro-elasticity. The high performance framework is a generic domain-aware tensor contraction engine specifically designed to metaprogrammatically optimise variational forms of different classes of electromechanics.

### Chapter 9:

To this end, in chapter 9, a new high performance tensor contraction framework for the numerical analysis of coupled electromechanics on streaming architectures is presented. In addition to explicit SIMD instructions and smart expression templates, the framework introduces domain specific constructs for the tensor cross product and its associated algebra. The two key ingredients of the presented expression template engine are as follows. First, the capability to mathematically transform complex chains of operations to simpler equivalent expressions, while potentially avoiding routes with higher levels of computational complexity and, second, to perform a compile time depth-first or breadth-first search to find the optimal contraction indices of a large tensor network in order to minimise the number of floating point operations. For optimisations of tensor contraction such as loop transformation, loop fusion and data locality optimisations, the framework relies heavily on compile time technologies. Every aspect of the framework is examined through relevant performance benchmarks, including the impact of data parallelism on the performance of isomorphic and nonisomorphic tensor products, the

FLOP and memory I/O optimality in the evaluation of tensor networks, the compilation cost and memory footprint of the framework and the performance of tensor cross product kernels. The framework is then applied to finite element analysis of coupled electro-mechanical problems to assess the speed-ups achieved in kernel-based numerical integration of complex electroelastic energy functionals. In this context, domain-aware expression templates combined with SIMD instructions are shown to provide a significant speed-up over the classical low-level style programming techniques.

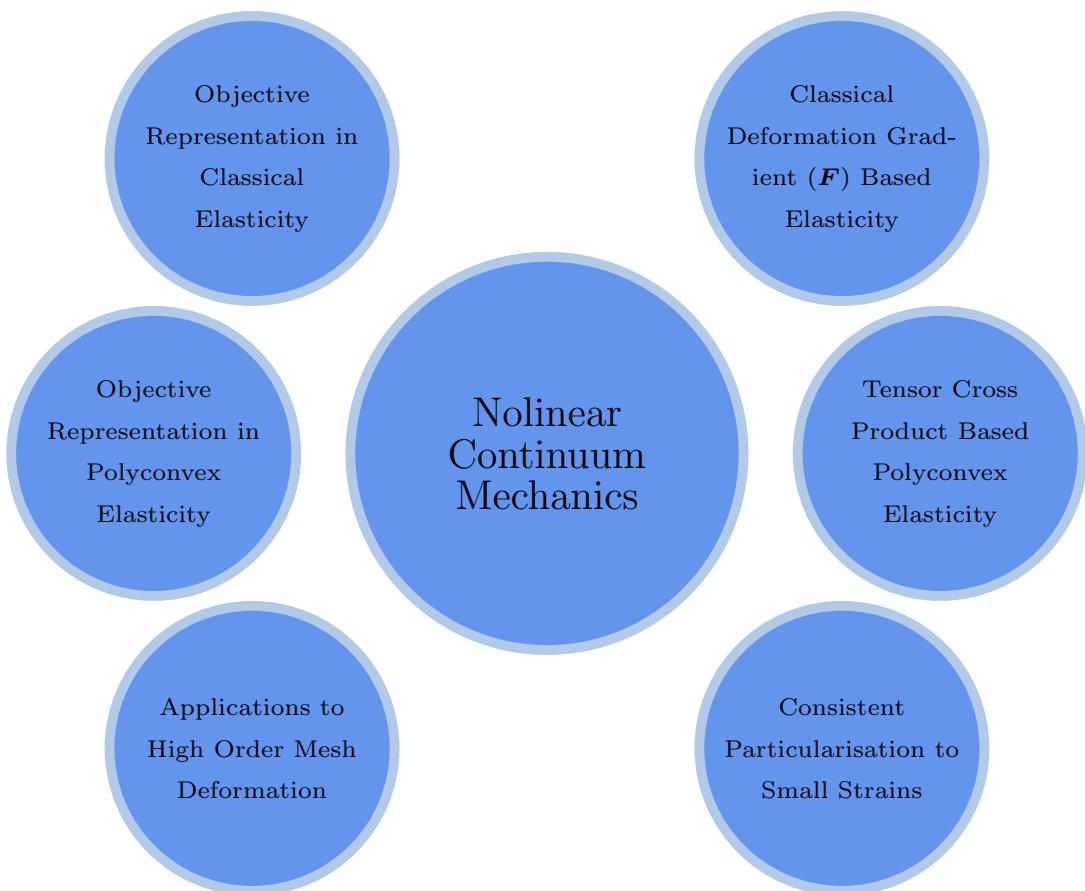
## Chapter 10: Concluding Remarks:

Finally in chapter 10, conclusions, remarks and a future perspective of the work is provided. This is once again divided into three parts. Each issue raised in the thesis is summarised and conclusions are given based on the current state of work and findings throughout the thesis. The thesis ends with providing outlook for future development and extension of the current platform on curvilinear mesh generation, numerical modelling of electromechanics and high performance computing fronts.



# Part 1:

## Nonlinear Continuum Mechanics: The Classical and Modern Approaches to Polyconvex Nonlinear Elasticity



## Chapter 2

# Nonlinear Continuum Mechanics

### 2.1 Introduction

Studying large strain elastic and inelastic response by finite elements or other computational techniques is a well established procedure in many areas of engineering analysis and design [30, 327, 127, 56, 66, 202, 68]. Often elasticity is described by means of a hyperelastic model defined in terms of a stored energy functional which depends on the deformation gradient of the mapping between initial and final configurations [30, 327, 127]. It has also been shown that for the model to be well defined in a mathematical sense, this dependency with respect to the deformation gradient has to be based upon appropriate convexity criteria [16, 48] which guarantees ellipticity and hence, the well-posedness of the governing equations. Ellipticity has therefore, important physical implications as it guarantees the existence of real wave speeds in the material in the vicinity of an equilibrium configuration and it is strongly related to material stability of the constitutive equations.

The simplest and most well known restriction on the constitutive equations is a convexity restriction upon the strain energy which would comply with ellipticity condition and would not exclude buckling effects. The loss ellipticity is known to be a major issue in modelling nonlinear materials which typically manifest itself in the form of localisation of deformations and shear bands [207, 25]. This convexity condition is called polyconvexity. Polyconvexity automatically ensures sequential weak lower semicontinuity of the strain energy [16, 48] and when enriched with appropriate coercivity or growth conditions, it guarantees the existence of minimisers for the total energy potential in nonlinear elasticity.

The classical approach to elastic response consists of ensuring that the defined stored energy function satisfies the polyconvexity condition first but then proceeds towards an evaluation of stresses and elasticity tensors by re-expressing the energy function in terms of the deformation gradient alone. This inevitably leads to the differentiation of inverse functions of the deformation gradient, its transpose or the inverse of the right Cauchy Green strain tensor. These derivatives are readily obtained using standard algebra but can lead to lengthy expressions [28]. Recently, Bonet, Gil and Ortigosa have studied the concept of polyconvexity in great depth and have shown that a new tensor cross product based algebra leads to a significant simplification of the algebra involved in consistent linearisation of the internal energy [29, 27, 112].

In this chapter we will discuss the classical and tensor cross product based approaches to polyconvex nonlinear elasticity. In particular, the chapter is divided into five sections, namely

1. **Section 2.2** discusses the fundamentals of nonlinear elasticity using a classical approach using the deformation gradient tensor as the driving kinematics.
2. **Section 2.3** discusses the objective representation in nonlinear elasticity using the right Cauchy Green strain tensor for expressing internal energy densities and the subsequent linearisation and further algebra therein.
3. **Section 2.4** motivates the concept of polyconvexity in nonlinear mechanics and presents the tensor cross product based formulation for polyconvex elasticity and the simplifica-

tions that the tensor cross product algebra brings forth to the equations of a deformable system.

4. **Section 2.5** discusses the objective representation of polyconvexity in nonlinear mechanics and presents the tensor cross product based formulation for re-expressing polyconvex elasticity in terms of symmetric kinematic measures.
5. **Section 2.6** presents the spatial representation of polyconvexity in nonlinear mechanics and presents the tensor cross product based formulation for re-expressing polyconvex elasticity in an updated Lagrangian setting.

## 2.2 The classical approach to nonlinear elasticity

In this section, essential concepts of nonlinear elasticity are discussed in its classical version. This formulation entails only the definition of the deformation gradient tensor and the subsequent governing equations and constitutive laws are formulated according to this kinematic measure.

### 2.2.1 Kinematics

Let us consider the motion of a body which in its initial configuration is defined by a domain  $V$  of boundary  $\partial V$  with outward unit normal  $\mathbf{N}$ . After the motion, the body occupies a final configuration defined by a domain  $v$  of boundary  $\partial v$  with outward unit normal  $\mathbf{n}$ , as shown in Figure 2.1. The pseudo-time ( $t$ ) dependent mapping field  $\phi$  links a material particle from initial configuration  $\mathbf{X}$  to final configuration  $\mathbf{x}$  according to  $\mathbf{x} = \phi(\mathbf{X}, t)$ . The deformation

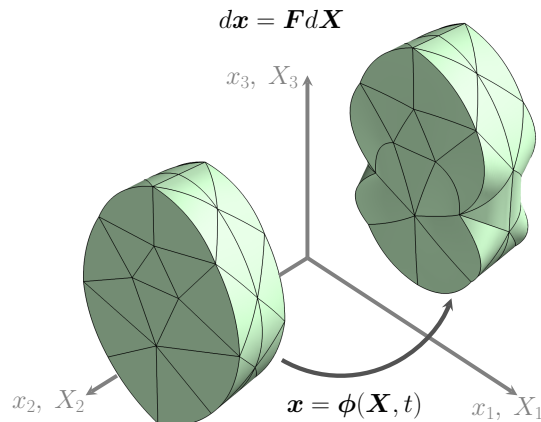


Figure 2.1: Motion map of a body  $V$

gradient tensor  $\mathbf{F}$  is defined as

$$\mathbf{F} = \nabla_0 \mathbf{x} = \frac{\partial \phi(\mathbf{X}, t)}{\partial \mathbf{X}}, \quad (2.1)$$

where  $\nabla_0(\cdot)$  is the Lagrangian (initial configuration) gradient operator.<sup>1</sup> As shown in Figure 2.1,  $\mathbf{F}$  is the kinematic measure relating the differential fibre elements from initial  $d\mathbf{X}$  to final  $d\mathbf{x}$  configuration. In addition, the cofactor  $\mathbf{H}$  (or area map) and the Jacobian  $J$  (or volume map) of the deformation are defined as

$$\mathbf{H} = J \mathbf{F}^{-T}; \quad (2.2a)$$

$$J = \det \mathbf{F}. \quad (2.2b)$$

---

<sup>1</sup>Throughout this work, the symbol  $(\cdot)$  indicates the scalar product  $\mathbf{a} \cdot \mathbf{b} = a_i b_i$ , the symbol  $(:)$ , the double contraction operation  $\mathbf{A} : \mathbf{B} = A_{ij} B_{ij}$ , the symbol  $(\times)$ , the cross product between vectors  $[\mathbf{a} \times \mathbf{b}]_i = \epsilon_{ijk} a_j b_k$  and the symbol  $(\otimes)$ , the outer or dyadic product  $[\mathbf{a} \otimes \mathbf{b}]_{ij} = a_i b_j$ . The Einstein summation convention is followed throughout, wherever indices appear.

Let us define  $\delta\mathbf{u}$  and  $\Delta\mathbf{u}$  as virtual and incremental variations of  $\mathbf{x}$ , respectively, where it will be assumed that  $\delta\mathbf{u}$  and  $\Delta\mathbf{u}$  satisfy compatible homogeneous displacement based boundary conditions that vanishes on  $\partial_u V$ , where  $\partial_u V$  is part of the boundary subjected to suitable essential (Dirichlet) boundary condition(s). The first and second directional derivatives of the deformation gradient tensor  $\mathbf{F}$  with respect to virtual and incremental variations of the geometry can then be evaluated as

$$D\mathbf{F}[\delta\mathbf{u}] = \nabla_0 \delta\mathbf{u}; \quad (2.3a)$$

$$D^2\mathbf{F}[\delta\mathbf{u}; \Delta\mathbf{u}] = \mathbf{0}. \quad (2.3b)$$

Analogously, the first and second directional derivatives of the cofactor of the deformation gradient tensor  $\mathbf{H}$  can be evaluated as

$$D\mathbf{H}[\delta\mathbf{u}] = \left[ (\mathbf{H} : \nabla_0 \delta\mathbf{u}) \mathbf{I} - \mathbf{H}(\nabla_0 \delta\mathbf{u})^T \right] \mathbf{F}^{-T}; \quad (2.4a)$$

$$\begin{aligned} D^2\mathbf{H}[\delta\mathbf{u}; \Delta\mathbf{u}] &= \left( \left[ (\mathbf{H} : \nabla_0 \Delta\mathbf{u}) \mathbf{I} - \mathbf{H}(\nabla_0 \Delta\mathbf{u})^T \right] \mathbf{F}^{-T} : \nabla_0 \delta\mathbf{u} \right. \\ &\quad \left. - \left[ (\mathbf{H} : \nabla_0 \Delta\mathbf{u}) \mathbf{I} - \mathbf{H}(\nabla_0 \Delta\mathbf{u})^T \right] (\nabla_0 \delta\mathbf{u})^T \right) \mathbf{F}^{-T} \\ &\quad - \left[ (\mathbf{H} : \nabla_0 \delta\mathbf{u}) \mathbf{I} - \mathbf{H}(\nabla_0 \delta\mathbf{u})^T \right] \mathbf{F}^{-T} (\nabla_0 \Delta\mathbf{u})^T \mathbf{F}^{-T}. \end{aligned} \quad (2.4b)$$

Finally, the first and second directional derivatives of the Jacobian of the deformation gradient tensor  $J$  are computed as

$$DJ[\delta\mathbf{u}] = \mathbf{H} : \nabla_0 \delta\mathbf{u}; \quad (2.5a)$$

$$D^2J[\delta\mathbf{u}; \Delta\mathbf{u}] = \nabla_0 \delta\mathbf{u} : \left[ (\mathbf{H} : \nabla_0 \Delta\mathbf{u}) \mathbf{I} - \mathbf{H}(\nabla_0 \Delta\mathbf{u})^T \right] \mathbf{F}^{-T}. \quad (2.5b)$$

## 2.2.2 Governing equations of continuum mechanics

Let us assume that the domain defined by the deformable body is subjected to a body force per unit of undeformed volume  $\mathbf{f}_0$  and a traction force per unit of undeformed area  $\mathbf{t}_0$  applied on  $\partial_t V \in \partial V$ , such that  $\partial_t V \cup \partial_u V = \partial V$  and  $\partial_t V \cap \partial_u V = \emptyset$ . The conservation of linear momentum in the global form leads to the integral of the translational equilibrium equations as

$$\int_V \mathbf{f}_0 dV + \int_{\partial_t V} \mathbf{t}_0 dA = \mathbf{0}. \quad (2.6)$$

The above integral equation governing the physics of a deformable system, can be summarised in the local (strong) form and Lagrangian setting as follows [30, 29, 28].

$$\text{DIV} \mathbf{P} + \mathbf{f}_0 = \mathbf{0} \quad \text{in } V; \quad (2.7a)$$

$$\mathbf{P}\mathbf{N} = \mathbf{t}_0 \quad \text{on } \partial_t V; \quad (2.7b)$$

$$\phi = \bar{\phi} \quad \text{on } \partial_u V. \quad (2.7c)$$

where DIV is the Lagrangian divergence operator and  $\mathbf{P}$  is the first Piola-Kirchhoff stress tensor. The rotational equilibrium dictates that  $\mathbf{F}^T \mathbf{P} = \mathbf{P} \mathbf{F}^T$ .

## 2.2.3 The internal energy density in hyperelasticity

For the closure of the system of equations defined by (2.7), an additional constitutive law is needed relating deformation and stresses in the continuum. In the case of reversible elasticity,

where thermal effects and any other possible state variables (i.e. accumulated plastic deformation) are disregarded, the internal energy density  $e$  per unit of undeformed volume can be solely defined in terms of the deformation, namely  $e = e(\nabla_0 \mathbf{x})$ . In this case, combination of (2.7) and the first law of thermodynamics yields

$$De[\delta \mathbf{u}] = \mathbf{P} : \nabla_0 \delta \mathbf{u}; \quad \mathbf{P} = \frac{\partial e(\mathbf{F})}{\partial \mathbf{F}} \Big|_{\mathbf{F}=\nabla_0 \mathbf{x}}, \quad (2.8)$$

where the subscript  $\mathbf{F} = \nabla_0 \mathbf{x}$  denotes that  $\mathbf{F}$  is calculated from the deformation of the geometry  $\mathbf{x}$ . This distinction is necessary as independent variations of  $\mathbf{F}$  and  $\mathbf{x}$  are allowed. With an iterative type of solution process such as Newton-Raphson in mind, it is useful to derive the tangent elasticity operator. This is typically evaluated in terms of a fourth order tangent elasticity tensor  $\tilde{\mathcal{C}}$  defined by

$$D^2e[\delta \mathbf{u}; \Delta \mathbf{u}] = \nabla_0 \delta \mathbf{u} : D\mathbf{P}[\Delta \mathbf{u}] = \nabla_0 \delta \mathbf{u} : \tilde{\mathcal{C}} : \nabla_0 \Delta \mathbf{u}, \quad (2.9)$$

where

$$\tilde{\mathcal{C}} = \frac{\partial \mathbf{P}}{\partial \mathbf{F}} \Big|_{\mathbf{F}=\nabla_0 \mathbf{x}} = \frac{\partial^2 e(\mathbf{F})}{\partial \mathbf{F} \partial \mathbf{F}} \Big|_{\mathbf{F}=\nabla_0 \mathbf{x}} \quad (2.10)$$

#### 2.2.4 Material characterisation in the reference configuration

A simple internal energy functional  $e^{mn}$  expressed in terms of the deformation gradient tensor is the Mooney-Rivlin model, written as

$$e^{mn}(\mathbf{F}) = \mu_1 II_{\mathbf{F}} + \mu_2 II_{\mathbf{H}} + f(J), \quad (2.11)$$

where

$$f(J) = -2(\mu_1 + 2\mu_2)\ln J + \frac{\kappa}{2}(J-1)^2, \quad (2.12)$$

and  $II_{(\bullet)}$  denotes the squared of the  $L^2$  norm of the entity  $(\bullet)$  and  $\{\mu_1, \mu_2, \kappa\}$  are positive material constants. For this material model, the first Piola-Kirchhoff stress tensor  $\mathbf{P}$  can be computed as

$$\mathbf{P} = 2\mu_1 \mathbf{F} + \frac{2\mu_2}{J} \left[ (\mathbf{H} : \mathbf{H}) \mathbf{I} - \mathbf{H}^T \mathbf{H} \right] \mathbf{H} + f'(J), \quad (2.13)$$

where

$$f'(J) = \left[ \kappa(J-1) - \frac{2}{J}(\mu_1 + 2\mu_2) \right] \mathbf{H}. \quad (2.14)$$

Analogously, the fourth order tangent elasticity tensor  $\mathcal{C}$  can be computed as

$$\begin{aligned} \tilde{\mathcal{C}} &= 2\mu_1 \mathbf{I} + \frac{4\mu_2}{J^2} \left[ (\mathbf{H} : \mathbf{H}) \mathbf{I} - \mathbf{H}^T \mathbf{H} \right] \mathbf{H} \otimes \mathbf{H} \\ &\quad - \frac{2\mu_2}{J^2} \left[ (\mathbf{H}^T \mathbf{H}) \mathbf{H} \otimes \mathbf{H} + \mathbf{H} \otimes (\mathbf{H}^T \mathbf{H}) \mathbf{H} + (\mathbf{H} : \mathbf{H}) \mathbf{H} \otimes \mathbf{H} \right] \\ &\quad + \frac{2\mu_2}{J^2} \left[ (\mathbf{H}^T \mathbf{H}) \otimes \mathbf{H} + \mathbf{H} \otimes (\mathbf{H}^T \mathbf{H}) + (\mathbf{H}^T \mathbf{H}) \otimes (\mathbf{H}^T \mathbf{H}) \right] + f''(J), \end{aligned} \quad (2.15)$$

where

$$f''(J) = \frac{1}{J^2} \left[ (\mu_1 + 2\mu_2) + \kappa J(J-1) \right] \mathbf{H} \otimes \mathbf{H}. \quad (2.16)$$

As can be observed from (2.13) and (2.15), the classical continuum mechanics approach to formulating hyperelasticity based on the deformation gradient tensor  $\mathbf{F}$  leads to an extremely cumbersome algebra, requiring computation of the inverse of gradient multiple times.

## 2.3 The objective representation in classical elasticity

In this section, the kinematics, governing equations and constitutive law of nonlinear elasticity is going to be re-formulated and presented in terms of objective (materially frame indifferent kinematics). This formulation will come handy in our future development in the later chapters.

### 2.3.1 Kinematics

The requirement for objectivity or material frame indifference (i.e. invariance with respect to rotations in the material configuration) implies that internal energy functionals must be independent of the rotational components of the deformation gradient tensor  $\mathbf{F}$  and its cofactor  $\mathbf{H}$ . Hence, a function of these tensor via symmetric tensors are often used in expressing the internal energy. The right Cauchy-Green strain tensor  $\mathbf{C} = \mathbf{F}^T \mathbf{F}$  is the archetypal tensor being utilised in this regard. This is augmented by its symmetric cofactor  $\mathbf{G} = \mathbf{H}^T \mathbf{H}$  to re-express the internal energy. For the sake of consistency, here we also utilise the kinematic measure  $C = \det \mathbf{C} = J^2$ . The first and second directional derivatives of the right Cauchy-Green strain tensor  $\mathbf{C}$  with respect to virtual and incremental variation of the geometry can now be evaluated

$$DC[\delta \mathbf{u}] = D(\mathbf{F}^T \mathbf{F})[\delta \mathbf{v}] = (\nabla_0 \delta \mathbf{u})^T \mathbf{F} + \mathbf{F}^T \nabla_0 \delta \mathbf{u}, \quad (2.17a)$$

$$D^2 \mathbf{C}[\delta \mathbf{u}; \Delta \mathbf{u}] = (\nabla_0 \delta \mathbf{u})^T (\nabla_0 \Delta \mathbf{u}) + (\nabla_0 \Delta \mathbf{u})^T (\nabla_0 \delta \mathbf{u}). \quad (2.17b)$$

Similarly, for the co-factor  $\mathbf{G}$ , the first and second derivatives are

$$DG[\delta \mathbf{u}] = \left[ (\mathbf{G} : DC[\delta \mathbf{u}]) \mathbf{I} - \mathbf{G}(DC[\delta \mathbf{u}])^T \right] \mathbf{C}^{-1}, \quad (2.18a)$$

$$\begin{aligned} D^2 \mathbf{G}[\delta \mathbf{u}; \Delta \mathbf{u}] &= \left( \left[ (\mathbf{G} : DC[\Delta \mathbf{u}]) \mathbf{I} - \mathbf{G}(DC[\Delta \mathbf{u}])^T \right] \mathbf{C}^{-1} : DC[\delta \mathbf{u}] \right. \\ &\quad \left. - \left[ (\mathbf{G} : DC[\Delta \mathbf{u}]) \mathbf{I} - \mathbf{G}(DC[\Delta \mathbf{u}])^T \right] (DC[\delta \mathbf{u}])^T \right) \mathbf{C}^{-1} \\ &\quad - \left[ (\mathbf{G} : DC[\delta \mathbf{u}]) \mathbf{I} - \mathbf{G}(DC[\delta \mathbf{u}])^T \right] \mathbf{C}^{-1} (DC[\Delta \mathbf{u}])^T \mathbf{C}^{-1}. \end{aligned} \quad (2.18b)$$

and finally, for the Jacobian  $C$  the first and second derivates are

$$DC[\delta \mathbf{u}] = \mathbf{G} : DC[\delta \mathbf{u}]; \quad (2.19a)$$

$$D^2 C[\delta \mathbf{u}; \Delta \mathbf{u}] = DC[\delta \mathbf{u}] : \left[ (\mathbf{G} : DC[\Delta \mathbf{u}]) \mathbf{I} - \mathbf{G}(DC[\Delta \mathbf{u}])^T \right] \mathbf{C}^{-1}. \quad (2.19b)$$

### 2.3.2 The internal energy density in hyperelasticity

The internal energy density  $e = e(\nabla_0 \mathbf{x})$  defined in the previous section, can be re-written in terms of the Cauchy Green tensor as  $e(\nabla_0 \mathbf{x}) = e_{\text{sym}}(\mathbf{C})$ . In combination with (2.7) and the first law of thermodynamics we now obtain

$$De_{\text{sym}}[\delta \mathbf{u}] = \mathbf{S} : \frac{1}{2} DC[\delta \mathbf{u}]; \quad \mathbf{S} = 2 \frac{\partial e_{\text{sym}}(\mathbf{C})}{\partial \mathbf{C}} \Big|_{\mathbf{C}=\mathbf{C}_x}, \quad (2.20)$$

where  $\mathbf{S}$  is the symmetric second Piola-Kirchhoff stress tensor, such that  $\mathbf{S} = \mathbf{F}^{-1} \mathbf{P}$ . Similarly, the fourth order tangent elasticity tensor (with slight abuse of notation, expressed again as  $\mathbf{C}$ ) required for Newton-Raphson procedure can be computed as

$$D^2 e_{\text{sym}}[\delta \mathbf{u}; \Delta \mathbf{u}] = \frac{1}{2} DC[\delta \mathbf{u}] : DS[\Delta \mathbf{u}] = \frac{1}{2} DC[\delta \mathbf{u}] : \mathbf{C} : \frac{1}{2} DC[\Delta \mathbf{u}], \quad (2.21)$$

where

$$\mathbf{C} = 2 \frac{\partial \mathbf{S}}{\partial \mathbf{C}} \Big|_{\mathbf{C}=\mathbf{C}_x} = 4 \frac{\partial^2 e(\mathbf{C})}{\partial \mathbf{C} \partial \mathbf{C}} \Big|_{\mathbf{C}=\mathbf{C}_x} \quad (2.22)$$

### 2.3.3 Material characterisation in the reference configuration

The Mooney-Rivlin model defined in (2.11) in terms of  $\mathbf{F}$  can be re-expressed in terms of  $\mathbf{C}$  as

$$e_{\text{sym}}^{mn}(\mathbf{C}) = \mu_1 I_{\mathbf{C}} + \mu_2 I_{\mathbf{G}} + f(C), \quad (2.23)$$

where  $I_{\mathbf{A}} = \mathbf{A} : \mathbf{I} = \text{tr}(\mathbf{A})$  for any second order tensor  $\mathbf{A}$  and

$$f(C) = -2(\mu_1 + 2\mu_2)\ln\sqrt{C} + \frac{\kappa}{2}(\sqrt{C} - 1)^2, \quad (2.24)$$

For this material model, the second Piola-Kirchhoff stress tensor  $\mathbf{S}$  can be computed as

$$\mathbf{S} = 2\mu_1 \mathbf{I} + 2\mu_2 \left[ \text{tr}(\mathbf{C}^{-1}) \mathbf{I} - \mathbf{C}^{-1} \right] \mathbf{G} + f'(C), \quad (2.25)$$

where

$$f'(C) = \frac{1}{C} \left[ \kappa(\sqrt{C} - 1) - (\mu_1 + 2\mu_2) \right] \mathbf{G}. \quad (2.26)$$

Analogously, the fourth order tangent elasticity tensor  $\mathbf{C}$  can be computed as

$$\mathbf{C} = \frac{4\mu_2}{C^2} \left[ \text{tr}(\mathbf{G}) \mathbf{G} \otimes \mathbf{G} - \mathbf{G} \otimes (\mathbf{G}^T \mathbf{G}) - (\mathbf{G}^T \mathbf{G}) \otimes \mathbf{G} \right. \quad (2.27)$$

$$\left. - \frac{1}{2} \text{tr}(\mathbf{G}) [\mathbf{G}]_{IK} [\mathbf{G}]_{JL} - \frac{1}{2} \text{tr}(\mathbf{G}) [\mathbf{G}]_{IL} [\mathbf{G}]_{JK} + [\mathbf{G}]_{IK} [\mathbf{G}^T \mathbf{G}]_{JL} + [\mathbf{G}^T \mathbf{G}]_{IK} [\mathbf{G}]_{JL} \right] + f''(C), \quad (2.28)$$

where

$$f''(C) = \frac{\kappa}{C\sqrt{C}} \mathbf{G} \otimes \mathbf{G} - \frac{2}{C} \left[ \kappa(\sqrt{C} - 1) - (\mu_1 + 2\mu_2) \right] [\mathbf{G}]_{IK} [\mathbf{G}]_{JL}. \quad (2.29)$$

As can be observed from (2.25) and (2.28), the classical continuum mechanics approach to formulating hyperelasticity based on the Cauchy-Green strain tensor  $\mathbf{C}$  leads to an extremely cumbersome algebra, requiring computation of the inverse of gradient, multiple times. In the next section, we will have a look at polyconvex nonlinear elasticity using a new approach based on the tensor cross product algebra [28, 29] which will significantly simplify the algebra involved in formulating nonlinear hyperelastic problems.

## 2.4 The tensor cross product based approach to polyconvex elasticity

We will now discuss the concept of polyconvexity and re-formulate the governing equations of nonlinear continuum mechanics based on the a tensor cross product formulation, recently reported by [28, 29]. In principle, the approach entails formulating the nonlinear mechanics equations in terms of the deformation gradient tensor and its minors, i.e. its cofactor and its Jacobian.

### 2.4.1 Kinematics

Let us reconsider the motion of a deformable body which in its initial configuration is defined by a domain  $V$  of boundary  $\partial V$  with outward unit normal  $\mathbf{N}$ . After the motion, the body occupies a final configuration defined by a domain  $v$  of boundary  $\partial v$  with outward unit normal  $\mathbf{n}$ , as shown in Figure 4.1. The pseudo-time ( $t$ ) dependent mapping field  $\phi$  links a material particle from initial configuration  $\mathbf{X}$  to final configuration  $\mathbf{x}$  according to  $\mathbf{x} = \phi(\mathbf{X}, t)$ . The deformation gradient tensor  $\mathbf{F}$  is defined as

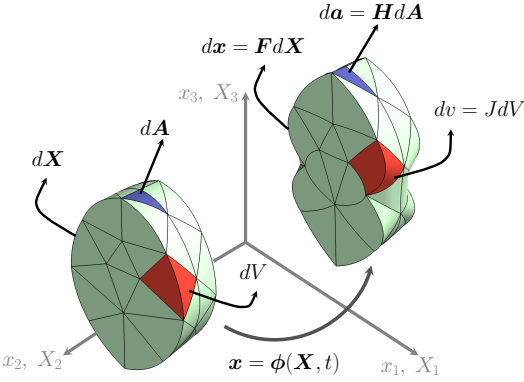


Figure 2.2: Motion map of a body  $V$  and the kinematic measures  $\{\mathbf{F}, \mathbf{H}, J\}$ .

$$\mathbf{F} = \nabla_0 \mathbf{x} = \frac{\partial \phi(\mathbf{X}, t)}{\partial \mathbf{X}}, \quad (2.30)$$

where  $\nabla_0(\cdot)$  is the Lagrangian (initial configuration) gradient operator. In addition, with the help of the tensor cross product operations, the cofactor and Jacobian ( $\mathbf{H} = \text{Cof}\mathbf{F}$  and  $J = \det\mathbf{F}$ ) of the deformation are defined as, [65, 28, 29]

$$\mathbf{H} = \frac{1}{2} \mathbf{F} \times \mathbf{F}; \quad H_{iI} = \frac{1}{2} \mathcal{E}_{ijk} \mathcal{E}_{IJK} F_{jJ} F_{kK}; \quad (2.31a)$$

$$J = \frac{1}{3} \mathbf{H} : \mathbf{F}; \quad J = \frac{1}{3} H_{iI} F_{iI}. \quad (2.31b)$$

As shown in Figure 4.1,  $\{\mathbf{F}, \mathbf{H}, J\}$  are the kinematic measures relating the differential fibre, area and volume elements from initial  $\{d\mathbf{X}, d\mathbf{A}, dV\}$  to final  $\{dx, da, dv\}$  configuration. Once again, defining  $\delta\mathbf{u}$  and  $\Delta\mathbf{u}$  as virtual and incremental variations of  $\mathbf{x}$ , respectively, assuming that both  $\delta\mathbf{u}$  and  $\Delta\mathbf{u}$  satisfy compatible homogeneous displacement based boundary conditions, the first and second directional derivatives of the kinematic measures  $\{\mathbf{F}, \mathbf{H}, J\}$  with respect to virtual and incremental variations of the geometry can then be evaluated as

$$D\mathbf{F}[\delta\mathbf{u}] = \nabla_0 \delta\mathbf{u}; \quad (2.32a)$$

$$D^2\mathbf{F}[\delta\mathbf{u}; \Delta\mathbf{u}] = \mathbf{0}; \quad (2.32b)$$

$$D\mathbf{H}[\delta\mathbf{u}] = \mathbf{F} \times \nabla_0 \delta\mathbf{u}; \quad (2.32c)$$

$$D^2\mathbf{H}[\delta\mathbf{u}; \Delta\mathbf{u}] = \nabla_0 \delta\mathbf{u} \times \nabla_0 \Delta\mathbf{u}; \quad (2.32d)$$

$$DJ[\delta\mathbf{u}] = \mathbf{H} : \nabla_0 \delta\mathbf{u}; \quad (2.32e)$$

$$D^2J[\delta\mathbf{u}; \Delta\mathbf{u}] = \mathbf{F} : (\nabla_0 \delta\mathbf{u} \times \nabla_0 \Delta\mathbf{u}). \quad (2.32f)$$

#### 2.4.2 The internal energy density in polyconvex hyperelasticity

In the context of nonlinear elasticity, the concept of polyconvexity was first introduced by Ball [16, 17] in order to establish sufficient conditions for the existence of solutions in nonlinear elasticity. It is recognised these days [28, 29, 271, 270, 27] that polyconvexity is a useful mathematical requirement that can be used to ensure the well-posedness of the equations in the large strain regime. The internal energy density  $e$ , encapsulating the constitutive information necessary to close the system of governing equations defined earlier can be re-written in terms of the fundamental kinematics as

$$e(\mathbf{F}) = \tilde{W}(\mathbf{F}, \mathbf{H}, J), \quad (2.33)$$

where  $\tilde{W}$  represents a polyconvex energy functional in terms of the extended set of arguments  $\mathcal{V}_{FHJ} = \{\mathbf{F}, \mathbf{H}, J\}$ . Following [29], the first Piola-Kirchhoff stress tensor and can be obtained

from the linearisation of the polyconvex energy as

$$De[\delta\mathbf{u}] = D\tilde{W}[D\mathbf{F}[\delta\mathbf{u}], D\mathbf{H}[\delta\mathbf{u}], DJ[\delta\mathbf{u}]] = (\boldsymbol{\Sigma}_{\mathbf{F}} + \boldsymbol{\Sigma}_{\mathbf{H}} \times \mathbf{F} + \boldsymbol{\Sigma}_J \mathbf{H}) : \nabla_0 \delta\mathbf{u}. \quad (2.34)$$

Comparison of (2.34) against (2.8), leads to the evaluation of the first Piola-Kirchoff tensor

$$\mathbf{P} = \boldsymbol{\Sigma}_{\mathbf{F}} + \boldsymbol{\Sigma}_{\mathbf{H}} \times \mathbf{F} + \boldsymbol{\Sigma}_J \mathbf{H}; \quad P_{IJ} = \Sigma_{F_{IJ}} + \mathcal{E}_{ijk} \mathcal{E}_{IJK} \Sigma_{H_{IJ}} F_{kK} + \Sigma_J H_{IJ}, \quad (2.35)$$

where  $\Sigma_{\mathbf{A}} = \frac{\partial \tilde{W}}{\partial \mathbf{A}}$ , where  $\mathbf{A}$  can represent any element from the set  $\mathcal{V}_{FHJ}$ . Further consistent linearisation of the polyconvex energy required for Newton-Raphson iteration leads to the constitutive and geometric terms, which following [28, 29], can be computed as

$$D^2 e[\delta\mathbf{u}; \Delta\mathbf{u}] = [\mathbb{M}_{\delta}^{FHJ}]^T [\mathbb{H}_{\tilde{W}}] [\mathbb{M}_{\Delta}^{FHJ}] + (\boldsymbol{\Sigma}_{\mathbf{H}} + \boldsymbol{\Sigma}_J \mathbf{F}) : (\nabla_0 \delta\mathbf{u} \times \nabla_0 \Delta\mathbf{u}), \quad (2.36)$$

where

$$\begin{aligned} [\mathbb{M}_{\delta}^{FHJ}] &= [(\nabla_0 \delta\mathbf{u}) : (\mathbf{F} \times \nabla_0 \delta\mathbf{u}) : (\mathbf{H} : \nabla_0 \delta\mathbf{u})], \\ [\mathbb{M}_{\Delta}^{FHJ}] &= \begin{bmatrix} : \nabla_0 \Delta\mathbf{u} \\ : (\mathbf{F} \times \nabla_0 \Delta\mathbf{u}) \\ (\mathbf{H} : \nabla_0 \Delta\mathbf{u}) \end{bmatrix}, \end{aligned}$$

and  $\mathbb{H}_{\tilde{W}}$  represents the symmetric positive definite Hessian operator given by

$$[\mathbb{H}_{\tilde{W}}] = \begin{bmatrix} \tilde{W}_{\mathbf{FF}} & \tilde{W}_{\mathbf{FH}} & \tilde{W}_{\mathbf{FJ}} \\ \tilde{W}_{\mathbf{HF}} & \tilde{W}_{\mathbf{HH}} & \tilde{W}_{\mathbf{HJ}} \\ \tilde{W}_{\mathbf{JF}} & \tilde{W}_{\mathbf{JH}} & \tilde{W}_{\mathbf{JJ}} \end{bmatrix}, \quad (2.37)$$

where  $W_{\mathbf{AB}} = \frac{\partial^2 \tilde{W}}{\partial \mathbf{A} \partial \mathbf{B}}$ , where  $\mathbf{A}$  and  $\mathbf{B}$  can represent any two elements from the set  $\mathcal{V}_{FHJ}$ . In effect, the above expression for the elasticity tensor separates the material dependencies or physics of the problem (encapsulated in the Hessian) from the geometry dependencies included via the initial stress term. From (2.37) the tangent elasticity tensor  $\tilde{\mathcal{C}}$  described in (2.10) can alternatively be described in terms of the set of work-conjugates  $\mathcal{V}_{FHJ}$  as

$$\begin{aligned} \tilde{\mathcal{C}} = & W_{\mathbf{FF}} + \mathbf{F} \times (W_{\mathbf{HH}} \times \mathbf{F}) + W_{\mathbf{JJ}} \mathbf{H} \otimes \mathbf{H} + 2(W_{\mathbf{FH}} \times \mathbf{F})^{\text{sym}} \\ & + 2(W_{\mathbf{FJ}} \otimes \mathbf{H})^{\text{sym}} + 2((\mathbf{F} \times W_{\mathbf{HJ}}) \otimes \mathbf{H})^{\text{sym}} + \mathcal{A} \end{aligned} \quad (2.38)$$

where

$$\mathcal{A}_{IjJ} = \mathcal{E}_{ijp} \mathcal{E}_{IJP} (\boldsymbol{\Sigma}_{\mathbf{H}} + \boldsymbol{\Sigma}_J \boldsymbol{\Sigma}_{\mathbf{H}})_{pP}.$$

Furthermore, for any symmetric fourth order tensor, its symmetric version can be computed as  $\mathcal{T}_{iIjJ}^{\text{sym}} = \frac{1}{2}(\mathcal{T}_{iIjJ} + \mathcal{T}_{jJiI})$ . Due to the disappearance of inverse operations, this alternative representation of the Hessian has a much lower computational cost in comparison to (2.15).

### 2.4.3 Material characterisation in the reference configuration

The Mooney-Rivlin model defined in (2.11) in terms of  $\mathbf{F}$  is indeed a simple internal energy functional which complies with the definition of polyconvexity in (2.33)

$$\tilde{W}^{mn}(\mathbf{F}, \mathbf{H}, J) = \mu_1 II_{\mathbf{F}} + \mu_2 II_{\mathbf{H}} + f(J). \quad (2.39)$$

Using (2.35), the first Piola-Kirchhoff stress tensor  $\mathbf{P}$  for this model can be computed as

$$\mathbf{P} = 2\mu_1 \mathbf{F} + 2\mu_2 \mathbf{H} \times \mathbf{F} + f'(J) \mathbf{H}, \quad (2.40)$$

and the non-zero components of the Hessian operator  $\mathbb{H}_{\tilde{W}^{mn}}$  are given by

$$\tilde{W}_{\mathbf{FF}}^{mn} = 2\mu_1 \mathcal{I}; \quad \tilde{W}_{\mathbf{HH}}^{mn} = 2\mu_2 \mathcal{I}; \quad \tilde{W}_{\mathbf{JJ}}^{mn} = f''(J). \quad (2.41)$$

The tensor  $\tilde{\mathcal{C}}$  can now be obtained from (2.41) using (2.38).

## 2.5 The objective representation in polyconvex elasticity

The requirement for objectivity or material frame indifference, and in particular our motivation for particularisation of polyconvex nonlinear elasticity to small strains dictate that the polyconvex internal energy be represented through a set of symmetric kinematic measures. These kinematic measures were already introduced in section 2.3 as  $\{\mathbf{C}, \mathbf{G}, C\}$ . It is however important to note that, the objective representation of the internal energy in terms of  $\{\mathbf{C}, \mathbf{G}, C\}$  may not necessarily be convex in any components of the set  $\{\mathbf{C}, \mathbf{G}, C\}$ . It is merely an objective re-expression of the internal energy in terms of a symmetric kinematic set.

### 2.5.1 Objective kinematics

The symmetric kinematic measures  $\{\mathbf{C}, \mathbf{G}, C\}$  introduced in section 2.3 can be used to re-express the equations of polyconvex elasticity in an objective setting. Using the tensor cross product, we can re-write the this set of kinematics as

$$\mathbf{C} = \mathbf{F}^T \mathbf{F}; \quad C_{IJ} = F_{IM} F_{MJ} \quad (2.42a)$$

$$\mathbf{G} = \frac{1}{2} \mathbf{C} \times \mathbf{C}; \quad G_{iI} = \frac{1}{2} \mathcal{E}_{ijk} \mathcal{E}_{IJK} C_{jJ} C_{kK}; \quad (2.42b)$$

$$C = \frac{1}{3} \mathbf{G} : \mathbf{C}; \quad C = \frac{1}{3} G_{iI} C_{iI}. \quad (2.42c)$$

The first and second directional derivatives of the symmetric kinematic measures with respect to virtual and incremental variation of the geometry can now be expressed using the cross product algebra, as

$$DC[\delta \mathbf{u}] = D(\mathbf{F}^T \mathbf{F})[\delta \mathbf{u}] = (\nabla_0 \delta \mathbf{u})^T \mathbf{F} + \mathbf{F}^T \nabla_0 \delta \mathbf{u}; \quad (2.43a)$$

$$D^2 \mathbf{C}[\delta \mathbf{u}; \Delta \mathbf{u}] = (\nabla_0 \delta \mathbf{u})^T (\nabla_0 \Delta \mathbf{u}) + (\nabla_0 \Delta \mathbf{u})^T (\nabla_0 \delta \mathbf{u}); \quad (2.43b)$$

$$DG[\delta \mathbf{u}] = \mathbf{C} \times DC[\delta \mathbf{u}]; \quad (2.43c)$$

$$D^2 \mathbf{G}[\delta \mathbf{u}; \Delta \mathbf{u}] = \mathbf{C} \times D^2 \mathbf{C}[\delta \mathbf{u}; \mathbf{u}] + DC[\Delta \mathbf{u}] \times DC[\delta \mathbf{u}]; \quad (2.43d)$$

$$DC[\delta \mathbf{u}] = \mathbf{G} : DC[\delta \mathbf{u}]; \quad (2.43e)$$

$$\begin{aligned} D^2 \mathbf{C}[\delta \mathbf{u}; \Delta \mathbf{u}] &= D^2 \mathbf{C}[\delta \mathbf{u}; \Delta \mathbf{u}] : \mathbf{G} + DC[\delta \mathbf{u}] : (DC[\Delta \mathbf{u}] \times \mathbf{C}) \\ &= D^2 \mathbf{C}[\delta \mathbf{u}; \Delta \mathbf{u}] : \mathbf{G} + \mathbf{C} : (DC[\delta \mathbf{u}] \times DC[\Delta \mathbf{u}]). \end{aligned} \quad (2.43f)$$

### 2.5.2 The internal energy density in objective polyconvex hyperelasticity

The internal energy density  $e$ , encapsulating the constitutive information necessary to close the system of governing equations defined earlier can be re-written in terms of the symmetric kinematic measures from its polyconvex description (2.33) as

$$e(\nabla_0 \mathbf{x}) \underset{\Leftarrow}{=} \tilde{W}(\mathbf{F}, \mathbf{H}, J) \underset{\Rightarrow}{=} W(\mathbf{C}, \mathbf{G}, C), \quad (2.44)$$

where  $W$  represents an energy functional with respect to the extended set of symmetric mechanical kinematics  $\mathcal{V}_{CGC} = \{\mathbf{C}, \mathbf{G}, C\}$ . It is worth noting that  $W$  is not strictly convex with respect to the individual components of the set  $\mathcal{V}$ , but rather an objective re-expression of the polyconvex functional  $\tilde{W}$ , in that in (2.44),  $W$  is identical to  $\tilde{W}$ . Notice that, constructing a polyconvex energy (i.e.  $\tilde{W}$ ) is a necessary first step for a materially frame indifferent representation (i.e.  $W$ ), but the vice-versa is not true, in that an objective energy may not necessarily be convex with respect to its set of independent symmetric kinematics. Combination of (2.44) and the first law of thermodynamics yield a set of work conjugates for the symmetric mechanical kinematic set  $\mathcal{V}_{CGC} = \{\mathbf{C}, \mathbf{G}, C\}$ , defined as [29]

$$De[\delta \mathbf{u}] = DW[DC[\delta \mathbf{u}], DG[\delta \mathbf{u}], DC[\delta \mathbf{u}]] = (\Sigma_C + \Sigma_G \times C + \Sigma_C G) : \frac{1}{2} DC[\delta \mathbf{u}]. \quad (2.45)$$

Comparison of (2.45) against (2.20), leads to the evaluation of the second Piola-Kirchoff tensor

$$\mathbf{S} = \boldsymbol{\Sigma}_C + \boldsymbol{\Sigma}_G \times \mathbf{C} + \boldsymbol{\Sigma}_C \mathbf{G}. \quad (2.46)$$

where  $\boldsymbol{\Sigma}_A = 2\frac{\partial W}{\partial A}$ , where  $A$  can represent any element from the set  $\mathcal{V}_{CGC}$ . Further consistent linearisation of the polyconvex energy required for Newton-Raphson iteration, leads to the constitutive and geometric terms, which following [28, 29], can be computed as

$$\begin{aligned} D^2e[\delta\mathbf{u}; \Delta\mathbf{u}] &= [\mathbb{M}_\delta^{CGC}]^T [\mathbb{H}_W] [\mathbb{M}_\Delta^{CGC}] + (\boldsymbol{\Sigma}_G + \boldsymbol{\Sigma}_C \mathbf{C}) : (\mathbf{F}^T \nabla_0 \delta\mathbf{u} \times \mathbf{F}^T \nabla_0 \Delta\mathbf{u}) \\ &\quad + \mathbf{S} : [(\nabla_0 \delta\mathbf{u})^T (\nabla_0 \Delta\mathbf{u})], \end{aligned} \quad (2.47)$$

where

$$\begin{aligned} [\mathbb{M}_\delta^{CGC}] &= [(\mathbf{F}^T \nabla_0 \delta\mathbf{u}) : (\mathbf{C} \times \mathbf{F}^T \nabla_0 \delta\mathbf{u}) : (\mathbf{G} : \mathbf{F}^T \nabla_0 \delta\mathbf{u})], \\ [\mathbb{M}_\Delta^{CGC}] &= \begin{bmatrix} : \mathbf{F}^T \nabla_0 \Delta\mathbf{u} \\ : (\mathbf{C} \times \mathbf{F}^T \nabla_0 \Delta\mathbf{u}) \\ (\mathbf{G} : \mathbf{F}^T \nabla_0 \Delta\mathbf{u}) \end{bmatrix}, \end{aligned}$$

and  $\mathbb{H}_W$  represents the symmetric positive definite Hessian operator given by

$$[\mathbb{H}_W] = \begin{bmatrix} W_{CC} & W_{CG} & W_{CC} \\ W_{GC} & W_{GG} & W_{GC} \\ W_{CC} & W_{CG} & W_{CC} \end{bmatrix}, \quad (2.48)$$

where  $W_{AB} = 4\frac{\partial^2 W}{\partial A \partial B}$ , where  $A$  and  $B$  can represent any two elements from the set  $\mathcal{V}_{CGC}$ . From (2.48) the tangent elasticity tensor  $\mathbf{C}$  described in (2.22), can alternatively be described in terms of the set of work-conjugates  $\mathcal{V}_{CGC}$  as

$$\begin{aligned} \mathbf{C} &= W_{CC} + \mathbf{C} \times (W_{GG} \times \mathbf{C}) + W_{CC} \mathbf{G} \otimes \mathbf{G} + 2(W_{CG} \times \mathbf{C})^{\text{sym}} \\ &\quad + 2(W_{CC} \otimes \mathbf{G})^{\text{sym}} + 2((\mathbf{C} \times W_{GC}) \otimes \mathbf{G})^{\text{sym}} + \mathbf{B} \end{aligned} \quad (2.49)$$

where

$$\mathcal{B}_{IjJ} = \mathcal{E}_{ijp} \mathcal{E}_{IJP} (\boldsymbol{\Sigma}_G + \boldsymbol{\Sigma}_C \boldsymbol{\Sigma}_G)_{pP}.$$

It is important to note, that as opposed to the polyconvex variant of the above Hessian operator expressed in terms of the fundamental kinematic set  $\mathcal{V}_{FHJ} = \{\mathbf{F}, \mathbf{H}, J\}$  in (2.37), the Hessian operator in (2.48) is not strictly positive definite as polyconvexity is not imposed with respect to the set  $\mathcal{V}_{CGC}$  and hence ellipticity (i.e. rank-one convexity) of the internal energy based on this constitutive term alone cannot be established.

### 2.5.3 Material characterisation in the reference configuration

The polyconvex Mooney-Rivlin model defined in (2.39) in terms of  $\{\mathbf{F}, \mathbf{H}, J\}$  can be re-expressed in terms of symmetric kinematic set  $\mathcal{V}_{CGC}$  complying to the definition given in (2.44)

$$W^{mn}(\mathbf{C}, \mathbf{G}, C) = \mu_1 I_C + \mu_2 I_G + f(C). \quad (2.50)$$

Using (2.46), the second Piola-Kirchhoff stress tensor  $\mathbf{S}$ , for this model can be computed as

$$\mathbf{S} = 2\mu_1 \mathbf{I} + 2\mu_2 \mathbf{I} \times \mathbf{C} + f'(C) \mathbf{G},$$

and the only non-zero component of the Hessian operator  $\mathbb{H}_{W^{mn}}$  are given by

$$W_{CC}^{mn} = 4f''(C). \quad (2.51)$$

The tensors  $\mathbf{C}$  can now be obtained from (2.51) using (2.49).

## 2.6 Polyconvex nonlinear elasticity in spatial setting

In this section, the polyconvex nonlinear elasticity is presented in the spatial setting. Our future development on a unified continuum mechanics formulation for linear, geometrically linearised and nonlinear approach to elasticity would be based on these formulation and on an updated Lagrangian framework.

### 2.6.1 The Cauchy stress tensor and spatial tangent operator

With a particularisation to the case of small strains in mind, in addition to the first and second Piola-Kirchoff stress tensors, it is also necessary to derive expressions for the Cauchy  $\boldsymbol{\sigma}$  (or Kirchhoff  $\boldsymbol{\tau}$ ) stress tensors. The expressions for the Cauchy stress tensor and spatial tangent elasticity tensor can be derived using the standard push forward operations [30], for the case of classical elasticity

$$\boldsymbol{\tau} = J\boldsymbol{\sigma} = \mathbf{F}\mathbf{S}\mathbf{F}^T; \quad (2.52)$$

$$J\mathbf{c} = [\mathbf{C}]_{IJKL}[\mathbf{F}]_{iI}[\mathbf{F}]_{jJ}[\mathbf{F}]_{kK}[\mathbf{F}]_{lL}, \quad (2.53)$$

where  $\boldsymbol{\sigma}$  is the symmetric second order Cauchy stress tensor and  $\mathbf{c}$  is the fourth order tangent elasticity operator in spatial setting. For the case of polyconvex elasticity, similar push forward operations can be applied on the work-conjugates to obtain the Cauchy stress tensor as

$$J\boldsymbol{\sigma} = \boldsymbol{\tau} = J(\boldsymbol{\sigma}_C + \boldsymbol{\sigma}_G \times \mathbf{I} + \sigma_C \mathbf{I}) \quad (2.54)$$

where  $\mathbf{I}$  denotes the second order identity tensor and the spatial work conjugates are given

$$J\boldsymbol{\sigma}_C = \mathbf{F}\boldsymbol{\Sigma}_C\mathbf{F}^T; \quad J\boldsymbol{\sigma}_G = \mathbf{H}\boldsymbol{\Sigma}_G\mathbf{H}^T; \quad J\sigma_C = C\Sigma_C. \quad (2.55)$$

The spatial form of the tangent operator can be computed using the standard push-forward operations to yield

$$\begin{aligned} D^2e[\delta\mathbf{u}; \Delta\mathbf{u}] &= [\mathbb{S}_\delta]^T \phi_*[\mathbb{H}_W] [\mathbb{S}_\Delta] + J(\boldsymbol{\sigma}_G + \sigma_C \mathbf{I}) : (\nabla\delta\mathbf{u} \times \nabla\Delta\mathbf{u}) \\ &\quad + J\boldsymbol{\sigma} : \left[ (\nabla\delta\mathbf{v})^T (\nabla\Delta\mathbf{u}) \right], \end{aligned} \quad (2.56)$$

where

$$[\mathbb{S}_\delta] = [\nabla\delta\mathbf{u} : (\nabla\delta\mathbf{u} \times \mathbf{I}) : (\nabla\delta\mathbf{u} : \mathbf{I})], \quad (2.57)$$

$$[\mathbb{S}_\Delta] = \begin{bmatrix} : \nabla\Delta\mathbf{u} \\ : (\nabla\Delta\mathbf{u} \times \mathbf{I}) \\ (\nabla\Delta\mathbf{u} : \mathbf{I}) \end{bmatrix}, \quad (2.58)$$

with the fourth order tensor  $\mathbf{c}$  given as

$$J\phi_*[\mathbb{H}_W] = \begin{bmatrix} (W_{CC})_{IJKL}\mathbf{F}_{iI}\mathbf{F}_{jJ}\mathbf{F}_{kK}\mathbf{F}_{lL} & (W_{CG})_{IJKL}\mathbf{F}_{iI}\mathbf{F}_{jJ}\mathbf{H}_{kK}\mathbf{H}_{lL} & J^2(W_{CC})_{IJ}\mathbf{F}_{iI}\mathbf{F}_{jJ} \\ (W_{GC})_{KLIJ}\mathbf{H}_{kK}\mathbf{H}_{lL}\mathbf{F}_{iI}\mathbf{F}_{jJ} & (W_{GG})_{IJKL}\mathbf{H}_{iI}\mathbf{H}_{jJ}\mathbf{H}_{kK}\mathbf{H}_{lL} & J^2(W_{GC})_{IJ}\mathbf{H}_{iI}\mathbf{H}_{jJ} \\ J^2(W_{CC})_{JI}\mathbf{F}_{iI}\mathbf{F}_{jJ} & J^2(W_{CG})_{JI}\mathbf{H}_{iI}\mathbf{H}_{jJ} & J^2(W_{CC})J^2 \end{bmatrix}. \quad (2.59a)$$

### 2.6.2 Governing equations of continuum mechanics in spatial setting

Let us assume that the domain defined by the deformable body is subjected to a body force per unit of deformed volume  $\mathbf{f}$  and a traction force per unit of deformed area  $\mathbf{t}$  applied on  $\partial_t v \in \partial v$ , such that  $\partial_t v \cup \partial_u v = \partial v$  and  $\partial_t v \cap \partial_u v = \emptyset$ . The conservation of linear momentum in the global from leads to the integral of the translational equilibrium equations as

$$\int_v \mathbf{f} dv + \int_{\partial_t v} \mathbf{t} da = \mathbf{0}. \quad (2.60)$$

The above integral equation governing the physics of a deformable system, can be summarised in the local (strong) form and spatial setting as follows [30, 29, 28].

$$\operatorname{div}\boldsymbol{\sigma} + \mathbf{f} = \mathbf{0} \quad \text{in } v; \quad (2.61\text{a})$$

$$\boldsymbol{\sigma}\mathbf{n} = \mathbf{t} \quad \text{on } \partial_t v; \quad (2.61\text{b})$$

$$\phi = \bar{\phi} \quad \text{on } \partial_u v. \quad (2.61\text{c})$$

## 2.7 The tensor cross product

One of the key elements of in the development of the current framework proposed is the extension of the standard vector cross product to define the cross product between second order tensors and between tensors and vectors and high order tensors. This rediscovers the work of de Boer [65] which, to the best knowledge of the author, first appeared in [28, 29] as an English language publication.

### 2.7.1 Definition for second order tensors and associated properties

The original nomenclature for the tensor cross product discussed in [65] is “Das äußere Tensorprodukt von Tensoren” which has been translated here as tensor cross product.

The left cross product of a vector  $\mathbf{v}$  and a second order tensor  $\mathbf{A}$  to give a second order tensor denoted  $\mathbf{v} \times \mathbf{A}$  is defined so that when applied to a general vector  $\mathbf{w}$  gives:

$$(\mathbf{v} \times \mathbf{A}) \mathbf{w} = \mathbf{v} \times (\mathbf{A} \mathbf{w}); \quad (\mathbf{v} \times \mathbf{A})_{ij} = \mathcal{E}_{ikl} v_k A_{lj} \quad (2.62)$$

where  $\mathcal{E}_{ikl}$  denote the standard third order alternating tensor components, repeated indices indicate summation and  $\times$  is the standard vector cross product. The above operation is in fact equivalent to performing a standard cross product between each row of  $\mathbf{A}$  and  $\mathbf{v}$ . Similarly, the right cross product of a second order tensor  $\mathbf{A}$  by a vector  $\mathbf{v}$  to give a second order tensor denoted  $\mathbf{A} \times \mathbf{v}$  is defined so that for every vector  $\mathbf{w}$  the following relationship applies:

$$(\mathbf{A} \times \mathbf{v}) \mathbf{w} = \mathbf{A} (\mathbf{v} \times \mathbf{w}); \quad (\mathbf{A} \times \mathbf{v})_{ij} = \mathcal{E}_{jkl} A_{ik} v_l. \quad (2.63)$$

The effect is now to replace the rows of  $\mathbf{A}$  by the cross products of its original rows by  $\mathbf{v}$ . Finally, the cross product of two second order tensors  $\mathbf{A}$  and  $\mathbf{B}$  to give a new second order tensor denoted  $\mathbf{A} \times \mathbf{B}$  is defined so that for any arbitrary vectors  $\mathbf{v}$  and  $\mathbf{w}$  gives:

$$\mathbf{v} \cdot (\mathbf{A} \times \mathbf{B}) \mathbf{w} = (\mathbf{v} \times \mathbf{A}) : (\mathbf{B} \times \mathbf{w}); \quad (\mathbf{A} \times \mathbf{B})_{ij} = \mathcal{E}_{ikl} \mathcal{E}_{jmn} A_{km} B_{ln}. \quad (2.64)$$

In this work, the tensor cross product will be mostly applied between two-point tensors, however high order tensor cross products are also evaluated in the final chapter. For this purpose, the above definition can be particularised to second order two-point tensors or material tensors as,

$$(\mathbf{A} \times \mathbf{B})_{iI} = \mathcal{E}_{ijk} \mathcal{E}_{IJK} A_{jJ} B_{kK}; \quad (\mathbf{A} \times \mathbf{B})_{IJ} = \mathcal{E}_{IKL} \mathcal{E}_{JMN} A_{KM} B_{LN}. \quad (2.65)$$

The practical evaluation of these products in the box below. It is easy to show using simply algebraic manipulations based on the permutation properties of  $\mathcal{E}$  or the fact that  $\mathcal{E}_{ijk} \mathcal{E}_{kln} = \delta_{il} \delta_{jn} - \delta_{in} \delta_{jl}$ , that the above tensor cross products satisfy the following properties (note that  $\mathbf{v}, \mathbf{v}_1, \mathbf{v}_2, \mathbf{w}, \mathbf{w}_1$  and  $\mathbf{w}_2$  denote arbitrary vectors and  $\mathbf{A}, \mathbf{A}_1, \mathbf{A}_2, \mathbf{B}, \mathbf{B}_1, \mathbf{B}_2$  and  $\mathbf{C}$  are second order tensors):

$$\mathbf{A} \times \mathbf{B} = \mathbf{B} \times \mathbf{A}; \quad (2.66\text{a})$$

$$(\mathbf{A} \times \mathbf{B})^T = \mathbf{A}^T \times \mathbf{B}^T; \quad (2.66\text{b})$$

$$\mathbf{A} \times (\mathbf{B}_1 + \mathbf{B}_2) = \mathbf{A} \times \mathbf{B}_1 + \mathbf{A} \times \mathbf{B}_2; \quad (2.66\text{c})$$

$$\alpha (\mathbf{A} \times \mathbf{B}) = (\alpha \mathbf{A}) \times \mathbf{B} = \mathbf{A} \times (\alpha \mathbf{B}); \quad (2.66\text{d})$$

$$(\mathbf{A} \times \mathbf{B}) : \mathbf{C} = (\mathbf{B} \times \mathbf{C}) : \mathbf{A} = (\mathbf{A} \times \mathbf{C}) : \mathbf{B}; \quad (2.66e)$$

$$\mathbf{A} \times \mathbf{I} = (\text{tr} \mathbf{A}) \mathbf{I} - \mathbf{A}^T; \quad (2.66f)$$

$$\mathbf{I} \times \mathbf{I} = 2\mathbf{I}; \quad (2.66g)$$

$$(\mathbf{A} \times \mathbf{A}) : \mathbf{A} = 6 \det \mathbf{A}; \quad (2.66h)$$

$$\text{Cof} \mathbf{A} = \frac{1}{2} \mathbf{A} \times \mathbf{A}; \quad (2.66i)$$

$$(\mathbf{v}_1 \otimes \mathbf{v}_2) \times (\mathbf{w}_1 \otimes \mathbf{w}_2) = (\mathbf{v}_1 \times \mathbf{w}_1) \otimes (\mathbf{v}_2 \times \mathbf{w}_2); \quad (2.66j)$$

$$\mathbf{v} \times (\mathbf{A} \times \mathbf{w}) = (\mathbf{v} \times \mathbf{A}) \times \mathbf{w} = \mathbf{v} \times \mathbf{A} \times \mathbf{w}; \quad (2.66k)$$

$$\mathbf{A} \times (\mathbf{v} \otimes \mathbf{w}) = -\mathbf{v} \times \mathbf{A} \times \mathbf{w}; \quad (2.66l)$$

$$(\mathbf{A} \times \mathbf{B})(\mathbf{v} \times \mathbf{w}) = (\mathbf{Av}) \times (\mathbf{Bw}) + (\mathbf{Bv}) \times (\mathbf{Aw}); \quad (2.66m)$$

$$(\mathbf{A}_1 \times \mathbf{A}_2)(\mathbf{B}_1 \times \mathbf{B}_2) = (\mathbf{A}_1 \mathbf{B}_1) \times (\mathbf{A}_2 \mathbf{B}_2) + (\mathbf{A}_1 \mathbf{B}_2) \times (\mathbf{A}_2 \mathbf{B}_1); \quad (2.66n)$$

$$(\mathbf{A}_1 \mathbf{B}) \times (\mathbf{A}_2 \mathbf{B}) = (\mathbf{A}_1 \times \mathbf{A}_2) \text{Cof} \mathbf{B}. \quad (2.66o)$$

### 2.7.2 Definition of tensor cross product for some selected high order tensors

The tensor cross product can also be defined between tensors of any arbitrary order. In the following, the tensor cross products appearing in the later formulations are listed, where  $\mathcal{K}$  and  $\mathcal{L}$  represent third order tensors and  $\mathbb{M}$  and  $\mathbb{N}$  represent fourth order tensors. Note that for high order tensors, multiple definitions of the tensor cross product are possible.

$$[\mathcal{K} \times \mathbf{A}]_{PiI} = \mathcal{E}_{ijk} \mathcal{E}_{IJK} [\mathcal{K}]_{PjJ} [\mathbf{A}]_{kK}; \quad (2.67a)$$

$$[\mathbf{A} \times \mathcal{K}]_{iIP} = \mathcal{E}_{ijk} \mathcal{E}_{IJK} [\mathbf{A}]_{jJ} [\mathcal{K}]_{kKP}; \quad (2.67b)$$

$$[\mathbb{M} \times \mathbf{A}]_{pPiI} = \mathcal{E}_{ijk} \mathcal{E}_{IJK} [\mathbb{M}]_{pPjJ} [\mathbf{A}]_{kK}; \quad (2.67c)$$

$$[\mathbf{A} \times \mathbb{M}]_{iIpP} = \mathcal{E}_{ijk} \mathcal{E}_{IJK} [\mathbf{A}]_{jJ} [\mathbb{M}]_{kKpP}; \quad (2.67d)$$

$$[\mathcal{K} \times \mathcal{L}]_{PiIQ} = \mathcal{E}_{ijk} \mathcal{E}_{IJK} [\mathcal{K}]_{PjJ} [\mathcal{L}]_{kKQ}; \quad (2.67e)$$

$$[\mathcal{K} \times \mathcal{L}]_{PiIQ} = \mathcal{E}_{ijk} \mathcal{E}_{IJK} [\mathcal{K}]_{PjJ} [\mathcal{L}]_{QkK}; \quad (2.67f)$$

$$[\mathcal{K} \times \mathcal{L}]_{PQiI} = \mathcal{E}_{ijk} \mathcal{E}_{IJK} [\mathcal{K}]_{PjJ} [\mathcal{L}]_{kKQ}; \quad (2.67g)$$

$$[\mathcal{K} \times \mathcal{L}]_{PQiI} = \mathcal{E}_{ijk} \mathcal{E}_{IJK} [\mathcal{K}]_{PjJ} [\mathcal{L}]_{QkK}; \quad (2.67h)$$

$$[\mathcal{K} \times \mathcal{L}]_{iIPQ} = \mathcal{E}_{ijk} \mathcal{E}_{IJK} [\mathcal{K}]_{PjJ} [\mathcal{L}]_{kKQ}; \quad (2.67i)$$

$$[\mathcal{K} \times \mathcal{L}]_{iIPQ} = \mathcal{E}_{ijk} \mathcal{E}_{IJK} [\mathcal{K}]_{PjJ} [\mathcal{L}]_{QkK}; \quad (2.67j)$$

$$[\mathbb{M} \times \mathbb{N}]_{pPiIqQ} = \mathcal{E}_{ijk} \mathcal{E}_{IJK} [\mathbb{M}]_{pPjJ} [\mathbb{N}]_{kKqQ}; \quad (2.67k)$$

$$[\mathbb{M} \times \mathbb{N}]_{pPiIqQ} = \mathcal{E}_{ijk} \mathcal{E}_{IJK} [\mathbb{M}]_{pPjJ} [\mathbb{N}]_{qQkK}; \quad (2.67l)$$

$$[\mathbb{M} \times \mathbb{N}]_{pPqQiI} = \mathcal{E}_{ijk} \mathcal{E}_{IJK} [\mathbb{M}]_{pPjJ} [\mathbb{N}]_{kKqQ}; \quad (2.67m)$$

$$[\mathbb{M} \times \mathbb{N}]_{pPqQiI} = \mathcal{E}_{ijk} \mathcal{E}_{IJK} [\mathbb{M}]_{pPjJ} [\mathbb{N}]_{qQkK}; \quad (2.67n)$$

$$[\mathbb{M} \times \mathbb{N}]_{iIpPqQ} = \mathcal{E}_{ijk} \mathcal{E}_{IJK} [\mathbb{M}]_{pPjJ} [\mathbb{N}]_{kKqQ}; \quad (2.67o)$$

$$[\mathbb{M} \times \mathbb{N}]_{iIpPqQ} = \mathcal{E}_{ijk} \mathcal{E}_{IJK} [\mathbb{M}]_{pPjJ} [\mathbb{N}]_{qQkK}. \quad (2.67p)$$

**Explicit matrix form of tensor cross products:**

$$[\mathbf{v} \times \mathbf{A}] = \begin{bmatrix} v_y A_{zx} - v_z A_{yx} & v_y A_{zy} - v_z A_{yy} & v_y A_{zz} - v_z A_{yz} \\ v_z A_{xx} - v_x A_{zx} & v_z A_{xy} - v_x A_{zy} & v_z A_{xz} - v_x A_{zz} \\ v_x A_{yx} - v_y A_{xx} & v_x A_{yy} - v_y A_{xy} & v_x A_{yz} - v_y A_{xz} \end{bmatrix}$$

$$[\mathbf{A} \times \mathbf{w}] = \begin{bmatrix} A_{xy}v_z - A_{xz}v_y & A_{xz}v_x - A_{xx}v_z & A_{xx}v_y - A_{xy}v_x \\ A_{yy}v_z - A_{yz}v_x & A_{yz}v_x - A_{yx}v_z & A_{yx}v_y - A_{yy}v_x \\ A_{yx}v_z - A_{xx}v_y & A_{yy}v_x - A_{xy}v_z & A_{yz}v_y - A_{xz}v_x \end{bmatrix}$$

$$[\mathbf{A} \times \mathbf{B}] = \begin{bmatrix} [\mathbf{A} \times \mathbf{B}]_{xx} & [\mathbf{A} \times \mathbf{B}]_{xy} & [\mathbf{A} \times \mathbf{B}]_{xz} \\ [\mathbf{A} \times \mathbf{B}]_{yx} & [\mathbf{A} \times \mathbf{B}]_{yy} & [\mathbf{A} \times \mathbf{B}]_{yz} \\ [\mathbf{A} \times \mathbf{B}]_{zx} & [\mathbf{A} \times \mathbf{B}]_{zy} & [\mathbf{A} \times \mathbf{B}]_{zz} \end{bmatrix}$$

$$[\mathbf{A} \times \mathbf{B}]_{xx} = A_{yy}B_{zz} - A_{yz}B_{zy} + A_{zz}B_{yy} - A_{zy}B_{yz}$$

$$[\mathbf{A} \times \mathbf{B}]_{xy} = A_{yz}B_{zx} - A_{yx}B_{zz} + A_{zx}B_{yz} - A_{zz}B_{yx}$$

$$[\mathbf{A} \times \mathbf{B}]_{xz} = A_{yx}B_{zy} - A_{yy}B_{zx} + A_{zy}B_{yx} - A_{zx}B_{yy}$$

$$[\mathbf{A} \times \mathbf{B}]_{yx} = A_{xz}B_{zy} - A_{xy}B_{zz} + A_{zy}B_{xz} - A_{zz}B_{xy}$$

$$[\mathbf{A} \times \mathbf{B}]_{yy} = A_{zz}B_{xx} - A_{zx}B_{xz} + A_{xx}B_{zz} - A_{xz}B_{zx}$$

$$[\mathbf{A} \times \mathbf{B}]_{yz} = A_{zx}B_{xy} - A_{zy}B_{xx} + A_{xy}B_{zx} - A_{xx}B_{zy}$$

$$[\mathbf{A} \times \mathbf{B}]_{zx} = A_{xy}B_{yz} - A_{xz}B_{yy} + A_{yz}B_{xy} - A_{yy}B_{xz}$$

$$[\mathbf{A} \times \mathbf{B}]_{zy} = A_{xz}B_{yx} - A_{xx}B_{yz} + A_{yx}B_{xz} - A_{yz}B_{xx}$$

$$[\mathbf{A} \times \mathbf{B}]_{zz} = A_{xx}B_{yy} - A_{xy}B_{yx} + A_{yy}B_{xx} - A_{yx}B_{xy}$$



# High Order Curvilinear Mesh Generation - Integrating CAD & Finite Elements through Polyconvex Nonlinear Elasticity



# Chapter 3

# The Generation of High Order Curvilinear Meshes through Metric Controlled Polyconvex Nonlinear Elasticity

## 3.1 Introduction

In this chapter, the variational formulation and computational implementation of polyconvex nonlinear elasticity are discussed in the context of high order finite elements with an eye to utilise polyconvex nonlinear elasticity as an efficient tool for mesh deformation and metric controlled curvilinear mesh generation. As a result, the finite element examples of polyconvex nonlinear elasticity are discussed in the context of mesh generation and the benefits of polyconvexity in controlling fundamental distortion measures of curved meshes are highlighted.

The use of curved elements is nowadays accepted to be crucial in order to fully exploit the advantages of high-order discretisation methods [76, 18, 186, 329, 164, 274, 303, 273], but until relatively recently, the challenge of automatically generating high-order curvilinear meshes has been an obstacle for the widespread application of high-order methods [317]. Methods to produce high-order curvilinear meshes are traditionally classified into *direct* methods and *a posteriori* methods [74, 75]. Direct methods build the curvilinear high-order mesh directly from the CAD boundary representation of the domain whereas *a posteriori* approaches rely on mature low-order mesh generation algorithms to produce an initial mesh that is subsequently curved using different techniques, such as local modification of geometric entities [74, 75, 281, 187, 280], solid mechanics analogies [242, 328] or optimisation [304, 100].

Within the category of *a posteriori* approaches, the solid mechanics analogy first proposed in [242] has become increasingly popular. The main idea is to consider the initial, low-order, mesh as the undeformed configuration of an elastic solid. High-order nodal distributions are then inserted into all of the elements and then the nodes over element edges/faces in contact with the curved parts of the boundary are projected onto the true CAD boundary. The displacement required to move the nodes onto the true boundary is interpreted as an essential boundary condition within the solid mechanics analogy. The solution of the elastic problem provides the desired curvilinear mesh as the deformed configuration, as shown in Figure 3.1.

The initial approach proposed in [242] used a non-linear solid mechanics analogy with the neo-Hookean constitutive model. Several attempts to reduce the computational cost of this approach have been proposed based on a linear elastic analogy, see [328, 5]. It is clear that when large deformations are induced to produce the deformed curvilinear high-order mesh, a linear elastic model can result in non-valid elements due to the violation of the hypothesis of small deformations. In order to alleviate this problem, it is possible to split the desired (potentially large) displacement of boundary nodes into smaller load increments. Other approaches to increase the robustness of the linear elastic analogy have been recently introduced, for instance

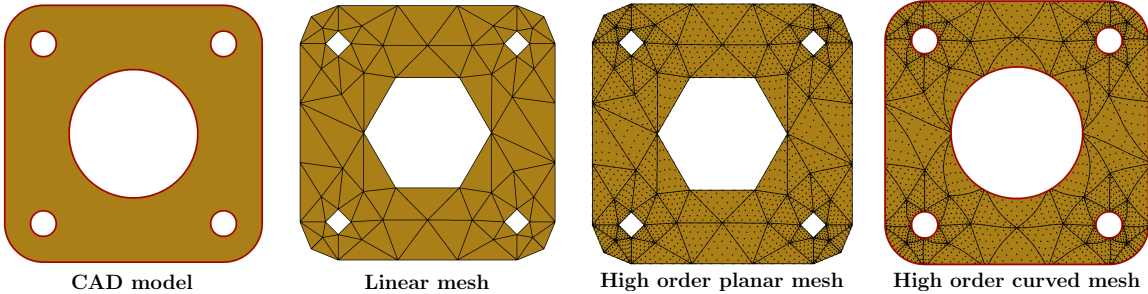


Figure 3.1: An a posteriori mesh deformation technique based on continuum mechanics analogy

in [218, 219], where *pseudo* thermal effects are introduced. It is worth noting that mesh moving strategies based on an elastic analogy have also been proposed and successfully used with a proven track record of robustness in the low-order context [301, 144, 289].

These approaches have been shown to be capable of producing curvilinear high-order meshes of highly complex geometrical configurations, including anisotropic boundary layer meshes around a full aircraft configuration [328, 254]. A comparative study of such techniques has been recently investigated in [254]. This work follows up on much of development reported in [254] in trying to propose a unified theoretical and computational solid mechanics framework for high order mesh deformation. The formulation advocated here encompasses the linear and non-linear formulations proposed in [242] and [328], respectively. In addition, a new incrementally linearised elasticity formulation, not previously applied to generate curvilinear high-order meshes, is proposed within this unified framework.

The polyconvex nonlinear elasticity has all the basic ingredients to generate curvilinear meshes with controlled metrics in terms of skewness, shape and size of the curved elements. Different distortion measures can be established for the quality of curved meshes based on the fundamental kinematic measures of polyconvex elasticity, which are in nature independent of the geometrical representation. These can be then utilised to evaluate the quality of the generated meshes for the different polynomial degrees.

Figure 3.1 shows a more in-depth step-by-step procedure for generating high order curved meshes. Typically, interaction with CAD geometry during the high order mesh deformation is necessary for acquiring information about topological curves and surfaces in the domain, further healing of the geometry and correcting the linear mesh which could be misrepresented from the actual CAD definition due to many tolerances and floating point issues that low mesh generators suffer from. From this perspective, the solid mechanics analogy is eyed as a means of closely bridging the gap between finite elements and computer aided design.

It should be noted that much of the work in this chapter is based on the authors work on curvilinear mesh generation presented in [254]. This chapter embarks from where we left off in the previous chapter on nonlinear continuum mechanics formulation for polyconvex elasticity. The polyconvex strain energies seem to be an ideal candidate for mesh deformation as they already encode the fundamental distortion measures necessary to control the quality of the high order mesh, i.e. edge distortion (skewness), surface distortion (shape) and volume distortion (size). To this end, we revisit the fundamentals of nonlinear continuum mechanics yet again in this chapter within the context of mesh moving techniques. This chapter is organised as follows. In section 3.2, the fundamentals of non-linear continuum mechanics are briefly revisited by following some recent developments in [28, 29], where the kinematics of the non-linear continua and the principle of virtual work for a displacement-based formulation, in material and spatial settings, are presented. The new consistent incrementally linearised approach is detailed in section 3.3 and the material characterisation for all the different formulations is described in detail in section 3.4. Using the derivation of all the formulations from an energy principle, a range of quality measures are proposed in section 3.5 and their relations with existing quality indicators is briefly discussed. Finally, section 3.8 presents a number of numerical examples both in two and three dimensions and an extensive comparison of performances

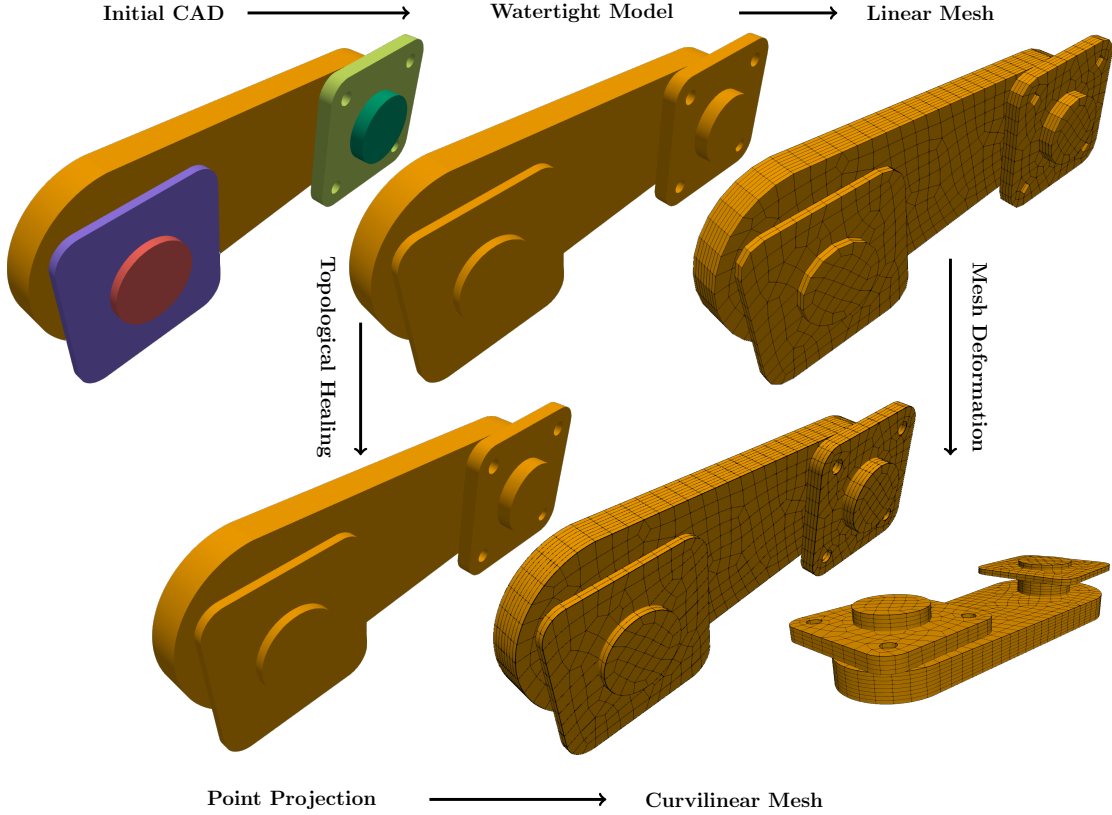


Figure 3.2: Schematic representation of an a posteriori mesh deformation technique based on continuum mechanics analogy

of the different formulations is presented. The examples include geometries appearing in a range of areas of computational mechanics, e.g. computational solid mechanics, computational fluid dynamics, computational electromagnetics and computational bio and electromechanics. Meshes are produced for a variety of degrees of approximation and for interior and exterior domains, illustrating the potential of the proposed framework. Throughout this chapter the letter  $p$  is used to denote polynomial enrichment over triangles, quadrilaterals, tetrahedra and hexahedra.

## 3.2 Non-linear continuum mechanics for mesh deformation

### 3.2.1 Kinematics

Let us reconsider the motion of a continuum from its initial undeformed (planar mesh in this case) configuration  $\Omega_0 \subset \mathbb{R}^d$ , with boundary  $\partial\Omega_0$  and outward unit normal  $\mathbf{n}_0$ , into its final deformed (curved mesh in this case) configuration  $\Omega \subset \mathbb{R}^d$ , with boundary  $\partial\Omega$  and outward unit normal  $\mathbf{n}$ , where  $d$  represents the number of spatial dimensions. In the context of curved mesh generation, the initial (undeformed) configuration  $\Omega_0$  represents a linear mesh with planar faces (edges in two dimensions) and the final (deformed) configuration  $\Omega$  represents the final curved high-order mesh, as illustrated in Figure 4.1. The motion is described by a mapping  $\phi$  which links a material particle from material configuration  $\mathbf{X}$  to spatial configuration  $\mathbf{x}$  according to  $\mathbf{x} = \phi(\mathbf{X})$ . The strain measures  $\{\mathbf{F}, \mathbf{H}, J\}$  introduced in the previous chapter can be re-written as

$$d\mathbf{x} = \mathbf{F} d\mathbf{X}; \quad d\mathbf{a} = \mathbf{H} d\mathbf{A}; \quad d\Omega = J d\Omega_0. \quad (3.1)$$

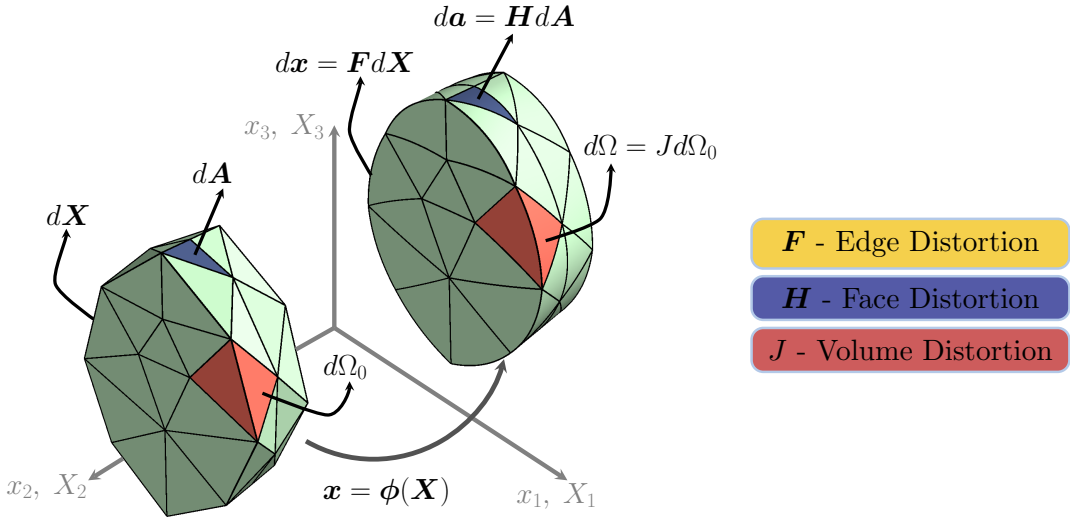


Figure 3.3: Deformation map of a linear mesh to curvilinear mesh and the related quality measures  $\mathbf{F}$ ,  $\mathbf{H}$  and  $J$ .

The fundamental strain measures  $\{\mathbf{F}, \mathbf{H}, J\}$ , also illustrated in Figure 4.1, encode the essential modes of deformation, necessary to characterise the quality of high order curvilinear meshes.

### 3.2.2 The principle of virtual work in the material and spatial settings

While a myriad of methodologies can be applied to solve for the deformation of a continuum described by the motion map  $\phi$ , such as optimisation, Laplacian smoothing and rezoning techniques [74, 75, 187, 280, 281, 102, 223, 95, 197, 315, 33], in the context of continuum mechanics, the deformation of a continuum from its undeformed configuration to its deformed configuration can be posed as a minimisation of the total potential energy  $\Pi$ , subjected to certain desired constraints [202, 127, 30]. In other words, the displacement of a deformable body can be obtained by finding the stationary condition of the total potential energy, also called the principle of virtual work (or variational principle), of the internal energy density, described in chapter 2. For problems of mesh deformation, we follow an objective representation of the internal energy discussed in chapter 2 and represented by  $\Psi(\mathbf{C}) = e_{\text{sym}}(\mathbf{C})$ , here. Hence, in our setting, we can write the potential energy as

$$\Pi(\phi^*) = \inf_{\phi \in \mathcal{V}} \left\{ \int_{\Omega_0} \Psi(\mathbf{C}) d\Omega_0 \right\}, \quad (3.2)$$

where  $\mathcal{V} = \{\phi \in [\mathcal{H}^1(\Omega_0)]^d : \phi(\mathbf{X}) = \bar{\mathbf{x}} \text{ on } \partial\Omega_0\}$ . It is worth noting that, the problem of a posteriori curved mesh generation is purely Dirichlet driven and no external forces are considered. In that the Dirichlet boundary conditions are imposed on the whole boundary corresponding to the displacement needed to place the high-order nodes on the CAD boundary entities, at position  $\bar{\mathbf{x}}$ .

Following our development in section 2.3, the stationary condition of the total potential energy in (3.2) obtained after linearisation with respect to virtual and incremental variation of geometry  $\delta\mathbf{u}$  and  $\Delta\mathbf{u}$ , leads to the principle of virtual work in the material configuration

$$D\Pi(\phi^*)[\delta\mathbf{u}] = \int_{\Omega_0} D\Psi(\mathbf{C})[\delta\mathbf{u}] d\Omega_0 = \int_{\Omega_0} \mathbf{S} : \frac{1}{2} D\mathbf{C}[\delta\mathbf{u}] d\Omega_0 = 0. \quad (3.3)$$

Equation (3.3) results in a system of non-linear equations that need to be solved through an iterative scheme and the necessary tangent operator required to facilitate convergence of the

non-linear iterative scheme (e.g. Newton-Rapshon) can be determined by computing the second directional derivative of the total potential energy

$$\begin{aligned} D^2\Pi(\phi^*)[\delta\mathbf{u}; \Delta\mathbf{u}] &= \int_{\Omega_0} D^2\Psi(\mathbf{C})[\delta\mathbf{u}; \Delta\mathbf{u}] d\Omega_0 \\ &= \int_{\Omega_0} \left( \frac{1}{2} D\mathbf{C}[\delta\mathbf{u}] : \mathbf{C} : \frac{1}{2} D\mathbf{C}[\Delta\mathbf{u}] + \mathbf{S} : \frac{1}{2} D^2\mathbf{C}[\delta\mathbf{u}; \Delta\mathbf{u}] \right) d\Omega_0. \end{aligned} \quad (3.4)$$

Following our development in section 2.6, in order to establish a unified framework for various solid mechanics approaches discussed in this work, it is convenient to re-express (3.3) in the spatial configuration

$$D\Pi(\phi^*)[\delta\mathbf{u}] = \int_{\Omega} \boldsymbol{\sigma} : \boldsymbol{\varepsilon}(\delta\mathbf{u}) d\Omega = 0, \quad (3.5)$$

where  $\boldsymbol{\varepsilon}(\mathbf{a})$  is the small strain tensor given by  $\boldsymbol{\varepsilon}(\mathbf{a}) = \frac{1}{2}(\nabla\mathbf{a} + (\nabla\mathbf{a})^T)$  and  $\nabla$  is the gradient operator in the spatial configuration such that  $\nabla_0\mathbf{a} = \nabla\mathbf{a}\mathbf{F}$ . Analogously, the second directional derivative of the total potential energy (3.4) can be re-expressed in the spatial configuration as

$$D^2\Pi(\phi^*)[\delta\mathbf{u}; \Delta\mathbf{u}] = \int_{\Omega} (\boldsymbol{\varepsilon}(\delta\mathbf{u}) : \mathbf{c} : \boldsymbol{\varepsilon}(\Delta\mathbf{u}) + \boldsymbol{\sigma} : [(\delta\mathbf{u})^T \nabla \Delta\mathbf{u}]) d\Omega \quad (3.6)$$

where the Cauchy stress tensor  $\boldsymbol{\sigma}$  and the spatial fourth order tangent elasticity tensor  $\mathbf{c}$  are obtained using the standard push-forward operations described in (4.45). In this setting, the first and second terms in the right hand side of (3.6) yield the constitutive and the geometric/initial stiffness components, respectively.

### 3.3 A consistent incrementally linearised solid mechanics approach

The standard non-linear solid mechanics methodology described in the previous section can be proven costly (due to the iterative nature of the solution finding process) when the ultimate goal is solely to deform a mesh in order to conform to the exact geometry. Alternative solid mechanics methodologies have been developed in the past, based on a variety of linearised elasticity approaches [328, 5, 218]. It is worth emphasising that, to guarantee and/or maintain previously mentioned mathematical requirements for the linearised strain energy density, a linearised solid mechanics approach must emanate from an underlying non-linear variational principle, as the notion of objectivity and polyconvexity cannot be invoked in small strains. This is typically achieved by consistent linearisation of the total potential energy (3.2) through a Taylor series expansion. To illustrate this, let us consider the total potential energy in (3.2), cast in the form of an iterative (Newton-Raphson) scheme

$$\Pi(\phi_{n+1}^*) = \inf_{\phi_{n+1} \in \mathcal{V}_{n+1}} \left\{ \int_{\Omega_0} \Psi(\mathbf{C}_{n+1}) d\Omega_0 \right\} \quad (3.7)$$

where  $\mathcal{V}_{n+1} = \{\phi_{n+1} \in [\mathcal{H}^1(\Omega_0)]^d : \phi_{n+1}(\mathbf{X}) = \bar{\mathbf{x}}_{n+1} \text{ on } \partial\Omega_0\}$  and  $\mathbf{x}_{n+1} = \phi_{n+1}(\mathbf{X})$  is the position vector of the material points at increment  $n+1$ , which can be evaluated through an incremental displacement  $\mathbf{u}$  superimposed on the deformed configuration at increment  $n$ , i.e.  $\mathbf{x}_{n+1} = \mathbf{x}_n + \mathbf{u}$ , as illustrated in Figure 3.4. At increment  $n$ , the current position vector  $\mathbf{x}_n$ , the state of deformation gradient  $\mathbf{F}_n$  and, subsequently, the Cauchy-Green strain  $\mathbf{C}_n$  are fully known. In a non-linear regime, the motion of the continuum from  $n$  to  $n+1$  is solved iteratively, as the amount of displacements, the state of deformation gradient  $\mathbf{F}_{n+1}$  and the Cauchy-Green strain  $\mathbf{C}_{n+1}$  cannot be determined explicitly.

However, in the context of high-order curved mesh generation, it is convenient to approximate (3.7) through a Taylor series expansion of the form

$$\Pi(\phi_{n+1}^*) \approx \Pi_{\text{lin}}(\mathbf{x}_n^* + \mathbf{u}^*) = \inf_{\mathbf{u} \in \mathcal{U}} \left\{ \int_{\Omega_0} \left( \Psi(\mathbf{C}_n) + D\Psi(\mathbf{C}_n)[\mathbf{u}] + \frac{1}{2} D^2\Psi(\mathbf{C}_n)[\mathbf{u}; \mathbf{u}] \right) d\Omega_0 \right\} \quad (3.8)$$

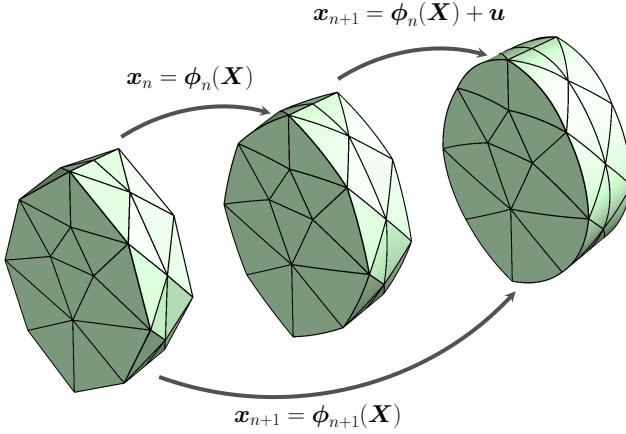


Figure 3.4: Schematic representation of an incrementally linearised solid mechanics approach.

where  $\mathcal{U} = \{\mathbf{u} \in [\mathcal{H}^1(\Omega_n)]^d : \mathbf{u} = \bar{\mathbf{u}} \text{ on } \partial\Omega_n\}$ . Certainly, embedded in the definition of the new total potential energy ( $\Pi_{\text{lin}}$ ) in (3.8) are the first and second directional derivatives of the non-linear total potential energy (3.2), where the virtual and incremental variations, namely  $\mathbf{v}$  and  $\mathbf{w}$ , are now replaced with  $\mathbf{u}$ . Hence, unlike (3.3), (3.8) is fully and consistently linearised in  $\mathbf{u}$ . Furthermore, notice that the first term in the integrand in (3.8) is a constant term describing the state of strain energy density at increment  $n$ , which vanishes at the moment of computing the stationary point of (3.8). In fact, the stationary condition of the linearised total potential energy (3.8) is identical to the stationary condition of the following potential energy

$$\Pi_u(\mathbf{u}^*) = \inf_{\mathbf{u} \in \mathcal{U}} \left\{ \int_{\Omega_0} \left( D\Psi(\mathbf{C}_n)[\mathbf{u}] + \frac{1}{2} D^2\Psi(\mathbf{C}_n)[\mathbf{u}; \mathbf{u}] \right) d\Omega_0 \right\}. \quad (3.9)$$

Substituting for (3.5-3.6) in (3.9), we obtain the spatial form of the linearised total potential energy as

$$\Pi_u(\mathbf{u}^*) = \inf_{\mathbf{u} \in \mathcal{U}} \left\{ \int_{\Omega_n} \left( \boldsymbol{\sigma}_n : \boldsymbol{\varepsilon}_n(\mathbf{u}) + \frac{1}{2} \boldsymbol{\varepsilon}_n(\mathbf{u}) : \mathbf{c}_n : \boldsymbol{\varepsilon}_n(\mathbf{u}) + \frac{1}{2} \boldsymbol{\sigma}_n : \left( (\nabla_n \mathbf{u})^T (\nabla_n \mathbf{u}) \right) \right) d\Omega_n \right\} \quad (3.10)$$

where the subscript  $n$  denotes the state of deformation, stresses, tangent elasticity and the volume at increment  $n$ , namely  $\boldsymbol{\varepsilon}_n$ ,  $\boldsymbol{\sigma}_n$ ,  $\mathbf{c}_n$  and  $\Omega_n$ . In addition,  $\nabla_n$  represents the spatial gradient operator at increment  $n$ . The stationary condition of (3.10), obtained after the linearisation with respect to the virtual displacement  $\mathbf{v}$ , leads to the principle of virtual work

$$D\Pi_u(\mathbf{u}^*)[\mathbf{v}] = \int_{\Omega_n} \left( \underbrace{\boldsymbol{\sigma}_n : \boldsymbol{\varepsilon}_n(\mathbf{v})}_{\mathcal{R}_n} + \underbrace{\boldsymbol{\varepsilon}_n(\mathbf{u}) : \mathbf{c}_n : \boldsymbol{\varepsilon}_n(\mathbf{v})}_{\mathcal{C}_n} + \underbrace{\boldsymbol{\sigma}_n : ((\nabla_n \mathbf{u})^T (\nabla_n \mathbf{v}))}_{\mathcal{G}_n} \right) d\Omega_n = 0. \quad (3.11)$$

It is worth noting that, in the right hand side of (3.11), the first term  $\mathcal{R}_n$  corresponds to the residual stresses, the second term  $\mathcal{C}_n$  to the linearised constitutive stiffness term and the last term  $\mathcal{G}_n$  to the geometric stiffness term. The emergence of the geometric stiffness term is due to consistent linearisation of the non-linear total potential energy, which would not have appeared, had the starting point not been chosen to correspond to a non-linear total potential energy, as also described in [130] (pp. 104) and in [202]. As will be seen in the numerical examples, in the context of high-order curved mesh generation, the geometric stiffness term, stiffens the interior elements of the computational mesh against severe distortion, hence producing meshes with better quality. Note that unlike in the non-linear analysis, since (3.11) is linear in  $\mathbf{u}$ , a further linearisation is not required.

Formulation \ Computational Requirement	Requires increments	Requires iteration	Accounts for stresses	Tangent operator evaluation
Non-linear elasticity	✓	✓	✓	Per iteration
Consistent Incrementally Linearised (CIL)	✓	✗	✓	Per increment
Inconsistent Incrementally Linearised	✓	✗	✓	Once at the origin
Incremental Linear Elasticity (ILE)	✓	✗	✗	Once at the origin
Classical linear elasticity	✗	✗	✗	Once at the origin

Table 3.1: Computational requirement of different solid mechanics formulations for curved mesh generation

If a single increment is used to reach the final curved mesh, i.e. when  $n = 0$ , the equations of classical linear elasticity are recovered. Note that, in the context of linearised approaches there are a multitude of heuristic formulations which do not necessarily come from a variational principle. In fact, apart from the case when all the terms  $\{\mathcal{R}_n, \mathcal{C}_n, \mathcal{G}_n\}$  are present in the principle of virtual work, all the other formulations based on the combinations of these terms lead to non-consistent formulations. For the sake of completeness, the four distinct linearised cases used in the literature of curved mesh generation are identified in the following; [see also Table 3.1 for a schematic comparison of these cases and their associated computational requirement]:

1. When the state of deformation at increment  $n + 1$  is obtained by computing the residual stresses, the constitutive stiffness and the geometric stiffness at the previous deformed configuration i.e. based on  $\{\mathcal{R}_n, \mathcal{C}_n, \mathcal{G}_n\}$ . This consistent incrementally linearised methodology for high-order curved mesh generation, was first presented in [254].
2. When the residual stresses at increment  $n + 1$  are obtained from the previous deformed configuration based on  $\mathcal{R}_n$ , but the constitutive stiffness is evaluated at the initial undeformed (or stress-free) configuration i.e.  $\mathcal{C}_0$  and the geometric stiffness term is absent from the formulation. The technique developed by [218] falls into this category.
3. When both the residual stresses and constitutive stiffness at increment  $n + 1$  are computed based on the initial undeformed configuration i.e.  $\mathcal{R}_0$  and  $\mathcal{C}_0$  and the geometric stiffness term is absent from the formulation, but the geometry itself is updated incrementally such that  $\mathbf{x}_{n+1} = \mathbf{x}_n + \mathbf{u}$ . This approach has been pursued in [328, 5] and from here onwards we will refer to this approach as the incremental linear elastic approach.
4. When  $n = 0$  or in other words, when the residual stresses, constitutive stiffness and geometric stiffness are evaluated once at the initial undeformed configuration  $\{\mathcal{R}_0, \mathcal{C}_0, \mathcal{G}_0\}$  i.e. particularisation to the case of classical linear elasticity.

### 3.4 Polyconvexity, non-polyconvexity and material characterisation for different formulations

Apart from satisfying the requirements of existence of minimisers, objectivity and favourably polyconvexity, the choice of material generally imposes further physical requirements on the internal energy density. For an isotropic material, the internal energy density can be written as a function of three independent invariants as

$$\Psi(\mathbf{C}) = \Psi_{\text{iso}}(I_1, I_2, I_3), \quad I_1 = \mathbf{I} : \mathbf{C}; \quad I_2 = \mathbf{I} : \mathbf{G}; \quad I_3 = C, \quad (3.12)$$

where the three isotropic invariants  $I_1$ ,  $I_2$  and  $I_3$  are indeed further related to the fundamental kinematic measures as<sup>1</sup>

$$I_1 = \mathbf{F} : \mathbf{F}; \quad I_2 = \mathbf{H} : \mathbf{H}; \quad I_3 = J^2. \quad (3.13)$$

<sup>1</sup>Note that for plane strain problems, the first two isotropic invariants are identical i.e.  $I_1 = I_2$ .

Furthermore, for a transversely isotropic material, the strain energy density can be expressed as

$$\Psi(\mathbf{C}) = \Psi_{\text{aniso}}(I_1, I_2, I_3, I_4, I_5), \quad I_4 = \mathbf{N} \cdot \mathbf{CN}, \quad I_5 = \mathbf{N} \cdot \mathbf{C}^2 \mathbf{N}, \quad (3.14)$$

where the two transversely isotropic invariants  $I_4$  and  $I_5$  are indeed related to the fundamental kinematic measure  $\mathbf{F}$  as

$$I_4 = \mathbf{FN} \cdot \mathbf{FN} = \mathbf{N} \cdot \mathbf{CN}; \quad I_5 = \mathbf{CN} \cdot \mathbf{CN} = \mathbf{F}^T \mathbf{FN} \cdot \mathbf{F}^T \mathbf{FN}, \quad (3.15)$$

where  $\mathbf{N}$  is the unit Lagrangian vector characterising the direction of transverse isotropy. It is worth emphasising that (3.13) and (3.15) represent a set of independent invariants that can be used to construct isotropic and transversely isotropic strain energy density expressions, respectively<sup>2</sup>. Any other invariant used to construct the strain energy density, would be a linear combination of the aforementioned invariants. As will be discussed later, these invariants play a key role in quantifying the quality of generated curvilinear meshes.

To establish a unified framework for the different solid mechanics formulations presented in the previous section and to further facilitate a comparison among them, it is essential that material parameters are calibrated such that the strain energies (and consequently the stresses and the constitutive tensors) for the different formulations are identical at the initial undeformed configuration. To this end, in this section, we discuss characterisation of material constants through an example of a hyperelastic neo-Hookean model. More sophisticated internal energies accounting for near incompressibility and transverse isotropy are also considered and will be discussed subsequently.

### 3.4.1 Material characterisation for the nonlinear hyperelastic case

Let us consider a compressible neo-Hookean model which is also considered, for instance in [242] in the context of high-order curvilinear mesh deformation. The strain energy density of the material is given by

$$\Psi^{\text{neo}}(\mathbf{C}) = \frac{\mu}{2}(I_1 - 3) + f(I_3), \quad f(I_3) = \frac{\lambda}{2}(\sqrt{I_3} - 1)^2 - \mu \ln(\sqrt{I_3}), \quad (3.16)$$

where  $\mu$  and  $\lambda$  are two material constants. Note that this model can be obtained by setting  $\beta = 0$  and  $\alpha = \frac{\mu}{2}$  in the more sophisticated compressible Mooney-Rivlin model presented later. Following the procedure outlined in the previous section, the Cauchy stress tensor and the tangent elasticity tensor can be obtained as

$$\boldsymbol{\sigma}^{\text{neo}} = \frac{\mu}{J} \mathbf{b} + \left( \lambda(J-1) - \frac{\mu}{J} \right) \mathbf{I} \quad (3.17)$$

$$\mathbf{c}^{\text{neo}} = \lambda(2J-1) \mathbf{I} \otimes \mathbf{I} + \left( \frac{\mu}{J} - \lambda(J-1) \right) \boldsymbol{\mathcal{I}} \quad (3.18)$$

where  $\mathbf{b} = \mathbf{FF}^T$  is the left Cauchy-Green strain tensor and  $\boldsymbol{\mathcal{I}}$  is the symmetric fourth order identity tensor  $[\boldsymbol{\mathcal{I}}]_{ijkl} = \delta_{ik}\delta_{jl} + \delta_{il}\delta_{jk}$ , where  $\delta_{mn}$  denotes the Kronecker delta.

### 3.4.2 Material characterisation for the classical linear elastic case

For the classical compressible linear elastic constitutive model, the strain energy is defined as

$$\Psi_{\text{lin}}(\boldsymbol{\varepsilon}) = \frac{\lambda_{\text{lin}}}{2} (\text{tr} \boldsymbol{\varepsilon})^2 + \mu_{\text{lin}} \boldsymbol{\varepsilon} : \boldsymbol{\varepsilon}, \quad (3.19)$$

---

<sup>2</sup>To satisfy polyconvexity in a transversely isotropic material, the independent invariant  $I_5$  is instead given by

$$I_5 = \mathbf{HN} \cdot \mathbf{HN} = \mathbf{N} \cdot \mathbf{GN}.$$

where  $\lambda_{\text{lin}}$  and  $\mu_{\text{lin}}$  represent the well-known Lamé parameters. The Cauchy stress tensor and the tangent elasticity tensor are then obtained as

$$\boldsymbol{\sigma}_{\text{lin}} = \lambda_{\text{lin}} \text{tr} \boldsymbol{\varepsilon} \mathbf{I} + 2\mu_{\text{lin}} \boldsymbol{\varepsilon} \quad (3.20)$$

$$\mathbf{c}_{\text{lin}} = \lambda_{\text{lin}} \mathbf{I} \otimes \mathbf{I} + \mu_{\text{lin}} \mathbf{I}. \quad (3.21)$$

It is worth noting that the approach pursued in [328, 218] corresponds to a linear elastic approach with only the geometry being updated at each increment  $\mathbf{x} = \mathbf{x}_n$ .

Comparison of the tangent elasticity tensor of the neo-Hookean model (3.18) evaluated at the origin (i.e.  $J = 1$ ) to its linear elastic counterpart (3.21), a relationship between material constants can be defined as

$$\mu = \mu_{\text{lin}}, \quad \lambda = \lambda_{\text{lin}}.$$

In the case of the neo-Hookean material model the relationship between material constants is *one-to-one*, whereas for more complex material models dependent upon more than two constants, one can arrive at correlations between those and the Lamé constants, preferably having to fix some of those constants. The calibration of material constants of a nonlinear or linearised energy functional against the linear elastic model is key to the comparison of the approaches. In practice, normally the Young's modulus ( $E$ ) and Poisson's ratio ( $\nu$ ) of the material are provided, which for the three-dimensional and plane strain isotropic cases are related to the Lamé constants as

$$\lambda_{\text{lin}} = \frac{E\nu}{(1+\nu)(1-2\nu)}, \quad \mu_{\text{lin}} = \frac{E}{2(1+\nu)}. \quad (3.22)$$

To facilitate a comparison between material models for producing the higher-order curvilinear meshes, all isotropic materials described in the next three subsections can be expressed in terms of the Poisson's ratio  $\nu$  using (3.22).

### 3.4.3 A modified Mooney-Rivlin model for mesh deformation

Another model apart from the neo-Hookean model which would be used frequently for our continuum mechanics based mesh deformation is the modified polyconvex Mooney-Rivlin model, whose internal energy, Cauchy stress tensor and tangent elasticity operator are given as below [28, 29]

$$\Psi(\mathbf{C}) = \alpha I_1 + \beta I_2 - 4\beta \sqrt{I_3} - 2\alpha \ln \sqrt{I_3} + \frac{\lambda}{2} (\sqrt{I_3} - 1)^2 - (3\alpha - \beta); \quad (3.23a)$$

$$\boldsymbol{\sigma} = \frac{2}{J} \left( \alpha + \beta (\mathbf{b} \times \mathbf{I}) \right) \mathbf{b} + \left( \lambda(J-1) - 4\beta - \frac{2\alpha}{J} \right) \mathbf{I}; \quad (3.23b)$$

$$\begin{aligned} [\mathbf{c}]_{ijkl} &= \frac{2\beta}{J} \left( 2 [\mathbf{b}]_{ij} [\mathbf{b}]_{kl} - [\mathbf{b}]_{ik} [\mathbf{b}]_{jl} - [\mathbf{b}]_{il} [\mathbf{b}]_{jk} \right) + \left( \lambda(2J-1) - 4\beta \right) \delta_{ij} \delta_{kl} \\ &\quad - \left( \lambda(J-1) - 4\beta - \frac{2\alpha}{J} \right) \left( \delta_{ik} \delta_{jl} + \delta_{il} \delta_{jk} \right), \end{aligned} \quad (3.23c)$$

where for all of our analyses we fix  $\alpha = \beta$ .

### 3.4.4 A nearly incompressible polyconvex Mooney-Rivlin model

An incompressible version of the Mooney-Rivlin model can be considered to allow the curvilinear meshes to maintain a balanced scaled Jacobian across all elements. The internal energy, the Cauchy stress tensor and the tangent elasticity operator of this model are given as below

$$\Psi(\mathbf{C}) = \alpha I_3^{-1/3} I_1 + \beta I_3^{-1} I_2^{3/2} + \frac{\kappa}{2} (\sqrt{I_3} - 1)^2 - (3\alpha + 3\sqrt{3}\beta); \quad (3.24a)$$

$$\boldsymbol{\sigma} = 2\alpha J^{-5/3} \mathbf{b} + \left( \kappa(J-1) - \frac{2\alpha}{3} J^{-5/3} \text{tr} \mathbf{b} + \beta J^{-3} \text{tr} \mathbf{g}^{3/2} \right) \mathbf{I} - 3\beta J^{-3} \text{tr} \mathbf{g}^{1/2} \mathbf{g}; \quad (3.24b)$$

$$\begin{aligned}
[\mathbf{c}]_{ijkl} = & -\frac{4\alpha}{3}J^{-5/3}\left([\mathbf{b}]_{ij}\delta_{kl} + \delta_{ij}[\mathbf{b}]_{kl}\right) \\
& + \left(\frac{4\alpha}{9}J^{-5/3}[\mathbf{b}]_{mm} + \beta J^{-3}([\mathbf{g}]_{mm})^{3/2} + \kappa(2J-1)\right)\delta_{ij}\delta_{kl} \\
& + \left(\frac{2\alpha}{3}J^{-5/3}[\mathbf{b}]_{mm} - \beta J^{-3}([\mathbf{g}]_{mm})^{3/2} - \kappa(J-1)\right)\left(\delta_{ik}\delta_{jl} + \delta_{il}\delta_{jk}\right) \\
& - 3\beta J^{-3}([\mathbf{g}]_{mm})^{1/2}\left(\delta_{ij}[\mathbf{g}]_{kl} + [\mathbf{g}]_{ij}\delta_{kl}\right) + 6\beta J^{-3}([\mathbf{g}]_{mm})^{1/2}\left(\delta_{ik}[\mathbf{g}]_{jl} + [\mathbf{g}]_{il}\delta_{jk}\right) \\
& + 3\beta J^{-3}([\mathbf{g}]_{mm})^{-1/2}[\mathbf{g}]_{ij}[\mathbf{g}]_{kl},
\end{aligned} \tag{3.24c}$$

with the following relationship for material properties holding at the origin

$$\begin{aligned}
2\alpha + 3\sqrt{3}\beta &= \mu_{\text{lin}}; \\
\kappa - \frac{4}{3}\alpha - 2\sqrt{3}\beta &= \lambda_{\text{lin}},
\end{aligned}$$

where for all of our analyses we fix  $\alpha = \frac{\mu_{\text{lin}}}{2}$ .

### 3.4.5 A transversely isotropic non-polyconvex model

For comparison and as a matter of pinpointing the effect of anisotropy in generating curvilinear meshes, we consider a transversely isotropic material model presented in [26]. The internal energy, Cauchy stress tensor and tangent elasticity operator of this model are given as below

$$\Psi(\mathbf{C}) = \alpha(I_1 - 3) + \beta(I_2 - 3) - \tilde{\mu}\ln\sqrt{I_3} + \frac{\lambda}{2}(\sqrt{I_3} - 1)^2 \tag{3.25a}$$

$$\begin{aligned}
\boldsymbol{\sigma} = & \frac{2}{J}\left(\alpha + \beta(\mathbf{b} \times \mathbf{I})\right)\mathbf{b} + \left(\lambda(J-1) - \frac{\tilde{\mu}}{J}\right)\mathbf{I} + \frac{2\eta_1}{J}\mathbf{F}\mathbf{N} \otimes \mathbf{F}\mathbf{N} + \frac{2\eta_2}{J}(\mathbf{F}\mathbf{N} \cdot \mathbf{F}\mathbf{N} - 1)\mathbf{b} \\
& + \frac{2\eta_2}{J}(\text{tr}\mathbf{b} - 3)\mathbf{F}\mathbf{N} \otimes \mathbf{F}\mathbf{N} + \frac{4\gamma}{J}(\mathbf{F}\mathbf{N} \cdot \mathbf{F}\mathbf{N} - 1)\mathbf{F}\mathbf{N} \otimes \mathbf{F}\mathbf{N} \\
& - \frac{\eta_1}{J}\left(\mathbf{F}\mathbf{N} \otimes \mathbf{b}\mathbf{F}\mathbf{N} + \mathbf{b}\mathbf{F}\mathbf{N} \otimes \mathbf{F}\mathbf{N}\right);
\end{aligned} \tag{3.25b}$$

$$\begin{aligned}
[\mathbf{c}]_{ijkl} = & \frac{2\beta}{J}\left(2[\mathbf{b}]_{ij}[\mathbf{b}]_{kl} - [\mathbf{b}]_{ik}[\mathbf{b}]_{jl} - [\mathbf{b}]_{il}[\mathbf{b}]_{jk}\right) + \lambda(2J-1)\delta_{ij}\delta_{kl} \\
& + \left(\tilde{\mu} - \lambda(J-1)\right)\left(\delta_{ik}\delta_{jl} + \delta_{il}\delta_{jk}\right) + \frac{4\eta_2}{J}([\mathbf{b}]_{ij}[\mathbf{F}\mathbf{N}]_k[\mathbf{F}\mathbf{N}]_l + [\mathbf{F}\mathbf{N}]_i[\mathbf{F}\mathbf{N}]_j[\mathbf{b}]_{kl}) \\
& + \frac{8\gamma}{J}[\mathbf{F}\mathbf{N}]_i[\mathbf{F}\mathbf{N}]_j[\mathbf{F}\mathbf{N}]_k[\mathbf{F}\mathbf{N}]_l - \frac{2\eta_1}{J}\left([\mathbf{b}]_{jk}[\mathbf{F}\mathbf{N}]_i[\mathbf{F}\mathbf{N}]_l + [\mathbf{b}]_{ik}[\mathbf{F}\mathbf{N}]_j[\mathbf{F}\mathbf{N}]_l\right),
\end{aligned} \tag{3.25c}$$

with the following relationship for material properties holding at the origin

$$\begin{aligned}
\tilde{\mu} &= 2\alpha + 4\beta; \\
\alpha + \beta &= \frac{E}{4(1+\nu)}; \\
\eta_1 &= 4\alpha - G_A; \\
12\alpha + \lambda &= C_{11}; \\
4\eta_2 &= C_{13} - 4\alpha - \lambda; \\
8\gamma &= C_{33} - 12\alpha + 4\eta_1 - 8\eta_2 - \lambda,
\end{aligned}$$

where  $C_{11}$ ,  $C_{13}$ ,  $C_{33}$ ,  $G_A$ ,  $E$  and  $\nu$  are the components of transversely isotropic linear elastic material, where the subscript  $A$  denotes the direction of anisotropy. For all the analyses we

fix  $\alpha = \beta$ . Notice that, the non-polyconvex nature of this material model is also used later to showcase the loss of ellipticity in the context of mesh deformation.

A detailed comparison of all these material models for mesh deformation is performed in the numerical examples sections.

### 3.5 Mesh quality (distortion) measures

Quality or distortion measures are traditionally used both in a low and high-order finite element context in order to quantify the approximation properties induced by a computational mesh. In a standard high-order finite element formulation, measures involving the Jacobian of the isoparametric mapping have been extensively used [105, 328], in particular the so-called scaled Jacobian. This measure only quantifies volumetric deformations and alternative measures that exploit different modes of deformation and account for shape, skewness and degeneracy of elements have only been recently considered [102, 101]. However, it is worth noting that not all of these quality measures can be regarded as independent quantities.

In the unified solid mechanics framework proposed here, due to the derivation of all the approaches from an energy principle, we propose five quality measures that are defined in terms of the invariants of (3.13) and (3.15), used to construct the strain energy. The quality measures for a generic element  $e$  are

$$Q_j^e = \sqrt{\frac{\min_{\xi \in R} \{I_j\}}{\max_{\xi \in R} \{I_j\}}} \quad \text{for } j = 1, \dots, 5, \quad (3.26)$$

where  $R$  denotes the reference element employed in the isoparametric formulation, with local coordinates  $\xi$ . If necessary, further quality measures can be obtained through a linear combination of the invariants  $I_j$  which will be independent of the geometrical parametrisation.

In practice, the invariants are evaluated at a discrete set of points within the reference element, usually the quadrature points that will be employed during a computational simulation. For the numerical examples presented here, a quadrature rule is used that integrates polynomials of degree up to  $2p$ , where  $p$  is the order of approximation.

In order to obtain a representative quality measure for a given computational mesh, a variety of statistical data can be reported, such as the mean quality or the standard deviation. However, in the numerical examples presented here, the mesh quality is defined by computing the minimum over all the elements, namely  $Q_j = \min_e \{Q_j^e\}$ . Despite this being the least favourable choice, it is well known that a few low quality elements can substantially deteriorate the overall quality of a finite element simulation, specially if these elements are near a curved boundary. Several numerical examples in two and three dimensions are used in the next section to evaluate the performance of different approaches for a posteriori mesh generation. The objective is to produce meshes where the minimum quality is as high as possible as this will provide the better approximation properties of a high-order finite element solver.

From the mesh distortion point of view, the first quality measure  $Q_1$ , quantifies fibre deformation (for instance, distortion of the edges of an element), the second quality measure  $Q_2$ , quantifies surface deformation (for instance, distortion of the faces of an element) and the third quality measure  $Q_3$ , quantifies volumetric deformation (distortion of the element itself). In fact, it is worth noting that the scaled Jacobian corresponds to the quality measure  $Q_3$ . For simplicial elements (i.e. triangles and tetrahedra), this measure is identical to the Jacobian of the deformation gradient tensor  $J$  because the isoparametric mapping for a simplicial elements with planar faces (or edges in two dimensions) is affine. This result is valid because, in the context of a posteriori high-order mesh generation, the undeformed configuration typically corresponds to a mesh formed by elements with planar faces (or edges).

The quality measures  $Q_4$  and  $Q_5$ , based on the two anisotropic invariants, quantify the distortion in the direction of anisotropy. These measures can only be utilised when the internal energy of the material is anisotropic and, since in the context of curved mesh generation this

is not often the case, their usage remains limited. Moreover, anisotropic quality measures are typically dependent on the geometrical parametrisation.

Finally, it should be emphasised that, in contrast to the non-linear approach, the solution of the incrementally linearised problem in (3.9), does not correspond to the minimisation of the total potential energy (3.7) with respect to the fundamental strain measures  $\{\mathbf{F}, \mathbf{H}, J\}$  per se, but rather with respect to the incrementally linearised versions of these quantities. Furthermore, it is easy to identify that for plane strain problems, the first and the second invariants are indeed identical i.e.  $I_1 = I_2$  which in turn translates into the corresponding quality measures being identical  $Q_1 = Q_2$ . This is only true for two-dimensional plane strain problems.

It should be noted that, in the case of classical linear elasticity (when the geometry is not updated), the five quality measures are not independent. The three quality measures based on the isotropic invariants are reduced to a single quantity, namely

$$\begin{aligned} D I_1[\delta \mathbf{u}]_{\mathbf{F}=\mathbf{I}} &= 2 (\mathbf{F} : \nabla_0 \delta \mathbf{u})_{\mathbf{F}=\mathbf{I}} = 2 \mathbf{I} : \nabla_0 \delta \mathbf{u} = 2 \text{tr} \delta \boldsymbol{\varepsilon} \\ D I_2[\delta \mathbf{u}]_{\mathbf{F}=\mathbf{I}} &= \mathbf{I} : \left( \mathbf{C} \times ((\nabla_0 \delta \mathbf{u})^T \mathbf{F} + \mathbf{F}^T \nabla_0 \delta \mathbf{u}) \right)_{\mathbf{F}=\mathbf{I}} \\ &= \mathbf{I} : (\mathbf{I} \times 2 \nabla_0 \delta \mathbf{u}) = 2 \nabla_0 \delta \mathbf{u} : (\mathbf{I} \times \mathbf{I}) = 2 \nabla_0 \mathbf{u} : 2 \mathbf{I} = 4 \text{tr} \delta \boldsymbol{\varepsilon} \\ D I_3[\delta \mathbf{u}]_{\mathbf{F}=\mathbf{I}} &= \left( \mathbf{G} : ((\nabla_0 \delta \mathbf{u})^T \mathbf{F} + \mathbf{F}^T \nabla_0 \delta \mathbf{u}) \right)_{\mathbf{F}=\mathbf{I}} = 2 \text{tr} \delta \boldsymbol{\varepsilon} \end{aligned}$$

and the two anisotropic measures reduce to a different measure, namely

$$\begin{aligned} D I_4[\delta \mathbf{u}]_{\mathbf{F}=\mathbf{I}} &= 2 \nabla_0 \delta \mathbf{u} : (\mathbf{N} \otimes \mathbf{N}) \\ D I_5[\delta \mathbf{u}]_{\mathbf{F}=\mathbf{I}} &= \left( (\mathbf{C} \mathbf{N} \otimes \mathbf{N} + \mathbf{N} \otimes \mathbf{C} \mathbf{N}) : ((\nabla_0 \delta \mathbf{u})^T \mathbf{F} + \mathbf{F}^T \nabla_0 \delta \mathbf{u}) \right)_{\mathbf{F}=\mathbf{I}} = 4 \nabla_0 \delta \mathbf{u} : \mathbf{N} \otimes \mathbf{N}. \end{aligned}$$

Furthermore, it is easy to identify that for plane strain problems, the first and the second invariants are indeed identical i.e.  $I_2^{2D} = I_1^{2D}$

## 3.6 Projection techniques

A myriad of projection techniques can be used to place the high order nodes on to the actual CAD boundary. In this section we will have a brief look at these techniques. Three projection techniques are going to be discussed in this section, namely:

1. Orthogonal projection
2. Isometric projection
3. Isoparametric projection

The most popular projection technique is perhaps the orthogonal projection technique. In the orthogonal projection technique, as the name implies, the nodes from planar surfaces are projected to the actual CAD boundary using the minimum distance (Euclidean distance) metric. This is shown in Figure 3.5(a). Notice that in Figure 3.5 only side of the triangular element is curved. The nodes are projected in such a way such that the projected node on the CAD curve makes for the closest orthogonal distance from the the node on the planar edge of the triangle. The second approach, called the isometric or arc-length projection technique, shown in Figure 3.5(b), uses the relative distance of the nodes on the planar edge/face to place the node on to the CAD curve/surface, in that the technique is distance preserving (hence the name isometric). This requires computing the length of the arc a priori for each CAD curve/surface. As a result the projected nodes always preserve the same relative distance. Both orthogonal and isometric approaches only modify the curved edges/faces of a planar

mesh. The third approach called the isoparametric approach uses the parametric description of CAD and the isoparametric nature of finite elements to directly map nodes from planar faces to curved faces. The isoparametric projection typically modifies all the nodes on the surface, as shown in Figure 3.5(c).

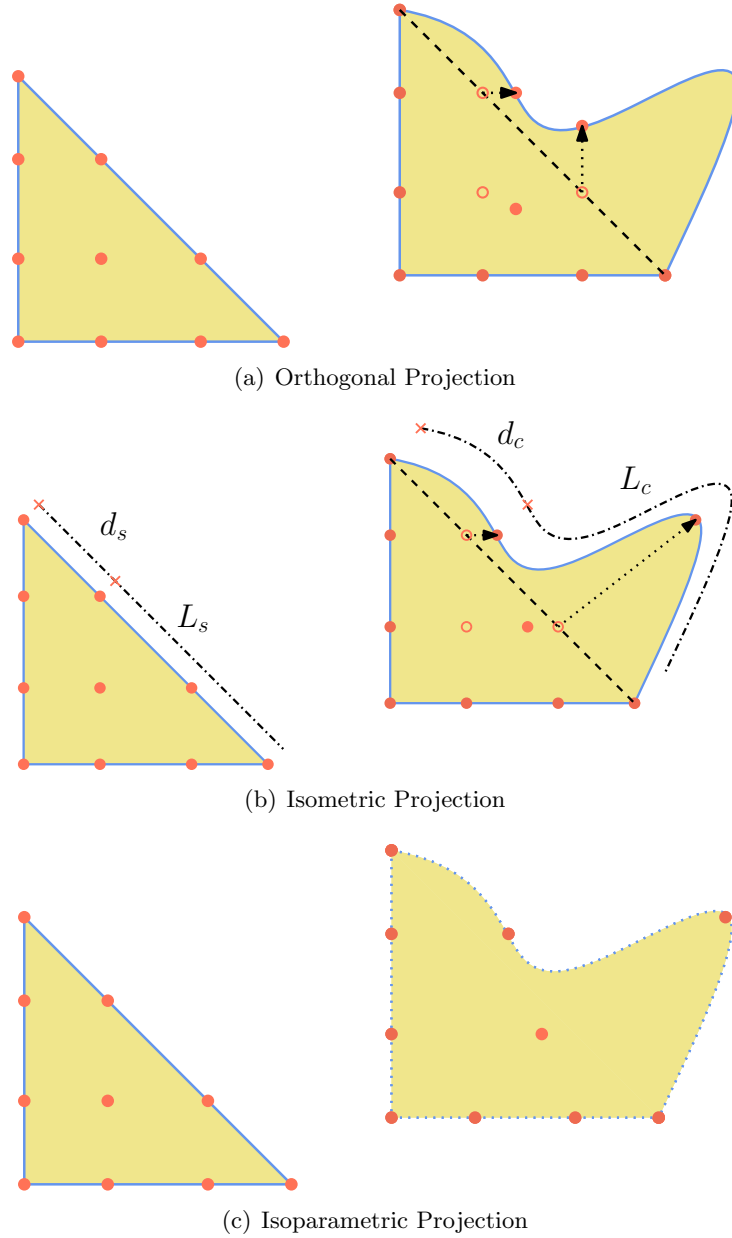


Figure 3.5: Types of projection techniques used for placing high order nodes on to the actual CAD boundary

Typically an isoparametric projection is the desired one and can be ultimately used for NURBS-enhanced finite element method as well [274, 273]. However, since the isoparametric projection also modifies the linear mesh, it is numerically less robust mainly due to inaccuracies and tolerances used during linear mesh generation. Occasionally, these issues can be worked around however, in some corner cases this introduces additional difficulties. Both isoparametric and isometric techniques also suffer from the so-called trespassing issue that is they can either project a node to a point in space where no CAD curve/surface exists or project the node on to the neighbouring surface in the vicinity of a curve intersection. However, the isoparametric approach is the least costly projection technique. Figure 3.6 shows the tradeoff between computational cost and numerical robustness of the aforementioned projection techniques.

In this work a mixed projection technique is followed, such that the ultimate projection

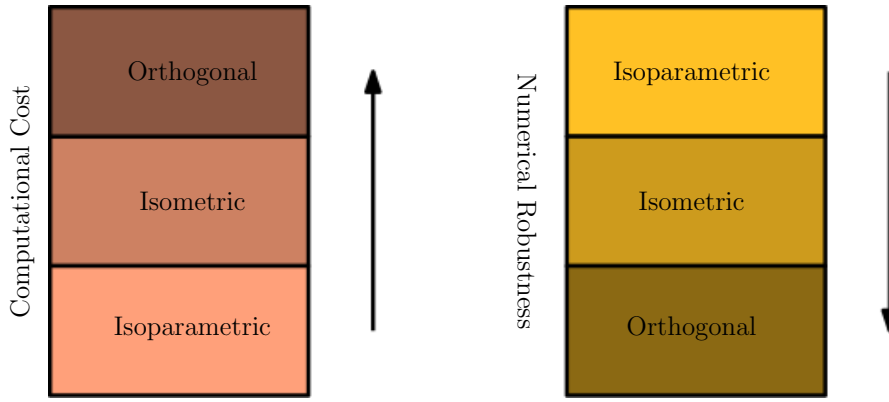


Figure 3.6: Characteristics of different projection techniques

strategy used is decided by the user. If isoparametric or isometric projection techniques are used, a verification step is performed using orthogonal projection. If the orthogonal projection fails to project the node from the planar surface to a CAD curve/surface, the actual projection technique for that mesh edge/face is abandoned and the whole mesh edge/face is re-projected using only the orthogonal projection technique. This mixed projection strategy is shown in Figure 3.7.

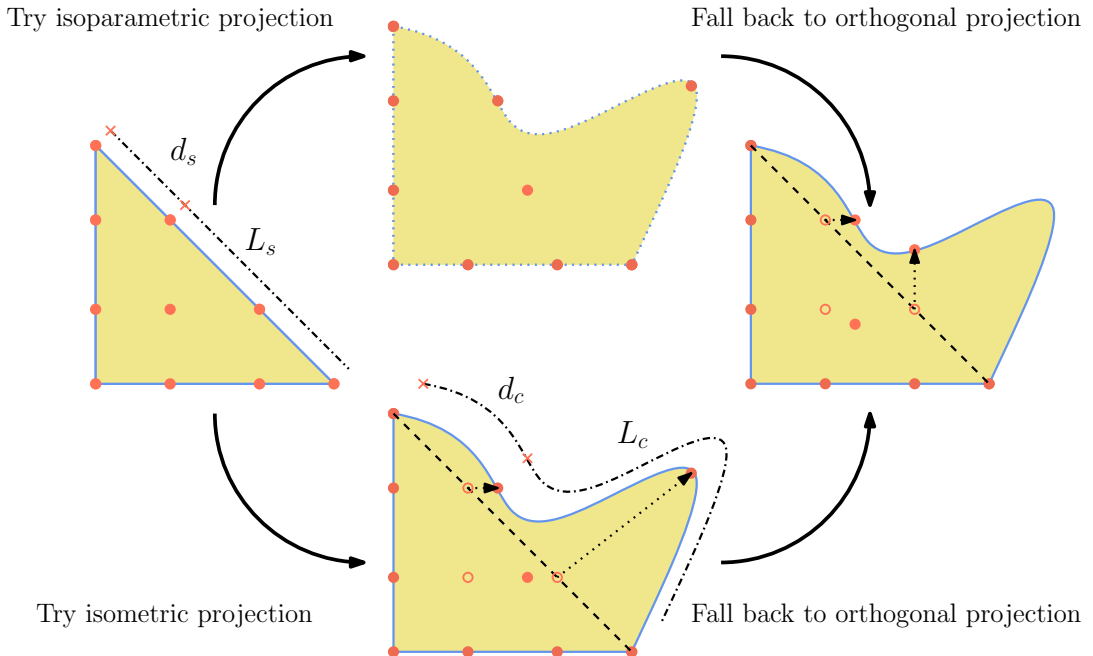


Figure 3.7: Mixed projection strategy

### 3.7 Multi-level mesh deformation technique

All mesh generators are essentially hierachic in nature, in that, first the CAD curves are discretised to edges, then the CAD surfaces are discretised to surface elements and finally the domain enclosed by surfaces is meshed using volume elements [106, 261, 243, 174, 182, 267, 268, 277]. It is essential to follow the same paradigm for solid mechanics based mesh deformation techniques (i.e. the solid mechanics mesh deformation analogy has to be performed at various levels), otherwise one may end up with self-intersecting, boundary piercing and invalid meshes. Such situations are more common in generating high order meshes, where untangling can

become problematic. A typical example of one of the most likely arising problem is shown in stage 4 of Figure 3.8 where the planar CAD surface is projected correctly but the interior nodes fall outside of the main computational mesh. This problem typically occurs when the CAD geometry consists of planar surfaces potentially with multiple curve intersection between them. In other words in a planar surface the projected node is always going to coincide with the actual node, since node projection does not have the knowledge of in-plane translation that would be necessary for successful mesh deformation. This problem can be successfully solved, if an in-plane solid mechanics problem is solved for each planar surface. This typically leads to a multi-level mesh deformation technique, implemented in this work. The multi-level mesh deformation technique, first checks for curve intersections and planar surfaces. Projecting onto curves is also useful for modelling curved rods and beams and can be hence termed the **one-dimensional step**. Next, all the 2D planar surfaces are solved for using a plane strain solid mechanics analogy for mesh deformation. This is certainly, the **two-dimensional step**, in which all the surfaces affected by the curve intersections are solved for and the high order curved surface mesh is produced. Finally, the final boundary conditions are computed from the first two steps and fed into a 3D solid mechanics problem and the whole computational mesh (volume) is solved for. This is the **three-dimensional step**. A graphic representation of the multi-level mesh deformation technique is shown in Figure 3.8. Note that the combination of different projection techniques and multi-level/hierarchic solid mechanics analogy for mesh deformation facilitates a unique framework for untangling high order curved mesh, by allowing the high order nodes to slide on curves and surfaces.

Note that, most mesh deformation techniques either do not have this capability or completely ignore the in-plane translation and node sliding step [242, 218, 219]. Some a posteriori curved mesh generation techniques use other post-processing and geometrical based mesh cosmetics to alleviate this problem. A different yet similar in spirit approach to allowing the nodes to slide on CAD curves has been recently presented in [265].

### 3.8 Representative examples

This section presents a detailed comparison of the various solid mechanics formulations considered in this work (refer to Table 3.1) for the a posteriori generation of high-order curvilinear meshes. The comparison focuses on the advantages and disadvantages of the various formulations, the influence of the material parameters, the degree of approximation obtained by using two and three dimensional examples and the monitoring of different quality measures. In this work, the only material parameter that is varied is the Poisson's ratio ( $\nu$ ). Notice that as detailed in [328], the Young's modulus has no real effect on the resulting high-order meshes because only Dirichlet boundary conditions are considered. Therefore, in all the examples we consider  $E = 10^5 \text{ GPa}$ ,  $E_A = \frac{5E}{2}$  and  $G_A = \frac{E}{2}$  and the Poisson's ratio is selected within the interval [0.001, 0.495].

To simplify the presentation, the following acronyms are utilised:

- Incremental Linear Elastic (ILE)
- Consistent Incrementally Linearised (CIL)

for incremental linear elastic and consistent incrementally linearised formulations, respectively. When these acronyms are not used in conjunction with a material model, the formulation should be assumed to correspond to a fully non-linear analysis. For the sake of brevity the names of the following two material models are also shortened to

- Nearly Incompressible Mooney-Rivlin (NI-MR)
- Transversely Isotropic (TI)

In all the examples, the linear system of equations resulting from the finite element discretisation, is solved using UMFPACK [64] and the Multi-frontal Massively Parallel Solver

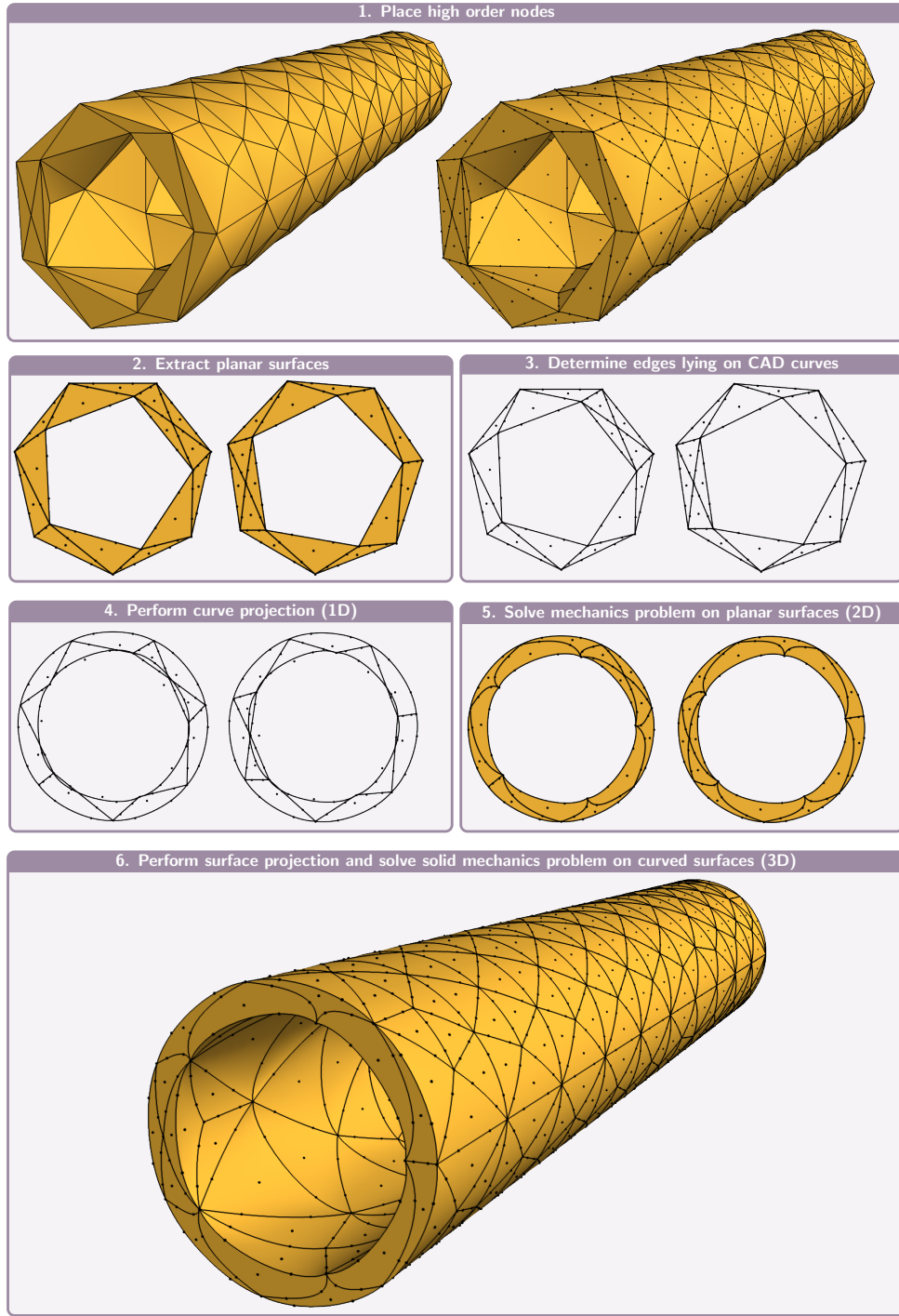


Figure 3.8: Multi-level projection and solid mechanics analogy for curves, followed by surfaces, followed by volumes

(MUMPS) [12] for the systems that result in two-dimensional and three-dimensional examples, respectively. The non-linear systems are solved using a standard Newton-Raphson algorithm where the tolerance is set to  $10^{-5}$ . Finally, it is worth noting that a standard isoparametric finite element formulation is considered throughout this work, using Lagrange polynomials with optimal distribution of nodes for interpolation [328] and also the optimal quadrature points for triangles and tetrahedra reported in [323] are considered for numerical integration.

The developed code, called **PostMesh**, has been released as an open-source software under MIT license and is available through the repository <https://github.com/romeric/PostMesh>.

### 3.8.1 Mesh of a mechanical component

As a first example we consider an isotropic mesh of a mechanical component. The geometry is given by 28 NURBS curves describing the boundary of the domain as depicted in Figure 3.9.

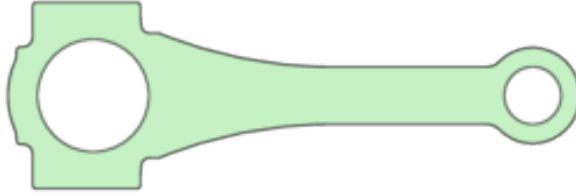


Figure 3.9: Geometry of mechanical component.

The initial linear triangular mesh is shown in Figure 3.10 (a), having 192 elements, 129 nodes and 68 boundary edges. The produced mesh using the ILE approach for a degree of approximation  $p=5$  is shown in Figure 3.10 (b), having 2,569 nodes.

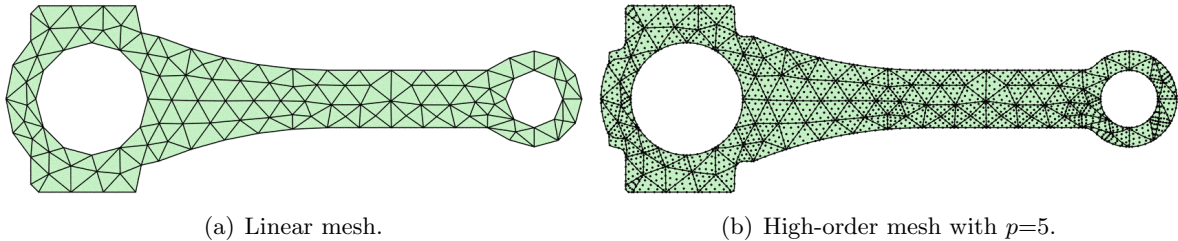


Figure 3.10: Isotropic mesh of mechanical component.

A detailed view of four high-order meshes produced using the same ILE approach is shown in Figure 3.11, showing the large distortion that is induced by the projection of the boundary nodes over the true boundary. In addition, the better approximation of the true boundary shown in Figure 3.9 as the polynomial order is increased, can be clearly observed.

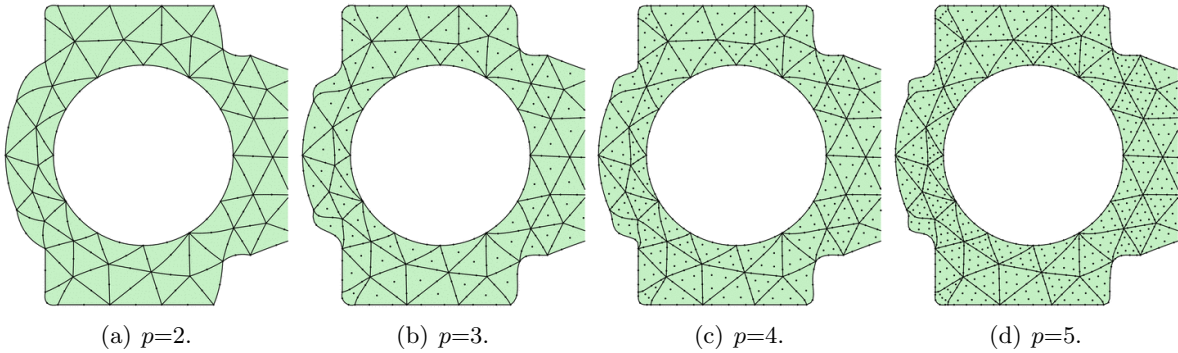


Figure 3.11: Detailed view of the high-order isotropic meshes of mechanical component.

### Effect of material properties

Figure 3.12 shows a comparison of the quality of the generated curvilinear meshes using linear, incrementally linearised and non-linear approaches. In all cases, the deformation of the boundary has been imposed using five increments and the minimum scaled Jacobian is used as a quality measure.

One can observe that the quality of the meshes produced with the ILE isotropic and CIL neo-Hookean approaches is almost identical, although the CIL neo-Hookean approach seems to provide better quality for high-order (e.g.  $p=5$ ) approximations and for values of the Poisson's

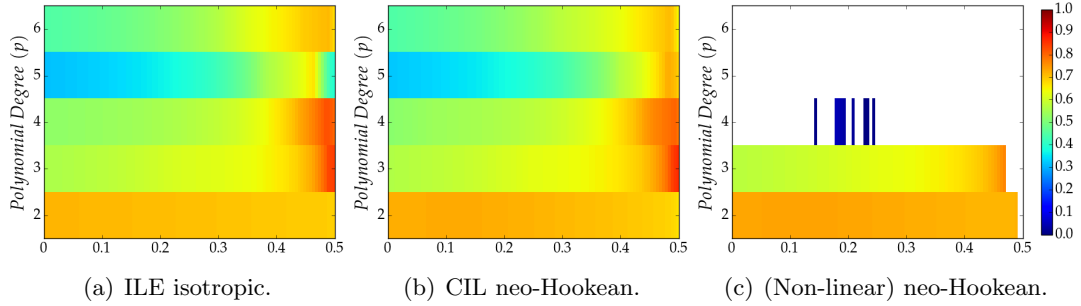


Figure 3.12: Minimum scaled Jacobian of the generated meshes as a function of the Poisson’s ratio and the polynomial degree.

ratio near the incompressible limit. Despite this difference, both approaches are able to produce high quality meshes for any degree of approximation tested. In contrast, the (non-linear) neo-Hookean approach fails to produce a high-order mesh for high-order approximations, except for a few cases where a low-quality mesh for  $p=4$  is produced. The quality of the produced meshes for lower order approximations (i.e.,  $p=3,4$ ) is similar to the quality produced by the ILE isotropic and CIL neo-Hookean approaches, but it is worth noting that the (non-linear) neo-Hookean approach also fails in the nearly incompressible region, whereas the ILE isotropic and CIL neo-Hookean approaches produce the best quality meshes in this scenario.

One should note that, unlike the linearised approaches wherein the internal nodes of the mesh move proportionally to the boundary nodes, in the non-linear approach the internal nodes can move arbitrarily within the element, and this can in turn affect the quality and approximation property of the produced meshes. In a purely displacement-based formulation, it is not possible to restrain the movement of internal nodes to a desired proportion. In this context, higher order gradient theories [214, 88, 19] and more elaborate mixed formulations [271, 28], offer a potential future research direction. From the mesh quality point of view, this makes the application of the non-linear approach for mesh deformation questionable, as under highly large and complex deformations, even more involved techniques such as line search and arc length [30] cannot help improve the Newton-Raphson to achieve convergence, other than perhaps enhancing the continuum using higher order gradient theories [214, 88, 19] and/or relying on a more sophisticated mixed formulation [271, 28].

### Effect of polyconvexity and the choice of material model

Next, we compare the effect of all the material models presented earlier in this chapter on the quality of generated meshes, for all the three approaches. Figure 3.13 shows the quality (minimum scaled Jacobian) as a function of the Poisson’s ratio for all the different models considered in this work, when a polynomial approximation of degree  $p=2$  is employed. For the transversely isotropic model, the negative  $x$ -axis is chosen as the direction of anisotropy for the interior elements. For the elements in the boundary, the direction of anisotropy is computed to be perpendicular to the unit normal to boundary edge. This technique is customary in the field of fibre-reinforced composites.

The results show that the quality displayed with neo-Hookean, Mooney-Rivlin and nearly incompressible materials is almost identical for any value of the Poisson’s ratio, whereas a different behaviour is obtained for the transversely isotropic model. The best quality is obtained with the ILE TI model and with a Poisson’s ratio near 0.5. However, it is worth emphasising that a small variability of the quality is obtained in all cases as all simulations provide a high-order mesh with quality belonging to [0.67,0.77].

Next, the same comparison is performed for higher order approximations, but the results with a Mooney-Rivlin and nearly incompressible models are omitted because, in all cases, the results are almost identical to those obtained with a neo-Hookean model. Figure 3.14 shows the quality (minimum scaled Jacobian) as a function of the Poisson’s ratio when a polynomial

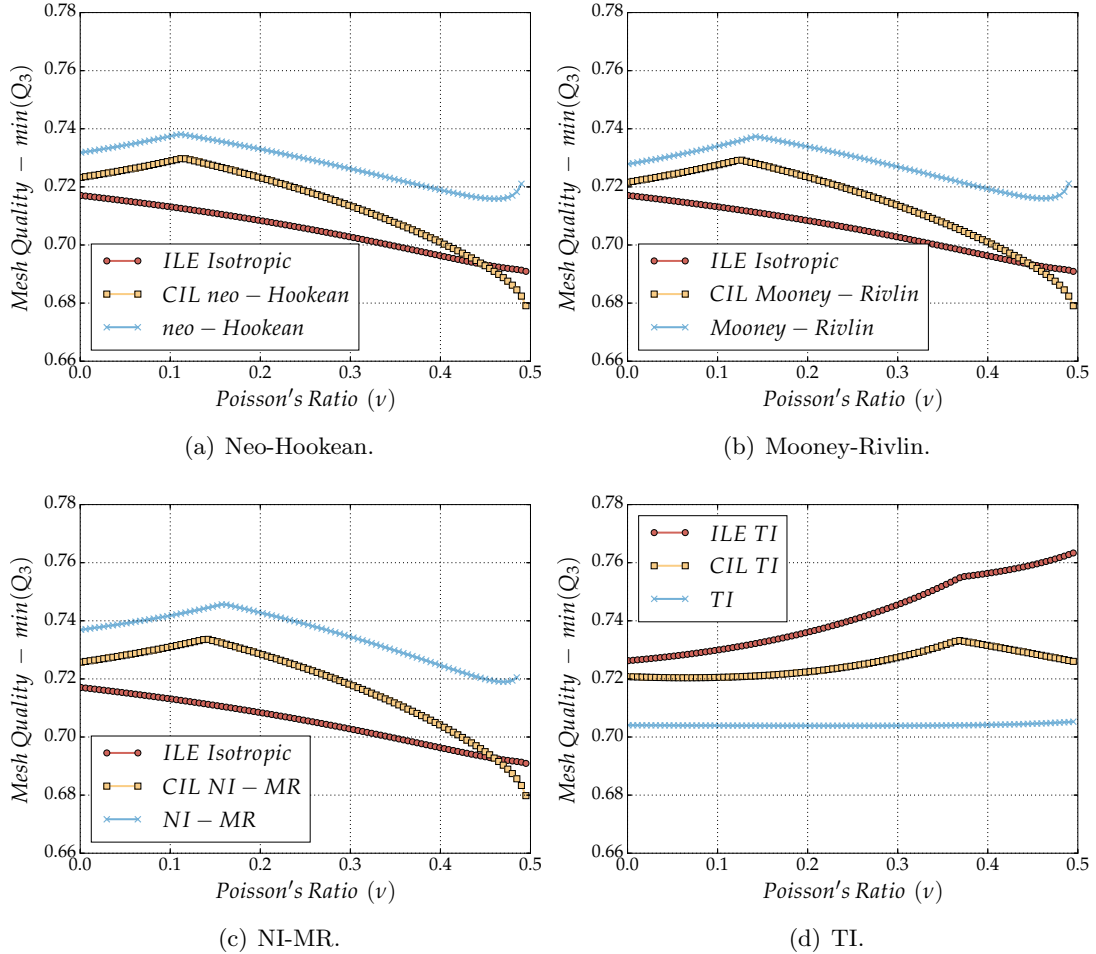


Figure 3.13: Minimum scaled Jacobian of the generated meshes as a function of the Poisson's ratio for  $p=2$  using the ILE isotropic, CIL and non-linear approaches with different material models.

approximation of degree  $p=3$  is considered.

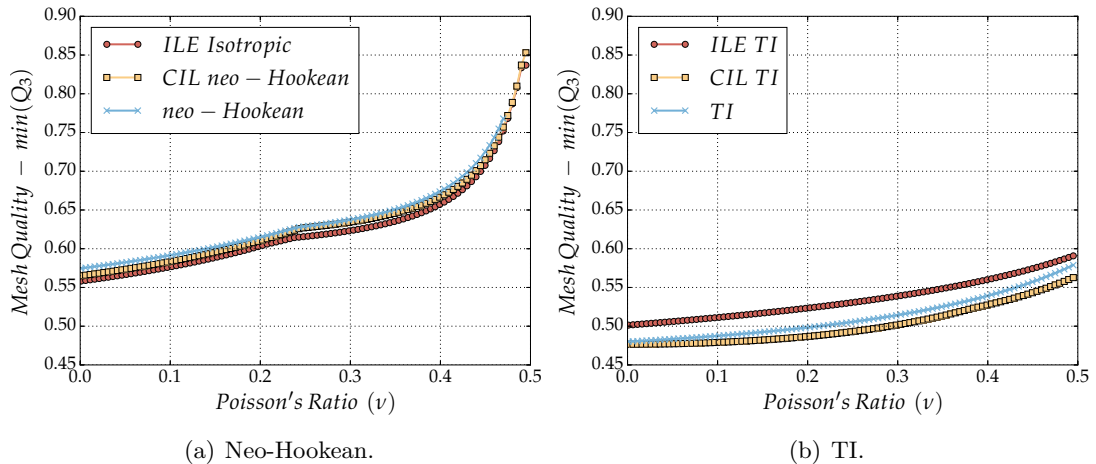


Figure 3.14: Minimum scaled Jacobian of the generated meshes as a function of the Poisson's ratio for  $p=3$  using the ILE isotropic, CIL and non-linear approaches with different material models.

A different trend is observed, when comparing the results with  $p=3$  to the results with  $p=2$  displayed in Figure 3.13. With  $p=3$  the quality of the mesh improves as the Poisson's ratio

is increased, providing the best results always when the incompressible limit is approached. This behaviour is expected in general because when the Poisson's ratio is taken near 0.5, the imposed displacement on the boundary induces a larger displacement of the interior nodes. In contrast, when a value of the Poisson's ratio near 0 is considered, the imposed displacement on the boundary induces small displacement on the interior nodes, resulting in more distorted elements (i.e. reduced quality elements). The reason why this expected behaviour was not obtained with  $p=2$  is attributed to the lack of resolution of the displacement field when the coarse mesh considered here, see Figure 3.10, is employed with a quadratic approximation. In fact, further simulations not reported here for brevity confirm that with a finer mesh the expected trend is obtained even with a degree of approximation  $p=2$ .

In addition, the results show that the quality of the meshes produced with ILE isotropic, CIL and non-linear approaches is almost identical if a neo-Hookean model is considered, whereas the use of a transversely isotropic model reveals some differences between the three approaches. The results demonstrate the significance of choosing a well-defined material model like neo-Hookean (with a quality reported near 0.85), in contrast with a transversely isotropic model (quality reported below 0.6 for any value of the Poisson's ratio), whose limitations would be discussed shortly. It is worth emphasising that the quality obtained with the Mooney-Rivlin and the NI-MR models is almost identical to that produced by the neo-Hookean model, so that any of the three models is equally suitable to produce high quality meshes in this example, since all these material models are mathematically well-defined.

### The choice of solid mechanics formulation

Finally, Figure 3.15 shows the quality (minimum scaled Jacobian) as a function of the Poisson's ratio when polynomial approximation of degrees  $p = \{4, 5, 6\}$  are considered. The conclusions that are implied by the results are similar to those obtained from the simulation with  $p=3$ . First, the quality obtained with the neo-Hookean model is similar for the ILE and CIL approaches whereas some differences are observed for the transversely isotropic model. However, in this case the non-linear approach is not able to converge, as already mentioned and shown in Figure 3.12. The quality of the produced meshes increases as the Poisson's ratio approaches 0.47 and the best results are obtained when a neo-Hookean (equivalently compressible or nearly incompressible Mooney-Rivlin) model is considered. It is worth mentioning that this example shows a slight drop in the quality of the mesh as the Poisson's ratio increases from 0.47 to 0.49. It should be noted that imposing the material to be incompressible in this example is not physically possible because the initial and deformed configuration have a pre-defined (and non-equal) volume as shown in Figure 3.12. Therefore, the results suggest that the Poisson's ratio should be carefully selected near the incompressible limit, but preferably of a value to ensure that some level of compressibility is allowed, for instance 0.45. This behaviour is only observed with  $p=6$  because for lower order approximations there is a lack of resolution to capture the displacement field.

The analysis for the different approaches and material models is summarised in Figure 3.16. This figure shows the mean and standard deviation of the scaled Jacobian for the ILE isotropic, CIL and non-linear approaches with different materials and degrees of approximation.

It can be concluded that the choice of material model does not play a major role, as long as the model is well-defined. As hinted before, unlike the other material models, the transversely isotropic (TI) material, does not correspond to a polyconvex energy functional, or more specifically, the invariant  $\mathbf{N} \cdot \mathbf{C}^2 \mathbf{N} = (\mathbf{F}^T \mathbf{F} \mathbf{N}) \cdot (\mathbf{F}^T \mathbf{F} \mathbf{N})$ , is not convex with respect to  $\mathbf{F}$ , and hence under highly large deformations, the model experiences instabilities in the form of loss of ellipticity which can manifest through shear-bands, fibre kinking if under compression or fibre de-bonding if under stretch; c.f. [207] and [208], for an intensive study on the loss of ellipticity for this invariant. The latter two phenomena (fibre kinking and de-bonding) also hold true for the transversely isotropic linear materials. As a consequence, it can be observed that the mean quality of the high-order meshes generated with a transversely isotropic material deteriorates as the order of approximation is increased, compared to the other material models.

Overall, the ILE isotropic approach is found to be the most robust, providing the best or

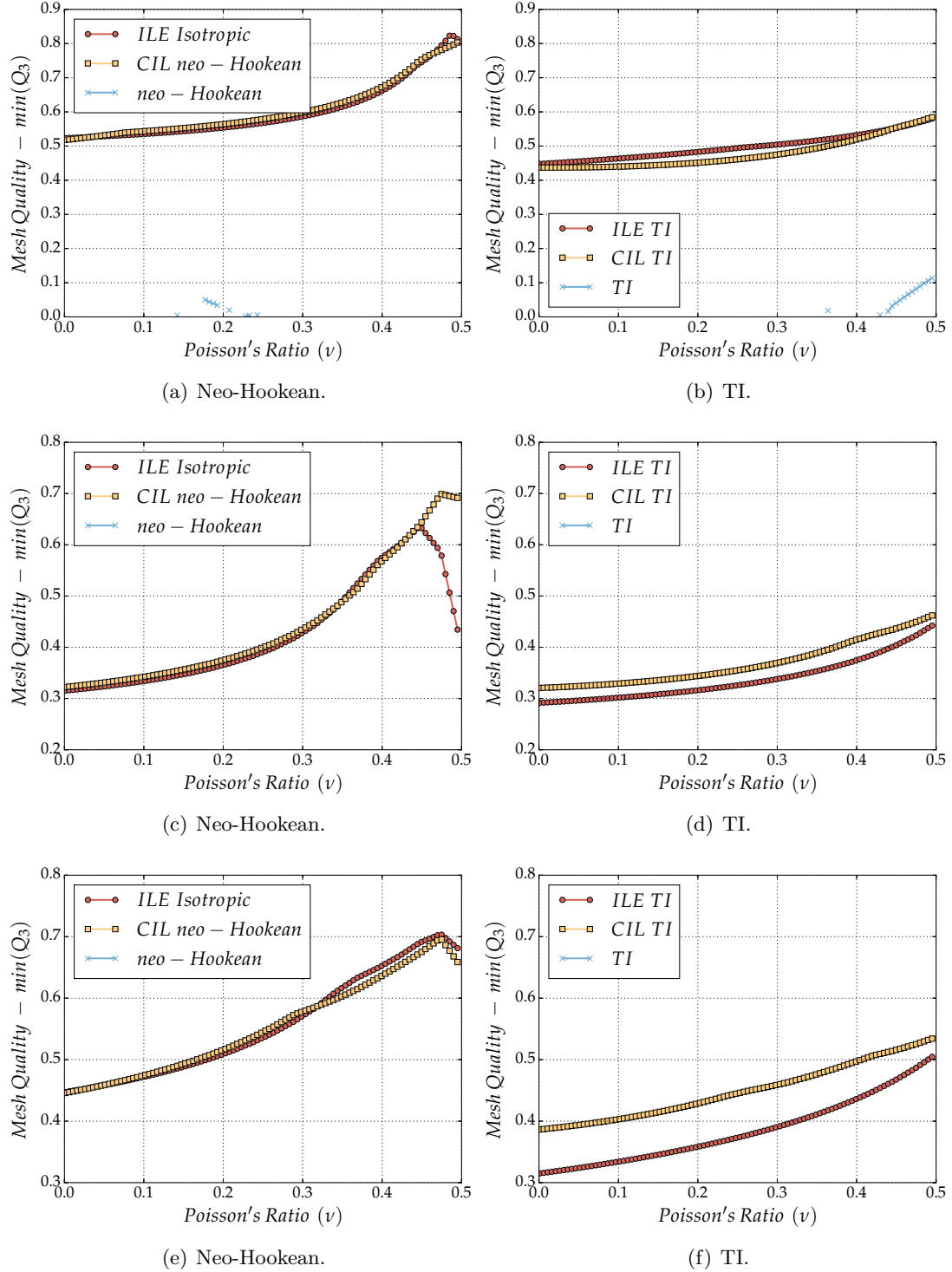


Figure 3.15: Minimum scaled Jacobian of the generated meshes as a function of the Poisson's ratio using the ILE isotropic, CIL and non-linear models with different material models and  $p=4$  (a,b),  $p=5$  (c,d) and  $p=6$  (e,f)

near the best mean quality for all orders of approximation. Also, it is worth noting that for all material models the standard deviation grows as the order of approximation is increased, implying that a good choice of the Poisson's ratio is more important as the order of approximation is increased.

Next, the effect of the Poisson's ratio, the different approaches and material models on the condition number of the system matrix is illustrated in Figure 3.17. The condition number is computed using the lower bound one-norm estimate of Higham [124].

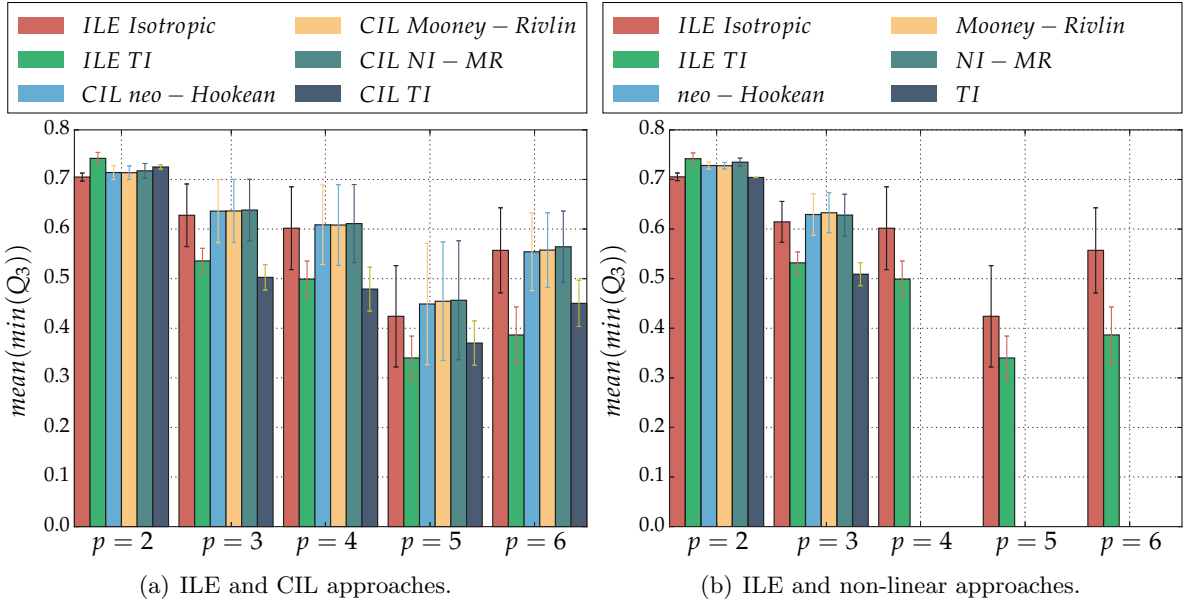


Figure 3.16: Mean value and standard deviation of the minimum scaled Jacobian of the generated meshes as a function of the Poisson's ratio for different materials and degrees of approximation.

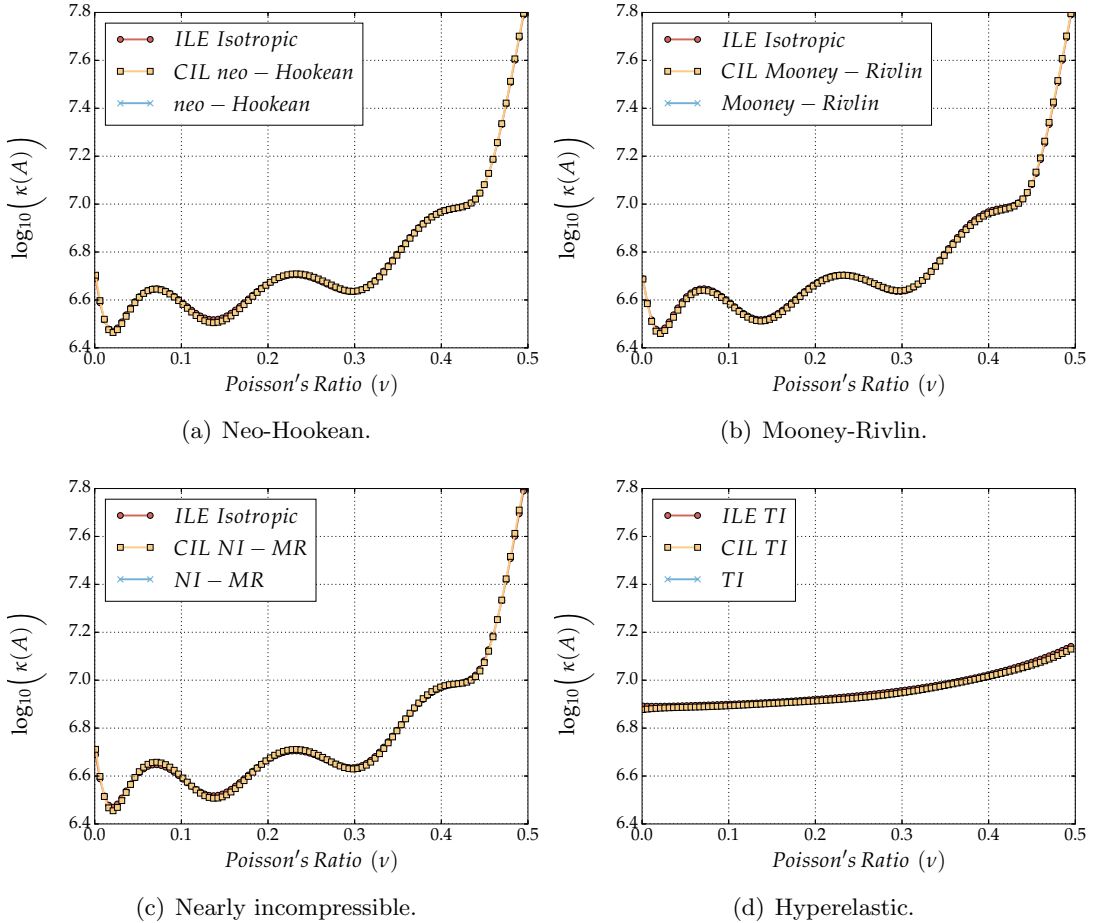


Figure 3.17: Condition number of the system matrix as a function of the Poisson's ratio for  $p=4$  using the ILE isotropic, CIL and non-linear approaches with different material models.

Again, the results show that the condition number with neo-Hookean, Mooney-Rivlin and NI-MR is almost identical for any value of the Poisson's ratio, whereas a different behaviour is

obtained for the transversely isotropic model. In all cases the condition number increases as the Poisson's ratio approaches the incompressible limit but it is worth noting that a slightly lower condition number is obtained when the transversely isotropic model is considered, irrespective of the use of ILE isotropic, CIL and non-linear approaches. This is inherently due to anisotropic nature of the model, as the deformation is not homogenous in every direction and hence the effect of Poisson's ratio is not equally pronounced for this model. The results with other degrees of approximation are omitted, as exactly the same behaviour is observed.

### Effect of different projection techniques

We next consider the effect of different projection techniques on the quality of the generated meshes. For 2D analysis one can only consider the isometric projection and the orthogonal projections. Figure 3.18 shows a comparison of the isometric and orthogonal projection techniques and its effect on the quality of for different Poisson's ratio and polynomial degree. As was mentioned earlier, the isometric and isoparametric projections are ideal as the maintain the relative distance of the nodes in the curved mesh. In contrary, the orthogonal projection performing a minimisation technique in Euclidean space can place the projected node arbitrarily. As can be seen, for certain geometrical representations and meshes this can affect the quality of the mesh adversely.

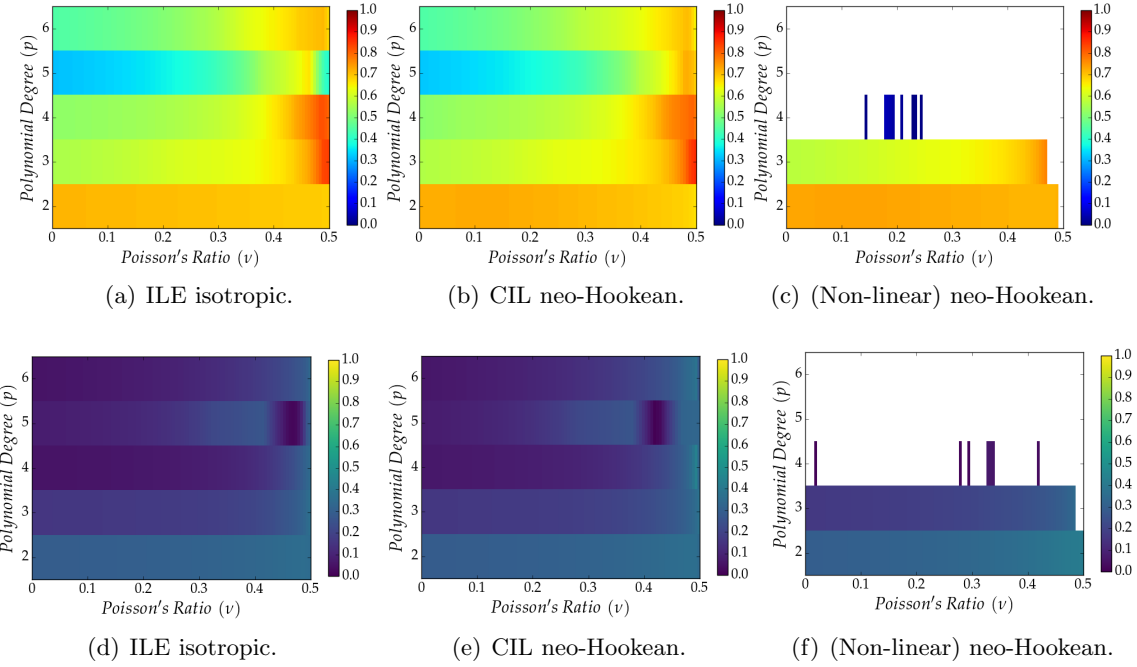


Figure 3.18: Minimum scaled Jacobian of the generated meshes as a function of the Poisson's ratio and the polynomial degree for isometric(a,b,c) and orthogonal(d,e,f) projection techniques.

### Computational cost of different formulations

The last analysis is aimed to compare the computational cost of each formulation with different material models and different orders of approximation  $p$ . As it is not feasible to a priori know the number of iterations required by the non-linear approach to converge, a comparison of the actual computing time is considered here.

Whilst theoretically, the non-linear approach should cost `number of iterations × number of increments` times more than the linear model, in practice, due to differences in the sparsity pattern and condition number of the system as well as CPU warm-up and pipelining, this is not often the case. In fact, comparison of non-linear against linear approaches is analogous to

cold versus hot benchmarking, in that with a higher number of iterations, the processor becomes progressively more accurate with branch prediction and guessing `jmp` operations, which helps improve processor pipelining. On the other hand, for highly non-linear problems, with every iteration of the non-linear analysis the condition number increases, hence impacting the run-time. With this in mind, we report the geometrical mean of 100 run-times, excluding the timing for the first 10 runs. An in-house tool similar to [Google Benchmark](#) is used for time measurements. For all time measurements, parallelisation has been turned off. Material data and  $p$  are deliberately chosen such that the non-linear analysis would converge. The analysis corresponds to  $\nu = 0.4$  with other parameters remaining constant as before.

Figure 3.19 shows the CPU time using the three formulations and different material models when the boundary displacement is imposed using five load increments using a polynomial approximation of degree  $p=2$  and  $p=3$ . The CPU timings have been normalised with respect

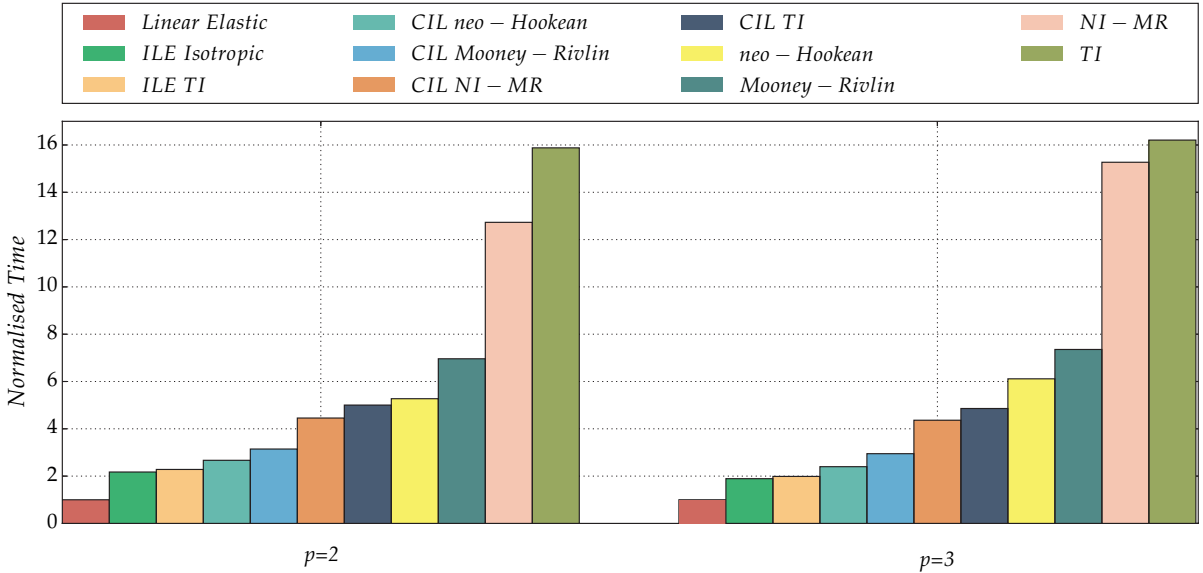


Figure 3.19: Computational cost of various material models using three different formulations with  $p=2$  (902 degrees of freedom) and  $p=3$  (1,930 degrees of freedom).

to that of classical linear elasticity (i.e. one increment). It is important to note that, due to the small size of the problem, all systems are solved using UMFPACK, the cost of solver is negligible and the condition number of the system does not adversely affect quadratic convergence of Newton-Raphson. Furthermore, for a problem of this size, a portion of the computational time corresponds to the overhead of function calls.

The computational cost associated with the different material models is clearly related to the cost of their tangent operator evaluation. In the case of linear elasticity, the tangent operator can be computed at the pre-processing stage. For a neo-Hookean model the two fourth order identity tensors  $\mathbf{I} \otimes \mathbf{I}$  ( $\delta_{ij}\delta_{kl}$ ) and  $\mathbf{I}'$  ( $\delta_{ik}\delta_{jl} + \delta_{il}\delta_{jk}$ ), appearing in the tangent operator, are compile time constants. For Mooney-Rivlin, nearly incompressible Mooney-Rivlin and transversely isotropic hyperelastic models, the dyadic products in the tangent operators are run-time variables and their computation is not always cache-friendly due to unavoidable strided indexing [c.f. last chapter on detailed analysis of tensor networks]. In fact for complex material models identifying the optimal contraction indices of tensor networks is not trivial [251, 245, 93]. Using Voigt notation and further permutations, these dyadic products can be transformed to further `gemm` calls, which eventually may or may not be beneficial. Also, the nearly incompressible and transversely isotropic hyperelastic models require computation of co-factors  $\mathbf{H}$  and  $\mathbf{HH}^T$ , at every quadrature point which are all  $O(n^3)$  in computational complexity.

In this example, the ILE isotropic approach is found to be the most competitive. This allows to conclude that, for this example, the ILE isotropic approach provides both the best

quality and the lowest computational cost compared to other approaches and material models. Furthermore, one should note that the qualities reported here are not indicative of the maximum quality that can be obtained, as the number of load increments is rather kept fixed to facilitate an impartial comparison between different approaches. Finally, although CPU time measurements are always dependent on the implementation, the results reported here provide a qualitative indication of the higher cost associated to a non-linear approach. The CPU timing, together with the already discussed convergence difficulties of non-linear approaches for high-order approximations, clearly provides an indication of the limited scope of such an approach for a posteriori high-order mesh generation.

### 3.8.2 Mesh around the SD7003 aerofoil

The second example considers anisotropic boundary layer meshes around the SD7003 aerofoil with different levels of stretching in the boundary layer. The detailed view near the leading edge of the initial linear triangular mesh shown in Figure 3.20 (a) corresponds to a stretching factor of 25 (measured as the length of the largest edge divided by the shortest edge for an element in the boundary layer), having 2,171 elements, 1,140 nodes and 85 edges on the curved boundary. The produced mesh using the ILE approach for a degree of approximation  $p=5$  is shown in Figure 3.20 (b), having 27,410 nodes.

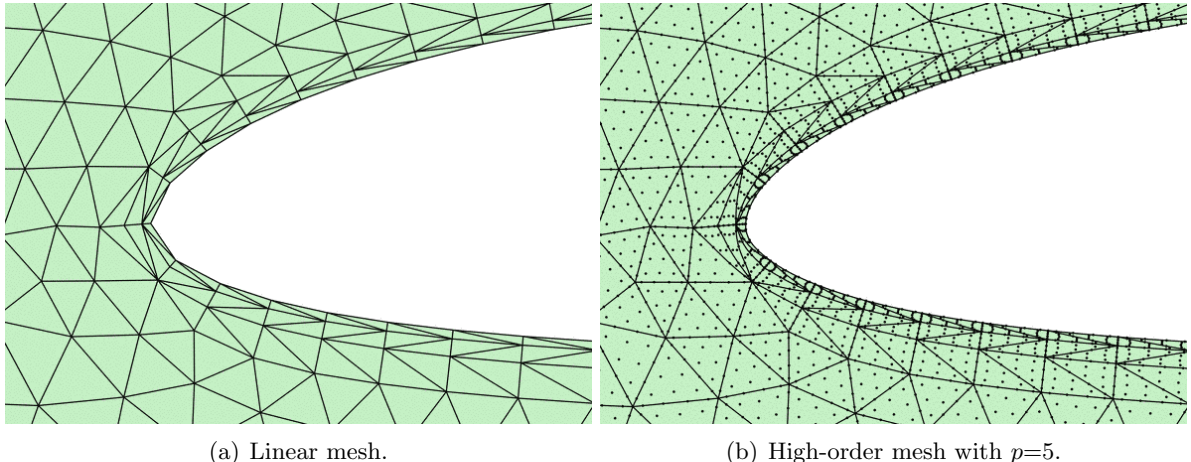


Figure 3.20: Boundary layer mesh around an aerofoil.

### The choice of different solid mechanics formulations on stretching

It should be mentioned that, similar to the previous example, it was found that the choice of material model does not have an effect on the quality of the curved meshes and that the transversely isotropic material shows a similar pattern of loss of ellipticity. In the light of these findings, we abandon the comparison of material models for the present example and unless otherwise stated, we only utilise the neo-Hookean model with its linearised version. In contrast, due to high level of stretching of the meshes considered here, the effect of the number of load increments on the quality of generated meshes will be investigated.

Figure 3.21 shows the quality of the high-order meshes, measured as the minimum scaled Jacobian, as a function of the Poisson's ratio and the number of load increments for the ILE isotropic, CIL neo-Hookean and (non-linear) neo-Hookean approaches.

Once more, the non-linear approach is not able to provide a solution in all cases (i.e. for all values of the Poisson's ratio and number of load increments). In fact, when it converges, the quality of the non-linear approach is generally lower than the quality of the ILE isotropic and the CIL neo-Hookean approaches. It can also be observed that the quality of the meshes produced with the ILE isotropic and the CIL neo-Hookean approaches is almost identical, for

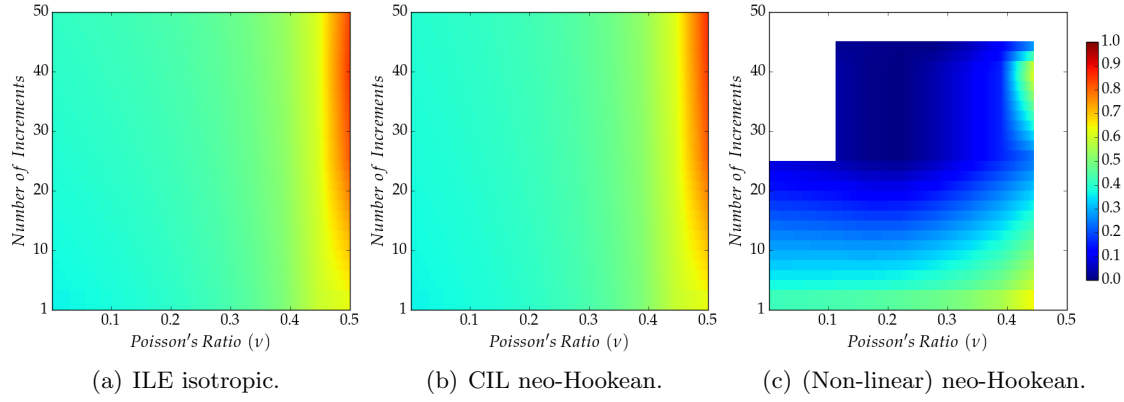


Figure 3.21: Minimum scaled Jacobian of the generated meshes with  $p=2$  as a function of the Poisson's ratio and the number of load increments.

any value of the Poisson's ratio and for any number of load increments. Finally, the results show that the best quality is obtained for value of the Poisson's ratio near the incompressible limit and ten load increments approximately. A further increase of the number of load increments does not improve substantially the quality of the meshes but it enables to obtain high quality meshes for slightly lower values of the Poisson's ratio.

Figure 3.22 shows the same analysis for meshes with significantly higher level of stretching, namely 100 and 800, for the same degree of approximation,  $p=2$ .

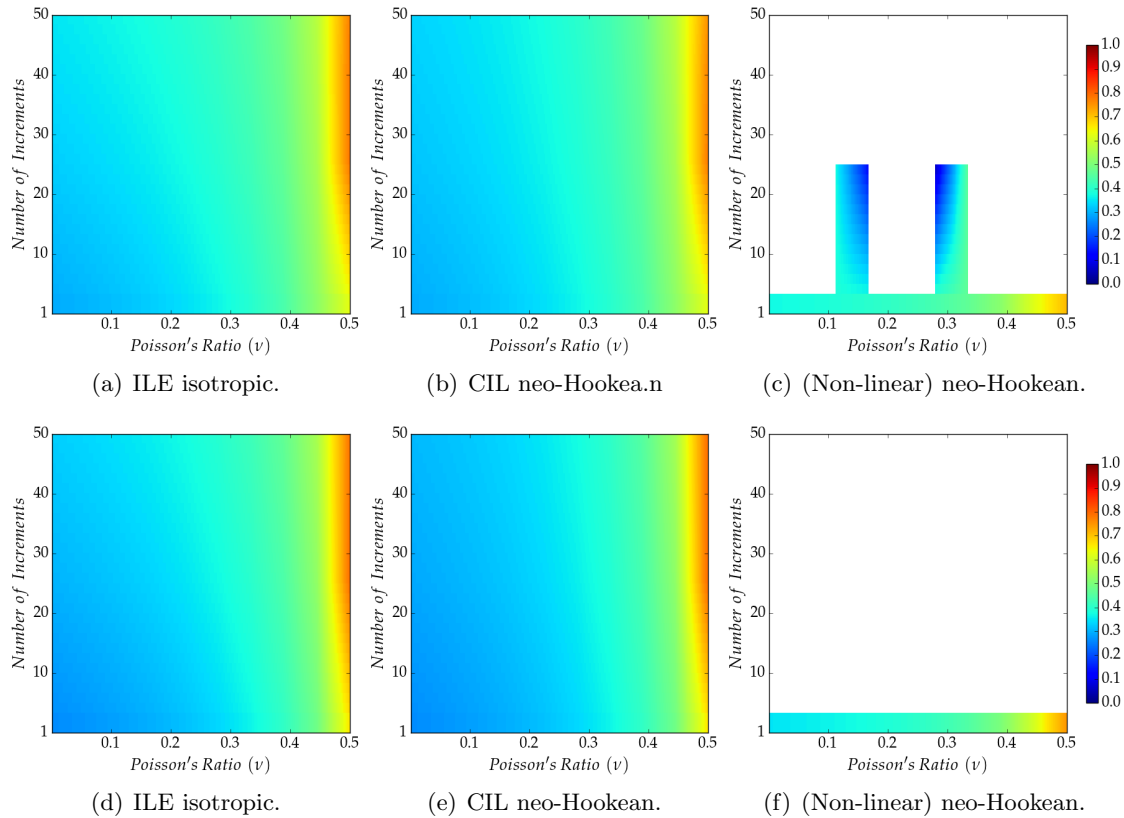


Figure 3.22: Minimum scaled Jacobian of generated meshes with  $p=2$  as a function of the Poisson's ratio and the number of load increments with a stretching of 100 in (a), (b) and (c) and with a stretching of 800 in (d), (e) and (f).

For these meshes, the non-linear approach is only able to provide a result in a few cases. In fact, further numerical experiments show that the higher the stretching, the more cases display no convergence of the non-linear approach. In addition, the quality of the meshes produced

with the ILE isotropic and the CIL neo-Hookean approaches is, again, almost identical, for any value of the Poisson's ratio and for any number of load increments, showing that the conclusions presented do not strongly depend on the level of stretching within the boundary layer.

### Effect of load increments

For the incremental linear elastic and the consistent incrementally linearised approaches, the number of load increments generally improves the mesh quality but the same is not true for the non-linear approach. If phenomena such as buckling, snap-back and snap through are not expected, the non-linear approach provides the same mesh quality irrespective of the number of increments. However, in the presence of buckling, it is possible to jump through snap-back/snap-through region with fewer load increments, but as the number of load increments is increased the buckling (i.e. snap-back/snap-through regions) cannot be avoided, which in the absence of an arc-length technique leads to non-convergence of the Newton-Raphson method. Furthermore, it is possible for the Newton-Rapshon scheme to converge just prior to the onset of buckling, at the cost of losing quadratic rate of convergence due to ill-conditioning of the system which essentially emanates from nearly zero Jacobian(s).

Next, the same analysis is performed for higher orders of approximation. Figure 3.23 and Figure 3.24 show the quality of the high-order meshes as a function of the Poisson's ratio and the number of load increments for the ILE isotropic, CIL neo-Hookean and (non-linear) neo-Hookean approaches, for a degree of approximation  $p=4$  and  $p=6$  respectively.

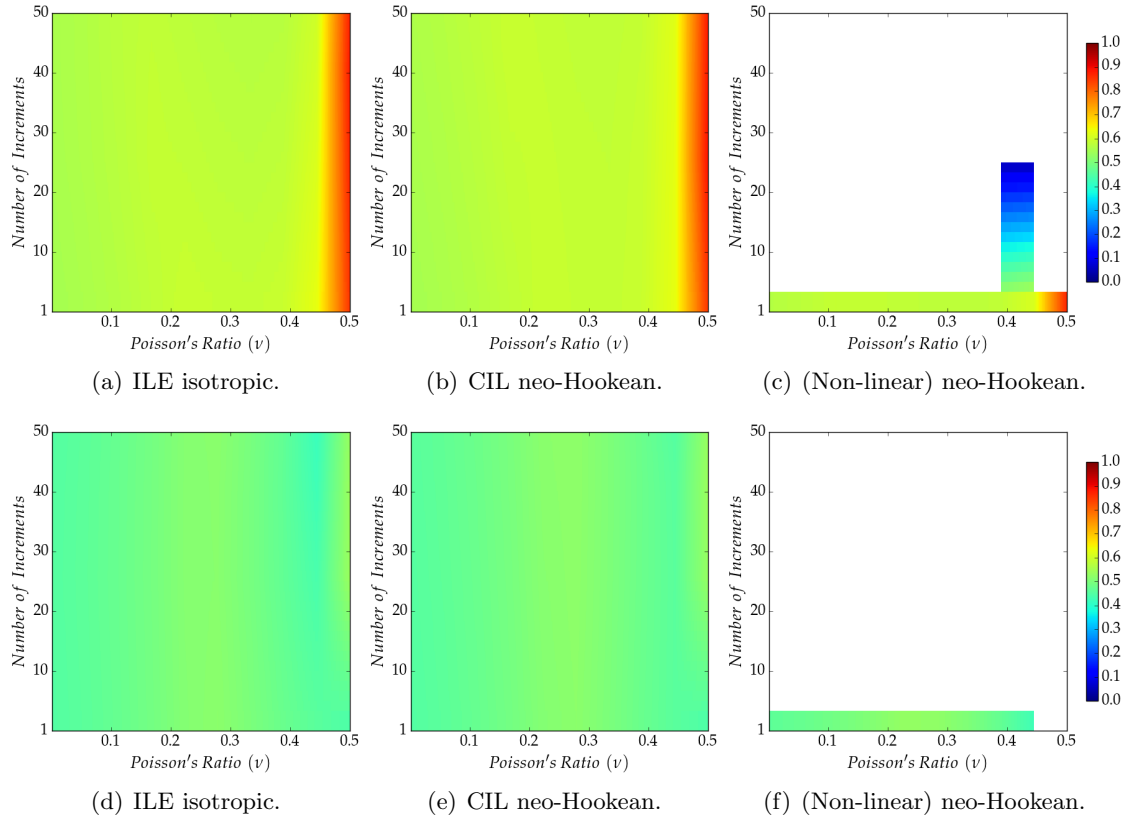


Figure 3.23: Minimum scaled Jacobian of the generated meshes with  $p=4$  as a function of the Poisson's ratio and the number of load increments with a stretching of 50 in (a), (b) and (c) and with a stretching of 400 in (d), (e) and (f).

For  $p=4$  the non-linear approach is unable to converge in the majority of cases. Only for a relatively low stretching, such as 50, and using one load increment, this approach provides a solution for any value of the Poisson's ratio. When the stretching is increased to 400, this approach fails to converge even when one increment is used if the Poisson's ratio is selected near

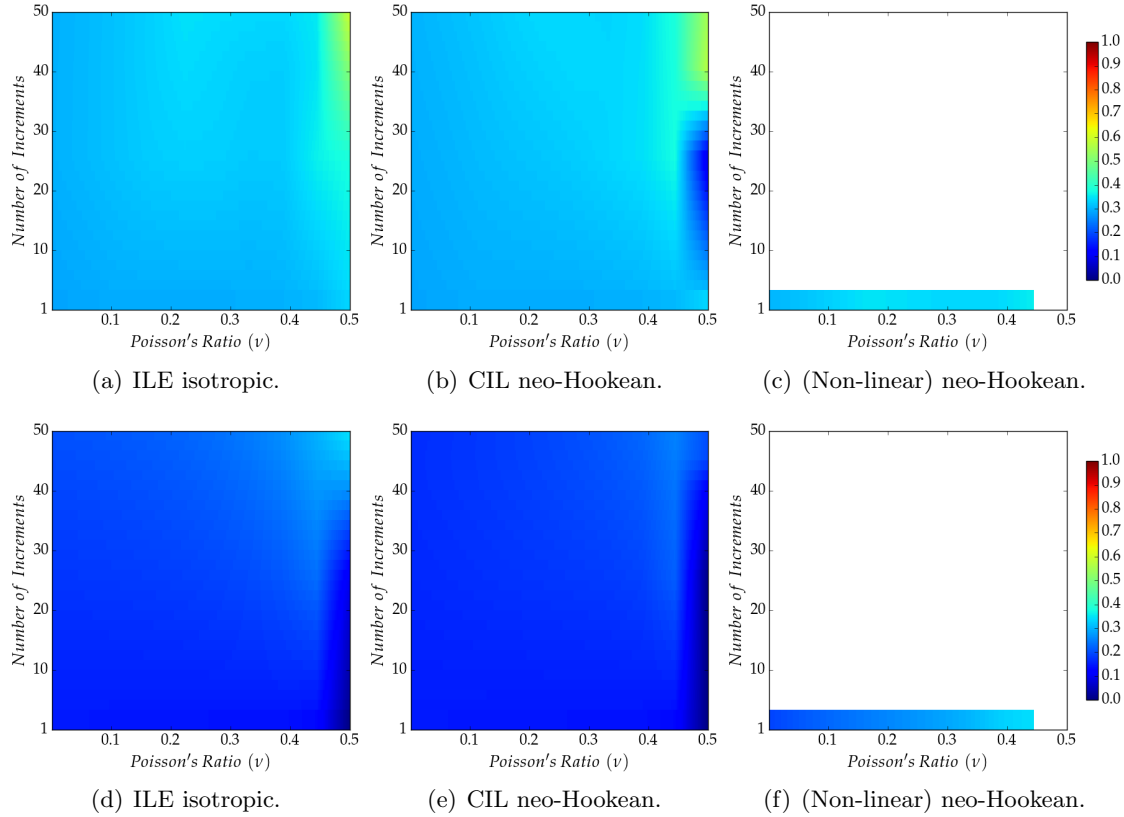


Figure 3.24: Minimum scaled Jacobian of the generated meshes with  $p=6$  as a function of the Poisson's ratio and the number of load increments with a stretching of 100 in (a), (b) and (c) and with a stretching of 800 in (d), (e) and (f).

the incompressible limit. For the ILE isotropic and CIL neo-Hookean approaches the quality of the produced meshes is, once more, almost identical for any value of the Poisson's ratio, number of increments and stretching. It worth noting that for this order of approximation, the increase in stretching translates into a significant decrease in the maximum quality that can be obtained with the ILE isotropic and CIL neo-Hookean approaches.

If the order of approximation is further increased to  $p=6$ , the problem becomes substantially more challenging and the quality of the produced meshes with either the ILE isotropic and CIL neo-Hookean approaches is significantly lower, as observed in Figure 3.24. For a stretching factor of 100, a higher number of load increments is required (approximately 40) compared to previous examples and a value of the Poisson's ratio near the incompressible limit is mandatory to obtain the best quality meshes. It is also worth noting that this example shows, for the first time, a subtle difference between the ILE isotropic and CIL neo-Hookean approaches. For a value of the Poisson's ratio near the incompressible limit, the CIL neo-Hookean approach requires more load increments than the ILE isotropic approach to obtain similar quality. The conclusions for a stretching factor of 800 are similar but, as it can be observed in Figure 3.24, both the ILE isotropic and CIL neo-Hookean approaches can only provide a maximum quality near 0.3. In this example, the non-linear approach shows once more the inability to converge in the majority of simulations.

To summarise, Figure 3.25 shows the ratio of the scaled Jacobian with 50 load increments over the classical linear elasticity (i.e. single increment), in a logarithmic scale. Note that, due to the logarithmic nature of this measure, a factor of zero implies no improvement and, furthermore, a slight improvement in terms of this factor can imply a significant change in terms of percentage value. For instance, for  $p = 6$ , and stretching of 1600, the scaled Jacobian improves from 0.0011 for a single increment to 0.3382 for 50 increments. It can be observed, that at high  $p$ , it is crucial to increase the number of load increments to obtain good quality

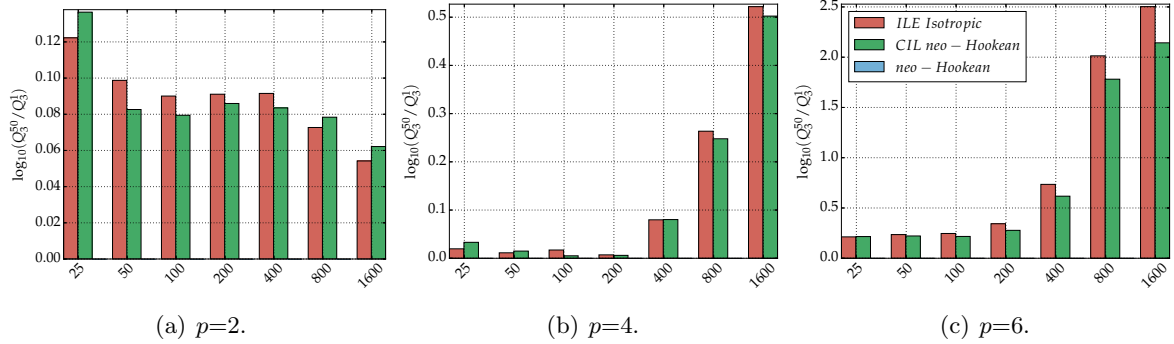


Figure 3.25: Ratio of the scaled Jacobian with 50 load increments over a single load increment (i.e. classical linear elasticity) for  $\nu=0.495$ . The  $x$ -label indicates the level of stretching.

meshes, specially if the stretching is also high. In contrast, for low-order approximations the gain obtained by increasing the number of load increments is marginal.

To further illustrate the improvement induced by an increase on the number of load increments in the quality of the generated meshes, Figure 3.26 shows a histogram of the quality for two different values of the Poisson's ratio, namely  $\nu = 0.11$  and  $\nu = 0.44$ , and for an increasing number of load increments. The simulations correspond to the mesh with stretching factor of

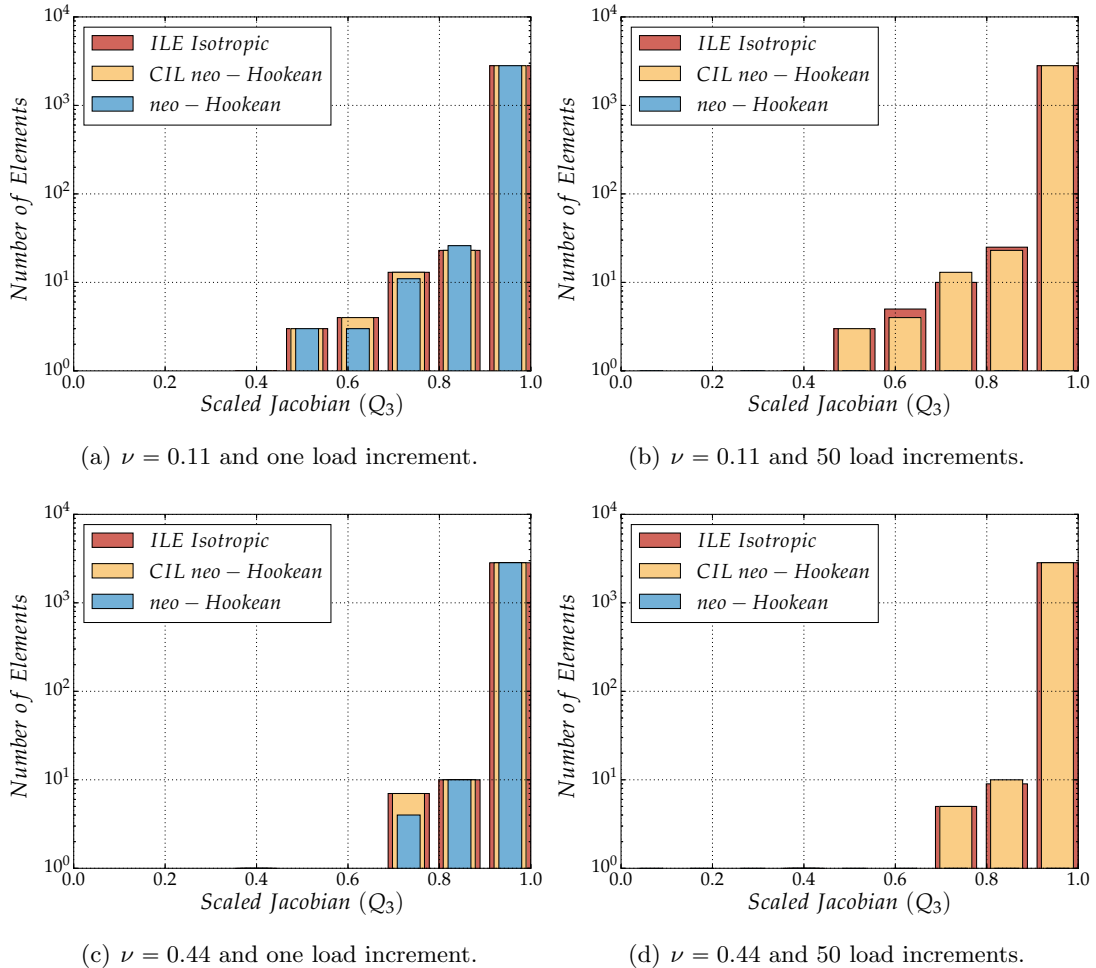


Figure 3.26: Distribution of scaled Jacobian throughout the mesh for  $p = 4$  and stretch level of 200.

200 and with a degree of approximation  $p=4$ .

A marginal difference is observed between the ILE isotropic and CIL neo-Hookean ap-

proaches both at lower values of Poisson's ratio as well as for values near the incompressible limit. As discussed earlier, this figure shows that the non-linear model is only able to converge when a few load increments are considered. However, note that due to the presence of the geometric stiffness term in the CIL approach, the interior elements are stiffened against heavy distortion and hence the CIL approach typically produces meshes with a slightly better distribution of the quality over the computational mesh, irrespective of the minimum value for quality measures. The results also show the improvement induced by an increase of the Poisson's ratio. For instance, Figure 3.26 (a) shows that the mesh contains a significant number of elements of quality 0.45 when the Poisson's ratio is 0.11 whereas the minimum quality of the mesh associated to Figure 3.26 (c), with a Poisson's ratio of 0.44, the minimum quality is near 0.75.

### The choice of right quality measures

Next, the quality of the generated meshes in terms of different measures is studied, namely the measures defined in Equation (3.26) that are defined in terms of the invariants in Equation (3.13). The two anisotropic mesh quality measures  $Q_4$  and  $Q_5$  are dropped from the comparison because they are only valid for the transversely isotropic material model, which has been shown to produce low quality meshes in the examples considered. It is worth emphasising that the qualities  $Q_1$  and  $Q_2$  are the same for two-dimensional plane strain problems.

Figure 3.27 shows the quality  $Q_1$  as a function of the Poisson's ratio and the number of load increments for the mesh with a stretching factor 50, 400 and 1600 and  $p=6$ .

The results show that the quality is substantially improved when the number of load increments is increased, as previously observed with the minimum scaled Jacobian as quality measure. However, in this example, increasing the Poisson's ratio near the incompressible limit induces a lower quality except if a large number of load increments is considered. As shown in previous examples, the ILE isotropic approach performs slightly better than the CIL approach when the Poisson's ratio is selected near the incompressible limit and the non-linear approach fails to converge in the majority of cases. Finally, by comparing Figure 3.27 and Figure 3.24, we can clearly observe that a value closer to one is obtained when using  $Q_1$  instead of the minimum scaled Jacobian. This behaviour is expected because, for this problem the deformation is primarily volumetric and the deviatoric contribution is negligible.

Figure 3.28 shows the three quality measures  $Q_1$ ,  $Q_2$  and  $Q_3$  as a function of the Poisson's ratio for the mesh with  $p=2$ , a stretching factor of 25 and using five load increments. The results confirm, numerically, that the quality measures  $Q_1$  and  $Q_2$  are the same for two-dimensional plane strain problems. It can also be observed that the ILE and CIL approaches produce meshes of the same quality, irrespectively of the measure used. In addition, the results illustrate that the quality measure  $Q_1$  (and  $Q_2$ ) is less influenced by changes on the Poisson's ratio, compared to  $Q_3$ . Finally, the results confirm, once more, the lower quality obtained with the non-linear approach compared to the ILE and CIL approaches, irrespective of the measure used.

In Figure 3.29, the effect of the stretching factor on the different quality measures is illustrated for the ILE isotropic approach using the mesh with  $p=4$  and by introducing five load increments. Almost identical results are obtained with the CIL neo-Hookean approach whereas the non-linear approach fails to converge in the majority of the cases.

The results show that the quality measure  $Q_1$  (and  $Q_2$ ) are less influenced by an increase in the stretching factor, compared to the minimum scaled Jacobian  $Q_3$ . In all cases, and for all values of the Poisson's ratio, the value of  $Q_1$  (and  $Q_2$ ) is approximately 0.9, whereas the quality  $Q_3$  can vary from 0.4 to 0.9 depending on the value of the Poisson's ratio and the level of stretching. When the quality  $Q_3$  is considered, the optimal value of the Poisson's ratio is clearly dependent on the level of stretching. For low to moderate stretching factors, a Poisson's ratio near the incompressible limit provides the highest quality whereas for very high stretching factors it is better to consider values in between 0.3 and 0.4.

Finally, Figure 3.30 shows the three quality measures  $Q_1$ ,  $Q_2$  and  $Q_3$  as a function of the Poisson's ratio for the mesh with  $p=6$ , a stretching factor of 200 and using five load increments.

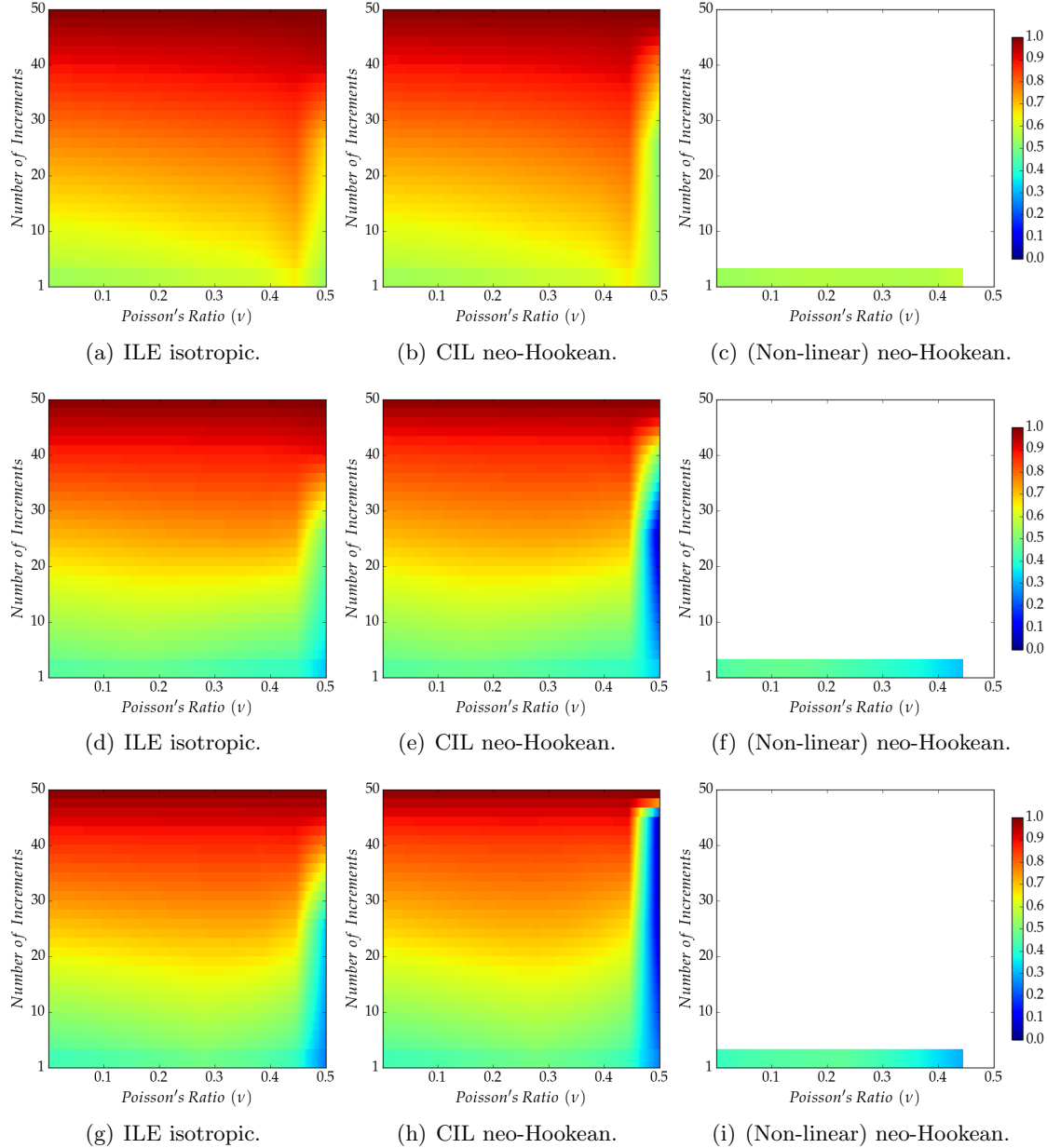


Figure 3.27: Quality  $Q_1$  of the generated meshes with  $p=6$  as a function of the Poisson's ratio and the number of load increments with a stretching of 50 (a,b,c), 400 (d,e,f) and 1600 (g,h,i).

The results correspond to the ILE isotropic and CIL neo-Hookean approaches because the non-linear approach fails to converge in all cases due to the high stretching and high-order considered in this example.

This example, shows a different behaviour of the ILE isotropic and CIL neo-Hookean approaches. The CIL approach shows a significant deterioration of the quality measure  $Q_1$  (and  $Q_2$ ) near the incompressible limit, whereas the ILE isotropic approach maintains a high quality for all values of the Poisson's ratio.

### Computational cost of different formulations

Next, under the same setting as in the previous problem, the computational time is analysed, for different formulations and using different material models. Figure 3.31 shows the CPU time using the three formulations and different material models when the boundary displacement is imposed using five load increments. The Poisson's ratio is  $\nu = 0.4$  and the order of approximation is  $p=2$ . These values are deliberately chosen such that the non-linear analysis converges

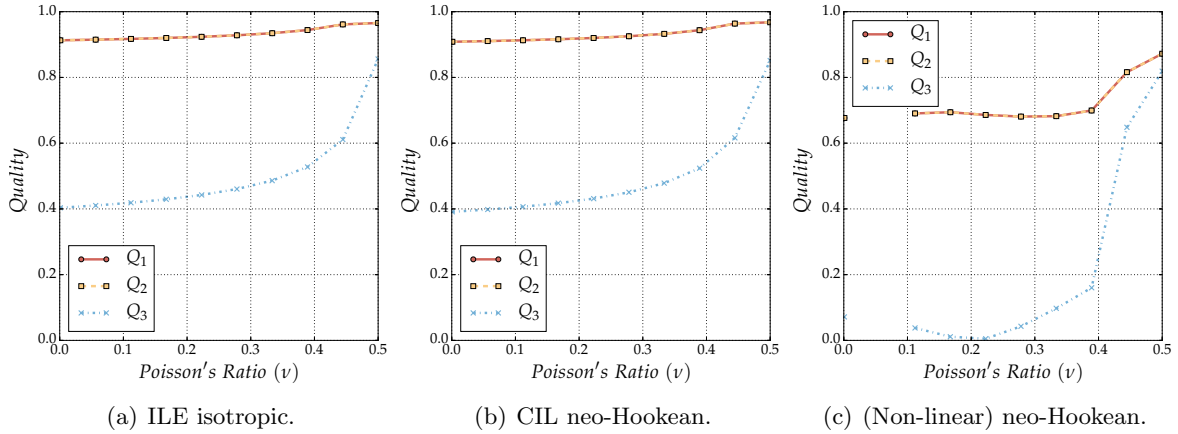


Figure 3.28: Different quality measures of the generated meshes with  $p=2$  as a function of the Poisson's ratio for the mesh with a stretching of 25 and using five load increments.

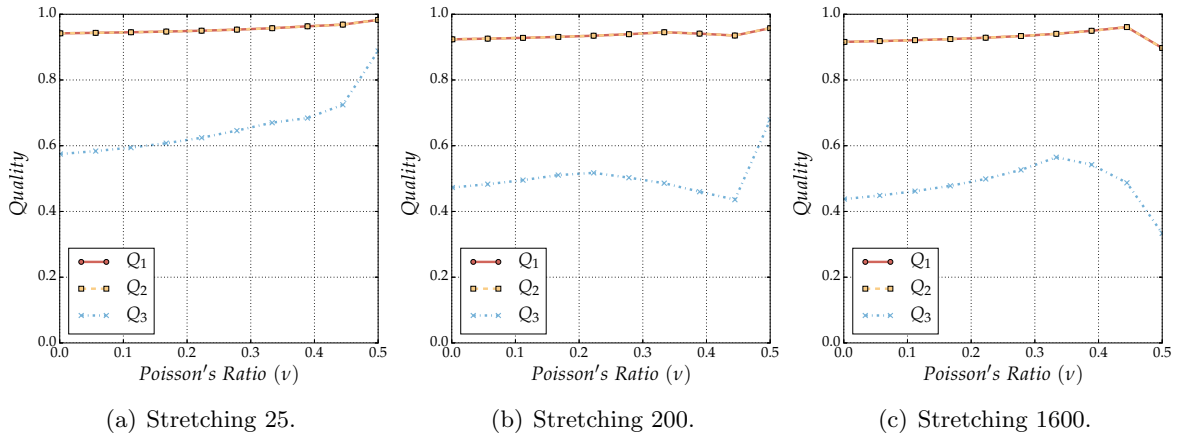


Figure 3.29: Different quality measures of the generated meshes with  $p=4$  as a function of the Poisson's ratio for the ILE isotropic approach and using five load increments.

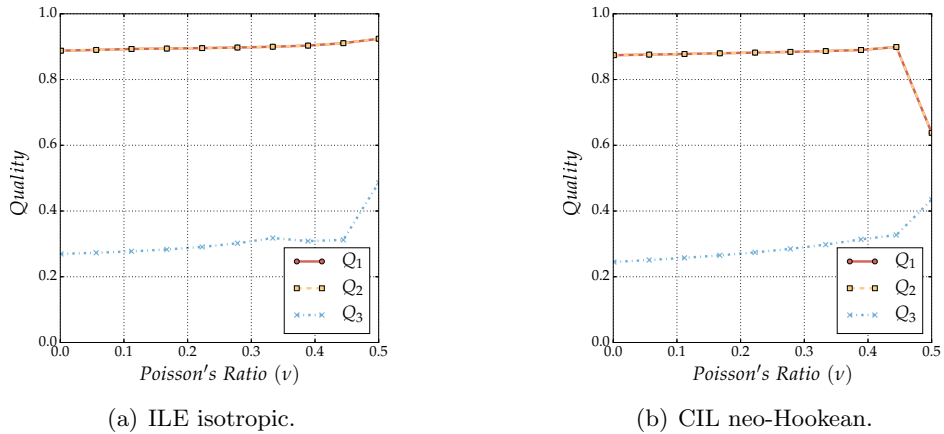


Figure 3.30: Different quality measures of the generated meshes with  $p=6$  as a function of the Poisson's ratio for the mesh with a stretching of 200 and using five load increments.

for most material models.

Compared to the previous problem, there is a significant increase in the degrees of freedom and hence the overhead of function calls is insignificant compared to the actual cost of computation.

For highly stretched meshes, the Newton-Raphson scheme loses quadratic convergence.

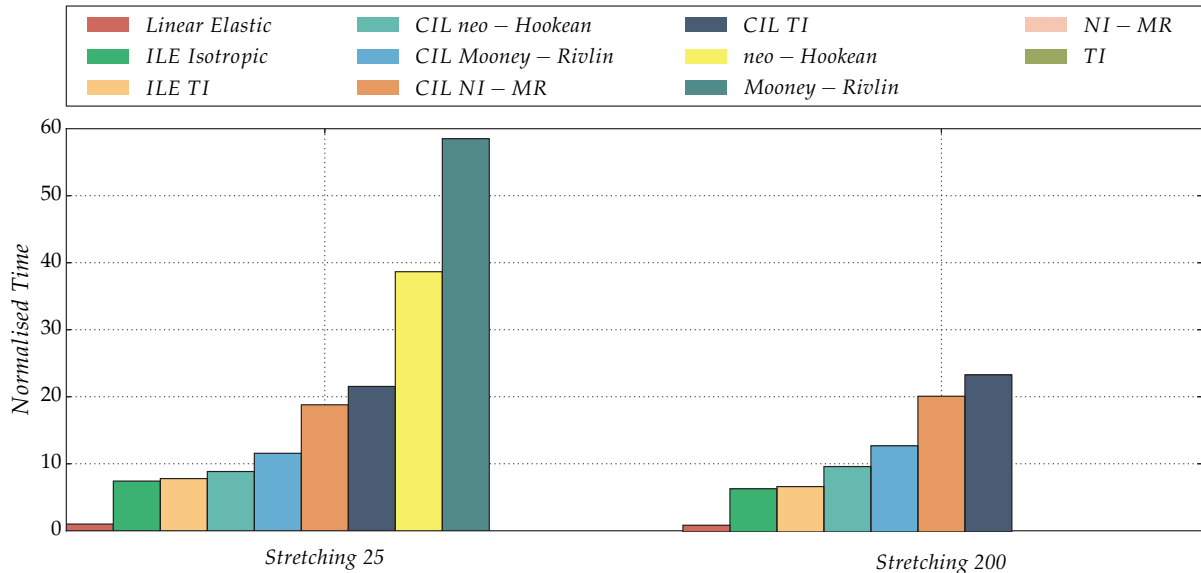


Figure 3.31: Computational cost of various material models using three different formulations and with different levels of stretching.

The increased number of iterations required and the higher cost of each iteration, due to ill-conditioning, makes the cost of the non-linear approach significantly higher. The ILE (isotropic and TI) approaches are found to be the most competitive. This allows to conclude that, as in the previous example, the ILE approaches provide both the best quality and the lowest computational cost compared to other approaches and material models.

### Effect of formulation and material models on $p$ -convergence

The last study for this example, involves a  $p$ -convergence analysis in order to illustrate the optimal approximation properties of the produced meshes. Given a smooth function defined in Cartesian coordinates, the strategy consists on computing the exact value of the solution at the mesh nodes. Then, the error between the approximated solution, interpolated from the nodal values, and the exact solution is computed at each integration point to compute the error in the  $\mathcal{L}^2(\Omega)$  norm.

Figure 3.32 shows the approximation error in the  $\mathcal{L}^2(\Omega)$  norm as a function of the square root of the number of degrees of freedom for two different levels of stretching and for a degree of approximation ranging from  $p=2$  up to  $p=9$ .

The results show the expected exponential convergence in the approximation of a smooth function. In addition, it is interesting to observe that the error is almost identical for the ILE and CIL approaches. This conclusion is in line with the previous analysis where it was shown that the quality of the meshes produced with the ILE and CIL approaches is almost identical, except in some extreme cases considering highly stretched meshes, high-orders of approximation and values of the Poisson's ratio near the incompressible limit. In contrast, the CIL TI approach, which was shown to produce lower quality for high-order approximation shows a deterioration in the convergence rate, which illustrates the importance of producing high quality meshes for finite element analysis. Finally, the results also show the ability to preserve the approximation properties independently on the level of stretching. A much more detailed analysis of approximation properties of curved elements is performed in chapter 4, in the context of convex multi-variable electro-elasticity.

### 3.8.3 Mesh around the NASA almond

The next example considers a tetrahedral mesh around the NASA almond, a popular geometry for benchmarking 3D radar cross section computations in computational electromagnet-

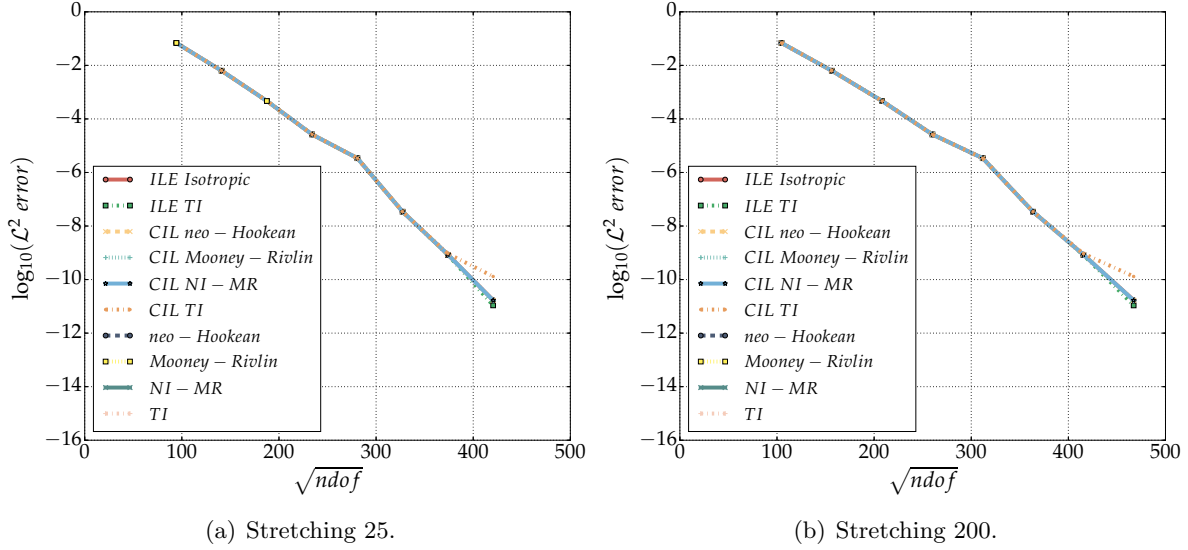


Figure 3.32: Approximation error in the  $\mathcal{L}^2(\Omega)$  norm as a function of the square root of the number of degrees of freedom

ics [77, 324]. Figure 3.33 shows the linear surface mesh of the almond, the high-order surface mesh corresponding to a degree of approximation  $p=4$  and a cut of the high-order volume mesh. The linear mesh contains 6,247 elements, 1,288 nodes and 688 faces on the almond.

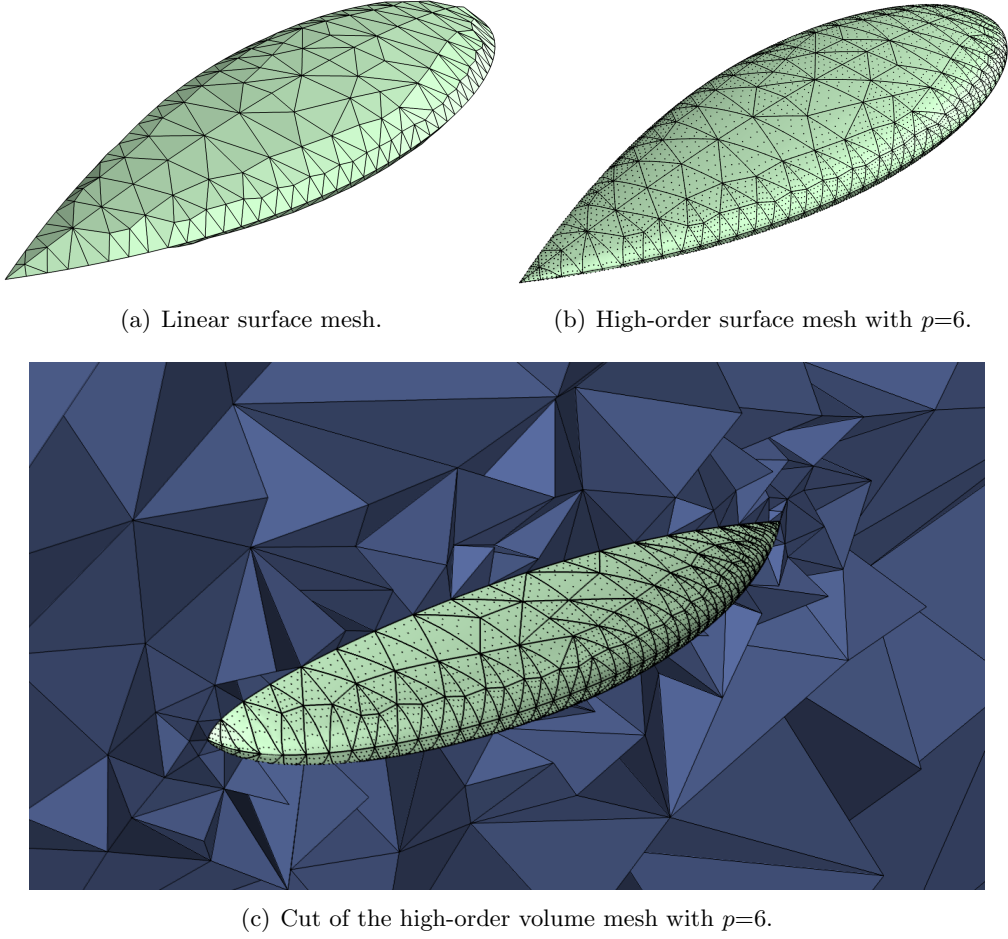


Figure 3.33: Isotropic mesh around the NASA almond.

The corresponding high-order mesh with  $p=6$  contains 233,205 nodes and 16,420 nodes to be

projected over the true almond geometry to obtain the Dirichlet boundary conditions of the solid mechanics problem.

Similar to the previous examples, the effect of the Poisson's ratio on the quality of the generated meshes is investigated first, for different degrees of approximation. Figure 3.34 shows the quality measure  $Q_1$  for the linear, incrementally linear and non-linear approaches. In all cases the imposed displacement on the boundary has been introduced using 10 load increments.

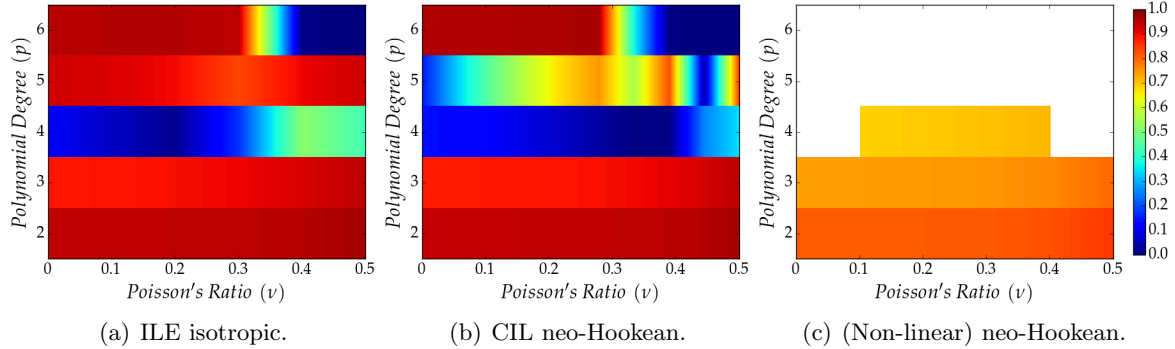


Figure 3.34: Quality measure  $Q_1$  of the generated meshes as a function of the Poisson's ratio and the polynomial degree.

Compared to the two-dimensional results of the isotropic meshes in Section 3.8.1, similar conclusions are derived here. First, the quality of both the meshes produced with the ILE isotropic and CIL neo-Hookean approaches is similar, although the ILE isotropic provides better quality near the incompressible limit and, for some particular choices of the approximation degree, for the whole range of values of the Poisson's ratio (e.g., for  $p=5$ ). As shown in previous examples, the non-linear approach produces good quality meshes for low-order approximations (i.e.,  $p=2,3$ ). For  $p=4$  a valid mesh is only obtained for values of the Poisson's ratio between 0.1 and 0.4, and no convergence is obtained if the order of approximation is further increased.

Similar conclusions are obtained if other quality measures are utilised. For instance, Figure 3.35 and Figure 3.36 show the same analysis in terms of the quality measures  $Q_2$  and  $Q_3$  respectively.

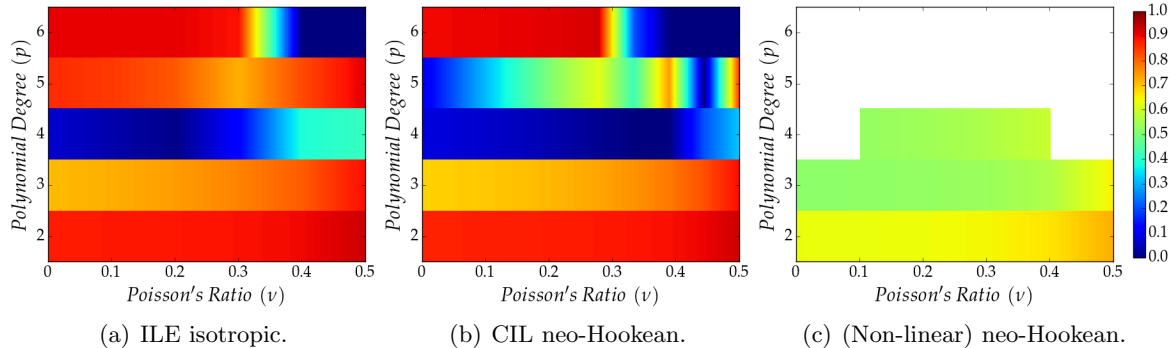


Figure 3.35: Quality measure  $Q_2$  of the generated meshes as a function of the Poisson's ratio and the polynomial degree.

Although the actual value of the quality is different, depending on the selected measure, the qualitative behaviour is the same compared to the quality  $Q_1$ . As reported earlier with the two dimensional examples, the quality measure that produces a lower absolute value is the scaled Jacobian,  $Q_3$ , traditionally used by the high-order mesh generation community. This is attributed to the motion resulting from an imposed boundary displacement that results from projecting the high-order nodes to the true CAD surface. In this scenario, the volumetric

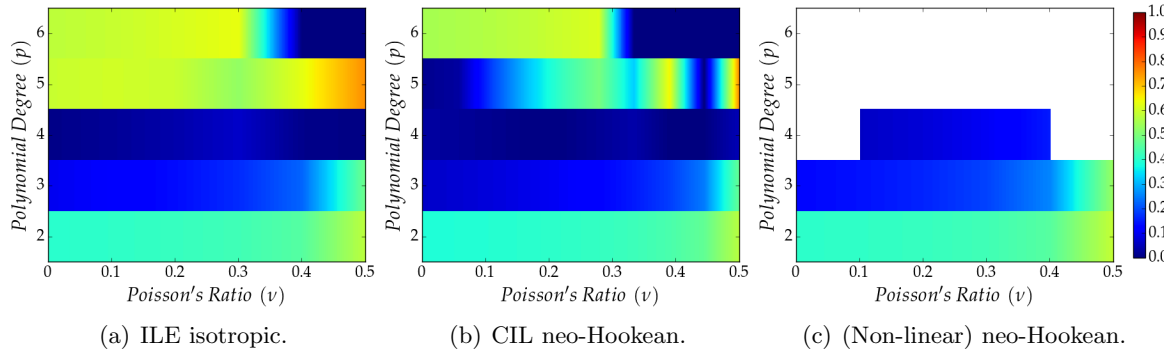


Figure 3.36: Quality measure  $Q_3$  of the generated meshes as a function of the Poisson's ratio and the polynomial degree.

deformation related to  $Q_3$ , is much more important than the deformations related to  $Q_1$  and  $Q_2$ .

Figure 3.37 shows the three quality measures  $Q_1$ ,  $Q_2$  and  $Q_3$  as a function of the Poisson's ratio for the mesh with  $p=3$  and using 10 load increments.

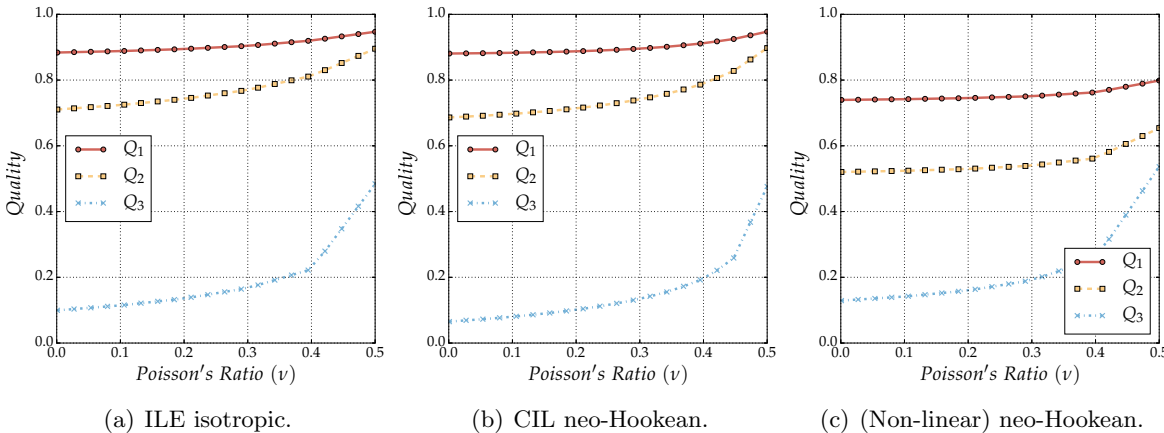


Figure 3.37: Different quality measures of the generated meshes with  $p=3$  as a function of the Poisson's ratio using 10 load increments.

The results confirm that, contrary to two dimensional plane strain problems, the quality measures  $Q_1$  and  $Q_2$  are different. It can be observed that the ILE and CIL approaches produce meshes of similar quality, irrespective of the measure considered. In addition, the results illustrate that the quality measure  $Q_1$  is less influenced by the Poisson's ratio whereas the quality  $Q_3$  shows a major dependence on this material parameter. Finally, the results shows that for low-order approximations the non-linear approach can produce meshes of slightly better scaled Jacobian compared to the ILE and CIL approaches although when the quality measures  $Q_1$  and  $Q_2$  are used, the non-linear approach produce the lowest quality meshes compared to the ILE and CIL approaches. This is again due to the non-proportional movement of the nodes in the non-linear approach, which results in distortion of edges and faces of the element, despite a reasonable volumetric deformation being maintained.

If a higher order of approximation is considered, say  $p=5$ , the non-linear approach fails to converge for any value of the Poisson's ratio, as illustrated in Figure 3.34. A comparison of the different quality measures for the ILE and CIL approaches is shown in Figure 3.38.

The results reveal important differences between the ILE and CIL approaches and illustrate the robustness of the ILE approach as the quality is significantly less dependent on the value of the Poisson's ratio selected, compared to the CIL approach. In fact, the results show that high quality meshes can be obtained for the ILE approach with any value of the Poisson's ratio,

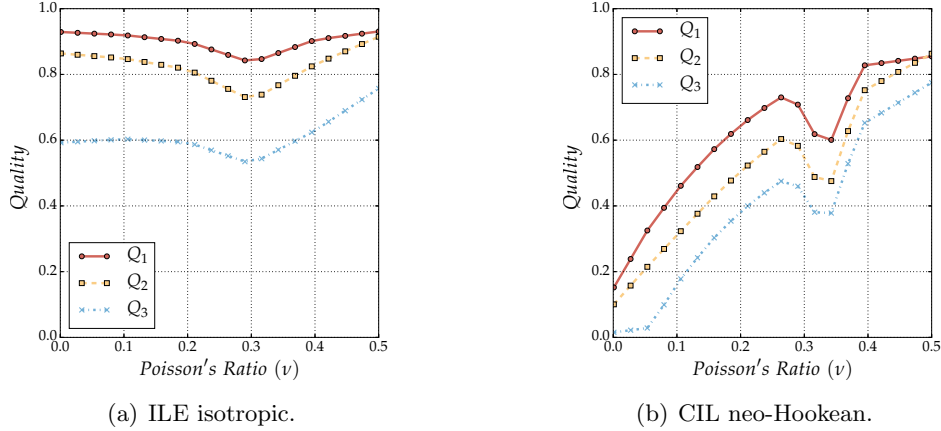


Figure 3.38: Different quality measures of the generated meshes with  $p=5$  as a function of the Poisson’s ratio using 10 load increments.

even with a value near 0, whereas a substantial decrease in the quality is observed if a Poisson’s ratio near 0 is selected for the CIL approach.

Next, the computational time is analysed. Figure 3.39 shows the CPU time using the three formulations and different material models when the boundary displacement is imposed using five load increments.

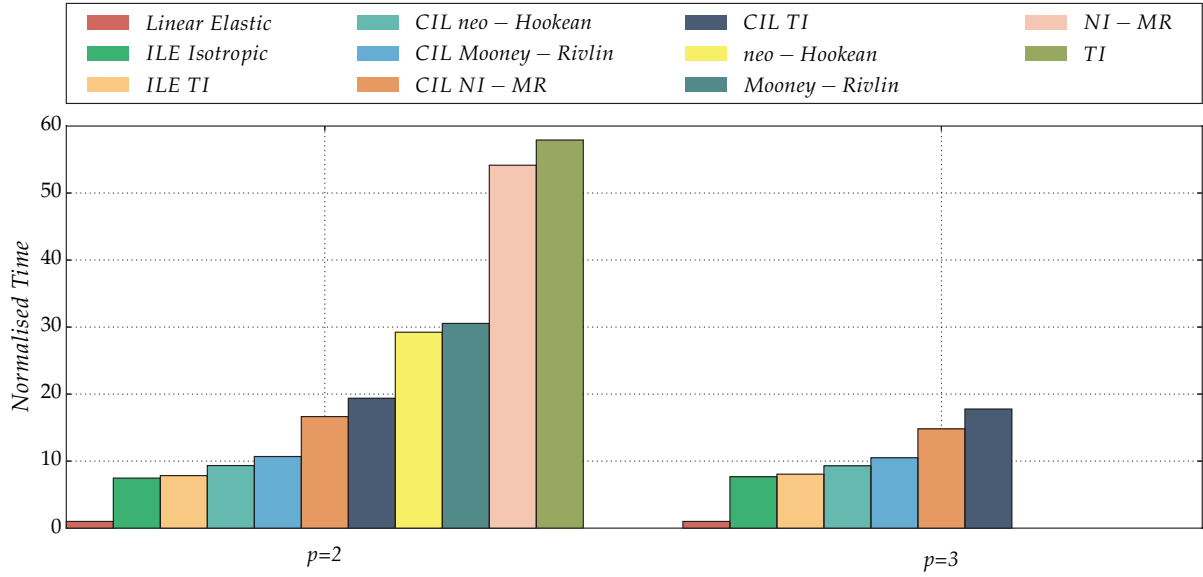


Figure 3.39: Computational cost of various material models using three different formulations with  $p=2$  (27,831 degrees of freedom) and  $p=3$  (90,648 degrees of freedom).

As carried out in the previous examples, the CPU time has been normalised with respect to that of classical linear elasticity and the geometrical mean of 100 run-times, excluding the timing for the first 10 runs, is reported. Compared to previous two-dimensional examples, the number of degrees of freedom is now significantly larger for a single core and, therefore, the cost of actual computation dominates over secondary effects such as inlining and branch prediction. The systems of linear equations are now solved using the Multi-frontal Massively Parallel Solver (MUMPS). It is interesting to observe that, despite these differences compared to the two-dimensional examples, similar conclusions are obtained from the CPU time analysis. Once more, both the ILE approaches are found to be the most competitive and the non-linear approaches the most computationally expensive. These results, together with the quality study presented in this section, enables to conclude that the ILE and CIL approaches are

recommended for producing high-order curvilinear meshes from an initial linear mesh.

To conclude,  $p$ -convergence analysis of the interpolation error is performed to illustrate the optimal approximation properties of the produced meshes. Following the strategy presented in Section 3.8.2, Figure 3.40 shows the approximation error in the  $\mathcal{L}^2(\Omega)$  norm as a function of the cubic root of the number of degrees of freedom for a degree of approximation ranging from  $p=2$  up to  $p=6$ .

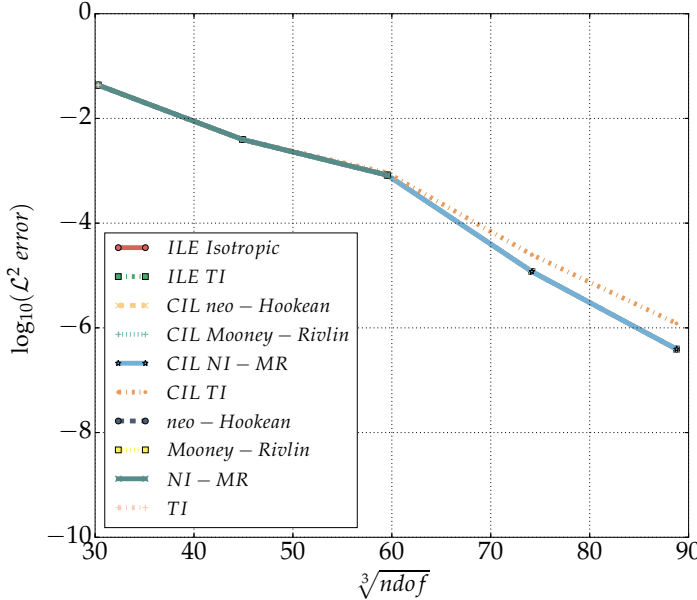


Figure 3.40: Approximation error in the  $\mathcal{L}^2(\Omega)$  norm as a function of the cubic root of the number of degrees of freedom.

The results show the expected exponential convergence in the approximation of a smooth function. In addition, it is interesting to observe that the error is almost identical for the ILE and CIL approaches. Once more, the CIL TI approach shows a slight deterioration in the rate of convergence for high-order approximations due to the lower quality of the meshes produced with this approach. This result in fact pin-points the importance of choosing a well-defined polyconvex material model, in the context of a posteriori mesh generation.

### 3.8.4 Meshes around full aircraft configurations

The next examples consider meshes around two full aircraft configurations, showing the capability of the proposed unified framework for generating meshes around realistic geometries of interest to the computational electromagnetics and computational fluid dynamics communities.

First, a tetrahedral mesh around a generic Falcon aircraft is considered. The linear mesh has 185,191 elements, 35,875 vertices and 16,922 triangular faces on the aircraft to be projected on the true CAD geometry to obtain the Dirichlet boundary condition for the solid mechanics problem. The corresponding CAD geometry has 54 surfaces with 240 intersection curves. For an interpolation degree of  $p=3$ , there are 876,988 nodes in the domain and 76,151 nodes on the aircraft that require projection.

Figure 3.41 shows the high-order surface mesh corresponding to a degree of approximation  $p=3$ , the higher order mesh showing elements with  $Q_3 < 0.9$  and a cut of the high-order volume mesh. The problem is solved using the CIL Mooney-Rivlin approach with  $\nu=0.45$  and 20 load increments. The minimum Scaled Jacobian for this mesh is  $Q_3 = 0.337$  and there are 181,251 elements (i.e. 97.87 percent of the total number of elements) for which  $Q_3 > 0.9$ . The minimum values of the other two quality measures, accounting for fibre and surface deformations, are  $Q_1 = 0.605$  and  $Q_2 = 0.467$ .

Next, a tetrahedral mesh around the DLR-F6 transport configuration is considered. The

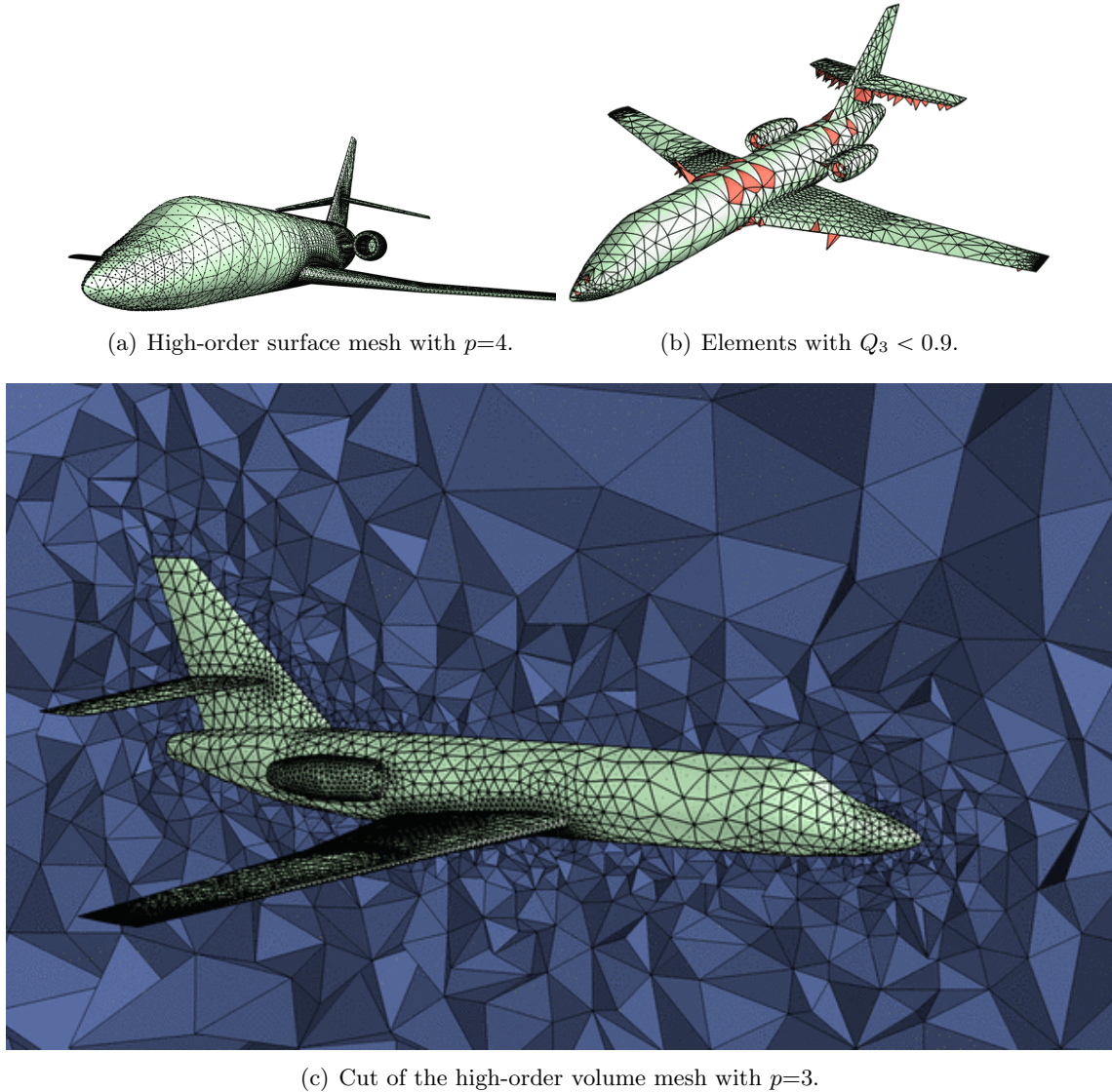


Figure 3.41: Isotropic mesh around a Falcon aircraft.

linear mesh has 68,571 elements, 31,080 vertices and 31,836 tetrahedral faces on the aircraft to be projected on the true CAD geometry to obtain the Dirichlet boundary conditions for the solid mechanics problem. The corresponding CAD geometry has 128 surfaces with 634 intersection curves. For an interpolation degree of  $p=4$ , there are 1,601,015 nodes on the domain and 255,584 nodes on the aircraft that require projection. The problem is solved using the ILE isotropic approach with  $\nu = 0.45$  and 100 load increments. The minimum values of the three quality measures for this mesh are  $Q_1 = 0.482$ ,  $Q_2 = 0.377$  and  $Q_3 = 0.329$ . Moreover there are only 11 elements with a quality  $Q_3 < 0.9$ . Figure 3.42 shows the linear surface mesh of the aircraft, the high-order surface mesh corresponding to a degree of approximation  $p=4$  and a cut of the high-order volume mesh.

Finally, a boundary layer tetrahedral mesh around the DLR-F6 transport configuration with a stretching of 317 is considered. The boundary layer has been constructed such that the final mesh is suitable for a compressible Navier-Stokes simulation up to a Reynolds number of approximately  $Re = 4 \times 10^7$ . The linear mesh 4,482,662 elements, 787,712 vertices and 110,458 triangular faces on the aircraft. Two curved boundary layer meshes are generated for this geometry with  $p = 3$  and  $p = 4$ , respectively. The resulting high-order mesh with  $p = 3$  has 20,434,689 nodes with 498,590 nodes on the aircraft and the  $p = 4$  mesh has 48,279,087 nodes with 885,712 nodes on the aircraft. These in turn correspond to 61,304,067 and 144,837,261 degrees of freedom for the elasticity solver. Both meshes are produced using

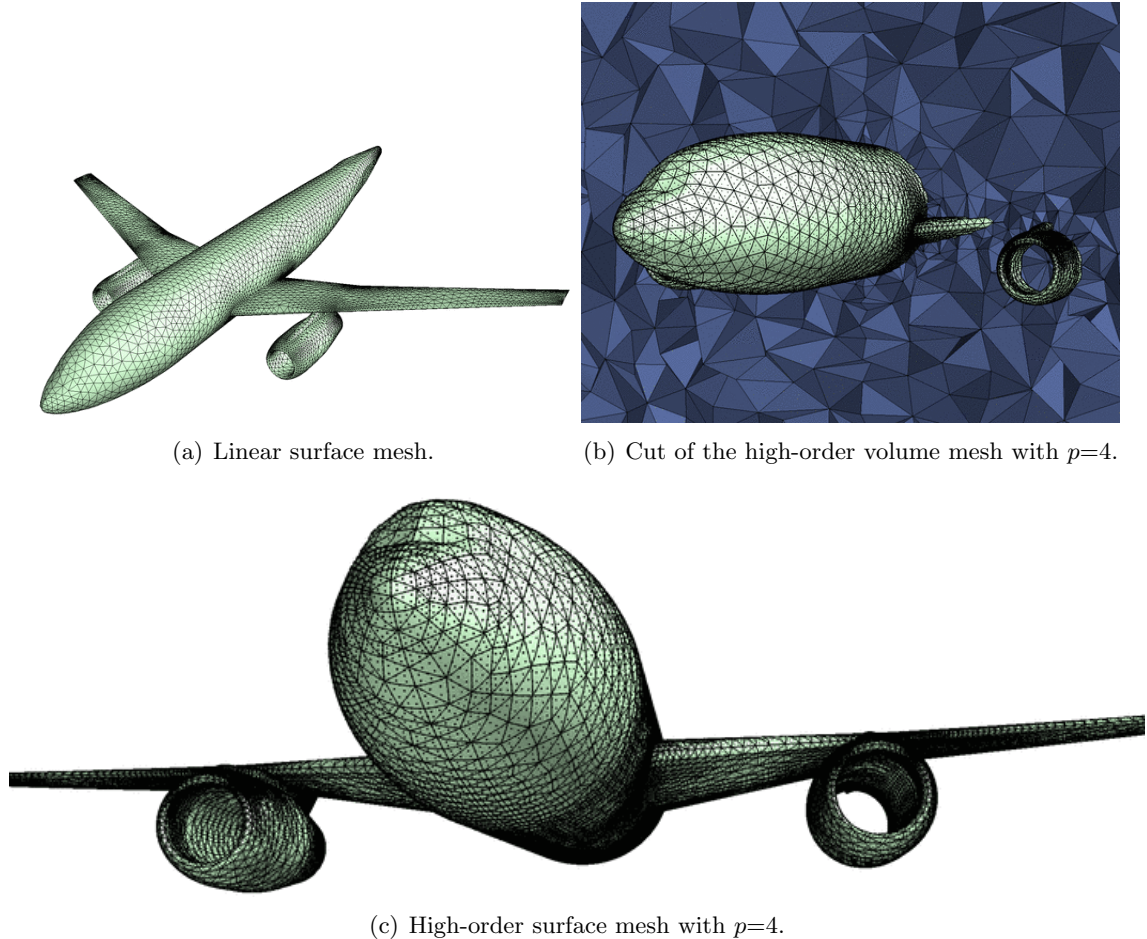


Figure 3.42: Isotropic mesh around the DLR-F6 transport configuration.

the ILE isotropic approach. The number of increments are chosen such that a balance is kept between computational cost and final quality of the computational mesh. This corresponds to 60 and 30 increments with a minimum scaled Jacobian of 0.06 and 0.02 for  $p = 3$  and  $p = 4$ , respectively. However, for both meshes, 99.5% of the elements have scaled Jacobian above 0.8.

Figure 3.43 shows the surface mesh of the aircraft for  $p = 4$  and cuts of the high-order volume mesh for  $p = 3$  and  $p = 4$ .

### 3.8.5 Meshes around full racing car configuration

We now consider an unstructured tetrahedral mesh around a full racing car configuration. The linear mesh has 184,463 elements, 43,206 vertices and 31,836 tetrahedral faces on the aircraft to be projected on the true CAD geometry to obtain the Dirichlet boundary conditions for the solid mechanics problem. The corresponding CAD geometry has 6,532 vertices 631 surfaces with 3,266 intersection curves and hence is sufficiently complicated. For an interpolation degree of  $p=5$ , there are 4,621,760 nodes on the domain and 2,670,660 nodes on the boundary that require projection. The problem is solved using the CIL Neo-Hookean approach with  $\nu = 0.4$  and 10 load increments. The minimum values of the three quality measures for this mesh are  $Q_1 = 0.533$ ,  $Q_2 = 0.416$  and  $Q_3 = 0.214$ . Moreover there are only 52 elements with a quality  $Q_3 < 0.8$ . It should be noted that the linear mesh obtained for this configuration has a coarse region which affects the high order mesh qualities, as can be seen in Figure 3.44(b). Figure 3.44 shows multiple profiles of the surface and cut volume mesh of the car.

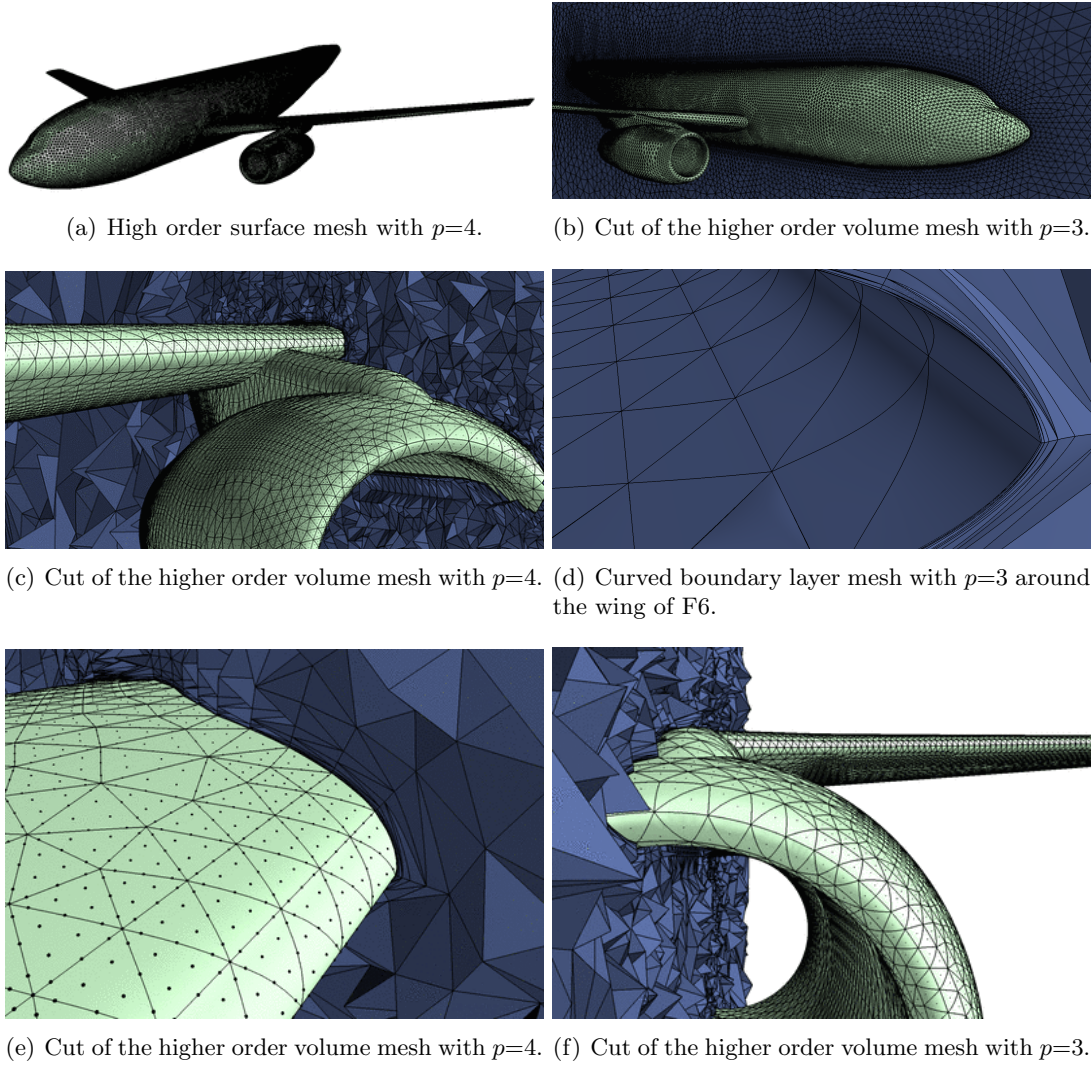


Figure 3.43: Boundary layer mesh around the DLR-F6 transport configuration.

### 3.8.6 Unstructured tetrahedral meshes of complex mechanical components

Three complex three-dimensional mechanical components are considered in this section. The Poisson's ratio for all the examples considered in this section is chosen as  $\nu = 0.45$ .

The first example considers a mechanical valve where the CAD geometry has 45 surfaces and 260 intersection curves. The linear mesh has 16,509 elements, 4,176 nodes and 5,364 triangular faces on the boundary. The resulting high order mesh with  $p = 5$  has 377,994 nodes and 67,047 nodes on the CAD surfaces. The problem is solved using the ILE isotropic approach with 5 load increments and the resulting minimum quality measures are  $Q_1 = 0.917$ ,  $Q_2 = 0.841$  and  $Q_3 = 0.768$ . Moreover, there are only 4 elements for which  $Q_3 < 0.9$ . Figure 3.45 shows two views of the generated high-order curved surface mesh corresponding to a degree of approximation  $p=5$ .

The second component considered is that of a drill with an extremely sharp groove. The linear mesh has 25,000 elements, 5,550 nodes and 4,904 triangular faces on the boundary. The corresponding CAD geometry has 33 surfaces with 176 intersection curves. The resulting high order mesh with  $p=5$  has 552,375 nodes and 61,306 nodes on the true CAD surface. The problem is solved using 20 steps of the CIL neo-Hookean model. Due to the extremely small slit, the mesh around this region is severely stretched and hence the minimum scaled Jacobian corresponds to  $Q_3 = 0.13$ . Figure 3.46 shows the linear surface mesh of the drill and different profiles of the high-order curved surface mesh corresponding to a degree of approximation  $p = 5$ .

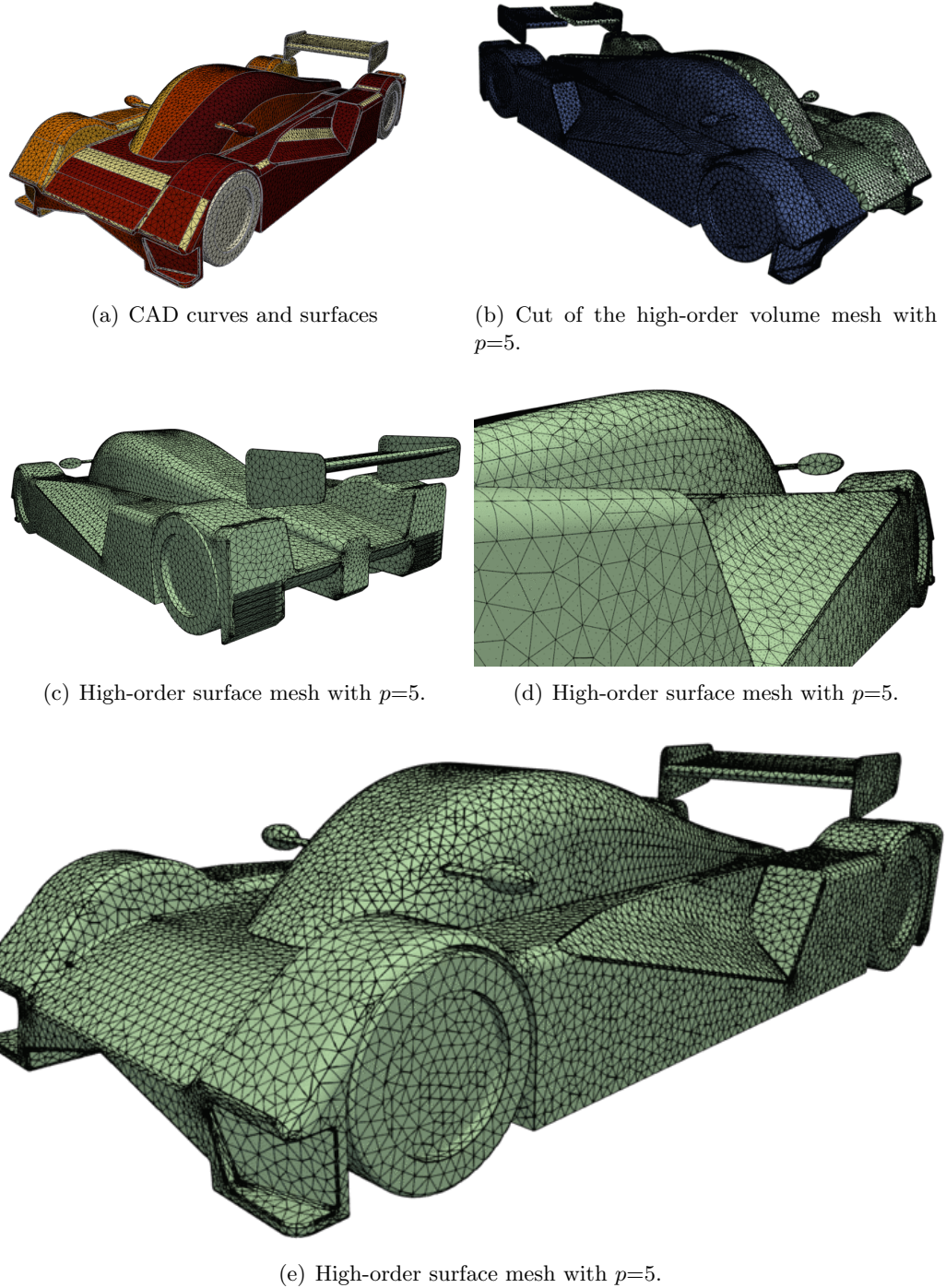


Figure 3.44: Isotropic mesh around the racing car.

The last example considers a more complex mechanical component and it has been selected to illustrate the robustness and potential of the proposed approach when dealing with complex geometries formed by a large number of surfaces. The corresponding CAD geometry has 638 surfaces with 3,459 intersection curves. The linear mesh has 64,599 elements 17,025 vertices and 23,506 triangular faces on the CAD boundary. The resulting high order mesh with  $p=4$  has 784,670 nodes and 187,903 nodes on the boundary. The problem is solved using the ILE isotropic approach with 200 load increments. The minimum values of the three quality measures for this mesh are  $Q_1 = 0.719$ ,  $Q_2 = 0.605$  and  $Q_3 = 0.451$ , respectively. Moreover, there are only 6 elements for which  $Q_3 < 0.9$ . Figure 3.47 shows different profiles of the high-order curved surface mesh corresponding to a degree of approximation  $p=4$ . Observe that in this mesh, there are 221 planar surfaces and the nodes lying on these surfaces require in-plane

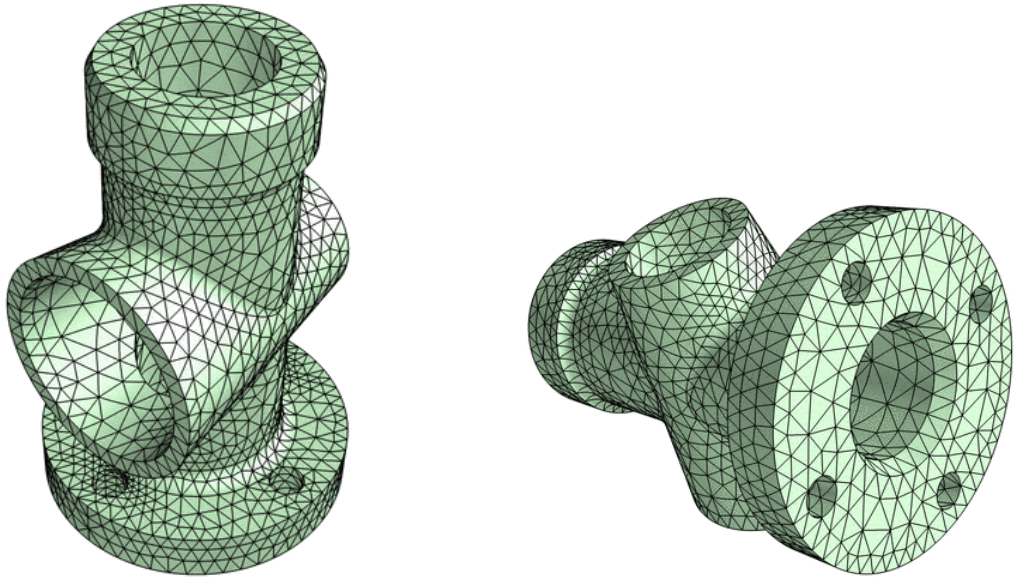


Figure 3.45: Two views of the high-order curved mesh of mechanical valve

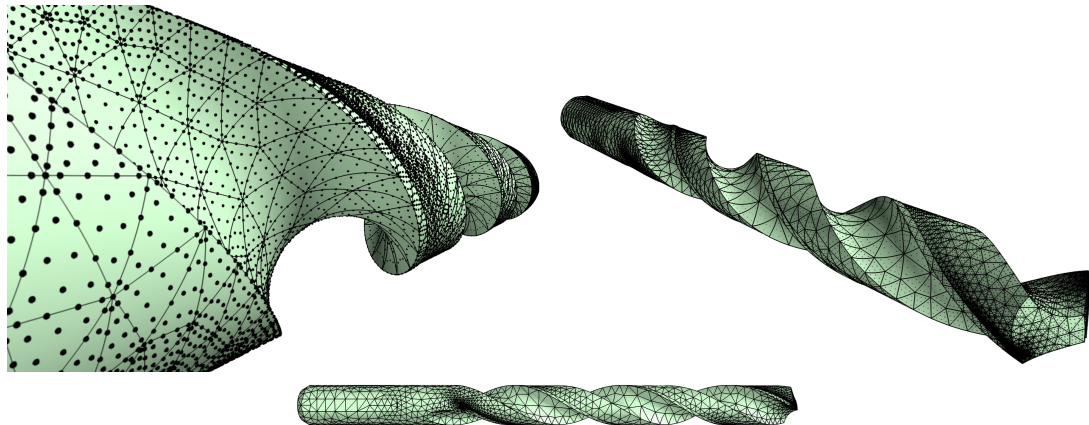


Figure 3.46: Two views of the high-order curved mesh of a drill

translations, which the proposed unified framework is capable of resolving.

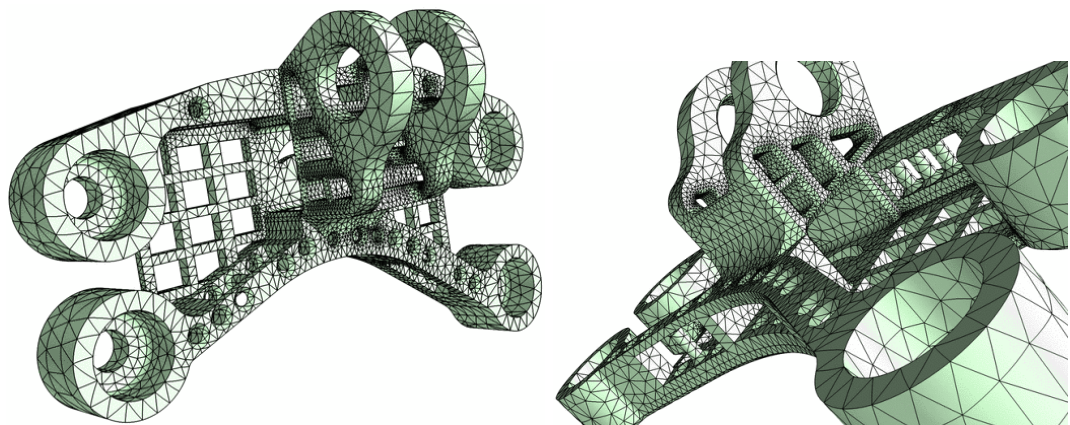


Figure 3.47: Two views of the high-order curved mesh of a complex mechanical component

### 3.8.7 Structured and unstructured curved hexahedral meshes

In this section we consider the case of structured and unstructured hexahedral mesh deformation. The Poisson's ratio for all the examples considered in this section is chosen as  $\nu = 0.45$ .

The first example considers a semi-structured hexahedral mesh of RAE2822 configuration where the CAD geometry has 4 surfaces and 12 intersection curves. The linear mesh has 383 elements 902 nodes and 900 quadrilateral faces on the boundary. The resulting high order mesh with  $p = 3$  has 14,596 nodes and 8,102 nodes on the CAD surfaces. The problem is solved using the ILE isotropic approach with 3 load increments and the resulting minimum quality measures are  $Q_1 = 0.987$ ,  $Q_2 = 0.952$  and  $Q_3 = 0.918$ . Figure 3.48 shows the CAD geometry and two views of the generated high-order curved surface mesh corresponding to a degree of approximation  $p=3$ .

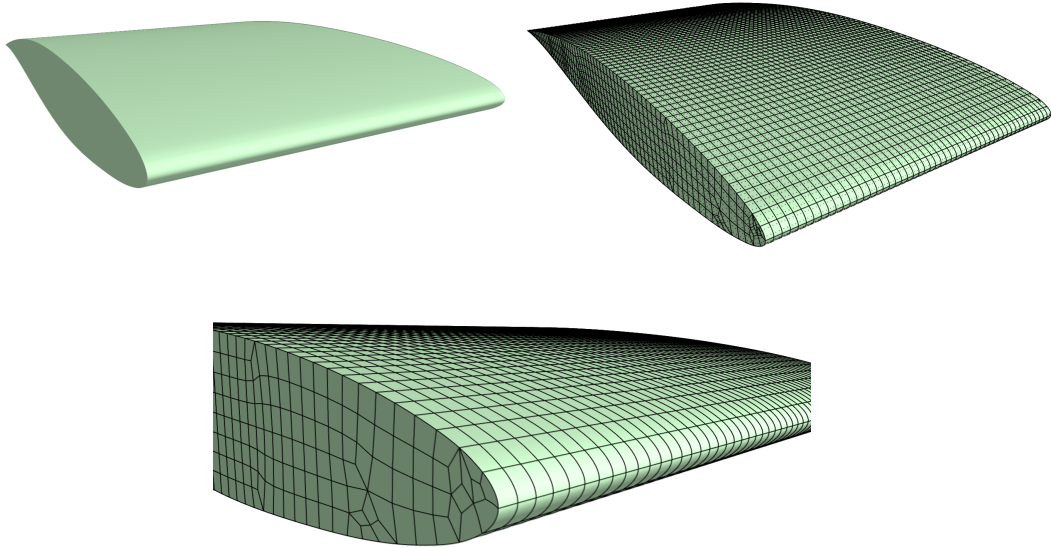


Figure 3.48: CAD geometry and two views of the high-order curved RAE2822 mesh

The hexahedral meshes considered earlier have been semi-structured. We now consider a completely unstructured hexahedral mesh of the popular propeller configuration shown in 3.8.7 . The corresponding CAD geometry has 724 vertices, 67 surfaces with 362 intersection curves, with 8 surfaces requiring 2D mesh deformation. The linear mesh has 423,196 elements 453,456 vertices and 15,304 quadrilateral faces on the CAD boundary. The resulting high order mesh with  $p=3$  has 11,563,199 nodes with 137,736 of them lying on the boundary. This results in a total of 34,689,597 degrees of freedom for the elasticity solver. The problem is solved using the CIL approach with Mooney-Rivlin model and Poisson's ratio 0.4. The minimum values of the three quality measures for this mesh are  $Q_1 = 0.922$ ,  $Q_2 = 0.901$  and  $Q_3 = 0.800$ , respectively. The distortion quality measures are shown in 3.8.7 with different profiles of the high-order curved surface and cut volume mesh.

The final example considers a fully unstructured hexahedral mesh of a simplified BMW-M6 car configuration. The corresponding CAD geometry has 1,152 vertices, 121 surfaces with 576 intersection curves, with 24 surfaces requiring in-plane translation (2D mesh deformation). The linear mesh has 2,978,096 elements 3,201,461 vertices and 58,308 quadrilateral faces on the CAD boundary. The resulting high order mesh with  $p=2$  has 24,330,028 nodes and 3,376,383 nodes on the boundary. This accounts for a total of 72,990,084 degrees of freedom for the elasticity solver. The problem is solved using the CIL approach with Mooney-Rivlin model and Poisson's ratio 0.4. The minimum values of the three quality measures for this mesh are  $Q_1 = 0.993$ ,  $Q_2 = 0.961$  and  $Q_3 = 0.906$ , respectively. The generated high order mesh has an excellent quality indeed .Figure 3.50 shows different profiles of the high-order curved surface and cut volume mesh.

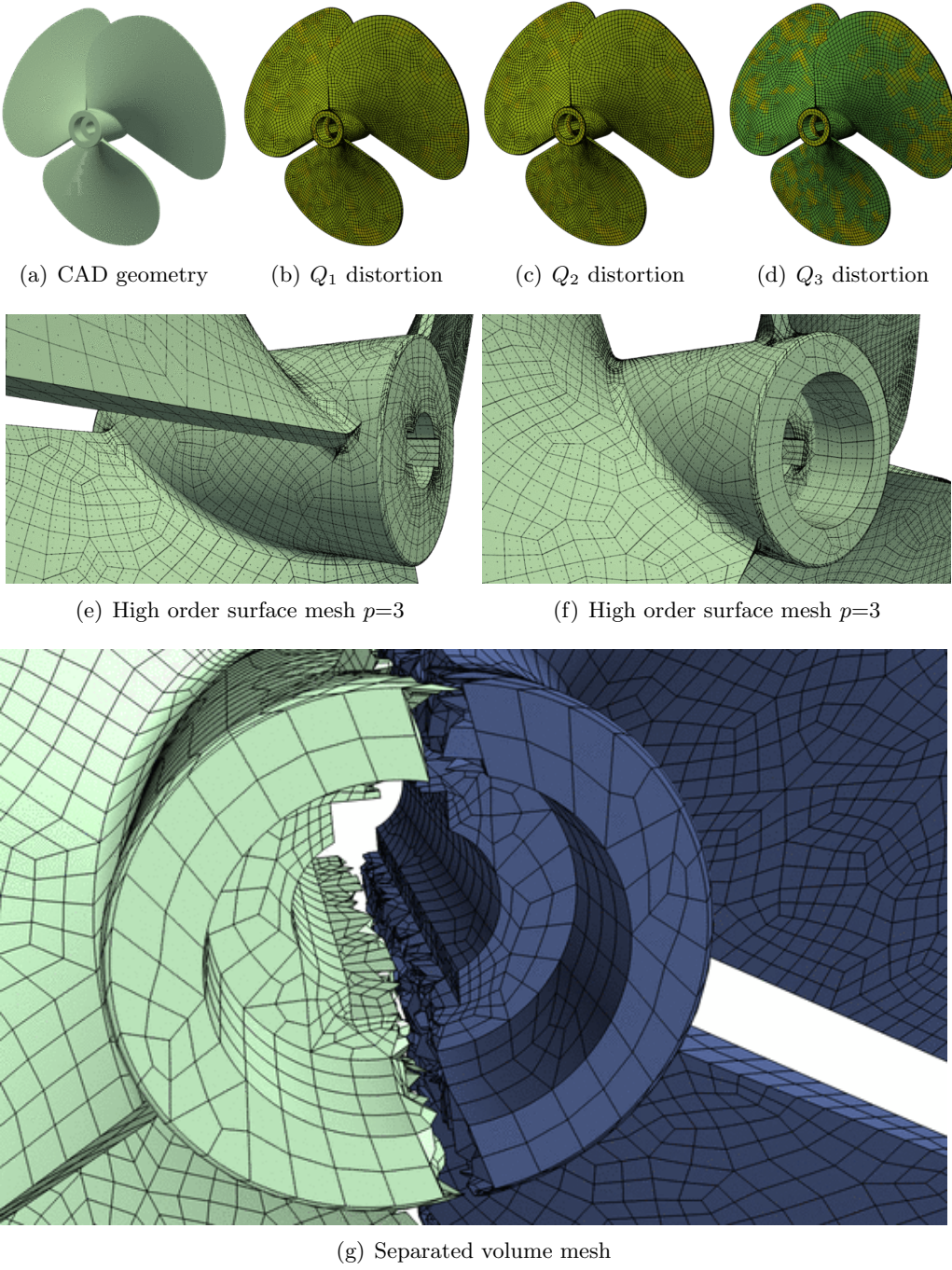


Figure 3.49: Multiple views of the high-order curved hexahedral mesh of propeller. The colorbar for distortion measures is scaled in  $[0,1]$  with minimum values  $Q_1 = 0.922$ ,  $Q_2 = 0.901$  and  $Q_3 = 0.800$

### 3.8.8 Unstructured prismatic and hybrid curved meshes

In this section, we consider the case of general polygonal shape elements and hybrid meshes. To this end, as a first example we reconsider the last geometry of mechanical component, considered in the previous section on hexahedral meshes. The linear mesh has 438 elements 570 vertices, 876 triangular faces and 135 quadrilateral faces on the CAD boundary. The resulting high order mesh with  $p=4$  has 18,855 nodes and 9,150 nodes on the boundary. The problem is solved using the ILE isotropic approach with 5 load increments. The minimum values of the three quality measures for this mesh are  $Q_1 = 0.789$ ,  $Q_2 = 0.751$  and  $Q_3 = 0.665$ , respectively. Note that the triangular surface mesh is generated without performing mesh

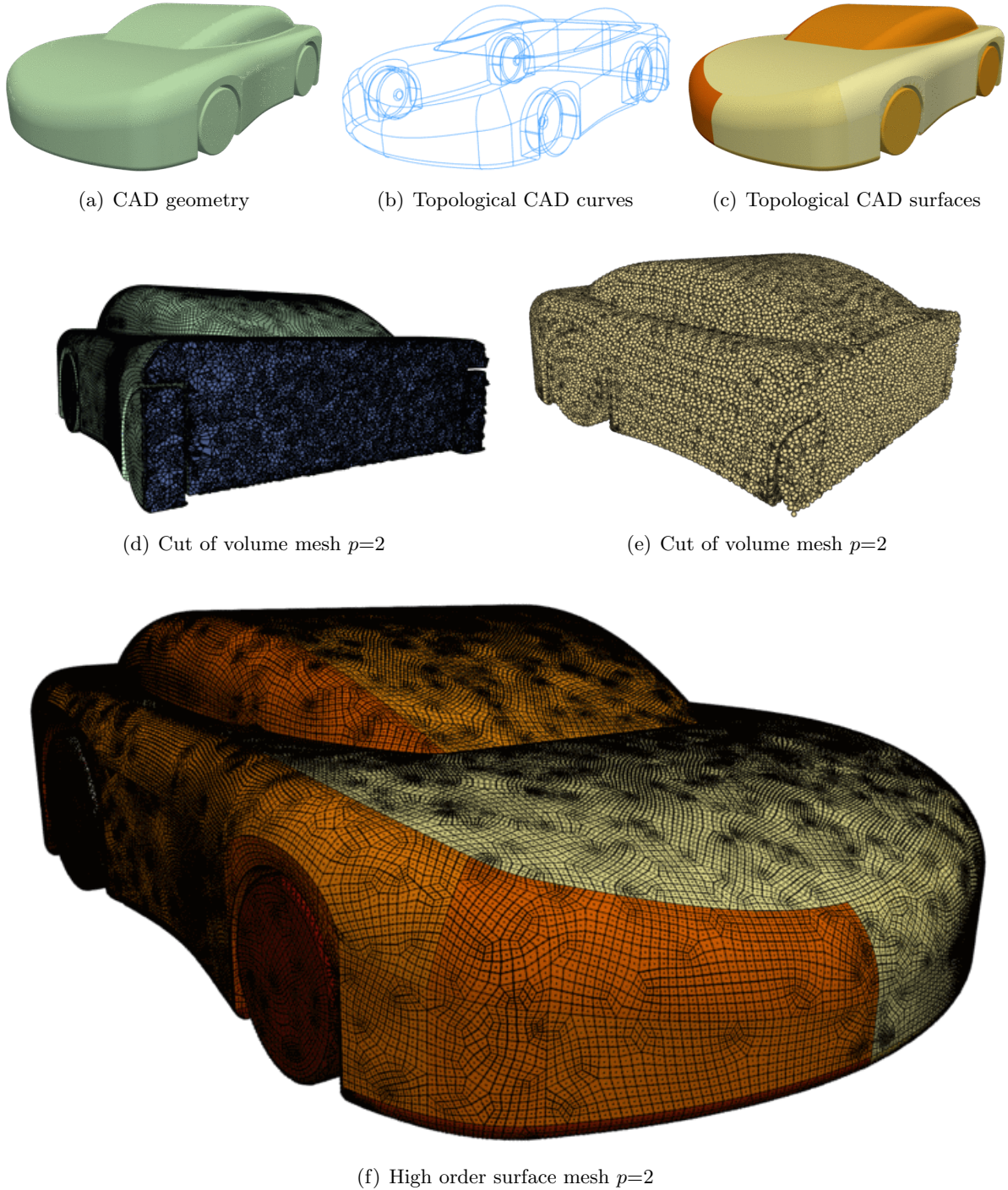


Figure 3.50: Multiple views of the high-order unstructured curved hexahedral mesh of the car configuration

enhancements (i.e. diagonal swapping). Figure 3.51 shows different profiles of the high-order curved surface mesh corresponding to a degree of approximation  $p=4$ . The presence of multiple planar surfaces require a multi-level mesh deformation technique, for this mesh.

The second example considers an inhomogenous plate with multiple holes, also considered in the previous section. The corresponding CAD geometry has 18 surfaces with 98 intersection curves. The linear mesh has 17,040 elements 11,649 vertices, 34,080 triangular faces and 8,740 quadrilateral faces on the CAD boundary. The resulting high order mesh with  $p=5$  has 1,141,329 nodes and 151,578 nodes on the boundary. The problem is solved using the nonlinear approach with Mooney-Rivlin model. The minimum values of the three quality measures for



Figure 3.51: CAD and high-order curved prismatic mesh of a mechanical component. The triangular surface mesh is generated without performing mesh enhancement (i.e. diagonal swapping)

this mesh are  $Q_1 = 0.881$ ,  $Q_2 = 0.856$  and  $Q_3 = 0.786$ , respectively. Figure 3.52 shows different profiles of the high-order curved surface mesh corresponding to a degree of approximation  $p=5$ .

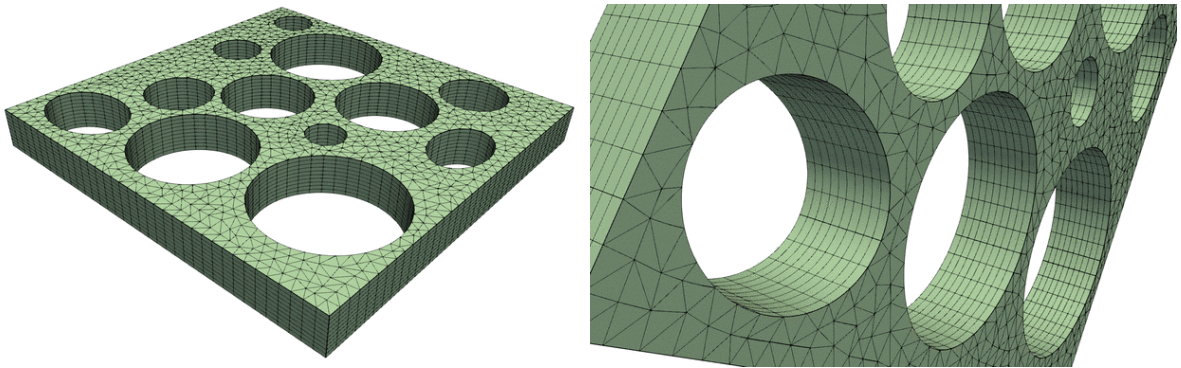


Figure 3.52: Two views of the high-order curved prismatic mesh of an inhomogenous plate

The third example considers a hybrid mesh of a mechanical component. The linear mesh consists of 1,392 hybrid tetrahedral, hexahedral and prismatic elements, 2,111 vertices, 384 triangular faces and 904 quadrilateral faces on the CAD boundary. The resulting high order mesh with  $p=2$  has 13,865 nodes and 5,146 nodes on the boundary. The problem is solved using the CIL approach with Mooney-Rivlin model. The minimum values of the three quality measures for this mesh are  $Q_1 = 0.772$ ,  $Q_2 = 0.714$  and  $Q_3 = 0.597$ , respectively. Figure 3.53 shows different profiles of the high-order curved surface mesh corresponding to a degree of approximation  $p=2$ . Notice that due to the nature of hybrid mesh the corresponding qualities are relatively lower, for this problem.

The fourth example considered is a hybrid quad dominant unstructured mesh of hand used in biomedical applications. The CAD geometry consists of 2,624 vertices, 1,312 intersection curves and 288. The linear mesh consists of 2,045,112 vertices, 46,070 quadrilateral faces and 9,124 triangular faces on the CAD boundary. The resulting high order mesh with  $p=2$  has 186,282 nodes lying on the boundary. The problem is solved using the CIL approach with Neo-Hookean model. The minimum values of the three quality measures for this mesh are  $Q_1 = 0.667$ ,  $Q_2 = 0.542$  and  $Q_3 = 0.401$  (corresponding to a hexahedral element), respectively. Figure 3.54 shows different profiles of the high-order curved surface mesh corresponding to a degree of approximation  $p=2$ .

The final example considers a hybrid quad dominant unstructured surface mesh of F16 fighter configuration. The consideration of surface mesh is to showcase the multi-level approach

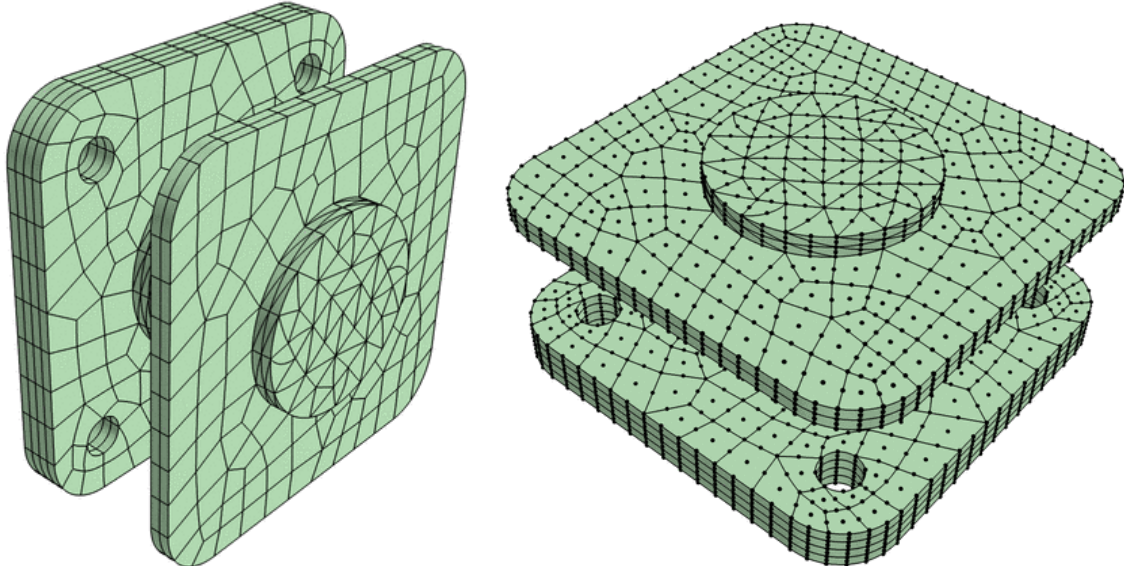


Figure 3.53: Two views of the high-order curved hybrid (tetrahedral, prismatic and hexahedral) mesh of a mechanical component

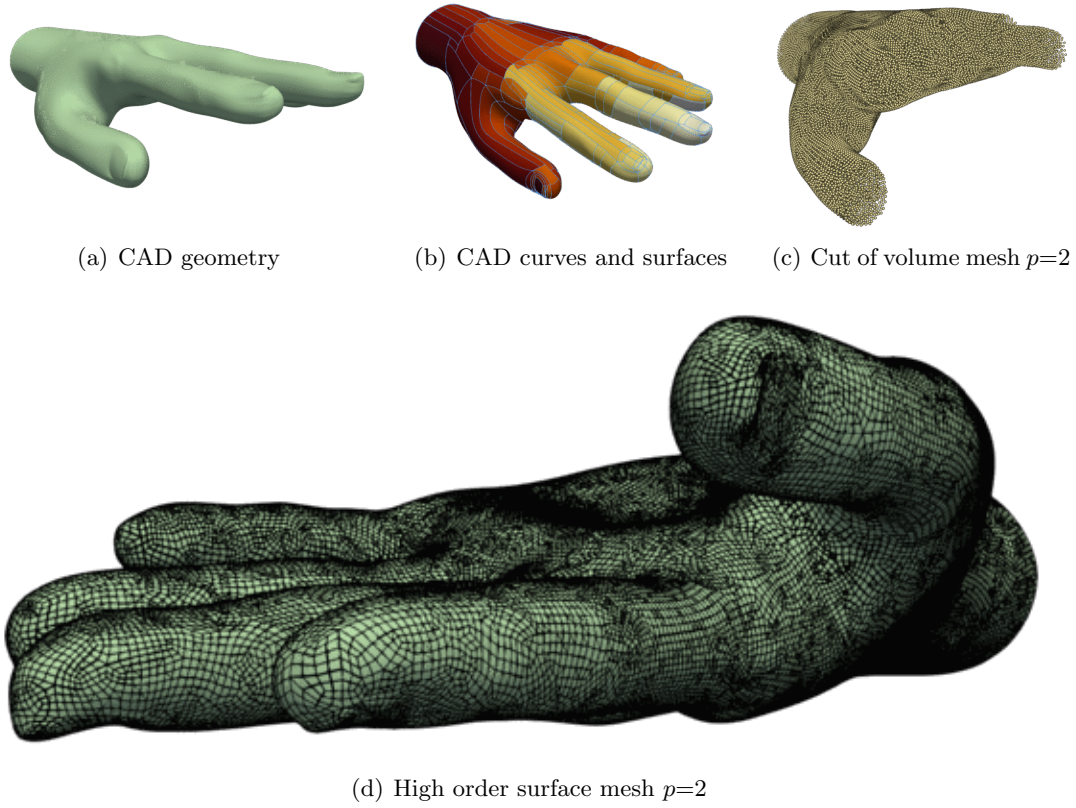


Figure 3.54: Multiple views of the high-order curved hex-dominant hand mesh

as the CAD geometry consists of multiple planes for which the solid mechanics analogy will have to be applied on. The CAD geometry consists of 1,048 vertices, 524 intersection curves and 83 surfaces of which 21 surfaces are plane and hence, require in-plane nodal translation. The linear mesh consists of 342,069 vertices, 307,858 quadrilateral faces and 68,412 triangular faces on the CAD boundary. The resulting high order mesh with  $p=2$  has 1,368,259 nodes all lying on the boundary. The problem is solved using the CIL approach with Mooney-Rivlin model. The minimum values of the three quality measures for this mesh are  $Q_1 = 0.883$ ,

$Q_2 = 0.871$  and  $Q_3 = 0.572$  (corresponding to a triangular element), respectively. Figure 3.55 shows different profiles of the high-order curved surface mesh corresponding to a degree of approximation  $p=2$ .

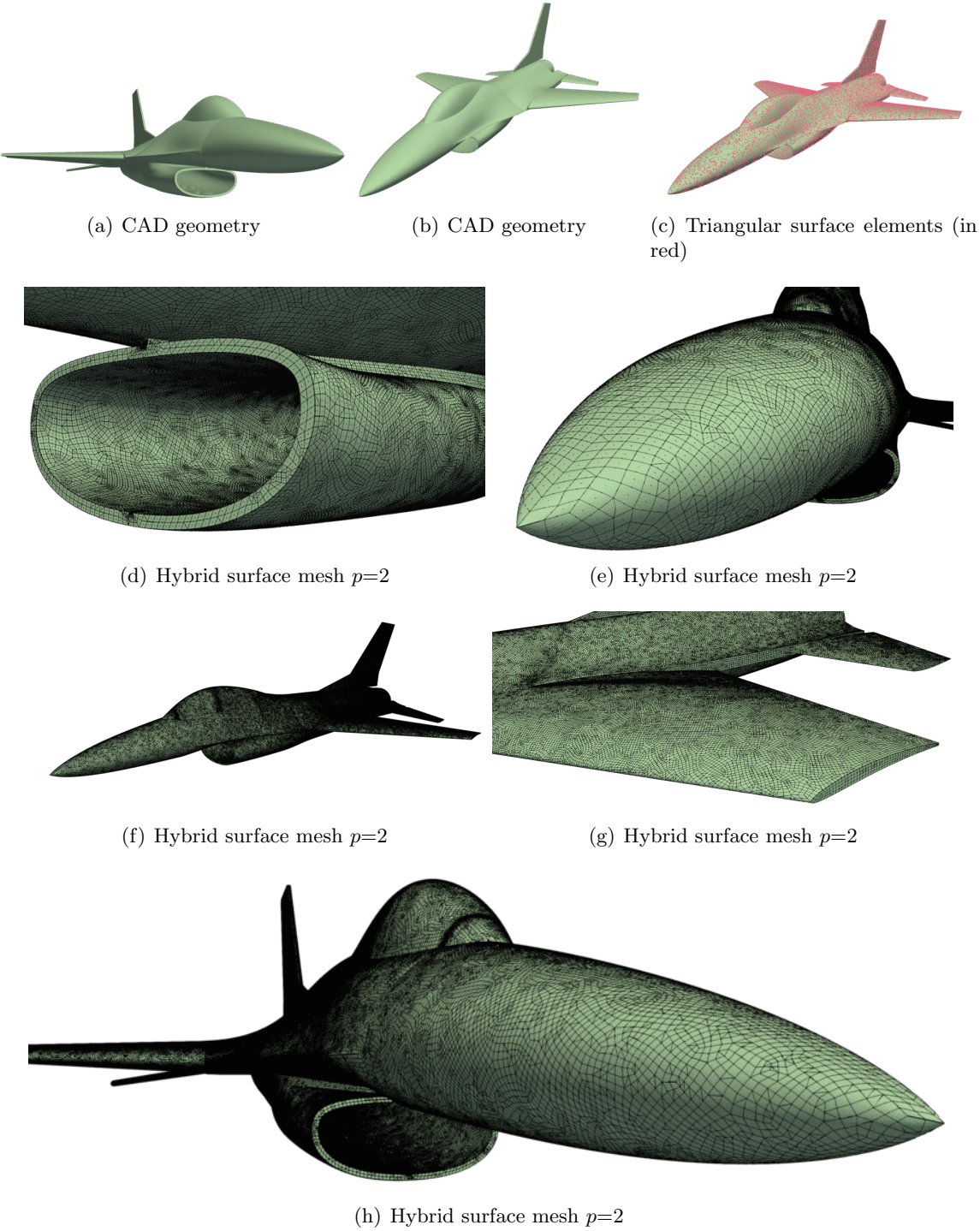


Figure 3.55: Multiple views of the high-order curved quad-dominant hybrid mesh of a F16 fighter

### 3.9 Conclusions

A unified framework for the generation of high-order curvilinear meshes derived via a solid mechanics analogy has been presented. This proposed theoretical and computational framework encompasses the incremental linear elastic approach (wherein only the geometry is updated

incrementally) and the fully non-linear approach, both previously applied in the context of a posteriori high-order mesh generation. In addition, the new incrementally linearised elasticity formulation (wherein the geometry, the tangent operator and the stresses are updated incrementally), not previously applied to generate curvilinear high-order meshes, is included within this unified framework. The material parameters are calibrated such that the tangent operators of all the aforementioned approaches with various material models are identical in the reference configuration, i.e. for the (undeformed) mesh with planar faces or edges. The derivation of all the approaches, based on energy principles, is used to propose mesh quality measures based on independent invariants of the strain energy density. The relation of the proposed quality measures with indicators previously used in the context of high-order curved mesh generation is discussed.

Several numerical examples are presented in both two and three dimensions, including realistic geometries of interest to the solids, fluids and electromagnetics communities. A detailed comparison of all the methodologies is made, including the quality of the generated high-order meshes, the influence of material parameters and load increments on the resulting meshes, the computational cost and the approximation properties of the meshes when applied to an isoparametric finite element formulation.

In terms of the material parameters, the use of a Poisson's ratio near the incompressible limit is generally advised in order to maximise the quality of the resulting mesh. For isotropic meshes, a low number of increments (e.g. five increments) is typically sufficient to obtain the maximum possible quality, whereas for highly stretched meshes and for high-orders of approximation (i.e.  $p > 4$ ) a higher number (e.g. 40 increments) is needed to obtain good quality meshes. Both factors are in fact related as the results show that a higher number of increments is needed when the Poisson's ratio approaches the incompressible limit.

When the material parameters are kept the same, all the linearised approaches, in particular, the incremental linear elastic and the consistent incrementally linearised approach produce meshes of very similar quality and only small differences are observed for highly stretched meshes when high-orders of approximation are used and the Poisson's ratio approaches the incompressible limit. In contrast, the non-linear approach has been found to produce poor quality elements when a high-order approximation is utilised. The non-proportional displacement of interior nodes with respect to the imposed displacement of boundary nodes has a significant negative impact on the convergence of the non-linear solver. Only for low-order approximations has the non-linear approach shown robustness and the ability to produce good quality meshes. The importance of having a well-defined internal energy for the non-linear material model has been illustrated using the transversely isotropic hyperelastic material. For highly stretched meshes, buckling can be expected in the non-linear analysis and the Dirichlet-driven nature of the problems demands a sophisticated and expensive arc-length technique to guarantee convergence, hindering its practical use in an a posteriori mesh generation framework.

The three quality measures proposed for isotropic materials, namely,  $Q_1$  related to fibre maps,  $Q_2$  related to surface maps and  $Q_3$  related to volume maps, show a similar trend with respect to the material parameters. In fact, the first two quality measures are identical for two dimensional plane strain problems. For all the examples considered,  $Q_3$  is the most impactful indicator, which corresponds to the so-called scaled Jacobian traditionally used by the high-order mesh generation community.

In terms of the computational cost, the non-linear approach is much more expensive than the linearised approaches. For highly stretched meshes, where the Newton-Raphson scheme may lose its quadratic convergence due to ill-conditioning of the system, a higher number of iterations is required and the solver time is drastically increased. The linearised approaches are not only much more economical but, in addition, more robust and produce better quality meshes.

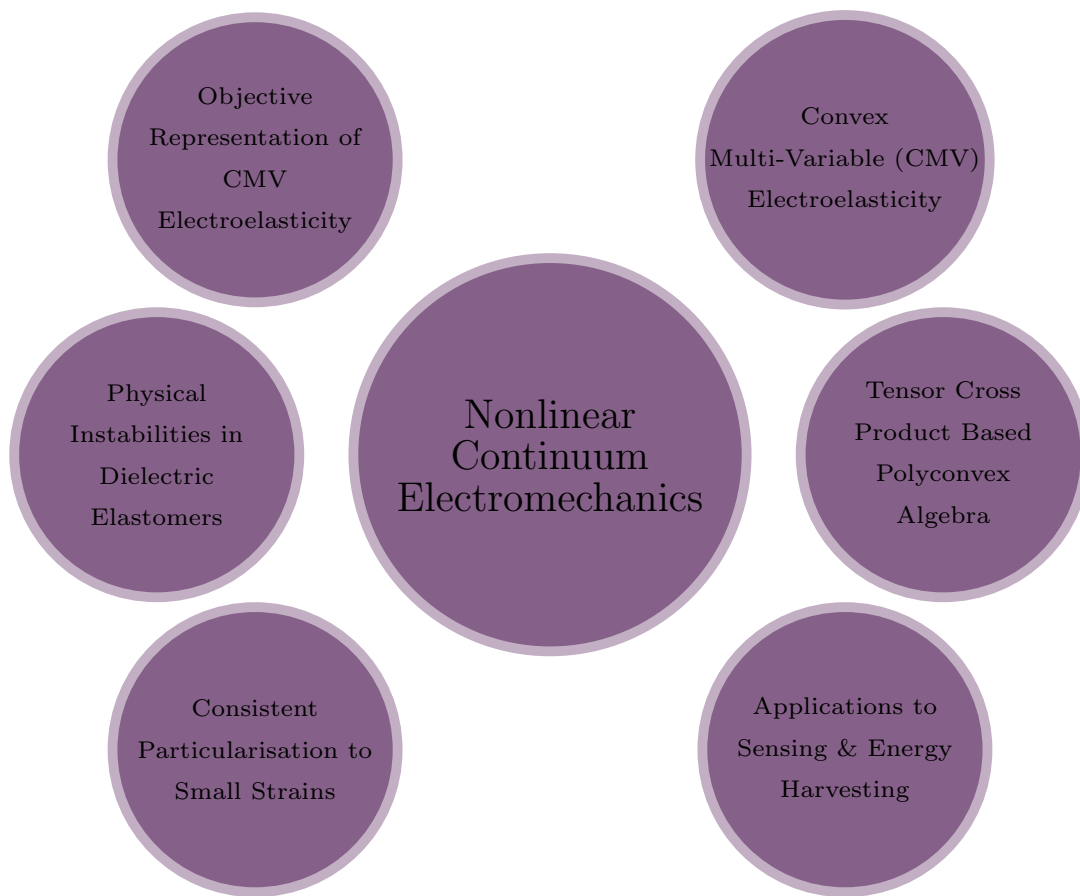
The approximation properties of the resulting meshes have been assessed and the results show that a similar quality of mesh (as indicated by  $Q_1$ ,  $Q_2$  and  $Q_3$ ) translates in similar interpolation errors (i.e. the quality indicators have been shown to be well chosen).

Finally, it is apparent by now that, the quality of a high order mesh depends on the restrictions imposed by the linear mesh. If a linear planar mesh is coarse in the vicinity of a steep curvature, the resulting elements in the high order mesh would experience a large distortion. However, the advantage of a posteriori approaches for mesh deformation based on solid mechanics analogy is in the fact that there are multitude of established efficient and parallel elasticity solver which can be utilised to generate computational meshes for realistic industrial geometries, whereas this is not often the case for a priori mesh generation algorithms.



# Part 2:

## Convex Multi-Variable Electromechanics



# Chapter 4

## Convex Multi-Variable Electromechanics

### 4.1 Introduction

In this chapter, the Convex Multi-Variable (CMV) class of electromechanics for large deformations large electric fields analyses is discussed. The CMV reversible nonlinear electro-elasticity is a direct extension of the polyconvex elasticity recently presented and thoroughly pursued by Gil and Ortigosa [113, 233, 232]. The variational framework for CMV designed to tackle materials, specially dielectric elastomers which are characterised by displaying extremely large deformations when exposed to a high electric field is shown to satisfy ellipticity and guarantee material stability for the entire range of deformation.

The point of departure for such formulations is an assumed energy functional for the coupled electromechanical system. Conceptually, essential and suitable mathematical requirements for the energy functional such as ellipticity [16, 202], multi-variable convexity [113, 233], coercivity [270] and material frame indifference [29] can only be studied in a large deformation context. From a phenomenological point of view, these requirements or rather restrictions have important physical implications, in particular in guaranteeing the positive definiteness of the generalised electromechanical acoustic tensor, existence of real wave speeds in the material in the vicinity of an equilibrium configuration and the electromechanical stability of the material [210, 233]. Apart from these requirements other forms of physical instabilities present in dielectric elastomers such as pull-in instability, snap-through and the formation, propagation and nucleation of wrinkles can also be studied solely in the finite deformation regime [246, 335, 198, 336, 177, 110, 216, 217].

Furthermore, the requirement for material frame indifference of the energy, dictates that convex multi-variable energies typically expressed in terms of fundamental kinematic measures  $\{\mathbf{F}, \mathbf{H}, J\}$  be re-expressed in terms of a set of symmetric kinematics  $\{\mathbf{C}, \mathbf{G}, C\}$  to guarantee the objectivity of the energy functional. This symmetrisation is in particular also redeeming from particularisation to small strain point of view.

In this chapter we will discuss the convex multi-variable electro-elasticity based on a tensor cross product formulation. In particular, the chapter is divided into four sections, namely

1. **Section 4.2** presents the concept of multi-variable convexity in nonlinear electromechanics and presents the tensor cross product based formulation for CMV and the simplifications that the tensor cross product algebra brings forth to the equations of massively deformable electro-active polymers.
2. **Section 4.3** discusses the objective representation of multi-variable convexity in nonlinear electromechanics and presents the tensor cross product based formulation for re-expressing CMV energies in terms of symmetric kinematic measures.
3. **Section 4.4** presents the spatial representation of multi-variable convexity in nonlinear electromechanics and presents the tensor cross product based formulation for re-

expressing CMV energies in an updated Lagrangian setting.

4. **Section 4.5** presents the Legendre transformation of the convex multi-variable internal energies to Helmholtz-like energies suitable for finite element implementation and the algebra involved therein.

## 4.2 Convex multi-variable electro-elasticity

In this section, essential concepts of electro-elasticity are discussed as a key application area for the current tensor contraction framework.

### 4.2.1 Kinematics

Let us consider the motion of an electro-mechanical body which in its initial configuration is defined by a domain  $V$  of boundary  $\partial V$  with outward unit normal  $\mathbf{N}$ . After the motion, the body occupies a final configuration defined by a domain  $v$  of boundary  $\partial v$  with outward unit normal  $\mathbf{n}$ , as shown in Figure 4.1. The pseudo-time ( $t$ ) dependent mapping field  $\phi$  links a material particle from initial configuration  $\mathbf{X}$  to final configuration  $\mathbf{x}$  according to  $\mathbf{x} = \phi(\mathbf{X}, t)$ . The deformation gradient tensor  $\mathbf{F}$  is defined as

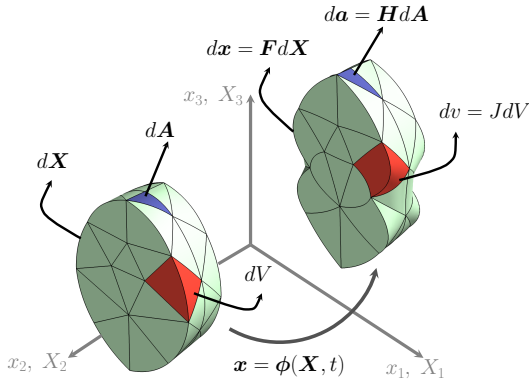


Figure 4.1: Motion map of a body  $V$  and the kinematic measures  $\{\mathbf{F}, \mathbf{H}, J\}$ .

$$\mathbf{F} = \nabla_0 \mathbf{x} = \frac{\partial \phi(\mathbf{X}, t)}{\partial \mathbf{X}}, \quad (4.1)$$

In addition, with the help of the tensor cross product operations, the cofactor and Jacobian ( $\mathbf{H} = \text{Cof}\mathbf{F}$  and  $J = \det \mathbf{F}$ ) of the deformation are defined as, [65, 28, 29]

$$\mathbf{H} = \frac{1}{2} \mathbf{F} \times \mathbf{F}; \quad H_{iI} = \frac{1}{2} \mathcal{E}_{ijk} \mathcal{E}_{IJK} F_{jJ} F_{kK}; \quad (4.2a)$$

$$J = \frac{1}{3} \mathbf{H} : \mathbf{F}; \quad J = \frac{1}{3} H_{iI} F_{iI}. \quad (4.2b)$$

As shown in Figure 4.1,  $\{\mathbf{F}, \mathbf{H}, J\}$  are the kinematic measures relating the differential fibre, area and volume elements from initial  $\{d\mathbf{X}, d\mathbf{A}, dV\}$  to final  $\{d\mathbf{x}, d\mathbf{a}, dv\}$  configuration.

### 4.2.2 Translational and rotational equilibrium

The kinematics of the electro-active continuum presented in subsection 4.2.1 must be described through the conservation of linear momentum. In the absence of inertial effects, the global conservation of linear momentum leads to the integral translational equilibrium equations

$$\int_{\partial_t V} \mathbf{t}_0 dA + \int_V \mathbf{f}_0 dV = \mathbf{0}, \quad (4.3)$$

where  $\mathbf{f}_0$  represents the body force per unit undeformed volume  $V$  and  $\mathbf{t}_0$  the traction force per unit undeformed area, applied on  $\partial_t V \subset \partial V$  such that  $\partial_t V \cup \partial_u V = \partial V$  and  $\partial_t V \cap \partial_u V = \emptyset$ . From (4.3), the local translational equilibrium equations and the associated boundary conditions can be written as

$$\text{DIV} \mathbf{P} + \mathbf{f}_0 = \mathbf{0} \quad \text{in } V; \quad (4.4a)$$

$$\mathbf{P} \mathbf{N} = \mathbf{t}_0 \quad \text{on } \partial_t V; \quad (4.4b)$$

$$\phi = (\phi)_{\partial_\phi V} \quad \text{on } \partial_u V, \quad (4.4c)$$

where  $\mathbf{P}$  represents the first Piola-Kirchoff stress tensor. Furthermore, conservation of rotational equilibrium leads to the well-known tensor condition  $\mathbf{P}\mathbf{F}^T = \mathbf{F}\mathbf{P}^T$ .

#### 4.2.3 Electrostatics: Gauss's and Faraday's laws

In addition to the conservation of translation and rotational equilibrium presented in subsection 4.2.2, the electro-active polymer represented by the continuum described in subsection 4.2.1 is subjected in its material configuration  $V$  to an electric volume charge  $\rho_0^e$  per unit of undeformed volume and an electric surface charge  $\omega_0^e$  per unit of undeformed area applied on  $\partial_\omega V \subset \partial V$ . Hence, in the absence of magnetic fields, the integral version of the Gauss's law can be written in a Lagrangian setting as

$$\int_{\partial_\omega V} \omega_0^e dA + \int_V \rho_0^e dV = 0. \quad (4.5)$$

From (4.5), the local version of Gauss's law and the associated boundary conditions can be written as

$$\text{DIV} \mathbf{D}_0 - \rho_0^e = 0 \quad \text{in } V; \quad (4.6a)$$

$$\mathbf{D}_0 \cdot \mathbf{N} = -\omega_0^e \quad \text{on } \partial_\omega V, \quad (4.6b)$$

where  $\mathbf{D}_0$  is the Lagrangian electric displacement vector. Furthermore, the integral version of the static Faraday's law can be written in a Lagrangian form for a closed curve  $\mathcal{C}$  embedded in  $V \cup \partial V$  as

$$\oint_{\mathcal{C}} \mathbf{E}_0 \cdot d\mathbf{X} = 0, \quad (4.7)$$

where  $\mathbf{E}_0$  is the Lagrangian or material electric field vector. The local version of (4.7) and the associated boundary conditions can be written as

$$\mathbf{E}_0 = -\nabla_0 \varphi \quad \text{in } V; \quad (4.8a)$$

$$\varphi = (\varphi)_{\partial_\varphi V} \quad \text{on } \partial_\varphi V, \quad (4.8b)$$

where  $\varphi$  is the scalar electric potential. In (4.8),  $\partial_\varphi V$  represents parts of the boundary  $\partial V$  where essential electric potential boundary conditions are applied such that  $\partial_\omega V \cup \partial_\varphi V = \partial V$  and  $\partial_\omega V \cap \partial_\varphi V = \emptyset$ . The spatial electric field vector  $\mathbf{E}$  can be obtained by performing the push forward (standard fibre transformation) on material electric field i.e.  $\mathbf{E}_0 = \mathbf{F}^T \mathbf{E}$ .

Let us define  $\delta\mathbf{u}$  and  $\Delta\mathbf{u}$  as virtual and incremental variations of  $\mathbf{x}$ , respectively and  $\delta\mathbf{D}_0$  and  $\Delta\mathbf{D}_0$  as virtual and incremental variations of  $\mathbf{D}_0$ , respectively, where it will be assumed that  $\delta\mathbf{u}$ ,  $\Delta\mathbf{u}$ ,  $\delta\mathbf{D}_0$  and  $\Delta\mathbf{D}_0$  satisfy compatible homogeneous displacement based boundary conditions that vanish on  $\partial_u V$  and  $\partial_\varphi V$ , respectively.

#### 4.2.4 The internal energy density in convex multi-variable electro-elasticity

For the closure of the system of equations defined by (4.4), (4.6) and (4.8), two additional constitutive laws are needed relating deformation and electric displacements to stresses and

electric fields in the continuum, satisfying appropriate constitutive inequalities, in particular ellipticity [78, 233]. In the case of reversible electro-elasticity, where thermal effects and electric polarisation induced hysteresis are disregarded, the internal energy density  $e$  per unit of undeformed volume can be solely defined in terms of the deformation and electric displacement, namely  $e = e(\nabla_0 \mathbf{x}, \mathbf{D}_0)$ . In this setting consistent linearisation of the internal energy  $e$  with respect of virtual and incremental variation of the geometry and electric displacement leads to

$$De[\delta \mathbf{u}; \delta \mathbf{D}_0] = \mathbf{P} : \nabla_0 \delta \mathbf{u} + \mathbf{E}_0 \cdot \delta \mathbf{D}_0, \quad (4.9)$$

where the first Piola-Kirchhoff stress tensor  $\mathbf{P}$  and the Lagrangian electric field  $\mathbf{E}_0$  are computed as

$$\mathbf{P} = \frac{\partial e(\mathbf{F}, \mathbf{D}_0)}{\partial \mathbf{F}} \Big|_{\mathbf{F}=\nabla_0 \mathbf{x}}; \quad \mathbf{E}_0 = \frac{\partial e(\mathbf{F}, \mathbf{D}_0)}{\partial \mathbf{D}_0} \Big|_{\mathbf{F}=\nabla_0 \mathbf{x}}, \quad (4.10)$$

Recently, Gil and Ortigosa [113, 233, 235, 234] have introduced the concept of multi-variable convexity (CMV), which satisfies the well-posedness of the governing equations described in subsection 4.2.2, and postulated as

$$e(\mathbf{F}, \mathbf{D}_0) = \tilde{W}(\mathbf{F}, \mathbf{H}, J, \mathbf{D}_0, \mathbf{d}); \quad \mathbf{d} = \mathbf{F}\mathbf{D}_0, \quad (4.11)$$

where  $\tilde{W}$  represents a convex multi-variable functional in terms of the extended set of arguments  $\mathcal{V}_{FHJD_0d} = \{\mathbf{F}, \mathbf{H}, J, \mathbf{D}_0, \mathbf{d}\}$ . Following [113], the first Piola-Kirchoff stress tensor and the electric field vector and can be obtained from the linearisation of the convex multi-variable energy as

$$\begin{aligned} De[\delta \mathbf{u}] &= D\tilde{W}[D\mathbf{F}[\delta \mathbf{u}], D\mathbf{H}[\delta \mathbf{u}], DJ[\delta \mathbf{u}], D\mathbf{D}_0[\delta \mathbf{u}], D\mathbf{d}[\delta \mathbf{u}]] \\ &= (\boldsymbol{\Sigma}_F + \boldsymbol{\Sigma}_H \times \mathbf{F} + \boldsymbol{\Sigma}_J \mathbf{H} + \boldsymbol{\Sigma}_d \otimes \mathbf{D}_0) : \nabla_0 \delta \mathbf{u}; \end{aligned} \quad (4.12a)$$

$$De[\delta \mathbf{D}_0] = D\tilde{W}[\delta \mathbf{D}_0, \delta \mathbf{F}\mathbf{D}_0] = (\boldsymbol{\Sigma}_{\mathbf{D}_0} + \mathbf{F}^T \boldsymbol{\Sigma}_d) \cdot \delta \mathbf{D}_0, \quad (4.12b)$$

from which the first Piola-Kirchhoff stress tensor and the electric field vector can be expressed as

$$\mathbf{P} = \boldsymbol{\Sigma}_F + \boldsymbol{\Sigma}_H \times \mathbf{F} + \boldsymbol{\Sigma}_J \mathbf{H} + \boldsymbol{\Sigma}_d \otimes \mathbf{D}_0; \quad P_{II} = \Sigma_{F_{II}} + \mathcal{E}_{ijk} \mathcal{E}_{IJK} \Sigma_{H_{jJ}} F_{kK} + \Sigma_J H_{II} + \Sigma_{d_I} D_{0I}; \quad (4.13)$$

$$\mathbf{E}_0 = \boldsymbol{\Sigma}_{\mathbf{D}_0} + \mathbf{F}^T \boldsymbol{\Sigma}_d; \quad E_{0I} = \Sigma_{D_{0I}} + F_{II} \Sigma_{d_I}, \quad (4.14)$$

where  $\Sigma_A = \frac{\partial W}{\partial A}$ , where  $A$  can represent any element from the set  $\mathcal{V}_{FHJD_0d}$ . Furthermore, consistent linearisation of the governing equations leads to

$$D^2 e[\delta \mathbf{u}, \delta \mathbf{D}_0; \Delta \mathbf{u}, \Delta \mathbf{D}_0] = [\nabla_0 \delta \mathbf{u} : \delta \mathbf{D}_0] \begin{bmatrix} \tilde{\mathcal{C}} & \tilde{\mathcal{Q}}^T \\ \tilde{\mathcal{Q}} & \tilde{\boldsymbol{\theta}} \end{bmatrix} \begin{bmatrix} : \nabla_0 \Delta \mathbf{u} \\ \Delta \mathbf{D}_0 \end{bmatrix} \quad (4.15)$$

with the constitutive tensors of the material namely, the fourth order elasticity tensor  $\tilde{\mathcal{C}}$ , the third order piezoelectric or coupling tensor  $\tilde{\mathcal{Q}}$  and the second order dielectric tensor  $\tilde{\boldsymbol{\theta}}$ , defined as

$$\tilde{\mathcal{C}} = \frac{\partial^2 e(\mathbf{F}, \mathbf{D}_0)}{\partial \mathbf{F} \partial \mathbf{F}} \Big|_{\mathbf{F}=\nabla_0 \mathbf{x}}; \quad \tilde{\mathcal{Q}} = \frac{\partial^2 e(\mathbf{F}, \mathbf{D}_0)}{\partial \mathbf{D}_0 \partial \mathbf{F}} \Big|_{\mathbf{F}=\nabla_0 \mathbf{x}}; \quad \tilde{\boldsymbol{\theta}} = \frac{\partial^2 e(\mathbf{F}, \mathbf{D}_0)}{\partial \mathbf{D}_0 \partial \mathbf{D}_0} \Big|_{\mathbf{F}=\nabla_0 \mathbf{x}}. \quad (4.16)$$

Analogous to (4.13), a more physically insightful representation of the tangent operator can be obtained as

$$\begin{aligned} D^2 e[\delta \mathbf{u}; \delta \mathbf{D}; \Delta \mathbf{u}; \Delta \mathbf{D}] &= [\mathbb{M}_\delta^{FHJD0d}]^T [\mathbb{H}_{\tilde{W}}] [\mathbb{M}_\Delta^{FHJD0d}] + (\boldsymbol{\Sigma}_H + \boldsymbol{\Sigma}_J \mathbf{F}) : (\nabla_0 \delta \mathbf{u} \times \nabla_0 \Delta \mathbf{u}) \\ &\quad + \boldsymbol{\Sigma}_d \cdot ((\nabla_0 \delta \mathbf{u}) \Delta \mathbf{D}_0 + (\nabla_0 \Delta \mathbf{u}) \delta \mathbf{D}_0), \end{aligned} \quad (4.17)$$

where

$$[\mathbb{M}_\delta^{FHJD0d}]^T = [(\nabla_0 \delta \mathbf{u}) : (\nabla_0 \delta \mathbf{u} \times \mathbf{F}) : (\nabla_0 \delta \mathbf{u} : \mathbf{H}) \quad \delta \mathbf{D}_0 \cdot ((\nabla_0 \delta \mathbf{u}) \mathbf{D}_0 + \mathbf{F} \delta \mathbf{D}_0)];$$

$$[\mathbb{M}_\Delta^{FHJD0d}] = \begin{bmatrix} (\nabla_0 \Delta \mathbf{u}) : \\ (\nabla_0 \Delta \mathbf{u} \times \mathbf{F}) : \\ (\nabla_0 \Delta \mathbf{u} : \mathbf{H}) \\ \Delta \mathbf{D}_0 \cdot \\ ((\nabla_0 \Delta \mathbf{u}) \mathbf{D}_0 + \mathbf{F} \Delta \mathbf{D}_0) \end{bmatrix},$$

with the Hessian operator  $[\mathbb{H}_{\tilde{W}}]$  defined as

$$[\mathbb{H}_{\tilde{W}}] = \begin{bmatrix} \tilde{W}_{FF} & \tilde{W}_{FH} & \tilde{W}_{FJ} & \tilde{W}_{FD_0} & \tilde{W}_{Fd} \\ \tilde{W}_{HF} & \tilde{W}_{HH} & \tilde{W}_{HJ} & \tilde{W}_{HD_0} & \tilde{W}_{Hd} \\ \tilde{W}_{JF} & \tilde{W}_{JH} & \tilde{W}_{JJ} & \tilde{W}_{JD_0} & \tilde{W}_{Jd} \\ \tilde{W}_{D_0F} & \tilde{W}_{D_0H} & \tilde{W}_{D_0J} & \tilde{W}_{D_0D_0} & \tilde{W}_{D_0D_0} \\ \tilde{W}_{dF} & \tilde{W}_{dH} & \tilde{W}_{dJ} & \tilde{W}_{dD_0} & \tilde{W}_{dd} \end{bmatrix}, \quad (4.18)$$

where  $W_{AB} = \frac{\partial^2 \tilde{W}}{\partial A \partial B}$ , where  $\mathbf{A}$  and  $\mathbf{B}$  can represent any two elements from the set  $\mathcal{V}_{FHJD0d}$ . Alternatively, following [113], the components  $\tilde{\mathcal{C}}$ ,  $\tilde{\mathcal{Q}}$  and  $\tilde{\boldsymbol{\theta}}$  can be defined in terms of the set of work-conjugates  $\mathcal{V}_{FHJD0d}$  as

$$\begin{aligned} \tilde{\mathcal{C}} = & W_{FF} + \mathbf{F} \times (W_{HH} \times \mathbf{F}) + W_{JJ} \mathbf{H} \otimes \mathbf{H} + \mathcal{C}_1 + 2(W_{FH} \times \mathbf{F})^{\text{sym}} \\ & + 2(W_{FJ} \otimes \mathbf{H})^{\text{sym}} + 2(W_{Fd} \otimes \mathbf{D}_0)^{\text{sym}} + 2((\mathbf{F} \times W_{HJ}) \otimes \mathbf{H})^{\text{sym}} \\ & + 2((\mathbf{F} \times W_{Hd}) \otimes \mathbf{D}_0)^{\text{sym}} + 2(\mathbf{H} \otimes (W_{Jd} \otimes \mathbf{D}_0))^{\text{sym}} + \mathcal{A}; \end{aligned} \quad (4.19a)$$

$$\tilde{\mathcal{Q}}^T = W_{FD_0} + \mathbf{F} \times W_{HD_0} + \mathbf{H} \otimes W_{JD_0} + \mathcal{Q}_1^T + \mathcal{Q}_2^T + \mathcal{Q}_3^T + \mathcal{Q}_4^T + \mathcal{Q}_5^T; \quad (4.19b)$$

$$\tilde{\boldsymbol{\theta}} = W_{D_0D_0} + (W_{D_0d} \mathbf{F} + \mathbf{F}^T W_{dD_0}) + \mathbf{F}^T W_{dd} \mathbf{F}, \quad (4.19c)$$

where

$$\mathcal{A}_{iIjJ} = \mathcal{E}_{ijp} \mathcal{E}_{IJp} (\Sigma_H + \Sigma_J \Sigma_H)_{pP}; \quad \mathcal{C}_{1iIjJ} = (W_{dd})_{ij} D_{0I} D_{0J},$$

and for any fourth order tensor  $\mathcal{T}$ ,  $\mathcal{T}_{iIjJ}^{\text{sym}} = \frac{1}{2}(\mathcal{T}_{iIjJ} + \mathcal{T}_{jJiI})$  and

$$\begin{aligned} [\mathcal{Q}_1^T]_{iIJ} &= [W_{dD_0}]_{iJ} D_{0I}; \\ [\mathcal{Q}_2^T]_{iIJ} &= [W_{Fd}]_{iIj} F_{jJ}; \\ [\mathcal{Q}_3^T]_{iIJ} &= [\mathbf{F} \times W_{HD_0}]_{iIj} F_{jJ}; \\ [\mathcal{Q}_4^T]_{iIJ} &= [\mathbf{H} \otimes W_{Jd}]_{iIj} F_{jJ}; \\ [\mathcal{Q}_5^T]_{iIJ} &= [W_{dd}]_{ij} F_{jJ} D_{0I} \end{aligned}$$

In the context of finite elements, equations (4.13-4.16) need to be evaluated at every quadrature point. Hence, the computational cost of numerical integration would be dictated primarily by the evaluation of the work-conjugates and the Hessian of the internal energy [254, 251].

It is important to note that, the convex multi-variable electro-elastic formulation described here is a direct extension of the polyconvex nonlinear elasticity presented in chapter 2. In fact equivalency could be established between the two as shown in Figure 4.2.

#### 4.2.5 A simple convex multi-variable constitutive model

A simple internal energy functional which complies with the definition of multi-variable convexity in (4.11), can be defined as

$$W = \mu_1 II_F + \mu_2 II_H + f(J) + \frac{1}{2\varepsilon_1} II_{D_0} + \frac{1}{2\varepsilon_2 J} II_d, \quad (4.20)$$

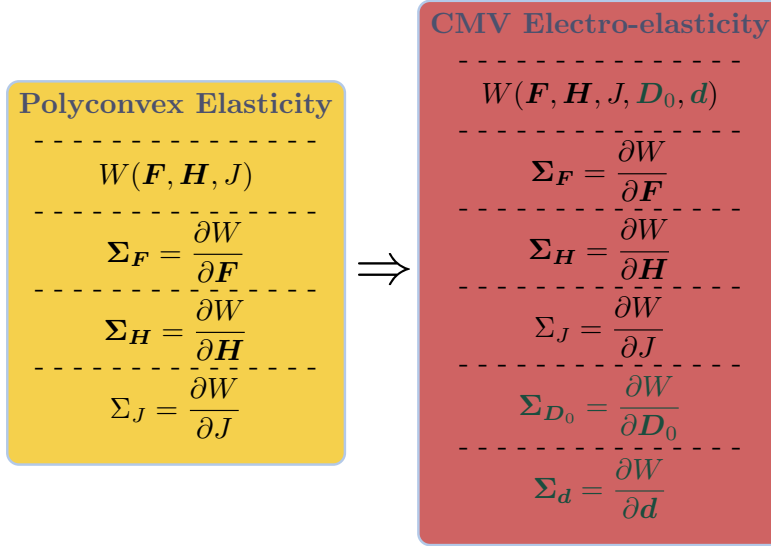


Figure 4.2: Extension of polyconvexity to Convex Multi-Variable (CMV) electro-elasticity, showing internal energy and the associated work-conjugates

where  $f(J)$  was introduced in (2.12) and  $\{\mu_1, \mu_2, \varepsilon_1, \varepsilon_2, \kappa\}$ , positive material constants. For this model,  $\mathbf{P}$  (4.13) and  $\mathbf{E}_0$  (4.14) are

$$\mathbf{P} = 2\mu_1 \mathbf{F} + 2\mu_2 \mathbf{H} \times \mathbf{F} + \left( f'(J) - \frac{1}{2\varepsilon_2 J^2} II_{\mathbf{d}} \right) \mathbf{H}; \quad \mathbf{E}_0 = \frac{1}{\varepsilon_1} \mathbf{D}_0 + \frac{1}{\varepsilon_2 J} \mathbf{F}^T \mathbf{d}, \quad (4.21)$$

and the non-zero components of the Hessian operator  $\mathbb{H}_{W_1}$  are defined as

$$\begin{aligned} W_{\mathbf{FF}} &= 2\mu_1 \mathbf{I}; & W_{\mathbf{HH}} &= 2\mu_2 \mathbf{I}; & W_{JJ} &= \left( f''(J) + \frac{1}{4\varepsilon_2 J^3} II_{\mathbf{d}} \right); \\ W_{J\mathbf{d}} &= -\frac{1}{\varepsilon_2 J^2} \mathbf{d}; & W_{\mathbf{D}_0\mathbf{D}_0} &= \frac{1}{\varepsilon_1} \mathbf{I}; & W_{\mathbf{dd}} &= \frac{1}{\varepsilon_2 J} \mathbf{I}, \end{aligned} \quad (4.22)$$

where  $f'(J)$  and  $f''(J)$  were defined in (2.14) and (2.16), respectively. The tensors  $\mathcal{C}$ ,  $\mathcal{Q}$  and  $\boldsymbol{\theta}$  can now be obtained from (4.22).

## 4.3 Objective representation in convex multi-variable electro-elasticity

### 4.3.1 Kinematics

Based on the fundamental kinematic measures  $\{\mathbf{F}, \mathbf{H}, J\}$  defined in (4.1) and (4.2), a set of symmetric kinematic measures namely  $\mathbf{C}$ ,  $\mathbf{G}$  and  $C$ , can be defined as described in chapter 2

$$\mathbf{C} = \mathbf{F}^T \mathbf{F}; \quad \mathbf{G} = \frac{1}{2} \mathbf{C} \times \mathbf{C} = \mathbf{H}^T \mathbf{H}; \quad C = \frac{1}{3} \mathbf{G} : \mathbf{C} = J^2, \quad (4.23)$$

where  $\mathbf{C}$  is the right Cauchy-Green strain tensor and  $\mathbf{G}$  and  $C$  are its co-factor and determinant, respectively. The directional derivatives of the kinematics with respect to incremental and virtual variation of the geometry can be computed as described in chapter 2.

### 4.3.2 The internal energy density in objective convex multi-variable electro-elasticity

The requirement for objectivity (i.e. invariance with respect to rotations in the material configuration) implies that  $e$  must be independent of the rotational components of deformation.

This can be facilitated by re-expressing the internal energy density in terms of a symmetric kinematic measure such as the symmetric right Cauchy-Green tensor  $\mathbf{C}$  as follows

$$e(\nabla_0 \mathbf{x}, \mathbf{D}_0) = e_{\text{sym}}(\mathbf{C}, \mathbf{D}_0). \quad (4.24)$$

In this setting consistent linearisation of the internal energy  $e$  with respect of virtual and incremental variation of the geometry and electric displacement leads to

$$De_{\text{sym}}[\delta \mathbf{u}; \delta \mathbf{D}_0] = \mathbf{S} : \frac{1}{2} D\mathbf{C}[\delta \mathbf{u}] + \mathbf{E}_0 \cdot \delta \mathbf{D}_0, \quad (4.25)$$

where the second Piola-Kirchhoff stress tensor  $\mathbf{S}$  and the Lagrangian electric field  $\mathbf{E}_0$  are computed as

$$\mathbf{S} = 2 \frac{\partial e_{\text{sym}}(\mathbf{C}, \mathbf{D}_0)}{\partial \mathbf{C}} \Big|_{\mathbf{F}=\nabla_0 \mathbf{x}}; \quad \mathbf{E}_0 = \frac{\partial e_{\text{sym}}(\mathbf{C}, \mathbf{D}_0)}{\partial \mathbf{D}_0} \Big|_{\mathbf{F}=\nabla_0 \mathbf{x}}, \quad (4.26)$$

wherein the first and second Piola-Kirchhoff tensors are related through  $\mathbf{P} = \mathbf{F}\mathbf{S}$ . For the requirement of objectivity, the convex multi-variable energy  $\tilde{W}$  (4.11) can be re-expressed in terms of a set of symmetric kinematics defined in (4.23)

$$e(\nabla_0 \mathbf{x}, \mathbf{D}_0) = e_{\text{sym}}(\mathbf{C}, \mathbf{D}_0) \underset{\Leftarrow}{=} \tilde{W}(\mathbf{F}, \mathbf{H}, J, \mathbf{D}_0, \mathbf{d}) \underset{\Rightarrow}{=} W_{\text{sym}}(\mathbf{C}, \mathbf{G}, C, \mathbf{D}_0), \quad (4.27)$$

where  $e_{\text{sym}}$  represents the internal energy in terms of the right Cauchy Green strain tensor  $\mathbf{C}$  and Lagrangian electric displacement  $\mathbf{D}_0$  and  $W_{\text{sym}}$  represents an internal energy defined in terms of the extended symmetric mechanical kinematic set  $\mathcal{V}_{\text{sym}}^m = \{\mathbf{C}, \mathbf{G}, C\}$  and the Lagrangian electric displacement  $\mathbf{D}_0$ . It is worth noting that  $W_{\text{sym}}$  is not strictly convex with respect to the individual components of the set  $\{\mathcal{V}_{\text{sym}}^m, \mathbf{D}_0\}$ , but rather an objective re-expression of the convex multi-variable functional  $W$ . Furthermore, the inclusion of the term  $\mathbf{d}$  in  $\tilde{W}$  is useful in the context of studying material stability [113] which can be re-expressed in terms of the combination of kinematics in  $\{\mathcal{V}_{\text{sym}}^m, \mathbf{D}_0\}$ . Notice that, constructing a convex multi-variable energy (i.e.  $\tilde{W}$ ) is a necessary first step for a materially frame indifferent representation (i.e.  $W_{\text{sym}}$ ), but the vice-versa is not necessarily true or at times even obtainable.

Definition of an objective internal energy density such as in (4.27) is an essential requirement for the particularisation of a multi-variable convex function to the case of small strains [254, 251]. Furthermore, this definition of the internal energy  $e_{\text{sym}}$  (4.27) facilitates the introduction of a new set of work-conjugates which can now be defined as

$$\boldsymbol{\Sigma}_C = 2 \frac{\partial W_{\text{sym}}}{\partial \mathbf{C}}; \quad \boldsymbol{\Sigma}_G = 2 \frac{\partial W_{\text{sym}}}{\partial \mathbf{G}}; \quad \boldsymbol{\Sigma}_C = 2 \frac{\partial W_{\text{sym}}}{\partial C}; \quad \boldsymbol{\Sigma}_{\mathbf{D}_0} = \frac{\partial W_{\text{sym}}}{\partial \mathbf{D}_0}. \quad (4.28)$$

For notational convenience, the following sets, featuring in subsequent sections, are introduced

$$\mathcal{V}_{\text{sym}}^m = \{\mathbf{C}, \mathbf{G}, C\}; \quad \Sigma_{\mathcal{V}_{\text{sym}}^m}^m = \{\boldsymbol{\Sigma}_C, \boldsymbol{\Sigma}_G, \boldsymbol{\Sigma}_C\}; \quad (4.29a)$$

$$\mathcal{V}^e = \{\mathbf{D}_0\}; \quad \Sigma_{\mathcal{V}^e}^e = \{\boldsymbol{\Sigma}_{\mathbf{D}_0}\}; \quad (4.29b)$$

$$\mathcal{V} = \{\mathcal{V}_{\text{sym}}^m, \mathcal{V}^e\}; \quad \Sigma_{\mathcal{V}} = \{\Sigma_{\mathcal{V}_{\text{sym}}^m}^m, \Sigma_{\mathcal{V}^e}^e\} \quad (4.29c)$$

Following [29, 113, 233], a physically more insightful representation for the second Piola-Kirchhoff stress tensor  $\mathbf{S}$  and the Lagrangian electric field  $\mathbf{E}_0$  can be obtained through consistent linearisation of (4.27)

$$\begin{aligned} De_{\text{sym}}[\delta \mathbf{u}] &= DW[D\mathbf{C}[\delta \mathbf{u}], D\mathbf{G}[\delta \mathbf{u}], DC[\delta \mathbf{u}], D\mathbf{D}_0[\delta \mathbf{u}]] \\ &= (\boldsymbol{\Sigma}_C + \boldsymbol{\Sigma}_G \times \mathbf{C} + \boldsymbol{\Sigma}_C \mathbf{G}) : \frac{1}{2} D\mathbf{C}[\delta \mathbf{u}]; \end{aligned} \quad (4.30a)$$

$$De_{\text{sym}}[\delta \mathbf{D}_0] = DW[\delta \mathbf{D}_0] = \boldsymbol{\Sigma}_{\mathbf{D}_0} \cdot \delta \mathbf{D}_0, \quad (4.30b)$$

from which the second Piola-Kirchoff stress tensor and the electric field vector can be expressed as

$$\mathbf{S} = \boldsymbol{\Sigma}_C + \boldsymbol{\Sigma}_G \times \mathbf{C} + \boldsymbol{\Sigma}_C \mathbf{G}; \quad (4.31)$$

$$\mathbf{E}_0 = \boldsymbol{\Sigma}_{D_0}. \quad (4.32)$$

Subsequently, the internal energy  $e_{\text{sym}} = e_{\text{sym}}(\mathbf{C}, \mathbf{D}_0)$  can be further linearised leading to a tangent operator (facilitating a Newton-Raphson solution) which can be defined as follows

$$D^2 e_{\text{sym}}[\delta \mathbf{u}, \delta \mathbf{D}_0; \Delta \mathbf{u}, \Delta \mathbf{D}_0] = [\tfrac{1}{2} D\mathbf{C}[\delta \mathbf{u}] : \delta \mathbf{D}_0] \begin{bmatrix} \mathcal{C} & \mathcal{Q}^T \\ \mathcal{Q} & \boldsymbol{\theta} \end{bmatrix} \begin{bmatrix} : \tfrac{1}{2} D\mathbf{C}[\Delta \mathbf{u}] \\ \Delta \mathbf{D}_0 \end{bmatrix} + \mathbf{S} : \frac{1}{2} D^2 \mathbf{C}[\delta \mathbf{u}; \Delta \mathbf{u}], \quad (4.33)$$

with the fourth order elasticity tensor  $\mathcal{C}$ , the third order coupling tensor  $\mathcal{Q}$  and the second order dielectric tensor  $\boldsymbol{\theta}$  defined as

$$\mathcal{C} = 4 \frac{\partial^2 e_{\text{sym}}(\mathbf{C}, \mathbf{D}_0)}{\partial \mathbf{C} \partial \mathbf{C}} \Big|_{\mathbf{F}=\nabla_0 \mathbf{x}}; \quad \mathcal{Q} = 2 \frac{\partial^2 e_{\text{sym}}(\mathbf{C}, \mathbf{D}_0)}{\partial \mathbf{D}_0 \partial \mathbf{C}} \Big|_{\mathbf{F}=\nabla_0 \mathbf{x}}; \quad \boldsymbol{\theta} = \frac{\partial^2 e_{\text{sym}}(\mathbf{C}, \mathbf{D}_0)}{\partial \mathbf{D}_0 \partial \mathbf{D}_0} \Big|_{\mathbf{F}=\nabla_0 \mathbf{x}}. \quad (4.34)$$

Analogous to (4.31), a more physically insightful representation of the tangent operator can be obtained as

$$D^2 e_{\text{sym}}[\delta \mathbf{u}; \delta \mathbf{D}_0; \Delta \mathbf{u}; \Delta \mathbf{D}_0] = [\mathbb{M}_\delta^{CGCD_0}]^T [\mathbb{H}_{W_{\text{sym}}}^{CGCD_0}] [\mathbb{M}_\Delta] + (\boldsymbol{\Sigma}_G + \boldsymbol{\Sigma}_C \mathbf{C}) : (\tfrac{1}{2} D\mathbf{C}[\delta \mathbf{u}] \times \tfrac{1}{2} D\mathbf{C}[\Delta \mathbf{u}]) + \mathbf{S} : [(\nabla_0 \delta \mathbf{u})^T (\nabla_0 \Delta \mathbf{u})], \quad (4.35)$$

where

$$\begin{aligned} [\mathbb{M}_\delta^{CGCD_0}]^T &= [\tfrac{1}{2} D\mathbf{C}[\delta \mathbf{u}] : \tfrac{1}{2} D\mathbf{G}[\delta \mathbf{u}] : \tfrac{1}{2} D\mathbf{C}[\delta \mathbf{u}] \cdot \delta \mathbf{D}_0]; \\ [\mathbb{M}_\Delta^{CGCD_0}] &= \begin{bmatrix} : \tfrac{1}{2} D\mathbf{C}[\Delta \mathbf{u}] \\ : \tfrac{1}{2} D\mathbf{G}[\Delta \mathbf{u}] \\ \tfrac{1}{2} D\mathbf{C}[\Delta \mathbf{u}] \\ \Delta \mathbf{D}_0 \end{bmatrix}, \end{aligned}$$

with the Hessian operator  $[\mathbb{H}_{W_{\text{sym}}}]$  defined as

$$[\mathbb{H}_{W_{\text{sym}}}] = \begin{bmatrix} 4W_{\text{sym}}_{CC} & 4W_{\text{sym}}_{CG} & 4W_{\text{sym}}_{CC} & 2W_{\text{sym}}_{CD_0} \\ 4W_{\text{sym}}_{GC} & 4W_{\text{sym}}_{GG} & 4W_{\text{sym}}_{GC} & 2W_{\text{sym}}_{GD_0} \\ 4W_{\text{sym}}_{CC} & 4W_{\text{sym}}_{CG} & 4W_{\text{sym}}_{CC} & 2W_{\text{sym}}_{CD_0} \\ 2W_{\text{sym}}_{D_0 C} & 2W_{\text{sym}}_{D_0 G} & 2W_{\text{sym}}_{D_0 C} & W_{\text{sym}}_{D_0 D_0} \end{bmatrix}, \quad (4.36)$$

where the components of  $\mathcal{C}$ ,  $\mathcal{Q}$  and  $\boldsymbol{\theta}$  can now be defined in terms of the set of work-conjugates  $\Sigma_V$  defined in (4.29) as follows

$$\begin{aligned} \mathcal{C} &= W_{\text{sym}}_{CC} + \mathbf{C} \times (W_{\text{sym}}_{GG} \times \mathbf{C}) + (W_{\text{sym}}_{CC} \mathbf{G} \otimes \mathbf{G}) + W_{\text{sym}}_{CG} \times \mathbf{C} + \mathbf{C} \times W_{\text{sym}}_{CG} \\ &\quad + W_{\text{sym}}_{CC} \otimes \mathbf{G} + \mathbf{G} \otimes W_{\text{sym}}_{CC} + (\mathbf{C} \times W_{\text{sym}}_{CC}) \otimes \mathbf{G} + \mathbf{G} \otimes (W_{\text{sym}}_{CC} \times \mathbf{C}); \end{aligned} \quad (4.37a)$$

$$\mathcal{Q}^T = W_{\text{sym}}_{CD_0} + \mathbf{C} \times W_{\text{sym}}_{D_0 C} + \mathbf{G} \otimes W_{\text{sym}}_{CD_0}; \quad (4.37b)$$

$$\boldsymbol{\theta} = W_{D_0 D_0}. \quad (4.37c)$$

It is important to note that, as opposed to the convex multi-variable Hessian operator expressed in terms of the fundamental kinematic set  $\{\mathbf{F}, \mathbf{H}, J, \mathbf{D}_0, \mathbf{d}\}$  in (4.18), the Hessian operator in (4.36) is not strictly positive definite as multi-variable convexity is not defined with respect to the set  $V_{\text{sym}}^m$  and, hence, ellipticity (i.e. rank-one convexity) of the internal energy based on this constitutive term alone cannot be established.

It is important to note that, the objective convex multi-variable electro-elastic formulation described here is a direct extension of the frame invariant polyconvex nonlinear elasticity presented in chapter 2. In fact equivalency could be established between the two as shown in Figure 4.3.

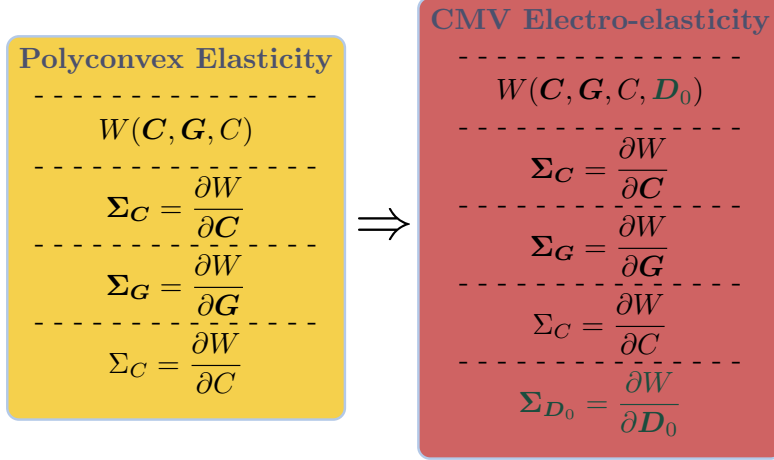


Figure 4.3: Extension of frame invariant polyconvexity to objective Convex Multi-Variable (CMV) electro-elasticity, showing internal energy and the associated work-conjugates

#### 4.3.3 A simple objective convex multi-variable constitutive model

A simple internal energy functional which complies with the definition of objective multi-variable convexity in (4.27), can be defined as

$$W = \mu_1 I_C + \mu_2 I_G + f(C) + \frac{1}{2\varepsilon_1} II_{D_0} + \frac{1}{2\varepsilon_2 \sqrt{C}} II_d, \quad (4.38)$$

where  $f(C)$  was introduced in (2.24). For this model,  $\mathbf{S}$  (4.31) and  $\mathbf{E}_0$  (4.32) are

$$\mathbf{S} = 2\mu_1 \mathbf{I} + 2\mu_2 \mathbf{I} \times \mathbf{C} + \left( f'(C) - \frac{1}{2\varepsilon_2 C} II_d \right) \mathbf{H}; \quad \mathbf{E}_0 = \frac{1}{\varepsilon_1} \mathbf{D}_0 + \frac{1}{\varepsilon_2 \sqrt{C}} \mathbf{F}^T \mathbf{d}, \quad (4.39)$$

and the non-zero components of the Hessian operator  $\mathbb{H}_{W_1}$  are defined as

$$W_{CC} = \left( f''(C) + \frac{1}{4\varepsilon_2 C \sqrt{C}} II_d \right); \quad W_{D_0 D_0} = \frac{1}{\varepsilon_1} \mathbf{I}, \quad (4.40)$$

where  $f'(C)$  and  $f''(C)$  were defined in (2.26) and (2.29), respectively. The tensors  $\mathcal{C}$ ,  $\mathcal{Q}$  and  $\boldsymbol{\theta}$  can now be obtained from (4.40).

### 4.4 Convex multi-variable electro-elasticity in spatial setting

In this section, the convex multi-variable electro-elasticity is presented in spatial setting. Our future development on a unified continuum electromechanics formulation for linear, geometrically linearised and nonlinear approach to electro-elasticity would be based on this formulation and in an updated Lagrangian framework.

#### 4.4.1 The Cauchy stress tensor, spatial electric field vector and tangent operator

With a particularisation to the case of small strains in mind, in addition to the first and second Piola-Kirchhoff stress tensors and Lagrangian electric field vector, it is also necessary to derive expressions for the Cauchy  $\boldsymbol{\sigma}$  (or Kirchhoff  $\boldsymbol{\tau}$ ) stress tensors and the spatial electric field vector  $\mathbf{E}$ . The expressions for the Cauchy stress tensor, spatial electric field vector and spatial tangent

elasticity tensor can be derived using the standard push forward operations [78, 318, 31], for the case of classical electro-elasticity

$$\boldsymbol{\tau} = J\boldsymbol{\sigma} = \mathbf{F}\mathbf{S}\mathbf{F}^T; \quad (4.41)$$

$$J\mathbf{c} = [\mathbf{C}]_{IJKL}[\mathbf{F}]_{iI}[\mathbf{F}]_{jJ}[\mathbf{F}]_{kK}[\mathbf{F}]_{lL}; \quad (4.42)$$

$$\mathbf{D}_0 = \mathbf{H}^T \mathbf{D}; \quad (4.43)$$

$$\mathbf{E} = \mathbf{F}^{-T} \mathbf{E}_0 \quad (4.44)$$

where  $\mathbf{D}_0$  is the spatial electric displacement vector and  $\boldsymbol{\sigma}$  is the symmetric second order Cauchy stress tensor and  $\mathbf{c}$  is the fourth order spatial tangent elasticity operator introduced in chapter 2. For the case of convex multi-variable electro-elasticity, similar push forward operations can be applied on the work-conjugates to obtain the Cauchy stress tensor and the spatial electric field vector as

$$J\boldsymbol{\sigma} = \boldsymbol{\tau} = J(\boldsymbol{\sigma}_C + \boldsymbol{\sigma}_G \times \mathbf{I} + \sigma_C \mathbf{I}); \quad (4.45)$$

$$\mathbf{E} = \mathbf{F}^{-T} \boldsymbol{\Sigma}_{D_0} \quad (4.46)$$

where the spatial work conjugates are given

$$J\boldsymbol{\sigma}_C = \mathbf{F} \boldsymbol{\Sigma}_C \mathbf{F}^T; \quad J\boldsymbol{\sigma}_G = \mathbf{H} \boldsymbol{\Sigma}_G \mathbf{H}^T; \quad J\sigma_C = C \Sigma_C. \quad (4.47)$$

The spatial form of the tangent operator can be computed using the standard push-forward operations to yield

$$\begin{aligned} D^2 e[\delta \mathbf{u}; \delta \mathbf{D}; \Delta \mathbf{u}; \Delta \mathbf{D}] &= [\mathbb{S}_\delta]^T \phi_* [\mathbb{H}_W] [\mathbb{S}_\Delta] + J(\boldsymbol{\sigma}_G + \sigma_C \mathbf{I}) : (\nabla \delta \mathbf{u} \times \nabla \Delta \mathbf{u}) \\ &\quad + J\boldsymbol{\sigma} : [(\nabla \delta \mathbf{v})^T (\nabla \Delta \mathbf{u})], \end{aligned} \quad (4.48)$$

where

$$[\mathbb{S}_\delta] = [\nabla \delta \mathbf{u} : (\nabla \delta \mathbf{u} \times \mathbf{I}) : (\nabla \delta \mathbf{u} : \mathbf{I}) \mathbf{H}^T \delta \mathbf{D}], \quad (4.49)$$

$$[\mathbb{S}_\Delta] = \begin{bmatrix} : \nabla \Delta \mathbf{u} \\ : (\nabla \Delta \mathbf{u} \times \mathbf{I}) \\ (\nabla \Delta \mathbf{u} : \mathbf{I}) \\ \cdot \mathbf{H}^T \Delta \mathbf{D} \end{bmatrix}, \quad (4.50)$$

with the fourth order tensor  $\mathbf{c}$  given as

$$\begin{aligned} &J\phi_* [\mathbb{H}_{W_{\text{symm}}}] \\ &= \begin{bmatrix} (W_{CC})_{IJKL} \mathbf{F}_{iI} \mathbf{F}_{jJ} \mathbf{F}_{kK} \mathbf{F}_{lL} & (W_{CG})_{IJKL} \mathbf{F}_{iI} \mathbf{F}_{jJ} \mathbf{H}_{kK} \mathbf{H}_{lL} & J^2 (W_{CC})_{IJ} \mathbf{F}_{iI} \mathbf{F}_{jJ} & (W_{CD_0})_{IJK} \mathbf{F}_{iI} \mathbf{F}_{jJ} \mathbf{F}_{kK} \\ (W_{GC})_{KLIJ} \mathbf{H}_{kK} \mathbf{H}_{lL} \mathbf{F}_{iI} \mathbf{F}_{jJ} & (W_{GG})_{IJKL} \mathbf{H}_{iI} \mathbf{H}_{jJ} \mathbf{H}_{kK} \mathbf{H}_{lL} & J^2 (W_{GC})_{IJ} \mathbf{H}_{iI} \mathbf{H}_{jJ} & (W_{GD_0})_{IJK} \mathbf{H}_{iI} \mathbf{H}_{jJ} \mathbf{H}_{kK} \\ J^2 (W_{CC})_{JI} \mathbf{F}_{iI} \mathbf{F}_{jJ} & J^2 (W_{CG})_{JI} \mathbf{H}_{iI} \mathbf{H}_{jJ} & J^2 (W_{CC}) J^2 & J^2 (W_{CD_0})_I \mathbf{F}_{ii} \\ (W_{D_0 C})_{KIJ} \mathbf{F}_{kK} \mathbf{F}_{iI} \mathbf{F}_{jJ} & (W_{D_0 G})_{KIJ} \mathbf{H}_{kK} \mathbf{H}_{iI} \mathbf{H}_{jJ} & J^2 (W_{D_0 C})_I \mathbf{F}_{ii} & (W_{D_0 D_0})_I \mathbf{F}_{ii} \mathbf{F}_{jj} \end{bmatrix}. \end{aligned} \quad (4.51a)$$

#### 4.4.2 Governing equations of continuum electromechanics in spatial setting

Let us assume that the domain defined by the deformable body is subjected to a body force per unit of deformed volume  $\mathbf{f}$  and a traction force per unit of deformed area  $\mathbf{t}$  applied on  $\partial_t v \in \partial v$ , such that  $\partial_t v \cup \partial_u v = \partial v$  and  $\partial_t v \cap \partial_u v = \emptyset$ . The conservation of linear momentum in the global from leads to the integral of the translational equilibrium equations as

$$\int_v \mathbf{f} dv + \int_{\partial_t v} \mathbf{t} da = \mathbf{0}. \quad (4.52)$$

The above integral equation governing the physics of a deformable system, can be summarised in the local (strong) form and spatial setting as follows [30, 29, 28].

$$\operatorname{div} \boldsymbol{\sigma} + \mathbf{f} = \mathbf{0} \quad \text{in } v; \quad (4.53\text{a})$$

$$\boldsymbol{\sigma} \mathbf{n} = \mathbf{t} \quad \text{on } \partial_t v; \quad (4.53\text{b})$$

$$\phi = \bar{\phi} \quad \text{on } \partial_u v. \quad (4.53\text{c})$$

In addition to the conservation of translation and rotational equilibrium in subsection 4.4.2, the electro-active polymer is subjected in its spatial configuration  $v$  to an electric volume charge  $\rho^e$  per unit of deformed volume and an electric surface charge  $\omega^e$  per unit of deformed area applied on  $\partial_\omega v \subset \partial v$ . Hence, in the absence of magnetic fields, the integral version of the Gauss's law can be written in a updated Lagrangian (spatial) setting as

$$\int_{\partial_\omega v} \omega^e da + \int_v \rho^e dV = 0. \quad (4.54)$$

From (4.54), the local version of Gauss's law and the associated boundary conditions can be written as

$$\operatorname{div} \mathbf{D} - \rho^e = 0 \quad \text{in } v; \quad (4.55\text{a})$$

$$\mathbf{D} \cdot \mathbf{n} = -\omega^e \quad \text{on } \partial_\omega v, \quad (4.55\text{b})$$

Furthermore, the integral version of the static Faraday's law can be written in a Lagrangian form for a closed curve  $\mathcal{C}$  embedded in  $v \cup \partial v$  as

$$\oint_{\mathcal{C}} \mathbf{E} \cdot d\mathbf{x} = 0, \quad (4.56)$$

The local version of (4.56) and the associated boundary conditions can be written as

$$\mathbf{E} = -\nabla \varphi \quad \text{in } v; \quad (4.57\text{a})$$

$$\varphi = (\varphi)_{\partial_\varphi v} \quad \text{on } \partial_\varphi v. \quad (4.57\text{b})$$

In (4.57),  $\partial_\varphi v$  represents parts of the boundary  $\partial v$  where essential electric potential boundary conditions are applied such that  $\partial_\omega v \cup \partial_\varphi v = \partial v$  and  $\partial_\omega v \cap \partial_\varphi v = \emptyset$ .

## 4.5 Helmholtz-like energy density and Legendre transformation

In the case of pursuing a standard variational implementation via the finite element method, where the scalar electric potential is preferred as an unknown over the electric displacement field vector, it is typically preferred to work with the Helmholtz's like energy  $\Phi = \Phi(\mathbf{C}, -\nabla_0 \varphi)$ , defined as [113, 233]

$$\Phi(\mathbf{C}, -\nabla_0 \varphi) = -\sup_{\mathbf{D}_0} \{-\nabla_0 \varphi \cdot \mathbf{D}_0 - e_{\text{sym}}(\mathbf{C}, \mathbf{D}_0)\}, \quad (4.58)$$

wherein the second Piola-Kirchhoff stress tensor  $\mathbf{S}$  and the Lagrangian electric displacement  $\mathbf{D}_0$  are computed as

$$\mathbf{S} = 2 \frac{\partial \Phi(\mathbf{C}, \mathbf{E}_0)}{\partial \mathbf{C}} \Big|_{\mathbf{E}_0 = -\nabla_0 \varphi}; \quad \mathbf{D}_0 = -\frac{\partial \Phi(\mathbf{C}, \mathbf{E}_0)}{\partial \mathbf{E}_0} \Big|_{\mathbf{E}_0 = -\nabla_0 \varphi}. \quad (4.59)$$

Further linearisation of the Helmholtz's energy leads to the three constitutive tensors analogous to (4.33)

$$\mathbf{C}_\Phi = \frac{\partial^2 \Phi(\mathbf{C}, \mathbf{E}_0)}{\partial \mathbf{C} \partial \mathbf{C}} \Big|_{\mathbf{E}_0 = -\nabla_0 \varphi}; \quad \mathbf{Q}_\Phi = \frac{\partial^2 \Phi(\mathbf{C}, \mathbf{E}_0)}{\partial \mathbf{C} \partial \mathbf{E}_0} \Big|_{\mathbf{E}_0 = -\nabla_0 \varphi}; \quad \mathbf{\Theta}_\Phi = \frac{\partial^2 \Phi(\mathbf{C}, \mathbf{E}_0)}{\partial \mathbf{E}_0 \partial \mathbf{E}_0} \Big|_{\mathbf{E}_0 = -\nabla_0 \varphi}, \quad (4.60)$$

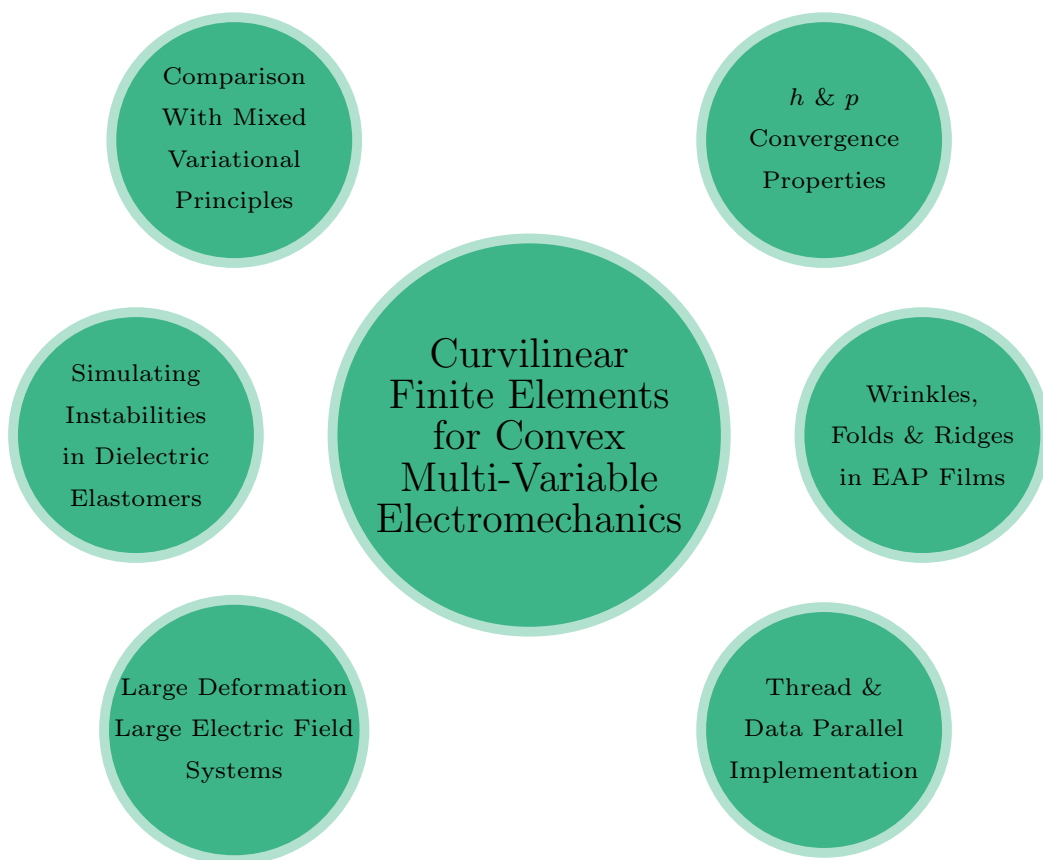
where the subscript  $\mathbf{E}_0 = -\nabla_0 \varphi$  implies that the electric field is computed from the gradient of the electric potential since, individual variations of the fields can also be assumed. When the internal energy is a complex multi-variable function of the set  $\mathcal{V}$ , the nonlinearity of the convex multi-variable function  $e_{sym}$  can make it impossible to obtain an explicit representation of the constitutive tensors in (4.60). Whence, it is typically more suitable to perform this step numerically, by utilising a nonlinear iterative scheme. In the context of finite element analysis, by exploiting the relationship between the internal energy and the Helmholtz's energy through the Legendre transform in (4.58), it is possible to compute, via a Newton-Raphson algorithm per quadrature point, these tensors as

$$[\boldsymbol{\theta}_\Phi]_{ij} = -[\boldsymbol{\theta}]_{ij}^{-1}; \quad [\boldsymbol{\mathcal{Q}}_\Phi]_{ijk} = -[\boldsymbol{\theta}_\Phi]_{mi} [\boldsymbol{\mathcal{Q}}]_{jkm}; \quad [\boldsymbol{\mathcal{C}}_\Phi]_{ijkl} = [\boldsymbol{\mathcal{C}}]_{ijkl} - [\boldsymbol{\mathcal{Q}}]_{ijm} [\boldsymbol{\mathcal{Q}}_\Phi]_{mkl}. \quad (4.61)$$

For a detailed representation of different electromechanical energies, the reader can refer to Gil and Ortigosa [113].



# Class 1: Curvilinear Finite Elements for Large Deformations - Large Electric Fields Electromechanics



# Chapter 5

## Curvilinear Finite Elements for Large Deformations - Large Electric Fields Electromechanics

### 5.1 Introduction

This chapter presents a high order finite element implementation of the convex multi-variable electro-elasticity for large deformations - large electric fields analyses combined with curvilinear meshes generated through the polyconvex elastic framework described in chapter 3. A great deal of emphasis is put on accurate geometrical representation of the electromechanical components throughout all the examples, by relying on the aforementioned curvilinear mesh generator. The performance of the method under near incompressibility and bending actuation scenarios is analysed with extremely thin and highly stretched components and compared to the performance of mixed variational principles recently reported by Gil and Ortigosa [113, 233, 232] for convex multi-variable electro-elasticity. Although convex multi-variable constitutive models are elliptic hence, materially stable for the entire range of deformations and electric fields, as presented in the last chapter, other forms of physical instabilities are not precluded in these models. In particular, physical instabilities present in dielectric elastomers such as pull-in instability, snap-through and the formation, propagation and nucleation of wrinkles and folds are numerically studied with a detailed precision in this chapter, verifying experimental findings [246, 335, 198]. To this end, we present virtual prototyping of many application-oriented dielectric elastomers carried out with an eye on pattern forming in soft robotics and other potential medical applications and the instabilities inherent in these components that could be harnessed for many other applications.

Admittedly, this class of electromechanics has been primarily applied to simplified geometries where the aim has been to verify ideas and the computational frameworks rather than to simulate realistic electromechanical components. Through simulations, we show instabilities and massive wrinkling in dielectric films. To the best of the author's knowledge, instabilities in Dielectric Elastomers (DEs) have not been numerically studied with this level of detail yet most of our simulations possessing millions of degrees of freedom and being as close to the realistic situations as possible. To be able to simulate such massive systems, efficient and meticulously designed thread and data parallel software libraries are needed. One such numerical framework is the outcome of this thesis, which combines many state of the art implementation designs for high order accurate simulation of convex multi-variable formulations for the analyses of dielectric elastomer films. This computational framework encompasses the curvilinear mesh generator developed in chapter 3 (**PostMesh**), utilises the data parallel capabilities of a newly developed tensor contraction framework **Fastor**, whose interface design is thoroughly discussed in the final chapter and integrates them all into one single open source computational framework called **Florence**, available under MIT license from <https://github.com/romeric/florence>. Some of the computational tools that Florence is built on are presented in

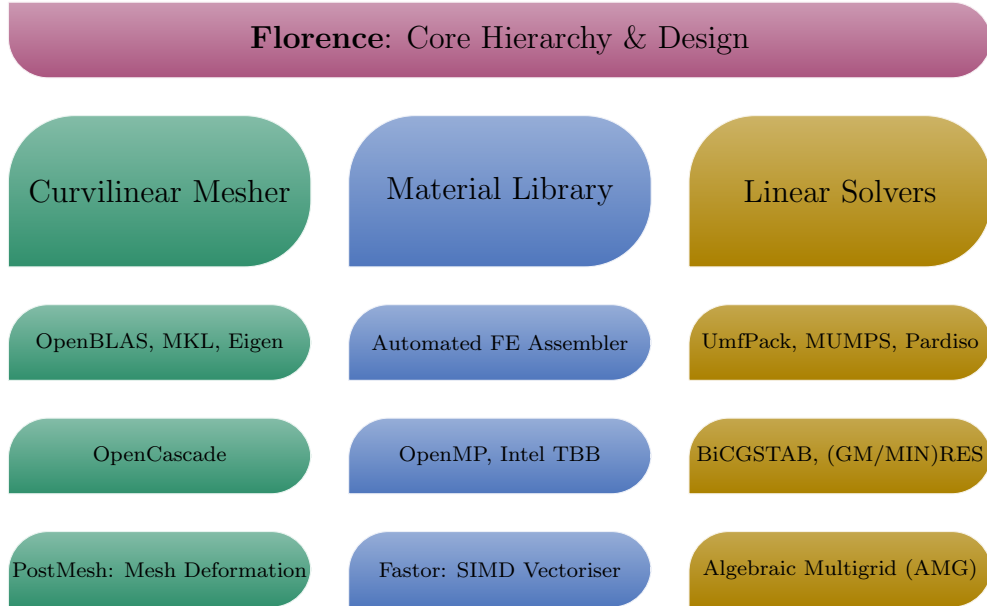


Figure 5.1: The developed massively parallel open source computational framework for high order curvilinear finite elements for CMV electromechanics, its requirements and dependencies

As can be seen from the Figure 5.1, the developed high performance high order curvilinear finite element framework for coupled electromechanical systems (**Florence**) depends on many other state of the art, open standard and open source technologies. In particular, a core constituent of the current framework is the curvilinear mesh generation framework (**PostMesh**) which itself is based on OpenCascade for CAD and geometry processing. This in combination with the use of optimised/vendor BLAS libraries help in building high order meshes in an efficient multi-threaded environment. The high order meshes are then curved using the poly-convex elasticity framework described in chapter 3. The second ingredient of the framework, is the convex multi-variable material library. These materials are typically defined programmatically at the energy level in a terse, intuitive and nearly mathematical format which are then automatically translated to efficient low-level multi-threaded C code, using a be-spoke finite element assembler in conjunction with OpenMP or Intel TBB. The tensor contraction engine **Fastor**, is used in this process to perform heavy compile time code transformation to emit FLOP optimal and further data parallel code for numerical integration of these material models. The aspect of high performance implementation of the code is described in detail in chapter 9. Finally, the framework has interfaces for a suite of massively parallel direct and iterative sparse linear solvers that can be used for solving the system of equations arising from high order finite element discretisation.

It should be noted that much of the work in this chapter is based on the authors work on convex multi-variable electromechanics presented in [253]. The chapter is organised as follows. In section 5.2, a variational framework for high order displacement-potential electromechanics is described. In section 9.3, a series of numerical examples pertaining to the capability of the current framework in modelling DEs are analysed, starting from the  $h$  and  $p$  convergence properties of the curvilinear finite element framework presented in subsection 5.3.1. The effect of accurate boundary representation using high order curvilinear finite elements is analysed in subsection 5.3.2 and compared to high order planar elements (elements with planar faces/edges). In subsection 5.3.3, the performance of the current high order finite element displacement-potential approach is compared to those of mixed Hu-Washizu formulations presented in [113, 233, 232]. Finally, a series of examples pertaining to the massive deformation of dielectric elastomers are presented in subsection 5.3.4. We also study the benefit of high order finite elements in simulating electromechanics. The inherent instabilities in DEs such as

pull-in instability and the formation of wrinkles are studied with detailed precision using  $h$  and  $p$  refinements, pinpointing the robustness and the high performant capability of the current framework.

## 5.2 Variational formulation

### 5.2.1 Displacement-electric potential based variational formulation

A variational principle can be established by the total energy minimisation defined in terms of the internal energy of the system  $e_{\text{sym}} = e_{\text{sym}}(\mathbf{C}, \mathbf{D}_0)$ . The total potential energy of the electro-active system in this case can be written in the complementary form as

$$\begin{aligned} \bar{\Pi}^e(\mathbf{x}^*, \mathbf{D}_0^*) &= \inf_{\mathbf{x}, \mathbf{D}_0} \left\{ \int_V e_{\text{sym}}(\mathbf{C}, \mathbf{D}_0) dV - \Pi_{\text{ext}}^m(\mathbf{x}) + \int_{\partial_\varphi V} (\mathbf{D}_0 \cdot \mathbf{N}) \bar{\varphi} dA \right\}; \\ \text{s.t. } &\begin{cases} \text{DIV} \mathbf{D}_0 = \rho_0 & \text{in } V \\ \mathbf{D}_0 \cdot \mathbf{N} = \omega_0 & \text{in } \partial_\omega V \end{cases}, \end{aligned} \quad (5.1)$$

where  $(\mathbf{x}^*, \mathbf{D}_0^*)$  denotes the exact solution and  $\Pi_{\text{ext}}^m(\mathbf{x})$  is the work done by external mechanical forces. Note that the last term in (5.1) accounts for the work done by the imposed essential boundary condition and its inclusion is necessary when starting from a complementary energy. The constraint defined by the Gauss's law is enforced as a Lagrange multiplier to yield an energy potential  $\Pi^e(\mathbf{x}^*, \varphi^*, \mathbf{D}_0^*)$  as

$$\begin{aligned} \Pi^e(\mathbf{x}^*, \varphi^*, \mathbf{D}_0^*) &= \inf_{\mathbf{x}, \mathbf{D}_0} \sup_{\varphi} \left\{ \int_V e_{\text{sym}}(\mathbf{C}, \mathbf{D}_0) dV - \int_V \mathbf{f}_0 \cdot \mathbf{x} dV - \int_{\delta_t V} \mathbf{t}_0 \cdot \mathbf{x} dA \right. \\ &\quad \left. + \int_V \varphi (\rho_0^e - \text{DIV} \mathbf{D}_0) dV + \int_{\partial_\omega V} \varphi (\omega_0^e - [\mathbf{D}_0] \cdot \mathbf{N}) dA + \int_{\partial_\varphi V} (\mathbf{D}_0 \cdot \mathbf{N}) \bar{\varphi} dA \right\}, \end{aligned} \quad (5.2)$$

Application of the Gauss divergence theorem to (5.2) yields an alternative representation of the variational principle as

$$\Pi_e(\mathbf{x}^*, \varphi^*, \mathbf{D}_0^*) = \inf_{\mathbf{x}, \mathbf{D}_0} \sup_{\varphi} \left\{ \int_V e_{\text{sym}}(\mathbf{C}, \mathbf{D}_0) dV + \int_V \mathbf{D}_0 \cdot \nabla_0 \varphi dV - \Pi_{\text{ext}}(\mathbf{x}, \varphi) \right\}, \quad (5.3)$$

where the electric potential  $\varphi$  acts as the Lagrange multiplier needed to enforce the constraints and  $(\mathbf{x}^*, \varphi^*, \mathbf{D}_0^*)$  denotes the exact solution and  $\Pi_{\text{ext}}(\mathbf{x}, \varphi)$  represents the external coupled electromechanical work additively decomposed into the purely mechanical  $\Pi_{\text{ext}}^m(\mathbf{x})$  and electrical  $\Pi_{\text{ext}}^e(\varphi)$  components

$$\begin{aligned} \Pi_{\text{ext}}^m(\mathbf{x}) &= \int_V \mathbf{f} \cdot \mathbf{x} dV + \int_{\delta_t V} \mathbf{t}_0 \cdot \mathbf{x} dA; \\ \Pi_{\text{ext}}^e(\varphi) &= - \int_V \rho_0^e \varphi dV - \int_{\partial_\omega V} \omega_0^e \varphi dA, \end{aligned}$$

where

$$\Pi_{\text{ext}}(\mathbf{x}, \varphi) = \Pi_{\text{ext}}^m(\mathbf{x}) + \Pi_{\text{ext}}^e(\varphi).$$

Application of the Legendre transform enables above variational principle (5.3) to be reformulated as

$$\Pi_\Phi(\mathbf{x}^*, \varphi^*) = \inf_{\mathbf{x}} \sup_{\varphi} \left\{ \int_V \Phi(\mathbf{C}, -\nabla_0 \varphi) dV - \Pi_{\text{ext}}(\mathbf{x}, \varphi) \right\}. \quad (5.4)$$

Note that the image of the Helmholtz-like energy  $\Pi_\Phi(\mathbf{x}^*, \varphi^*)$  is indeed identical to the image of the complementary energy, if one includes the contribution of Dirichlet forces as done in (5.1). This have been recognised recently by Miehe et. al. [210] although the author admittedly provides no solution to this problem. The appearance of the Dirichlet term in (5.1) can be proven easily if one starts from an appropriate Hu-Washizu principle.

In addition, it is worth mentioning that, the use of the term *Helmholtz-like* energy is due to the fact that the Helmholtz energy is predominantly used in the context of thermal problems for the free energy expressed in terms temperature and the Legendre transformation therein to obtain the internal energy expressed in terms of entropy.

The stationary condition of the Helmholtz-like functional in (5.4) with respect to changes in the geometry leads to the principle of virtual work (or power), written as

$$D\Pi_\Phi[\delta\mathbf{u}] = \int_V \mathbf{S} : \frac{1}{2} DC[\delta\mathbf{u}] dV - \Pi_{\text{ext}}[\delta\mathbf{u}]. \quad (5.5)$$

Analogously, the stationary point with respect to changes in the electric potential leads to the variational statement for the Gauss's law as

$$D\Pi_\Phi[\delta\varphi] = \int_V \mathbf{D} : \nabla_0 \delta\varphi dV - \Pi_{\text{ext}}[\delta\varphi]. \quad (5.6)$$

It is now straightforward to perform finite element discretisation of (5.4) in terms of  $\{\mathbf{x}, \varphi\}$ . This finite element discretisation is fairly standard and the interested reader can refer to the author's work [253, 233]. In the current setting, equal order high order isoparametric finite elements are utilised for the interpolation of the primary variables i.e.  $\{\mathbf{x}, \varphi\}$ . In this context, (5.4) can be solved for in a standard monolithic way as described in Algorithm 1.

---

**Algorithm 1** The nonlinear electromechanics solver

---

```

procedure MONOLITHIC SOLVER
    Input geometry, material properties and analysis parameters
    Initialise  $\mathbf{F} = \mathbf{0}$ ,  $\mathbf{x} = \mathbf{X}$  and  $\mathbf{R} = \mathbf{0}$ 
    for each increment  $n$  do
        Compute incremental nodal forces  $\Delta\mathbf{F}$ 
        Compute electromechanical nodal forces  $\mathbf{F} = \mathbf{F} + \Delta\mathbf{F}$ 
        Compute electromechanical residuals  $\mathbf{R} = \mathbf{R} - \Delta\mathbf{F}$ 
        while  $\|\mathbf{R}\|/\|\mathbf{F}\| > \text{tolerance}$  do
            Assemble  $\mathbf{K}$ 
            Solve  $\mathbf{Ku} = -\mathbf{R}$ 
            Update the geometry  $\mathbf{x} = \mathbf{x} + \mathbf{u}$ 
            for every quadrature point do
                Given  $\mathbf{E}_0$  compute  $\mathbf{D}_0$  implicitly via 4.37(c)
                Compute  $\mathcal{C}_\Phi, \mathcal{Q}_\Phi$  and  $\boldsymbol{\theta}_\Phi$  using (4.61)
                Compute second Piola-Kirchhoff stress tensor  $\mathbf{S}$  using (4.31)
            end for
            Compute traction forces  $\mathbf{T}$ 
            Find  $\mathbf{R} = \mathbf{T} - \mathbf{F}$ 
        end while
    end for
end procedure

```

---

### 5.3 Numerical examples

In this section a series of numerical examples for electromechanics are presented. These include a) (mesh refinement)  $h$  and (polynomial enrichment)  $p$  convergence studies for high

order displacement-potential formulation for convex multi-variable internal energies presented in section 5.2, b) the impact of accurate geometrical representations on the solution of large deformation electromechanical problems and, c) comparison of the current framework with the mixed Hu-Washizu variational principles presented in [233, 114]. Apart from these benchmark studies, a series of examples pertaining to the massive deformation and the instabilities in DEs such as the formation of folds and wrinkles is studied in detail using the current framework. The finite element implementation involves equal order standard isoparametric discretisation of the electromechanical variables  $\{\boldsymbol{x}, \varphi\}$ , starting with at least quadratic basis functions. As a standard nomenclature in high order finite element analysis, polynomial interpolation over tetrahedra are denoted by  $p$  and polynomial enrichment over hexahedra are denoted by  $q$ . Unless otherwise specified, for all the examples, the curvilinear meshes are generated using the consistently linearised solid mechanics analogy presented in chapter 3, using a Mooney-Rivlin model with a Poisson's ratio of 0.45 and 10 load increments. In addition, all the analyses are carried out with the high performance domain-specific data parallel tensor contraction finite element framework **Fastor** [251] also presented as the last chapter of this thesis and the massively parallel multi-frontal direct sparse solver **MUMPS** and **Pardiso** are primarily used for the solution of system of linear equations. For the purpose of assessing the performance of the proposed monolithic approach the final example is solved using the algebraic multigrid (AMG) solver with the standard Ruge-Stuben aggregations, c.f. [293, 103, 60, 311].

### 5.3.1 $h$ & $p$ convergence of the proposed high order framework

As a starting point, it is essential to examine the  $h$  and  $p$  convergence properties of the proposed high order displacement-potential formulation for large deformations large electric fields (fully coupled monolithic approach) described in chapter 4 and subsection 5.2.1. Hence, the objective of this example is to a) assess the convergence of different variables in  $\{\boldsymbol{x}, \varphi, \mathcal{V}, \Sigma_{\mathcal{V}}\}$  using  $h$  and  $p$  refinements, b) examine optimality of the algorithm in terms of convergence properties on high order curved tetrahedral and hexahedral meshes around a dielectric elastomeric patch, obtained using the mesh deformation technique described in [254] and, c) showcase the scalability of the framework with high polynomial enrichment. The geometry of the dielectric patch is shown in Figure 5.2. A similar convergence study for an eleven field Hu-Washizu type mixed variational formulation in terms of the set of unknowns  $\{\boldsymbol{x}, \mathbf{F}, \mathbf{H}, \mathbf{J}, \varphi, \mathbf{d}, \Sigma_{\mathbf{F}}, \Sigma_{\mathbf{H}}, \Sigma_{\mathbf{J}}, \Sigma_{\mathbf{D}_0}, \Sigma_{\mathbf{d}}\}$  is presented in [233]. The constitutive model considered is based on a convex multi-variable energy functional expressed in terms of the invariants of the set  $\mathcal{V}$  as follows

$$W_{el,1}(\mathbf{C}, \mathbf{G}, C, \mathbf{D}_0) = \mu_1 \sum_{i=1}^n \alpha_i I_{\mathbf{C}}^i + \mu_2 \sum_{i=1}^n \beta_i I_{\mathbf{G}}^i - 2 \left( \mu_1 \sum_{i=1}^n i \alpha_i 3^{i-1} + 2 \mu_2 \sum_{i=1}^n i \beta_i 3^{i-1} \right) \ln \sqrt{C} \\ + \frac{\lambda}{2} (\sqrt{C} - 1)^2 + \frac{1}{2\varepsilon_1} II_{\mathbf{D}_0} + \frac{1}{2\varepsilon_2 \sqrt{C}} II_{\mathbf{d}}, \quad (5.7)$$

where  $I_{(\bullet)}$  denotes the trace of the entity  $(\bullet)$  and  $II_{(\bullet)}$  the squared of the  $\mathcal{L}^2$  norm of the entity  $(\bullet)$  with  $II_{\mathbf{d}} = \mathbf{D}_0 \cdot \mathbf{C} \mathbf{D}_0$ . Furthermore,  $\{\mu_1, \mu_2, \lambda, \varepsilon_1, \varepsilon_2\}$  represent positive material constants with  $\alpha_i$ 's and  $\beta_i$ 's denoting scaling coefficients. The material parameters in (5.7) used for this example are presented in Table 5.1, where  $n = 2$ ,  $\alpha_1 = \beta_1 = 1$  and  $\alpha_2 = \beta_2 = 0.2$  are chosen. The problem is constructed so that smoothness of the solution is guaranteed. For that purpose,

$\mu_1$ (Pa)	$\mu_2$ (Pa)	$\lambda$ (Pa)	$\varepsilon_1$ (N/V <sup>2</sup> )	$\varepsilon_2$ (N/V <sup>2</sup> )
1	1/2	1	4	4

Table 5.1: Material properties for example 5.3.1

the following simple exact fields associated with the fields  $\boldsymbol{x}$  and  $\varphi$  are considered

$$\boldsymbol{x}^{\text{exact}} = \boldsymbol{X} + \begin{Bmatrix} \gamma_1 \sin X_1 \\ \gamma_2 \cos X_2 \\ \gamma_3(\sin X_3 + \cos X_3) \end{Bmatrix}; \quad \varphi^{\text{exact}} = \varphi_0 \sin X_1, \quad (5.8)$$

where for this benchmark example,  $\gamma_1 = 0.1$ ,  $\gamma_2 = 0.2$ ,  $\gamma_3 = 0.3$  and  $\varphi_0 = 10^4 V$  are chosen. The deformation gradient tensor and the Lagrangian electric field can now be computed as

$$\boldsymbol{F}^{\text{exact}} = \begin{bmatrix} 1 + \gamma_1 \cos X_1 & 0 & 0 \\ 0 & 1 - \gamma_2 \sin X_2 & 0 \\ 0 & 0 & 1 + \gamma_3(\cos X_3 - \sin X_3) \end{bmatrix}; \quad \boldsymbol{E}_0^{\text{exact}} = - \begin{Bmatrix} \varphi \cos X_1 \\ 0 \\ 0 \end{Bmatrix}. \quad (5.9)$$

The remaining exact fields in the set  $\mathcal{V}^{\text{exact}} = \{\boldsymbol{C}^{\text{exact}}, \boldsymbol{G}^{\text{exact}}, C^{\text{exact}}, \boldsymbol{D}_0^{\text{exact}}\}$  can now be obtained for the smooth displacement and electric potential fields, from (5.9). Application of (4.23) on (5.9) yields the exact right Cauchy-Green tensor, its cofactor and determinant for the smooth fields (5.8) as

$$\boldsymbol{C}^{\text{exact}} = \boldsymbol{F}^{\text{exact}}{}^T \boldsymbol{F}^{\text{exact}}; \quad \boldsymbol{G}^{\text{exact}} = \frac{1}{2} \boldsymbol{C}^{\text{exact}} \times \boldsymbol{C}^{\text{exact}}; \quad C^{\text{exact}} = \frac{1}{3} \boldsymbol{G}^{\text{exact}} : \boldsymbol{C}^{\text{exact}}. \quad (5.10)$$

Similarly, the Lagrangian electric displacement vector can be computed by applying (4.26) on (5.7) as

$$\boldsymbol{D}_0^{\text{exact}} = \left( \frac{1}{\varepsilon_1} \boldsymbol{I} + \frac{1}{\varepsilon_2 \sqrt{C^{\text{exact}}}} \boldsymbol{C}^{\text{exact}} \right)^{-1} \boldsymbol{E}_0^{\text{exact}}. \quad (5.11)$$

Once all the elements of the set  $\mathcal{V}^{\text{exact}}$  have been determined, it is possible to obtain the set of exact work conjugates  $\Sigma_{\mathcal{V}}^{\text{exact}} = \{\boldsymbol{\Sigma}_{\boldsymbol{C}}^{\text{exact}}, \boldsymbol{\Sigma}_{\boldsymbol{G}}^{\text{exact}}, \boldsymbol{\Sigma}_C^{\text{exact}}, \boldsymbol{\Sigma}_{\boldsymbol{D}_0}^{\text{exact}}\}$  via (4.28). These enable to compute the second Piola-Kirchhoff stress tensor  $\boldsymbol{S}^{\text{exact}}$  from (4.31). Finally, the associated volumetric force and electric charge in mechanical and electrical equilibrium with the exact first Piola-Kirchhoff stress tensor  $\boldsymbol{P}^{\text{exact}} = \boldsymbol{F}^{\text{exact}} \boldsymbol{S}^{\text{exact}}$  and exact Lagrangian electric displacement field  $\boldsymbol{D}_0^{\text{exact}}$  are determined from (4.4) and (4.55), respectively as

$$\boldsymbol{f}_0(\boldsymbol{x}^{\text{exact}}, \varphi^{\text{exact}}) = -\text{DIV} \boldsymbol{P}^{\text{exact}}; \quad \rho_0(\boldsymbol{x}^{\text{exact}}, \varphi^{\text{exact}}) = \text{DIV} \boldsymbol{D}_0^{\text{exact}}. \quad (5.12)$$

For the convergence studies, three different high order curvilinear unstructured tetrahedral meshes and one high order curvilinear structured hexahedral mesh for the dielectric patch in Figure 5.2 are considered with 532 elements, 9220 elements, 26807 elements for the first three and 5000 elements for the last one, respectively, as shown in Figure 5.4. As will be described shortly, these discretisations are chosen such that the maximum segment fitting in a curved element (denoted by  $h$ ) is successively refined for  $h$ -convergence. The placements of high order nodes on curved boundaries of the meshes are given particular importance, in that they have been computed through an arc-length based projection from high order planar meshes with Warburton nodal distribution [254]. The curved volume mesh is then obtained by applying the consistently linearised elastic analogy [254, 328, 5, 100]. It is worth mentioning that the quality of the curvilinear meshes directly impact the  $h$  and  $p$  convergence property (optimality) of the finite element interpolation scheme. To this end, Table 5.2 and Table 5.3 report the three fundamental quality measures (where  $Q_1$  quantifies distortion of edges,  $Q_2$  quantifies distortion of faces and  $Q_3$ , also known as scaled Jacobian, quantifies volumetric distortion of the element itself) of the curved tetrahedral and hexahedral meshes, respectively; c.f. [254]. Optimal symmetric quadrature rules for tetrahedra reported in [323] are utilised for numerical integration of high order tetrahedral elements. For hexahedral elements, a simple tensor product based quadrature rule is utilised.

For studying  $h$ -convergence properties, only tetrahedral meshes are considered. The convergence rate of different primary and derived variables  $\{\boldsymbol{x}, \varphi, \mathcal{V}, \Sigma_{\mathcal{V}}\}$  are then studied by comparing the interpolated solution and analytical solution for a fixed  $p$  and successive  $h$ -refinement,

$p$	Coarse (532 elements)				Medium (9220 elements)				Fine (26807 elements)			
	DoFs	$Q_1$	$Q_2$	$Q_3$	DoFs	$Q_1$	$Q_2$	$Q_3$	DoFs	$Q_1$	$Q_2$	$Q_3$
$p = 2$	$1027 \times 4$	0.888	0.875	0.790	$17934 \times 4$	0.962	0.924	0.885	$52590 \times 4$	0.953	0.909	0.866
$p = 3$	$3077 \times 4$	0.881	0.843	0.746	$54018 \times 4$	0.936	0.869	0.799	$158352 \times 4$	0.947	0.893	0.838
$p = 4$	$6861 \times 4$	0.874	0.813	0.738	$120473 \times 4$	0.926	0.850	0.771	$352838 \times 4$	0.935	0.871	0.800
$p = 5$	$12911 \times 4$	0.851	0.807	0.711	$226516 \times 4$	0.904	0.831	0.721	$662848 \times 4$	0.924	0.843	0.765
$p = 6$	$21759 \times 4$	0.846	0.771	0.652	$381373 \times 4$	0.891	0.828	0.713	$1115196 \times 4$	0.901	0.837	0.757

Table 5.2: Distortion quality of high order curvilinear tetrahedral meshes

$p$	DoFs	$Q_1$	$Q_2$	$Q_3$
$p = 2$	$49943 \times 4$	0.999	0.984	0.914
$p = 3$	$147364 \times 4$	0.993	0.972	0.889
$p = 4$	$341885 \times 4$	0.987	0.961	0.853
$p = 5$	$659106 \times 4$	0.981	0.934	0.820
$p = 6$	$1129027 \times 4$	0.971	0.900	0.797

Table 5.3: Distortion quality of high curvilinear hexahedral mesh

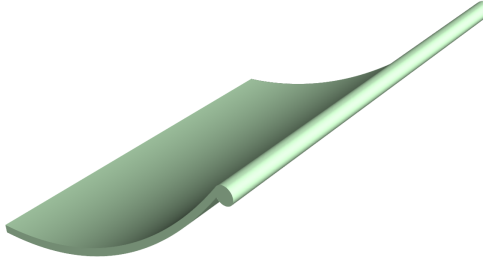


Figure 5.2: CAD geometry of the dielectric patch

similar to the strategy followed in [254, 233]. To monitor the convergence rate, the  $\mathcal{L}^2(V)$  norm of the error is computed for all quantities of interest. It is important to note, since the meshes are curvilinear (and unstructured), successive refinement based on element size or element edge size will not guarantee the expected  $h$ -convergence. As a result, the  $\mathcal{L}^2(V)$  norms of the variables are reported as a function the largest segment that can fit within a curved element. This can be seen as a generalisation of edge size based refinement, as for planar meshes, the largest segment represents the largest element edge. The computation of the largest segment for the computational mesh is carried out through a straight-forward sampling strategy illustrated in Figure 5.3 for triangular, quadrilateral, tetrahedral and hexahedral elements. After traversing the whole computational mesh, the minimum value of all the largest segments is chosen as  $h$ . For curvilinear meshes the  $\mathcal{L}^2(V)$  norms of the variables are reported as a function of the diameter (the largest segment that can fit within a curved region) of the element. After traversing the whole computational mesh, the minimum value of all the diameters is chosen as  $h$  [145, 285]. The tetrahedral meshes reported in Table 5.2 are chosen such that they correspond to successive refinement in this quantity.

Figure 5.5 shows  $h$ -convergence of the variables  $\{\mathbf{x}, \varphi, \mathcal{V}, \Sigma_{\mathcal{V}}\}$  for four levels of  $p$ -refinement (i.e.  $p = 2, 3, 4, 5$ ). Note that unlike in [233], while the displacements and electric potential are primary (solved) variables, the rest of variables are secondary (derived). As can be observed in Figure 5.5 for both low and high order polynomial interpolations, the expected rate of convergence is achieved for both primary ( $p + 1$  convergence rate) and derived ( $p$  convergence rate) variables. Notice that for this study, the multi-precision floating point library (MPFR) is utilised for arbitrary floating point accuracy. Apart from pinpointing the optimality and accuracy of the high order electromechanical solver on complex curved meshes, the  $h$ -convergence plots also prove that the framework scales reliably with high  $p$  and millions of degrees of freedom. Next, the  $p$ -convergence of tetrahedral elements for a fixed mesh (the finest mesh) is considered and compared to the  $p$ -convergence properties of hexahedral elements. Notice from Table 5.2 and Table 5.3 that the hexahedral mesh is chosen such that for every  $p$ , the number of nodes in the tetrahedral and hexahedral meshes are within a 5% difference. Once again, the degree of interpolation is successively increased leading to  $p$  convergence of

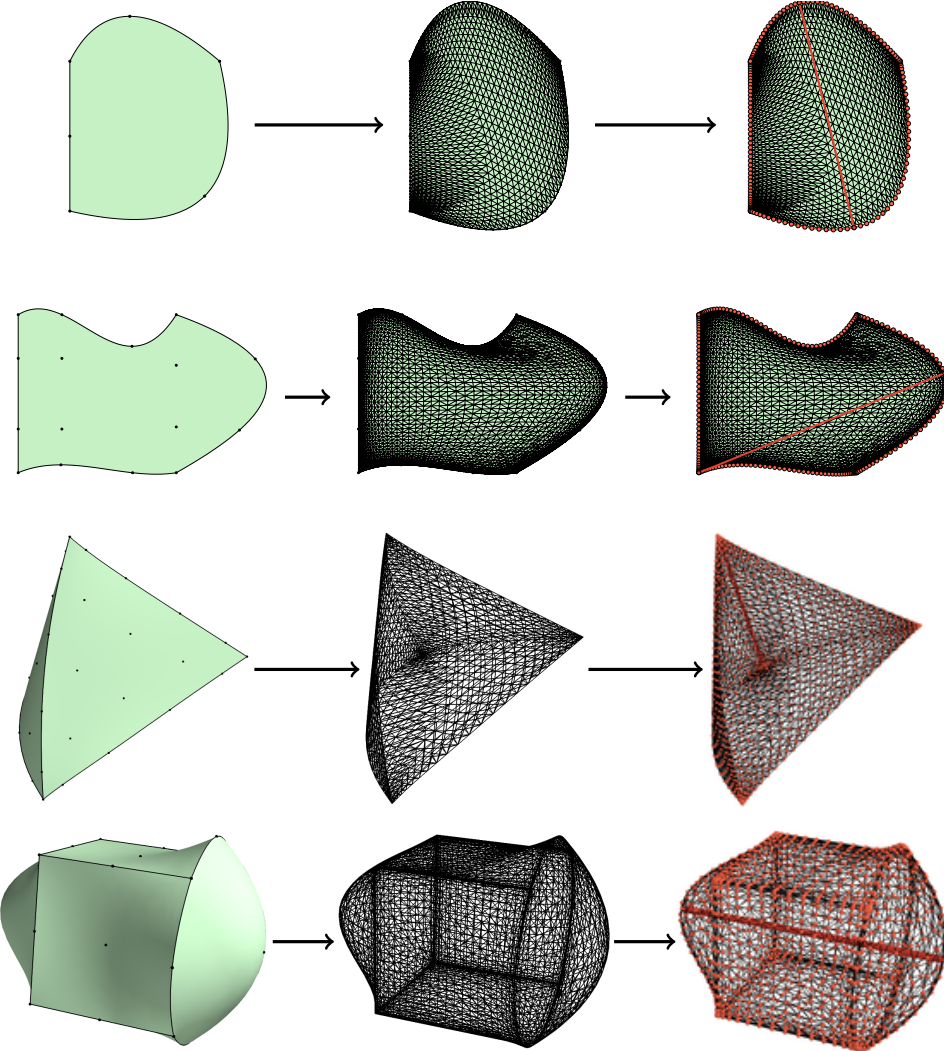


Figure 5.3: Illustration of computing the diameter (largest segment) in curvilinear meshes using sampling and tessellation strategy, for  $p=2$  triangle and  $q=3$  quadrilateral,  $p=5$  tetrahedra and  $q=2$  hexahedra

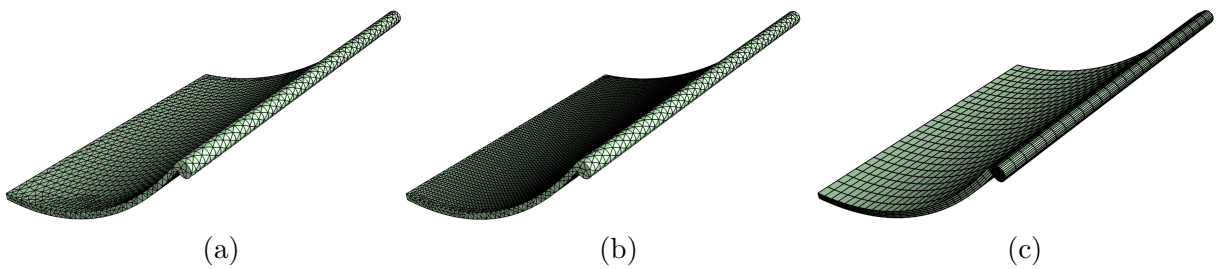


Figure 5.4: Three representative curvilinear meshes used for convergence studies; a) medium tetrahedral mesh (9220 elements) b) fine tetrahedral mesh (26807 elements), and c) fine hexahedral mesh (5000 elements)

the  $\mathcal{L}^2(V)$  norm of the same afore-mentioned quantities. Figure 5.6 shows  $p$  convergence of the  $\mathcal{L}^2(V)$  for arguments of the set  $\{\mathbf{x}, \varphi, \mathcal{V}, \Sigma\mathcal{V}\}$ . Once again, optimal rates of convergence for both curvilinear tetrahedral and hexahedral elements are obtained.

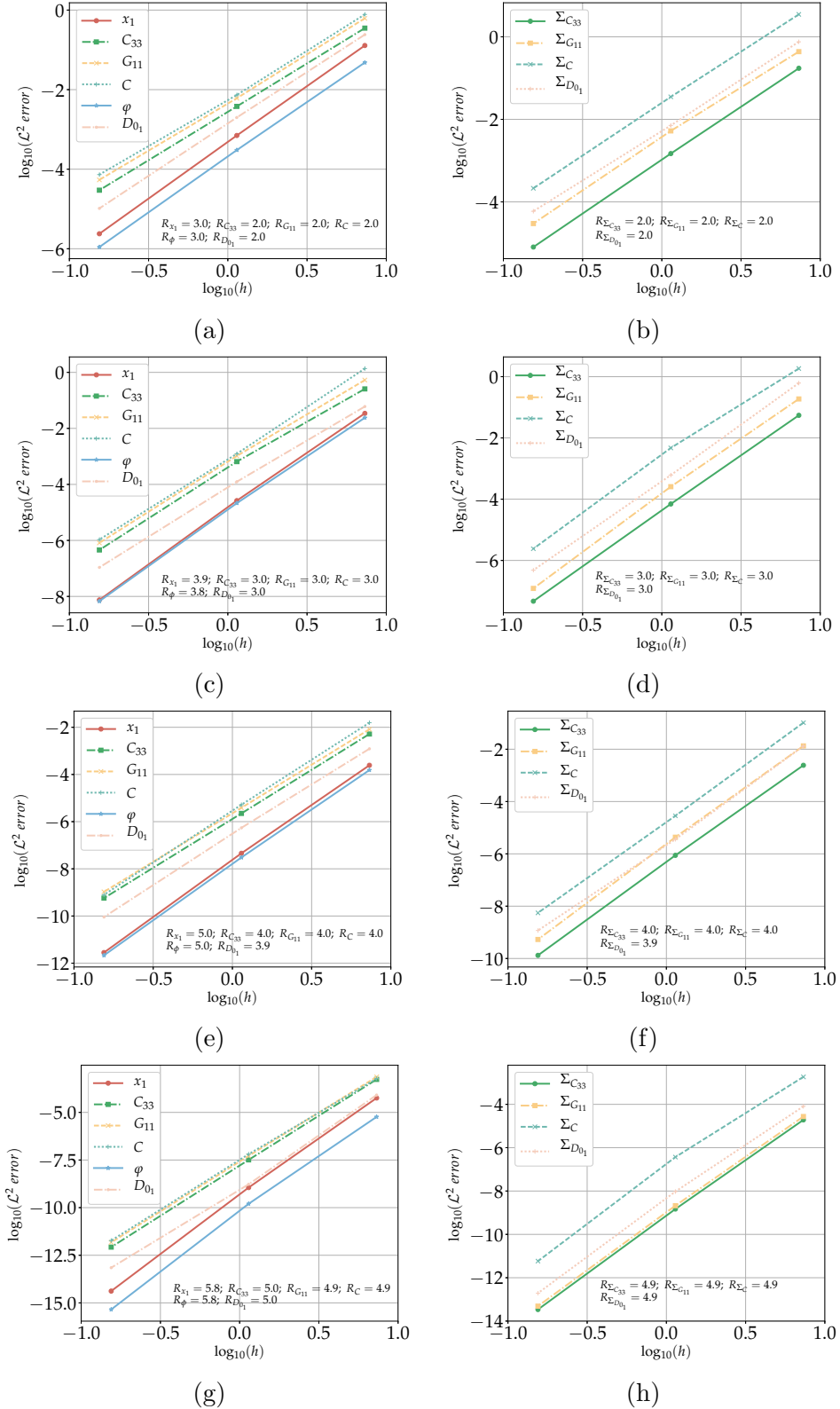


Figure 5.5:  $h$  convergence of  $\mathcal{L}^2(V)$  norm of the error for different kinematic and kinetic variables, (a) & (b)  $p = 2$ , (c) & (d)  $p = 3$ , (e) & (f)  $p = 4$  and (g) & (h)  $p = 5$ .  $R_\zeta$  indicates the rate of convergence of quantity  $\zeta$ .

### 5.3.2 Effect of accurate boundary representation in nonlinear electro-elasticity

Having studied the convergence properties of high order curvilinear finite elements for modelling convex multi-variable electromechanics in the previous section, the objective of this section is to

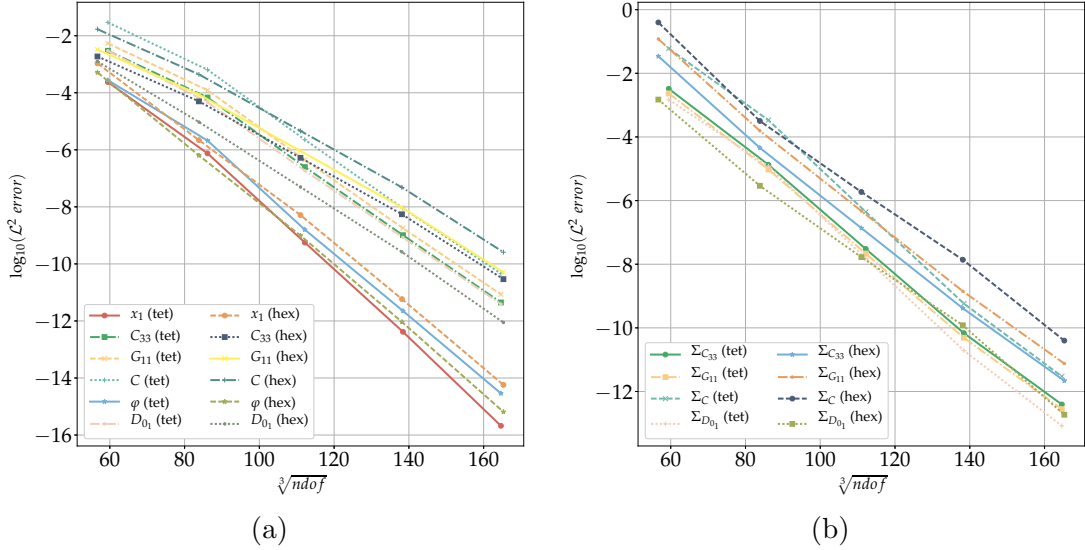


Figure 5.6:  $p$  convergence of  $\mathcal{L}^2(V)$  norm of the error for different kinematic and kinetic variables for mesh with 9220 elements.

examine if accurate geometrical representation through high order curvilinear finite elements, does play a role in capturing the physics of soft elastomeric materials better compared to the standard high order finite elements with planer faces/edges. The examples in this section are also motivated by the fact that, the vast majority of finite element simulations of electromechanical devices are carried out using either low order or high order finite elements with planer faces [269, 319, 240, 233, 114, 210, 241], with possible geometrical simplifications and at times even de-featuring [273].

To this end, the notable example of electromechanical plate with a hole is chosen for examination [269]. For this example, once again, one tetrahedral mesh and one hexahedral mesh is chosen and the polynomial degree is successively enriched, while keeping the mesh size  $h$  fixed. Additionally, for both examples, the material model chosen is based on the following convex multi-variable strain energy representation

$$W_{el,2} = \mu_1 I_C + \mu_2 I_G - 2(\mu_1 + \mu_2) \ln \sqrt{C} + \frac{\lambda}{2} (\sqrt{C} - 1)^2 + \frac{1}{2\varepsilon_1} II_{D_0} + \frac{1}{2\sqrt{C}\varepsilon_2} II_d, \quad (5.13)$$

with material constants as given in Table 5.4. The Poisson's ratio corresponding to parameters  $\mu_1$ ,  $\mu_2$  and  $\lambda$ , is  $\nu = 0.357$ . The mesh quality information for the plate with the hole is listed in

$\mu_1$ (Pa) 1e5	$\mu_2$ (Pa) 1e5	$\lambda$ (Pa) 5e5	$\varepsilon_1$ (N/V <sup>2</sup> ) $\varepsilon_0$	$\varepsilon_2$ (N/V <sup>2</sup> ) $5\varepsilon_0$
---------------------	---------------------	-----------------------	--	---

Table 5.4: Material parameters for (5.13) with the vacuum permittivity  $\varepsilon_0 = 8.85418781 \times 10^{-12}$  (N/V<sup>2</sup>)

Table 5.5 and the geometry and the tetrahedral and hexahedral meshes are shown in Figure 5.7 and Figure 5.8, respectively. A constant electric voltage of  $2 \times 10^8 V/m$  is applied through the

$p/q$	Tetrahedral			Hexahedral				
	DoFs	$Q_1$	$Q_2$	$Q_3$	DoFs	$Q_1$	$Q_2$	$Q_3$
$p/q = 2$	$340 \times 4$	0.982	0.965	0.948	$363 \times 4$	0.980	0.961	0.942
$p/q = 3$	$938 \times 4$	0.990	0.980	0.971	$1012 \times 4$	0.982	0.966	0.951
$p/q = 4$	$2021 \times 4$	0.986	0.973	0.960	$2165 \times 4$	0.981	0.963	0.947
$p/q = 5$	$3681 \times 4$	0.990	0.980	0.970	$3966 \times 4$	0.979	0.959	0.941
$p/q = 6$	$6097 \times 4$	0.990	0.979	0.969	$6559 \times 4$	0.977	0.955	0.935

Table 5.5: Distortion quality of high order curvilinear tetrahedral and hexahedral meshes whole thickness and symmetric mechanical Dirichlet boundary conditions are imposed on 1/4th

of the plate. This induces stretching of the electromechanical plate and as a result of the outer boundaries being fixed the plate is thickened in the region away from the hole and shrunk in thickness in the vicinity of the hole. Figure 5.9 shows the quadratic convergence of Newton-

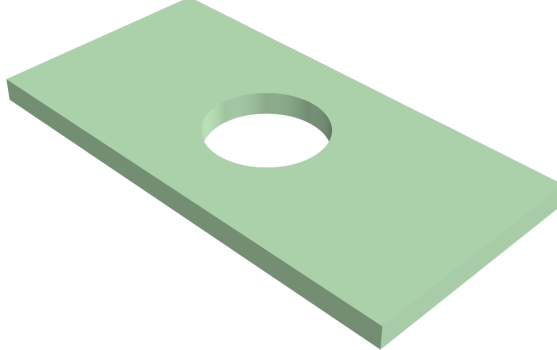


Figure 5.7: CAD representation of plate with circular hole with dimensions  $10 \times 20 \times 2 \text{ m}^3$ . The circular hole with a radius of  $5\text{m}$  is centred at  $[0, 0, 0]^T$

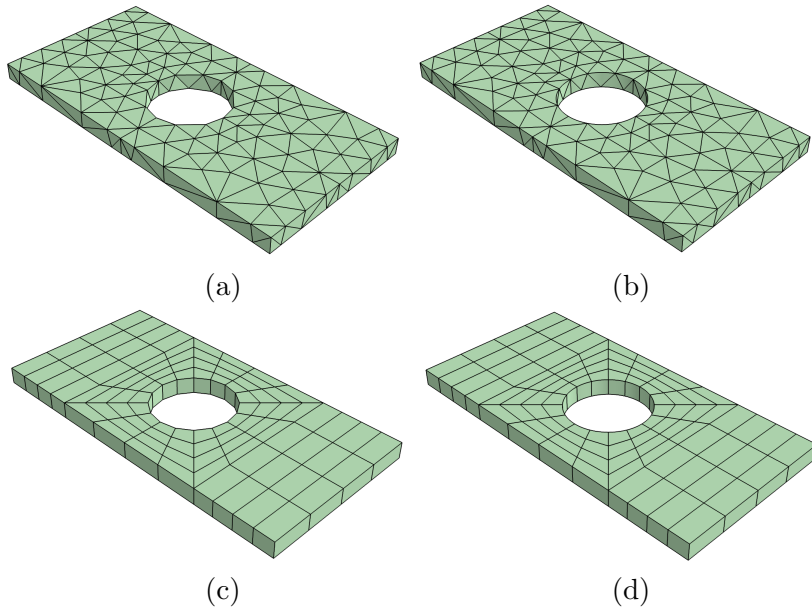


Figure 5.8: Curvilinear meshes used for comparison a)  $p = 3$  planar tetrahedra, b)  $p = 3$  curvilinear tetrahedra, c)  $p = 3$  planar hexahedra and, d)  $p = 3$  curvilinear hexahedra

Raphson for the last load increment for all polynomial degrees on curvilinear tetrahedral and hexahedral meshes, respectively. It is worth mentioning that, since the planar and curvilinear meshes do not possess the same volume, a systematic study of the difference in error norms of quantities is not feasible. However, since both planar and curved meshes share the same ( $p/q = 1$ ) vertices, a comparison of certain quantities of interest at these vertices can be carried out. Notice that since the node is shared between neighbouring elements appropriate stress recovery is required. This will lead to some oscillatory results in stresses (c.f. subsection 5.3.3 for further investigation in this regard). In the current setting, the order of quadrature rule to integrate stresses have been purposefully increased to  $2(p + 1)$  to remove these oscillations as far as feasible. Table 5.6 lists the results of  $\sigma_{xx}$ ,  $\sigma_{yy}$  and hydrostatic pressure  $p_{hyd}$  at the tip of the circular hole within the plate for planar and curvilinear tetrahedral meshes, for an intermediate load increment ( $n = 20$ ). From the table it is apparent that the planar mesh introduces a significant amount of stress concentration at the tip, whereas for curvilinear mesh the values of stresses at tip are significantly lower (although still existent and oscillatory in

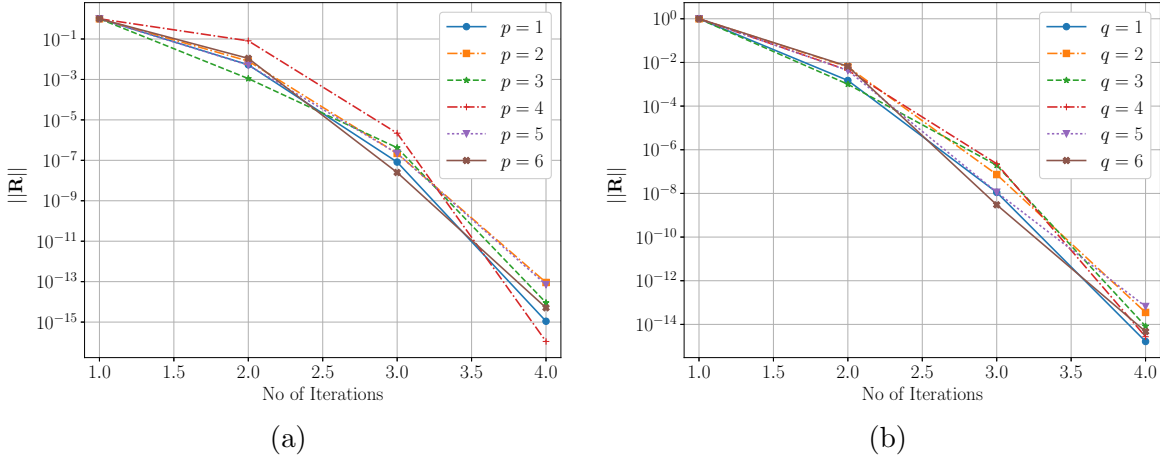


Figure 5.9: Quadratic convergence of Newton-Raphson on curvilinear a ) tetrahedral mesh and, b) hexahedral mesh

nature). Similarly, Table 5.7 lists the results of  $\sigma_{xx}$ ,  $\sigma_{yy}$  and hydrostatic pressure  $p_{hyd}$  at the tip of the circular hole within the plate for planar and curvilinear hexahedral meshes. A similar conclusion can be drawn for hexahedral meshes, where the stresses obtained on curvilinear mesh are consistently lower than those of planar mesh across all polynomial degrees. Notice that in line with the results from the previous section, with polynomial enrichment the concentration of stresses at the tip completely vanishes for curvilinear meshes. This is not the case for planar meshes regardless of enrichment, although they seem to converge to a particular value.

$p$	Planar			Curvilinear		
	$\sigma_{xx}$ (Pa)	$\sigma_{yy}$ (Pa)	$p_{hyd}$ (Pa)	$\sigma_{xx}$ (Pa)	$\sigma_{yy}$ (Pa)	$p_{hyd}$ (Pa)
$p = 2$	59.327	72.14	44.237	8.871	13.134	-9.721
$p = 3$	-18.569	-48.812	-21.979	-12.238	-6.544	-12.506
$p = 4$	-4.473	62.69	13.855	-21.267	8.097	-2.869
$p = 5$	-21.858	-33.012	-18.998	-5.964	-7.21	-2.802
$p = 6$	7.576	22.864	11.136	-0.931	-2.782	1.136

Table 5.6: Evolution of stresses at the circular tip of the plate for tetrahedral meshes

$p$	Planar			Curvilinear		
	$\sigma_{xx}$ (Pa)	$\sigma_{yy}$ (Pa)	$p_{hyd}$ (Pa)	$\sigma_{xx}$ (Pa)	$\sigma_{yy}$ (Pa)	$p_{hyd}$ (Pa)
$q = 2$	-35.733	389.798	115.414	-27.944	278.284	81.263
$q = 3$	-14.044	456.388	137.744	-10.701	329.368	98.884
$q = 4$	-0.833	497.554	166.209	-0.573	61.953	20.981
$q = 5$	-4.415	495.226	160.13	-3.302	36.381	11.642
$q = 6$	0.707	505.523	169.399	0.053	5.819	1.404

Table 5.7: Evolution of stresses at the circular tip of the plate for hexahedral meshes

A representation of stress concentration for the plate with circular hole is shown figuratively in Figure 5.10 only for  $p/q = 5$  meshes, for the final deformed configuration. It is evident from the figures that as opposed to the meshes with planar faces/edges, curvilinear meshes perform much better in reporting a smoother representation of the stress near the circular region. A similar conclusion is drawn across all polynomial degrees for tetrahedral and hexahedral elements (not reported, for the purpose of brevity). For instance, the maximum hydrostatic pressure at the tip of the circular hole within the plate located at  $[5, 20, 2]^T$  is  $p_{hyd} = -4.982 \times 10^4$  Pa for the hexahedral mesh with planar faces/edges, whereas only  $p_{hyd} = -0.104$  Pa for curvilinear hexahedral mesh. This clearly confirms that the appearance of non-physical stress concentrations can be significantly reduced through curvilinear meshes accurately representing the geometry. Similar behaviour has also been reported by the computational fluid dynamics community, where an inaccurate geometric representation leads to non-physical entropy production [274, 273]. However, it is important to note that, non-physical stress concentrations cannot be completely resolved using curvilinear meshes with standard finite elements without enhanc-

ing the finite element functional spaces either through blending functions [142, 296] or more generally through exact geometrical representation [272, 274, 273]. A similar study considering exact geometrical representation through NURBS-enhanced finite elements is reported in [273]. In line with the theme of this work, the aim of this study has been to assess and report the performance of curvilinear meshes in comparison to high order meshes with planar facets purely based on geometrical enhancements.

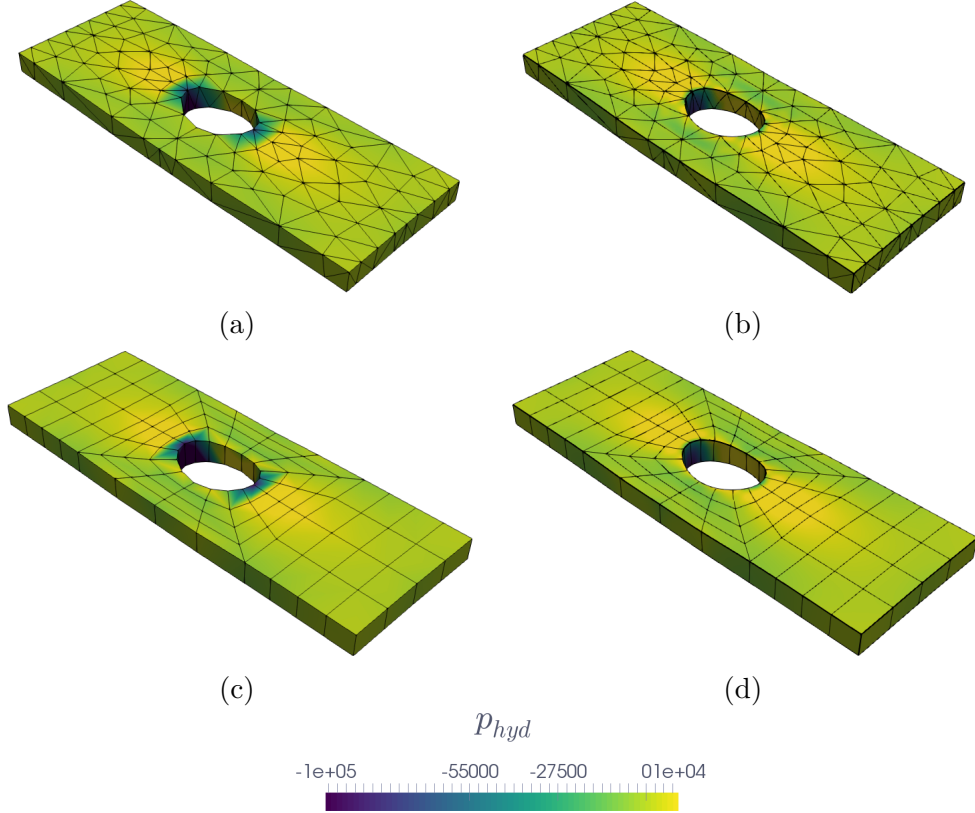


Figure 5.10: Evolution of voltage induced hydrostatic pressure in a plate with circular hole, a) planar  $p = 5$  mesh, b) curved  $p = 5$  mesh, c) planar  $q = 5$  mesh and, d) curved  $q = 5$  mesh

### 5.3.3 Comparison of higher order displacement potential based formulation with 11 field mixed formulation for electro-elasticity

The objective of the examples presented in this section is to compare the performance of the displacement-potential formulation (**DPF**) discretised using high order tetrahedral and hexahedral finite elements with the 11 field mixed Hu-Washizu variational formulation (**MWF**) (based on the set  $\{\mathbf{x}, \mathbf{F}, \mathbf{H}, J, \varphi, \mathbf{d}, \boldsymbol{\Sigma}_F, \boldsymbol{\Sigma}_H, \boldsymbol{\Sigma}_J, \boldsymbol{\Sigma}_{D_0}, \boldsymbol{\Sigma}_d\}$ ) for electro-elasticity presented in [113, 233, 114, 233], on curvilinear meshes. While for the **DPF** formulation, an equal order interpolation for all the variables ( $\mathbf{x}, \varphi$ ) is used (for tetrahedra and hexahedra), the **MWF** formulation utilises a quadratic interpolation for  $\mathbf{x}$  and  $\varphi$ , linear discontinuous interpolation for  $\mathbf{F}, \mathbf{H}, J, \mathbf{d}, \boldsymbol{\Sigma}_F, \boldsymbol{\Sigma}_H, \boldsymbol{\Sigma}_{D_0}, \boldsymbol{\Sigma}_d$  and a piecewise constant interpolation for  $J$  and  $\boldsymbol{\Sigma}_J$  and is primarily developed for 10-noded tetrahedra [233]. These formulations are compared against with an eye on two fundamental issues pertaining to the modelling of large deformation large electric field electromechanics namely, shear-locking and volumetric locking. To this end, three dielectric cantilever patches with aspect ratio  $\{10, 100, 1000\}$  are considered, as shown in Figure 5.11. The problem is analysed under compressible and nearly incompressible scenarios with Poisson's ratio 0.45 and 0.499 respectively. A series of curvilinear meshes are then produced for  $p = \{2, 3, 4, 5\}$  and  $q = \{2, 3, 4, 5\}$  for each aspect ratio. In addition, three  $h$ -refinement levels are considered using a coarse, a medium and a fine description for each aspect ratio and

each polynomial degree. An attempt is made to keep the total number of nodes in the computational mesh for every polynomial degree within the same range (within 5% difference). The necessary information regarding the quality of the curvilinear meshes are listed in Table 5.8 and Table 5.9, for tetrahedral meshes and hexahedral meshes, respectively. Note that, for a given  $p$  and  $h$ -refinement level, the size of the computational mesh is the same for all aspect ratios, in that, to obtain different aspect ratios, the mesh is appropriately scaled in the thickness direction. This certainly leads to extremely stretched elements but does not change the distortion of quality of the mesh as far as curvilinear mesh quality measures are concerned.

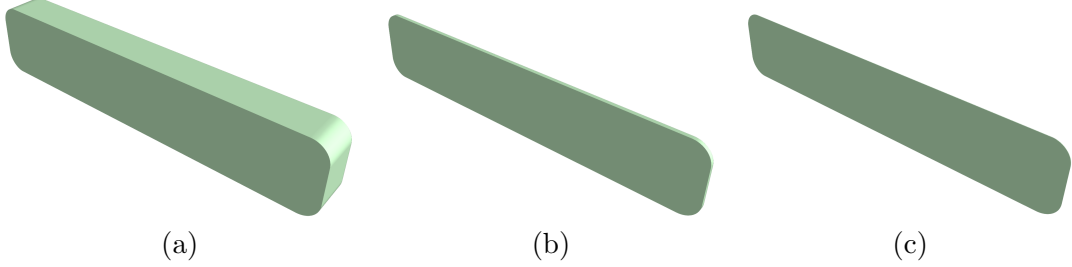


Figure 5.11: Geometry of the patch for three different aspect ratios a) 10, b) 100 and, c) 1000

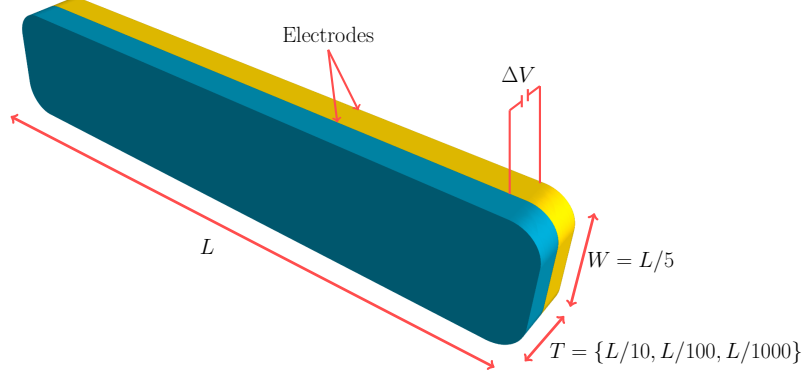


Figure 5.12: Description of the boundary conditions

<b><math>p</math></b>	Coarse				Medium				Fine			
	DoFs (N. Elements)	$Q_1$	$Q_2$	$Q_3$	DoFs (N. Elements)	$Q_1$	$Q_2$	$Q_3$	DoFs (N. Elements)	$Q_1$	$Q_2$	$Q_3$
$p = 2$	$2842 \times 4$ (1652)	0.971	0.943	0.909	$4686 \times 4$ (2730)	0.965	0.936	0.911	$9916 \times 4$ (5910)	0.980	0.959	0.938
$p = 3$	$2859 \times 4$ (396)	0.911	0.784	0.586	$4656 \times 4$ (710)	0.925	0.837	0.734	$9838 \times 4$ (1866)	0.952	0.898	0.836
$p = 4$	$2835 \times 4$ (126)	0.852	0.690	0.500	$4693 \times 4$ (326)	0.872	0.733	0.611	$9819 \times 4$ (698)	0.945	0.886	0.819
$p = 5$	$2856 \times 4$ (82)	0.873	0.758	0.651	$4651 \times 4$ (172)	0.952	0.908	0.866	$9889 \times 4$ (396)	0.944	0.890	0.840

Table 5.8: Distortion quality of high order curvilinear tetrahedral meshes

<b><math>p</math></b>	Coarse				Medium				Fine			
	DoFs (N. Elements)	$Q_1$	$Q_2$	$Q_3$	DoFs (N. Elements)	$Q_1$	$Q_2$	$Q_3$	DoFs (N. Elements)	$Q_1$	$Q_2$	$Q_3$
$q = 2$	$2885 \times 4$ (244)	0.972	0.987	0.957	$4665 \times 4$ (472)	0.986	0.970	0.953	$9805 \times 4$ (928)	0.990	0.980	0.969
$q = 3$	$2853 \times 4$ (76)	0.959	0.913	0.863	$4605 \times 4$ (148)	0.979	0.957	0.935	$9805 \times 4$ (292)	0.979	0.958	0.935
$q = 4$	$2873 \times 4$ (32)	0.818	0.618	0.361	$4650 \times 4$ (68)	0.950	0.897	0.842	$9793 \times 4$ (124)	0.950	0.898	0.842
$q = 5$	$2756 \times 4$ (16)	0.822	0.625	0.369	$4700 \times 4$ (32)	0.834	0.656	0.401	$9801 \times 4$ (64)	0.853	0.723	0.781

Table 5.9: Distortion quality of high order curvilinear hexahedral meshes

For comparison an ideal dielectric elastomer is considered with the following convex multi-variable internal energy description

$$W_{el,3} = \mu_1 I_C + \mu_2 I_G - 2(\mu_1 + \mu_2) \ln \sqrt{C} + \frac{\lambda}{2} (\sqrt{C} - 1)^2 + \frac{1}{2\varepsilon_1} II_d, \quad (5.14)$$

with the material parameters as given in Table 5.10.

Parameters	$\mu_1$ (Pa)	$\mu_2$ (Pa)	$\lambda$ (Pa)	$\varepsilon_1$ (N/V <sup>2</sup> )
Values (for $\nu = 0.45$ )	1e5	0	9e5	$4\varepsilon_0$
Values (for $\nu = 0.499$ )	1e5	0	4.99e7	$4\varepsilon_0$

Table 5.10: Material parameters for (5.14) with the vacuum permittivity  $\varepsilon_0 = 8.85418781 \times 10^{-12}$  (N/V<sup>2</sup>)

In order to be able to apply appropriate boundary conditions, it is made sure that all computational meshes have at least two elements across the thickness. For every aspect ratio, the patch is clamped at  $[0, X, Y]^T$  and a constant electric voltage is applied across the half thickness  $T/2$  (where  $T$  represents the patch thickness), as shown in Figure 5.12. It is certainly not feasible to apply the same amount of electric voltage while varying the patch aspect ratio and hence Table 5.11 lists the Dirichlet boundary conditions considered for the three aspect ratios.

Aspect Ratio	10	100	1000
Electric Voltage (V/m)	1e7	7.5e4	1.8e2

Table 5.11: Applied electric voltage as Dirichlet boundary condition for three aspect ratios

In order to compare different kinematic and kinetic quantities of interest for different formulations, two different physical points in the patches are considered namely,  $A$  - the node located at  $[L, W/2, T/2]^T$ , and  $B$  - the point interior to the computational mesh  $[0.98L, 0.49W, 0.49T]^T$  (c.f. Figure 5.12).

Table 5.12 and Table 5.13 compare the results obtained for different kinematics and kinetics quantities with displacement potential formulation using high order tetrahedral and hexahedral elements with the 11 field mixed formulations, for aspect ratio 10 and Poisson's ratio 0.45 and 0.499, respectively. For this comparison, the problem is solved in 50 load increments and the comparison is performed at increment 12, which corresponds to the onset of nonlinear deformation. The first observation from the tables is that the **DPF** based discretisations have an asymptotically upper bound convergence while the **MWF** based results have an asymptotically lower bound convergence. This can be observed studying the convergence of a given quantity for a fixed polynomial degree and successive  $h$ -refinements. This convergence pattern is more pronounced in the case of **MWF**. Consequently, for a fixed polynomial degree, it can be observed that **MWF** has a consistent 2%-5% higher displacements and strains estimate rate.

Regarding the stresses, as can be seen from the  $\sigma_{xz}$  results, the differences between the formulations are significant. While the results for the **MWF** show a convergence pattern, the results of the **DPF** do not seem to converge as coherently, with some clear pressure oscillations (as  $p/q$  and  $h$ -refinements are carried out). The  $\sigma_{zz}$  and hydrostatic pressure still do not seem to be affected, primarily due to the fact that these components have a much higher electro-mechanical stress contribution coming from the electric displacement (which is the applied Dirichlet boundary condition).

The conclusion drawn from the above set of results is that for thick electromechanical beams both high order **DPF** and **MWF** implementations capture the physical behaviour of the system accurately without showing any signs of shear or volumetric lockings. Importantly, this signifies that high order discretisations can capture nearly incompressible scenarios reliably [302, 143, 321]. The oscillations in stresses is an expected phenomenon for **DPF** implementations [233, 271, 28] which seems to persist even with polynomial enrichment. Unlike the problems reported in subsection 5.3.1, the convergence rate of stresses here can not be ascertained, since the polynomial enrichment here, comes with the trade-off of coarsening the computational mesh to keep the problem size the same. In this regard, **MWF** implementation maintains a consistent accuracy by virtue of explicitly solving for kinetic variables.

Note that, so far only the aspect ratio of the patch has been considered and no remarks have been made regarding the aspect ratio of the elements in the mesh. It is important to

mention that high order elements are at a severe disadvantage here compared to their low-order or **MWF** counterparts in that, polynomial enrichment leading to coarsening of the mesh also inherently implies dramatic stretching for high order elements. It is certainly not feasible to control the aspect ratio of the patch and the aspect ratio of the elements at the same time, while also having to keep the size of the computational mesh the same across all polynomial enrichments. This also signifies that, for  $p = q$ , the computational meshes do not necessarily exhibit the same elemental aspect ratios. It is still astounding to observe that, high order elements perform fairly well regardless.

Quantity	Refinement	$p = 2$	$p = 3$	$p = 4$	$p = 5$	$q = 2$	$q = 3$	$q = 4$	$q = 5$	11Mixed
$u_x^A(m)$	Coarse	0.15	0.1506	0.1502	0.1505	0.1505	0.1506	0.1506	0.1506	0.1595
	Medium	0.1505	0.1503	0.1505	0.1506	0.1506	0.1506	0.1507	0.1506	0.1542
	Fine	0.1505	0.1508	0.1505	0.1506	0.1506	0.1506	0.1507	0.1506	0.1535
$u_z^A(m)$	Coarse	0.9572	0.9555	0.9565	0.9551	0.958	0.9597	0.9598	0.9603	1.049
	Medium	0.9566	0.9576	0.9603	0.9596	0.9583	0.96	0.9604	0.9603	1.0022
	Fine	0.9571	0.96	0.9597	0.9594	0.9585	0.96	0.9604	0.9603	0.9948
$F_{xz}^A$	Coarse	-0.0176	-0.0186	-0.018	-0.0184	-0.0178	-0.0184	-0.0183	-0.0183	-0.0199
	Medium	-0.0183	-0.0181	-0.018	-0.0183	-0.0178	-0.0185	-0.0183	-0.0183	-0.0191
	Fine	-0.0183	-0.0186	-0.0178	-0.0184	-0.0178	-0.0185	-0.0183	-0.0183	-0.0191
$H_{zx}^A$	Coarse	-0.0184	-0.0184	-0.0182	-0.0186	-0.0181	-0.0184	-0.0183	-0.0183	-0.0198
	Medium	-0.0184	-0.0181	-0.0183	-0.0182	-0.018	-0.0185	-0.0184	-0.0183	-0.019
	Fine	-0.0184	-0.0181	-0.0186	-0.0184	-0.018	-0.0185	-0.0184	-0.0183	-0.0192
$\sigma_{xz}^B(\text{Pa})$	Coarse	68.817	-34.4955	8.4401	2.5424	20.9594	-16.3045	-4.2272	-8.6977	-24.0193
	Medium	1.5908	-10.4219	16.6441	-17.0173	11.9318	-4.436	-4.8418	-8.9388	-15.3804
	Fine	-3.9871	-63.5881	19.221	-15.5529	7.1833	-4.433	-4.8497	-8.9573	-4.7419
$\sigma_{zz}^B(\text{Pa})$	Coarse	228.8202	242.9458	167.4105	225.4981	227.3906	208.8909	220.5269	233.9105	262.6845
	Medium	226.3231	304.8385	190.6815	232.3852	228.7893	202.9177	228.5124	234.1146	262.0383
	Fine	226.7235	228.4325	192.3997	227.9372	229.1137	202.8566	228.503	234.1104	233.9687
$p_{hyd}^B(\text{Pa})$	Coarse	258.7676	262.7815	228.257	256.8133	249.9223	258.8183	253.0553	260.2188	283.1432
	Medium	256.2272	239.7233	239.8217	256.7475	249.6441	259.3416	254.3613	260.1902	279.219
	Fine	257.2179	258.3805	255.9474	256.809	249.4617	259.3333	254.3594	260.1998	229.3169

Table 5.12: Comparison of high order displacement potential and 11 field mixed formulations for different kinematic and kinetic measures, for aspect ratio 10 and Poisson's ratio 0.45

Quantity	Refinement	$p = 2$	$p = 3$	$p = 4$	$p = 5$	$q = 2$	$q = 3$	$q = 4$	$q = 5$	11Mixed
$u_x^A(m)$	Coarse	0.1603	0.1614	0.1606	0.1576	0.1621	0.1607	0.1613	0.1603	0.1682
	Medium	0.1609	0.1606	0.1609	0.1603	0.1622	0.1607	0.1614	0.1603	0.1647
	Fine	0.1611	0.1612	0.1611	0.1599	0.1622	0.1607	0.1614	0.1603	0.1641
$u_z^A(m)$	Coarse	1.0215	1.0273	1.0274	0.949	1.0265	1.031	1.0299	1.0198	1.109
	Medium	1.0256	1.028	1.0213	1.0175	1.0282	1.0306	1.0317	1.0197	1.0737
	Fine	1.0256	1.0304	1.0326	1.0175	1.0286	1.0306	1.0317	1.0198	1.0659
$F_{xz}^A$	Coarse	-0.0189	-0.0201	-0.019	-0.019	-0.0203	-0.0187	-0.0201	-0.0191	-0.021
	Medium	-0.0195	-0.0188	-0.0189	-0.0193	-0.0203	-0.0187	-0.0202	-0.0191	-0.0205
	Fine	-0.0197	-0.0198	-0.0191	-0.0212	-0.0203	-0.0187	-0.0202	-0.0191	-0.0205
$H_{zx}^A$	Coarse	-0.02	-0.02	-0.0193	-0.0191	-0.0204	-0.0192	-0.0198	-0.0194	-0.0209
	Medium	-0.0197	-0.0195	-0.0194	-0.0192	-0.0205	-0.0191	-0.02	-0.0194	-0.0204
	Fine	-0.0198	-0.019	-0.0198	-0.0199	-0.0205	-0.0191	-0.02	-0.0194	-0.0205
$\sigma_{xz}^B(\text{Pa})$	Coarse	89.1516	-23.91	14.7041	0.2679	7.9494	39.9045	-41.9385	17.966	-25.4328
	Medium	10.3683	60.0207	38.6844	-20.1666	6.9024	27.4752	-32.0594	17.139	-18.2278
	Fine	-3.7742	-90.0163	12.6685	-	6.0727	27.538	-32.0799	17.0549	-4.8466
$\sigma_{zz}^B(\text{Pa})$	Coarse	234.1627	260.194	146.468	244.717	143.7517	299.7924	199.8753	270.1902	376.1902
	Medium	245.7591	362.475	203.2137	255.0402	144.1905	299.4855	200.6011	270.5423	282.167
	Fine	233.4144	265.2387	177.1516	192.5099	144.4195	299.4976	200.6389	270.5092	204.6006
$p_{hyd}^B(\text{Pa})$	Coarse	273.3164	279.5418	241.9163	274.1948	273.0657	273.9475	273.383	273.9117	402.374
	Medium	273.4977	272.6952	253.7051	274.2576	273.0683	273.934	273.4753	273.9096	294.6149
	Fine	273.7066	274.0771	259.1145	270.249	273.0699	273.9341	273.4752	273.9103	246.635

Table 5.13: Comparison of high order displacement potential and 11 field mixed formulations for different kinematic and kinetic measures, for aspect ratio 10 and Poisson's ratio 0.499

Turning the attention to thinner beams, the results for the patch with the aspect ratio 100 are analogous to those with the aspect ratio 10 and offer no further insight, and are hence omitted for the purpose of brevity. The same analysis is then carried out with extremely thin beams with aspect ratio 1000 featuring highly stretched elements. The corresponding loading from Table 5.11 is applied. Table 5.14 and Table 5.15 compare the results obtained for different kinematics and kinetics quantities with displacement potential formulation using high order tetrahedral and hexahedral elements with the 11 field mixed formulations, for aspect ratio 1000 and Poisson's ratio 0.45 and 0.499, respectively.

As can be observed from the tables, the  $p = 2$  elements exhibit severe shear locking in this case. Comparing the results of thick and thin beams, it is evident that this phenomenon occurs solely due to the high aspect ratio (slenderness of the beam) [206, 205]. Interestingly, although not as dramatic, the **MWF** implementation also exhibits shear locking. On the other

hand, hexahedral elements have a consistent performance across all polynomial degrees. It is important to mention that, this phenomenon can not be attributed to the nearly incompressible nature of the material, due to two reasons. First, for  $p = 2$  elements, the thick beams do not exhibit locking neither at  $\nu = 0.45$  nor at  $\nu = 0.499$ . Second, **MWF** performs specifically well for nearly incompressible scenarios and explicitly solves for the  $J$  variable through an augmented Hu-Washizu variational principle [113]. Also notice that, for this aspect ratio, even  $p = 3$  elements exhibit some amount of locking. The oscillations in the stress on the other hand, for **DPF** formulations is huge, at high polynomial degrees. This is in part due to the fact that, higher order elements are much more stretched. For instance, the coarsest  $p = 5$  elements have an aspect ratio of 215 and the coarsest  $q = 5$  elements have an aspect ratio of 450.

Quantity	Refinement	$p = 2$	$p = 3$	$p = 4$	$p = 5$	$q = 2$	$q = 3$	$q = 4$	$q = 5$	11Mixed
$u_x^A(m)$	Coarse	-0.0057	-0.037	-0.04437	-0.0478	-0.0566	-0.056	-0.0536	-0.0527	0.0005
	Medium	0.0021	-0.049	-0.0473	-0.0487	-0.057	-0.0571	-0.0529	-0.0532	-0.0156
	Fine	0.0017	-0.0483	-0.0494	-0.0499	-0.0572	-0.0572	-0.0537	-0.0561	-0.0252
$u_z^A(m)$	Coarse	0.0437	2.3622	2.8948	2.9245	3.0755	3.0593	2.9972	3.0944	0.5598
	Medium	0.0677	2.7467	2.9379	2.9545	3.0875	3.0916	2.9803	3.0929	1.672
	Fine	0.2951	2.7054	2.9584	2.9941	3.0927	3.0956	3.0022	3.0972	2.094
$F_{xz}^A$	Coarse	-0.0074	-0.0467	-0.0435	-0.0235	-0.0604	-0.0599	-0.0589	-0.054	-0.0004
	Medium	-0.0013	-0.0541	-0.0437	-0.0444	-0.0606	-0.0606	-0.0586	-0.055	-0.0001
	Fine	-0.0061	-0.0547	-0.0537	-0.0455	-0.0606	-0.0607	-0.059	-0.0516	-0.0003
$H_{zx}^A$	Coarse	-0.0075	-0.0467	-0.04535	-0.0235	-0.0604	-0.06	-0.0589	-0.054	-0.0406
	Medium	-0.0013	-0.0541	-0.0438	-0.0445	-0.0606	-0.0606	-0.0586	-0.0551	-0.0106
	Fine	-0.0061	-0.0547	-0.0537	-0.0456	-0.0607	-0.0607	-0.059	-0.0516	-0.0345
$\sigma_{xz}^B(\text{Pa})$	Coarse	18.3433	-0.0816	-1.2205	-0.9087	0.6522	0.5042	-0.4751	0.7071	-0.1453
	Medium	-0.0358	-1.1296	8.3123	2.6078	0.7813	0.3317	0.2968	1.1267	0.4453
	Fine	-0.1437	-0.8996	1.2107	3.3222	0.892	0.333	0.2834	1.1086	0.1926
$\sigma_{zz}^B(\text{Pa})$	Coarse	-32.2983	-15.9872	541.2936	63.4422	0.0401	0.1828	0.8809	-0.7323	1.6931
	Medium	-1.173	-10.6548	327.1866	120.7646	-0.0127	0.1375	0.1661	0.2904	4.1625
	Fine	-0.3662	2.8504	23.2398	4.5291	-0.0542	0.1445	0.0937	0.308	14.0885
$p_{hyd}^B(\text{Pa})$	Coarse	-24.8172	-23.6293	410.2216	42.8566	2.7135	2.8305	3.7971	2.0094	-4.2656
	Medium	-8.1182	-16.7676	308.1874	111.348	2.6489	2.8169	2.8075	2.4095	5.391
	Fine	-6.7439	-3.6837	26.1795	10.0663	2.5984	2.8229	2.7651	2.4154	15.0638

Table 5.14: Comparison of high order displacement potential and 11 field mixed formulations for different kinematic and kinetic measures, for aspect ratio 1000 and Poisson's ratio 0.45

Quantity	Refinement	$p = 2$	$p = 3$	$p = 4$	$p = 5$	$q = 2$	$q = 3$	$q = 4$	$q = 5$	11Mixed
$u_x^A(m)$	Coarse	0.0022	-0.0329	-0.0563	-0.0564	-0.0603	-0.0618	-0.0607	-0.0618	0.0004
	Medium	0.0022	-0.0489	-0.0559	-0.0574	-0.0642	-0.0615	-0.0615	-0.0605	-0.0194
	Fine	0.0022	-0.0434	-0.0577	-0.0582	-0.0614	-0.0616	-0.0615	-0.0615	-0.0312
$u_z^A(m)$	Coarse	0.0062	2.1839	2.9353	3.0931	3.1536	3.2548	3.2635	3.2618	0.5988
	Medium	0.0024	2.496	2.9301	2.9984	3.2623	3.2082	3.2936	3.2518	1.8414
	Fine	0.0104	2.8819	2.933	2.9997	3.2017	3.2099	3.1395	3.2548	2.3124
$F_{xz}^A$	Coarse	-0.0007	-0.0441	-0.0505	-0.0515	-0.0626	-0.0691	-0.0603	-0.0621	-0.0004
	Medium	-0.0002	-0.0565	-0.0564	-0.0526	-0.0643	-0.063	-0.0592	-0.0044	-0.0001
	Fine	-0.0002	-0.0501	-0.0561	-0.0582	-0.063	-0.063	-0.0613	-0.0593	-0.0004
$H_{zx}^A$	Coarse	-0.0007	-0.0441	-0.0205	-0.0515	-0.0627	-0.0691	-0.0604	-0.0621	-0.0448
	Medium	-0.0002	-0.0565	-0.0565	-0.0527	-0.0643	-0.063	-0.0592	-0.0044	-0.0115
	Fine	-0.0002	-0.0501	-0.0561	-0.0583	-0.063	-0.063	-0.0613	-0.0593	-0.038
$\sigma_{xz}^B(\text{Pa})$	Coarse	-0.058	-1.0561	0.2593	0.191	0.7204	0.7001	0.7089	0.7071	-0.2034
	Medium	-0.0656	-1.022	5.1248	-39.3918	0.8225	0.5512	0.3729	-9.6306	0.6378
	Fine	-0.1293	-0.8051	10.014	28.8039	0.8635	0.5506	0.364	-	0.2668
$\sigma_{zz}^B(\text{Pa})$	Coarse	47.1482	-	-33.2631	538.5343	-2.8369	3.3726	3.3814	3.3796	2.1594
	Medium	0.6649	395.4936	49.3672	-	2113.4412	-4.1608	6.1501	1.802	2217.1176
	Fine	-0.6984	13.3289	330.097	2189.0055	-5.4436	6.173	1.4294	3478.8777	14.6644
$p_{hyd}^B(\text{Pa})$	Coarse	38.1504	-	-41.0376	528.9243	0.4472	6.5811	6.5899	6.5881	-5.0029
	Medium	-7.9517	407.0878	40.8982	-	985.5186	-0.8781	9.456	5.1897	739.779
	Fine	-9.1691	5.7871	350.556	710.8945	-2.1342	9.4748	4.8289	1165.274	15.8006

Table 5.15: Comparison of high order displacement potential and 11 field mixed formulations for different kinematic and kinetic measures, for aspect ratio 1000 and Poisson's ratio 0.499

The conclusion drawn from the experiments so far is that, both **DPF** and **MWF** are capable of capturing the behaviour of compressible and nearly incompressible dielectric elastomers fairly well. However, for thin beams, low order **DPF** discretisations on tetrahedra as well **MWF** suffer from shear locking (resolvable through the use of a finer discretisation), while high order **DPF** discretisations are able to cope up with thin beams and resolve the primary variables accurately at the expense of a huge oscillation in derived variables such as stresses. To separate the issue of volumetric and shear locking further a different set of experiments

are now considered using only **DPF** implementation by applying an extremely high electric voltage on the patches and lowering the Poisson's ratio to  $\nu = 0.35$ . The loading scenario for different aspect ratios is listed in Table 5.16.

Aspect Ratio	10	100	1000
Electric Voltage ( $V/m$ )	$2.6e7$	$1e5$	$4e2$

Table 5.16: Applied electric voltage as Dirichlet boundary condition for three aspect ratios

Figure 5.13 shows the hydrostatic pressure for the patch with aspect ratio 10 (thick) solved with the medium mesh. Once again, it can be seen that even for large deformations and finite strains, the **DPF** implementation with tetrahedra does not suffer from any locking, although some oscillation in the pressure could be observed, across all polynomial degrees. Similarly, Figure 5.14 shows the evolution of the co-factor component  $H_{13}$  on the coarse mesh. For this aspect ratio, which could be considered a thin beam, **DPF** implementation with tetrahedra once again produces accurate results.

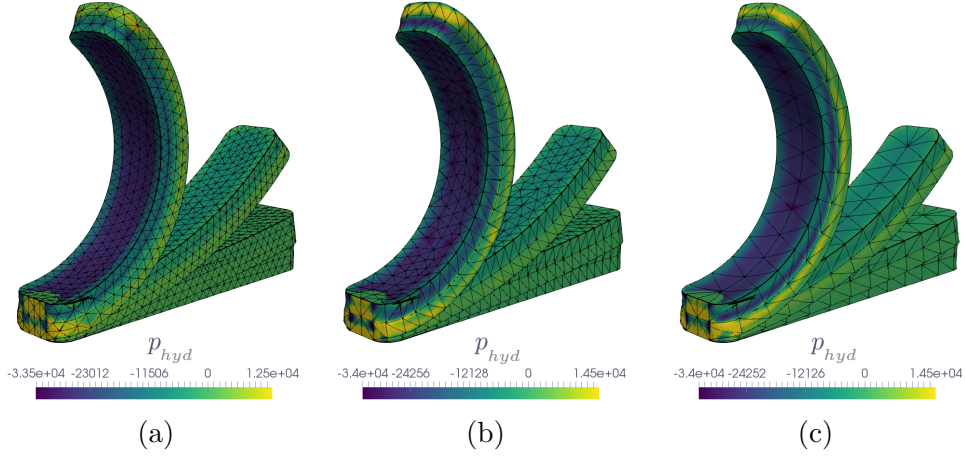


Figure 5.13: Voltage induced hydrostatic pressure  $p_{hyd}$  for the medium mesh using a)  $p = 2$ , b)  $p = 3$  and, c)  $p = 4$

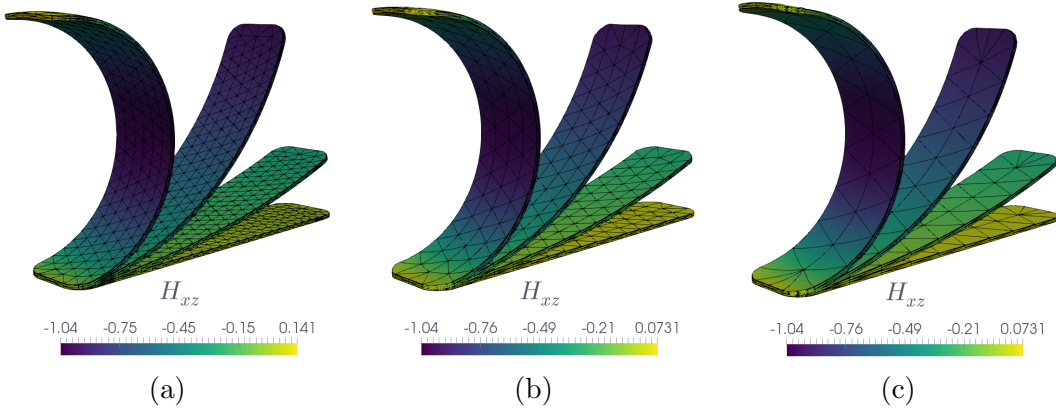


Figure 5.14: Voltage induced large strain ( $H_{xz}$ ) for the coarse mesh using a)  $p = 2$ , b)  $p = 3$  and, c)  $p = 4$

As evident by now, the challenging problem is the extremely thin beams with aspect ratio 1000 shown in Figure 5.14 . Notice that both  $p = 2$  and  $p = 3$  elements exhibit severe shear locking for this aspect ratio, confirming the fact that this locking is purely due to stretching of the elements. Only  $p = 4$  elements (and beyond) are able to capture this deformation accurately. Interestingly, as shown in Figure 5.16 the  $q = 2$  elements also lock at this level of deformation. Certainly, the problem of shear locking could in part be remedied by using

$h$ -refinement. As shown in Figure 5.17, even with the fine mesh the  $q = 2$  elements suffer from shear locking.

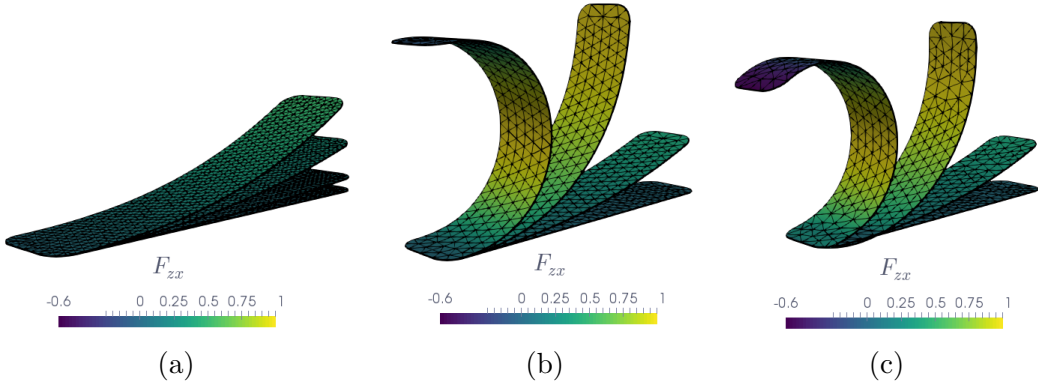


Figure 5.15: Voltage induced large strain ( $F_{zx}$ ) for the fine mesh using a)  $p = 2$ , b)  $p = 3$  and, c)  $p = 4$

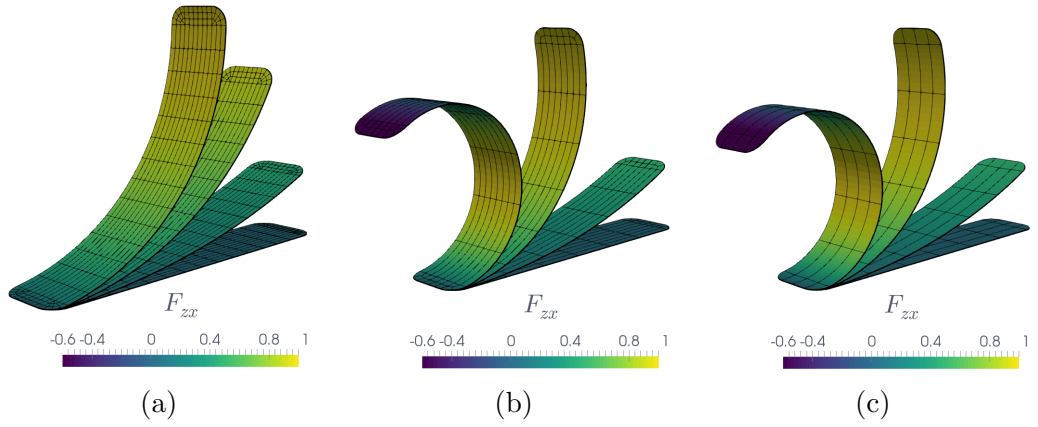


Figure 5.16: Voltage induced large strain ( $F_{zx}$ ) for the fine mesh using a)  $q = 2$ , b)  $q = 3$  and, c)  $q = 4$

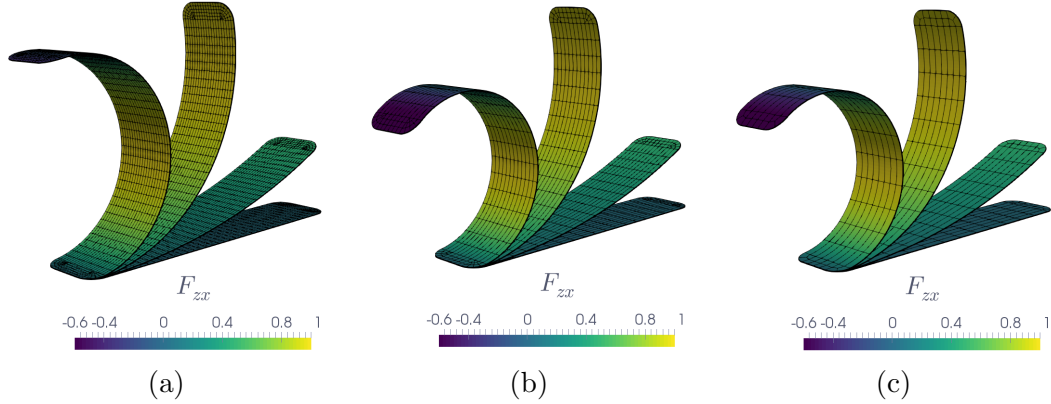


Figure 5.17: Voltage induced large strain ( $F_{zx}$ ) for the fine mesh using a)  $q = 2$ , b)  $q = 3$  and, c)  $q = 4$

The examples presented here show a clear advantage for the application of high order elements in electromechanics. Modelling of dielectric elastomeric beams with high aspect ratio is indeed a challenging problem. Mixed formulations based on convex multi-variable electro-elastic strain energies have an unrivalled performance in capturing the pressure and other derived quantities of interest, but still could suffer from shear locking at extremely high aspect

ratios. Note that the performance of high order elements could still be superior if the element's aspect ratio was preserved during polynomial enrichment (which was not the case for here). The analyses performed in this section was carried out with the clear goal of keeping the size of the computational domain the same across all polynomial enrichments.

### 5.3.4 Virtual prototyping of massive deformations and instabilities in dielectric elastomers through high performance numerical simulations

The objective of this section is to numerically study the behaviour of highly stretchable dielectric elastomers undergoing massive deformations through virtual prototyping of a series of electromechanical components. One of the main goals of these set of examples is to gain insights into the onset of instabilities such as pull-in instability [246, 335] and the subsequent formation of wrinkles in dielectric elastomers. The occurrence of these phenomena have been experimentally verified by Plante and Dubowsky [246], where a large applied electric potential has led to massive deformation of a dielectric elastomer sheet with eventual partial wrinkling of the sheet. Zhao et. al. [335], Mao [198] and others [336, 177] have also reported instabilities in DEs through numerical studies, albeit in relatively simplified settings. Here, an attempt is made to model dielectric elastomeric components which could potentially be applied as compliant actuators in soft robotics, medical devices and similar applications. From a computational point of view, four ingredients are needed to simulate such massive deformations in DEs namely, a) a convex multi-variable expansion of the electromechanical internal energy ensuring ellipticity [113, 233, 232, 114] b) accurate representation of the dielectric elastomeric components, c) high order finite element analyses to capture extreme deformations and finally, d) high performance kernels for rapid prototyping and modelling DEs. Having established all the aforementioned necessities, a diligent endeavour is put in the upcoming examples to present application-oriented numerical modelling of dielectric elastomers. Unless otherwise specified, all the examples in this section are modelled using the ideal dielectric elastomer material presented in (5.13) with material parameters listed in Table 5.4. For majority of these examples, the meshes are extremely fine in order to capture the formation of wrinkles (despite polynomial enrichment) and, as a consequence, the distortion quality of curvilinear meshes are almost unity.

#### A massively deformable dielectric cylinder

The first example considered is that of a dielectric shell-like cylindrical structure shown in Figure 5.18(a) with  $10m$  outer radius,  $0.333m$  thickness and  $25m$  length, centred at  $[0, 0, 0]^T$ . The model is made up of 27000 ( $p = 3$ ) curvilinear tetrahedral elements with 179122 points in the computational mesh corresponding to a total of 716488 degrees of freedom (shown in Figure 5.18(b)). An ideal dielectric elastomer is used as material model and the material

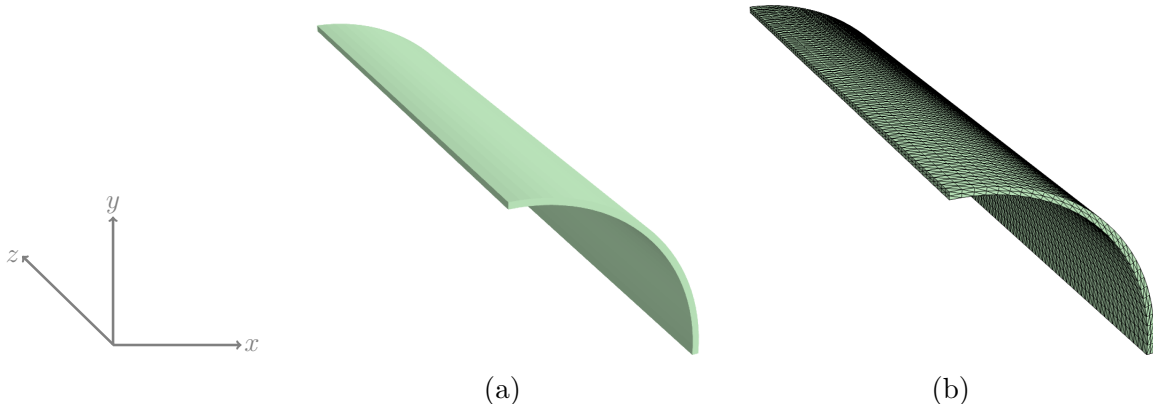


Figure 5.18: Geometry and a curved tetrahedral mesh of the dielectric shell-like cylindrical structure with  $10m$  radius  $0.333m$  thickness and  $25m$  length, centred at  $[0, 0, 0]^T$

properties are shown in Table 5.17. The following set of boundary conditions are applied.

$\mu_1$ (Pa)	$\mu_2$ (Pa)	$\lambda$ (Pa)	$\varepsilon_1^{-1}$ ( $V^2/N$ )	$\varepsilon_2$ ( $N/V^2$ )
$1e5$	0	$4e5$	0	$4\varepsilon_0$

Table 5.17: Material parameters with the vacuum permittivity  $\varepsilon_0 = 8.85418781 \times 10^{-12}$  (N/V<sup>2</sup>)

$$\begin{aligned} u_y = 0 [m] & \quad \text{at } \mathbf{X} = [0, y, z]^T; \\ u_x = 0 [m] & \quad \text{at } \mathbf{X} = [x, 0, z]^T; \\ \mathbf{u} = \mathbf{0} [m] & \quad \text{at } \mathbf{X} = [10, y, z]^T; \\ \varphi = 0 [V] & \quad \text{at } R_{in}; \\ \omega_0 = 1.4 \times 10^{-4} \Lambda [Q/m^2] & \quad \text{at } R_{out}, \end{aligned}$$

where  $R_{in} = 9.6667m$  is the inner radius,  $R_{out} = 10m$  is the outer radius and  $\Lambda$

$$\Lambda \in [0, 1] \subset \mathbb{R}$$

is simply a load factor controlling the application of surface charge such that,  $\Lambda = 0$ . represents start of the load increment and  $\Lambda = 1$ . represents end of the load increment (application of full load). The usage of load factor as a pseudo-time step to quantify the application of load is a standard practice in nonlinear quasi-static analyses [68, 56, 66]. The above non-uniform set of boundary conditions causes the cylinder to deform asymmetrically. Furthermore, the disparity in electric charge between the electrodes across the thickness causes the thickness to shrink. As shown in Figure 5.19, when the voltage is small, the elastomer deforms slightly, and the charge increases with the electric voltage approximately linearly. As the voltage increases, the elastomer's surface area expands significantly, and a small increase in the voltage adds a large amount of displacement on the cylinder. Consequently, after the voltage reaches a maximum value the voltage needed to maintain the charge drops [246]. This corresponds to the pull-in instability [335] causing regions of the cylinder to snap-back to fully new configuration possessing a different thickness. As more charge is applied at this state, the difference between the thick and thin regions causes the surface of the cylinder to fold and form wrinkles. This can be clearly observed in Figure 5.19(c,f). Notice that at the extreme loading state the elements closer to symmetry surfaces become considerably thinner and a complete zone of compression is formed at this region. Since the formation of wrinkles causes the cylinder to maintain different circumferential expansion at different regions along the length, one measure to quantify actuation property is to report the electric voltage as a function of circumferential expansion. One such graph is shown in Figure 5.20 for different positions along the length of the cylinder. The figure confirms the experimental findings in [246] that the formation of wrinkles is beyond the point of pull-in instability, when the surface is a mixture of thinner and thicker regions.

Next, two  $q = 3$  hexahedral meshes are chosen for the cylinder and two sets of boundary conditions are applied on each one respectively. The meshes correspond to 1.5M and 3.2M degrees of freedom, approximately. The first set of boundary conditions is similar to the previous analysis, however instead of surface charge now an electric potential of  $5.2 \times 10^7 V$  is applied at the inner radius. The second set of boundary conditions corresponds to

$$\begin{aligned} \mathbf{u} = \mathbf{0} [m] & \quad \text{at } \mathbf{X} = [0, y, z]^T; \\ \mathbf{u} = \mathbf{0} [m] & \quad \text{at } \mathbf{X} = [x, 0, z]^T; \\ \varphi = 0 [V] & \quad \text{at } R_{in}; \\ \varphi = 5.2 \times 10^7 \Lambda [V] & \quad \text{at } R_{out}, \end{aligned}$$

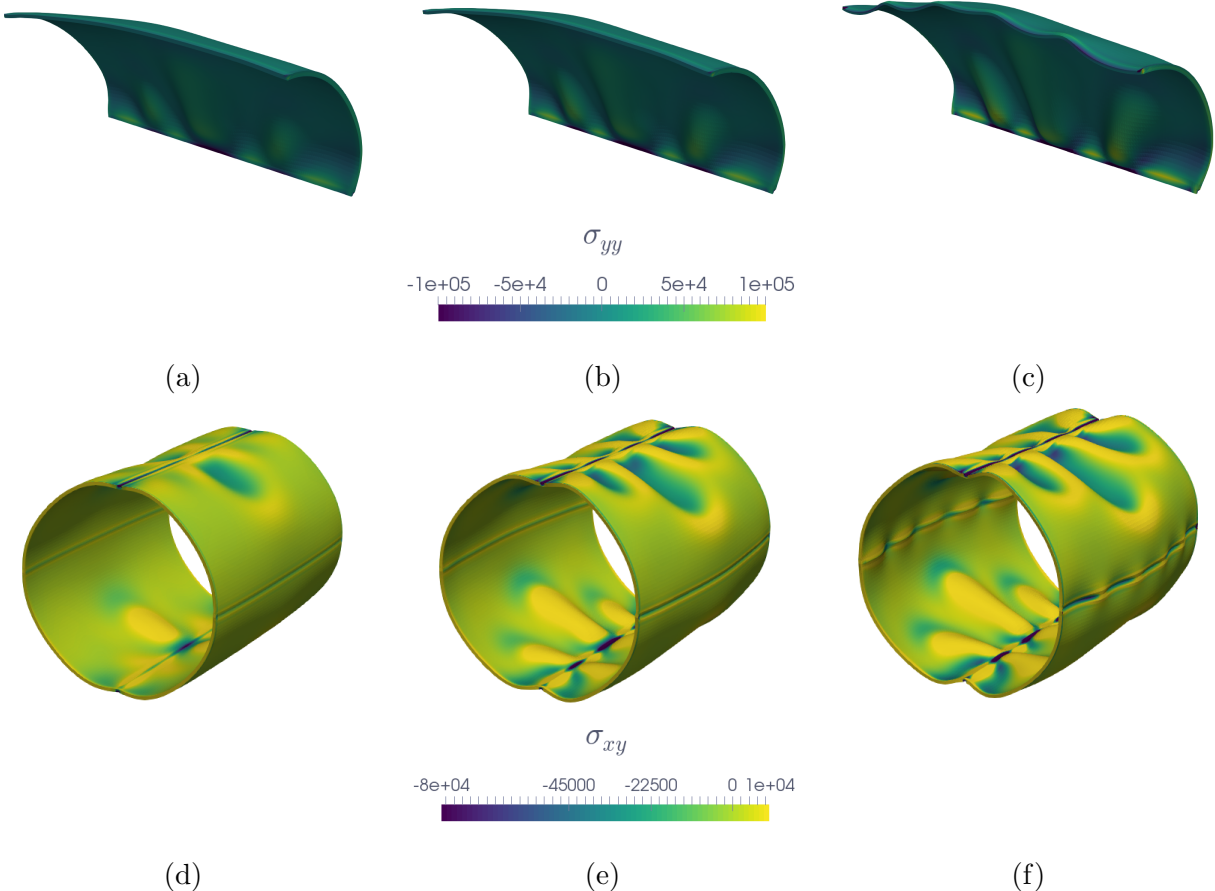


Figure 5.19: Evolution of charge induced stresses in dielectric cylindrical structure with accumulated load factor  $\Lambda$  being a)  $\sigma_{yy}$  at  $\Lambda = 0.678$  b)  $\sigma_{yy}$  at  $\Lambda = 0.785$ , c)  $\sigma_{yy}$  at  $\Lambda = 1.0$  d)  $\sigma_{xy}$  at  $\Lambda = 0.678$  e)  $\sigma_{xy}$  at  $\Lambda = 0.785$ , f)  $\sigma_{xy}$  at  $\Lambda = 1.0$

where  $\Lambda$  is now the load factor quantifying the application of electric potential for the nonlinear quasi-static analysis. Due to symmetry, only 1/8th of geometries are analysed. Figure 5.21 shows the evolution of the  $F_{xz}$  component of the deformation gradient tensor with voltage history. The first observation is that since the boundary condition is now through applied voltage and not electric charge as in the previous analysis, the voltage will always constantly increase and hence there is no negative or downward slope in voltage vs strain curves, up until the point of electric breakdown. The second observation from Figure 5.21 is that, unlike in the case of applied charge where the surfaces near symmetry boundary conditions become thinner, here these surfaces undergo twisting to accommodate for the constant applied electric voltage. The formation of coarse wrinkles at  $[0, x, y]^T$  is not present in this case.

Finally, unlike the two previous analyses, the third example with the second set of boundary conditions for the hexahedral mesh mentioned above is completely uniform in terms of loading. As can be seen in Figure 5.22 this set of boundary conditions imposes a homogeneous circumferential expansion. However, once the electric voltage is high enough, coarse wave-like wrinkles starting from the central point along the length of the cylinder are formed propagating towards the two ends of the cylinder.

The above three examples of cylindrical shell-like DEs pinpoint the different actuation properties that can be activated different sets of boundary conditions. In addition, they verify the capability of the current framework to cope with extremely fine meshes and high polynomial enrichment to capture massive deformations and wrinkling in dielectric elastomers.

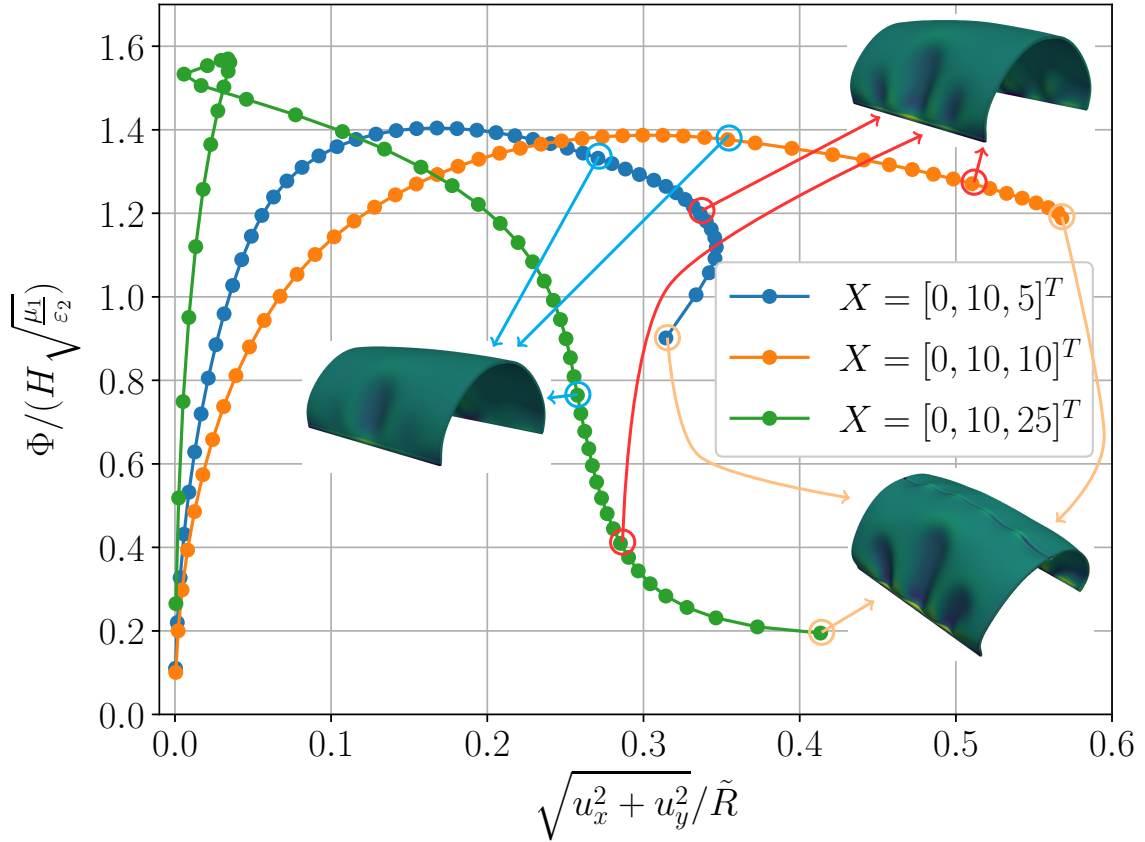


Figure 5.20: Non-dimensional quantity  $\Phi/(H \sqrt{\frac{\mu_1}{\varepsilon_2}})$  quantifying electric voltage as a function of circumferential expansion, showing points of snap-through, pull-in instability and formation of coarse wrinkles in dielectric elastomer.  $H$  stands for thickness and  $\tilde{R} = 9.8333$  is the averaged radius accounting for thickness stretch

### Capsule

The next example considered is that of a dielectric capsule, shown in Figure 5.23(a,b) centered at  $[0, 0, 0]^T$  with an in-plane radius of  $10m$ , thickness of  $0.5m$  and a bulging factor of  $2m$  in the out of plane direction. The mesh considered (shown in Figure 5.23(c)) has 10112 elements and for an interpolation degree  $q = 3$  there are 365584 points in the computational mesh which corresponds to 1462336 degrees of freedom. Due to symmetry, only 1/4th of the geometry is analysed. A set of symmetric mechanical Dirichlet boundary conditions are applied on the mesh with an applied electric voltage across the thickness, as described in the following.

$$\begin{aligned}
 \mathbf{u} &= \mathbf{0} \text{ [m]} & \text{at } \mathbf{X} &= [0, y, z]^T; \\
 u_z &= 0 \text{ [m]} & \text{at } \mathbf{X} &= [x, 0, z]^T; \\
 \varphi &= 0 \text{ [V]} & \text{at } R_{in}; \\
 \varphi &= 2.5 \times 10^7 \Lambda \text{ [V]} & \text{at } R_{out}.
 \end{aligned}$$

This problem is in particular interesting in shape and pattern forming through actuation. Figure 5.24 shows the hydrostatic pressure at different loading stages. As can be observed the capsule undergoes massive deformation to adopt a squared shape from an initial circular configuration, as the electric voltage is applied. The capsule deforms significantly when the electric voltage is high to adopt the new shape. After the point of snap-through as more voltage is applied, a compression zone is formed at the centre. As the electric voltage is increased, this

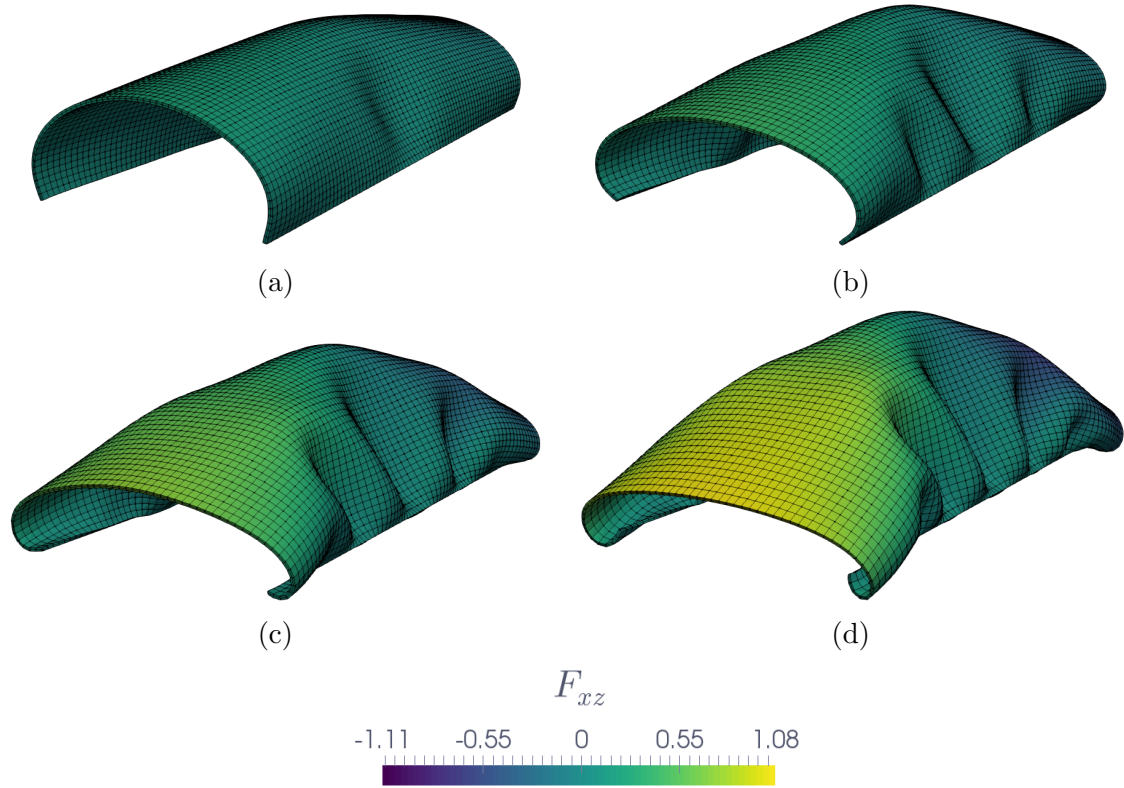


Figure 5.21: Evolution of voltage induced strain  $F_{xz}$  in dielectric cylindrical structure with accumulated load factor  $\Lambda$  being a)  $\Lambda = 0.538$  b)  $\Lambda = 0.769$ , c)  $\Lambda = 0.923$  and, d)  $\Lambda = 1.0$

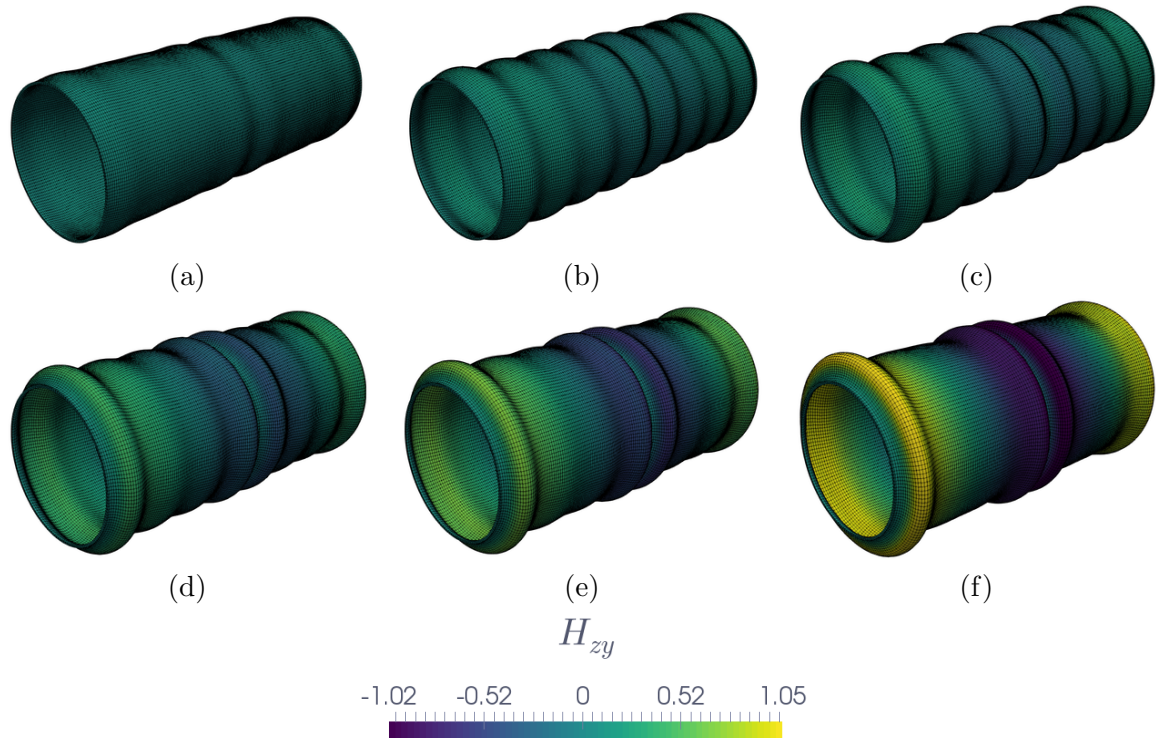


Figure 5.22: Evolution of voltage induced strain (co-factor of the deformation gradient)  $H_{zy}$  in dielectric cylindrical structure with accumulated load factor  $\Lambda$  being a)  $\Lambda = 0.490$  b)  $\Lambda = 0.686$ , c)  $\Lambda = 0.784$ , d)  $\Lambda = 0.882$ , e)  $\Lambda = 0.941$  and, f)  $\Lambda = 1.0$

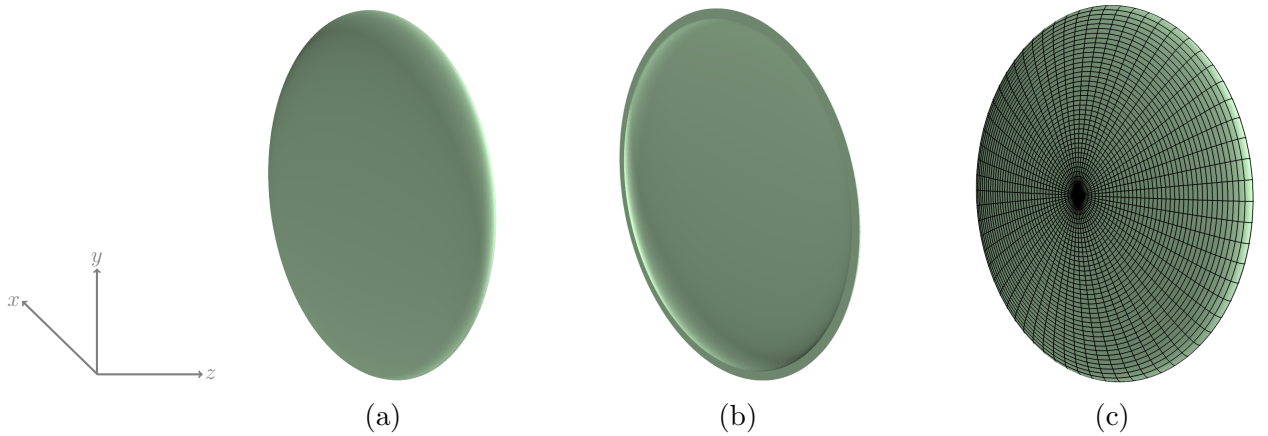


Figure 5.23: Dielectric capsule centred at  $[0, 0, 0]^T$  with an in-plane radius of 10m, thickness of 0.5m and a bulging factor of 2m a,b) CAD geometry and c)  $q = 3$  structured hexahedral mesh

compression zone rapidly moves from the centre towards the edges of the deformed capsule signalling the propagation of compressed band through a highly inflated capsule. The occurrence of this phenomenon is indeed analogous to the ones reported in the previous section, in that, after the point of pull-in instability the thicker regions expand at the expense of the thinner region resulting in zones of compression and propagation of pressure as a wave through the capsule.

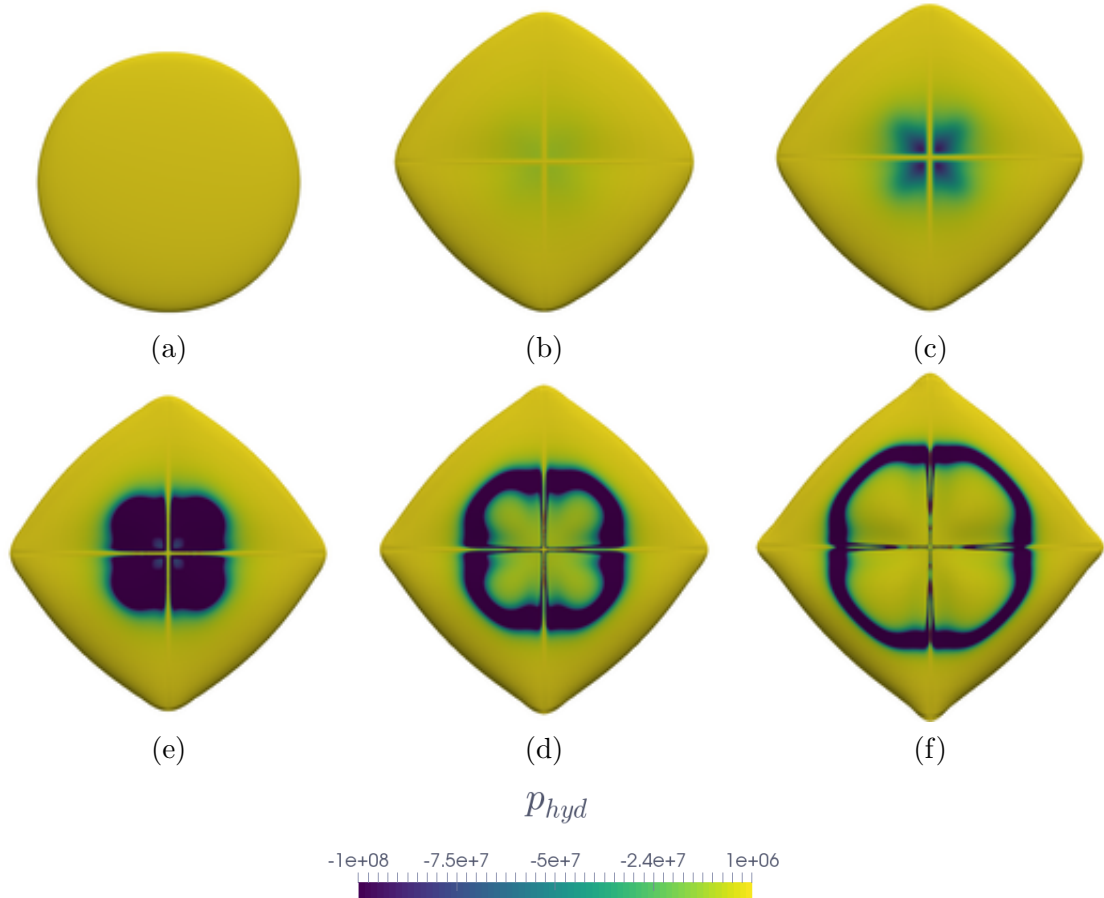


Figure 5.24: Evolution of voltage induced hydrostatic pressure in dielectric capsule with the accumulated load factor  $\Lambda$  being a)  $\Lambda = 0.411$ , b)  $\Lambda = 0.767$ , c)  $\Lambda = 0.823$ , d)  $\Lambda = 0.882$ , e)  $\Lambda = 0.946$  and, f)  $\Lambda = 1.0$

### Capturing folds and coarse wrinkles in dielectric plates with and without inclusions

The objective of this study is to show the effect of inclusions and the capability of the current high order curvilinear framework in capturing folds and coarse wrinkles with very coarse meshes through polynomial enrichments. To this effect, two dielectric plates are considered one without holes or inclusions and one with multiple circular inclusions distributed non-homogeneously through the plate, as shown in Figure 5.25. The mesh considered for the plate without inclusion is an extremely coarse  $12 \times 12 \times 1$  structured hexahedral mesh (with only one element across the thickness). For a polynomial degree of  $q = 6$  there are 37303 points in the computational mesh corresponding to a total of 149212 degrees of freedom. For the plate with inclusions, the mesh considered is an unstructured tetrahedral with 2147 elements, as shown in Figure 5.25(d). For an interpolation degree of  $p = 4$ , there are 26943 points in the computational mesh corresponding to a total of 107772 degrees of freedom.

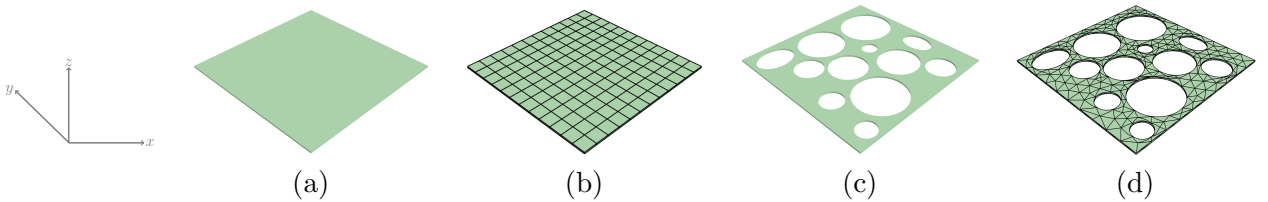


Figure 5.25: Geometries and meshes for the dielectric plates of size  $100 \times 100 \times 1 m^3$ , a,b) without inclusions and, c,d) with inclusions

The following set of boundary conditions are applied on both plates

$$\begin{aligned}
 \mathbf{u} &= \mathbf{0} [m] & \text{at } \mathbf{X} &= [0, y, 0]^T; \\
 \mathbf{u} &= \mathbf{0} [m] & \text{at } \mathbf{X} &= [100, y, 0]^T; \\
 \mathbf{u} &= \mathbf{0} [m] & \text{at } \mathbf{X} &= [x, 0, 0]^T; \\
 \mathbf{u} &= \mathbf{0} [m] & \text{at } \mathbf{X} &= [x, 100, 0]^T; \\
 \varphi &= 0 [V] & \text{at } \mathbf{X} &= [x, y, 0]^T; \\
 \varphi &= 4.98 \times 10^7 \Lambda [V] & \text{at } \mathbf{X} &= [x, y, 1]^T.
 \end{aligned}$$

Figure 5.26 shows the evolution of deformation in the plate (without inclusions) at multiple loading stages and Figure 5.27 shows the final configuration of the plate. The formation of folds and coarse wrinkles can be clearly seen from the figures. Notice how the high order curvilinear elements are able to capture this intrinsic property of dielectric elastomers with a very coarse discretisation.

Similarly, Figure 5.28 shows the evolution of strain component  $F_{xz}$  in the plate with inclusions at multiple loading stages and Figure 5.29 shows the final configuration of the plate. The formation of folds can be clearly seen from the figures. However, unlike in the case of plate with no inclusions, the deformation pattern is completely non-uniform and the plate does not deform as much. Once again, notice how the high order curvilinear elements are able to capture foldings in dielectric elastomers with an increased level of detail despite a coarse discretisation.

It should be noted that, in the electromechanics community most researchers use low order preferably linear and planar  $q = 1$  elements for their simulation. To this end, Figure 5.30 shows the performance of different polynomial degrees in capturing coarse wrinkles, in a slightly modified geometry i.e. the same plate but a square hole in the center. Notice from the figure that  $q = 1$  elements at this level of refinement fail to present a good description of the voltage induced deformation in the plate.

Finally, the same plate is now analysed but under application of a surface charge of  $2.5 \times 10^{-4} Q/m^2$ . Figure 5.31 shows the evolution of norm of displacement under various stages of

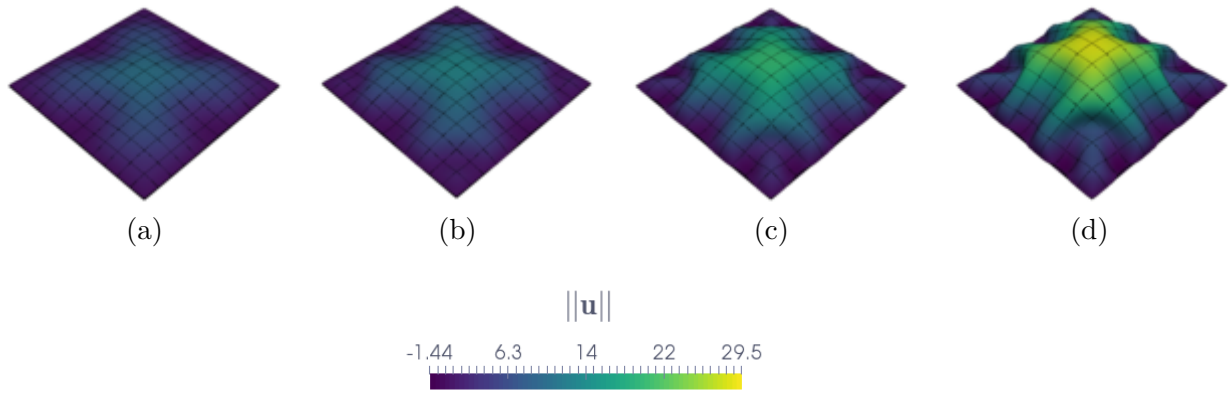


Figure 5.26: Evolution of norm of displacements in dielectric plate with the accumulated load factor  $\Lambda$  being a)  $\Lambda = 0.482$ , b)  $\Lambda = 0.602$ , c)  $\Lambda = 0.843$  and, d)  $\Lambda = 1.0$

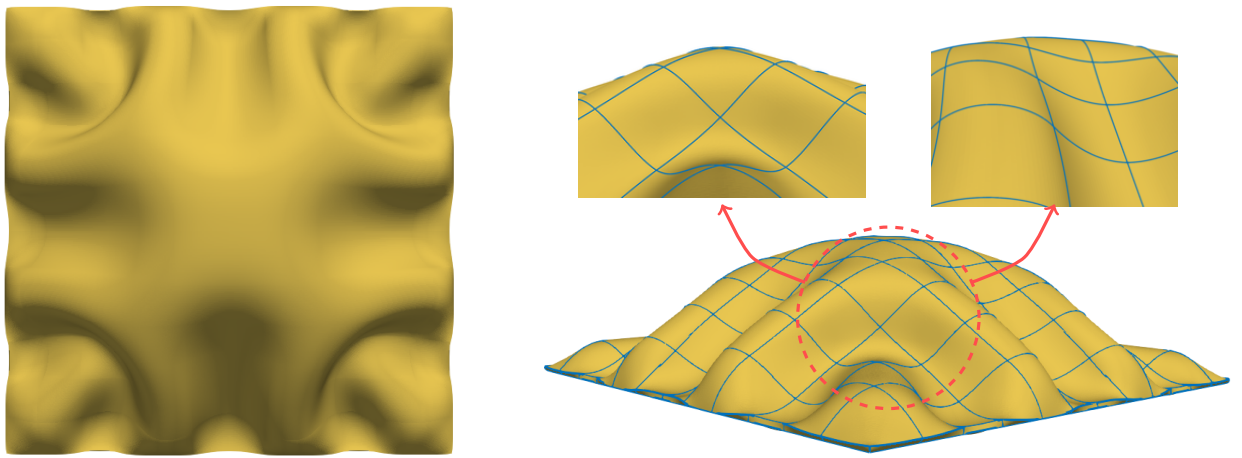


Figure 5.27: Formation of folds in dielectric plate (at the final deformed configuration) captured on a  $12 \times 12 \times 1$  hexahedral mesh with  $q = 6$  polynomial interpolation

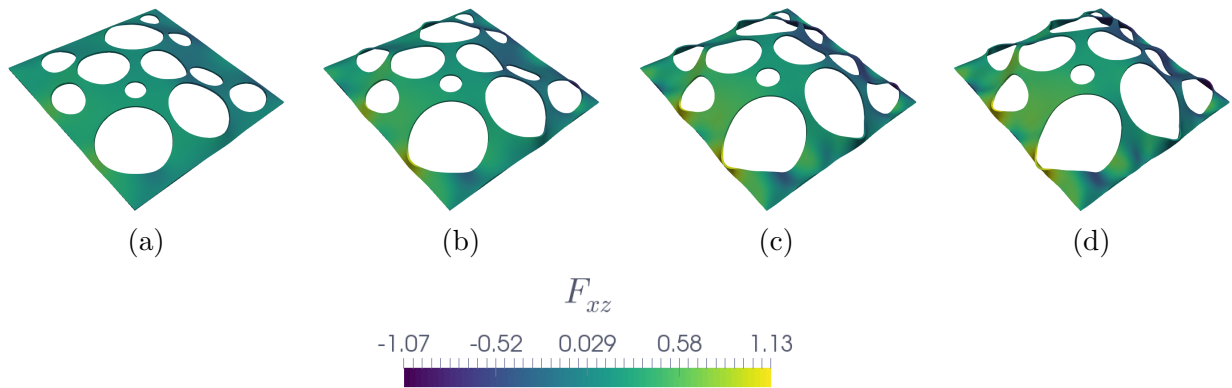


Figure 5.28: Evolution of strains  $F_{xz}$  in dielectric plate with inclusions with the accumulated load factor  $\Lambda$  being a)  $\Lambda = 0.482$ , b)  $\Lambda = 0.602$ , c)  $\Lambda = 0.843$  and, d)  $\Lambda = 1.0$

loading (without the color contours). As can be seen under the application of surface charge the problem is more stable and the analysis can be performed at a much higher loading stage leading to a severe formation of folds and multiple stages of snap-through.

While folding and the formation of single layer coarse wrinkles can be captured accurately using the high order curvilinear elements, as presented in the next section, multi-layer wrinkling

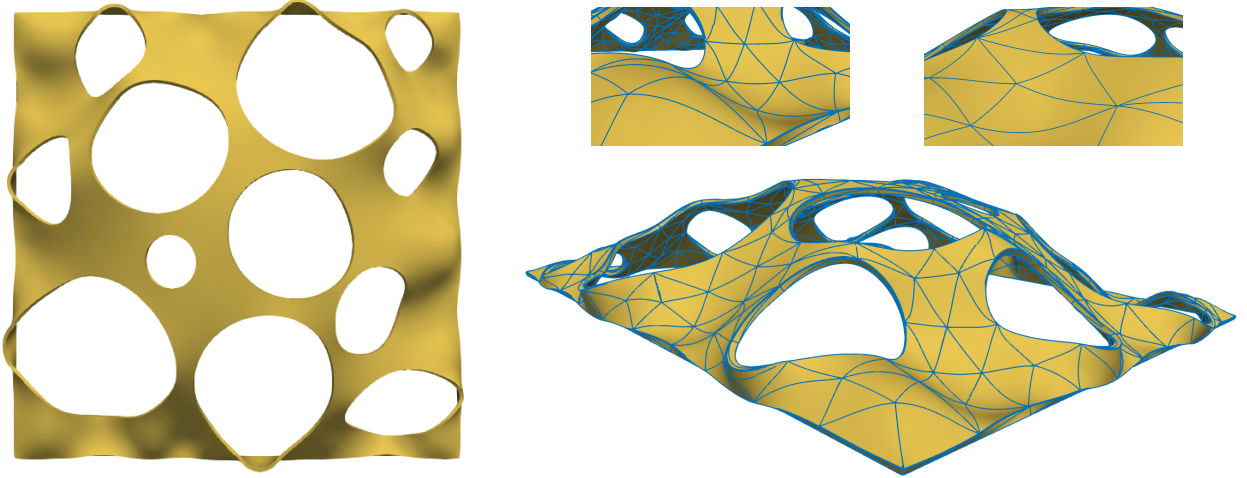


Figure 5.29: Formation of folds in dielectric plate with inclusions (at the final deformed configuration) captured on an unstructured tetrahedral mesh with  $p = 4$  polynomial interpolation

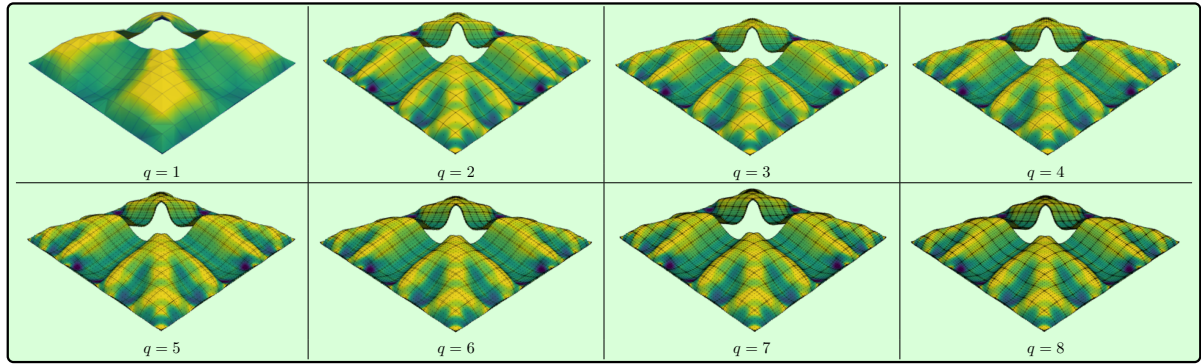


Figure 5.30: A comparison of performance of high order curvilinear elements in capturing wrinkles

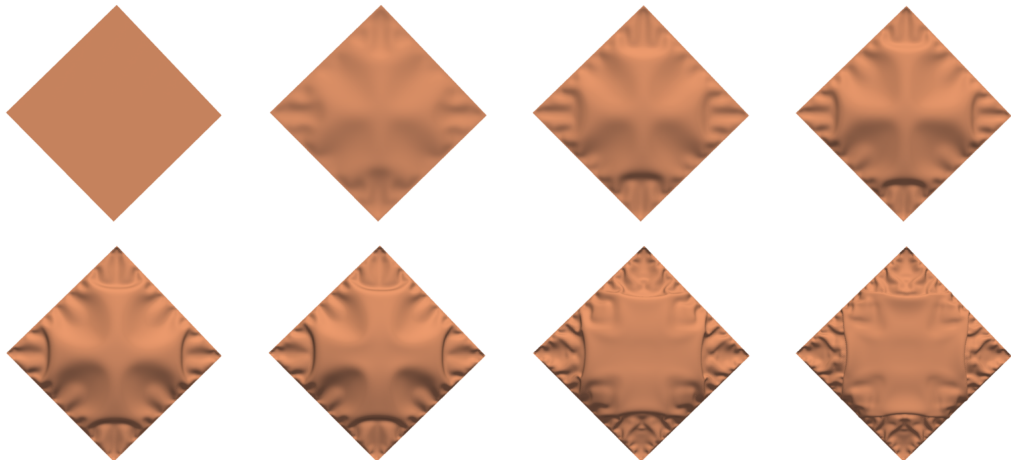


Figure 5.31: Evolution of norm of displacements in dielectric plate under the application of surface charge

and the propagation and nucleation of extremely fine wrinkles would still require a refined computational mesh.

### Dielectric thin film undergoing massive wrinkling

The objective of this final example is to study the voltage induced instability in a thin dielectric elastomeric film undergoing massive formation, propagation and nucleation of wrinkles. Instabilities in the form of wrinkling have also been studied in [198, 336, 177]. For the analysis, a hexahedral mesh with two polynomial enrichments is considered namely  $q = 2$  and  $q = 6$  with 268140 and 1.4M degrees of freedom, respectively. The latter allows for a highly detailed propagation of wrinkles through the film in terms of geometry and solution accuracy. The CAD geometry and mesh of the film are shown in Figure 5.32 with 100m radius and 1m thickness centred at  $[0, 0, 0]^T$ .

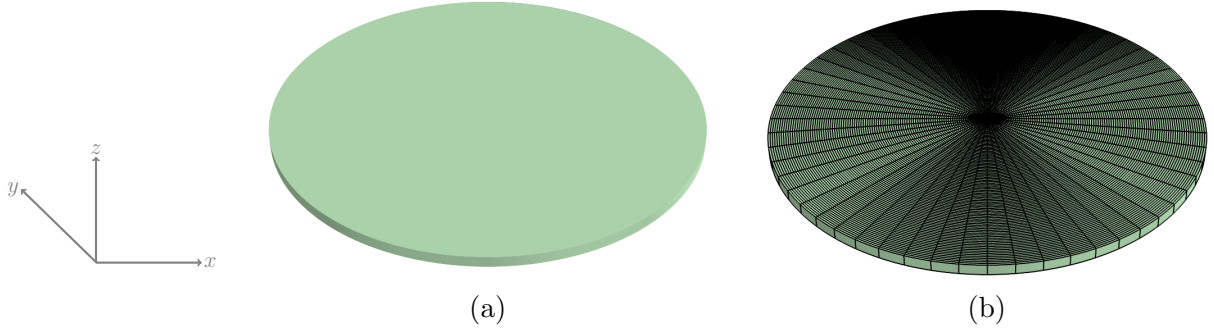


Figure 5.32: Dielectric thin film with 100m radius and 1m thickness centred at  $[0, 0, 0]^T$ , a) CAD geometry and, b)  $q = 2$  mesh

The following set of boundary conditions is applied on the film

$$\begin{aligned} \mathbf{u} = \mathbf{0} \text{ [m]} & \quad \text{at } \mathbf{X} = [x, y, 0]^T \text{ s.t. } x^2 + y^2 = 100^2; \\ \varphi = 0 \text{ [V]} & \quad \text{at } \mathbf{X} = [x, y, 0]^T; \\ \varphi = 5 \times 10^7 \Lambda \text{ [V]} & \quad \text{at } \mathbf{X} = [x, y, 1]^T. \end{aligned}$$

This above set of boundary conditions essentially implies fixing the mechanical variables at the outer boundary of the base of the film and applying an electric voltage across the thickness of the film. This forces the film to bend perpendicularly and expand in area. The electric voltage is applied adaptively on the film through 1000 load increments. Figure 5.33 shows the evolution of stress components  $\sigma_{xz}$  and  $\sigma_{yz}$  in dielectric film for  $q = 2$  mesh. As can be observed under low electric voltage, the region near the boundary of the circular film starts bulging up. This allows the film to expand in area and shrink in thickness in this region. As the voltage is increased the thick regions surrounding the thin ones start to expand and bulge facilitating the formation and further propagation of wrinkles. Under further increase in voltage all the regions start to possess similar thickness and the film straightens again allowing for nucleation of many wrinkles. The process of wrinkling starts once again, when the voltage is further increased. The process keeps repeating itself as voltage keeps increasing up until the point of complete electric breakdown. Note that the formation of deep channels near the boundary require polynomial enhancement despite a very fine mesh to capture the massive voltage induced bending caused by wrinkles.

The same problem is then analysed using  $q = 6$  elements, however now after the formation a certain number of wrinkles in the film, the load is released. Figure 5.34 shows the deformation history of the film together with the evolution of hydrostatic pressure. As the load is released, the deep channels around the boundary start to move inwards, leaving a thick bended layer behind. As the whole load cycle is completed the film starts flattening and forming a plate with multiple tiny wrinkles on the surface.

Finally, the aspect ratio of the film is decreased from 1/100 to 1/20 i.e. the radius is decreased to 20m and the same problem with release load cycle is analysed using the  $q = 6$  mesh. The

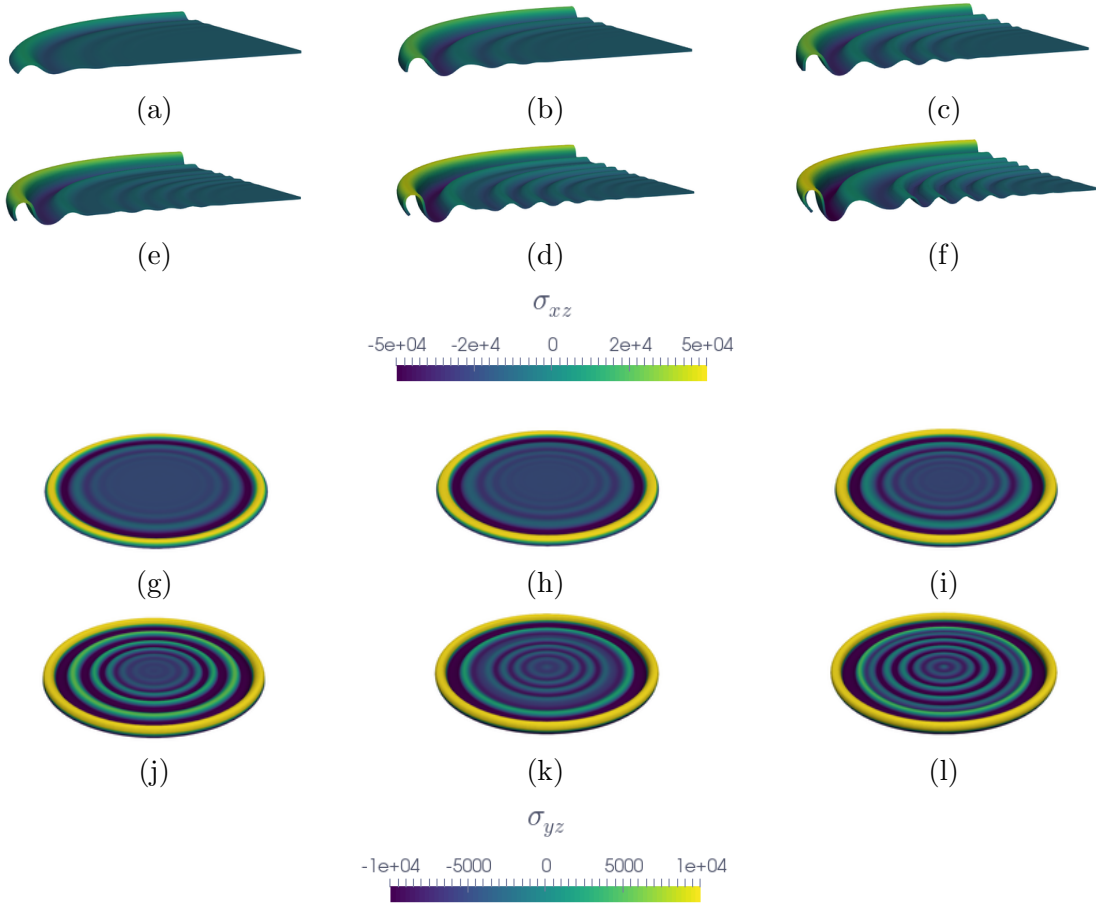


Figure 5.33: Evolution of voltage induced stress components  $\sigma_{xz}$  (a,b,c,d,e,f) and  $\sigma_{yz}$  (g,h,i,j,k,l) in dielectric film with the accumulated load factor  $\Lambda$  being a,g)  $\Lambda = 0.580$ , b,h)  $\Lambda = 0.725$ , c,i)  $\Lambda = 0.798$ , d,j)  $\Lambda = 0.870$ , e,k)  $\Lambda = 0.943$  and, f,l)  $\Lambda = 1.0$

deformation pattern is the same as in the previous analysis, however, since now there is little room for the formation of multiple thick and thin regions, wrinkling is limited. As shown in Figure 5.35 a deep channel is formed near the boundary that starts propagating inwards till it reaches the centre. The film starts occupying a balloon shape at this stage. As the voltage is increased, the centre of the film starts bending in the opposite direction, allowing the formation of another layer of wrinkles to propagate outwards. Once the wrinkle is propagated through the film by reaching the boundaries, another layer of wrinkles starting from the centre starts propagating outwards. The process is repeated and in the process, multiple wrinkles start nucleating before hitting the boundary. Under the completion of the release cycle, the film starts flattening leaving multiple extremely fine wrinkles behind on the surface.

Overall, the problem of analysing the formation of wrinkles in dielectric elastomers is a challenging one, in that it requires a very fine mesh. With coarse meshes it is possible to capture folds using high order curvilinear elements, however multi-layer wrinkling might not even occur using coarse meshes. Even high polynomial enrichments do not allow for a wave like deformation of a single element in a wrinkled state, and hence  $h$ -refinement is absolutely necessary. Where polynomial enrichment really helps is in massive bending of single elements during the formation of deep channels. The examples discussed afore, pinpoint the robustness and the high performant capability of the framework in capturing massive deformations and wrinkling in dielectric elastomers with a remarkable level of detail.

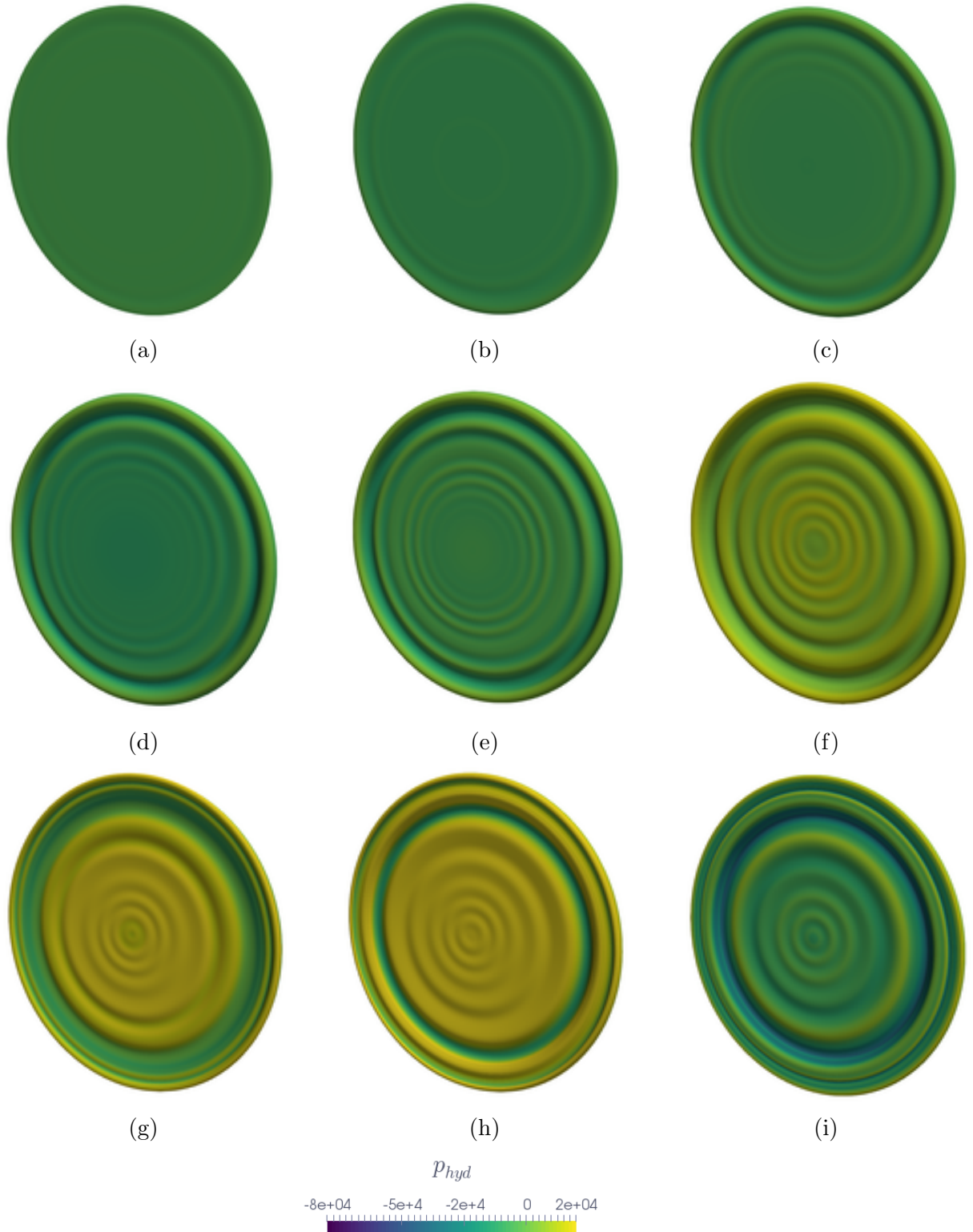


Figure 5.34: Evolution of voltage induced hydrostatic pressure in dielectric film with the accumulated load factor  $\Lambda$  being a)  $\Lambda = 0.221$ , b)  $\Lambda = 0.332$ , c)  $\Lambda = 0.443$ , d)  $\Lambda = 0.554$ , e)  $\Lambda = 0.665$ , f)  $\Lambda = 0.887$ , g)  $\Lambda = 0.943$ , h)  $\Lambda = 0.971$ , and, i)  $\Lambda = 1.0$

### Dielectric hemispherical film undergoing massive wrinkling

The objective of this example is to once again study the voltage induced instability in a thin dielectric elastomeric hemispherical film undergoing massive formation, propagation and nucleation of wrinkles. For the analysis, a hexahedral mesh with polynomial enrichment  $q = 2$

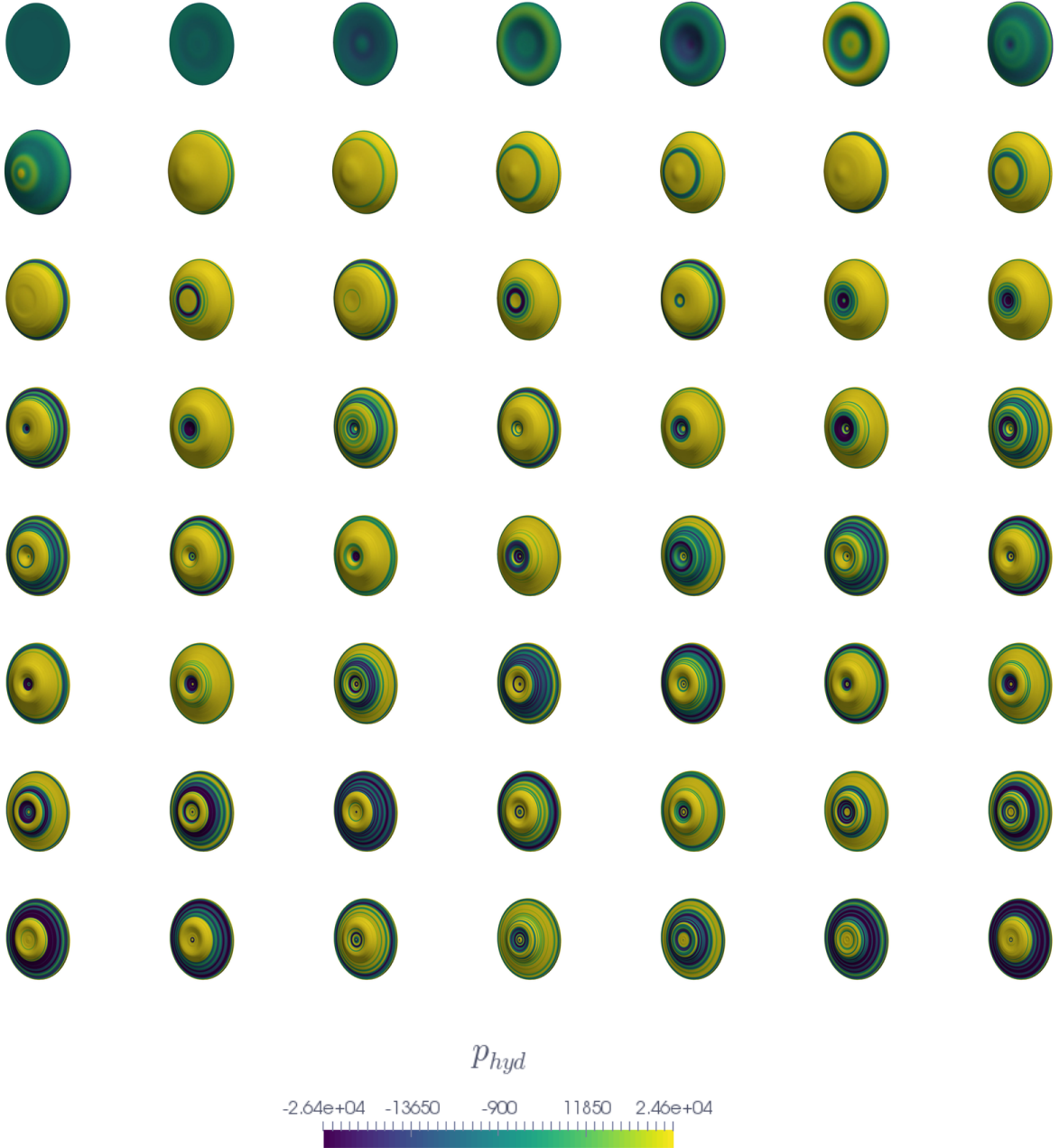


Figure 5.35: Evolution of voltage induced hydrostatic pressure in dielectric film with the accumulated load factor  $\Lambda$  being (left to right - top to bottom)  $\Lambda = 0.0, \Lambda = 0.124, \Lambda = 0.249, \Lambda = 0.374, \Lambda = 0.499, \Lambda = 0.624, \Lambda = 0.749, \Lambda = 0.874, \Lambda = 0.886, \Lambda = 0.899, \Lambda = 0.911, \Lambda = 0.918, \Lambda = 0.921, \Lambda = 0.924, \Lambda = 0.928, \Lambda = 0.93, \Lambda = 0.934, \Lambda = 0.936, \Lambda = 0.94, \Lambda = 0.942, \Lambda = 0.949, \Lambda = 0.952, \Lambda = 0.955, \Lambda = 0.958, \Lambda = 0.96, \Lambda = 0.962, \Lambda = 0.964, \Lambda = 0.965, \Lambda = 0.966, \Lambda = 0.968, \Lambda = 0.969, \Lambda = 0.97, \Lambda = 0.971, \Lambda = 0.972, \Lambda = 0.974, \Lambda = 0.975, \Lambda = 0.976, \Lambda = 0.978, \Lambda = 0.979, \Lambda = 0.98, \Lambda = 0.981, \Lambda = 0.982, \Lambda = 0.984, \Lambda = 0.985, \Lambda = 0.986, \Lambda = 0.988, \Lambda = 0.989, \Lambda = 0.99, \Lambda = 0.991, \Lambda = 0.992, \Lambda = 0.994, \Lambda = 0.995, \Lambda = 0.996, \Lambda = 0.998, \Lambda = 0.999$  and,  $\Lambda = 1.0$

is considered, where the number of degrees of freedom in the computational mesh are almost 7.6M. This allows for a highly detailed propagation of wrinkles through the film in terms of geometry and solution accuracy. The CAD geometry and mesh of the film are shown in Figure 5.36 with 10mm radius and 0.1mm thickness centred at  $[0, 0, 0]^T$ . Due to symmetry only 1/4th of the geometry is solved for. We solve for three different set of boundary conditions for

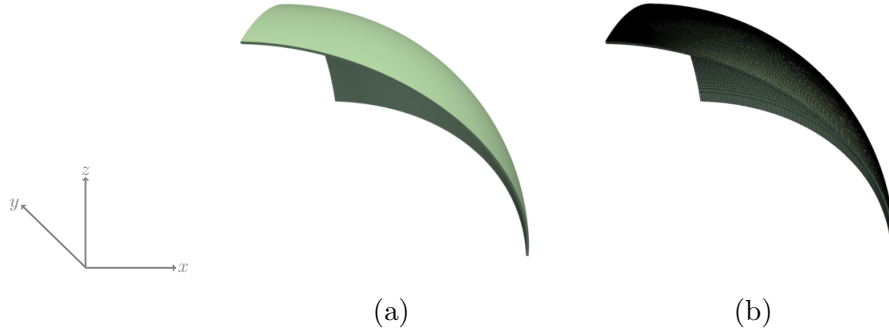


Figure 5.36: Dielectric arc with  $10\text{mm}$  radius and  $0.1\text{mm}$  thickness centred at  $[0, 0, 0]^T$ , a) CAD geometry and, b)  $q = 2$  mesh

this geometry. The first situation is when all the faces of the geometry shown above (except conic faces) are mechanical fixed in all direction and electric potential is applied through the thickness. This can be written as The following set of boundary conditions is applied on the film

$$\begin{aligned}
 \mathbf{u} &= \mathbf{0} [\text{mm}] & \text{at } \mathbf{X} &= [0, y, z]^T; \\
 \mathbf{u} &= \mathbf{0} [\text{mm}] & \text{at } \mathbf{X} &= [x, 0, z]^T; \\
 \mathbf{u} &= \mathbf{0} [\text{mm}] & \text{at } \mathbf{X} &= [x, y, 0]^T; \\
 \varphi &= 0 [V] & \text{at } R &= R_{in}; \\
 \varphi &= 5 \times 10^3 \Lambda [V] & \text{at } R &= R_{out}.
 \end{aligned}$$

Figure 5.37 shows the evolution of hydrostatic pressure in dielectric hemispherical sheet for  $q = 2$  mesh. As can be observed due to the nature of the boundary condition, under low electric voltage, the region near the boundary of the film starts bulging up. This allows the film to expand in area and shrink in thickness in this region. As the voltage is increased the thick regions surrounding the thin ones start to expand and bulge facilitating the formation wrinkles, in this region. As can be observed the formation of coarse wrinkles around edges is primarily due to the boundary conditions in that the mechanical degrees of freedom are fixed around this region. In these example we in particular show the capabilities of the current high order convex multi-variable electromechanical formulation for capturing folds and wrinkles. A more detailed analysis could be carried out to obtain the points of snap-through and critical voltage for the design of these devices.

The next boundary condition corresponds to a set of symmetric boundary conditions at the edges except the base  $z = 0$ , in that

$$\begin{aligned}
 u_x &= 0 [\text{mm}] & \text{at } \mathbf{X} &= [0, y, z]^T; \\
 u_y &= 0 [\text{mm}] & \text{at } \mathbf{X} &= [x, 0, z]^T; \\
 \mathbf{u} &= \mathbf{0} [\text{mm}] & \text{at } \mathbf{X} &= [x, y, 0]^T; \\
 \mathbf{u} &= \mathbf{0} [\text{mm}] & \text{at } \mathbf{X} &= [0, 0, R_{in}]^T; \\
 \varphi &= 0 [V] & \text{at } R &= R_{in}; \\
 \varphi &= 5 \times 10^3 \Lambda [V] & \text{at } R &= R_{out}.
 \end{aligned}$$

The tip point of the arc at the pole to allow a more rigorous formation of wrinkles. At the absence of this mechanical fixture, the dielectric arc will have more capacity to expand uniformly and develop less dramatic wrinkles.

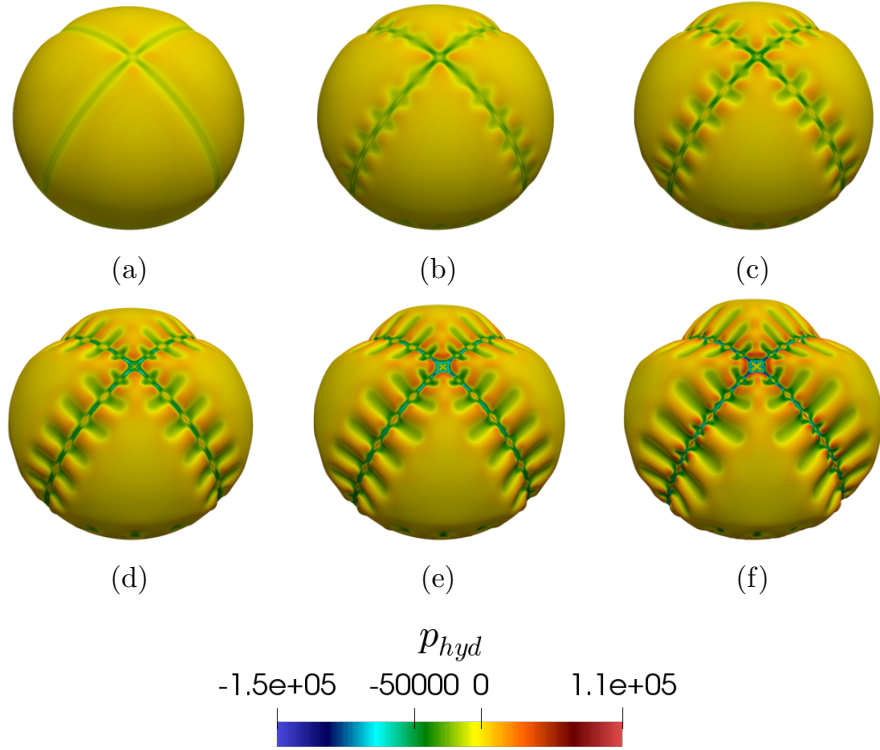


Figure 5.37: Evolution of voltage induced hydrostatic pressure in dielectric film with the accumulated load factor  $\Lambda$  being a)  $\Lambda = 0.489$ , b)  $\Lambda = 0.653$ , c)  $\Lambda = 0.734$ , d)  $\Lambda = 0.857$ , e)  $\Lambda = 0.938$ , and, f)  $\Lambda = 1.0$

Figure 5.38 shows the evolution of strains in dielectric hemispherical sheet. As can be observed due to the symmetric nature of the boundary condition, there is no bulding of the dielectric sheet near the corners but more uniform wave like wrinkles are formed initiating from the top (pole) of the arc and travelling downwards. This allows the film to expand in area and shrink in thickness once again. As the voltage is increased the tip of the spherical arc gets distored heavily and the component reaches a geometrical tolerance in terms of functionality. This behaviour could be remedied numerically by refining the mesh around the tip which has been the case for this problem. However, even with fine meshes there would finally reach a point where the dielectric film would be in a severely non-functional state.

The other way to allow formation of multiple wrinkles, is to fix the region around the tip of the hemispherical film using a cap holding mechanism shown as follows. The associated boundary condition for this case (the third case) is given as follows

$$\begin{aligned}
 u_x &= 0 \text{ [mm]} & \text{at } \mathbf{X} &= [0, y, z]^T; \\
 u_y &= 0 \text{ [mm]} & \text{at } \mathbf{X} &= [x, 0, z]^T; \\
 \mathbf{u} &= \mathbf{0} \text{ [mm]} & \text{at } \mathbf{X} &= [x, y, 0]^T; \\
 \mathbf{u} &= \mathbf{0} \text{ [mm]} & \text{at } \mathbf{X} &= [0, y, z]^T \cup [x, 0, z]^T \text{ s.t. } R = R_{in}; \\
 \varphi &= 0 \text{ [V]} & \text{at } R &= R_{in}; \\
 \varphi &= 5 \times 10^3 \Lambda \text{ [V]} & \text{at } R &= R_{out}.
 \end{aligned}$$

The fourth item in the above boundary condition set essentially implies fixing the arc in from inside around the edges where symmetry boundary conditions are imposed. This allows the arc to roll on one side (outwards) and in the process expand. However, the existence of a cap holding the region around the tip means that this expansion is not possible beyond a limit and wrinkles should be expected in the vicinity of this region. This problem is once again

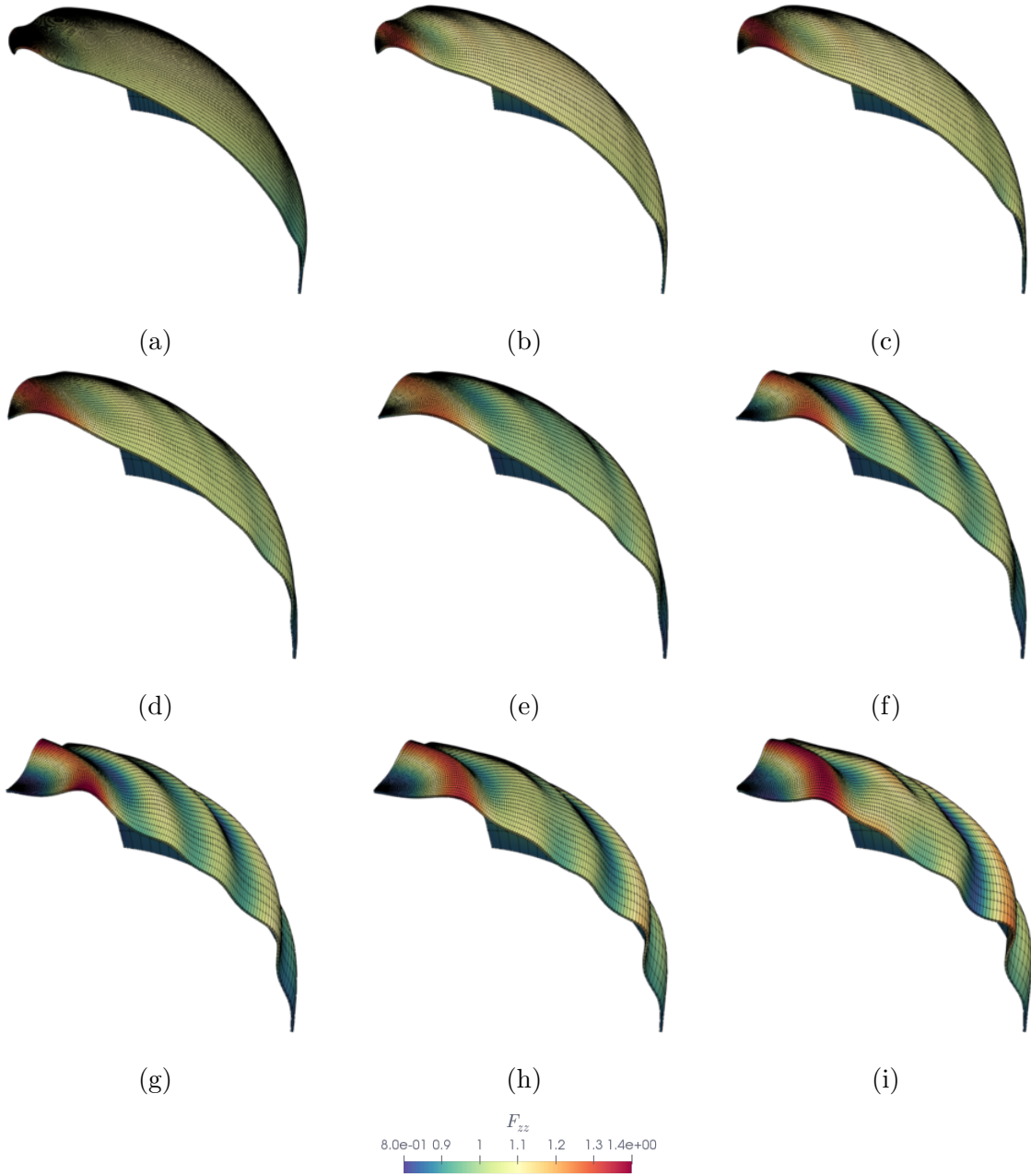


Figure 5.38: Evolution of voltage induced strain in dielectric film with the accumulated load factor  $\Lambda$  being a)  $\Lambda = 0.489$ , b)  $\Lambda = 0.653$ , c)  $\Lambda = 0.734$ , d)  $\Lambda = 0.857$ , e)  $\Lambda = 0.938$ , f)  $\Lambda = 1.0$ , g)  $\Lambda = 0.857$ , h)  $\Lambda = 0.938$ , and, i)  $\Lambda = 1.0$

using 350 load increments and the load is released in the last 100 increments

Figure 5.41 shows the evolution of strains in dielectric hemispherical sheet. As can be observed, similar to the first example, due to the nature of the boundary condition, under low electric voltage, the region near the boundary that is near the cap fixture in this case starts to form wrinkles very early on. The most exciting stage during the analysis is the unloading stage where multiple layers of wrinkles are being formed. Since the unloading happens beyond the critical voltage limit, the film has already formed many regions with different levels of thickness. As the unloading occurs the wrinkles propagate through the thin regions much faster than the thick region making the wrinkles stick deeper into the thick regions for a longer time and as a result these thick regions get distorted heavily, whereas the thin regions experience faster propagation of wrinkles and less formation of channels. A close up of this phenomenon is shown in Figure 5.40.

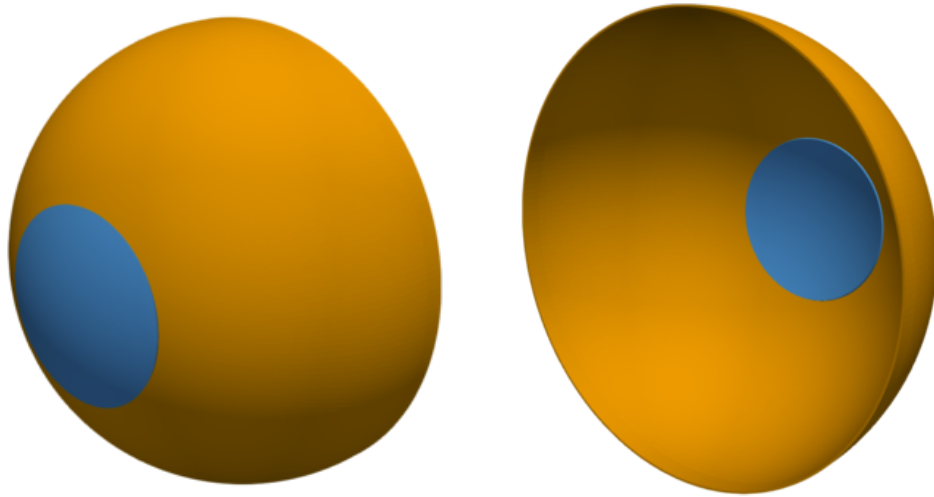


Figure 5.39: Rear and front view of cap fixture mechanism for hemispherical dielectric film

## 5.4 Conclusions

A high order finite element implementation of the convex multi-variable electro-elasticity for large deformations large electric fields simulations was presented in this chapter. Accurate geometrical representation through a high performance curvilinear finite element framework based on a posteriori mesh deformation technique is developed to accurately discretise the underlying displacement-potential variational formulation. The performance of the method under near incompressibility and bending actuation scenarios is analysed with extremely thin and highly stretched components and compared to the performance of mixed variational principles. Although convex multi-variable constitutive models are elliptic and hence, materially stable for the entire range of deformations and electric fields, other forms of physical instabilities are not precluded in these models. In particular, physical instabilities present in dielectric elastomers such as pull-in instability, snap-through and the formation, propagation and nucleation of wrinkles and folds are numerically studied with a detailed precision in this work, verifying experimental findings. In this context, the combination of  $h$  and  $p$  refinement proves to be essential to capture the inherent instabilities in dielectric elastomers. While the formation of folds and coarse wrinkles can be accurately captured by high order curvilinear elements using extremely coarse meshes, nucleation of wrinkles and multi-layer wrinkling require mesh refinement in addition to polynomial enrichment.

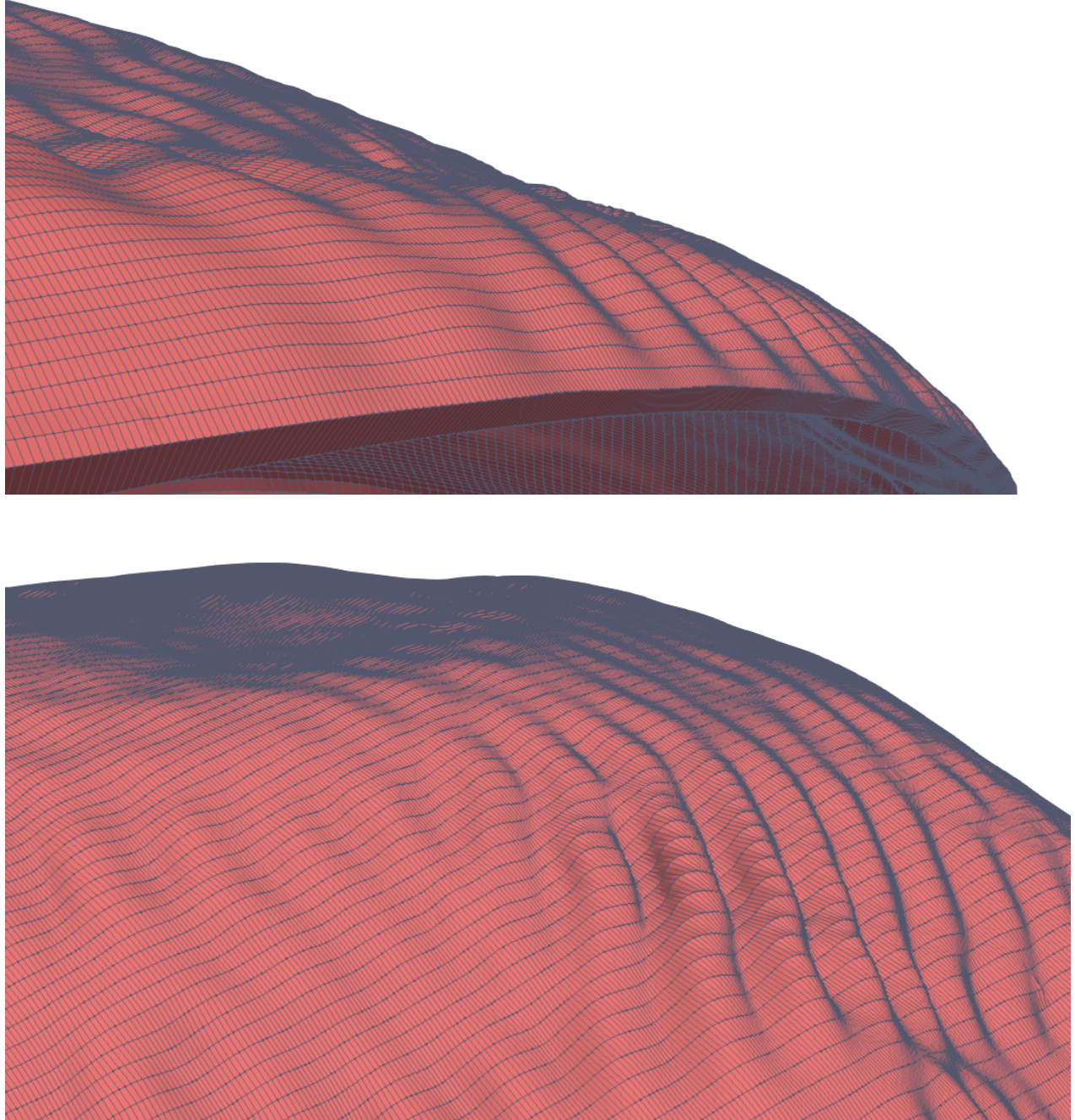


Figure 5.40: Close up of thick regions experiencing deeper formation of wrinkles

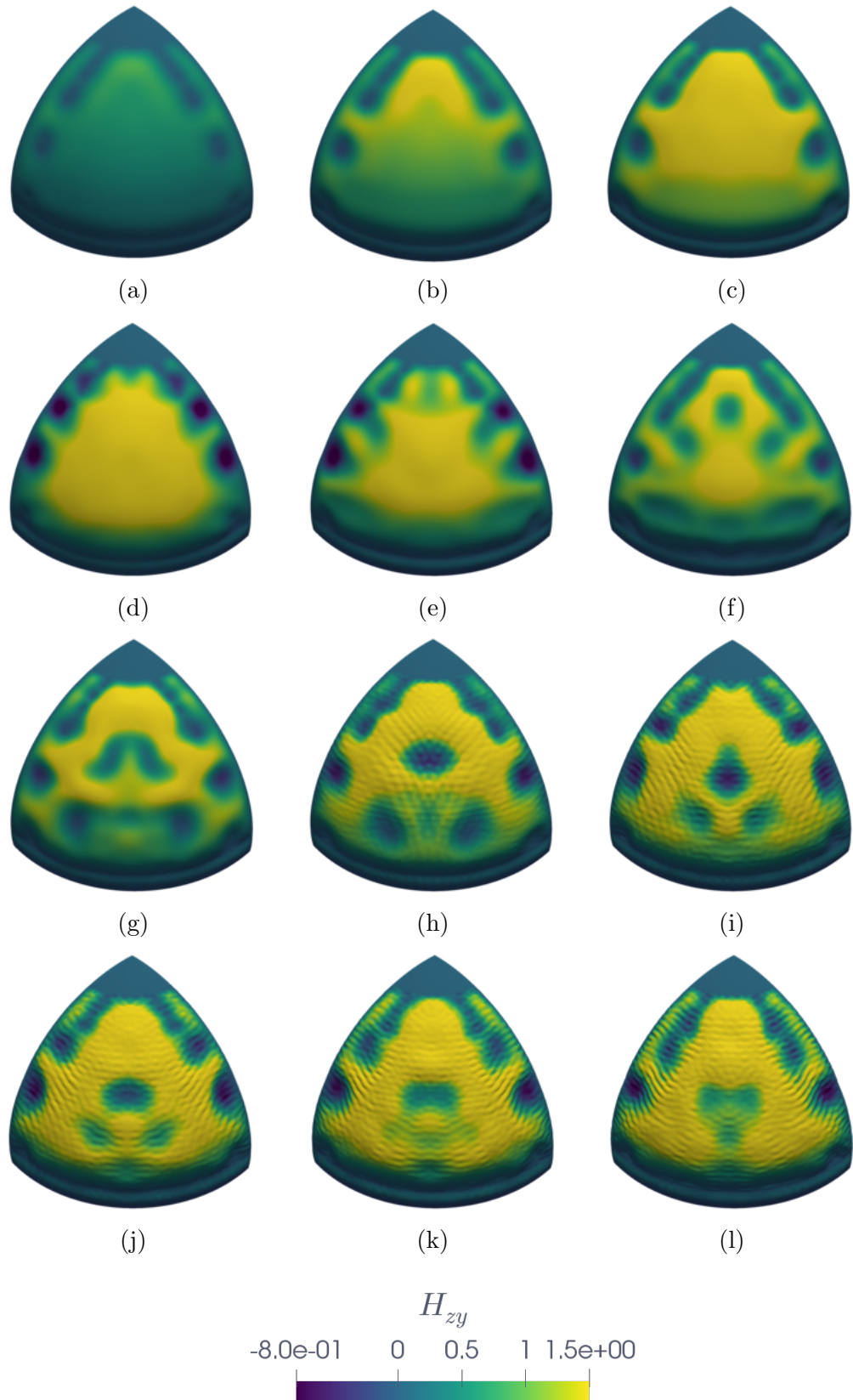
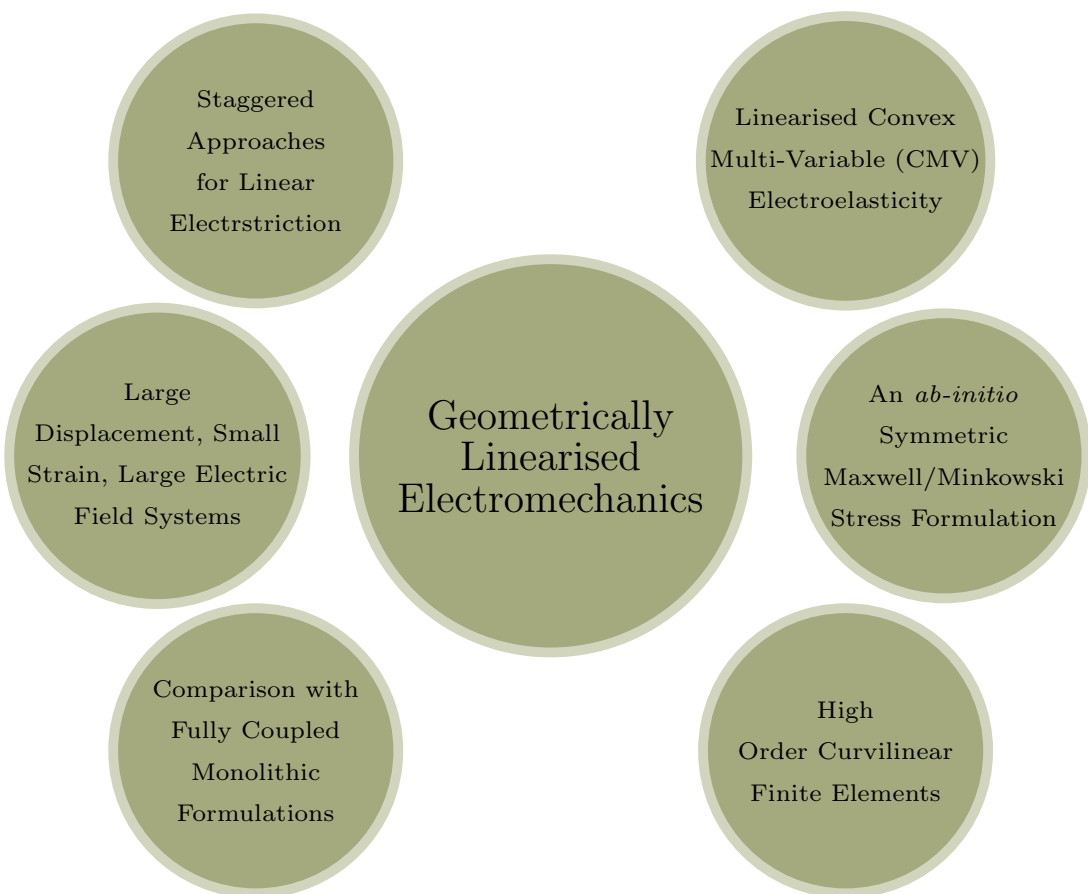


Figure 5.41: Evolution of voltage induced strain  $H_{zy}$  in dielectric film with the accumulated load factor  $\Lambda$  being a)  $\Lambda = 0.228$ , b)  $\Lambda = 0.293$ , c)  $\Lambda = 0.358$ , d)  $\Lambda = 0.488$ , e)  $\Lambda = 0.553$ , and, f)  $\Lambda = 0.618$ , g)  $\Lambda = 0.749$ , h)  $\Lambda = 0.830$ , i)  $\Lambda = 0.912$ , j)  $\Lambda = 0.944$ , k)  $\Lambda = 0.973$ , and, l)  $\Lambda = 1.0$



# Class 2: Curvilinear Finite Elements for Small Deformations - Large Electric Fields Electromechanics



# Chapter 6

## Curvilinear Finite Elements for Small Deformations - Large Electric Fields Electromechanics

### 6.1 Introduction

In an important intermediate class of problems for electromechanics, the large deformation characteristics of the system are neglected, whereas the nonlinearity still present in the material emanates from the electrostriction of the material through the Maxwell (for vacuum  $V_\infty$ ) or Minkowski (for material  $V$ ) stress tensors [89, 171, 241, 111]. Theoretical aspects of these formulations were first introduced in Landau and Lifshitz [171]. The practical relevance of Maxwell stress tensor has led to a widespread utilisation of these formulations for exploiting electrostriction and magnetostriction. Unfortunately, electrostrictive models based on the utilisation of Minkowski stress tensor, in the generic case of anisotropy do not satisfy material frame indifference (i.e. objectivity or invariance of the energy with respect to rotations) of the electromechanical (total) stress tensor, due to the inherent non-symmetric nature of the Minkowski stress. Several authors in the past have used *ad-hoc* solutions, such as symmetrisation of the total stress tensor, or consideration of the conservation of angular momentum in the formulation, as a remedy [241, 262]. Nevertheless, the extended electromechanical Hessian still remains non-symmetric, which dictates the development of specialised non-symmetric finite element frameworks. Recently, Bustamente [38] has shown that physically admissible energy functionals can be constructed by choosing suitable constitutive restrictions such that their linearisation yields symmetric objective Minkowski-type stresses. The merit of starting from an energy principle is that no symmetrisation is required for the stresses and the resulting finite element discretisation is guaranteed to be symmetric.

This chapter presents a computational framework suitable for geometrically linearised small deformation large electric field electromechanics. A convex multi-variable strain energy description based on the works of Gil and Ortigosa [113, 233, 232] is chosen for modelling EAPs under actuation and energy harvesting scenarios. For the case of small strains, following Bustamente [38], this chapter extends the framework developed by Gil and Ortigosa [113, 233] to the case of geometrically linearised electrostriction, to redress the aforementioned inconsistencies for the class of intermediate formulations. Importantly, all the aforementioned mathematical requirements are imposed at a large deformation level to arrive at a physically admissible energy functional. In this context, convex multi-variable energies typically expressed in terms of fundamental kinematic measures  $\{\mathbf{F}, \mathbf{H}, J\}$  are re-expressed in terms of a set of symmetric kinematics  $\{\mathbf{C}, \mathbf{G}, C\}$  to guarantee the objectivity of the energy functional. Linearisation with respect to geometrical fields is then performed by perturbing the energy in the vicinity of the reference configuration. Analogous to [254], this is achieved through a staggered scheme where the equations of electrostatics are solved in a nonlinear fashion whereas the linearised mechanical equations are updated incrementally.

It should be noted that much of the work in this chapter is based on the authors work on linearised electromechanics presented in [253, 175]. The chapter is organised as follows. In section 6.2 we discuss the kinematics of the linearised electromechanics together with an appropriate variational formulation. This is followed by numerical examples in section 6.3, showcasing the realm of applicability and benefits of the linearised scheme in capturing small strains yet large displacements in electromechanical systems. Finally conclusions are given in section 6.4.

## 6.2 Incrementally linearised electromechanics

### 6.2.1 Symmetric linearised kinematics

Typically when strains are small i.e.  $\mathbf{E} \ll 1$ , (where  $\mathbf{E} = \frac{1}{2}(\mathbf{C} - \mathbf{I})$  is the Green-Lagrange strain tensor, in this case), the nonlinear term(s) in the kinematics can be ignored such that, if  $\mathbf{u}$  is the displacement vector, then

$$\mathbf{F} = \nabla_0 \mathbf{u} + \mathbf{I}; \quad (6.1a)$$

$$\mathbf{C} = \mathbf{F}^T \mathbf{F} = \left( \nabla_0 \mathbf{u} + \mathbf{I} \right)^T \left( \nabla_0 \mathbf{u} + \mathbf{I} \right) \quad (6.1b)$$

$$= \mathbf{I} + \left( (\nabla_0 \mathbf{u})^T + \nabla_0 \mathbf{u} \right) + (\nabla_0 \mathbf{u})^T (\nabla_0 \mathbf{u}),$$

$$\mathbf{E} = \frac{1}{2} \left( (\nabla_0 \mathbf{u})^T + \nabla_0 \mathbf{u} \right) + \frac{1}{2} (\nabla_0 \mathbf{u})^T (\nabla_0 \mathbf{u}), \quad (6.1c)$$

where the small strain tensor can be approximated as

$$\boldsymbol{\varepsilon} = \frac{1}{2} \left( (\nabla \mathbf{u})^T + \nabla \mathbf{u} \right), \quad (6.2)$$

where the distinction between material configuration and spatial configuration is now irrelevant. The internal energy is subsequently expressed in terms of  $\boldsymbol{\varepsilon}$  and linearised. Besides, (6.2) can be identified as a Taylor series expansion of a nonlinear strain measure (Green-Lagrange strain tensor  $\mathbf{E}$  in this case) up to the first order term, i.e. we can essentially write

$$\boldsymbol{\varepsilon} = \frac{1}{2} \left( (\nabla \mathbf{u})^T + \nabla \mathbf{u} \right) + O(\nabla \mathbf{u})^2. \quad (6.3)$$

The nature of this approximation inherently limits the choice of linearised internal energies that can be constructed for representing a wide range of physically plausible modes of deformation [32, 137], specifically the ones suitable for electromechanical applications. Furthermore during consistent linearisation of the potential energy, second directional derivatives are required which heralds an up to second order Taylor series expansion of the kinematics. To this end, a set of symmetric linearised kinematics can be introduced using  $\{\mathbf{C}, \mathbf{G}, \mathbf{C}\}$  as the starting point and a Taylor series expansion of up to second order term, where virtual and incremental variations are now both denoted by  $\mathbf{u}$ , itself

$$\bar{\mathbf{C}} = \left[ \mathbf{C} + \frac{1}{2} D\mathbf{C}[\mathbf{u}] + \frac{1}{4} D^2\mathbf{C}[\mathbf{u}] \right]_{\mathbf{F}=\mathbf{I}} + O(D\mathbf{C}[\mathbf{u}])^3 \quad (6.4a)$$

$$= \mathbf{I} + \frac{1}{2} \left( (\nabla \mathbf{u})^T + \nabla \mathbf{u} \right) + \frac{1}{4} \left( (\nabla \mathbf{u})^T (\nabla \mathbf{u}) + (\nabla \mathbf{u})^T (\nabla \mathbf{u}) \right),$$

$$\bar{\mathbf{G}} = \left[ \mathbf{G} + \frac{1}{2} D\mathbf{G}[\mathbf{u}] + \frac{1}{4} D^2\mathbf{G}[\mathbf{u}] \right]_{\mathbf{F}=\mathbf{I}} + O(D\mathbf{G}[\mathbf{u}])^3; \quad (6.4b)$$

$$= \mathbf{I} + \frac{1}{2} \mathbf{I} \times \left( (\nabla \mathbf{u})^T + \nabla \mathbf{u} \right) + \frac{1}{4} \mathbf{I} \times \left( (\nabla \mathbf{u})^T (\nabla \mathbf{u}) + (\nabla \mathbf{u})^T (\nabla \mathbf{u}) \right)$$

$$\begin{aligned}
& + \frac{1}{4} \left( (\nabla \mathbf{u})^T + \nabla \mathbf{u} \right) \times \left( (\nabla \mathbf{u})^T + \nabla \mathbf{u} \right) + O(D\mathbf{G}[\mathbf{u}])^3; \\
\bar{\mathbf{C}} &= \left[ C + \frac{1}{2} DC[\mathbf{u}] + \frac{1}{4} D^2 C[\mathbf{u}] \right]_{\mathbf{F}=\mathbf{I}} + O(DC[\mathbf{u}])^3 \\
&= 1 + \left( (\nabla \mathbf{u})^T + \nabla \mathbf{u} \right) : \mathbf{I} + \frac{1}{4} \mathbf{I} : \left( (\nabla \mathbf{u})^T (\nabla \mathbf{u}) + (\nabla \mathbf{u})^T (\nabla \mathbf{u}) \right) \\
&+ \frac{1}{4} \mathbf{I} : \left[ \left( (\nabla \mathbf{u})^T + \nabla \mathbf{u} \right) \times \left( (\nabla \mathbf{u})^T + \nabla \mathbf{u} \right) \right] + O(DC[\mathbf{u}])^3.
\end{aligned} \tag{6.4c}$$

It is easy to identify the emergence classical small strain tensor  $\boldsymbol{\varepsilon} = \frac{1}{2} \left( (\nabla \mathbf{u})^T + \nabla \mathbf{u} \right)$ . However, importantly new high order terms also arise in this process, which in the presence of a suitable strain energy typically lead to some kind of prestress effect [131]. Furthermore, it should be noted that the above Taylor series expansion is exact in  $\mathbf{C}$ , in the sense

$$D^3 \mathbf{C}[\mathbf{u}] = \mathbf{0} \quad \Rightarrow \quad O(D\mathbf{C}[\mathbf{u}])^3 = 0, \tag{6.5}$$

Although, this approximation is not exact in  $\mathbf{G}$  and  $\mathbf{C}$ . This one of the fundamental reasons, why in chapter 3 the variational principle for consistent incrementally linearised approach was presented in terms of  $\mathbf{C}$  alone. In order to have a unified framework, the variational formulation in the last chapter and consequently in this chapter are also going to be in terms of  $\mathbf{C}$  alone.

### 6.2.2 Variational Formulation

As discussed in section 6.1, a particular class of coupling in electromechanics deals with small strains coupled with nonlinear electrostatics. To this end, the variational principle described in chapter 4 can be particularised for the case of small strains. Extending, the strategy presented in [254, 253, 14], let us consider the total potential energy (5.4) cast in an iterative (Newton-Raphson) form

$$\Pi_{\Phi_{\text{int}}}(\mathbf{x}_{k+1}^{*^{n+1}}, \varphi_{k+1}^{*^{n+1}}) = \int_V \Phi(\mathbf{C}_{k+1}^{n+1}, -(\nabla_0 \varphi)_{k+1}^{n+1}) dV, \tag{6.6}$$

where superscripts denote increments and subscripts denote iterations. A geometrically linearised formulation for electro-elasticity can be obtained by perturbing the potential energy (6.6). However note that in contrast to the approach presented in [254], particularisation of (6.6) for small strains through consistent linearisation with respect to the variations in electrostatic fields and mechanical fields cannot be performed simultaneously, as it leads to high order tensorial quantities without clear physical interpretations. However, as shown in Figure 6.1, for small deformations, the geometry could be solved for incrementally with only the electrostatic equations requiring a full Newton-Raphson procedure. This gives rise to the staggered scheme presented in the following subsection.

### 6.2.3 The staggered approach to incrementally linearised electromechanics

To elaborate the staggered approach emanating from the variational principle, let us reconsider (6.6) which in fully discretised form (using the finite element method) can be written as

$$\begin{bmatrix} \mathbf{K}_{\mathbf{uu}}^{n+1} & \mathbf{K}_{\mathbf{u}\phi}^{n+1} \\ \mathbf{K}_{\phi\mathbf{u}}^{n+1} & \mathbf{K}_{\phi\phi}^{n+1} \end{bmatrix} \begin{bmatrix} \mathbf{U}_{\mathbf{u}}^{n+1} \\ \mathbf{U}_{\phi}^{n+1} \end{bmatrix} = - \begin{bmatrix} \mathbf{R}_{\mathbf{u}}^{n+1} \\ \mathbf{R}_{\phi}^{n+1} \end{bmatrix}, \tag{6.7}$$

where  $\mathbf{K}_{\mathbf{uu}}$  represents the fully discrete purely mechanical stiffness matrix,  $\mathbf{K}_{\phi\phi}$  the fully discrete matrix associated with electrostatic variable(s) and  $\mathbf{K}_{\mathbf{u}\phi}$  and  $\mathbf{K}_{\phi\mathbf{u}}$  the fully discrete electromechanical coupled matrices. The above discrete form particularised to the staggered case of (5.3) can be established as shown in Algorithm 2. Algorithm 2 in particular implies a

staggered system in which the geometry is updated incrementally, but the associated electrostatic variables are solved for iteratively. More specifically, as shown in Figure 6.1 the geometry, the mechanical and the coupling matrices are frozen during the iterative (implicit) solution of the electrostatic variables. An algorithmic representation of this staggered scheme is presented in Algorithm 2 where  $\mathbf{N}$  represents the external electrical nodal force vector. Note that an initial step for solving the mechanical variables is necessary in this case i.e.  $\mathbf{K}_{\mathbf{uu}_0^0} \mathbf{U}_{\mathbf{u}_0^0} = -\mathbf{R}_{\mathbf{u}_0^0}$  to account for Dirichlet driven problems. Since the above staggered approach requires the solution of a scalar field electric potential through solving the discretised Gauss's law, the saving in computational cost can be tremendous within its range of applicability (small strains). However as the voltage induced deformation increases a high number of increments might be needed to obtain the results of fully nonlinear monolithic approach. This staggered scheme can be termed as traction based staggered approach to electromechanics, as the electrical solution is fed into the mechanical problem through traction boundary conditions.

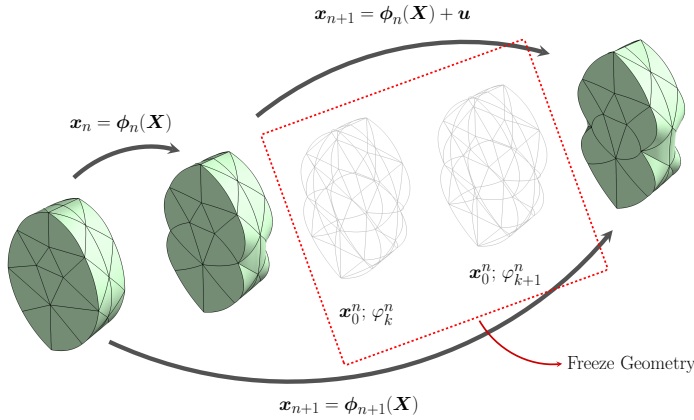


Figure 6.1: Schematic representation of the staggered incrementally linearised scheme.

---

**Algorithm 2** The incrementally linearised electromechanics solver

---

**procedure** STAGGERED SOLVER

Assemble & solve the mechanical problem  $\mathbf{K}_{\mathbf{uu}_0^0} \mathbf{U}_{\mathbf{u}_0^0} = -\mathbf{R}_{\mathbf{u}_0^0}$

**for** each increment  $n$  **do**

Compute electrostatic residual  $\hat{\mathbf{R}}_{\phi_0}^{n+1} = \mathbf{R}_{\phi_0}^{n+1} - \mathbf{K}_{\phi\mathbf{u}_0^n} \mathbf{U}_{\mathbf{u}_0^n}$

**while**  $\|\hat{\mathbf{R}}_{\phi_{k+1}}^{n+1}\| > \text{tolerance}$  **do**

Assemble & solve the electrostatic problem  $\mathbf{K}_{\phi\phi_{k+1}}^{n+1} \mathbf{U}_{\phi_{k+1}}^{n+1} = -\hat{\mathbf{R}}_{\phi_{k+1}}^{n+1}$

Compute electrostatic traction forces  $\mathbf{T}_{\phi_{k+1}}^{n+1}$

Update electrostatic residual  $\hat{\mathbf{R}}_{\phi_{k+1}}^{n+1} = \mathbf{T}_{\phi_{k+1}}^{n+1} - \mathbf{N}_{\phi_{k+1}}^{n+1}$

Accumulate mechanical residual  $\mathbf{R}_{\phi\mathbf{u}_{k+1}}^{n+1} = \mathbf{T}_{\mathbf{u}_{k+1}}^{n+1} - \mathbf{N}_{\mathbf{u}_{k+1}}^{n+1}$

**end while**

Compute the force vector  $\mathbf{F}_{\mathbf{u}\phi_0^n} = \mathbf{K}_{\mathbf{u}\phi_0^n} \mathbf{U}_{\phi_{k+1}}^{n+1}$

Solve the corrected mechanical problem  $\mathbf{K}_{\mathbf{uu}_0^n} \mathbf{U}_{\mathbf{u}_0^{n+1}} = -\mathbf{R}_{\mathbf{u}_0^n} - \mathbf{R}_{\phi\mathbf{u}_{k+1}}^{n+1} + \mathbf{F}_{\mathbf{u}\phi_0^n}$

Update the geometry  $\mathbf{x}^{n+1} = \mathbf{x}^n + \mathbf{U}_{\mathbf{u}_0^{n+1}}$

Assemble  $\mathbf{K}_{\mathbf{uu}_0^{n+1}}$ ,  $\mathbf{K}_{\mathbf{u}\phi_0^{n+1}}$  and  $\mathbf{K}_{\phi\mathbf{u}_0^{n+1}}$

Set  $n + 1$  to  $n$

**end for**

**end procedure**

---

A slightly modified version of this scheme is presented in Algorithm 3 where in this case the newly computed electric potential is used to update the coupling (off-diagonal) blocks of the coupled system and then the traction forces coming from electrical solution is computed

through this coupling sub-matrix. This approach can be termed as potential based staggered approach. In practice, the results obtained with these two approaches are not far different from each other, and hence we will not delve into discussing this aspect.

---

**Algorithm 3** The incrementally linearised electromechanics solver

---

**procedure** STAGGERED SOLVER

Assemble & solve the mechanical problem  $\mathbf{K}_{\mathbf{uu}_0}^0 \mathbf{U}_{\mathbf{u}_0}^0 = -\mathbf{R}_{\mathbf{u}_0}^0$

**for** each increment  $n$  **do**

Compute electrostatic residual  $\hat{\mathbf{R}}_{\phi_0}^{n+1} = \mathbf{R}_{\phi_0}^{n+1} - \mathbf{K}_{\phi\mathbf{u}_0}^n \mathbf{U}_{\mathbf{u}_0}^n$

**while**  $\|\hat{\mathbf{R}}_{\phi_{k+1}}^{n+1}\| > tolerance$  **do**

Assemble & solve the electrostatic problem  $\mathbf{K}_{\phi\phi_{k+1}}^{n+1} \mathbf{U}_{\phi_{k+1}}^{n+1} = -\hat{\mathbf{R}}_{\phi_{k+1}}^{n+1}$

Compute electrostatic traction forces  $\mathbf{T}_{\phi_{k+1}}^{n+1}$

Update electrostatic residual  $\hat{\mathbf{R}}_{\phi_{k+1}}^{n+1} = \mathbf{T}_{\phi_{k+1}}^{n+1} - \mathbf{N}_{\phi_{k+1}}^{n+1}$

Accumulate mechanical residual  $\mathbf{R}_{\phi\mathbf{u}_{k+1}}^{n+1} = \mathbf{T}_{\mathbf{u}_{k+1}}^{n+1} - \mathbf{N}_{\mathbf{u}_{k+1}}^{n+1}$

**end while**

Assemble  $\mathbf{K}_{\mathbf{u}\phi_0}^{n+1}$

Compute the force vector  $\mathbf{F}_{\mathbf{u}\phi_0}^{n+1} = \mathbf{K}_{\mathbf{u}\phi_0}^{n+1} \mathbf{U}_{\phi_{k+1}}^{n+1}$

Solve the corrected mechanical problem  $\mathbf{K}_{\mathbf{uu}_0}^n \mathbf{U}_{\mathbf{u}_0}^{n+1} = -\mathbf{R}_{\mathbf{u}_0}^n - \mathbf{R}_{\phi\mathbf{u}_{k+1}}^{n+1} + \mathbf{F}_{\mathbf{u}\phi_0}^{n+1}$

Update the geometry  $\mathbf{x}^{n+1} = \mathbf{x}^n + \mathbf{U}_{\mathbf{u}_0}^{n+1}$

Assemble  $\mathbf{K}_{\mathbf{uu}_0}^{n+1}$  and  $\mathbf{K}_{\phi\mathbf{u}_0}^{n+1}$

Set  $n + 1$  to  $n$

**end for**

**end procedure**

---

In the current setting, similar to our previous developments, equal order high order isoparametric finite elements are utilised to solve for the primary variables i.e.  $\{\mathbf{x}, \varphi\}$ .

## 6.3 Numerical examples

In this section a series of numerical examples for geometrically linearised electromechanics are presented. These include comparison of monolithic (nonlinear) approach with the incrementally linearised staggered approach and the range of applicability of the latter approach in actuation. Apart from these benchmark studies, a series of examples pertaining to the small deformation are showcased. We will in particular, also showcase that the current staggered approach also copes up really well with large displacement small strain problems. The finite element implementation involves equal order standard isoparametric discretisation of the electromechanical variables  $\{\mathbf{x}, \varphi\}$ , starting with at least quadratic basis functions. Unless otherwise specified, for all the examples, the curvilinear meshes are generated using the consistently linearised solid mechanics analogy presented in [254, 328], using a Mooney-Rivlin model with a Poisson's ratio of 0.45 and 10 load increments. In addition, all the analyses are carried out with the high performance domain-specific data parallel tensor contraction finite element framework **Fastor** based on the authors' previous work [251] and the massively parallel multi-frontal direct sparse solver **MUMPS** is used for the solution of system of linear equations.

### 6.3.1 An electromechanical plate with multiple holes

The objective of this example is to study the performance and the range of applicability of the staggered approach for small strain actuation and energy harvesting problems. To this end, two actuation problems are considered, based on two material models. For the first problem, the material model used is that of (5.13) with material constant given by (5.4). This problem is in particular a simple one due to the fact that electric field is a linear function of electric displacement and hence chosen for the purpose of benchmarking the staggered scheme. For the

second problem, the following stabilised convex multi-variable energy functional is considered [232]

$$\begin{aligned} W_{el,2} = & \mu_1 I_C + \mu_2 I_G - (2\mu_1 + 4\mu_2 + 12\mu_e) \ln \sqrt{C} + \frac{\lambda}{2} (\sqrt{C} - 1)^2 + \frac{1}{2\varepsilon_1} II_{D_0} + \frac{1}{2\varepsilon_2 \sqrt{C}} II_d \\ & + \mu_e \left( I_C^2 + \frac{2}{\mu_e \varepsilon_e} I_C II_d + \frac{1}{\mu_e^2 \varepsilon_e^2} II_d^2 \right), \end{aligned} \quad (6.8)$$

with material properties listed in Table 6.1. In this model the electric field and electric displace-

$\mu_1$ (Pa)	$\mu_2$ (Pa)	$\mu_e$ (Pa)	$\lambda$ (Pa)	$\varepsilon_1^{-1}$ (V <sup>2</sup> /N)	$\varepsilon_2$ (N/V <sup>2</sup> )	$\varepsilon_2$ (N/V <sup>2</sup> )
2.3e4	1.15e5	800	8e5	0	4.5 $\varepsilon_0$	1050 $\varepsilon_0$

Table 6.1: Material parameters for (6.8) with the vacuum permittivity  $\varepsilon_0 = 8.85418781 \times 10^{-12}$  (N/V<sup>2</sup>)

ment are coupled implicitly and hence this model tests the true performance of the staggered approach. The computational meshes considered are shown in Figure 6.2 together with the CAD geometry. The mesh has 3819 elements and for an interpolation degree  $p = 3$  there are 47317 points in the mesh corresponding to a total of 189268 degrees of freedom. To study

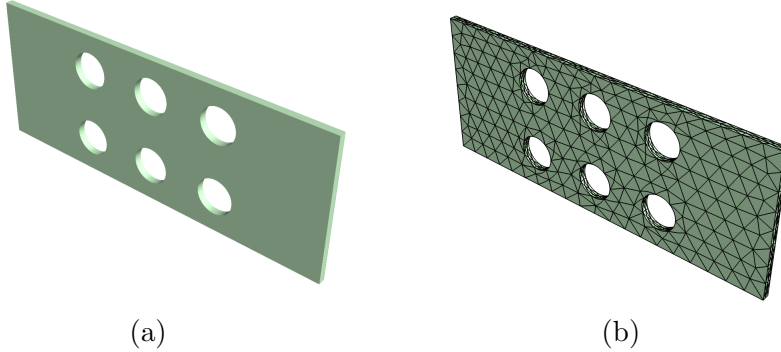


Figure 6.2: Electromechanical plate with holes a) CAD geometry and, b)  $p = 4$  curvilinear mesh

the performance of the staggered scheme the error incurred in staggered scheme is quantified relative to (fully nonlinear) monolithic approach as

$$\|e\|_{\mathcal{L}^2}^{\text{staggered}} = \left[ \frac{\|\boldsymbol{\eta}_{\text{monolithic}} - \boldsymbol{\eta}_{\text{staggered}}\|}{\|\boldsymbol{\eta}_{\text{monolithic}}\|} \right]^{\frac{1}{2}}. \quad (6.9)$$

Typically, the range of applicability of the staggered electrostrictive scheme can be determined by successively increasing the electric voltage and observing the error produced by the scheme [335]. In the current setting, the following non-dimensional quantity is chosen to quantify the increase in electric voltage

$$\mathcal{W} = \Phi / (H \sqrt{\frac{\mu}{\varepsilon}}), \quad (6.10)$$

where  $\Phi$  denotes the applied potential and  $H$  represents the plate thickness. For the ideal dielectric model  $\mu$  and  $\varepsilon$  can be related to material parameters as

$$\mu = 2(\mu_1 + \mu_2); \quad \frac{1}{\varepsilon} = \frac{1}{\varepsilon_1} + \frac{1}{\varepsilon_2}. \quad (6.11)$$

Similarly, for the stabilised material described in (6.8),  $\mu$  and  $\varepsilon$  can be found as

$$\mu = 2(\mu_1 + 2\mu_2 + 6\mu_e); \quad \frac{1}{\varepsilon} = \frac{1}{\varepsilon_1} + \frac{1}{\varepsilon_2} + \frac{12}{\varepsilon_e}. \quad (6.12)$$

The plate is clamped at the two ends along the length and the electric voltage is applied through the thickness of the plate such that  $\mathcal{W}$  increases from 0.1 to 1.0. Figure 6.3 shows the relative  $L^2$  norm of the staggered approach as function of number of increments for different values of  $\mathcal{W}$ . As can be observed, certainly as the  $\mathcal{W}$  and hence the voltage induced deformation increases, the error incurred in staggered approach increases. The convergence of the staggered approach is approximately linear for both models. Interestingly, even under the application of extremely high voltage, the results of the staggered scheme seem to converge to the results of the monolithic approach. However, opting for such high number of increments may not be computationally practical. For engineering accuracy and large scale problems, the staggered scheme pays off as it only involves an iterative solution of the Gauss's law for the scalar electric potential.

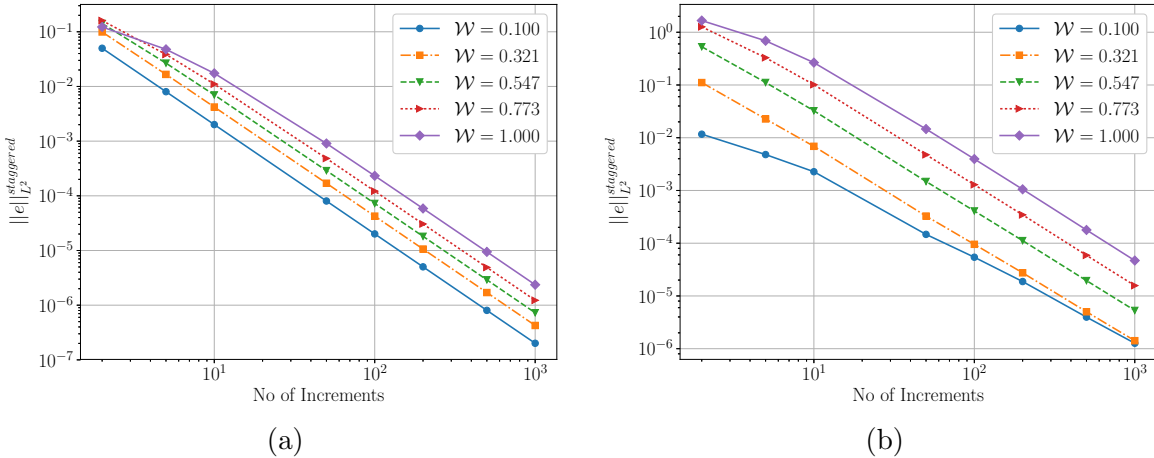


Figure 6.3: Convergence of the staggered scheme with respect to the monolithic solver as a function of increase in applied voltage quantified by  $\mathcal{W}$  as defined in (6.10)

Finally, Figure 6.4 shows the amount of voltage induced strains in the plate. Notice that despite large displacements, the strains are still small within the context of dielectric elastomers.

### 6.3.2 A simplified jelly fish undergoing voltage induced large displacement

In this section we consider, a simplified jelly fish example, modelled as half of a hollow ellipsoidal structure as shown in Figure 6.5. The geometry has a thickness of 1mm, with inner radius 49mm and outer radius 50mm, and the major axis of the ellipsoid being 250mm. An ideal dielectric elastomer is used for the analysis with  $p = 3$  for the analysis. The mesh has 97084 elements and 561954 nodes on the domain

The problem is solved by fixed the jelly fish geometry in the base and applying an electric potential of 5kV across the thickness. The problem is solved dynamically using a Newmark's Beta method using 200 time steps for 120 seconds. Figure 6.6 shows the deformation of the jelly fish through time. As can be seen from the figure, it is evident that the jelly fish is experiencing large displacements although the straining in the ellipsoid is not that massive. This confirms that the current staggered approach is capable of capturing large displacements if the strains are still small.

### 6.3.3 A self-rolling electromechanical actuator

In this section we consider a cylindrical electromechanical actuator which undergoes self-rolling under the action of electric potential. The problem is once again solved using the staggered

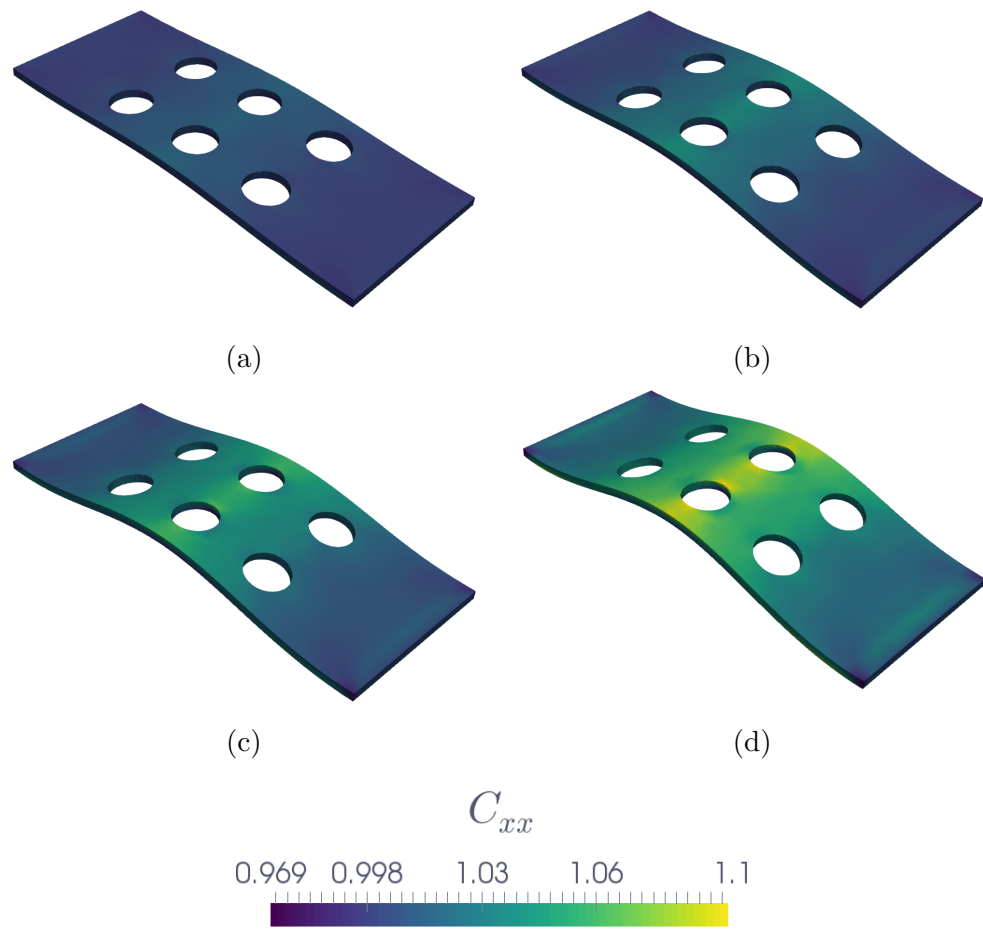
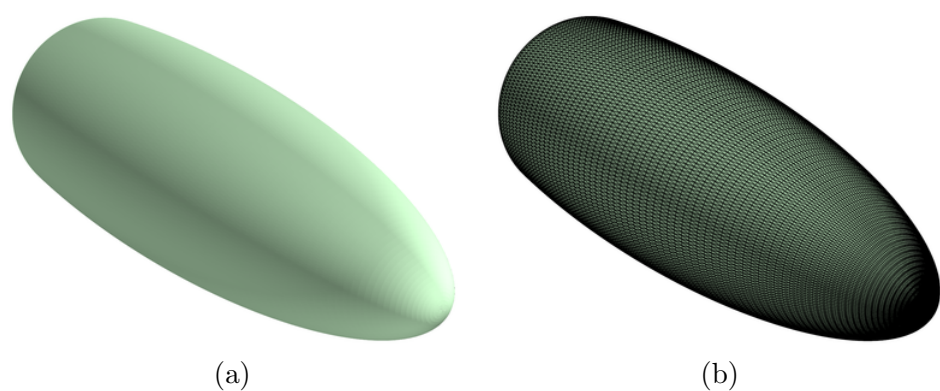
Figure 6.4: Voltage induced strains  $C_{xx}$  in electromechanical plate

Figure 6.5: Geometry and mesh of the tetrahedral ellipsoidal jelly fish

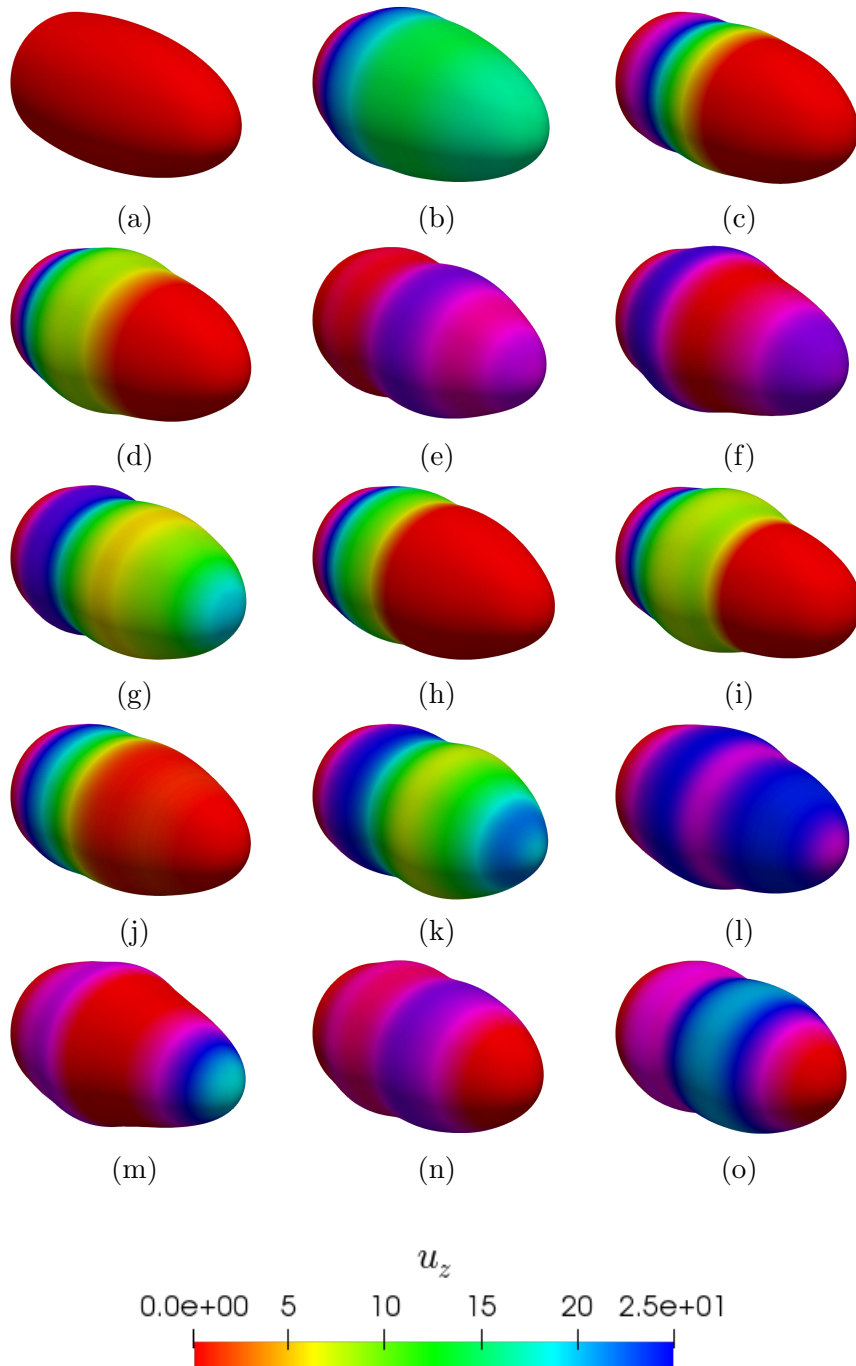


Figure 6.6: Voltage induced displacements  $u_z$  in jelly fish at time steps a) 1, b) 20, c) 40, d) 60, e) 80, f) 100, g) 120, h) 130, i) 140, j) 150, k) 160, l) 170, m) 180, n) 190, o) 200

presented in this chapter. The geometry of the cylinder is exactly the same as the cylinder considered in chapter 5, shown in Figure 5.18. We consider a  $q = 2$  hexahedral elements for this analysis.

The cylinder is fixed on all but faces except the surfaces of revolution and an electric potential of  $5 \times 10^7 \text{ V}$  is applied through the thickness. The problem is solved using the staggered approach with an ideal dielectric elastomer. The problem is once again solved dynamically with 900 time steps over 60 seconds. However, this problem is virtually designed in a particular way such that every 20 percent loading there is 5 seconds of constant loading. Figure 6.7 shows the voltage induced deformation of the cylinder using the staggered scheme. As can be observed the staggered scheme is once again to capture massive displacements induced due to applied voltage. As can be seen the maximum strain induced is only 4 percent.

## 6.4 Conclusions

A staggered scheme for geometrically linearised electromechanics based on convex multi-variable energies was presented in this chapter. The linearised variational formulation leads to symmetric Minkowski stresses without the need for further *ad-hoc* symmetrisation used in the literature. The resulting high order curvilinear finite elements used for discretisation is solved using a staggered approach such that the only the nonlinear electrostatic equations are solved iteratively. The mechanical problem is frozen during these iterations and update using either electrically induced tractions or electric potential per increment. The formulation is essentially similar in spirit to the linearised elasticity problem presented in chapter 3. Through numerical examples we have shown that the staggered scheme is able to capture large displacements as well as long as the strains induced in the components are relatively small. This is in particular very interesting, since the many problems exhibit large displacements without undergoing large strains and the computational time savings for these problems using a staggered approach is going to be significant.

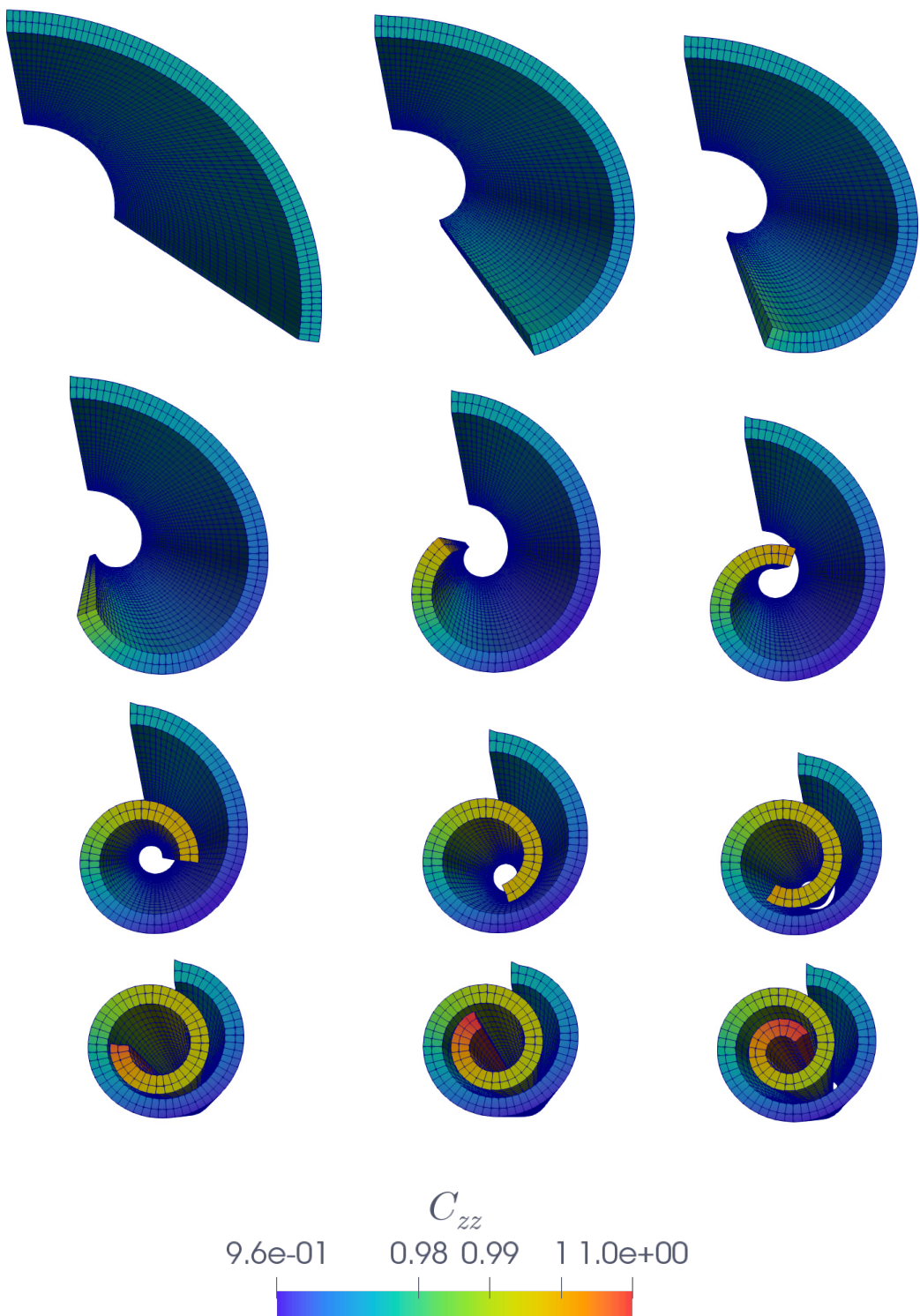


Figure 6.7: Voltage induced strains  $C_{xz}$  in electromechanical plate



# Class 3: High Order Finite Elements For Linear Piezoelectric Continua & Beams



# Chapter 7

## Linearised Electromechanics - Particularisation to Sensing and Energy Harvesting Piezoelectric Continua & Beams

### 7.1 Introduction

In this chapter, a new computational framework is introduced for the analysis of three dimensional linear piezoelectric beams and continua using  $hp$ -finite elements. Unlike existing publications on piezoelectric beams, the framework is extremely generic and suitable for static, modal and dynamic analyses; it is not restricted to either actuation or energy harvesting applications and, moreover, it can cope with any anisotropy or electric polarisation orientation. Derived from first principles, namely the fundamental equations of continuum piezoelectricity, a new set of beam balance equations is presented based on a Taylor series expansion for the displacement and electric potential across the cross section of the beam. The coupled nature of the piezoelectric phenomenon at a beam level arises via a series of mechanical (and electrical counterparts) stress and strain cross sectional area resultants. To benchmark the numerical algorithm, and in order to aid prospective researchers, a new closed-form solution is presented for the case of cantilever type systems subjected to end tip mechanical/electrical loads. To the best of the authors' knowledge, the analytical solution for this prototypical example has not been previously presented. Numerical aspects of the  $hp$ -discretisation are investigated including the exponential convergence of the  $hp$ -refinements and the consideration of linear or quadratic electric potential expansions across the cross section of the beam.

It should be noted that much of the work in this chapter is based on the authors work on linear theory of piezoelectricity presented in [250]. The structure of the chapter is as follows. Section 7.2 describes the balance equations of electromechanics and in Section 7.3 we introduce the kinematics and electrostatics of three-dimensional piezoelectric beams. Section 7.4 describes the variational formulation from which the mechanical and electrical cross sectional balance equations are obtained in Section 7.5. Analytical solutions for planar piezoelectric beams are presented in Section 7.6 and the  $hp$ -finite element discretisation of the variational formulation is presented in Section 7.7. Finally, in Section 7.8 a series of numerical simulations ranging from static to modal and dynamic analyses are reported.

### 7.2 Balance equations of electromechanics

Let  $\Omega \subset \mathbb{R}^3$  be a bounded contractible domain occupied by a continuum during the time interval  $[0, T]$  and  $\Gamma$  be its boundary, equipped with a unit outward normal  $\mathbf{n}$ , as shown in

Figure 7.1. In this case, the static Faraday and Gauss laws can be summarised as follows

$$\operatorname{curl} \mathbf{E} = \mathbf{0} \quad \text{and} \quad \operatorname{div} \mathbf{D} + \rho^e = 0 \quad \text{in } \Omega \times [0, T], \quad (7.1)$$

where  $\mathbf{E}$  denotes the electric field intensity vector,  $\mathbf{D}$  is the electric displacement vector and  $\rho^e$  is the volume charge density. As  $\Omega$  is a contractible domain, the electric field vector  $\mathbf{E}$  can be reformulated as  $\mathbf{E} = -\nabla\phi$ , where  $\phi$  is a scalar potential field. Dirichlet and Neumann boundary conditions can then be introduced as

$$\phi = \bar{\psi} \quad \text{on} \quad \Gamma^\psi \times [0, T], \quad (7.2a)$$

$$\mathbf{D} \cdot \mathbf{n} = \omega \quad \text{on} \quad \Gamma^D \times [0, T]. \quad (7.2b)$$

where  $\Gamma = \Gamma^D \cup \Gamma^\psi$  and  $\Gamma^D \cap \Gamma^\psi = \emptyset$ . In the context of small deformations, the motion of the continuum can be defined by a displacement field  $\mathbf{u} : \Omega \times [0, T] \rightarrow \mathbb{R}^3$ , such that  $(\mathbf{x}, t) \mapsto \mathbf{u}(\mathbf{x}, t)$ , where  $\mathbf{x} \in \Omega$  represents a material point and  $t \in [0, T]$  the time. The conservation of linear momentum equation is defined as

$$\operatorname{div} \boldsymbol{\sigma} + \rho \mathbf{b} = \rho \ddot{\mathbf{u}} \quad \text{in } \Omega \times [0, T], \quad (7.3)$$

where  $\rho$  is the density of the continuum,  $\boldsymbol{\sigma}$  is the symmetric (conservation of angular momentum) Cauchy stress tensor,  $\mathbf{b}$  is a body force per unit of mass and a superimposed dot (double dot) indicates partial (double) differentiation with respect to time (e.g.  $\dot{\cdot} := \frac{\partial}{\partial t}$  and  $\ddot{\cdot} := \frac{\partial^2}{\partial t^2}$ ). Dirichlet, Neumann and initial conditions can be introduced as

$$\mathbf{u} = \bar{\mathbf{u}} \quad \text{on} \quad \Gamma^u \times [0, T], \quad (7.4a)$$

$$\boldsymbol{\sigma} \mathbf{n} = \mathbf{t} \quad \text{on} \quad \Gamma^\sigma \times [0, T], \quad (7.4b)$$

$$\mathbf{u} = \mathbf{u}_0 \quad \text{in} \quad \bar{\Omega} \times 0, \quad (7.4c)$$

$$\dot{\mathbf{u}} = \dot{\mathbf{u}}_0 \quad \text{in} \quad \bar{\Omega} \times 0, \quad (7.4d)$$

where  $\Gamma = \Gamma^\sigma \cup \Gamma^u$  and  $\Gamma^\sigma \cap \Gamma^u = \emptyset$ . The coupled electro-mechanical initial boundary value problem, defined by equations (7.1) to (7.4), must be complemented with two closure equations related to the electro-mechanical nature of the continuum. For a conservative material, the closure equations can be derived from the enthalpy density of the system  $\Psi$  defined in terms of the electric field vector  $\mathbf{E}$  and the small strain tensor  $\boldsymbol{\varepsilon}$  as follows

$$\boldsymbol{\sigma}(\boldsymbol{\varepsilon}, \mathbf{E}) := \frac{\partial \Psi(\boldsymbol{\varepsilon}, \mathbf{E})}{\partial \boldsymbol{\varepsilon}} \quad \text{and} \quad \mathbf{D}(\boldsymbol{\varepsilon}, \mathbf{E}) := -\frac{\partial \Psi(\boldsymbol{\varepsilon}, \mathbf{E})}{\partial \mathbf{E}}, \quad \boldsymbol{\varepsilon} := \frac{1}{2} (\nabla \mathbf{u} + \nabla \mathbf{u}^T), \quad (7.5)$$

expressing the total Cauchy stress tensor  $\boldsymbol{\sigma}$  and the electric displacement vector  $\mathbf{D}$  in terms of the electric field  $\mathbf{E}$  and the small strain tensor  $\boldsymbol{\varepsilon}$ . A variety of electro-mechanical constitutive models are available in the literature defined in terms of different enthalpy expressions [111, 142]. In the case of linear piezoelectricity,  $\boldsymbol{\sigma}$  and  $\mathbf{D}$  obtained this way render algebraic summations of mechanical  $(\cdot)^m$  and electrical  $(\cdot)^e$  components.

The electric displacement  $\mathbf{D}$  can be expanded as

$$\mathbf{D} = \mathbf{D}^m + \mathbf{D}^e; \quad \mathbf{D}^m := \mathcal{P} : \boldsymbol{\varepsilon}, \quad \mathbf{D}^e := \boldsymbol{\epsilon} \mathbf{E}, \quad (7.6)$$

where  $\boldsymbol{\epsilon}$  is the symmetric second order dielectric permittivity tensor and  $\mathcal{P}$  is the third order piezoelectric tensor verifying  $[\mathcal{P}]_{ijk} = [\mathcal{P}]_{ikj}$ . Analogously, the total Cauchy stress tensor  $\boldsymbol{\sigma}$  can be decomposed additively as

$$\boldsymbol{\sigma} = \boldsymbol{\sigma}^m + \boldsymbol{\sigma}^e; \quad \boldsymbol{\sigma}^m := \mathcal{C} : \boldsymbol{\varepsilon}, \quad \boldsymbol{\sigma}^e := -\mathbf{E} \cdot \mathcal{P}. \quad (7.7)$$

Piezoelectric materials exhibit anisotropic behaviour and, hence,  $\mathcal{C}$  is the general fourth order anisotropic elasticity tensor satisfying  $[\mathcal{C}]_{ijkl} = [\mathcal{C}]_{jikl} = [\mathcal{C}]_{ijlk} = [\mathcal{C}]_{klij}$ . It is important to emphasise that the conservation of angular momentum requires the symmetry of  $\boldsymbol{\sigma}$  but not

of its individual components  $\boldsymbol{\sigma}^m$  and  $\boldsymbol{\sigma}^e$ . Finally, the initial boundary value problem of the coupled problem is defined by equations (7.1)-(7.4), (7.6)-(7.7).

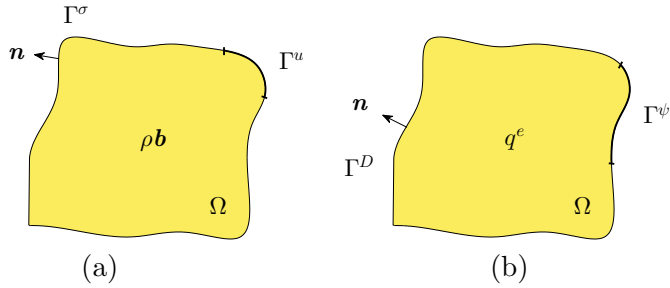


Figure 7.1: Decomposition of (a) Mechanical Boundary  $\Gamma = \Gamma^\sigma \cup \Gamma^u$  and  $\Gamma^\sigma \cap \Gamma^u = \emptyset$  and (b) Electrical Boundary  $\Gamma = \Gamma^D \cup \Gamma^\psi$  and  $\Gamma^D \cap \Gamma^\psi = \emptyset$

## 7.3 Kinematics and electrostatics of three-dimensional piezo-electric beams

### 7.3.1 Kinematics

Let us consider the motion of a beam  $\Omega \subset \mathbb{R}^3$  as shown in Figure 7.2 [57]. The beam in the undeformed configuration has a straight axis of length  $l$  and is completely characterised with an orthonormal reference triad  $\{e_1, e_2, e_3\}$ , where  $e_3$  is parallel to the beam axis and  $\{e_\alpha\}(\alpha = 1, 2)$  lie in the plane which defines the cross sectional area  $A$  (with boundary  $\partial A$ ) of the beam  $\Omega = A \times l^1$ . Assuming for simplicity that this reference frame (placed at  $[0, 0, x_3]^T$ ) coincides with the global one (placed at  $[0, 0, 0]^T$ ), as shown in Figure 7.2, the beam current configuration  $\mathbf{x} = [x_1, x_2, x_3]^T$  can be defined through a mapping  $\varphi : \Omega \times [0, T] \rightarrow \mathbb{R}^3$  as

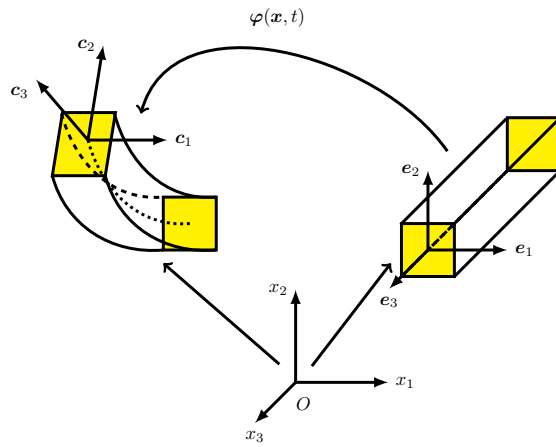


Figure 7.2: Motion of beam in  $\mathbb{R}^3$ . The initial orthonormal triad  $\{e_1, e_2, e_3\}$  transforms to the orthonormal triad  $\{c_1, c_2, c_3\}$ .

$$(\mathbf{x}, t) \mapsto \varphi(\mathbf{x}, t) = x_3 e_3 + \mathbf{w}(x_3, t) + \boldsymbol{\Lambda}(x_3, t) \mathbf{p}(x_1, x_2), \quad (7.8)$$

---

<sup>1</sup>Throughout the remainder of the chapter, any Greek indices will be assumed to vary in the integer interval [1,2] and Latin indices to vary in the integer interval [1,2,3].

where  $\mathbf{p}(x_1, x_2) := x_\alpha \mathbf{e}_\alpha$  is the position vector of a material point within the cross section  $A$  with respect to the origin of the triad  $\{\mathbf{e}_1, \mathbf{e}_2, \mathbf{e}_3\}$ <sup>2</sup>,  $\mathbf{w}(x_3, t)$  is the displacement vector of the reference triad origin and  $\boldsymbol{\Lambda}(x_3, t)$  is an orthogonal tensor evaluated at the triad origin and representing the transformation of the reference orthonormal triad  $\{\mathbf{e}_1, \mathbf{e}_2, \mathbf{e}_3\}$  to a new orthonormal triad  $\{\mathbf{c}_1, \mathbf{c}_2, \mathbf{c}_3\}$  according to  $\mathbf{c}_i = \boldsymbol{\Lambda} \mathbf{e}_i$ . It is well known, this rotation tensor  $\boldsymbol{\Lambda}$  can be obtained in terms of the exponential mapping of a skew symmetric second order tensor  $\hat{\boldsymbol{\theta}}$  and can be expanded in the form

$$\boldsymbol{\Lambda} = \exp(\hat{\boldsymbol{\theta}}) = \mathbf{I} + \hat{\boldsymbol{\theta}} + \frac{1}{2!} \hat{\boldsymbol{\theta}}^2 + \frac{1}{3!} \hat{\boldsymbol{\theta}}^3 + \dots \text{ as } \|\hat{\boldsymbol{\theta}}\| \rightarrow 0 \quad (7.9)$$

where  $\|\cdot\|$  denotes the standard Euclidean vector norm and  $\hat{\boldsymbol{\theta}}$  is the skew-symmetric tensor associated with  $\boldsymbol{\theta}$  [126]. Note that for any arbitrary vector  $\mathbf{v} \in \mathbb{R}^3$  the following identity is fulfilled

$$\boldsymbol{\theta} \times \mathbf{v} = \hat{\boldsymbol{\theta}} \mathbf{v}. \quad (7.10)$$

In the case of small rotations and neglecting high order terms, the rotation tensor can be approximated as  $\boldsymbol{\Lambda} \simeq \mathbf{I} + \hat{\boldsymbol{\theta}}$  yielding a final displacement field  $\mathbf{u} : \Omega \times [0, T] \rightarrow \mathbb{R}^3$  (refer to equation (7.8)) defined as

$$(\mathbf{x}, t) \mapsto \mathbf{u}(\mathbf{x}, t) = \mathbf{w}(x_3, t) + \boldsymbol{\theta}(x_3, t) \times \mathbf{p}(x_1, x_2), \quad (7.11)$$

where the vectors  $\mathbf{w} = w_i \mathbf{e}_i$  and  $\boldsymbol{\theta} = \theta_i \mathbf{e}_i$  are collectively called the generalised beam displacements. Expression (7.11) represents a time dependent affine mapping for any material point contained within the cross sectional area  $A$  of the beam. Noticing that  $\nabla \mathbf{u} = \frac{\partial \mathbf{u}}{\partial x_i} \otimes \mathbf{e}_i$  and  $\frac{\partial \mathbf{p}}{\partial x_\alpha} = \mathbf{e}_\alpha$ , the small strain tensor  $\boldsymbol{\epsilon}$  can be rewritten as

$$\boldsymbol{\epsilon} = \frac{1}{2} \left[ (\boldsymbol{\epsilon}^m + \boldsymbol{\kappa}^m \times \mathbf{p}) \otimes \mathbf{e}_3 + \mathbf{e}_3 \otimes (\boldsymbol{\epsilon}^m + \boldsymbol{\kappa}^m \times \mathbf{p}) \right], \quad (7.12)$$

where

$$\boldsymbol{\epsilon}^m := \frac{\partial \mathbf{w}}{\partial x_3} + \mathbf{e}_3 \times \boldsymbol{\theta}, \quad \boldsymbol{\kappa}^m := \frac{\partial \boldsymbol{\theta}}{\partial x_3}, \quad (7.13)$$

are called the strain resultants of the linear beam model, which characterise translational deformation and rotational deformation, respectively.

### 7.3.2 Electrical Mapping

Similar to the previous section, we postulate a Taylor series expansion for the electric potential  $\phi : \Omega \times [0, T] \rightarrow \mathbb{R}$  in the form

$$(\mathbf{x}, t) \mapsto \phi(\mathbf{x}) = \phi|_{(0,0,x_3,t)} + \mathbf{p}(x_1, x_2) \cdot \nabla \phi|_{(0,0,x_3,t)} + \frac{1}{2} \mathbf{p}(x_1, x_2) \cdot \mathbf{H}_\phi|_{(0,0,x_3,t)} \mathbf{p}(x_1, x_2) + \dots \text{ as } \|\mathbf{p}(x_1, x_2)\| \rightarrow 0 \quad (7.14)$$

in terms of the time dependent electric potential  $\phi$ , its vector gradient  $\nabla \phi$  and its second order tensor Hessian  $\mathbf{H}_\phi$  defined at the reference triad origin  $[0, 0, x_3]^T$ . It is possible to neglect high order terms  $\mathcal{O}(\|\mathbf{p}(x_1, x_2)\|^3)$  by assuming that the spatial variation of the electric potential in the cross section of the beam is sufficiently well defined via  $\nabla \phi$  and  $\mathbf{H}_\phi$ , in line with references [39, 166]. Notice that any lower order electric potential interpolation across the section of the beam would yield a non-varying electric field vector  $\mathbf{E}$  across  $A$ . With this assumption in place, we can introduce an approximate electric potential field  $\psi : \Omega \times [0, T] \rightarrow \mathbb{R}$  defined as

$$(\mathbf{x}, t) \mapsto \psi(\mathbf{x}, t) := \phi(x_3, t) + \mathbf{p}(x_1, x_2) \cdot \boldsymbol{\beta}(x_3, t) + \frac{1}{2} \mathbf{p}(x_1, x_2) \cdot \boldsymbol{\gamma}(x_3, t) \mathbf{p}(x_1, x_2), \quad (7.15)$$

---

<sup>2</sup>Note that unless otherwise stated, Einstein's summation convention will be assumed.

where  $\psi$  represents a parabolic expansion across the cross sectional area  $A$  of the beam, completely defined in terms of  $\phi$ ,  $\beta$  and  $\gamma$ , namely scalar, vector and symmetric second order tensor beam axis-varying functions. It is important to remark that the only approximation for the distribution of the electric potential is established across the section of the beam (see Figure 7.3). The variation along the beam axis remains without any approximation.

The electric field vector  $\mathbf{E}$  can now be obtained by computing the gradient of the newly introduced electric potential  $\psi$  as  $\mathbf{E} := -\nabla\psi$  yielding (refer to equation (7.15)), after some algebraic manipulation

$$\mathbf{E} = -\epsilon^e - (\mathbf{e}_3 \otimes \mathbf{p})\kappa^e - \mathbf{V} : \varsigma^e - \mathbf{W} : \gamma, \quad (7.16)$$

where

$$\epsilon^e := \frac{\partial\phi}{\partial x_3} \mathbf{e}_3 + \beta, \quad \kappa^e := \frac{\partial\beta}{\partial x_3}, \quad \varsigma^e := \frac{\partial\gamma}{\partial x_3}, \quad (7.17)$$

with the third order tensors  $\mathbf{V}$  and  $\mathbf{W}$  defined by

$$\mathbf{V} := \mathbf{e}_3 \otimes \frac{1}{2}(\mathbf{p} \otimes \mathbf{p}), \quad \mathbf{W} := \mathbf{e}_\alpha \otimes \frac{1}{2}(\mathbf{p} \otimes \mathbf{e}_\alpha + \mathbf{e}_\alpha \otimes \mathbf{p}). \quad (7.18)$$

Considering equation (7.16), it is interesting to notice the similarities with the definition of the small strain tensor  $\boldsymbol{\epsilon}$  (7.12). Notice how the first two terms on the right hand side of equation (7.16) stem from the linear contribution in (7.15) (as in formula (7.12)) whereas the last two terms stem from the quadratic contribution in (7.15).

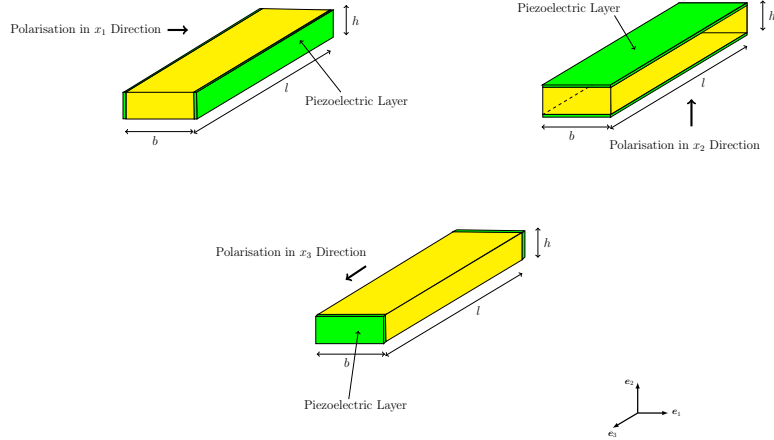


Figure 7.3: Electrostatics of a three-dimensional piezoelectric beam

The new initial boundary value problem, adapted to a three-dimensional beam problem, is then defined by equations (7.1-7.7) and (7.11,7.15), which combine the governing equations of both elastodynamics and electrostatics, initial and boundary conditions, the coupling electro-mechanical equations for  $\sigma$  and  $\mathbf{D}$ , the beam kinematics assumption  $\mathbf{u}$  and the electric potential spatial distribution  $\psi$ . Notice that the initial and boundary conditions must be compatible with the assumptions for the beam kinematics and the electric potential spatial distribution. The variables of the resulting electromechanical beam model in a general three-dimensional beam problem are  $\{\mathbf{w}, \boldsymbol{\theta}, \phi, \beta, \gamma\}$  defined in  $l \times [0, T]$ .

## 7.4 Variational formulation

In order to establish the variational formulation of the problem, the following spaces of admissible trial functions  $\mathbf{u}$  and  $\psi$  are considered:

$$\mathcal{V}_{\bar{\mathbf{u}}}^{\mathbf{u}} := \{\mathbf{u} \mid \mathbf{u} := \mathbf{w} + \boldsymbol{\theta} \times \mathbf{p}, \quad \mathbf{u} = \bar{\mathbf{u}} \text{ on } \Gamma^u \times [0, T]\}, \quad (7.19)$$

$$\mathcal{V}_{\bar{\psi}}^{\psi} := \left\{ \psi \mid \psi := \phi + \mathbf{p} \cdot \boldsymbol{\beta} + \frac{1}{2} \mathbf{p} \cdot \boldsymbol{\gamma} \cdot \mathbf{p}, \quad \psi = \bar{\psi} \text{ on } \Gamma^{\psi} \times [0, T] \right\}, \quad (7.20)$$

with the component functions  $\{(\mathbf{w} \cdot \mathbf{e}_i), (\boldsymbol{\theta} \cdot \mathbf{e}_i), \phi, (\boldsymbol{\beta} \cdot \mathbf{e}_{\alpha}), (\mathbf{e}_{\alpha} \cdot \boldsymbol{\gamma} \mathbf{e}_{\beta})\} \in H^1(\Omega)$ . Following a standard variational methodology [111, 142], the variational form (virtual work) of the initial boundary value problem is given as:

Find  $(\mathbf{u}, \psi) \in \mathcal{V}_{\bar{\mathbf{u}}}^{\mathbf{u}} \times \mathcal{V}_{\bar{\psi}}^{\psi}$  such that

$$\delta W(\mathbf{u}, \psi; \delta \mathbf{u}, \delta \psi) := \delta W_{iner} + \delta W_{int}^m + \delta W_{int}^e - \delta W_{ext}^m - \delta W_{ext}^e = 0, \quad (7.21)$$

for all  $(\delta \mathbf{u}, \delta \psi) \in \mathcal{V}_0^{\mathbf{u}} \times \mathcal{V}_0^{\psi}$  where

$$\delta W_{iner} := \int_{\Omega} \rho \ddot{\mathbf{u}} \cdot \delta \mathbf{u} \, d\Omega, \quad (7.22a)$$

$$\delta W_{int}^m := \int_{\Omega} \boldsymbol{\sigma} : \delta \boldsymbol{\epsilon} \, d\Omega, \quad (7.22b)$$

$$\delta W_{ext}^m := \int_{\Omega} \rho \mathbf{b} \cdot \delta \mathbf{u} \, d\Omega + \int_{\Gamma^{\sigma}} \mathbf{t} \cdot \delta \mathbf{u} \, d\Gamma, \quad (7.22c)$$

$$\delta W_{int}^e := - \int_{\Omega} \mathbf{D} \cdot \delta \mathbf{E} \, d\Omega, \quad (7.22d)$$

$$\delta W_{ext}^e := \int_{\Omega} \rho^e \delta \psi \, d\Omega + \int_{\Gamma^D} \omega \delta \psi \, d\Gamma, \quad (7.22e)$$

represent the different contributions (e.g. inertial, internal, external, mechanical, electrical) to the total virtual work and

$$\delta \boldsymbol{\epsilon} = \frac{1}{2} \left( \nabla \delta \mathbf{u} + (\nabla \delta \mathbf{u})^T \right), \quad \delta \mathbf{E} = -\nabla \delta \psi. \quad (7.23)$$

Substituting the expressions for  $\delta \mathbf{u}$  (7.19) and  $\delta \psi$  (7.20) into equation (7.23) results in

$$\delta \boldsymbol{\epsilon} = \frac{1}{2} \left[ (\delta \boldsymbol{\epsilon}^m + \delta \boldsymbol{\kappa}^m \times \mathbf{p}) \otimes \mathbf{e}_3 + \mathbf{e}_3 \otimes (\delta \boldsymbol{\epsilon}^m + \delta \boldsymbol{\kappa}^m \times \mathbf{p}) \right], \quad (7.24a)$$

$$\delta \mathbf{E} = -\delta \boldsymbol{\epsilon}^e - (\mathbf{e}_3 \otimes \mathbf{p}) \delta \boldsymbol{\kappa}^e - \boldsymbol{\mathcal{V}} : \delta \boldsymbol{\varsigma}^e - \boldsymbol{\mathcal{W}} : \delta \boldsymbol{\gamma}, \quad (7.24b)$$

where

$$\delta \boldsymbol{\epsilon}^m := \frac{\partial \delta \mathbf{w}}{\partial x_3} + \mathbf{e}_3 \times \delta \boldsymbol{\theta}, \quad \delta \boldsymbol{\kappa}^m := \frac{\partial \delta \boldsymbol{\theta}}{\partial x_3}, \quad (7.25a)$$

$$\delta \boldsymbol{\epsilon}^e := \frac{\partial \delta \phi}{\partial x_3} \mathbf{e}_3 + \delta \boldsymbol{\beta}, \quad \delta \boldsymbol{\kappa}^e := \frac{\partial \delta \boldsymbol{\beta}}{\partial x_3}, \quad \delta \boldsymbol{\varsigma}^e := \frac{\partial \delta \boldsymbol{\gamma}}{\partial x_3}, \quad (7.25b)$$

represent the virtual mechanical and electrical beam strains.

Substituting the expressions for  $\mathbf{u}$  (7.11) and  $\delta \mathbf{u}$  (7.19) into (7.22a) yields (after integration over the cross sectional area  $A$ ) the inertial virtual work

$$\delta W_{iner} = \int_l \left[ \delta \mathbf{w} \cdot \left( \mathbf{A}_D \ddot{\mathbf{w}} + \mathbf{S}_D \ddot{\boldsymbol{\theta}} \right) + \delta \boldsymbol{\theta} \cdot \left( \mathbf{S}_D^T \ddot{\mathbf{w}} + \mathbf{I}_D \ddot{\boldsymbol{\theta}} \right) \right] dx_3, \quad (7.26)$$

where

$$\mathbf{A}_D := \int_A \rho \mathbf{I} dA, \quad \mathbf{S}_D := \int_A \rho \hat{\mathbf{p}} \, dA, \quad \mathbf{I}_D := \int_A \rho \hat{\mathbf{p}} \hat{\mathbf{p}}^T dA, \quad (7.27)$$

represent the mass  $\mathbf{A}_D$ , first area moment  $\mathbf{S}_D$  and second area moment  $\mathbf{I}_D$  tensors of the cross sectional area  $A$ . Notice that  $\hat{\mathbf{p}}$  represents the skew symmetric tensor associated with the position vector  $\mathbf{p}$ . When considering a reference frame whose origin coincides with the centre of mass of the cross sectional area  $A$ , then  $\mathbf{S}_D = \mathbf{0}$ . Moreover, if the reference frame is aligned along the so-called principal directions, the second area moment tensor  $\mathbf{I}_D$  becomes diagonal.

Analogously, substituting the expression for  $\delta\epsilon$  (7.24a) into (7.22b) yields (after integration over the cross sectional area  $A$ ) the internal mechanical virtual work

$$\delta W_{int}^m = \int_l [\delta\epsilon^m \cdot \mathbf{Q}^m + \delta\kappa^m \cdot \mathbf{M}^m] dx_3, \quad (7.28)$$

with

$$\mathbf{Q}^m := \int_A \boldsymbol{\sigma} \mathbf{e}_3 dA, \quad \mathbf{M}^m := \int_A \mathbf{p} \times (\boldsymbol{\sigma} \mathbf{e}_3) dA. \quad (7.29)$$

In above equation (7.28),  $\mathbf{Q}^m$  represents the internal shear/axial force whereas  $\mathbf{M}^m$  represents the internal bending/torsion moment.

Substituting the expression for  $\delta\mathbf{u}$  (7.19) into (7.22c) yields (after integration over the cross sectional area  $A$ ) the mechanical external virtual work

$$\delta W_{ext}^m = [\delta\mathbf{w} \cdot \mathbf{Q}^m + \delta\theta \cdot \mathbf{M}^m]_0^l + \int_l [\delta\mathbf{w} \cdot \mathbf{q}^m + \delta\theta \cdot \mathbf{m}^m] dx_3, \quad (7.30)$$

where

$$\mathbf{q}^m := \int_A \rho \mathbf{b} dA + \int_{\partial A} \mathbf{t} d\Gamma, \quad \mathbf{m}^m := \int_A (\mathbf{p} \times \rho \mathbf{b}) dA + \int_{\partial A} (\mathbf{p} \times \mathbf{t}) d\Gamma. \quad (7.31)$$

In above equations (7.30) and (7.31),  $\mathbf{q}^m$  and  $\mathbf{m}^m$  represent a possible external distributed force and moment, respectively, acting along the beam axis. The first term in squared brackets on the right hand side of equation (7.30) represents mechanical actions (force and moment) applied at both ends of the beam, namely  $x_3 = 0$  and  $x_3 = l$ .

From the electrical point of view, substituting the expression for  $\delta\mathbf{E}$  (7.24b) into (7.22d) yields (after integration over the cross sectional area  $A$ ) the internal electrical virtual work

$$\delta W_{int}^e = \int_l [\delta\epsilon^e \cdot \mathbf{Q}^e + \delta\kappa^e \cdot \mathbf{M}^e + \delta\zeta^e : \mathbf{O}^e + \delta\gamma : \mathbf{P}^e] dx_3, \quad (7.32)$$

where

$$\mathbf{Q}^e := \int_A \mathbf{D} dA, \quad \mathbf{M}^e := \int_A (\mathbf{D} \cdot \mathbf{e}_3) \mathbf{p} dA, \quad (7.33a)$$

$$\mathbf{P}^e := \int_A \mathbf{D} \cdot \mathbf{W} dA, \quad \mathbf{O}^e := \int_A \mathbf{D} \cdot \mathbf{V} dA. \quad (7.33b)$$

In above equations (7.32) and (7.33a), it is very interesting to observe the similarities between  $\mathbf{Q}^e$  and  $\mathbf{M}^e$  and their mechanical counterparts (7.29), namely  $\mathbf{Q}^m$  and  $\mathbf{M}^m$ , respectively. In addition, due to the quadratic nature of the electric potential distribution, two extra second order tensors arise, that is  $\mathbf{P}^e$  and  $\mathbf{O}^e$  expressed in terms of the third order tensors  $\mathbf{W}$  and  $\mathbf{V}$  already defined in (7.18).

Finally, substituting the expression for  $\delta\psi$  (7.20) into (7.22e) yields (after integration over the cross sectional area  $A$ ) the electrical external virtual work as

$$\delta W_{ext}^e = [\delta\phi (\mathbf{Q}^e \cdot \mathbf{e}_3) + \delta\beta \cdot \mathbf{M}^e + \delta\gamma : \mathbf{O}^e]_0^l + \int_l [\delta\phi q^e + \delta\beta \cdot \mathbf{m}^e + \delta\gamma : \mathbf{o}^e] dx_3, \quad (7.34)$$

where

$$q^e := \int_A \rho^e dA + \int_{\partial A} \omega d\Gamma, \quad (7.35a)$$

$$\mathbf{m}^e := \int_A \rho^e \mathbf{p} dA + \int_{\partial A} \omega \mathbf{p} d\Gamma, \quad (7.35b)$$

$$\mathbf{o}^e := \int_A \frac{\rho^e}{2} (\mathbf{p} \otimes \mathbf{p}) dA + \int_{\partial A} \frac{\omega}{2} (\mathbf{p} \otimes \mathbf{p}) d\Gamma. \quad (7.35c)$$

Again, it is interesting to note the similarities between the above expressions  $q^e$ ,  $\mathbf{m}^e$  (7.35) and those of  $\mathbf{q}^m$ ,  $\mathbf{m}^m$  (7.31). In above equation (7.34),  $q^e$ ,  $\mathbf{m}^e$  and  $\mathbf{o}^e$  represent possible

distributed electrical effects per unit of length. Moreover,  $(\mathbf{Q}^e \cdot \mathbf{e}_3)$ ,  $\mathbf{M}^e$  and  $\mathbf{O}^e$  represent electrical actions applied at both ends of the beam, namely  $x_3 = 0$  and  $x_3 = L$ .

For completeness, the final virtual work expression characterising the behaviour of the piezoelectric beam can be written as

Find  $(\mathbf{u}, \psi) \in \mathcal{V}_{\mathbf{u}}^{\mathbf{u}} \times \mathcal{V}_{\psi}^{\psi}$  such that

$$\delta W := \delta W_{iner} + \delta W_{int} - \delta W_{ext} = 0, \quad (7.36)$$

for all  $(\delta \mathbf{u}, \delta \psi) \in \mathcal{V}_{\mathbf{0}}^{\mathbf{u}} \times \mathcal{V}_0^{\psi}$  where

$$\delta W_{iner} = \int_l [\delta \mathbf{w} \cdot (\mathbf{A}_D \ddot{\mathbf{w}} + \mathbf{S}_D \ddot{\boldsymbol{\theta}}) + \delta \boldsymbol{\theta} \cdot (\mathbf{S}_D^T \ddot{\mathbf{w}} + \mathbf{I}_D \ddot{\boldsymbol{\theta}})] dx_3, \quad (7.37a)$$

$$\begin{aligned} \delta W_{int} &= \int_l [\delta \boldsymbol{\epsilon}^m \cdot \mathbf{Q}^m + \delta \boldsymbol{\kappa}^m \cdot \mathbf{M}^m] dx_3 \\ &\quad + \int_l [\delta \boldsymbol{\epsilon}^e \cdot \mathbf{Q}^e + \delta \boldsymbol{\kappa}^e \cdot \mathbf{M}^e + \delta \boldsymbol{\varsigma}^e : \mathbf{P}^e + \delta \boldsymbol{\gamma} : \mathbf{O}^e] dx_3, \end{aligned} \quad (7.37b)$$

$$\begin{aligned} \delta W_{ext} &= [\delta \mathbf{w} \cdot \mathbf{Q}^m + \delta \boldsymbol{\theta} \cdot \mathbf{M}^m]_0^l + \int_l [\delta \mathbf{w} \cdot \mathbf{q}^m + \delta \boldsymbol{\theta} \cdot \mathbf{m}^m] dx_3 \\ &\quad + [\delta \phi(\mathbf{Q}^e \cdot \mathbf{e}_3) + \delta \boldsymbol{\beta} \cdot \mathbf{M}^e + \delta \boldsymbol{\gamma} : \mathbf{O}^e]_0^l + \int_l [\delta \phi q^e + \delta \boldsymbol{\beta} \cdot \mathbf{m}^e + \delta \boldsymbol{\gamma} : \mathbf{o}^e] dx_3. \end{aligned} \quad (7.37c)$$

## 7.5 Mechanical and electrical cross sectional balance equations

### 7.5.1 Beam balance equations

As it is well known in standard beam theory [126], further manipulation of the above variational form (7.36)-(7.37) can lead to the so-called beam balance equations, which are indeed written as,

$$\frac{\partial \mathbf{Q}^m}{\partial x_3} + \mathbf{q}^m = \mathbf{A}_D \ddot{\mathbf{w}} + \mathbf{S}_D \ddot{\boldsymbol{\theta}}, \quad \text{in } l \times [0, T], \quad (7.38a)$$

$$\frac{\partial \mathbf{M}^m}{\partial x_3} - \mathbf{Q}^m \times \mathbf{e}_3 + \mathbf{m}^m = \mathbf{S}_D^T \ddot{\mathbf{w}} + \mathbf{I}_D \ddot{\boldsymbol{\theta}}, \quad \text{in } l \times [0, T], \quad (7.38b)$$

$$\frac{\partial (\mathbf{Q}^e \cdot \mathbf{e}_3)}{\partial x_3} + q^e = 0, \quad \text{in } l \times [0, T], \quad (7.38c)$$

$$\frac{\partial \mathbf{M}^e}{\partial x_3} - (\mathbf{I} - \mathbf{e}_3 \otimes \mathbf{e}_3) \mathbf{Q}^e + \mathbf{m}^e = \mathbf{0}, \quad \text{in } l \times [0, T], \quad (7.38d)$$

$$\frac{\partial \mathbf{O}^e}{\partial x_3} - \mathbf{P}^e + \mathbf{o}^e = \mathbf{0}, \quad \text{in } l \times [0, T], \quad (7.38e)$$

The above set of equations represent a set of balance equations in terms of internal area resultants  $\mathbf{Q}^m$ ,  $\mathbf{M}^m$ ,  $\mathbf{Q}^e$ ,  $\mathbf{M}^e$ ,  $\mathbf{P}^e$  and  $\mathbf{O}^e$ . Initial conditions (7.4c-7.4d), boundary conditions (7.2a,7.4a), mechanical strains (7.12-7.13) and their electrical counterparts (7.16-7.17) complement the above system of partial differential equations (7.38) to form the initial boundary value problem of the three-dimensional piezoelectric beam. Specifically, compatible initial conditions can be defined in terms of axis varying functions  $\mathbf{w}_0, \dot{\mathbf{w}}_0, \boldsymbol{\theta}_0, \dot{\boldsymbol{\theta}}_0 : [0, l] \rightarrow \mathbb{R}^3$  as

$$\mathbf{u}(x_1, x_2, x_3, t) = \mathbf{w}_0(x_3) + \boldsymbol{\theta}_0(x_3) \times \mathbf{p}(x_1, x_2) \quad \text{in } \Omega \times 0, \quad (7.39a)$$

$$\dot{\mathbf{u}}(x_1, x_2, x_3, t) = \dot{\mathbf{w}}_0(x_3) + \dot{\boldsymbol{\theta}}_0(x_3) \times \mathbf{p}(x_1, x_2) \quad \text{in } \Omega \times 0, \quad (7.39b)$$

Dirichlet (and corresponding Neumann) boundary conditions can be defined at either end of the beam  $x_3 = 0$  or  $x_3 = l$  by

$$\mathbf{w} = \bar{\mathbf{w}}, \quad \boldsymbol{\theta} = \bar{\boldsymbol{\theta}}, \quad \phi = \bar{\phi}, \quad \boldsymbol{\beta} = \bar{\boldsymbol{\beta}}, \quad \boldsymbol{\gamma} = \bar{\boldsymbol{\gamma}}, \quad (7.40a)$$

$$\mathbf{Q}^m = \bar{\mathbf{Q}}^m, \quad \mathbf{M}^m = \bar{\mathbf{M}}^m, \quad \mathbf{Q}^e \cdot \mathbf{e}_3 = \bar{\mathbf{Q}}^e, \quad \mathbf{M}^e = \bar{\mathbf{M}}^e, \quad \mathbf{O}^e = \bar{\mathbf{O}}^e. \quad (7.40b)$$

Naturally, wherever a Dirichlet boundary condition is defined, a corresponding Neumann boundary condition cannot be used. Finally, in order to close the system defined by (7.12-7.13), (7.38), (7.39) and (7.40), it is necessary to establish relationships between the internal area resultants and the mechanical/electrical strains.

### 7.5.2 Internal area resultants

From the mechanical standpoint, having introduced the additive decomposition of the total Cauchy stress tensor  $\boldsymbol{\sigma}$  in equation (7.7), we now proceed to find the traction vector acting in a cross sectional area  $A$  of the beam defined by the outward unit normal  $\mathbf{e}_3$ , namely  $\boldsymbol{\sigma}\mathbf{e}_3$ . For the mechanical contribution  $\boldsymbol{\sigma}^m$ , combining equations (7.7) and (7.12), it yields

$$\boldsymbol{\sigma}^m \mathbf{e}_3 = \boldsymbol{\Xi}(\boldsymbol{\epsilon}^m + \hat{\mathbf{p}}^T \boldsymbol{\kappa}^m), \quad [\boldsymbol{\Xi}]_{ij} = [\mathcal{C}]_{ikjl}[\mathbf{e}_3]_k[\mathbf{e}_3]_l. \quad (7.41)$$

Analogously, for the electrical contribution  $\boldsymbol{\sigma}^e$ , combining equations (7.7) and (7.16), it yields

$$\boldsymbol{\sigma}^e \mathbf{e}_3 = \boldsymbol{\Theta}(\boldsymbol{\epsilon}^e + (\mathbf{e}_3 \otimes \mathbf{p})\boldsymbol{\kappa}^e + \boldsymbol{\mathcal{V}} : \boldsymbol{\varsigma}^e + \boldsymbol{\mathcal{W}} : \boldsymbol{\gamma}), \quad [\boldsymbol{\Theta}]_{ij} = [\mathcal{P}]_{jik}[\mathbf{e}_3]_k. \quad (7.42)$$

The first internal area resultant  $\mathbf{Q}^m$ , also known as the axial/shear force, can now be computed from equations (7.29), (7.41) and (7.42) as

$$\mathbf{Q}^m = \mathbf{A}^m \boldsymbol{\epsilon}^m + \mathbf{S}^m \boldsymbol{\kappa}^m + \mathbf{A}_1^e \boldsymbol{\epsilon}^e + \mathbf{S}_1^e \boldsymbol{\kappa}^e + \mathbf{S}_2^e : \boldsymbol{\gamma} + \mathbf{I}_1^e : \boldsymbol{\varsigma}^e, \quad (7.43)$$

where

$$\begin{aligned} \mathbf{A}^m &:= \int_A \boldsymbol{\Xi} dA, & \mathbf{S}^m &:= \int_A \boldsymbol{\Xi} \hat{\mathbf{p}}^T dA, & \mathbf{A}_1^e &:= \int_A \boldsymbol{\Theta} dA, \\ \mathbf{S}_1^e &:= \int_A \boldsymbol{\Theta}(\mathbf{e}_3 \otimes \mathbf{p}) dA, & \mathbf{I}_1^e &:= \int_A \boldsymbol{\Theta} \boldsymbol{\mathcal{V}} dA, & \mathbf{S}_2^e &:= \int_A \boldsymbol{\Theta} \boldsymbol{\mathcal{W}} dA, \end{aligned}$$

The first two terms on the right hand side of (7.43) stem from strain contributions whereas the remainder stem from electrical contributions. The second internal area resultant  $\mathbf{M}^m$ , also known as bending/torsion moment, can also be computed from equations (7.29), (7.41) and (7.42) as

$$\mathbf{M}^m = (\mathbf{S}^m)^T \boldsymbol{\epsilon}^m + \mathbf{I}^m \boldsymbol{\kappa}^m + \mathbf{S}_3^e \boldsymbol{\epsilon}^e + \mathbf{I}_2^e \boldsymbol{\kappa}^e + \mathbf{I}_3^e : \boldsymbol{\gamma} + \mathbf{G}_1^e : \boldsymbol{\varsigma}^e, \quad (7.45)$$

where

$$\begin{aligned} \mathbf{I}^m &:= \int_A \hat{\mathbf{p}} \boldsymbol{\Xi} \hat{\mathbf{p}}^T dA, & \mathbf{S}_3^e &:= \int_A \hat{\mathbf{p}} \boldsymbol{\Theta} dA, & \mathbf{I}_2^e &:= \int_A \hat{\mathbf{p}} \boldsymbol{\Theta}(\mathbf{e}_3 \otimes \mathbf{p}) dA, \\ \mathbf{G}_1^e &:= \int_A \hat{\mathbf{p}} \boldsymbol{\Theta} \boldsymbol{\mathcal{V}} dA, & \mathbf{I}_3^e &:= \int_A \hat{\mathbf{p}} \boldsymbol{\Theta} \boldsymbol{\mathcal{W}} dA. \end{aligned}$$

From the electrical standpoint, having introduced the additive decomposition of the electric displacement  $\mathbf{D}$  in equation (7.6), we can obtain after combining equations (7.6), (7.12) and (7.16)

$$\mathbf{D}^m = \boldsymbol{\Theta}^T(\boldsymbol{\epsilon}^m + \hat{\mathbf{p}}^T \boldsymbol{\kappa}^m), \quad (7.47)$$

and

$$\mathbf{D}^e = -\boldsymbol{\epsilon}(\boldsymbol{\epsilon}^e + (\mathbf{e}_3 \otimes \mathbf{p})\boldsymbol{\kappa}^e + \boldsymbol{\mathcal{V}} : \boldsymbol{\varsigma}^e + \boldsymbol{\mathcal{W}} : \boldsymbol{\gamma}). \quad (7.48)$$

The third internal area resultant  $\mathbf{Q}^e$  can now be computed from equations (7.33a), (7.47) and (7.48) as

$$\mathbf{Q}^e = (\mathbf{A}_1^e)^T \boldsymbol{\epsilon}^m + (\mathbf{S}_3^e)^T \boldsymbol{\kappa}^m - \mathbf{A}_2^e \boldsymbol{\epsilon}^e - \mathbf{S}_4^e \boldsymbol{\kappa}^e - \mathbf{S}_5^e : \boldsymbol{\gamma} - \mathbf{I}_4^e : \boldsymbol{\varsigma}^e, \quad (7.49)$$

where

$$\begin{aligned} \mathbf{A}_2^e &:= \int_A \boldsymbol{\epsilon} dA, & \mathbf{S}_4^e &:= \int_A \boldsymbol{\epsilon} (\mathbf{e}_3 \otimes \mathbf{p}) dA, \\ \mathbf{I}_4^e &:= \int_A \boldsymbol{\epsilon} \mathcal{V} dA, & \mathbf{S}_5^e &:= \int_A \boldsymbol{\epsilon} \mathcal{W} dA. \end{aligned}$$

Analogously, the fourth  $\mathbf{M}^e$ , fifth  $\mathbf{P}^e$  and sixth  $\mathbf{O}^e$  internal area resultants can be computed from equations (7.33a-7.33b), (7.47) and (7.48) as

$$\begin{aligned} \mathbf{M}^e &= (\mathbf{S}_1^e)^T \boldsymbol{\epsilon}^m + (\mathbf{I}_2^e)^T \boldsymbol{\kappa}^m - (\mathbf{S}_4^e)^T \boldsymbol{\epsilon}^e - \mathbf{I}_5^e \boldsymbol{\kappa}^e - \mathbf{I}_6^e : \boldsymbol{\gamma} - \mathbf{G}_2^e : \boldsymbol{\varsigma}^e, \\ \mathbf{P}^e &= (\mathbf{S}_2^e)^T \boldsymbol{\epsilon}^m + (\mathbf{I}_3^e)^T \boldsymbol{\kappa}^m - (\mathbf{S}_5^e)^T \boldsymbol{\epsilon}^e - (\mathbf{I}_6^e)^T \boldsymbol{\kappa}^e - \mathbf{I}_7^e : \boldsymbol{\gamma} - \mathbf{G}_3^e : \boldsymbol{\varsigma}^e, \\ \mathbf{O}^e &= (\mathbf{I}_1^e)^T \boldsymbol{\epsilon}^m + (\mathbf{G}_1^e)^T \boldsymbol{\kappa}^m - (\mathbf{I}_4^e)^T \boldsymbol{\epsilon}^e - (\mathbf{G}_2^e)^T \boldsymbol{\kappa}^e - (\mathbf{G}_3^e)^T : \boldsymbol{\gamma} - \mathbf{J}^e : \boldsymbol{\varsigma}^e, \end{aligned} \quad (7.51)$$

where

$$\begin{aligned} \mathbf{I}_5^e &:= \int_A (\mathbf{p} \otimes \mathbf{e}_3) \boldsymbol{\epsilon} (\mathbf{e}_3 \times \mathbf{p}) dA, & \mathbf{J}^e &:= \int_A \mathcal{V}^{*T} \boldsymbol{\epsilon} \mathcal{V} dA, & \mathbf{I}_6^e &:= \int_A (\mathbf{p} \otimes \mathbf{e}_3) \boldsymbol{\epsilon} \mathcal{W} dA, \\ \mathbf{G}_2^e &:= \int_A (\mathbf{p} \otimes \mathbf{e}_3) \boldsymbol{\epsilon} \mathcal{V} dA, & \mathbf{G}_3^e &:= \int_A \mathcal{W}^{*T} \boldsymbol{\epsilon} \mathcal{V} dA, & \mathbf{I}_7^e &:= \int_A \mathcal{W}^{*T} \boldsymbol{\epsilon} \mathcal{W} dA. \end{aligned}$$

Finally, we can summarise all of the above relationships between internal area resultants and mechanical/electrical strains in the following table matrix format<sup>3</sup>

$\begin{bmatrix} \mathbf{Q}^m \\ \mathbf{M}^m \\ \mathbf{Q}^e \\ \mathbf{M}^e \\ \mathbf{P}^e \\ \mathbf{O}^e \end{bmatrix} = \begin{bmatrix} \mathbf{A}^m & \mathbf{S}^m & \mathbf{A}_1^e & \mathbf{S}_1^e & \mathbf{S}_2^e & \mathbf{I}_1^e \\ & \mathbf{I}^m & \mathbf{S}_3^e & \mathbf{I}_2^e & \mathbf{I}_3^e & \mathbf{G}_1^e \\ & & -\mathbf{A}_2^e & -\mathbf{S}_4^e & -\mathbf{S}_5^e & -\mathbf{I}_4^e \\ & & & -\mathbf{I}_5^e & -\mathbf{I}_6^e & -\mathbf{G}_2^e \\ & & & & -\mathbf{I}_7^e & -\mathbf{G}_3^e \\ & Sym & & & & -\mathbf{J}^e \end{bmatrix} \begin{bmatrix} \boldsymbol{\epsilon}^m \\ \boldsymbol{\kappa}^m \\ \boldsymbol{\epsilon}^e \\ \boldsymbol{\kappa}^e \\ :\boldsymbol{\gamma} \\ :\boldsymbol{\varsigma}^e \end{bmatrix}. \quad (7.53) \end{bmatrix}$
--

As expected, the resulting matrix is symmetric and has a saddle point structure due to its derivation from the enthalpy density of the system. In the case of dealing with a homogeneous material across the section of the beam, namely constant mechanical and electrical properties within the area section  $A$ , if the origin of the reference triad  $\{\mathbf{e}_1, \mathbf{e}_2, \mathbf{e}_3\}$  is chosen as the centre of mass of the section, then the tensors  $\mathbf{S}^m$ ,  $\mathbf{S}_k^e$  ( $k = 1 \dots 5$ ) and  $\mathbf{G}_k^e$  ( $k = 1 \dots 3$ ) vanish (e.g. their integrand is of odd order in the position vector  $\mathbf{p}$ ). Finally, we note that the initial boundary value problem representing the behaviour of a piezoelectric three-dimensional beam is defined by equations (7.12), (7.13), (7.38), (7.39), (7.40) and (7.53).

## 7.6 Analytical solution of planar piezoelectric beams

The aim of this section is to present closed-form solutions for some particular cases of piezoelectric beams, which will enable the benchmarking of the finite element implementation presented in a subsequent section of this chapter. In addition, the presentation of closed-form solutions is of interest to prospective researchers in order to validate their piezoelectric beam models. To the best of our knowledge, closed-form solutions of two-way coupled piezoelectric beams with quadratic distribution of electric potential within the cross section do not exist in the literature.

<sup>3</sup>Notice that the entries in columns one to four correspond to second order tensors whereas the entries in columns five and six correspond to third order tensors.

We will focus on the analysis of two-dimensional beams (placed on the plane defined by  $Ox_1x_3$ ) where distributed effects along the beam will be disregarded (i.e.  $\mathbf{q}^m = \mathbf{0}$ ,  $\mathbf{m}^m = \mathbf{0}$ ,  $q^e = 0$ ,  $\mathbf{m}^e = \mathbf{0}$ ,  $\mathbf{o}^e = \mathbf{0}$ ) and we will seek solutions to static problems where inertial terms are neglected (e.g.  $\rho = 0$ ). In addition, we will particularise our solutions to beams with homogeneous cross sectional area where the origin of the reference frame coincides with the centre of mass of the section.

For simplicity, the displacement  $\mathbf{w}$  of the cross sectional reference frame origin is considered perpendicular to the beam axis, namely  $\mathbf{w} \cdot \mathbf{e}_3 = 0$ , and no torsion along the beam axis is considered either,  $\theta \cdot \mathbf{e}_3 = 0$ . In this case, the problem is fully described by the following five variables  $\{w := \mathbf{w} \cdot \mathbf{e}_1, \theta := \theta \cdot \mathbf{e}_2, \phi, \beta := \mathbf{\beta} \cdot \mathbf{e}_1, \gamma := \mathbf{e}_1 \cdot \mathbf{\gamma} \cdot \mathbf{e}_1\} : [0, l] \rightarrow \mathbb{R}$ . Substitution of equations (7.53) into the beam balance equations (7.38) yields, after redefinition of the beam coordinate axis as  $x \in [0, l]$ ,

$$a_1 \left( \frac{dw}{dx} - \theta \right) + a_2 \beta + a_3 \frac{d\phi}{dx} + \frac{a_{14}}{2} \frac{d\gamma}{dx} = \bar{Q}^m, \quad (7.54a)$$

$$a_4 \frac{d^2\theta}{dx^2} - a_5 \frac{d^2\beta}{dx^2} - a_{15} \frac{d\gamma}{dx} + a_1 \left( \frac{dw}{dx} - \theta \right) + a_2 \beta + a_3 \frac{d\phi}{dx} + \frac{a_{14}}{2} \frac{d\gamma}{dx} = 0, \quad (7.54b)$$

$$a_6 \left( \frac{dw}{dx} - \theta \right) - a_7 \beta - a_8 \frac{d\phi}{dx} - \frac{a_{16}}{2} \frac{d\gamma}{dx} = \bar{Q}^e, \quad (7.54c)$$

$$a_9 \frac{d^2\theta}{dx^2} + a_{10} \frac{d^2\beta}{dx^2} + \frac{a_{17}}{2} \frac{d\gamma}{dx} + a_{11} \left( \frac{dw}{dx} - \theta \right) - a_{12} \beta - a_{13} \frac{d\phi}{dx} = 0, \quad (7.54d)$$

$$\begin{aligned} \frac{d}{dx} \left[ \frac{a_{18}}{2} \left( \frac{dw}{dx} - \theta \right) - \frac{1}{2} \left( a_{19} \beta + a_{20} \frac{d\phi}{dx} \right) - \frac{a_{21}}{4} \frac{d\gamma}{dx} \right] \\ + a_{22} \frac{d\theta}{dx} + a_{23} \frac{d\beta}{dx} + a_{24} \gamma = 0, \end{aligned} \quad (7.54e)$$

where coefficients  $a_k$  ( $k = 1 \dots 24$ ), expressed in terms of mechanical, electrical and geometrical properties, are defined as

$$\begin{aligned} a_1 &:= \mu A k_s, & a_2 &:= \mathcal{P}_{113} A k_s, & a_3 &:= \mathcal{P}_{313} A k_s, & a_4 &:= EI, \\ a_5 &:= \mathcal{P}_{333} I, & a_6 &:= \mathcal{P}_{313} A, & a_7 &:= \epsilon_{13} A, & a_8 &:= \epsilon_{33} A, \\ a_9 &:= \mathcal{P}_{333} I, & a_{10} &:= \epsilon_{33} I, & a_{11} &:= \mathcal{P}_{113} A, & a_{12} &:= \epsilon_{11} A, \\ a_{13} &:= \epsilon_{13} A, & a_{14} &:= \mathcal{P}_{313} I, & a_{15} &:= \mathcal{P}_{133} I, & a_{16} &:= \epsilon_{33} I, \\ a_{17} &:= \epsilon_{13} I, & a_{18} &:= \mathcal{P}_{313} I, & a_{19} &:= \epsilon_{13} I, & a_{20} &:= \epsilon_{33} I, \\ a_{21} &:= \epsilon_{33} J, & a_{22} &:= \mathcal{P}_{133} I, & a_{23} &:= \epsilon_{13} I, & a_{24} &:= \epsilon_{11} I, \end{aligned}$$

where  $A$  is the cross sectional area,  $I := \int_A (x_1)^2 dA$  is the second moment of area of the section,  $J := \int_A (x_1)^4 dA$  is the fourth moment of area of the section,  $E$  is the Young modulus,  $\mu$  is the shear modulus,  $\mathcal{P}_{ijk}$  are piezoelectric coefficients and  $\epsilon_{ij}$  are dielectric coefficients.  $k_s$  represents a shear factor correction for the section [126] that will be taken as one unless otherwise stated. Together with appropriate boundary conditions (7.40), the piezoelectric beam problem is completely closed with the above set of equations (7.54). Note that we have assumed that all material and geometric beam properties remain constant throughout the beam length.

The set of boundary conditions considered for a cantilever problem are

$$w = 0, \quad \theta = 0, \quad \phi = 0, \quad \beta = 0, \quad \gamma = 0, \quad \text{at } x = 0, \quad (7.55a)$$

$$Q^m = \bar{Q}^m, \quad M^m = 0, \quad Q^e = \bar{Q}^e, \quad M^e = 0, \quad O^e = 0, \quad \text{at } x = l, \quad (7.55b)$$

where  $Q^m := \mathbf{Q}^m \cdot \mathbf{e}_1$ ,  $M^m := \mathbf{M}^m \cdot \mathbf{e}_2$ ,  $Q^e := \mathbf{Q}^e \cdot \mathbf{e}_3$ ,  $M^e := \mathbf{M}^e \cdot \mathbf{e}_1$  and  $O^e := \mathbf{e}_1 \cdot \mathbf{O}^e \mathbf{e}_1$ . As it is common in piezoelectric beam literature [92, 39, 152], for the electrical part we have postulated similar Dirichlet and Neumann boundary conditions to those of the mechanical problem i.e. all electric variables are zero at the fixed end and the derivatives are specified at

the free end in a coupled fashion. From (7.54a) and (7.54c) we can deduce  $(\frac{dw}{dx} - \theta)$  and  $\frac{d\phi}{dx}$  as

$$\left( \frac{dw}{dx} - \theta \right) = \frac{\bar{Q}^m}{a_1} - \frac{a_2}{a_1} \beta - \frac{a_3}{a_1} \frac{d\phi}{dx} - \frac{1}{2} \frac{a_{14}}{a_1} \frac{d\gamma}{dx}, \quad (7.56a)$$

$$\frac{d\phi}{dx} = \frac{a_6}{a_1 b_2} \bar{Q}^m - \frac{\bar{Q}^e}{b_2} - \frac{b_1}{b_2} \beta - \frac{b_8}{b_2} \frac{d\gamma}{dx}, \quad (7.56b)$$

where coefficients  $b_1$ ,  $b_2$  and  $b_8$  are defined in A. After back substitution into (7.54b), (7.54d) and (7.54e), we obtain

$$a_4 \frac{d^2\theta}{dx^2} - a_5 \frac{d^2\beta}{dx^2} - a_{15} \frac{d\gamma}{dx} + \bar{Q}^m = 0, \quad (7.57a)$$

$$a_9 \frac{d^2\theta}{dx^2} + a_{10} \frac{d^2\beta}{dx^2} + b_9 \frac{d\gamma}{dx} - b_5 \beta + b_6 \bar{Q}^m + b_7 \bar{Q}^e = 0, \quad (7.57b)$$

$$\frac{d^2\gamma}{dx^2} + k_1^2 \gamma + m_1 \frac{d\beta}{dx} + m_3 \frac{d\theta}{dx} = 0, \quad (7.57c)$$

where coefficients  $b_5$ ,  $b_6$ ,  $b_7$ ,  $b_9$ ,  $m_1$ ,  $m_1$ ,  $m_3$  and  $k_1$  are defined in A. The above three equations (7.57), together with relevant boundary conditions, can be integrated to solve for  $\theta$ ,  $\beta$  and  $\gamma$ . Then, by using equations in (7.56), the remaining variables  $w$  and  $\phi$  can be obtained.

The solution of these equations would require four piezoelectric parameters  $\mathcal{P}_{113}$ ,  $\mathcal{P}_{133}$ ,  $\mathcal{P}_{313}$  and  $\mathcal{P}_{333}$ , three dielectric parameters  $\epsilon_{11}$ ,  $\epsilon_{13}$  and  $\epsilon_{33}$  and two mechanical parameters  $\mu$  and  $E$ . From a practical viewpoint, piezoelectric materials having all of the above material parameters non-zero are rare and the solution obtained using this approach would be too lengthy to be reported. For such closed-form solutions, the reader can refer to [249].

We identify two practically feasible scenarios for the above set of differential equations (7.57). Firstly, the case where the electric potential distribution is assumed to vary linearly within the cross section. Secondly, the case where the electric potential distribution is assumed to vary quadratically within the cross section but the electric permittivity tensor  $\epsilon$  is considered to be diagonal and the piezoelectric component  $\mathcal{P}_{133} = 0$ . The most notable piezoelectric materials, such as PZT-5H, PZT-5A, Quartz and many others, share these features.

### 7.6.1 Linear electric potential distribution within the cross section

In this case, the equations in (7.57) reduce to

$$a_4 \frac{d^2\theta}{dx^2} - a_5 \frac{d^2\beta}{dx^2} + \bar{Q}^m = 0, \quad (7.58a)$$

$$a_9 \frac{d^2\theta}{dx^2} + a_{10} \frac{d^2\beta}{dx^2} - b_5 \beta + b_6 \bar{Q}^m + b_7 \bar{Q}^e = 0, \quad (7.58b)$$

with the following set of boundary conditions

$$\theta|_{x=0} = 0, \quad \beta|_{x=0} = 0, \quad (7.59a)$$

$$\left. \frac{d\theta}{dx} \right|_{x=l} = 0, \quad \left. \frac{d\beta}{dx} \right|_{x=l} = 0. \quad (7.59b)$$

The final closed-form solution of this problem yields

$$\begin{aligned}
\beta(x) &:= \frac{(\bar{Q}^m b_3 + \bar{Q}^e b_4)}{k^2} g(x), \\
\phi(x) &:= \left( \frac{\bar{Q}^m a_6}{a_1 b_2} - \frac{\bar{Q}^e}{b_2} \right) x - \frac{b_1 (\bar{Q}^m b_3 + \bar{Q}^e b_4)}{b_2 k^3} f(x), \\
\theta(x) &:= \frac{\bar{Q}^m l x}{a_4} - \frac{\bar{Q}^m x^2}{2a_4} + \frac{a_5 (\bar{Q}^m b_3 + \bar{Q}^e b_4)}{a_4 k^2} g(x), \\
w(x) &:= \left[ \frac{\bar{Q}^m}{a_1} + \frac{a_3 (\bar{Q}^e a_1 - \bar{Q}^m a_6)}{a_1^2 b_2} \right] x + \frac{\bar{Q}^m L x^2}{2a_4} - \frac{\bar{Q}^m x^3}{6a_4} + (\bar{Q}^m b_3 + \bar{Q}^e b_4) h(x), \\
f(x) &:= \frac{\sinh(kl - kx) - \sinh(kl) + kx \cosh(kl)}{\cosh(kl)}, \\
g(x) &:= 1 - \frac{\cosh(kl - kx)}{\cosh(kl)}, \\
h(x) &:= \frac{(a_1 a_5 b_2 - a_2 a_4 b_2 + a_3 a_4 b_1) [\sinh(kl - kx) - \sinh(kl) + kx \cosh(kl)]}{a_1 a_4 b_2 k^3 \cosh(kl)},
\end{aligned}$$

where the new coefficients  $b_3$ ,  $b_4$  and  $k$  are defined in A.

### 7.6.2 Quadratic electric potential distribution within the cross section

In the case of quadratic electric potential distribution, a diagonal electric permittivity tensor and piezoelectric component  $\mathcal{P}_{133} = 0$ , which is the case for a major class of piezoceramics [331] and, specifically, the ones used in piezoelectric beam literature [80, 2, 90, 92, 22, 307, 308, 152], the three differential equations (7.57) take the form,

$$a_4 \frac{d^2 \theta}{dx^2} - a_5 \frac{d^2 \beta}{dx^2} + \bar{Q}^m = 0, \quad (7.60a)$$

$$a_9 \frac{d^2 \theta}{dx^2} + a_{10} \frac{d^2 \beta}{dx^2} - b_5 \beta + b_6 \bar{Q}^m + b_7 \bar{Q}^e = 0, \quad (7.60b)$$

$$\frac{d^2 \gamma}{dx^2} + k_1^2 \gamma + m_1 \frac{d\beta}{dx} = 0, \quad (7.60c)$$

with the following set of boundary conditions,

$$\theta|_{x=0} = 0, \quad \beta|_{x=0} = 0, \quad \gamma|_{x=0} = 0, \quad (7.61a)$$

$$\left. \frac{d\theta}{dx} \right|_{x=l} = 0, \quad \left. \frac{d\beta}{dx} \right|_{x=l} = 0, \quad \left. \frac{d\gamma}{dx} \right|_{x=l} = m_2, \quad (7.61b)$$

where  $m_2$  is a coefficient which depends on the electromechanical loading and the electric gradient  $\beta$  at  $x = l$ , as given in A. The final closed form of this problem is defined for the mechanical variables as

$\theta(x) := \frac{\bar{Q}^m l x}{a_4} - \frac{\bar{Q}^m x^2}{2 a_4} + \frac{a_5 (\bar{Q}^m b_3 + \bar{Q}^e b_4)}{a_4 k^2} \left[ 1 - \frac{\cosh(kl - kx)}{\cosh(kl)} \right],$ $w(x) := \frac{\bar{Q}^m x}{a_1} + \frac{\bar{Q}^m l x^2}{2 a_4} - \frac{\bar{Q}^m x^3}{6 a_4} + \frac{a_5 (\bar{Q}^m b_3 + \bar{Q}^e b_4) x}{a_4 k^2} + g_1(x) + g_2(x) + g_3(x)$ $+ g_4(x) + g_5(x) + g_6(x) + g_7(x) + g_8(x) + g_9(x) + g_{10}(x) + g_{11}(x) + g_{12}(x),$ $g_1(x) := \frac{a_5 (\bar{Q}^m b_3 + \bar{Q}^e b_4) [\sinh(kl - kx) - \sinh(kl)]}{a_4 k^3 \cosh(kl)},$ $g_2(x) := -\frac{a_2 (\bar{Q}^m b_3 + \bar{Q}^e b_4)}{a_1} \left[ \frac{\sinh(kl - kx) + kx \cosh(kl) - \sinh(kl)}{k^3 \cosh(kl)} \right],$ $g_3(x) := -\frac{a_3}{a_1} \left( \frac{a_6 \bar{Q}^m}{a_1 b_2} - \frac{\bar{Q}^e}{b_2} \right) x,$ $g_4(x) := \frac{a_3 b_1 (\bar{Q}^m b_3 + \bar{Q}^e b_4)}{a_1 b_2} \left[ \frac{\sinh(kl - kx) + kx \cosh(kl) - \sinh(kl)}{k^3 \cosh(kl)} \right],$ $g_5(x) := \frac{a_3 b_8}{a_1 b_2} \left[ \frac{m_2 \sinh(k_1 x) (k^2 - k_1^2)}{\cosh(k_1 l) (k^2 k_1 - k_1^3)} + \frac{m_1 (\bar{Q}^m b_3 + \bar{Q}^e b_4) \sinh(kl - kx)}{\cosh(kl) (k k_1^2 - k^3)} \right],$ $g_6(x) := -\frac{a_3 b_8 m_1 (\bar{Q}^m b_3 + \bar{Q}^e b_4)}{a_1 b_2} \left[ \frac{2k \sinh(k_1 x) - \sinh(kl) (e^{(kl+2k_1 x)} + k_1 e^{k_1(l-x)})}{2 \cosh(kl) \cosh(k_1 l) (k k_1^3 - k^3 k_1)} \right],$ $g_7(x) := \frac{a_3 b_8 m_1 (\bar{Q}^m b_3 + \bar{Q}^e b_4)}{a_1 b_2} \left[ \frac{\sinh(kl) (e^{kl} + k_1 e^{k_1 l})}{2 \cosh(kl) \cosh(k_1 l) (k k_1^3 - k^3 k_1)} \right],$ $g_8(x) := -\frac{a_3 b_8 m_1 (\bar{Q}^m b_3 + \bar{Q}^e b_4)}{a_1 b_2} \left[ \frac{\sinh(kl)}{\cosh(kl) (k k_1^2 - k^3)} \right],$ $g_9(x) := -\frac{a_{14}}{2 a_1} \left[ \frac{m_2 \sinh(k_1 x) (k^2 - k_1^2)}{\cosh(k_1 l) (k^2 k_1 - k_1^3)} + \frac{m_1 (\bar{Q}^m b_3 + \bar{Q}^e b_4) \sinh(kl - kx)}{\cosh(kl) (k k_1^2 - k^3)} \right],$ $g_{10}(x) := -\frac{a_{14} m_1 (\bar{Q}^m b_3 + \bar{Q}^e b_4)}{2 a_1} \left[ \frac{2k \sinh(k_1 x) - \sinh(kl) (e^{(kl+2k_1 x)} + k_1 e^{k_1(l-x)})}{2 \cosh(kl) \cosh(k_1 l) (k k_1^3 - k^3 k_1)} \right],$ $g_{11}(x) := \frac{a_{14} m_1 (\bar{Q}^m b_3 + \bar{Q}^e b_4)}{2 a_1} \left[ \frac{\sinh(kl)}{\cosh(kl) (k k_1^2 - k^3)} \right],$ $g_{12}(x) := -\frac{a_{14} m_1 (\bar{Q}^m b_3 + \bar{Q}^e b_4)}{2 a_1} \left[ \frac{\sinh(kl) (e^{kl} + k_1 e^{k_1 l})}{2 \cosh(kl) \cosh(k_1 l) (k k_1^3 - k^3 k_1)} \right],$
--

and similarly for the electrical variables as

$$\begin{aligned}
\phi(x) &:= \left( \frac{\bar{Q}^m a_6}{a_1 b_2} - \frac{\bar{Q}^e}{b_2} \right) x + f_1(x) + f_2(x) + f_3(x) + f_4(x) + f_5(x), \\
\beta(x) &:= \frac{(\bar{Q}^m b_3 + \bar{Q}^e b_4)}{k^2} \left[ 1 - \frac{\cosh(kl - kx)}{\cosh(kl)} \right], \\
\gamma(x) &:= \frac{m_2 \sinh(k_1 x) (k^2 - k_1^2)}{\cosh(k_1 l) (k^2 k_1 - k_1^3)} + \frac{m_1 (\bar{Q}^m b_3 + \bar{Q}^e b_4) \sinh(kl - k x)}{\cosh(kl) (k k_1^2 - k^3)} + f_6(x), \\
f_1(x) &:= -\frac{b_1 (\bar{Q}^m b_3 + \bar{Q}^e b_4)}{b_2} \left[ \frac{\sinh(kl - kx) + kx \cosh(kl) - \sinh(kl)}{k^3 \cosh(kl)} \right], \\
f_2(x) &:= -\frac{b_8}{b_2} \left[ \frac{m_2 \sinh(k_1 x) (k^2 - k_1^2)}{\cosh(k_1 l) (k^2 k_1 - k_1^3)} + \frac{m_1 (\bar{Q}^m b_3 + \bar{Q}^e b_4) \sinh(kl - kx)}{\cosh(kl) (k k_1^2 - k^3)} \right], \\
f_3(x) &:= -\frac{b_8 m_1 (\bar{Q}^m b_3 + \bar{Q}^e b_4)}{b_2} \left[ \frac{2k \sinh(k_1 x) - \sinh(kl) (e^{(kl+2k_1 x)} + k_1 e^{k_1(l-x)})}{2 \cosh(kl) \cosh(k_1 l) (k k_1^3 - k^3 k_1)} \right], \\
f_4(x) &:= \frac{b_8 m_1 (\bar{Q}^m b_3 + \bar{Q}^e b_4)}{b_2} \left[ \frac{\sinh(kl)}{\cosh(kl) (k k_1^2 - k^3)} \right], \\
f_5(x) &:= -\frac{b_8 m_1 (\bar{Q}^m b_3 + \bar{Q}^e b_4)}{b_2} \left[ \frac{\sinh(kl) (e^{kl} + k_1 e^{k_1 l})}{2 \cosh(kl) \cosh(k_1 l) (k k_1^3 - k^3 k_1)} \right], \\
f_6(x) &:= \frac{m_1 (\bar{Q}^m b_3 + \bar{Q}^e b_4)}{2 \cosh(kl) \cosh(k_1 l) (k k_1^3 - k^3 k_1)} [2k \sinh(k_1 x) - \sinh(kl) (e^{(kl+2k_1 x)} + k_1 e^{k_1(l-x)})],
\end{aligned}$$

where the new coefficients  $m_1$  and  $k$  are defined in A.

## 7.7 The Finite Element Discretisation

The finite element discretisation of (7.36) follows naturally by introducing a non-overlapping partition of  $l$  into a series of one-dimensional elements. In particular, we choose to employ the  $hp$ -version of the finite element method as it is known to overcome the problems of locking associated with low-order approaches [295, 47, 111]. We introduce a set of  $H^1$  conforming interpolatory functions,  $\mathcal{V}_{hp} \subset H^1(\Omega)$ , where the subscript  $h$  refers to the mesh spacing and  $p$  to the polynomial degree. In the  $hp$ -finite element method it is possible to construct a discretisation where the order of the elements varies throughout the mesh (the so-called  $p$ -adaptivity) but, in our case, we adopt the simplest configuration and fix the polynomial degree of the bases to be the same everywhere throughout the domain. The corresponding discrete weak variational statement is: Find  $(\mathbf{u}_{hp}, \psi_{hp}) \in \mathcal{V}_{\bar{\mathbf{u}}}^{\mathbf{u}} \cap \mathcal{V}_{hp}^{\mathbf{u}} \times \mathcal{V}_{\psi}^{\psi} \cap \mathcal{V}_{hp}^{\psi}$  such that

$$\delta W := \delta W_{iner} + \delta W_{int} - \delta W_{ext} = 0, \quad (7.62)$$

for all  $(\delta \mathbf{u}_{hp}, \delta \psi_{hp}) \in \mathcal{V}_0^{\mathbf{u}} \cap \mathcal{V}_{hp}^{\mathbf{u}} \times \mathcal{V}_0^{\psi} \cap \mathcal{V}_{hp}^{\psi}$  where

$$\mathcal{V}_{hp}^{\mathbf{u}} := \{\mathbf{u}_{hp} \mid \mathbf{u}_{hp} := \mathbf{w}_{hp} + \boldsymbol{\theta}_{hp} \times \mathbf{p}\}, \quad (7.63)$$

$$\mathcal{V}_{hp}^{\psi} := \left\{ \psi_{hp} \mid \psi_{hp} := \phi_{hp} + \mathbf{p} \cdot \boldsymbol{\beta}_{hp} + \frac{1}{2} \mathbf{p} \cdot \boldsymbol{\gamma}_{hp} \cdot \mathbf{p} \right\}, \quad (7.64)$$

with the component functions  $\{(\mathbf{w}_{hp} \cdot \mathbf{e}_i), (\boldsymbol{\theta}_{hp} \cdot \mathbf{e}_i), \phi_{hp}, (\boldsymbol{\beta}_{hp} \cdot \mathbf{e}_\alpha), (\mathbf{e}_\alpha \cdot \boldsymbol{\gamma}_{hp} \mathbf{e}_\beta)\} \in \mathcal{V}_{hp}$ .

Discussions of suitable sets of hierachic basis functions for  $\mathcal{V}_{hp}$ , which have implementation advantages over standard Lagrangian nodal basis functions, can be found in a range of

texts (e.g. [69, 296, 148]) and, therefore, will not be discussed further here. For details of the numerical treatment of these elements, and our specific implementation, we refer to the aforementioned references and [249].

## 7.8 Numerical examples

The numerical examples presented in this section have been carried out using FEAPB, a cross-platform  $hp$ -finite element analysis program for piezoelectric beams [248], developed based on the theoretical formulation outlined in this chapter and distributed as a free software under the terms of GNU General Public License at <https://github.com/romeric/FEAPB>.

The piezoelectric material properties used in Examples 7.8.1 and 7.8.2 are presented below in Voigt notation and taken from [22]. Note that for shear actuator problems, the electric permittivity tensor is not required since the problem is purely mechanical.

$$\mathcal{C} = \begin{bmatrix} 126 & 79.5 & 84.1 & 0 & 0 & 0 \\ 79.5 & 126 & 84.1 & 0 & 0 & 0 \\ 84.1 & 84.1 & 117 & 0 & 0 & 0 \\ 0 & 0 & 0 & 23.3 & 0 & 0 \\ 0 & 0 & 0 & 0 & 23.3 & 0 \\ 0 & 0 & 0 & 0 & 0 & 23.25 \end{bmatrix} GPa,$$

$$\epsilon = \begin{bmatrix} 1.505 & 0 & 0 \\ 0 & 1.505 & 0 \\ 0 & 0 & 1.3 \end{bmatrix} 10^{-8} \frac{C}{Vm},$$

$$\mathcal{P} = \begin{bmatrix} 0 & 0 & 0 & 0 & 17 & 0 \\ 0 & 0 & 0 & 17 & 0 & 0 \\ -6.5 & -6.5 & 23.3 & 0 & 0 & 0 \end{bmatrix} \frac{C}{m^2}.$$

The material properties of AT-cut Quartz, of density  $\rho = 2649 \frac{kg}{m^3}$ , used in Example 7.8.4, are given below [331].

$$\mathcal{C} = \begin{bmatrix} 86.74 & -8.25 & 27.15 & -3.66 & 0 & 0 \\ & 129.77 & -7.42 & 5.7 & 0 & 0 \\ & & 102.83 & 9.92 & 0 & 0 \\ & & & 38.61 & 0 & 0 \\ & & & & 68.81 & 2.53 \\ & & & & & 29.01 \end{bmatrix} \times 10^9 \frac{N}{m^2},$$

$$\epsilon = \begin{bmatrix} 39.21 & 0 & 0 \\ & 39.82 & 0.86 \\ & & 40.42 \end{bmatrix} \times 10^{-12} \frac{C}{Vm},$$

$$\mathcal{P} = \begin{bmatrix} 0.171 & 0 & 0 \\ -0.152 & 0 & 0 \\ -0.0187 & 0 & 0 \\ 0.067 & 0 & 0 \\ 0 & 0.108 & -0.0761 \\ 0 & -0.095 & 0.067 \end{bmatrix} \frac{C}{m^2}.$$

In order to benchmark the  $hp$ -finite element scheme proposed, we define for a tensor (e.g. scalar, vector or second order) field  $\zeta : [0, l] \times t \rightarrow \mathbb{R}^n$ , where  $n$  is the dimension of the tensor field, the following  $L^2$  and  $H^1$  norms

$$\|\zeta\|_{L^2} := \left[ \int_l \zeta : \zeta dx_3 \right]^{1/2},$$

$$\|\zeta\|_{H^1} := \left[ \int_l \left( \zeta : \zeta + \frac{\partial \zeta}{\partial x_3} : \frac{\partial \zeta}{\partial x_3} \right) dx_3 \right]^{1/2}, \quad (7.65)$$

associated with the magnitude of the tensor field  $\zeta$ . In our case,  $\zeta$  can be any of the mechanical and electrical unknowns, namely  $w, \theta, \phi, \beta$  and  $\gamma$ . In addition, the following energy norm can be defined

$$\|\boldsymbol{\pi}\|_E := \left[ \int_l \frac{1}{2} (\boldsymbol{\varepsilon}^m \cdot \mathbf{Q}^m + \boldsymbol{\kappa}^m \cdot \mathbf{M}^m + \boldsymbol{\varepsilon}^e \cdot \mathbf{Q}^e + \boldsymbol{\kappa}^e \cdot \mathbf{Q}^e + \boldsymbol{\varsigma}^e : \mathbf{P}^e + \boldsymbol{\gamma}^e \cdot \mathbf{O}^e) dx_3 \right]^{1/2}, \quad (7.66)$$

where  $\boldsymbol{\pi}$  gathers all the mechanical and electrical unknowns. This enables the definition of the following error norms  $\|\zeta_{hp} - \zeta\|_{L^2}/\|\zeta\|_{L^2}$ ,  $\|\zeta_{hp} - \zeta\|_{H^1}/\|\zeta\|_{H^1}$  and  $\|\boldsymbol{\pi}_{hp} - \boldsymbol{\pi}\|_E/\|\boldsymbol{\pi}\|_E$ , which can then be used to assess the convergence of the algorithm under  $h$ - or  $p$ -refinement.

### 7.8.1 The benchmark problem

To begin our numerical examples, we first benchmark the finite element implementation against the analytical solution provided in Section 7.6 and A. The example considered for the benchmark problem is a two dimensional cantilever beam, of height 1mm and length 10mm, under the action of a unit tip load  $\bar{Q}^m = 1N$  and zero electric displacement resultant  $\bar{Q}^e = 0C$ . The beam is assumed to be of a single fibre polarised along the length as shown in Figure 7.4, with material properties as given above. To quantify the error incurred in all the variables

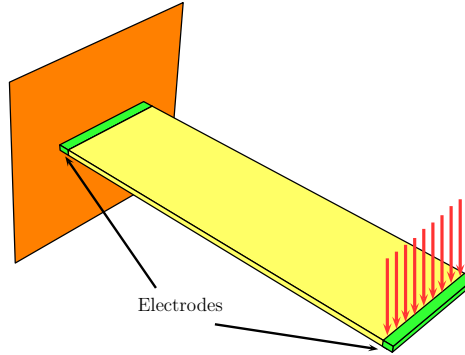


Figure 7.4: Cantilever beam polarised along the length

$\{w, \theta, \phi, \beta, \gamma\}$  of the finite element implementation, we compute the  $L^2$ ,  $H^1$  and energy norms of the error (as described above) for various mesh sizes and polynomial enhancements. In Figures 7.5 and 7.6, each line represents a fixed polynomial degree  $p$  and each data point on a given line represents a mesh size  $h$ . Unless otherwise stated, for this analysis, the basis functions of degree  $p = 1, 2, 3, 4$  with equally-spaced mesh sizes have been used namely  $h = 0.4, 0.2, 0.133, 0.1$  which correspond to 25, 50, 75 and 100 elements, respectively.

For  $hp$ -refinement, we put emphasis on the case of quadratic electric potential distribution within the cross section whose closed-form solution is provided in subsection 7.6.2. The solution for a linear electric potential distribution model can be considered as a special case of the quadratic one for which we only list the tip values of non-zero variables,  $\{w, \theta, \beta\}$  and their point-wise percentage error, see Table 7.1 and 7.2. Also note that for the quadratic case *only*, to get non-zero  $\gamma$  and  $\phi$  and show their convergence, we tune an additional piezoelectric parameter i.e.  $\mathcal{P}_{333} = 20C/m^2$ . In the following plots, slope indicates the rate of convergence. The absolute relative  $L^2$  norm of the error in all the variables is shown in Figure 7.5.

Table 7.1: Convergence of Numerical Scheme for Tip Values

<i>hp</i> -Refinement	$w_{x=L}$ (mm)	$\theta_{x=L}$ (rad)	$\beta_{x=L}$ (rad)
$h = 5, p = 1$	0.019382	0.002871	20.090531
$h = 5, p = 2$	0.034576	0.005128	47.566588
$h = 5, p = 3$	0.034623	0.005128	35.849481
Exact	0.034623	0.005128	35.849481

Table 7.2: Point-wise % Error Incurred in Table 7.1

<i>hp</i> -Refinement	% Error $w$	% Error $\theta$	% Error $\beta$
$h = 5, p = 1$	44.018998	44.019046	43.958656
$h = 5, p = 2$	0.134194	4.550137e-05	32.684178
$h = 5, p = 3$	8.161727e-07	2.385000e-12	4.784048e-07

These convergence rates are in good agreement with theoretical predictions [296, 148]. In fact, in some cases, the convergence rate is far superior, for instance, as it can be observed in the convergence of the electric potential (Figure 7.5b) with quadratic basis function  $p = 2$ . The stagnation in convergence occurs when the numerical solution reaches the analytical solution (Figure 7.5a), which normally happens at a higher value than the computer language floating-point precision.

A similar trend is observed with the convergence of the  $H^1$  norm of the error, shown in Figure 7.6. Again, the convergence rate is in agreement with theoretical predictions [296].

To further elaborate the overall convergence of the problem, we compute the energy norm of the error for both linear and quadratic electric potential distributions, but this time with a fixed mesh size and uniformly increased interpolation degree. In other words, we report the energy norm of the error with  $p$ -refinement, as shown in Figure 7.7. In addition, by means of the error measured in the energy norm, we also compare the convergence of the problem and the ability to overcome locking by increasing the degree of interpolation.

This is an important advantage of  $hp$ -finite element analysis and, although well known in the context of linear elasticity [296, 111, 142], we believe to the best of our knowledge it is missing in the piezoelectric literature.

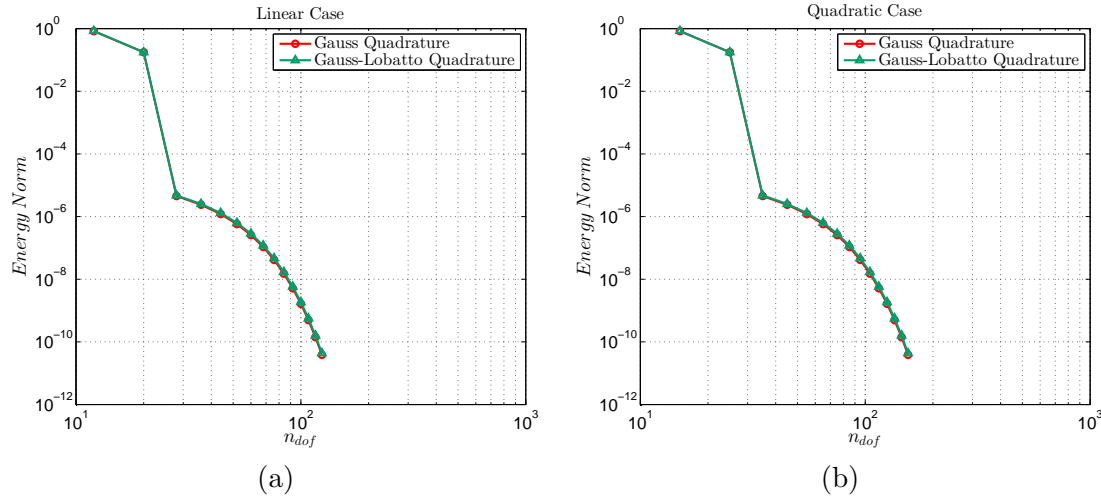


Figure 7.7: Convergence of the energy norm of the error under  $p$ -refinement and with different numerical integration techniques. (a) Linear electric potential distribution. (b) Quadratic electric potential distribution.

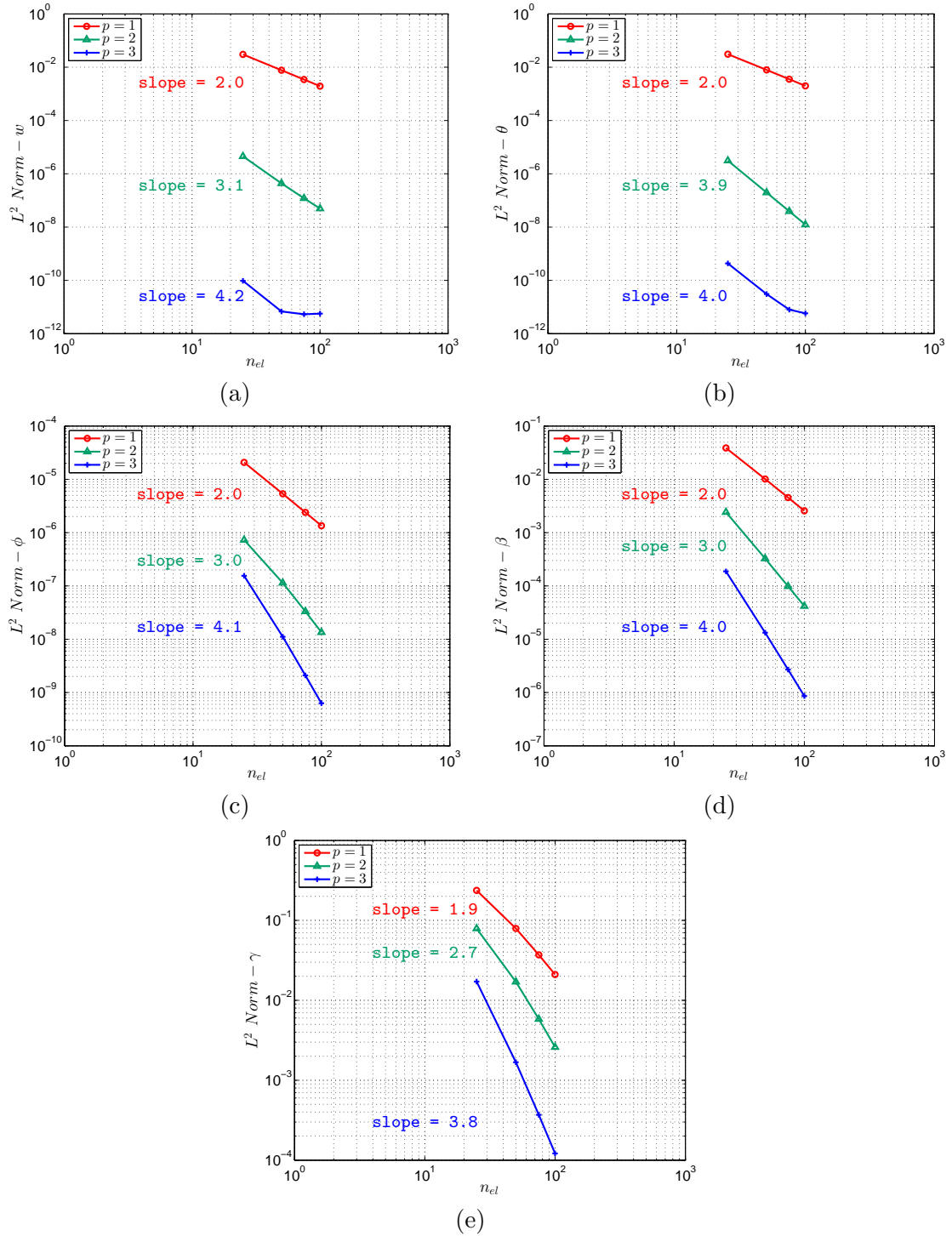


Figure 7.5: Convergence of the error measured in the  $L^2$  norm for the variables (a)  $w$ ; (b)  $\theta$ ; (c)  $\phi$ ; (d)  $\beta$ ; (e)  $\gamma$

### 7.8.2 Shear actuator problem

In this example, we consider a composite piezoelectric beam that has a well-established solution. The shear actuator initially proposed by Zhang and Sun [334] has been analysed analytically in [334, 9], numerically in [9, 22, 39] and experimentally in [15]. In our presentation, we wish to make the distinction that our approach, unlike the majority of these models, is not restricted to actuation-only scenarios. Indeed, the proposed beam model incorporates electrical degrees of freedom and hence can also be applied to energy harvesting scenarios. In fact, shear actuator

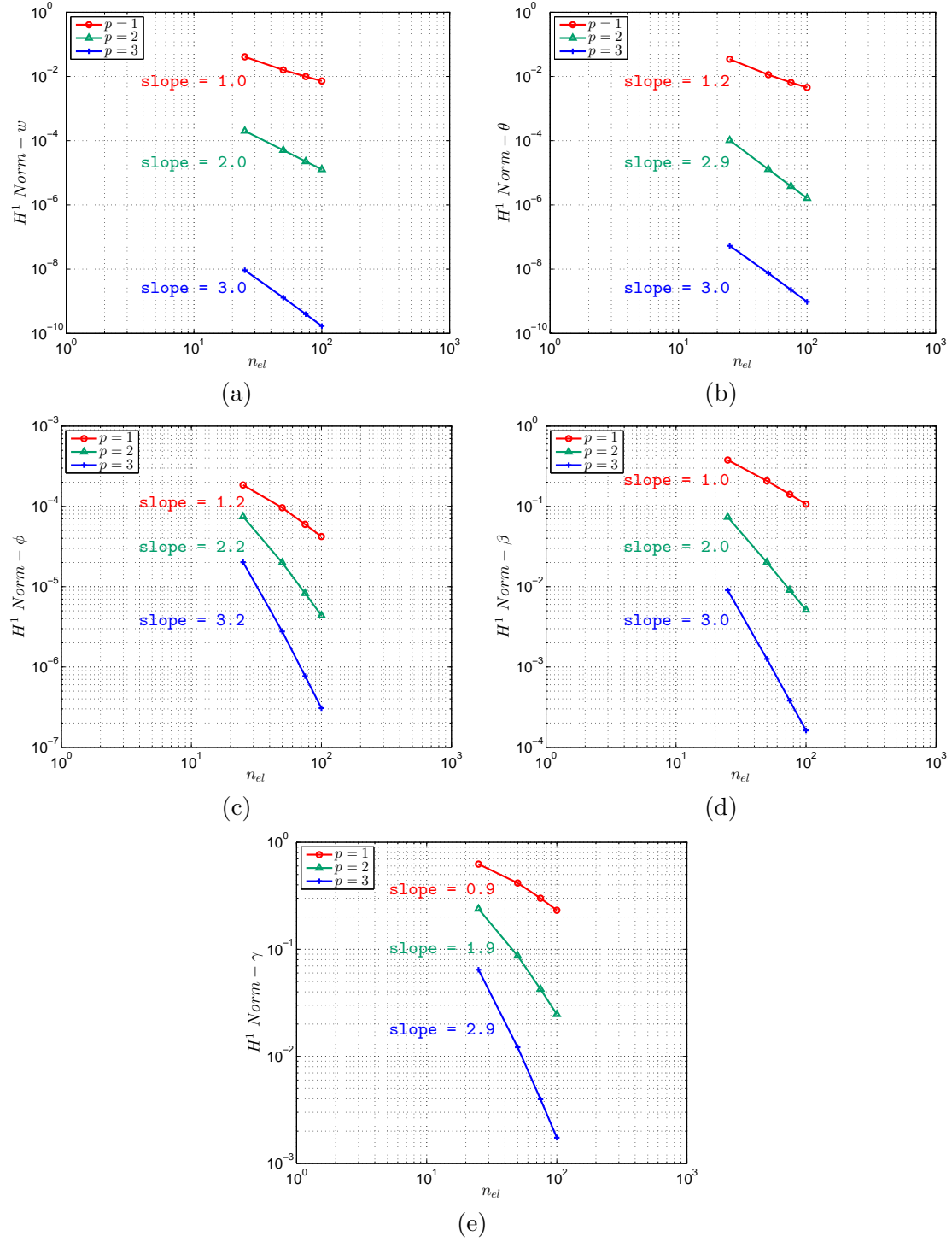


Figure 7.6: Convergence of the error measured in the  $H^1$  norm for the variables (a)  $w$ ; (b)  $\theta$ ; (c)  $\phi$ ; (d)  $\beta$ ; (e)  $\gamma$

models which consider all composite layers as Timoshenko beams, can be regarded as a special case of the present formulation. For instance, the closed form solutions presented in [9] are based on equations (7.38a) and (7.38b).

The presented results correspond to when the shear actuator is analysed in a two-dimensional setting where the width of the beam is assumed to be 1mm, the length of the beam as 100mm, thickness of piezoelectric layer as 2mm and thickness of each Aluminum layer as 8mm [334], as shown in Figure 7.8. Piezoelectric material properties are given above. The modulus of elasticity and Poisson's ratio of Aluminum are 70.3 GPa and 0.345, respectively.

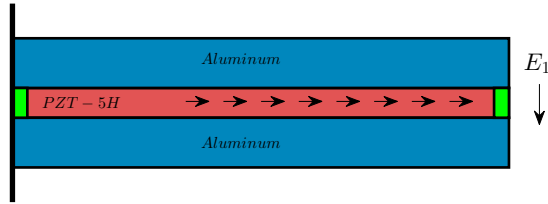


Figure 7.8: Geometry of the shear actuator

Despite having shown here in a cantilever setting, the shear actuator has also been analysed for various other mechanical end boundary conditions, such as clamped-clamped and clamped-hinged situations, for instance by Aldraihem [9]. The electric loading corresponds to an electric field  $E_1$  of  $10V/mm$  applied perpendicular to the polarisation direction, as shown in Figure 7.8. In our setting, this requires prescribing all the electric degrees of freedom with a value of  $\beta = 10V/mm$  and zero for the rest of the electrical unknowns in all nodes.

The cross-sectional properties of the composite beam are calculated numerically, which also makes the present finite element formulation amenable to multi-layer composites and non-rectangular geometries. In the following, finite element solutions are compared with the analytical solutions provided by [9] for a Timoshenko model, for all the aforementioned boundary conditions. The beam is discretised with 20 quadratic elements.

It should be pointed out that Zhang and Sun [334] and Benjeddou et al. [22] model the non-electroactive layers of the shear actuator as an Euler-Bernoulli beam, which further requires imposing compatibility constraints in the interface between the various layers. Following [9], for a Timoshenko model, a shear factor of  $k_s = 2/3$  or less is required to capture the results of the Euler-Bernoulli model, as shown in Figure 7.9d. For the purpose of comparison a shear factor of  $5/6$  has been used in the rest of the test cases shown in Figure 7.9.

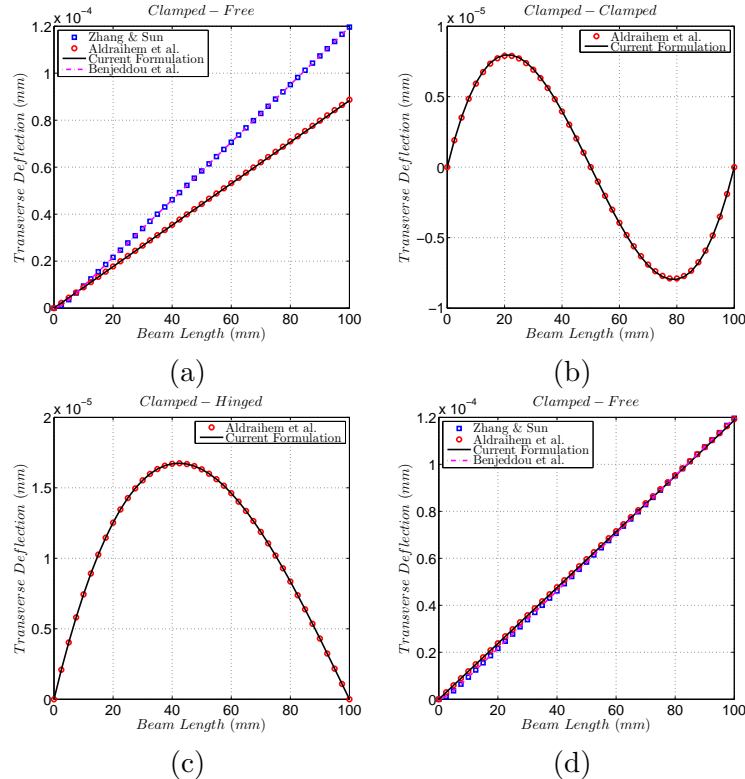


Figure 7.9: Transverse deflection obtained with various models (Shear factor  $k_s = 5/6$ ). (a) Clamped-free; (b) Clamped-clamped; (c) Clamped-hinged; (d) Clamped-free with shear factor  $k_s = 0.62$ .

### 7.8.3 Ambient vibration energy harvester undergoing coupled bending-torsion

In this example, we analyse a fully three-dimensional piezoelectric energy harvesting beam undergoing coupled bending-torsion vibration. As reported in [2], coupled bending-torsion energy harvesters can function on broader frequency ranges and are advantageous in improving the efficiency of energy harvesting. To this effect, we analyse a fibre of AT-cut Quartz with material properties as given above and dimensions defined by length  $40\text{mm}$ , height  $0.9\text{mm}$  and width  $12\text{mm}$ .

To start with, we first compute some selected natural frequencies of the beam. The dimensions of the beam are chosen such that one of these modes (i.e. sixth mode) correspond to twisting. To obtain the natural frequencies, we employ 50 elements of degree  $p = 3$ . Unless otherwise stated, the results reported here are with second order electric potential distribution across the cross section. The natural frequencies corresponding to modes 1, 2, 3 and 6 are listed in Table 7.3 and hardly vary with respect to those corresponding to purely mechanical beam problem without any piezoelectric interaction. Hence, the natural frequencies can be verified with closed-form formulas, for instance those provided in [257]. Many researchers [92, 90, 80, 2] tend to place a point mass at the tip of the beam in order to reduce the frequency spectrum. We have opted for using directly the frequencies as obtained from the eigenvalue analysis of the beam problem.

Table 7.3: Natural frequencies of bending-torsion fibre (Hz)

Mode ( $i$ )	1	2	3	6
Frequency ( $f_i$ )	17.897759	111.999935	224.776362	1006.096205

The mode shapes corresponding to bending and torsion frequencies are shown in Figure 7.10. Note that for the purpose of plotting, the interior degrees of freedom are condensed out and the colours in the plot, which essentially show the absolute magnitude of mode deformation, are magnified appropriately.

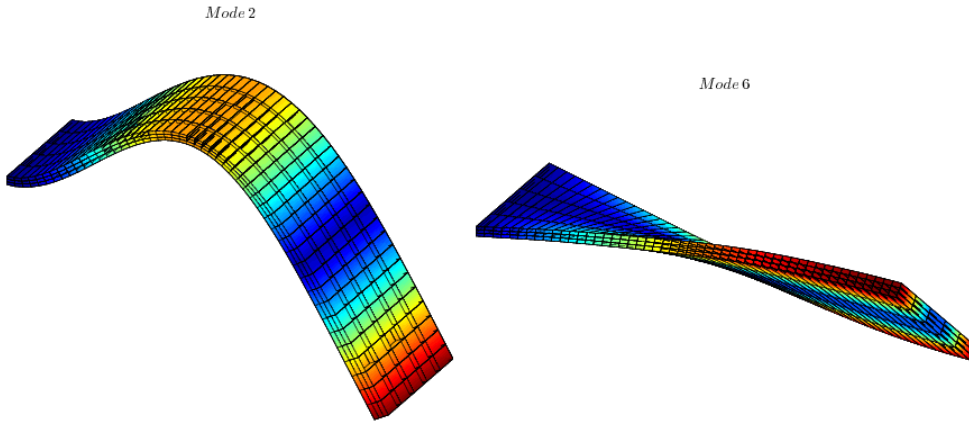


Figure 7.10: bending and torsion mode of bending-torsion fibre

Finally, a dynamic analysis is carried out, where the beam is subjected to a harmonic end point load. The frequency of excitation of the external forcing term is chosen sequentially equal to  $\omega_p \in [0.01, 0.1, 1.0, 10.0] \text{ rad/s}$ . While it is possible to excite the beam at different resonance frequencies, this would lead to irreproducible results from the experimental standpoint, due to the high value of the natural frequencies. In order to obtain a bounded solution, a damped system is introduced where classical Rayleigh damping [131] is used. The damping matrix  $\mathbf{C}$  is obtained as a linear combination of the mass  $\mathbf{M}$  and stiffness matrices  $\mathbf{K}$ , namely  $\mathbf{C} = a\mathbf{M} + b\mathbf{K}$ , where  $a = b = 0.01$  are used for this analysis.

The damped system subjected to the external forcing term is then solved via the Newmark's method using 50 quadratic elements of Lagrange-Gauss-Lobbato basis functions and the time-

step size is chosen as 1/500 s. An external forcing term defined by  $\mathbf{Q}^m \cdot \mathbf{e}_1 = P_0 \sin(\omega_P t)$  is applied at the tip, where  $\omega_P$  is the natural frequency of excitation (as listed above) and  $P_0$  the amplitude of the excitation chosen in this case as 100N. Figure 7.11 shows the time history of the external forcing term when  $\omega_P = 10\text{rad/sec}$ . Note that the external force  $\omega_P = 0.01\text{rad/sec}$  corresponds to a pulse loading. As can be observed, the external forcing term is applied for the first 30s and then removed (see Figure 7.11). The correct consideration of the multiple degrees of freedom of the system enables the accurate capturing of the energy of the beam model, superseding alternative approaches based on simplified structural models.

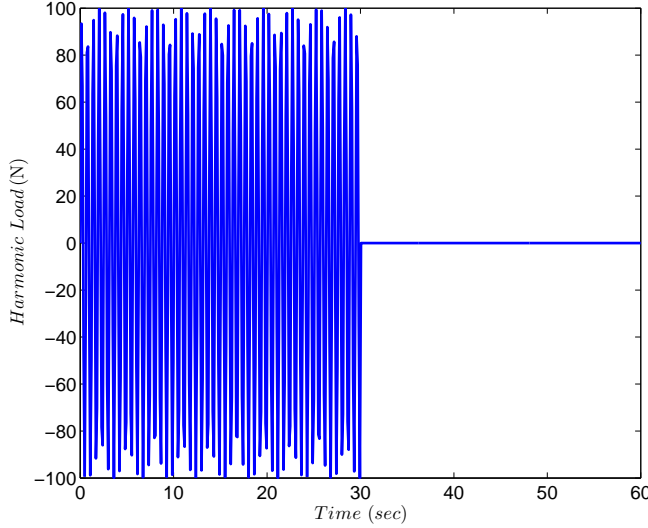


Figure 7.11: Harmonic vibration with frequency  $\omega_p = 10 \text{ rad/sec}$

The instantaneous electrical power  $P^e$  can be computed (refer to equation (7.32)) as

$$P^e = \int_l \left( \dot{\epsilon}^e \cdot \mathbf{Q}^e + \dot{\kappa}^e \cdot \mathbf{M}^e + \dot{\zeta}^e : \mathbf{P}^e + \dot{\gamma}^e : \mathbf{O}^e \right) dx_3. \quad (7.67)$$

In the finite element context, one needs to compute the electrical power at each time step by carrying out the normal post-processing used in stress recovery (i.e. perform numerical integration to obtain the desired quantity at Gauss points, while looping over elements). Due to the linear nature of the problem, the time derivative of the electrical variables (needed to evaluate  $P^e$ ) can be computed directly from the Newmark's method, without the need to resort to an ad-hoc numerical differentiation within every time step. Recall that whilst velocities and accelerations are part of the unknowns of the dynamic problem, the time rates of the electrical variables are not. The harvested power for the case of the damped system is shown in Figure 7.12, for the four different excitation frequencies listed above.

It should be noted that this power corresponds to an instantaneous power where it is assumed that the electrodes are not attached to an external resistor. In all the cases, the power history decreases dramatically after 30s, which is when the external forcing term is removed.

#### 7.8.4 Structural health assessment of a sophisticated multi-component actuation machine with multiple circular piezoelectric sensors - CAD driven high order curvilinear finite elements

In our final example, we consider finite element simulation of linear piezoelectricity at a continuum level. This problem entails analysis of an actuation machine with multiple piezoelectric sensor installed on its surface to monitor its functional life cycle and performance. The actuation machine has an extremely complicated CAD description with multiple inter connected assemblies. While some of the components of the machine are described using NURBS curves

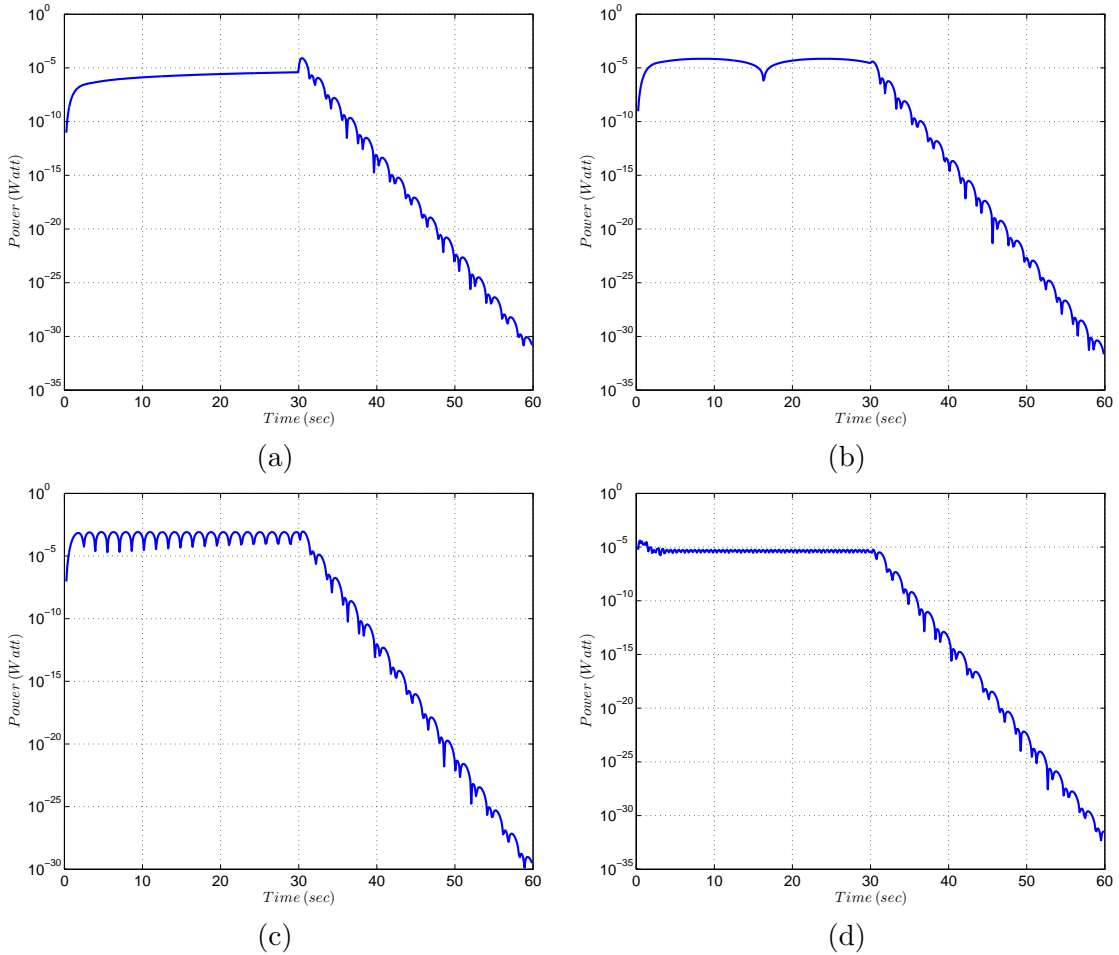


Figure 7.12: Harvested power at various frequencies: (a)  $\omega_P = 0.01 \text{ rad/sec}$ ; (b)  $\omega_P = 0.1 \text{ rad/sec}$ ; (c)  $\omega_P = 1 \text{ rad/sec}$ ; (d)  $\omega_P = 10 \text{ rad/sec}$

and B-Spline surfaces there are also multiple planes, conic regions and surfaces of revolutions which are described using standardised CAD specification (ISO 10303). Both isogeometric analysis and NURBS-enhanced finite elements fall short of dealing directly with these kind of topologies without converting the whole geometry to NURBS representation. Our developed curvilinear finite element is capable of working directly on these topologies without converting each individual component to NURBS descriptions and without moving away from the standard finite element functional spaces. On the other hand, positioning of piezoelectric sensors on to the CAD model requires a tight integration of geometrical design, curvilinear mesh generation and the finite elements in order to identify active and passive regions and impose the necessary boundary conditions which is again straightforward in our developed framework. Given the complexity of the problem, it is certain that there are no idealised settings and no exact or approximate analytical solution(s) for this problem and a three-dimensional computational study needs to be carried out.

The specification of this analysis falls under the sensing and structural health monitoring problems. The piezoelectric sensors attached on the surface of the machine are assumed to be PZT-5H with material properties given in the earlier section. Each sensor has a thickness of 1mm and is attached to the surface of the machine within designated cuts. The CAD geometry and the  $p = 4$  curvilinear mesh used for the analysis are shown in Figure 7.14. The overall dimensions of the machine are 133.37mm in the  $z$  direction (height), 133.5mm in the  $y$  direction (width) and 152.46mm in the  $x$  direction (length). It is assumed that the machine is structurally fixed at the base (Figure 7.14c) and bolted to the ground. It is also assumed that an entry shaft to top of the machine (main hole shown in Figure 7.14b) pressurises the entire assembly and challenges its structural endurance. The total number of degrees of freedom

in the system resulting from the  $p = 4$  finite element discretisation is approximately **60M** for the given computational mesh with 112819 elements. We use the high performance data parallel framework outlined in the next chapter to efficiently solve this problem. The problem is analysed dynamically using the generalised alpha method wherein the compressive pressure load of 50kPa caused by the connected shaft pressing the machine is applied monotonically over a long period of 300 seconds and then released during the second half of the simulation. The system is left undamped in this case. An open circuit configuration is adopted in that every sensor is assumed to have a zero electric potential at one of its ends.

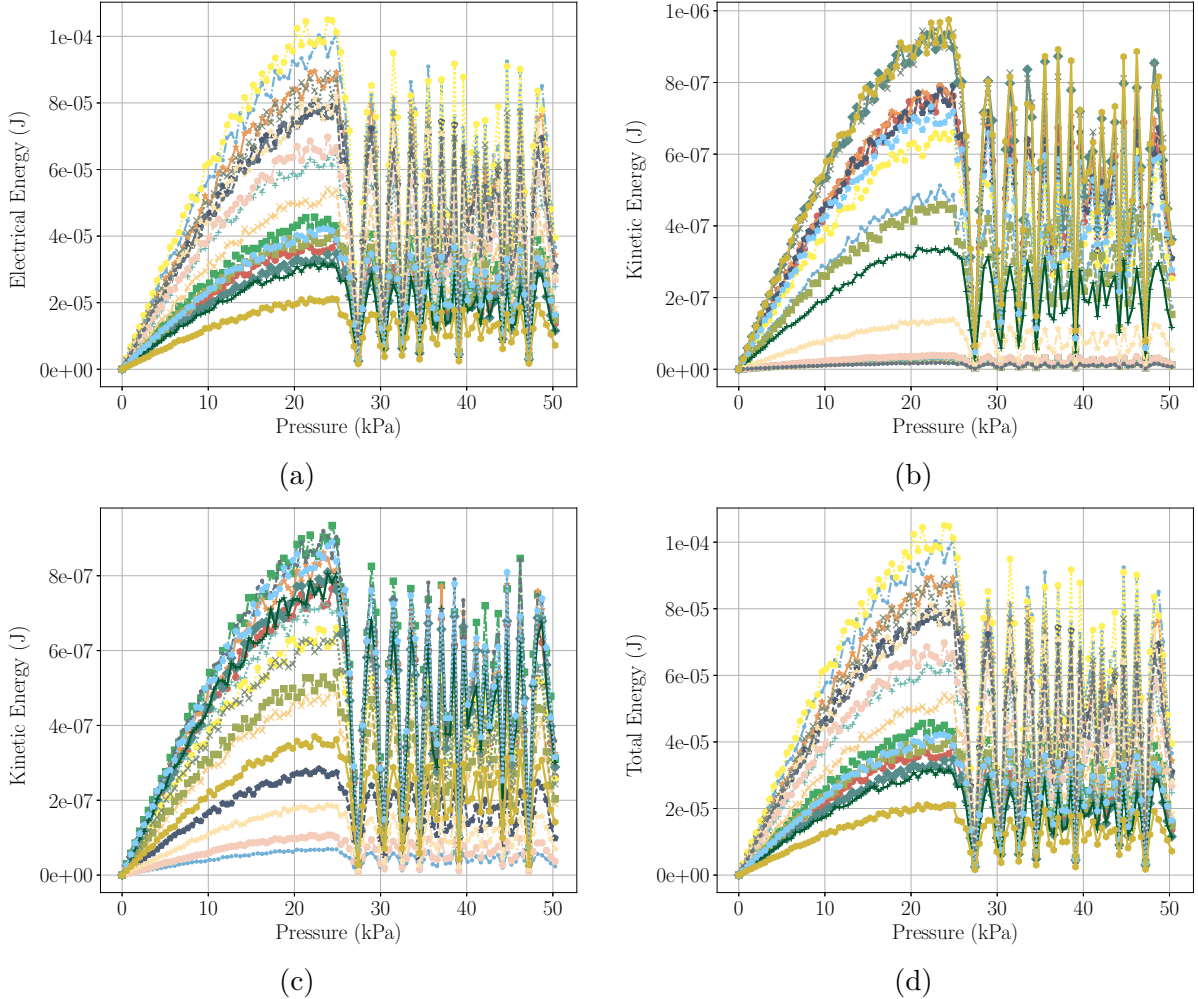


Figure 7.13: Measured total accumulated energies at each of the 17 piezoelectric sensors showing the (a) electrical energy, (b) strain energy, (c) vibration energy and, (d) total internal energy

Figure 7.15 shows the evolution of stress  $\sigma_{xy}$  in the machine as a result of continuous compressive pressure. Notice that, 552M further tetrahedral cells have been used as a result of further post-processing tessellation to extrapolate the results of the  $p = 4$  curved finite elements in order to obtain an extremely smooth and detailed representation of the evolution of the stresses. It can be observed that the our developed high order curvilinear finite element framework is capable of resolving the stress around NURBS boundaries with a remarkable level of detail.

An intuitive way to monitor the health of the machine is measure the contribution of electrical and strain energies accumulated in the sensors during the loading and unloading process. Figure 7.13 shows the evolution of electrical, strain and kinetic/vibrational energies during loading and unloading process for all 17 circular sensors (note that colours and marker styles are randomised). The energies are numerically computed over the entire region of every sensors. Since the system does not have damping, it can be seen that oscillations during

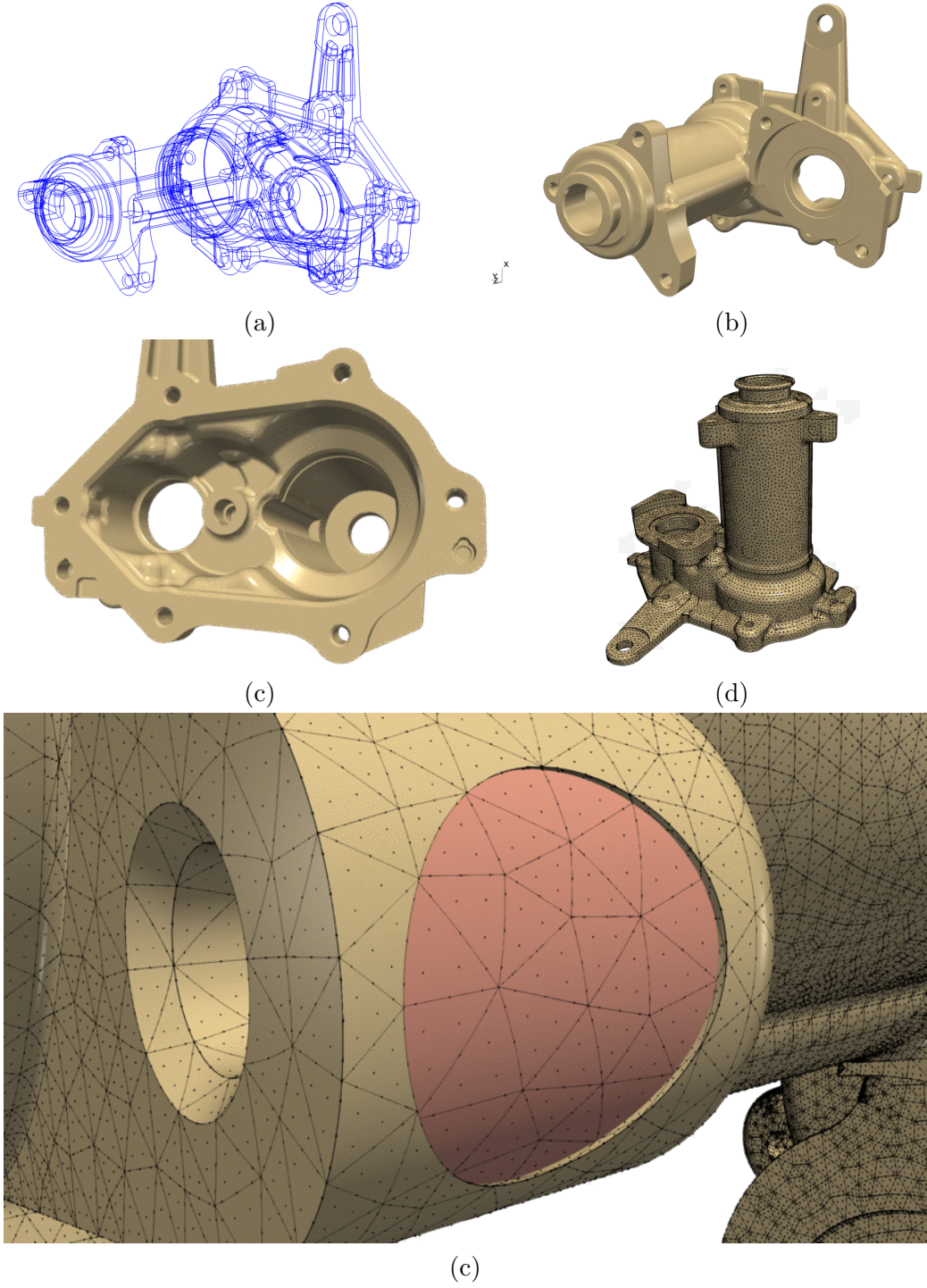


Figure 7.14: CAD model and  $p = 4$  curvilinear mesh of the actuation machine. The CAD model (after rigorous clean-up) is composed of 1207 topological surfaces, 5897 intersection curves (subfigure (a)), and 11794 topological vertices. Subfigure (e) shows the location of one of the 17 circular piezoelectric sensor patches installed on the machine. Positioning of sensors on to the CAD requires a tight integration of geometrical design and finite elements in order to identify active and passive regions and impose the necessary boundary conditions which is straightforward in our developed framework

unloading process keep intact. The major contribution in energy comes from the electrical energy of the system, however in the context of sensing within this problem the magnitudes add little insight into the state of the machine. The strain, vibrational, electrical and total internal energies of the system can all be investigated to monitor which areas in the machine are

experiencing strains. The sensors installed near the base/ground experience little deformation or vibration and hence signal the electric polarisation around the region is weak.

## 7.9 Conclusions

In this chapter, complete three-dimensional linear piezoelectric formulation for continua and beams and their *hp*-finite element implementation have been presented. A Timoshenko model, used to describe the kinematics of a straight axis beam, is complemented with a quadratic description of the electric potential across the cross section of the beam. The formulation is suitable to deal with static, modal and dynamic actuation and harvesting scenarios. Starting from the continuum level, a very clear description of the beam balance equations is presented by means of the introduction of suitable mechanical (and electrical counterparts) stress and strain resultants defined along the beam axis.

The chapter includes the closed-form solution for a two-dimensional piezoelectric cantilever beam subjected to static end tip mechanical and electrical loads and used to benchmark the numerical simulations through the use of suitable  $L^2$ ,  $H^1$  and energy error norms. In addition, the formulation has been also compared against existing literature [334, 9, 22] yielding excellent agreement in all cases. For shear-driven problems, a shear factor of 0.62 is suggested for the Timoshenko based solution in order to comply with that of layer-wise Euler-Bernoulli's approaches. Finally, three-dimensional continuum simulations have been carried to pinpoint the advanced computational capability and scalability of the framework for cases exact or approximate analytical solutions do not exist.

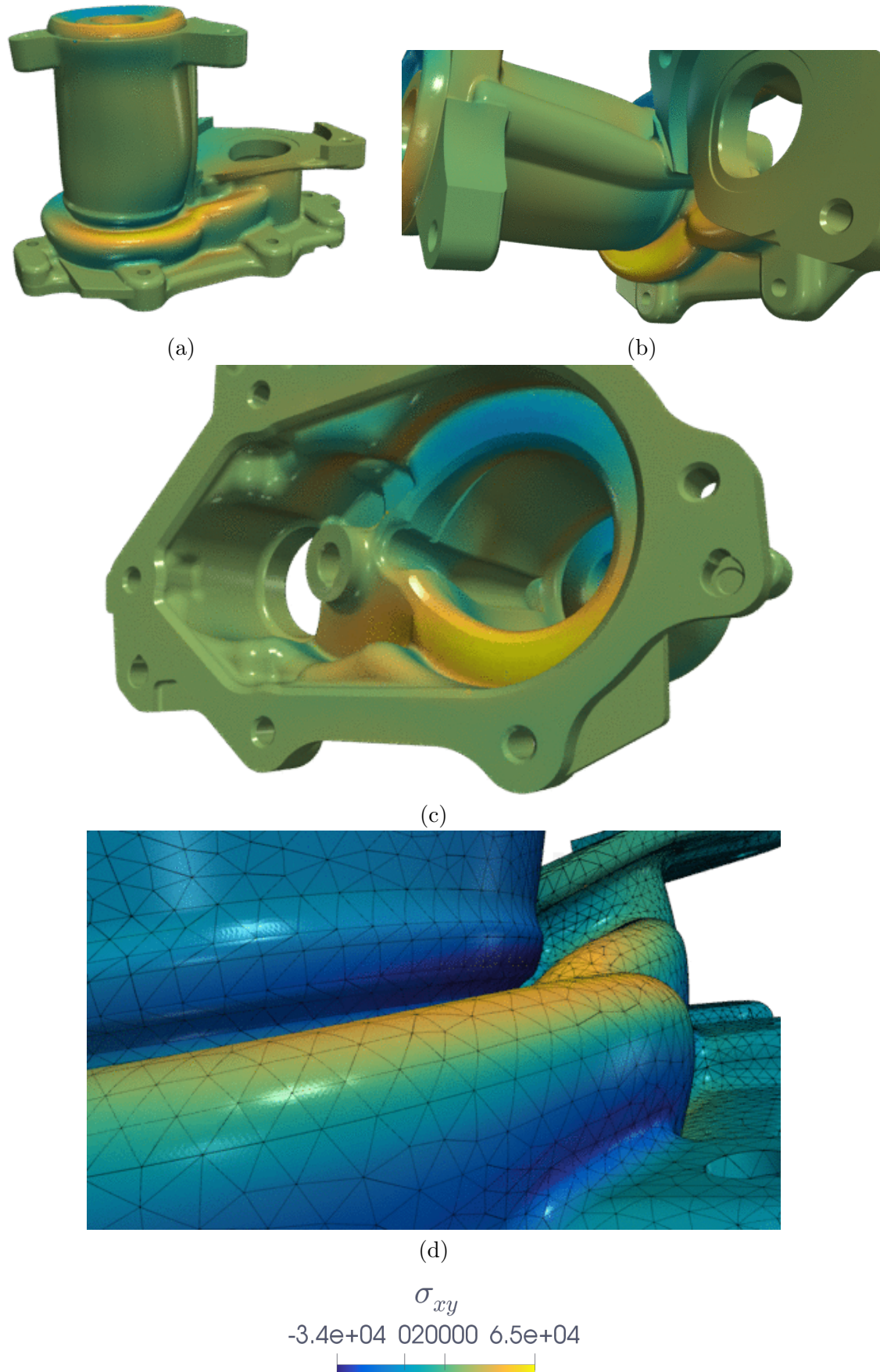


Figure 7.15: Evolution of stress  $\sigma_{xy}$  (Pa) in the machine as a result of continuous compressive pressure. **552M** further tetrahedral cells have been used to process an extremely smooth and detailed representation of the stress. Deformations are magnified by a factor of 5



# Class 4: High Order Finite Elements For Linear Flexoelectric Continua & Beams



# Chapter 8

## Linearised Electromechanics - Particularisation to Sensing and Energy Harvesting Flexoelectric Continua & Beams

### 8.1 Introduction

In this chapter, a family of numerical models for the phenomenological linear flexoelectric theory for continua and their particularisation to the case of three-dimensional beams based on a skew-symmetric couple stress theory is presented. In contrast to the traditional flexoelectric models which assume coupling between electric polarisation and strain gradients, we postulate an electric enthalpy in terms of linear invariants of curvature and electric field. This is achieved by introducing the axial curvature vector as a strain gradient measure. The implication of this assumption is many-fold. Firstly, for isotropic (non-piezoelectric) materials it allows constructing flexoelectric energies without breaking material symmetry. Secondly, nonuniform distribution of volumetric part of strains (volumetric strain gradients) do not generate electric polarisation, as confirmed by experimental evidence to be the case for some important classes of flexoelectric materials. Thirdly, a state of plane strain generates out of plane deformation through strain gradient effects. Finally, extension and shear coupling modes cannot be characterised individually as they contribute to the generation of electric polarisation as a whole. Four distinct variational principles are presented for both continuum and beam models namely, a displacement-potential formulation, a penalty formulation, a Lagrange-multiplier formulation and an augmented Lagrangian formulation. The three latter formulations facilitate incorporation of strain gradient measures in to a standard finite element scheme while maintaining the  $C^0$  continuity. The efficacy of high order finite elements along with the computational efficiency of mixed finite elements are utilised to develop a series of low and high order mixed finite element schemes for couple stress based flexoelectricity. Numerical results of finite element discretisations for the three latter variational formulations are benchmarked against available closed form solutions in regards to electromechanical coupling efficiency. A detailed comparison of the developed couple stress based flexoelectric model with the standard strain gradient flexoelectric models is performed for the case of Barium Titanate where a myriad of simple analytical solutions are proposed in order to quantitatively describe the similarities and dissimilarities in effective electromechanical coupling under these two theories. It is observed that, if the same experimental flexoelectric constants are fitted in to both theories, the current couple stress theory in general, reports stronger electromechanical conversion efficiency. Finally, nanocompression of a complex flexoelectric conical pyramid for which analytical solution cannot be established is numerically studied at an unprecedented level of detail to pinpoint the robustness and advanced computational scalability of the framework.

Much of the work in this chapter is based on the authors work on couple stress based flexo-

electric formulation for continua and beams presented in [252]. The structure of the paper is as follows. In section 8.2, the balance equations of electromechanics in a generalised micropolar continuum is presented. In section 8.3, the skew-symmetric couple stress model as a rotationally constrained case of the micropolar theory is discussed and the corresponding variational formulations are presented in section 8.4. In section 8.5 the couple stress problem is casted under the kinematics and electrostatics of three-dimensional flexoelectric beams and the associated weak and strong forms derived. Finite element discretisation of the variational formulations is presented in section 8.6. In section 8.7 a series of elementary and advanced computational simulations to study the electromechanical efficiency and microstructural dependency under static and dynamic settings are reported. Finally, in section 8.8 a set of conclusions are given.

## 8.2 Balance equations of electromechanics in micropolar continuum

Let  $\Omega \subset \mathbb{R}^3$  be a bounded contractible domain occupied by a micropolar continuum during the time interval  $[0, T]$  and  $\Gamma$  be its boundary, equipped with a unit outward normal  $\mathbf{n}$ , as shown in Figure 8.1. In this case, the static Faraday and Gauss laws can be summarised as follows

$$\nabla \times \mathbf{E} = \mathbf{0} \quad \text{and} \quad \operatorname{div} \tilde{\mathbf{D}} - \rho^e = 0 \quad \text{in } \Omega \times [0, T], \quad (8.1)$$

where  $\nabla \times$  denotes the curl operator,  $\mathbf{E}$  is the electric field intensity vector,  $\tilde{\mathbf{D}}$  is the electric displacement vector and  $\rho^e$  is the volume charge density. As  $\Omega$  is a contractible domain, the electric field vector  $\mathbf{E}$  can be reformulated as  $\mathbf{E} = -\nabla\psi$ , where  $\psi$  is a scalar potential field. Dirichlet and Neumann boundary conditions can then be introduced as

$$\psi = \bar{\psi} \quad \text{on} \quad \Gamma^\psi \times [0, T], \quad (8.2a)$$

$$\tilde{\mathbf{D}} \cdot \mathbf{n} = -q_0 \quad \text{on} \quad \Gamma^D \times [0, T]. \quad (8.2b)$$

where  $\Gamma = \Gamma^D \cup \Gamma^\psi$  and  $\Gamma^D \cap \Gamma^\psi = \emptyset$ . In the context of small deformations, the motion of the continuum can be defined by a displacement field  $\mathbf{u} : \Omega \times [0, T] \rightarrow \mathbb{R}^3$ , such that  $(\mathbf{x}, t) \mapsto \mathbf{u}(\mathbf{x}, t)$ , where  $\mathbf{x} \in \Omega$  represents a material point and  $t \in [0, T]$  the time. The conservation of linear momentum equation is defined as

$$\operatorname{div} \tilde{\boldsymbol{\sigma}} + \rho \mathbf{b} = \rho \ddot{\mathbf{u}} \quad \text{in } \Omega \times [0, T], \quad (8.3)$$

where  $\rho$  is the density of the continuum,  $\tilde{\boldsymbol{\sigma}}$  is the non-symmetric force stress tensor,  $\mathbf{b}$  is a body force per unit of mass and a superimposed dot (double dot) indicates partial (double) differentiation with respect to time (e.g.  $\dot{\cdot} := \frac{\partial}{\partial t}$  and  $\ddot{\cdot} := \frac{\partial^2}{\partial t^2}$ ). Dirichlet, Neumann and initial conditions can be introduced as

$$\mathbf{u} = \bar{\mathbf{u}} \quad \text{on} \quad \Gamma^u \times [0, T], \quad (8.4a)$$

$$\tilde{\boldsymbol{\sigma}} \mathbf{n} = \mathbf{t} \quad \text{on} \quad \Gamma^\sigma \times [0, T], \quad (8.4b)$$

$$\mathbf{u} = \mathbf{u}_0 \quad \text{in} \quad \bar{\Omega} \times 0, \quad (8.4c)$$

$$\dot{\mathbf{u}} = \dot{\mathbf{u}}_0 \quad \text{in} \quad \bar{\Omega} \times 0, \quad (8.4d)$$

where  $\Gamma = \Gamma^\sigma \cup \Gamma^u$  and  $\Gamma^\sigma \cap \Gamma^u = \emptyset$ . The vector  $\mathbf{t}$  in (8.4b) represents the force-traction. In the context of small rotations, the angular motion of the continuum can be defined by a field of proper orthogonal rotations  $\boldsymbol{\omega} : \Omega \times [0, T] \rightarrow \mathbf{SO}(3)$ , such that the mapping,  $(\mathbf{x}, t) \mapsto \boldsymbol{\omega}(\mathbf{x}, t)$  is an isometric linear transformation. The conservation of angular momentum is defined as

$$\operatorname{div} \tilde{\boldsymbol{\mu}} + \boldsymbol{\xi} : \tilde{\boldsymbol{\sigma}}^T + \rho \mathbf{l} = \rho \mathbf{J} \ddot{\boldsymbol{\omega}} \quad \text{in } \Omega \times [0, T], \quad (8.5)$$

where  $\tilde{\boldsymbol{\mu}}$  is the couple (hyperstress) stress tensor,  $\mathbf{l}$  is the body couple,  $\mathbf{J}$  is the rotational or spin inertia (determined by the shape and size of micro-continuum elements, [67]) and  $\boldsymbol{\xi}$  is the

third order permutation tensor<sup>1</sup>. Dirichlet, Neumann and initial conditions can be introduced as

$$\omega = \bar{\omega} \quad \text{on} \quad \Gamma^\omega \times [0, T], \quad (8.6a)$$

$$\tilde{\mu}n = m \quad \text{on} \quad \Gamma^\mu \times [0, T], \quad (8.6b)$$

$$\omega = \omega_0 \quad \text{in} \quad \bar{\Omega} \times 0, \quad (8.6c)$$

$$\dot{\omega} = \dot{\omega}_0 \quad \text{in} \quad \bar{\Omega} \times 0, \quad (8.6d)$$

where  $\Gamma = \Gamma^\mu \cup \Gamma^\omega$  and  $\Gamma^\mu \cap \Gamma^\omega = \emptyset$ . The vector  $m$  in (8.6b) represents the moment-traction, see Figure 8.1. For the full set of corrected boundary conditions in couple stress elasticity refer to [194, 109]. The coupled electro-mechanical initial boundary value problem, defined by equations (8.1) to (8.6), must be complemented with three closure equations related to the electro-mechanical nature of the generalised continuum. For a conservative material, the closure equations can be derived from the enthalpy density of the system  $\Psi$  defined in terms of the small strain tensor  $\tilde{\epsilon}$ , the curvature tensor  $\tilde{\chi}$  the electric field vector  $E$  as follows

$$\tilde{\sigma}(\tilde{\epsilon}, \tilde{\chi}, E) := \frac{\partial \tilde{\Psi}(\epsilon, \tilde{\chi}, E)}{\partial \tilde{\epsilon}}, \quad (8.7)$$

$$\tilde{\mu}(\tilde{\epsilon}, \tilde{\chi}, E) := \frac{\partial \tilde{\Psi}(\tilde{\epsilon}, \tilde{\chi}, E)}{\partial \tilde{\chi}}, \quad (8.8)$$

$$\tilde{D}(\tilde{\epsilon}, \tilde{\chi}, E) := -\frac{\partial \tilde{\Psi}(\tilde{\epsilon}, \tilde{\chi}, E)}{\partial E}, \quad (8.9)$$

expressing the force stress tensor  $\tilde{\sigma}$ , the couple stress tensor  $\tilde{\mu}$  and the electric displacement vector  $\tilde{D}$  in terms of the small strain tensor  $\tilde{\epsilon}$ , the curvature tensor  $\tilde{\chi}$  and the electric field  $E$  where the compatibility equations (kinematic measures), are defined in the classical Cosserat sense [229, 225, 32]

$$\tilde{\epsilon} := \nabla u - \hat{\omega}, \quad \tilde{\chi} := \nabla \omega, \quad (8.10)$$

where the following relationships exist between the axial vector and its dual skew-symmetric tensor

$$\hat{\omega} := \omega \times I, \quad \omega = \text{axl}(\hat{\omega}).$$

A variety of electro-mechanical constitutive models are available in the literature defined in terms of different enthalpy expressions, such as in [44, 279, 117, 269, 111]. In the case of linear flexoelectricity,  $\tilde{\sigma}$ ,  $\tilde{\mu}$  and  $\tilde{D}$  obtained this way render algebraic summations of mechanical (strain related)  $(\cdot)^m$ , micro-mechanical (curvature/strain gradient related)  $(\cdot)^g$  and electrical  $(\cdot)^e$  components. For instance, the electric displacement vector  $\tilde{D}$  can be expanded as

$$\tilde{D} = \tilde{D}^m + \tilde{D}^g + \tilde{D}^e; \quad \tilde{D}^m := \tilde{e} : \tilde{\epsilon}, \quad \tilde{D}^g := \tilde{f} : \tilde{\chi}, \quad D^e := \epsilon E, \quad (8.11)$$

where  $\epsilon$  is the symmetric second order dielectric permittivity tensor,  $\tilde{e}$  is the third order piezoelectric tensor and  $\tilde{f}$  is the third order flexoelectric tensor. Note that due to the asymmetric nature of strain and curvature tensors, there is no symmetry restriction on  $\tilde{e}$  and  $\tilde{f}$ , thus allowing for more general electromechanical couplings, [44]. Analogously, the force stress tensor  $\tilde{\sigma}$  can be decomposed additively as

$$\tilde{\sigma} = \tilde{\sigma}^m + \tilde{\sigma}^g + \tilde{\sigma}^e; \quad \tilde{\sigma}^m := \tilde{\mathcal{C}} : \tilde{\epsilon}, \quad \tilde{\sigma}^g := \tilde{\mathcal{D}} : \tilde{\chi}, \quad \tilde{\sigma}^e := -E \cdot \tilde{e}, \quad (8.12)$$

<sup>1</sup>It is important to note that all tensor fields  $(\tilde{\cdot})$  represent micropolar quantities, differentiating them with their counterparts in couple stress theory. In general, when the grapheme  $(\sim)$  does not appear, such as on electric field  $E$ , it implies that the definition of the field/quantity is the same in both theories.

Furthermore, unless specified otherwise, all tensor fields  $(\hat{\cdot})$  represent skew-symmetric tensors dual to their corresponding axial vector  $(\cdot)$ .

and the couple stress tensor  $\tilde{\chi}$  can be additively decomposed as

$$\tilde{\mu} = \tilde{\mu}^m + \tilde{\mu}^g + \tilde{\mu}^e; \quad \tilde{\mu}^m := \tilde{\varepsilon} : \tilde{\mathcal{D}}, \quad \tilde{\mu}^g := \tilde{\mathcal{B}} : \tilde{\chi}, \quad \tilde{\mu}^e := -\mathbf{E} \cdot \tilde{\mathbf{f}}. \quad (8.13)$$

where  $\tilde{\mathcal{C}}$  is the fourth order anisotropic elasticity tensor and  $\tilde{\mathcal{B}}$  and  $\tilde{\mathcal{D}}$  are fourth order tensors characterising the behaviour of micro-continuum. Note that, for centrosymmetric materials, coupling between the strain tensor  $\tilde{\varepsilon}$  and the curvature tensor  $\tilde{\chi}$  is not possible as this breaks the point symmetry, and invariance of the strain energy requires  $\tilde{\mathcal{D}} = \mathbf{0}$ , [229, 168]. Finally, the initial boundary value problem of the coupled system is defined by equations (8.1)-(8.6), (8.11)-(8.13).

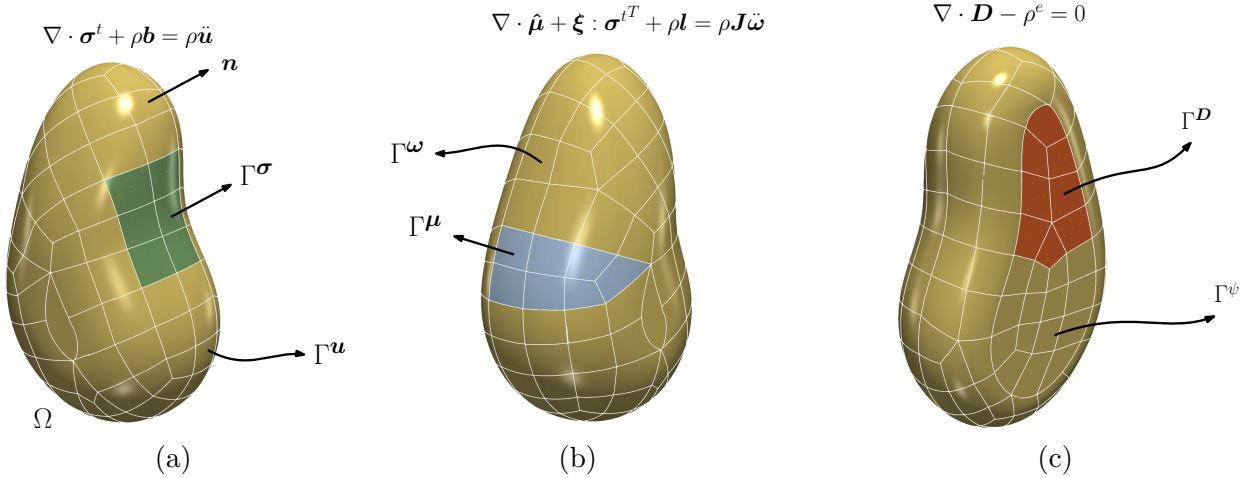


Figure 8.1: Schematic representation of the governing equations of couple stress and the decomposition of the boundary of a couple stress continua into a) displacements and tractions,  $\Gamma = \Gamma^\sigma \cup \Gamma^u$  and  $\Gamma^\sigma \cap \Gamma^u = \emptyset$ , b) rotations and couples/moments  $\Gamma = \Gamma^\mu \cup \Gamma^\omega$  and  $\Gamma^\mu \cap \Gamma^\omega = \emptyset$  and, c) surface charge and electric flux,  $\Gamma = \Gamma^D \cup \Gamma^\psi$  and  $\Gamma^D \cap \Gamma^\psi = \emptyset$ . Note that, while the boundary conditions associated with the electrostatics of the system are independent in couple stress theory when the rotations are constrained and individual variations of the fields are not allowed, it is only possible to apply two tangential components of moments on a traction boundary  $\Gamma^\sigma$ , and/or two tangential components of rotations on a displacement boundary  $\Gamma^u$  [215, 154, 228]. Note that  $\sigma^t$  represents the non-symmetric stress tensor defined in section 8.3.)

### 8.3 The skew-symmetric couple stress theory

The linear couple stress theory is formally a limit case of linear micropolar theory. The fundamental assumption is to enforce the following constraint on the rotations of the substructure

$$\boldsymbol{\omega}(\mathbf{x}, t) = \frac{1}{2} \nabla \times \mathbf{u}(\mathbf{x}, t) \quad \text{in } \Omega \times [0, T]. \quad (8.14)$$

Equation (8.14) is in fact the infinitesimal rotation (vorticity) vector of Cauchy elasticity. As discussed in B.1, this limit model can be obtained from the linear isotropic Cosserat model, provided appropriate boundary traction forces are considered as well [109, 221]. However, the consequence of imposing this constraint in general implies the indeterminacy of the couple stresses, as the spherical part of the curvature energy vanishes, see B.1. Furthermore, the strain tensor becomes symmetric, that is

$$\tilde{\varepsilon} = \varepsilon, \quad (8.15)$$

where  $\varepsilon$  represent the symmetric small strain tensor work conjugate to the force stress tensor of Cauchy elasticity  $\sigma$  and the curvature tensor in (8.10) remains unchanged. Furthermore,

the grapheme ( $\sim$ ) can be dropped from all quantities. Recently, [310] has shown that only the skew-symmetric part of the gradient of rotation is a thermodynamically valid state variable. The definition of the curvature tensor as the skew-symmetric part of gradient of rotation has been extensively studied in [300, 118, 117, 61, 62], giving rise to skew-symmetric couple stress theories. Hence, the couple stress curvature  $\chi$  has a dual representation

$$\hat{\chi} = \nabla^{skew} \omega = \nabla^{skew} \nabla^{skew} \mathbf{u} \quad \text{or} \quad \chi = \frac{1}{4} \nabla \times \nabla \times \mathbf{u}, \quad (8.16)$$

where

$$\chi = \text{axl}(\hat{\chi}), \quad \hat{\chi} = \chi \times \mathbf{I},$$

where  $\nabla^{skew}$  denotes the skew-symmetric part of the gradient. This definition of curvature vector opens new opportunities for modelling flexoelectricity in centrosymmetric materials, since the electric enthalpy can be defined in terms of linear invariants of the axial curvature vector and electric field, without breaking the symmetry. This also shows that the isotropic modified couple stress models developed by [330, 236, 189] cannot be generalised for the flexoelectric case as any linear invariant of symmetric curvature tensor in the enthalpy breaks the symmetry.

In light of (8.15) and in order to further simplify the process of material characterisation, the most well established couple stress models assume an additive decomposition of the internal energy of the system into a macromechanical energy expressed in terms of the invariants of classical strain tensor, a micromechanical energy expressed in terms of the invariants of the curvature vector and a couple term imposing the couple stress constraint [330, 236, 109]. Extending this to the case of flexoelectricity, the total internal energy of the electromechanical system can be written as

$$\begin{aligned} \check{\Psi}(\nabla^{sym} \mathbf{u}, \nabla^{skew} \mathbf{u}, \omega, \mathbf{E}(\psi)) &= \Psi(\epsilon(\mathbf{u}), \nabla \times \mathbf{u}, \omega, \mathbf{E}(\psi)) \\ &= \Psi_{mac}(\epsilon(\mathbf{u}), \mathbf{E}(\psi)) + \Psi_{mic}(\chi(\omega), \mathbf{E}(\psi)) + \Psi_{con}(\nabla \times \mathbf{u}, \omega), \end{aligned} \quad (8.17)$$

where  $\Psi_{con}(\nabla \times \mathbf{u}, \omega)$  typically takes the form shown in B.1 if different variations of the fields are considered and vanishes if the couple stress constraint is strongly enforced.

*Remark:* When coupled invariants of strain and curvature are neglected the constitutive term  $\mathcal{D}$  in (8.13) vanishes and consideration of infinitesimal strain tensor  $\epsilon$  leads to a symmetric local (Cauchy) stress and a symmetric constitutive tangent operator. However, a skew-symmetric non-local stress tensor  $\hat{\sigma}^g$  (dual to vector  $\sigma^g$ ) [see (8.12)] still emerges from the enforcement of the couple stress constraint which is not work-conjugate to  $\epsilon$ . In other words,  $\hat{\sigma}^g$  can be treated as a geometric term. This renders a non-symmetric total force stress tensor  $\sigma^t$  that contains both constitutive and geometric contributions. Certainly, this is also true for the classical indeterminate couple stress theory of [215] (i.e. the presence of body couples in the total force stress tensor); c.f. page 101 in [84]. This together with the issue of associated traction boundary conditions (see Figure 8.1) is arguably the most critiqued part of couple stress theory and an intensive part of recent developments by Neff and co-workers [228, 194, 109, 221, 220]. In essence, the equations of linear momentum and angular momentum can be re-written as

$$\text{div} \sigma^t + \rho \mathbf{b} = \rho \ddot{\mathbf{u}} \quad \text{in } \Omega \times [0, T], \quad (8.18)$$

$$\text{div} \hat{\mu} + \xi : \hat{\sigma}^{gT} + \rho \mathbf{l} = \rho \mathbf{J} \ddot{\omega} \quad \text{in } \Omega \times [0, T]. \quad (8.19)$$

We note that, in couple stress theories the effect of micro-inertia (angular velocities) can be neglected due to their associated moment of inertia being quadratic in characteristic length scale, [104]. Additionally, since the body couple term  $\rho \mathbf{l}$  performs work against  $\delta \omega$  and  $\delta \omega$  can be written in terms of  $\delta \mathbf{u}$  (where  $\delta \omega$  and  $\delta \mathbf{u}$  are possible boundary compatible variations of  $\omega$  and  $\mathbf{u}$ , respectively) the body couple can be transformed to a body force and a traction force contribution [118]. This leaves us with angular momentum equation of the form

$$-\nabla \times \mu + \xi : \hat{\sigma}^{gT} = \xi : (\hat{\sigma}^{gT} - \nabla \mu) = \mathbf{0} \quad \text{in } \Omega \times [0, T], \quad (8.20)$$

which implies

$$\hat{\boldsymbol{\sigma}}^g{}^T = \nabla \boldsymbol{\mu} \quad \text{in } \Omega \times [0, T], \quad (8.21)$$

signifying that in skew-symmetric couple stress theory,  $\hat{\boldsymbol{\sigma}}^g/\boldsymbol{\sigma}^g$  is not an independent quantity and can in fact be linked to the couple stress vector  $\boldsymbol{\mu}$  which itself is a constitutive stress. As a consequence,  $\hat{\boldsymbol{\sigma}}^g$ , and  $\hat{\boldsymbol{\mu}}$  contribute to the traction boundary condition. Subjected to the consideration of suitable boundary conditions, the skew-symmetric couple stress theory discussed here can be regarded as a restrictive case of the indeterminate couple stress theory of Mindlin and Tiersten, [228]. However, all the difficulties in boundary conditions can be circumvented if independent variations of the fields  $\mathbf{u}$  and  $\boldsymbol{\omega}$  are considered [226].

---

## 8.4 Variational formulations in couple stress based electromechanics of continua

In this section, four different variational formulations for couple stress based electromechanics are described in the continuum setting namely, a displacement potential formulation, a lagrange multiplier formulation, an augmented Lagrangian formulation and a penalty formulation.

### 8.4.1 The displacement-potential variational formulation

A two-field variational formulation can be established by strongly imposing the couple stress constraint. Focusing on the electro-elastodynamics of the conservative flexoelectric system, the internal and external forces together with the motion between times  $T_0 = 0$  and  $T$ , can be determined from a Hamilton's principle, [71, 294]. To this effect, we introduce the Lagrangian  $\mathcal{L}$  as

$$\mathcal{L}(\mathbf{u}, \dot{\mathbf{u}}, \psi) = \mathcal{K}(\dot{\mathbf{u}}) - \Pi_{\text{int}}(\mathbf{u}, \psi) - \Pi_{\text{ext}}(\mathbf{u}, \psi) \quad (8.22)$$

where  $\mathcal{K}$  is the kinetic energy of the body expressed as a function of velocity  $\dot{\mathbf{u}}$  and  $\Pi$  the total potential energy of the system, containing the work of internal and external electromechanical forces such that

$$\mathcal{K}(\dot{\mathbf{u}}) = \frac{1}{2} \int_{\Omega} \rho \dot{\mathbf{u}} \cdot \dot{\mathbf{u}} \, dV, \quad (8.23a)$$

$$\Pi_{\text{int}}(\mathbf{u}, \psi) = \int_{\Omega} \Psi(\boldsymbol{\varepsilon}(\mathbf{u}), \boldsymbol{\omega}(\mathbf{u}), \psi) \, dV = \int_{\Omega} \Psi_{mac}(\boldsymbol{\varepsilon}(\mathbf{u}), \mathbf{E}(\psi)) + \Psi_{mic}(\boldsymbol{\chi}(\mathbf{u}), \mathbf{E}(\psi)) \, dV, \quad (8.23b)$$

$$\Pi_{\text{ext}}(\mathbf{u}, \psi) = \int_{\Omega} \rho \left( \mathbf{b} \cdot \mathbf{u} + \mathbf{l} \cdot \boldsymbol{\omega}(\mathbf{u}) \right) - \rho_0 \psi \, dV + \int_{\Gamma} \mathbf{t} \cdot \mathbf{u} + \mathbf{m} \cdot \boldsymbol{\omega}(\mathbf{u}) - q_0 \psi \, dA \quad (8.23c)$$

Considering the action integral as the integral of the Lagrangian over the time interval  $t = [0, T]$ , the Hamilton's principle states that the mapping satisfying the equations of motion and electrostatics can be obtained by making the action integral stationary with respect to all possible mappings which are compatible with the boundary conditions. In the present case this leads to the following Euler-Lagrange equations

$$\frac{\partial \mathcal{L}}{\partial \mathbf{u}} - \frac{d}{dt} \frac{\partial \mathcal{L}}{\partial \dot{\mathbf{u}}} = \mathbf{0}, \quad \frac{\partial \mathcal{L}}{\partial \psi} = 0. \quad (8.24)$$

Denoting the virtual and incremental variations of displacements and electric potential as  $\delta \mathbf{u}$ ,  $\Delta \mathbf{u}$ ,  $\delta \psi$  and  $\Delta \psi$  respectively leading to

$$\delta \boldsymbol{\omega} = \frac{1}{2} \nabla \times \delta \mathbf{u}, \quad \Delta \boldsymbol{\omega} = \frac{1}{2} \nabla \times \Delta \mathbf{u}. \quad (8.25)$$

The stationary condition of the kinetic energy then becomes

$$\frac{d}{dt} \frac{\partial \mathcal{L}}{\partial \dot{\mathbf{u}}} = \frac{d}{dt} \frac{\partial \mathcal{K}}{\partial \dot{\mathbf{u}}} = \int_{\Omega} \rho \ddot{\mathbf{u}} \cdot \delta \mathbf{u} \, dV. \quad (8.26)$$

The stationary conditions of the internal energy can be found by computing the directional derivative of the energy with respect to virtual variations of displacements and electric potential as

$$D\Pi_{\text{int}}[\delta \mathbf{u}] = \int_{\Omega} \left( \frac{\partial \Psi}{\partial \boldsymbol{\varepsilon}} : \delta \boldsymbol{\varepsilon} + \left( \frac{\partial \Psi}{\partial \boldsymbol{\omega}} \times \mathbf{I} \right) : \delta \hat{\boldsymbol{\omega}} + \frac{\partial \Psi}{\partial \boldsymbol{\chi}} \cdot \delta \boldsymbol{\chi} \right) \, dV = \int_{\Omega} \left( \boldsymbol{\sigma} : \delta \boldsymbol{\varepsilon} + \hat{\boldsymbol{\sigma}}^g : \delta \hat{\boldsymbol{\omega}} + \boldsymbol{\mu} \cdot \delta \boldsymbol{\chi} \right), \quad (8.27a)$$

$$D\Pi_{\text{int}}[\delta \psi] = \int_{\Omega} \frac{\partial \Psi}{\partial \mathbf{E}} \cdot \delta \mathbf{E} \, dV = - \int_{\Omega} \mathbf{D} \cdot \delta \mathbf{E} \, dV, \quad (8.27b)$$

where  $\delta \boldsymbol{\varepsilon}$ ,  $\delta \boldsymbol{\chi}$  and  $\delta \mathbf{E}$  represent virtual variations of strain tensor, curvature vector and electric field vector respectively. Moreover, without loss of generality,  $\boldsymbol{\sigma}$  now represents the total constitutive tensor which might or might not include gradient effects depending on material symmetry; see (8.12).<sup>2</sup> Analogously, consistent linearisation of the external work leads to

$$D\Pi_{\text{ext}}[\delta \mathbf{u}] = \int_{\Omega} \rho \left( \mathbf{b} \cdot \delta \mathbf{u} + \mathbf{l} \cdot \delta \boldsymbol{\omega} \right) \, dV + \int_{\Gamma} \left( \mathbf{t} \cdot \delta \mathbf{u} + \mathbf{m} \cdot \delta \boldsymbol{\omega} \right) \, dA, \quad (8.28a)$$

$$D\Pi_{\text{ext}}[\delta \psi] = - \int_{\Omega} \rho_0 \psi \, dV - \int_{\Gamma} q_0 \psi \, dA, \quad (8.28b)$$

where  $\delta \boldsymbol{\omega}$  is defined in (8.25). For the purpose of finite element implementation it is also necessary to compute the relevant tangent operators through further consistent linearisation of (8.28) which can be written as (the symmetric terms are omitted)

$$\begin{aligned} D\Pi_{\text{int}}[\delta \mathbf{u}; \Delta \mathbf{u}] &= \int_{\Omega} \left( \Delta \boldsymbol{\varepsilon} : \frac{\partial^2 \Psi}{\partial \boldsymbol{\varepsilon} \partial \boldsymbol{\varepsilon}} : \delta \boldsymbol{\varepsilon} + \Delta \boldsymbol{\chi} \cdot \frac{\partial^2 \Psi}{\partial \boldsymbol{\chi} \partial \boldsymbol{\chi}} \cdot \delta \boldsymbol{\chi} \right) \, dV \\ &\quad + \int_{\Omega} \left( \Delta \boldsymbol{\varepsilon} : \frac{\partial^2 \Psi}{\partial \boldsymbol{\varepsilon} \partial \boldsymbol{\chi}} \cdot \delta \boldsymbol{\chi} + \Delta \boldsymbol{\chi} \cdot \frac{\partial^2 \Psi}{\partial \boldsymbol{\chi} \partial \boldsymbol{\varepsilon}} : \delta \boldsymbol{\varepsilon} \right) \, dV \\ &= \int_{\Omega} \left( \Delta \boldsymbol{\varepsilon} : \mathcal{C} : \delta \boldsymbol{\varepsilon} + \Delta \boldsymbol{\chi} \cdot \mathcal{B} \cdot \delta \boldsymbol{\chi} \right) \, dV \\ &\quad + \int_{\Omega} \left( \Delta \boldsymbol{\varepsilon} : \mathcal{D} \cdot \delta \boldsymbol{\chi} + \Delta \boldsymbol{\chi} \cdot \mathcal{D}^T : \delta \boldsymbol{\varepsilon} \right) \, dV, \end{aligned} \quad (8.29a)$$

$$\begin{aligned} D\Pi_{\text{int}}[\delta \mathbf{u}; \Delta \psi] &= \int_{\Omega} \left( \Delta \mathbf{E} \cdot \frac{\partial^2 \Psi}{\partial \boldsymbol{\varepsilon} \partial \mathbf{E}} : \delta \boldsymbol{\varepsilon} + \Delta \mathbf{E} \cdot \frac{\partial^2 \Psi}{\partial \boldsymbol{\chi} \partial \mathbf{E}} \cdot \delta \boldsymbol{\chi} \right) \, dV \\ &= - \int_{\Omega} \left( \Delta \mathbf{E} \cdot \mathbf{e} : \delta \boldsymbol{\varepsilon} + \Delta \mathbf{E} \cdot \mathbf{f} \cdot \delta \boldsymbol{\chi} \right) \, dV, \end{aligned} \quad (8.29b)$$

$$D\Pi_{\text{int}}[\delta \psi, \Delta \psi] = \int_{\Omega} \Delta \mathbf{E} \cdot \frac{\partial^2 \Psi}{\partial \mathbf{E} \partial \mathbf{E}} \cdot \delta \mathbf{E} \, dV = - \int_{\Omega} \Delta \mathbf{E} \cdot \boldsymbol{\epsilon} \cdot \delta \mathbf{E} \, dV, \quad (8.29c)$$

where  $\Delta \boldsymbol{\varepsilon}$ ,  $\Delta \boldsymbol{\chi}$  and  $\Delta \mathbf{E}$  represent incremental variations of strain tensor, curvature vector and electric field vector respectively. Furthermore, the coupled terms in (8.29a) vanish for isotropic materials. Note that upon performing further integration by part on (8.27) new boundary terms emerge that contribute to traction force and couple force [228]. In general, the total force stress can be written as

$$\boldsymbol{\sigma}^t = \boldsymbol{\sigma} + \hat{\boldsymbol{\sigma}}^g, \quad \text{where} \quad \hat{\boldsymbol{\sigma}}^g = \frac{1}{2} (\nabla \times \boldsymbol{\mu}) \times \mathbf{I}. \quad (8.30)$$

---

<sup>2</sup>Depending on the notation, the work-conjugacy between  $\delta \boldsymbol{\chi}$  and  $\boldsymbol{\mu}$  can also be written in terms of their dual representation  $\hat{\mu}_{ij} : \delta \hat{\chi}_{ij} = \xi_{ijk} \xi_{ijl} \mu_k \delta \chi_l = 2 \mu_k \delta \chi_k$ ,

which shows that the proper work-conjugate to  $\delta \boldsymbol{\chi}$  is in fact  $2\boldsymbol{\mu}$ . For notational convenience, here it is assumed that this factor is embedded in the definition of the axial couple stress vector  $\boldsymbol{\mu}$ .

The set of equations in (8.27), (8.28) and (8.29) facilitate straightforward finite element discretisation in terms of displacements and electric potential. This formulation however, dictates  $C^1$  continuity for displacements. This inevitably requires the use of non-standard finite element function spaces and is not pursued here.

#### 8.4.2 The penalty formulation

A natural way to formulate the couple stress flexoelectric problem is to treat the vorticity of the substructure  $\boldsymbol{w}$  as an independent field and impose the couple stress constraint weakly through a penalty approximation. In this case the potential energy of the system is given by

$$\tilde{\Pi}_{\text{int}}(\boldsymbol{u}, \boldsymbol{\omega}, \psi) = \int_{\Omega} \tilde{\Psi}(\boldsymbol{\varepsilon}(\boldsymbol{u}), \boldsymbol{\chi}(\boldsymbol{\omega}), \boldsymbol{E}(\psi)) \, dV + \int_{\Omega} \frac{\kappa}{2} \left\| \frac{1}{2} \nabla \times \boldsymbol{u} - \boldsymbol{\omega} \right\|^2 \, dV, \quad (8.31)$$

where  $\|\cdot\|$  is the Frobenius norm. As shown in B.1, the elegance of this formulation comes from the fact that  $\kappa$  can be treated as the Cosserat modulus and hence, the formulation adheres to a physically meaningful treatment of couple stress flexoelectricity.

Avoiding redundant derivations of stationary conditions of kinetic and external energies and focussing only on the internal energy, the first directional derivative of the (8.31) with respect to the virtual variations of displacements, vorticity and electric potential yields

$$D\tilde{\Pi}_{\text{int}}[\delta \boldsymbol{u}] = \int_{\Omega} \boldsymbol{\sigma} : \delta \boldsymbol{\varepsilon} \, dV + \int_{\Omega} \kappa \left( \frac{1}{2} \nabla \times \boldsymbol{u} - \boldsymbol{\omega} \right) \cdot \left( \frac{1}{2} \nabla \times \delta \boldsymbol{u} \right) \, dV, \quad (8.32a)$$

$$D\tilde{\Pi}_{\text{int}}[\delta \boldsymbol{\omega}] = \int_{\Omega} \boldsymbol{\mu} \cdot \delta \boldsymbol{\chi} \, dV - \int_{\Omega} \kappa \left( \frac{1}{2} \nabla \times \boldsymbol{u} - \boldsymbol{\omega} \right) \cdot \delta \boldsymbol{\omega} \, dV, \quad (8.32b)$$

$$D\tilde{\Pi}_{\text{int}}[\delta \psi] = - \int_{\Omega} \boldsymbol{D} \cdot \delta \boldsymbol{E} \, dV, \quad (8.32c)$$

For the purpose of finite element implementation it is also necessary to compute the relevant tangent operators through further consistent linearisation of (8.32)

$$D\tilde{\Pi}_{\text{int}}[\delta \boldsymbol{u}; \Delta \boldsymbol{u}] = \int_{\Omega} \Delta \boldsymbol{\varepsilon} : \boldsymbol{\mathcal{C}} : \delta \boldsymbol{\varepsilon} \, dV + \int_{\Omega} \kappa \left( \frac{1}{2} \nabla \times \Delta \boldsymbol{u} \right) \cdot \left( \frac{1}{2} \nabla \times \delta \boldsymbol{u} \right) \, dV, \quad (8.33a)$$

$$D\tilde{\Pi}_{\text{int}}[\delta \boldsymbol{u}; \Delta \boldsymbol{\omega}] = - \int_{\Omega} \kappa \Delta \boldsymbol{\omega} \cdot \left( \frac{1}{2} \nabla \times \delta \boldsymbol{u} \right) \, dV + \int_{\Omega} \Delta \boldsymbol{\chi} \cdot \boldsymbol{\mathcal{D}}^T : \delta \boldsymbol{\varepsilon} \, dV, \quad (8.33b)$$

$$D\tilde{\Pi}_{\text{int}}[\delta \boldsymbol{u}; \Delta \psi] = - \int_{\Omega} \delta \boldsymbol{E} \cdot \boldsymbol{e} : \delta \boldsymbol{\varepsilon} \, dV, \quad (8.33c)$$

$$D\tilde{\Pi}_{\text{int}}[\delta \boldsymbol{\omega}; \Delta \boldsymbol{\omega}] = \int_{\Omega} \Delta \boldsymbol{\chi} \cdot \boldsymbol{\mathcal{B}} \cdot \delta \boldsymbol{\chi} \, dV + \int_{\Omega} \kappa \Delta \boldsymbol{\omega} \cdot \delta \boldsymbol{\omega} \, dV, \quad (8.33d)$$

$$D\tilde{\Pi}_{\text{int}}[\delta \boldsymbol{\omega}; \Delta \psi] = - \int_{\Omega} \Delta \boldsymbol{E} \cdot \boldsymbol{f} \cdot \delta \boldsymbol{\chi} \, dV, \quad (8.33e)$$

$$D\tilde{\Pi}_{\text{int}}[\delta \psi, \Delta \psi] = - \int_{\Omega} \Delta \boldsymbol{E} \cdot \boldsymbol{\epsilon} \cdot \delta \boldsymbol{E} \, dV, \quad (8.33f)$$

where the second integrand in (8.33b) vanishes for isotropic materials. Note that, with a slight abuse of notation the kinematic variables and their work-conjugates have not been renamed, although strictly speaking their description under displacement-potential and penalty formulations are not the same. Analogous to displacement potential formulation, the total force stress tensor in the penalty formulation can be written as

$$\boldsymbol{\sigma}^t = \boldsymbol{\sigma} + \hat{\boldsymbol{\sigma}}^g, \quad \text{where} \quad \hat{\boldsymbol{\sigma}}^g = \kappa \left( \frac{1}{2} \nabla \times \boldsymbol{u} - \boldsymbol{\omega} \right) \times \boldsymbol{I}, \quad (8.34)$$

which shows that the penalty parameter  $\kappa$  is indeed the Cosserat modulus and the constraint will be imposed if  $\kappa \rightarrow \infty$ . In essence, this is an approximate enforcement, however the advantage of this formulation certainly, lies in the fact that it does not introduce a new variable for the enforcement of the constraint. Finite element discretisation of this formulation is presented in section 8.6.

### 8.4.3 The Lagrange multiplier formulation

The couple stress constraint can also be imposed exactly albeit in a weak sense through the so-called Lagrange multiplier approach. In this formulation, a new variable is introduced to impose the constraint and the internal energy of the system is given by

$$\bar{\Pi}_{\text{int}}(\boldsymbol{u}, \boldsymbol{\omega}, \boldsymbol{s}, \psi) = \int_{\Omega} \dot{\Psi}(\boldsymbol{\varepsilon}(\boldsymbol{u}), \boldsymbol{\chi}(\boldsymbol{\omega}), \boldsymbol{E}(\psi)) \, dV + \int_{\Omega} \boldsymbol{s} \cdot \left( \frac{1}{2} \nabla \times \boldsymbol{u} - \boldsymbol{\omega} \right) \, dV, \quad (8.35)$$

where  $\boldsymbol{s}$  is the vector of Lagrange multipliers enforcing the constraint. Focussing only on the internal energy, the first directional derivative of the (8.39) with respect to the virtual variations of displacements, vorticity, Lagrange multiplier and electric potential yields

$$D\bar{\Pi}_{\text{int}}[\delta \boldsymbol{u}] = \int_{\Omega} \boldsymbol{\sigma} : \delta \boldsymbol{\varepsilon} \, dV + \int_{\Omega} \boldsymbol{s} \cdot \left( \frac{1}{2} \nabla \times \delta \boldsymbol{u} \right) \, dV, \quad (8.36a)$$

$$D\bar{\Pi}_{\text{int}}[\delta \boldsymbol{\omega}] = \int_{\Omega} \boldsymbol{\mu} \cdot \delta \boldsymbol{\chi} \, dV - \int_{\Omega} \boldsymbol{s} \cdot \delta \boldsymbol{\omega} \, dV, \quad (8.36b)$$

$$D\bar{\Pi}_{\text{int}}[\delta \boldsymbol{s}] = \int_{\Omega} \delta \boldsymbol{s} \cdot \left( \frac{1}{2} \nabla \times \boldsymbol{u} - \boldsymbol{\omega} \right) \, dV, \quad (8.36c)$$

$$D\bar{\Pi}_{\text{int}}[\delta \psi] = - \int_{\Omega} \boldsymbol{D} \cdot \delta \boldsymbol{E} \, dV, \quad (8.36d)$$

For the purpose of finite element implementation it is also necessary to compute the relevant tangent operators through further consistent linearisation of (8.36)

$$D\bar{\Pi}_{\text{int}}[\delta \boldsymbol{u}; \Delta \boldsymbol{u}] = \int_{\Omega} \Delta \boldsymbol{\varepsilon} : \boldsymbol{\mathcal{C}} : \delta \boldsymbol{\varepsilon} \, dV, \quad (8.37a)$$

$$D\bar{\Pi}_{\text{int}}[\delta \boldsymbol{u}; \Delta \boldsymbol{\omega}] = \int_{\Omega} \Delta \boldsymbol{\chi} \cdot \boldsymbol{\mathcal{D}}^T : \delta \boldsymbol{\varepsilon} \, dV, \quad (8.37b)$$

$$D\bar{\Pi}_{\text{int}}[\delta \boldsymbol{u}; \Delta \boldsymbol{s}] = \int_{\Omega} \Delta \boldsymbol{s} \cdot \left( \frac{1}{2} \nabla \times \delta \boldsymbol{u} \right) \, dV, \quad (8.37c)$$

$$D\bar{\Pi}_{\text{int}}[\delta \boldsymbol{u}; \Delta \psi] = - \int_{\Omega} \delta \boldsymbol{E} \cdot \boldsymbol{e} : \delta \boldsymbol{\varepsilon} \, dV, \quad (8.37d)$$

$$D\bar{\Pi}_{\text{int}}[\delta \boldsymbol{\omega}; \Delta \boldsymbol{\omega}] = \int_{\Omega} \Delta \boldsymbol{\chi} \cdot \boldsymbol{\mathcal{B}} \cdot \delta \boldsymbol{\chi} \, dV + \int_{\Omega} \kappa \Delta \boldsymbol{\omega} \cdot \delta \boldsymbol{\omega} \, dV, \quad (8.37e)$$

$$D\bar{\Pi}_{\text{int}}[\delta \boldsymbol{\omega}; \Delta \boldsymbol{s}] = - \int_{\Omega} \Delta \boldsymbol{s} \cdot \delta \boldsymbol{\omega} \, dV, \quad (8.37f)$$

$$D\bar{\Pi}_{\text{int}}[\delta \boldsymbol{\omega}; \Delta \psi] = - \int_{\Omega} \Delta \boldsymbol{E} \cdot \boldsymbol{f} \cdot \delta \boldsymbol{\chi} \, dV, \quad (8.37g)$$

$$D\bar{\Pi}_{\text{int}}[\delta \boldsymbol{s}; \Delta \boldsymbol{s}] = 0, \quad (8.37h)$$

$$D\bar{\Pi}_{\text{int}}[\delta \psi, \Delta \psi] = - \int_{\Omega} \Delta \boldsymbol{E} \cdot \boldsymbol{\epsilon} \cdot \delta \boldsymbol{E} \, dV, \quad (8.37i)$$

where (8.37b) vanishes for isotropic materials. Note that, with a slight abuse of notation, the kinematic variables and their work-conjugates have not been renamed, although strictly speaking their description compared to the last two variational formulations have changed. The total force stress tensor can now be written as

$$\boldsymbol{\sigma}^t = \boldsymbol{\sigma} + \hat{\boldsymbol{\sigma}}^g, \quad \text{where} \quad \hat{\boldsymbol{\sigma}}^g = \frac{1}{2} \boldsymbol{s} \times \boldsymbol{I}, \quad (8.38)$$

which shows that the Lagrange multiplier  $\boldsymbol{s}$  can be interpreted as the skew-symmetric part of total force stress tensor emanating from microstructural contribution.

#### 8.4.4 The augmented Lagrangian formulation

From a numerical implementation point of view, the Lagrange multiplier approach leads to the popular saddle point problem that typically occurs in constrained energy minimisation problems such as incompressibility. Hence, it is at times advantageous to add a penalty type *regularisation* term to the internal energy of the system. This approach is termed as the augmented Lagrangian formulation and the internal energy of the system is given by

$$\check{\Pi}_{\text{int}}(\mathbf{u}, \boldsymbol{\omega}, \mathbf{s}, \psi) = \int_{\Omega} \Psi(\boldsymbol{\varepsilon}(\mathbf{u}), \boldsymbol{\chi}(\boldsymbol{\omega}), \mathbf{E}(\psi)) \, dV + \int_{\Omega} \mathbf{s} \cdot \left( \frac{1}{2} \nabla \times \mathbf{u} - \boldsymbol{\omega} \right) \, dV + \int_{\Omega} \frac{1}{2\kappa} \mathbf{s} \cdot \mathbf{s} \, dV. \quad (8.39)$$

Consistent linearisation of this energy is similar to the Lagrange multiplier formulation and the only two new terms arising are

$$D\check{\Pi}_{\text{int}}[\delta \mathbf{s}] = \int_{\Omega} \delta \mathbf{s} \cdot \left( \frac{1}{2} \nabla \times \mathbf{u} - \boldsymbol{\omega} \right) \, dV + \int_{\Omega} \frac{1}{\kappa} \mathbf{s} \cdot \delta \mathbf{s} \, dV, \quad (8.40)$$

$$D\check{\Pi}_{\text{int}}[\delta \mathbf{s}; \Delta \mathbf{s}] = \int_{\Omega} \frac{1}{\kappa} \Delta \mathbf{s} \cdot \delta \mathbf{s} \, dV, \quad (8.41)$$

and the total force stress tensor remains unchanged. Finite element implementation of all the three mixed formulations presented here are discussed in section 8.6.

### 8.5 Couple-stress flexoelectric theory for three-dimensional beams

Having established a curvature-induced flexoelectric theory through couple stress formulation for the continua, in this section, we turn our attention to couple stress flexoelectricity in three-dimensional beams. Extending the work of [250] on piezoelectric beams to flexoelectricity, we start with kinematics and electrostatics of a generic three-dimensional beam. Work-conjugates and area resultants are then introduced to facilitate similar variational formulations for beams. The Euler-Lagrange equations of three-dimensional beams are then derived in a compact form to facilitate interested readers with their closed form solutions.

#### 8.5.1 Kinematics of three-dimensional flexoelectric beams

Let us consider the motion of a beam  $\Omega \subset \mathbb{R}^3$  as shown in Figure 8.2. The beam in the undeformed configuration has a straight axis of length  $l$  and is completely characterised with an orthonormal reference triad  $\{\mathbf{e}_1, \mathbf{e}_2, \mathbf{e}_3\}$ , where  $\mathbf{e}_3$  is parallel to the beam axis and  $\{\mathbf{e}_\alpha\} (\alpha = 1, 2)$  lie in the plane which defines the cross sectional area  $A$  (with boundary  $\partial A$ ) of the beam  $\Omega = A \times l^3$ . Assuming for simplicity that this reference frame (placed at  $[0, 0, x_3]^T$ ) coincides with the global one (placed at  $[0, 0, 0]^T$ ), as shown in Figure 8.2, the displacements of the beam considering small rotations can be described as; see [250]

$$(\mathbf{x}, t) \mapsto \mathbf{u}(\mathbf{x}, t) = \mathbf{w}(x_3, t) + \boldsymbol{\theta}(x_3, t) \times \mathbf{p}(x_1, x_2), \quad (8.42)$$

where  $\mathbf{p}(x_1, x_2) := x_\alpha \mathbf{e}_\alpha$  is the position vector of a material point within the cross section  $A$  with respect to the origin of the triad  $\{\mathbf{e}_1, \mathbf{e}_2, \mathbf{e}_3\}$ . Vectors  $\mathbf{w} = w_i \mathbf{e}_i$  and  $\boldsymbol{\theta} = \theta_i \mathbf{e}_i$  are collectively called the generalised beam displacements. Expression (8.42) represents a time dependent affine mapping for any material point contained within the cross sectional area  $A$  of the beam. Noticing that  $\nabla \mathbf{u} = \frac{\partial \mathbf{u}}{\partial x_i} \otimes \mathbf{e}_i$  and  $\frac{\partial \mathbf{p}}{\partial x_\alpha} = \mathbf{e}_\alpha$ , the small strain tensor  $\boldsymbol{\varepsilon}$  can be rewritten as

$$\boldsymbol{\varepsilon} = \frac{1}{2} \left[ (\boldsymbol{\varepsilon}^m + \boldsymbol{\kappa}^m \times \mathbf{p}) \otimes \mathbf{e}_3 + \mathbf{e}_3 \otimes (\boldsymbol{\varepsilon}^m + \boldsymbol{\kappa}^m \times \mathbf{p}) \right], \quad (8.43)$$

---

<sup>3</sup>Throughout the remainder of the paper, any Greek indices will be assumed to vary in the integer interval [1,2] and Latin indices to vary in the integer interval [1,2,3].

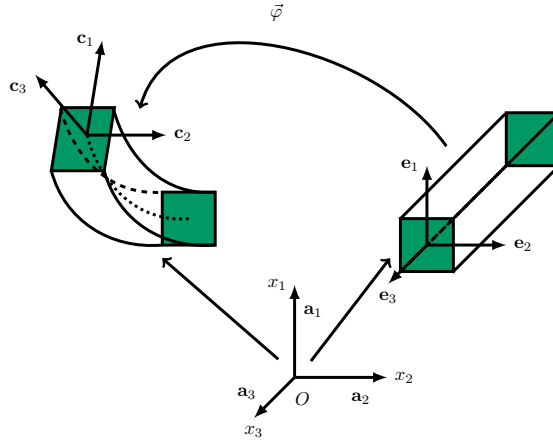


Figure 8.2: Motion of Beam in  $\mathbb{R}^3$ . The initial orthonormal triad  $\{e_1, e_2, e_3\}$  transforms to the orthonormal triad  $\{c_1, c_2, c_3\}$ .

where

$$\boldsymbol{\epsilon}^m := \frac{\partial \mathbf{w}}{\partial x_3} + \mathbf{e}_3 \times \boldsymbol{\theta}, \quad \boldsymbol{\kappa}^m := \frac{\partial \boldsymbol{\theta}}{\partial x_3}, \quad (8.44)$$

are called the strain measures of the linear beam model, which characterise translational deformation and rotational deformation, respectively. The explicit form of the strain tensor is

$$\boldsymbol{\varepsilon} = \frac{1}{2} \begin{bmatrix} 0 & 0 & \frac{\partial w_1}{\partial x_3} - \theta_2 - \frac{\partial \theta_3}{\partial x_3} \\ 0 & \frac{\partial w_2}{\partial x_3} + \theta_1 + \frac{\partial \theta_3}{\partial x_3} & \frac{\partial w_3}{\partial x_3} + x_2 \frac{\partial \theta_1}{\partial x_3} - x_1 \frac{\partial \theta_2}{\partial x_3} \\ sym & \frac{\partial w_3}{\partial x_3} + x_2 \frac{\partial \theta_1}{\partial x_3} - x_1 \frac{\partial \theta_2}{\partial x_3} & \end{bmatrix}. \quad (8.45)$$

As it is well known in classical beam theories and can also be seen clearly from (8.45), there is no deformation within the cross-section of the beam ( $\mathbf{e}_\alpha \cdot \boldsymbol{\varepsilon} \mathbf{e}_\beta = 0$ ). Following our argument in subsection 8.4.1, and with finding the beam balance equations of flexoelectric beams in mind, from the onset, we strongly impose the couple stress constraint (8.14), to obtain

$$(\mathbf{x}, t) \mapsto \boldsymbol{\omega}(\mathbf{x}, t) = \frac{1}{2} \nabla \times \left( \mathbf{w}(x_3, t) + \boldsymbol{\theta}(x_3, t) \times \mathbf{p}(x_1, x_2) \right), \quad (8.46)$$

where on the right hand side of (8.46) we have substituted the continuum displacements in terms of beam's generalised displacements using (8.42). Similar to the strain tensor, the symmetric and skew-symmetric parts of gradient of  $\boldsymbol{\omega}$  can be written in their matrix form as

$$\nabla^{sym} \boldsymbol{\omega} = \frac{1}{4} \begin{bmatrix} -\frac{\partial \theta_3}{\partial x_3} & 0 & \omega_{1,3} \\ 0 & -\frac{\partial \theta_3}{\partial x_3} & \omega_{2,3} \\ sym & 2 \frac{\partial \theta_3}{\partial x_3} & \end{bmatrix}, \quad \nabla^{skew} \boldsymbol{\omega} = \frac{1}{4} \begin{bmatrix} 0 & 0 & \omega_{1,3} \\ 0 & 0 & \omega_{2,3} \\ -\omega_{1,3} & -\omega_{2,3} & 0 \end{bmatrix}, \quad (8.47)$$

where

$$\omega_{1,3} = \frac{\partial \theta_1}{\partial x_3} - \frac{\partial^2 w_2}{\partial x_3^2} - x_1 \frac{\partial^2 \theta_3}{\partial x_3^2}, \quad \omega_{2,3} = \frac{\partial \theta_2}{\partial x_3} + \frac{\partial^2 w_1}{\partial x_3^2} - x_2 \frac{\partial^2 \theta_3}{\partial x_3^2}.$$

From (8.47) we observe that the symmetric part vorticity gradient is deviatoric i.e.  $\text{tr}(\nabla^{sym} \boldsymbol{\omega}) = 0$ . However, the non-zero diagonal components of symmetric part of the gradient still contribute to the uniform contraction of the cross section by an amount proportional to  $(-\frac{\partial \theta_3}{\partial x_3})$  and increase the torsional rigidity of the beam by an amount proportional to  $(2 \frac{\partial \theta_3}{\partial x_3})$ . From the point of view of classical beam theories, it is essential that the strain measures should not include cross-sectional deformation. This further justifies the use of a skew-symmetric curvature tensor as a fundamental kinematic measure however, it should be noted that, the conformal variant of

the couple stress theory recently reported by [109] based on the kinematic measure  $\nabla \times \boldsymbol{\varepsilon}$  also excludes these cross-sectional rotational modes. The axial curvature vector defined in (8.16) can now be written in terms of the beam kinematics

$$\boldsymbol{\chi} = \frac{1}{4} \mathbf{e}_3 \times \left( \mathbf{e}_3 \times (\boldsymbol{\epsilon}^g + \boldsymbol{\kappa}^g \times \mathbf{p}) \right) = \frac{1}{4} \bar{\mathbf{I}}(\boldsymbol{\epsilon}^g + \boldsymbol{\kappa}^g \times \mathbf{p}), \quad (8.48)$$

where

$$\boldsymbol{\epsilon}^g = \frac{\partial^2 \mathbf{w}}{\partial x_3^2} + \boldsymbol{\kappa}^m \times \mathbf{e}_3, \quad \boldsymbol{\kappa}^g = \frac{\partial^2 \boldsymbol{\theta}}{\partial x_3^2}, \quad (8.49)$$

are the strain gradient measures of the linear beam model, augmenting the classical strain measures (8.44) and

$$\bar{\mathbf{I}} = \mathbf{e}_3 \otimes \mathbf{e}_3 - \mathbf{I}. \quad (8.50)$$

The symmetric part of the gradient of rotation utilised in the purely mechanical planar beam theories developed by [236, 237], [189, 258, 283, 284] can also be represented in a compact form including the torsional terms as

$$(\nabla^{sym} \boldsymbol{\omega})_3 = \text{axl}(\nabla^{skew} \boldsymbol{\omega}) \times \mathbf{e}_3 + 2\boldsymbol{\kappa}_3^m \mathbf{e}_3, \quad (8.51)$$

where the subscript 3 in (8.51) represents the longitudinal ( $\mathbf{e}_3$ ) direction.<sup>4</sup>

### 8.5.2 Electrical Mapping

Following our recent development in [250], similar to the beam kinematics, we approximate electric potential  $\psi : \Omega \times [0, T] \rightarrow \mathbb{R}$  across the cross section of the beam through a Taylor series expansion, defined as

$$(\mathbf{x}, t) \mapsto \psi(\mathbf{x}, t) := \phi(x_3, t) + \mathbf{p}(x_1, x_2) \cdot \boldsymbol{\beta}(x_3, t) + \frac{1}{2} \mathbf{p}(x_1, x_2) \cdot \boldsymbol{\gamma}(x_3, t) \mathbf{p}(x_1, x_2), \quad (8.52)$$

where  $\psi$  represents a parabolic expansion across the cross sectional area  $A$  of the beam, completely defined in terms of  $\phi$  the electric potential at the reference triad origin  $[0, 0, x_3]^T$ , its gradient  $\boldsymbol{\beta}$  and its Hessian  $\boldsymbol{\gamma}$ , namely scalar, vector and symmetric second order tensor beam axis-varying functions. It is important to remark that the only approximation for the distribution of the electric potential is established across the section of the beam (see Figure 8.3). The variation along the beam axis remains without any approximation.

The electric field vector  $\mathbf{E}$  can now be obtained by computing the gradient of the newly introduced electric potential  $\psi$  as  $\mathbf{E} := -\nabla \psi$  yielding (refer to equation (8.52)), after some algebraic manipulation

$$\mathbf{E} = -\boldsymbol{\epsilon}^e - (\mathbf{e}_3 \otimes \mathbf{p}) \boldsymbol{\kappa}^e - \mathbf{V} : \boldsymbol{\varsigma}^e - \mathbf{W} : \boldsymbol{\gamma}, \quad (8.53)$$

where

$$\boldsymbol{\epsilon}^e := \frac{\partial \phi}{\partial x_3} \mathbf{e}_3 + \boldsymbol{\beta}, \quad \boldsymbol{\kappa}^e := \frac{\partial \boldsymbol{\beta}}{\partial x_3}, \quad \boldsymbol{\varsigma}^e := \frac{\partial \boldsymbol{\gamma}}{\partial x_3}, \quad (8.54)$$

with the third order tensors  $\mathbf{V}$  and  $\mathbf{W}$  defined by

$$\mathbf{V} := \mathbf{e}_3 \otimes \frac{1}{2} (\mathbf{p} \otimes \mathbf{p}), \quad \mathbf{W} := \mathbf{e}_3 \otimes \frac{1}{2} (\mathbf{p} \otimes \mathbf{e}_3 + \mathbf{e}_3 \otimes \mathbf{p}). \quad (8.55)$$

Considering equation (8.53), it is interesting to notice the similarities with the definition of the small strain tensor  $\boldsymbol{\varepsilon}$  (8.43). Notice how the first two terms on the right hand side of

---

<sup>4</sup>Interestingly, a direct consequence of (8.50) for the case of skew-symmetric couple stress theory is that, the couple stress resultants are first projected on to the axis of the beam prior to area integration. In classical beam theory, this projection vanishes due to the symmetry of Cauchy stresses i.e.  $\mathbf{e}_i \times (\boldsymbol{\sigma} \mathbf{e}_i) = \mathbf{0}$ ; see [126].

equation (8.53) stem from the linear contribution in (8.52) (as in formula (8.43)) whereas the last two terms stem from the quadratic contribution in (8.52).

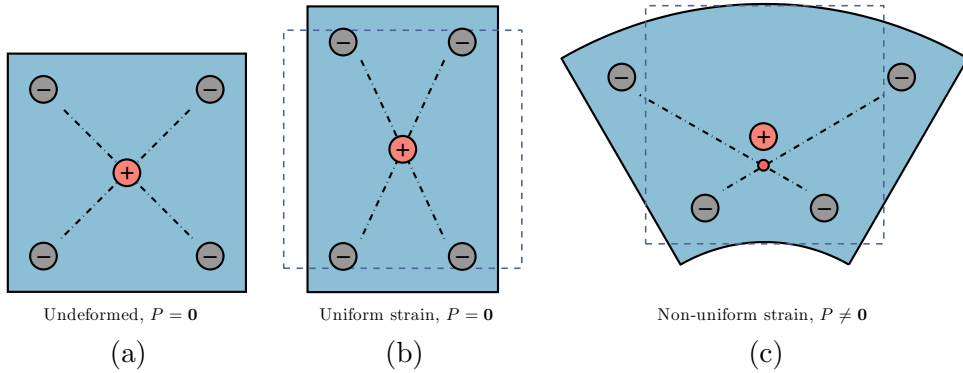


Figure 8.3: A schematic representation of electric polarisation in a centrosymmetric lattice beam, (a) undeformed state - no polarisation, (b) when uniformly strained, the atomic displacements of the centrosymmetric lattice will follow the elastic medium approximation resulting in no polarisation, (c) when strained non-uniformly, the atomic displacements no longer follow the elastic medium approximation and the symmetry restriction (symmetrical movement of ions) is broken resulting in electric polarisation opposite to the direction of applied strain, [338, 72].

The new initial boundary value problem, adapted to a three-dimensional beam problem, is then defined by equations (8.1,8.3,8.5) and (8.42,8.52), which combine the governing equations of both elastodynamics and electrostatics, initial and boundary conditions, the coupling electro-mechanical equations for  $\boldsymbol{\sigma}$ ,  $\chi$  and  $\mathbf{D}$ , the beam kinematics assumption  $\mathbf{u}$  and the electric potential spatial distribution  $\psi$ .

### 8.5.3 Displacement-potential variational formulation for flexoelectric beams

In order to establish the variational formulation of the problem at a beam level, we consider virtual variations of displacements and electric potential  $\delta\mathbf{u}$  and  $\delta\psi$ , satisfying appropriate boundary conditions. Analogous to continuum formulation and following [250], we can rewrite the variational form (virtual work) of the initial boundary value problem at beam level as

$$\delta W(\mathbf{u}, \psi; \delta\mathbf{u}, \delta\psi) := \delta W_{iner} + \delta W_{int}^m + \delta W_{int}^g + \delta W_{int}^e - \delta W_{ext}^m - \delta W_{ext}^g - \delta W_{ext}^e = 0, \quad (8.56)$$

where  $W$  represents the total work including strain-induced, curvature-induced and polarisation-induced internal and their corresponding external work, such that

$$\delta W_{iner} := \int_{\Omega} \rho \ddot{\mathbf{u}} \cdot \delta \mathbf{u} \, d\Omega, \quad (8.57a)$$

$$\delta W_{int}^m := \int_{\Omega} \boldsymbol{\sigma} : \delta \boldsymbol{\varepsilon} \, d\Omega + \int_{\Omega} \hat{\boldsymbol{\sigma}}^g : \delta \hat{\boldsymbol{\omega}} \, d\Omega, \quad (8.57b)$$

$$\delta W_{int}^g := \int_{\Omega} \boldsymbol{\mu} \cdot \delta \boldsymbol{\chi} \, d\Omega, \quad (8.57c)$$

$$\delta W_{ext}^m := \int_{\Omega} \rho \mathbf{b} \cdot \delta \mathbf{u} \, d\Omega + \int_{\Gamma_{\sigma}} \mathbf{t} \cdot \delta \mathbf{u} \, d\Gamma, \quad (8.57d)$$

$$\delta W_{ext}^g := \frac{1}{2} \left[ \int_{\Omega} \rho \mathbf{b} \cdot (\nabla \times \delta \mathbf{u}) \, d\Omega + \int_{\Gamma_{\mu}} \mathbf{m} \cdot (\nabla \times \delta \mathbf{u}) \, d\Gamma \right], \quad (8.57e)$$

$$\delta W_{int}^e := - \int_{\Omega} \mathbf{D} \cdot \delta \mathbf{E} \, d\Omega, \quad (8.57f)$$

$$\delta W_{ext}^e := \int_{\Omega} \rho^e \delta \psi \, d\Omega + \int_{\Gamma_D} q_0 \delta \psi \, d\Gamma, \quad (8.57g)$$

represent the different contributions (e.g. inertial, internal, external, mechanical, electrical) to the total virtual work. Substituting the expressions for  $\delta\mathbf{u}$  (8.42) and  $\delta\psi$  (8.52) into equation (8.43), (8.48) and (8.53) results in

$$\delta\boldsymbol{\epsilon} = \frac{1}{2} \left[ (\delta\boldsymbol{\epsilon}^m + \delta\boldsymbol{\kappa}^m \times \mathbf{p}) \otimes \mathbf{e}_3 + \mathbf{e}_3 \otimes (\delta\boldsymbol{\epsilon}^m + \delta\boldsymbol{\kappa}^m \times \mathbf{p}) \right], \quad (8.58a)$$

$$\delta\boldsymbol{\chi} = \frac{1}{4} \bar{\mathbf{I}}(\delta\boldsymbol{\epsilon}^g + \delta\boldsymbol{\kappa}^g \times \mathbf{p}), \quad (8.58b)$$

$$\delta\mathbf{E} = -\delta\boldsymbol{\epsilon}^e - (\mathbf{e}_3 \otimes \mathbf{p})\delta\boldsymbol{\kappa}^e - \mathbf{V} : \delta\boldsymbol{\varsigma}^e - \mathbf{W} : \delta\boldsymbol{\gamma}, \quad (8.58c)$$

where

$$\delta\boldsymbol{\epsilon}^m := \frac{\partial \delta\mathbf{w}}{\partial x_3} + \mathbf{e}_3 \times \delta\boldsymbol{\theta}, \quad \delta\boldsymbol{\kappa}^m := \frac{\partial \delta\boldsymbol{\theta}}{\partial x_3}, \quad (8.59a)$$

$$\delta\boldsymbol{\epsilon}^g := \frac{\partial^2 \delta\mathbf{w}}{\partial x_3^2} + \delta\boldsymbol{\kappa}^m \times \mathbf{e}_3, \quad \delta\boldsymbol{\kappa}^g := \frac{\partial^2 \delta\boldsymbol{\theta}}{\partial x_3^2}, \quad (8.59b)$$

$$\delta\boldsymbol{\epsilon}^e := \frac{\partial \delta\phi}{\partial x_3} \mathbf{e}_3 + \delta\boldsymbol{\beta}, \quad \delta\boldsymbol{\kappa}^e := \frac{\partial \delta\boldsymbol{\beta}}{\partial x_3}, \quad \delta\boldsymbol{\varsigma}^e := \frac{\partial \delta\boldsymbol{\gamma}}{\partial x_3}, \quad (8.59c)$$

represent the virtual mechanical and electrical beam strains. Substituting the expressions for  $\mathbf{u}$  and  $\delta\mathbf{u}$  (8.42) into (8.57a) yields (after integration over the cross sectional area  $A$ ) the inertial virtual work

$$\delta W_{iner} = \int_l \left[ \delta\mathbf{w} \cdot (\mathbf{A}_D \ddot{\mathbf{w}} + \mathbf{S}_D \ddot{\boldsymbol{\theta}}) + \delta\boldsymbol{\theta} \cdot (\mathbf{S}_D^T \ddot{\mathbf{w}} + \mathbf{I}_D \ddot{\boldsymbol{\theta}}) \right] dx_3, \quad (8.60)$$

where

$$\mathbf{A}_D := \int_A \rho \mathbf{I} dA, \quad \mathbf{S}_D := \int_A \rho \hat{\mathbf{p}} dA, \quad \mathbf{I}_D := \int_A \rho \hat{\mathbf{p}} \hat{\mathbf{p}}^T dA, \quad (8.61)$$

represent the mass  $\mathbf{A}_D$ , first area moment  $\mathbf{S}_D$  and second area moment  $\mathbf{I}_D$  tensors of the cross sectional area  $A$ . Notice that  $\hat{\mathbf{p}}$  represents the skew symmetric tensor associated with the axial vector  $\mathbf{p}$ . When considering a reference frame whose origin coincides with the centre of mass of the cross sectional area  $A$ , then  $\mathbf{S}_D = \mathbf{0}$ . Moreover, if the reference frame is aligned along the so-called principal directions, the second area moment tensor  $\mathbf{I}_D$  becomes diagonal.

Analogously, substituting the expression for  $\delta\boldsymbol{\epsilon}$  (8.58a) into (8.57b) yields (after integration over the cross sectional area  $A$ ) the internal mechanical virtual work

$$\delta W_{int}^m = \int_l [\delta\boldsymbol{\epsilon}^m \cdot \mathbf{Q}^m + \delta\boldsymbol{\kappa}^m \cdot \mathbf{M}^m] dx_3, \quad (8.62)$$

with

$$\mathbf{Q}^m := \int_A \boldsymbol{\sigma} \mathbf{e}_3 dA, \quad \mathbf{M}^m := \int_A \mathbf{p} \times (\boldsymbol{\sigma} \mathbf{e}_3) dA. \quad (8.63)$$

In the above equation (8.62),  $\mathbf{Q}^m$  represents the internal shear/axial force whereas  $\mathbf{M}^m$  represents the internal bending/torsion moment.

Substituting the expression for  $\delta\mathbf{u}$  (8.42) into (8.57d) yields (after integration over the cross sectional area  $A$ ) the standard mechanical external virtual work

$$\delta W_{ext}^m = [\delta\mathbf{w} \cdot \mathbf{Q}^m + \delta\boldsymbol{\theta} \cdot \mathbf{M}^m]_0^l + \int_l [\delta\mathbf{w} \cdot \mathbf{q}^m + \delta\boldsymbol{\theta} \cdot \mathbf{m}^m] dx_3, \quad (8.64)$$

where

$$\mathbf{q}^m := \int_A \rho \mathbf{b} dA + \int_{\partial A} \mathbf{t} d\Gamma, \quad \mathbf{m}^m := \int_A (\mathbf{p} \times \rho \mathbf{b}) dA + \int_{\partial A} (\mathbf{p} \times \mathbf{t}) d\Gamma. \quad (8.65)$$

In above equations (8.64) and (8.65),  $\mathbf{q}^m$  and  $\mathbf{m}^m$  represent a possible external distributed force and moment, respectively, acting along the beam axis. The first term in squared brackets

on the right hand side of equation (8.64) represents mechanical actions (force and moment) applied at both ends of the beam, namely  $x_3 = 0$  and  $x_3 = l$ .

For the strain gradient (curvature) quantities, substituting the expression for  $\delta\chi$  (8.58b) into (8.57c) yields the micro-mechanical internal virtual work

$$\delta W_{int}^g = \int_l [\delta\epsilon^g \cdot \mathbf{Q}^g + \delta\kappa^g \cdot \mathbf{M}^g] dx_3, \quad (8.66)$$

with

$$\mathbf{Q}^g := \int_A \frac{1}{2} \bar{\mathbf{I}} \boldsymbol{\mu} dA, \quad \mathbf{M}^g := \int_A \mathbf{p} \times \left( \frac{1}{2} \bar{\mathbf{I}} \boldsymbol{\mu} \right) dA. \quad (8.67)$$

where  $\mathbf{Q}^g$  and  $\mathbf{M}^g$  can be interpreted as size-dependent shear force and bending/torsion moment emanating from the micro-structure. Comparing (8.63) and (8.67), it is evident that unlike the standard force stress resultants (based on  $\sigma e_3$ ), couple-stress resultants are integrated in the plane ( $e_3 \otimes e_3 - \mathbf{I} = \bar{\mathbf{I}}$ ) which is the direct consequence of couple stress constraint  $2\omega = \nabla \times \mathbf{u}$  and the axial curvature vector (8.48).

Substituting the expression for  $\delta\mathbf{u}$  (8.42) into (8.57e) yields (after integration over the cross sectional area  $A$ ) the micro-mechanical external virtual work

$$\delta W_{ext}^g = [\delta\mathbf{w} \cdot \mathbf{Q}^g + \delta\theta \cdot \mathbf{M}^g]_0^l + \int_l [\delta\mathbf{w} \cdot \mathbf{q}^g + \delta\theta \cdot \mathbf{m}^g] dx_3, \quad (8.68)$$

where

$$\begin{aligned} \mathbf{q}^g &:= \int_A \frac{\rho}{2} \nabla \times \mathbf{l} dA + \int_{\partial A} \frac{1}{2} \nabla \times \mathbf{m} d\Gamma, \\ \mathbf{m}^g &:= \int_A \left( \mathbf{p} \times \left( \frac{\rho}{2} \nabla \times \mathbf{l} \right) \right) dA + \int_{\partial A} \frac{1}{2} \left( \mathbf{p} \times (\nabla \times \mathbf{m}) \right) d\Gamma. \end{aligned} \quad (8.69)$$

In the above equations (8.68) and (8.69),  $\mathbf{q}^g$  and  $\mathbf{m}^g$  can be interpreted as the micro-mechanical external distributed force and moment, respectively, acting along the beam axis. We can merge the contribution of external forces of  $\delta W_{ext}^m$  (8.68) with  $\delta W_{ext}^g$  (8.64), as these are prescribed quantities carrying the same units, whose effects cannot be distinguished individually. Hence, in what follows, with slight abuse of notation, we assume

$$\mathbf{q}^m = \mathbf{q}^m + \mathbf{q}^g, \quad \mathbf{m}^m = \mathbf{m}^m + \mathbf{m}^g.$$

From the electrical point of view, substituting the expression for  $\delta\mathbf{E}$  (8.58c) into (8.57f) yields (after integration over the cross sectional area  $A$ ) the internal electrical virtual work

$$\delta W_{int}^e = \int_l [\delta\epsilon^e \cdot \mathbf{Q}^e + \delta\kappa^e \cdot \mathbf{M}^e + \delta\zeta^e : \mathbf{O}^e + \delta\gamma : \mathbf{P}^e] dx_3, \quad (8.70)$$

where

$$\mathbf{Q}^e := \int_A \mathbf{D} dA, \quad \mathbf{M}^e := \int_A (\mathbf{D} \cdot \mathbf{e}_3) \mathbf{p} dA, \quad (8.71a)$$

$$\mathbf{P}^e := \int_A \mathbf{D} \cdot \mathbf{W} dA, \quad \mathbf{O}^e := \int_A \mathbf{D} \cdot \mathbf{V} dA. \quad (8.71b)$$

In the above equations (8.70) and (8.71a), it is interesting to observe the similarities between  $\mathbf{Q}^e$  and  $\mathbf{M}^e$  and their mechanical counterparts (8.63), namely  $\mathbf{Q}^m$  and  $\mathbf{M}^m$ , respectively. In addition, due to the quadratic nature of the electric potential distribution, two extra second order tensors arise, that is  $\mathbf{P}^e$  and  $\mathbf{O}^e$  expressed in terms of the third order tensors  $\mathbf{W}$  and  $\mathbf{V}$  already defined in (8.55).

Finally, substituting the expression for  $\delta\psi$  (8.52) into (8.57g) yields (after integration over the cross sectional area  $A$ ) the electrical external virtual work as

$$\delta W_{ext}^e = [\delta\phi (\mathbf{Q}^e \cdot \mathbf{e}_3) + \delta\beta \cdot \mathbf{M}^e + \delta\gamma : \mathbf{O}^e]_0^l + \int_l [\delta\phi q^e + \delta\beta \cdot \mathbf{m}^e + \delta\gamma : \mathbf{o}^e] dx_3, \quad (8.72)$$

where

$$q^e := \int_A \rho^e dA + \int_{\partial A} q_0 d\Gamma, \quad (8.73a)$$

$$\mathbf{m}^e := \int_A \rho^e \mathbf{p} dA + \int_{\partial A} q_0 \mathbf{p} d\Gamma, \quad (8.73b)$$

$$\mathbf{o}^e := \int_A \frac{\rho^e}{2} (\mathbf{p} \otimes \mathbf{p}) dA + \int_{\partial A} \frac{q_0}{2} (\mathbf{p} \otimes \mathbf{p}) d\Gamma. \quad (8.73c)$$

Again, it is interesting to note the similarities between the above expressions  $q^e$ ,  $\mathbf{m}^e$  (8.73) and those of  $\mathbf{q}^m$ ,  $\mathbf{m}^m$  (8.65). In equation (8.72),  $q^e$ ,  $\mathbf{m}^e$  and  $\mathbf{o}^e$  represent possible distributed electrical effects per unit of length. Moreover,  $(\mathbf{Q}^e \cdot \mathbf{e}_3)$ ,  $\mathbf{M}^e$  and  $\mathbf{O}^e$  represent electrical actions applied at both ends of the beam, namely  $x_3 = 0$  and  $x_3 = L$ .

For completeness, the final virtual work expression characterising the behaviour of the piezoelectric beam can be written as

$$\delta W := \delta W_{iner} + \delta W_{int} - \delta W_{ext} = 0, \quad (8.74)$$

$$\delta W_{iner} = \int_l [\delta \mathbf{w} \cdot (\mathbf{A}_D \ddot{\mathbf{w}} + \mathbf{S}_D \ddot{\boldsymbol{\theta}}) + \delta \boldsymbol{\theta} \cdot (\mathbf{S}_D^T \ddot{\mathbf{w}} + \mathbf{I}_D \ddot{\boldsymbol{\theta}})] dx_3, \quad (8.75a)$$

$$\begin{aligned} \delta W_{int} &= \int_l [\delta \boldsymbol{\epsilon}^m \cdot \mathbf{Q}^m + \delta \boldsymbol{\kappa}^m \cdot \mathbf{M}^m] + [\delta \boldsymbol{\epsilon}^g \cdot \mathbf{Q}^g + \delta \boldsymbol{\kappa}^g \cdot \mathbf{M}^g] dx_3 \\ &\quad + \int_l [\delta \boldsymbol{\epsilon}^e \cdot \mathbf{Q}^e + \delta \boldsymbol{\kappa}^e \cdot \mathbf{M}^e + \delta \boldsymbol{\varsigma}^e : \mathbf{P}^e + \delta \boldsymbol{\gamma} : \mathbf{O}^e] dx_3, \end{aligned} \quad (8.75b)$$

$$\begin{aligned} \delta W_{ext} &= [\delta \mathbf{w} \cdot \mathbf{Q}^m + \delta \boldsymbol{\theta} \cdot \mathbf{M}^m]_0^l + \int_l [\delta \mathbf{w} \cdot \mathbf{q}^m + \delta \boldsymbol{\theta} \cdot \mathbf{m}^m] dx_3 \\ &\quad + \left[ \delta \mathbf{w} \cdot \frac{\partial \mathbf{Q}^g}{\partial x_3} + \delta \boldsymbol{\theta} \cdot \frac{\partial \mathbf{M}^g}{\partial x_3} \right]_0^l + \int_l \left[ \delta \mathbf{w} \cdot \frac{\partial \mathbf{q}^g}{\partial x_3} + \delta \boldsymbol{\theta} \cdot \frac{\partial \mathbf{m}^g}{\partial x_3} \right] dx_3 \\ &\quad + [\delta \phi (\mathbf{Q}^e \cdot \mathbf{e}_3) + \delta \boldsymbol{\beta} \cdot \mathbf{M}^e + \delta \boldsymbol{\gamma} : \mathbf{O}^e]_0^l + \int_l [\delta \phi q^e + \delta \boldsymbol{\beta} \cdot \mathbf{m}^e + \delta \boldsymbol{\gamma} : \mathbf{o}^e] dx_3. \end{aligned} \quad (8.75c)$$

#### 8.5.4 Internal area resultants for displacement-potential formulation

From the mechanical standpoint, having introduced the additive decomposition of the total Cauchy stress tensor  $\boldsymbol{\sigma}$  in equation (8.12), we now proceed to find the traction vector acting in a cross sectional area  $A$  of the beam defined by the outward unit normal  $\mathbf{e}_3$ , namely  $\boldsymbol{\sigma} \mathbf{e}_3$ . For the mechanical contribution  $\boldsymbol{\sigma}^m$ , (8.43) yields

$$\boldsymbol{\sigma}^m \mathbf{e}_3 = \boldsymbol{\Xi}(\boldsymbol{\epsilon}^m + \hat{\mathbf{p}}^T \boldsymbol{\kappa}^m), \quad [\boldsymbol{\Xi}]_{ij} = [\mathcal{C}]_{ikjl} [\mathbf{e}_3]_k [\mathbf{e}_3]_l. \quad (8.76)$$

For the nonlocal contribution of the force stress tensor  $\hat{\boldsymbol{\sigma}}^g$ , (8.48) yields

$$\hat{\boldsymbol{\sigma}}^g \mathbf{e}_3 = \boldsymbol{\Upsilon}_1(\boldsymbol{\epsilon}^m + \hat{\mathbf{p}}^T \boldsymbol{\kappa}^m), \quad \boldsymbol{\Upsilon}_1 = \frac{1}{2} \hat{\boldsymbol{\sigma}}^g \hat{\mathbf{I}}, \quad (8.77)$$

where  $\hat{\mathbf{I}}$  is the skew-symmetric tensor dual to  $\mathbf{e}_3$  given by

$$\hat{\mathbf{I}} = \begin{bmatrix} 0 & -1 & 0 \\ 1 & 0 & 0 \\ 0 & 0 & 0 \end{bmatrix}.$$

For anisotropic materials the nonlocal contribution of the force stress tensor  $\hat{\boldsymbol{\sigma}}^g$  also includes constitutive terms

$$\hat{\boldsymbol{\sigma}}^g \mathbf{e}_3 = \boldsymbol{\Upsilon}_2(\boldsymbol{\epsilon}^g + \hat{\mathbf{p}}^T \boldsymbol{\kappa}^g), \quad [\boldsymbol{\Upsilon}_2]_{ij} = \frac{1}{4} [\mathcal{D}]_{iklj} [\mathbf{e}_3]_k [\bar{\mathbf{I}}]_{lj}. \quad (8.78)$$

Analogously, for the electrical contribution  $\boldsymbol{\sigma}^e$ , (8.53) yields

$$\boldsymbol{\sigma}^e \mathbf{e}_3 = \boldsymbol{\Theta} (\boldsymbol{\epsilon}^e + (\mathbf{e}_3 \otimes \mathbf{p}) \boldsymbol{\kappa}^e + \boldsymbol{\mathcal{V}} : \boldsymbol{\varsigma}^e + \boldsymbol{\mathcal{W}} : \boldsymbol{\gamma}), \quad [\boldsymbol{\Theta}]_{ij} = [e]_{jik} [e_3]_k. \quad (8.79)$$

The first internal area resultant  $\mathbf{Q}^m$ , also known as the axial/shear force, can now be computed from equations (8.63), (8.76-8.79) as

$$\mathbf{Q}^m = \mathbf{A}^m \boldsymbol{\epsilon}^m + \mathbf{S}^m \boldsymbol{\kappa}^m + \mathbf{A}^{mg} \boldsymbol{\epsilon}^g + \mathbf{S}_1^{mg} \boldsymbol{\kappa}^g + \mathbf{A}_1^e \boldsymbol{\epsilon}^e + \mathbf{S}_1^e \boldsymbol{\kappa}^e + \mathbf{S}_2^e : \boldsymbol{\gamma} + \mathbf{I}_1^e : \boldsymbol{\varsigma}^e, \quad (8.80)$$

where

$$\begin{aligned} \mathbf{A}^m &:= \int_A \boldsymbol{\Xi} \, dA + \int_A \boldsymbol{\Upsilon}_1 \, dA, & \mathbf{S}^m &:= \int_A \boldsymbol{\Xi} \hat{\mathbf{p}}^T \, dA + \int_A \boldsymbol{\Upsilon}_1 \hat{\mathbf{p}}^T \, dA, & \mathbf{A}^{mg} &:= \int_A \boldsymbol{\Upsilon}_2 \, dA, \\ \mathbf{S}_1^{mg} &:= \int_A \boldsymbol{\Upsilon}_2 \hat{\mathbf{p}}^T \, dA, & \mathbf{A}_1^e &:= \int_A \boldsymbol{\Theta} \, dA, & \mathbf{S}_1^e &:= \int_A \boldsymbol{\Theta} (\mathbf{e}_3 \otimes \mathbf{p}) \, dA, \\ \mathbf{I}_1^e &:= \int_A \boldsymbol{\Theta} \boldsymbol{\mathcal{V}} \, dA, & \mathbf{S}_2^e &:= \int_A \boldsymbol{\Theta} \boldsymbol{\mathcal{W}} \, dA, \end{aligned}$$

The first two terms on the right hand side of (8.80) stem from strain contributions, the third and fourth terms stem from curvature contribution and the remainder stem from electrical contribution. The second internal area resultant  $\mathbf{M}^m$ , also known as bending/torsion moment, can also be computed from equations (8.63), (8.76) and (8.79) as

$$\mathbf{M}^m = (\mathbf{S}^m)^T \boldsymbol{\epsilon}^m + \mathbf{I}^m \boldsymbol{\kappa}^m + \mathbf{S}_2^{mg} \boldsymbol{\epsilon}^g + \mathbf{I}^{mg} \boldsymbol{\kappa}^g + \mathbf{S}_3^e \boldsymbol{\epsilon}^e + \mathbf{I}_2^e \boldsymbol{\kappa}^e + \mathbf{I}_3^e : \boldsymbol{\gamma} + \mathbf{G}_1^e : \boldsymbol{\varsigma}^e, \quad (8.82)$$

where

$$\begin{aligned} \mathbf{I}^m &:= \int_A \hat{\mathbf{p}} \boldsymbol{\Xi} \hat{\mathbf{p}}^T \, dA + \int_A \hat{\mathbf{p}} \boldsymbol{\Upsilon}_1 \hat{\mathbf{p}}^T \, dA, & \mathbf{S}_2^{mg} &:= \int_A \hat{\mathbf{p}} \boldsymbol{\Upsilon}_2 \, dA, & \mathbf{I}^{mg} &:= \int_A \hat{\mathbf{p}} \boldsymbol{\Upsilon}_2 \hat{\mathbf{p}}^T \, dA, \\ \mathbf{S}_3^e &:= \int_A \hat{\mathbf{p}} \boldsymbol{\Theta} \, dA, & \mathbf{I}_2^e &:= \int_A \hat{\mathbf{p}} \boldsymbol{\Theta} (\mathbf{e}_3 \otimes \mathbf{p}) \, dA, & \mathbf{G}_1^e &:= \int_A \hat{\mathbf{p}} \boldsymbol{\Theta} \boldsymbol{\mathcal{V}} \, dA, \\ \mathbf{I}_3^e &:= \int_A \hat{\mathbf{p}} \boldsymbol{\Theta} \boldsymbol{\mathcal{W}} \, dA. \end{aligned}$$

As mentioned before, couple-stress resultants are integrated in the cross-sectional plane  $\bar{\mathbf{I}}$ . For mechanical contribution  $\boldsymbol{\mu}^m$ , (8.43) yields

$$\frac{1}{2} \bar{\mathbf{I}} \boldsymbol{\mu}^m = \boldsymbol{\Upsilon}^T (\boldsymbol{\epsilon}^m + \hat{\mathbf{p}}^T \boldsymbol{\kappa}^m), \quad (8.84)$$

For micro-mechanical contributions  $\boldsymbol{\mu}^g$ , (8.48) yields

$$\frac{1}{2} \bar{\mathbf{I}} \boldsymbol{\mu}^g = \boldsymbol{\varrho} (\boldsymbol{\epsilon}^g + \hat{\mathbf{p}}^T \boldsymbol{\kappa}^g), \quad [\boldsymbol{\varrho}]_{ij} = \frac{1}{16} [\bar{\mathbf{I}}]_{ik} [\mathbf{B}]_{kl} [\bar{\mathbf{I}}]_{lj}. \quad (8.85)$$

Analogously, for electrical contributions  $\boldsymbol{\mu}^e$ , (8.53) yields

$$\frac{1}{2} \bar{\mathbf{I}} \boldsymbol{\mu}^e = \boldsymbol{\aleph} (\boldsymbol{\epsilon}^e + (\mathbf{e}_3 \otimes \mathbf{p}) \boldsymbol{\kappa}^e + \boldsymbol{\mathcal{V}} : \boldsymbol{\varsigma}^e + \boldsymbol{\mathcal{W}} : \boldsymbol{\gamma}), \quad \boldsymbol{\aleph} = \frac{1}{4} \bar{\mathbf{I}} \mathbf{f}^T. \quad (8.86)$$

The couple stress area resultants  $\mathbf{Q}^g$  and  $\mathbf{M}^g$ , can now be computed from equations (8.67), (8.84-8.79) as

$$\mathbf{Q}^g = (\mathbf{A}^{mg})^T \boldsymbol{\epsilon}^m + (\mathbf{S}_2^{mg})^T \boldsymbol{\kappa}^m + \mathbf{A}^g \boldsymbol{\epsilon}^g + \mathbf{S}^g \boldsymbol{\kappa}^g + \mathbf{A}^{ge} \boldsymbol{\epsilon}^e + \mathbf{S}_1^{ge} \boldsymbol{\kappa}^e + \mathbf{S}_2^{ge} : \boldsymbol{\gamma} + \mathbf{I}_1^{ge} : \boldsymbol{\varsigma}^e, \quad (8.87)$$

where

$$\mathbf{A}^g := \int_A \boldsymbol{\varrho} \, dA, \quad \mathbf{S}^g := \int_A \boldsymbol{\varrho} \hat{\mathbf{p}}^T \, dA, \quad \mathbf{A}_1^{ge} := \int_A \boldsymbol{\aleph} \, dA,$$

$$\mathbf{S}_1^{ge} := \int_A \aleph(\mathbf{e}_3 \otimes \mathbf{p}) dA, \quad \mathbf{I}_1^{ge} := \int_A \aleph \mathbf{V} dA, \quad \mathbf{S}_2^{ge} := \int_A \aleph \mathbf{W} dA,$$

and analogously for  $\mathbf{M}^g$

$$\mathbf{M}^g = (\mathbf{S}_1^{mg})^T \boldsymbol{\epsilon}^m + (\mathbf{I}^{mg})^T \boldsymbol{\kappa}^m + (\mathbf{S}^g)^T \boldsymbol{\epsilon}^g + \mathbf{I}^{mg} \boldsymbol{\kappa}^g + \mathbf{S}_3^{ge} \boldsymbol{\epsilon}^e + \mathbf{I}_2^{ge} \boldsymbol{\kappa}^e + \mathbf{I}_3^{ge} : \boldsymbol{\gamma} + \mathbf{G}_1^{ge} : \boldsymbol{\varsigma}^e, \quad (8.89)$$

where

$$\begin{aligned} \mathbf{I}^g &:= \int_A \hat{\mathbf{p}} \boldsymbol{\varrho} \hat{\mathbf{p}}^T dA, & \mathbf{S}_3^{ge} &:= \int_A \hat{\mathbf{p}} \aleph dA, & \mathbf{I}_2^{ge} &:= \int_A \hat{\mathbf{p}} \aleph(\mathbf{e}_3 \otimes \mathbf{p}) dA, \\ \mathbf{G}_1^{ge} &:= \int_A \hat{\mathbf{p}} \aleph \mathbf{V} dA, & \mathbf{I}_3^{ge} &:= \int_A \hat{\mathbf{p}} \aleph \mathbf{W} dA. \end{aligned}$$

From the electrical standpoint, having introduced the additive decomposition of the electric displacement  $\mathbf{D}$  in equation (8.11), we can obtain after combining equations (8.11), (8.43), (8.48) and (8.53)

$$\mathbf{D}^m = \boldsymbol{\Theta}^T (\boldsymbol{\epsilon}^m + \hat{\mathbf{p}}^T \boldsymbol{\kappa}^m), \quad (8.91)$$

$$\mathbf{D}^g = \aleph^T (\boldsymbol{\epsilon}^g + \hat{\mathbf{p}}^T \boldsymbol{\kappa}^g), \quad (8.92)$$

$$\mathbf{D}^e = -\boldsymbol{\epsilon} (\boldsymbol{\epsilon}^e + (\mathbf{e}_3 \otimes \mathbf{p}) \boldsymbol{\kappa}^e + \mathbf{V} : \boldsymbol{\varsigma}^e + \mathbf{W} : \boldsymbol{\gamma}). \quad (8.93)$$

The third internal area resultant  $\mathbf{Q}^e$  can now be computed from equations (8.71a), (8.91) and (8.93) as

$$\mathbf{Q}^e = (\mathbf{A}_1^e)^T \boldsymbol{\epsilon}^m + (\mathbf{S}_3^e)^T \boldsymbol{\kappa}^m + (\mathbf{A}^{ge})^T \boldsymbol{\epsilon}^g + (\mathbf{S}_3^{ge})^T \boldsymbol{\kappa}^g - \mathbf{A}_2^e \boldsymbol{\epsilon}^e - \mathbf{S}_4^e \boldsymbol{\kappa}^e - \mathbf{S}_5^e : \boldsymbol{\gamma} - \mathbf{I}_4^e : \boldsymbol{\varsigma}^e, \quad (8.94)$$

where

$$\begin{aligned} \mathbf{A}_2^e &:= \int_A \boldsymbol{\epsilon} dA, & \mathbf{S}_4^e &:= \int_A \boldsymbol{\epsilon}(\mathbf{e}_3 \otimes \mathbf{p}) dA, \\ \mathbf{I}_4^e &:= \int_A \boldsymbol{\epsilon} \mathbf{V} dA, & \mathbf{S}_5^e &:= \int_A \boldsymbol{\epsilon} \mathbf{W} dA. \end{aligned}$$

Analogously, the fourth  $\mathbf{M}^e$ , fifth  $\mathbf{P}^e$  and sixth  $\mathbf{O}^e$  internal area resultants can be computed from equations (8.71a-8.71b), (8.91) and (8.93) as

$$\begin{aligned} \mathbf{M}^e &= (\mathbf{S}_1^e)^T \boldsymbol{\epsilon}^m + (\mathbf{I}_2^e)^T \boldsymbol{\kappa}^m + (\mathbf{S}_1^{ge})^T \boldsymbol{\epsilon}^g + (\mathbf{I}_2^{ge})^T \boldsymbol{\kappa}^g \\ &\quad - (\mathbf{S}_4^e)^T \boldsymbol{\epsilon}^e - \mathbf{I}_5^e \boldsymbol{\kappa}^e - \mathbf{I}_6^e : \boldsymbol{\gamma} - \mathbf{G}_2^e : \boldsymbol{\varsigma}^e, \\ \mathbf{P}^e &= (\mathbf{S}_2^e)^T \boldsymbol{\epsilon}^m + (\mathbf{I}_3^e)^T \boldsymbol{\kappa}^m + (\mathbf{S}_2^{ge})^T \boldsymbol{\epsilon}^g + (\mathbf{I}_3^{ge})^T \boldsymbol{\kappa}^g \\ &\quad - (\mathbf{S}_5^e)^T \boldsymbol{\epsilon}^e - (\mathbf{I}_6^e)^T \boldsymbol{\kappa}^e - \mathbf{I}_7^e : \boldsymbol{\gamma} - \mathbf{G}_3^e : \boldsymbol{\varsigma}^e, \\ \mathbf{O}^e &= (\mathbf{I}_1^e)^T \boldsymbol{\epsilon}^m + (\mathbf{G}_1^e)^T \boldsymbol{\kappa}^m + (\mathbf{I}_1^{ge})^T \boldsymbol{\epsilon}^g + (\mathbf{G}_1^{ge})^T \boldsymbol{\kappa}^g \\ &\quad - (\mathbf{I}_4^e)^T \boldsymbol{\epsilon}^e - (\mathbf{G}_2^e)^T \boldsymbol{\kappa}^e - (\mathbf{G}_3^e)^T : \boldsymbol{\gamma} - \mathbf{J}^e : \boldsymbol{\varsigma}^e, \end{aligned}$$

where

$$\begin{aligned} \mathbf{I}_5^e &:= \int_A (\mathbf{p} \otimes \mathbf{e}_3) \boldsymbol{\epsilon}(\mathbf{e}_3 \times \mathbf{p}) dA, & \mathbf{J}^e &:= \int_A \mathbf{V}^{*T} \boldsymbol{\epsilon} \mathbf{V} dA, & \mathbf{I}_6^e &:= \int_A (\mathbf{p} \otimes \mathbf{e}_3) \boldsymbol{\epsilon} \mathbf{W} dA, \\ \mathbf{G}_2^e &:= \int_A (\mathbf{p} \otimes \mathbf{e}_3) \boldsymbol{\epsilon} \mathbf{V} dA, & \mathbf{G}_3^e &:= \int_A \mathbf{W}^{*T} \boldsymbol{\epsilon} \mathbf{V} dA, & \mathbf{I}_7^e &:= \int_A \mathbf{W}^{*T} \boldsymbol{\epsilon} \mathbf{W} dA. \end{aligned}$$

Finally, we can summarise all of the above relationships between internal area resultants and mechanical/electrical strains in the following table matrix format<sup>5</sup>

<sup>5</sup>Notice that the entries in columns one to four correspond to second order tensors whereas the entries in columns five and six correspond to third order tensors. Also note that for a third order tensor  $[\mathcal{A}]_{ijk}$ , we have defined a transpose operator  $\mathcal{A}^{*T} = [\mathcal{A}]_{kij}$

$$\left\{ \begin{array}{l} \mathbf{Q}^m \\ \mathbf{M}^m \\ \mathbf{Q}^g \\ \mathbf{M}^g \\ \mathbf{Q}^e \\ \mathbf{M}^e \\ \mathbf{P}^e \\ \mathbf{O}^e \end{array} \right\} = \left[ \begin{array}{cccccccc} \mathbf{A}^m & \mathbf{S}^m & \mathbf{A}^{mg} & \mathbf{S}_1^{mg} & \mathbf{A}_1^e & \mathbf{S}_1^e & \mathbf{S}_2^e & \mathbf{I}_1^e \\ & \mathbf{I}^m & \mathbf{S}_2^{mg} & \mathbf{I}^{mg} & \mathbf{S}_3^e & \mathbf{I}_2^e & \mathbf{I}_3^e & \mathbf{G}_1^e \\ & & \mathbf{A}^g & \mathbf{S}^g & \mathbf{A}^{ge} & \mathbf{S}_1^{ge} & \mathbf{S}_2^{ge} & \mathbf{I}_1^{ge} \\ & & & \mathbf{I}^g & \mathbf{S}_3^{ge} & \mathbf{I}_2^{ge} & \mathbf{I}_3^{ge} & \mathbf{G}_1^{ge} \\ & & & & -\mathbf{A}_2^e & -\mathbf{S}_4^e & -\mathbf{S}_5^e & -\mathbf{I}_4^e \\ & & & & & -\mathbf{I}_5^e & -\mathbf{I}_6^e & -\mathbf{G}_2^e \\ & & & & & & -\mathbf{I}_7^e & -\mathbf{G}_3^e \\ & & & & & & & -\mathbf{J}^e \end{array} \right]_{sym} \left\{ \begin{array}{l} \boldsymbol{\varepsilon}^m \\ \boldsymbol{\kappa}^m \\ \boldsymbol{\varepsilon}^g \\ \boldsymbol{\kappa}^g \\ \boldsymbol{\varepsilon}^e \\ \boldsymbol{\kappa}^e \\ \boldsymbol{\gamma} \\ \boldsymbol{\varsigma}^e \end{array} \right\} \quad (8.97)$$

This resulting Hessian operator is symmetric indefinite since it emanates from the enthalpy density of the system. In case of dealing with a homogeneous material across the section of the beam, namely constant mechanical and electrical properties within the area section  $A$ , if the origin of the reference triad  $\{e_1, e_2, e_3\}$  is chosen as the centre of mass of the section, then the tensors  $\mathbf{S}^m$ ,  $\mathbf{S}_k^e$  ( $k = 1 \dots 5$ ) and  $\mathbf{G}_k^e$  ( $k = 1 \dots 3$ ) vanish (e.g. their integrand is of odd order in the position vector  $\mathbf{p}$ ). Finally, the initial boundary value problem representing the behaviour of a flexoelectric three-dimensional beam is defined by equations (8.110), (8.111), (8.112) and (8.97).

### 8.5.5 The penalty formulation for flexoelectric beams

So far in the development of flexoelectric beam theory, we have assumed a strong enforcement of the couple stress constraint in order to be able to find the area resultants and balance equations governing the physics of flexoelectric beams. However, similar to the continuum formulation, the couple stress constraint can be imposed weakly through a penalty formulation. This essentially implies that the vorticity vector must be treated as an independent field and must have a description compatible with the rest of beam kinematic and electrostatic measures. In essence,  $\boldsymbol{\omega}$  can be described through the mapping

$$(\mathbf{x}, t) \mapsto \boldsymbol{\omega}(\mathbf{x}, t) = \boldsymbol{\omega}_c(x_3, t) + \boldsymbol{\omega}_p(x_3, t) \times \mathbf{p}(x_1, x_2), \quad (8.98)$$

where  $\boldsymbol{\omega}_c$  and  $\boldsymbol{\omega}_p$  characterise the vorticity of the beam along the axis and across the cross section of the beam, respectively. The curvature vector can now be written as

$$\boldsymbol{\chi} = \frac{1}{2} \mathbf{e}_3 \times \left( \boldsymbol{\epsilon}^g + \boldsymbol{\kappa}^g \times \mathbf{p} \right) = \frac{1}{2} \hat{\mathbf{I}} \left( \boldsymbol{\epsilon}^g + \boldsymbol{\kappa}^g \times \mathbf{p} \right), \quad (8.99)$$

where

$$\boldsymbol{\epsilon}^g = \frac{\partial \boldsymbol{\omega}_c}{\partial x_3}, \quad \boldsymbol{\kappa}^g = \frac{\partial \boldsymbol{\omega}_p}{\partial x_3} \times \mathbf{p}, \quad (8.100)$$

If we assume a slight abuse of notation in order not to rename the variables, interestingly, the variational formulation for the penalty approach in the beam setting remains the same as the displacement-potential formulation presented in (8.75). The changes that will have to be reflected are minor and in the area resultants emanating from (8.32) taking into account the total stress tensor (8.34). In principle, this also means substituting the new value of  $\boldsymbol{\chi}$  which entails exchanging the term  $\frac{1}{4} \bar{\mathbf{I}}$  with  $\frac{1}{2} \hat{\mathbf{I}}$ . Furthermore, the contribution of geometric stiffness in  $\mathbf{A}^m$  and  $\mathbf{S}^m$  in (8.80) and in  $\mathbf{I}^m$  in (8.82) disappear, as these contribution now explicitly perform work against  $\delta \boldsymbol{\omega}_c$  and  $\delta \boldsymbol{\omega}_p$ , respectively (the third term in square brackets in (8.102b)). Under this settings we can write the variational form as

$$\delta W := \delta W_{iner} + \delta W_{int} - \delta W_{ext} = 0, \quad (8.101)$$

$$\delta W_{iner} = \int_l \left[ \delta \mathbf{w} \cdot (\mathbf{A}_D \ddot{\mathbf{w}} + \mathbf{S}_D \ddot{\boldsymbol{\theta}}) + \delta \boldsymbol{\theta} \cdot (\mathbf{S}_D^T \ddot{\mathbf{w}} + \mathbf{I}_D \ddot{\boldsymbol{\theta}}) \right] dx_3, \quad (8.102a)$$

$$\begin{aligned} \delta W_{int} &= \int_l [\delta \boldsymbol{\epsilon}^m \cdot \mathbf{Q}^m + \delta \boldsymbol{\kappa}^m \cdot \mathbf{M}^m] + [\delta \boldsymbol{\epsilon}^g \cdot \mathbf{Q}^g + \delta \boldsymbol{\kappa}^g \cdot \mathbf{M}^g] + [\delta \boldsymbol{\omega}_c \cdot \bar{\mathbf{Q}}^m + \delta \boldsymbol{\omega}_p \cdot \bar{\mathbf{M}}^m] dx_3 \\ &\quad + \int_l [\delta \boldsymbol{\epsilon}^e \cdot \mathbf{Q}^e + \delta \boldsymbol{\kappa}^e \cdot \mathbf{M}^e + \delta \boldsymbol{\varsigma}^e : \mathbf{P}^e + \delta \boldsymbol{\gamma} : \mathbf{O}^e] dx_3, \end{aligned} \quad (8.102b)$$

$$\begin{aligned} \delta W_{ext} &= [\delta \mathbf{w} \cdot \mathbf{Q}^m + \delta \boldsymbol{\theta} \cdot \mathbf{M}^m]_0^l + \int_l [\delta \mathbf{w} \cdot \mathbf{q}^m + \delta \boldsymbol{\theta} \cdot \mathbf{m}^m] dx_3 \\ &\quad + [\delta \boldsymbol{\omega}_c \cdot \mathbf{Q}^g + \delta \boldsymbol{\omega}_p \cdot \mathbf{M}^g]_0^l + \int_l [\delta \boldsymbol{\omega}_c \cdot \mathbf{q}^g + \delta \boldsymbol{\omega}_p \cdot \mathbf{m}^g] dx_3 \\ &\quad + [\delta \phi(\mathbf{Q}^e \cdot \mathbf{e}_3) + \delta \boldsymbol{\beta} \cdot \mathbf{M}^e + \delta \boldsymbol{\gamma} : \mathbf{O}^e]_0^l + \int_l [\delta \phi q^e + \delta \boldsymbol{\beta} \cdot \mathbf{m}^e + \delta \boldsymbol{\gamma} : \mathbf{o}^e] dx_3. \end{aligned} \quad (8.102c)$$

where

$$\bar{\mathbf{Q}}^m := \int_A \hat{\boldsymbol{\sigma}}^g \mathbf{e}_3 dA, \quad \bar{\mathbf{M}}^m := \int_A \mathbf{p} \times (\hat{\boldsymbol{\sigma}}^g \mathbf{e}_3) dA. \quad (8.103)$$

### 8.5.6 The Lagrange multiplier and augmented Lagrangian formulations for flexoelectric beams

In case of beams, the variational form of the Lagrange multiplier and augmented Lagrangian formulations remain sufficiently similar to that of a penalty formulation. However, the Lagrange multiplier itself is treated as an independent quantity and should be described to have a description compatible to the vorticity vector. This implies that the Lagrange multiplier must the vorticity along the axis as well as across the cross-section of the beam. In other words the Lagrange multiplier  $\mathbf{s}$  can be prescribed through the following mapping

$$(\mathbf{x}, t) \mapsto \mathbf{s}(\mathbf{x}, t) = \mathbf{s}_c(x_3, t) + \mathbf{s}_p(x_3, t) \times \mathbf{p}(x_1, x_2), \quad (8.104)$$

where  $\mathbf{s}_c$  and  $\mathbf{s}_p$  characterise the variation of Lagrange multiplier along the axis and across the cross section of the beam, respectively. The variational form of the problem now takes the form

$$\delta W := \delta W_{iner} + \delta W_{int} - \delta W_{ext} = 0, \quad (8.105)$$

$$\delta W_{iner} = \int_l \left[ \delta \mathbf{w} \cdot (\mathbf{A}_D \ddot{\mathbf{w}} + \mathbf{S}_D \ddot{\boldsymbol{\theta}}) + \delta \boldsymbol{\theta} \cdot (\mathbf{S}_D^T \ddot{\mathbf{w}} + \mathbf{I}_D \ddot{\boldsymbol{\theta}}) \right] dx_3, \quad (8.106a)$$

$$\begin{aligned} \delta W_{int} &= \int_l [\delta \boldsymbol{\epsilon}^m \cdot \mathbf{Q}^m + \delta \boldsymbol{\kappa}^m \cdot \mathbf{M}^m] + [\delta \boldsymbol{\epsilon}^g \cdot \mathbf{Q}^g + \delta \boldsymbol{\kappa}^g \cdot \mathbf{M}^g] \\ &\quad + [\delta \boldsymbol{\omega}_c \cdot \bar{\mathbf{Q}}^g + \delta \boldsymbol{\omega}_p \cdot \bar{\mathbf{M}}^g] + [\delta \mathbf{s}_c \cdot \mathbf{Q}^s + \delta \mathbf{s}_p \cdot \mathbf{M}^s] dx_3 \\ &\quad + \int_l [\delta \boldsymbol{\epsilon}^e \cdot \mathbf{Q}^e + \delta \boldsymbol{\kappa}^e \cdot \mathbf{M}^e + \delta \boldsymbol{\varsigma}^e : \mathbf{P}^e + \delta \boldsymbol{\gamma} : \mathbf{O}^e] dx_3, \end{aligned} \quad (8.106b)$$

$$\begin{aligned} \delta W_{ext} &= [\delta \mathbf{w} \cdot \mathbf{Q}^m + \delta \boldsymbol{\theta} \cdot \mathbf{M}^m]_0^l + \int_l [\delta \mathbf{w} \cdot \mathbf{q}^m + \delta \boldsymbol{\theta} \cdot \mathbf{m}^m] dx_3 \\ &\quad + [\delta \boldsymbol{\omega}_c \cdot \mathbf{Q}^g + \delta \boldsymbol{\omega}_p \cdot \mathbf{M}^g]_0^l + \int_l [\delta \boldsymbol{\omega}_c \cdot \mathbf{q}^g + \delta \boldsymbol{\omega}_p \cdot \mathbf{m}^g] dx_3 \\ &\quad + [\delta \mathbf{s}_c \cdot \mathbf{Q}^s + \delta \mathbf{s}_p \cdot \mathbf{M}^s]_0^l + \int_l [\delta \mathbf{s}_c \cdot \mathbf{q}^s + \delta \mathbf{s}_p \cdot \mathbf{m}^s] dx_3 \\ &\quad + [\delta \phi(\mathbf{Q}^e \cdot \mathbf{e}_3) + \delta \boldsymbol{\beta} \cdot \mathbf{M}^e + \delta \boldsymbol{\gamma} : \mathbf{O}^e]_0^l + \int_l [\delta \phi q^e + \delta \boldsymbol{\beta} \cdot \mathbf{m}^e + \delta \boldsymbol{\gamma} : \mathbf{o}^e] dx_3. \end{aligned} \quad (8.106c)$$

where

$$\bar{\mathbf{Q}}^m := - \int_A \hat{\boldsymbol{\sigma}}^g \mathbf{e}_3 \, dA, \quad \bar{\mathbf{M}}^m := - \int_A \mathbf{p} \times (\hat{\boldsymbol{\sigma}}^g \mathbf{e}_3) \, dA, \quad (8.107)$$

and for Lagrange multiplier approach we have

$$\mathbf{Q}^s := \int_A (\nabla^{skew} \mathbf{u} - \hat{\boldsymbol{\omega}}) \mathbf{e}_3 \, dA, \quad \mathbf{M}^s := \int_A \mathbf{p} \times ((\nabla^{skew} \mathbf{u} - \hat{\boldsymbol{\omega}}) \mathbf{e}_3) \, dA, \quad (8.108a)$$

$$\mathbf{q}^s := \int_A (\nabla^{skew} \mathbf{u} - \hat{\boldsymbol{\omega}}) \mathbf{n} \, dA, \quad \mathbf{m}^s := \int_A \mathbf{p} \times ((\nabla^{skew} \mathbf{u} - \hat{\boldsymbol{\omega}}) \mathbf{n}) \, dA. \quad (8.108b)$$

whereas for augmented Lagrangian we obtain

$$\mathbf{Q}^s := \int_A [(\nabla^{skew} \mathbf{u} - \hat{\boldsymbol{\omega}}) + \frac{1}{\kappa} \mathbf{s} \times \mathbf{I}] \mathbf{e}_3 \, dA, \quad \mathbf{M}^s := \int_A \mathbf{p} \times [(\nabla^{skew} \mathbf{u} - \hat{\boldsymbol{\omega}}) + \frac{1}{\kappa} \mathbf{s} \times \mathbf{I}] \mathbf{e}_3 \, dA, \quad (8.109a)$$

$$\mathbf{q}^s := \int_A [(\nabla^{skew} \mathbf{u} - \hat{\boldsymbol{\omega}}) + \frac{1}{\kappa} \mathbf{s} \times \mathbf{I}] \mathbf{n} \, dA, \quad \mathbf{m}^s := \int_A \mathbf{p} \times [(\nabla^{skew} \mathbf{u} - \hat{\boldsymbol{\omega}}) + \frac{1}{\kappa} \mathbf{s} \times \mathbf{I}] \mathbf{n} \, dA. \quad (8.109b)$$

### 8.5.7 Governing equations of three-dimensional flexoelectric beams

As it is well known in standard beam theory, further manipulation of the displacement-potential variational form (8.74)-(8.75) can lead to the so-called beam balance equations [126], which are written as

$$\left( \frac{\partial^2 \mathbf{Q}^g}{\partial x_3^2} \right) + \frac{\partial \mathbf{Q}^m}{\partial x_3} + \mathbf{q}^m = \mathbf{A}_D \ddot{\mathbf{w}} + \mathbf{S}_D \ddot{\boldsymbol{\theta}}, \quad \text{in } l \times [0, T], \quad (8.110a)$$

$$\begin{aligned} & \left( \frac{\partial^2 \mathbf{M}^g}{\partial x_3^2} - \mathbf{e}_3 \times \frac{\partial \mathbf{Q}^g}{\partial x_3} \right) + \frac{\partial \mathbf{M}^m}{\partial x_3} \\ & - \mathbf{Q}^m \times \mathbf{e}_3 + \mathbf{m}^m = \mathbf{S}_D^T \ddot{\mathbf{w}} + \mathbf{I}_D \ddot{\boldsymbol{\theta}}, \quad \text{in } l \times [0, T], \end{aligned} \quad (8.110b)$$

$$\frac{\partial (\mathbf{Q}^e \cdot \mathbf{e}_3)}{\partial x_3} + q^e = 0, \quad \text{in } l \times [0, T], \quad (8.110c)$$

$$\frac{\partial \mathbf{M}^e}{\partial x_3} + \bar{\mathbf{I}} \mathbf{Q}^e + \mathbf{m}^e = \mathbf{0}, \quad \text{in } l \times [0, T], \quad (8.110d)$$

$$\frac{\partial \mathbf{O}^e}{\partial x_3} - \mathbf{P}^e + \mathbf{o}^e = \mathbf{0}, \quad \text{in } l \times [0, T], \quad (8.110e)$$

The above set of equations represent a set of balance equations in terms of internal area resultants  $\mathbf{Q}^g$ ,  $\mathbf{M}^g$ ,  $\mathbf{Q}^m$ ,  $\mathbf{M}^m$ ,  $\mathbf{Q}^e$ ,  $\mathbf{M}^e$ ,  $\mathbf{P}^e$  and  $\mathbf{O}^e$ . If we drop the terms in the bracket, the piezoelectric beam model of [250] is recovered. Initial conditions in (8.4), boundary conditions (8.2-8.4-8.6), strains measures (8.43-8.44), strain gradient measures (8.48-8.49) and the electrical counterparts (8.53-8.54) complement the above system of partial differential equations (8.110) to form the initial boundary value problem of the three-dimensional flexoelectric beam. Specifically, compatible initial conditions can be defined in terms of axis varying functions  $\mathbf{w}_0, \dot{\mathbf{w}}_0, \boldsymbol{\theta}_0, \dot{\boldsymbol{\theta}}_0 : [0, l] \rightarrow \mathbb{R}^3$  as

$$\mathbf{u}(x_1, x_2, x_3, t) = \mathbf{w}_0(x_3) + \boldsymbol{\theta}_0(x_3) \times \mathbf{p}(x_1, x_2) \quad \text{in } \Omega \times 0, \quad (8.111a)$$

$$\dot{\mathbf{u}}(x_1, x_2, x_3, t) = \dot{\mathbf{w}}_0(x_3) + \dot{\boldsymbol{\theta}}_0(x_3) \times \mathbf{p}(x_1, x_2) \quad \text{in } \Omega \times 0, \quad (8.111b)$$

Dirichlet (and corresponding Neumann) boundary conditions can be defined at either end of the beam  $x_3 = 0$  or  $x_3 = l$  by

$$\mathbf{w} = \bar{\mathbf{w}}, \quad \boldsymbol{\theta} = \bar{\boldsymbol{\theta}}, \quad \phi = \bar{\phi}, \quad \boldsymbol{\beta} = \bar{\boldsymbol{\beta}}, \quad \gamma = \bar{\gamma}, \quad (8.112a)$$

$$\mathbf{Q}^m = \bar{\mathbf{Q}}^m, \quad \mathbf{M}^m = \bar{\mathbf{M}}^m, \quad \mathbf{Q}^e \cdot \mathbf{e}_3 = \bar{\mathbf{Q}}^e, \quad \mathbf{M}^e = \bar{\mathbf{M}}^e, \quad \mathbf{O}^e = \bar{\mathbf{O}}^e, \quad (8.112b)$$

$$\mathbf{Q}^g = \bar{\mathbf{Q}}^g, \quad \mathbf{M}^g = \bar{\mathbf{M}}^g. \quad (8.112c)$$

If we consider a purely mechanical couple stress beam model, equations (8.110) and (8.112) can be reduced to those of [189](Eqs. 21-22) and [236](Eqs. 22-23) for planar beams, by dropping the torsional term  $\frac{\partial^2 \mathbf{M}^g}{\partial x_3^2}$  from (8.110b). Thus, the present beam model (8.110) is a fourth order differential equation in both  $\mathbf{w}$  and  $\boldsymbol{\theta} \cdot \mathbf{e}_3$ . It should be emphasised however, that the kinematics and constitutive relations of the present beam model are different. Due to the effect of couple stress quantities, namely moment-tractions and body couples having been merged with force-tractions and body forces, complicated boundary conditions (especially the body couple) of [189, 258, 283] do not appear in our formulation.

## 8.6 The finite element discretisation

The purpose of this section is to present a family of mixed finite element discretisation schemes to the couple stress flexoelectric theory of continua and beams. The point of departure is the respective variational formulations presented in the previous two sections in particular, the penalty formulation for continuum (8.32), the penalty formulation for beams (8.102), the Lagrange multiplier for continuum (8.36), the Lagrange multiplier for beams (8.106), the augmented Lagrangian formulation for continuum (8.40) and the augmented Lagrangian formulation for beams (8.106). The finite element discretisation follows naturally by introducing a non-overlapping partition of the domain  $\Omega$  into a series of one-dimensional (for beams) or two and/or three-dimensional (for continuum) elements, as shown in Figure 8.5 and Figure 8.4, respectively. Owing to the nature of the aforementioned variational formulations,  $C^0$  continuity can be retained for all variables by choosing the standard  $p$ -version of the finite element method [295, 47] for discretisation. For the penalty formulation this entails employing piece-wise continuous  $P_n$  interpolation functions for displacements  $\mathbf{u}$  while piece-wise discontinuous  $P_{n-1}^D$  interpolation functions for rotations  $\boldsymbol{\omega}$  (where  $n \geq 2 \in \mathbb{N}$  represents any arbitrary polynomial degree and  $D$  represents the discontinuous nature of the interpolation functions), subjected to the satisfaction of the inf-sup condition [34, 43]. Similarly, for Lagrange multiplier and augmented Lagrangian formulations piece-wise continuous  $P_n$  interpolation functions for displacements  $\mathbf{u}$  and electric potential  $\psi$  and piece-wise discontinuous  $P_{n-1}^D$  interpolation functions for the rotations  $\boldsymbol{\omega}$  and the Lagrange multiplier  $\mathbf{s}$  can be employed. These arrangements are shown in Figure 8.4 for triangles, quadrilaterals, tetrahedra and hexahedra, where the standard terminology in finite element is used (i.e. P representing the polynomial degree of interpolation bases for triangles and tetrahedral elements and Q denoting the polynomial degree of interpolation bases for quadrilateral and hexahedral elements). Similar discretisation methodology can be followed in the case of beams. While  $\{\mathbf{w}, \boldsymbol{\theta}, \psi, \beta, \gamma\}$  can be discretised using piece-wise continuous  $P_n$  interpolation functions,  $\{\boldsymbol{\omega}_c, \boldsymbol{\omega}_p, \mathbf{s}_c, \mathbf{s}_p\}$  can be discretised using piece-wise discontinuous  $P_{n-1}^D$  interpolation functions, subjected to the satisfaction of the inf-sup condition. These arrangements are shown in Figure 8.5.

To keep the presentation succinct, the details of finite element implementations are not discussed here. Finite element implementations of couple stress models for purely mechanical continuum elements are discussed in [42, 99] for penalty formulation and in [70, 167] for Lagrange multiplier formulation. The previous work of the authors also describe computational implementation of a series of mixed and high order finite element discretisations based on an enhanced set of variables in electromechanics for continuum and beam elements [233, 253, 235, 250]. It is worth noting that, due to the discontinuous nature of couple stress related variables, their corresponding contributions can be locally condensed out using static condensation leading to an extremely efficient implementation of couple stress flexoelectricity that can be easily incorporated in to an existing piezoelectric finite element software [251]. Furthermore, since at least a quadratic interpolation is used for displacements, the geometry of flexoelectric structures can be represented accurately using the recently developed isoparametric curvilinear finite element technology presented in [254, 253].

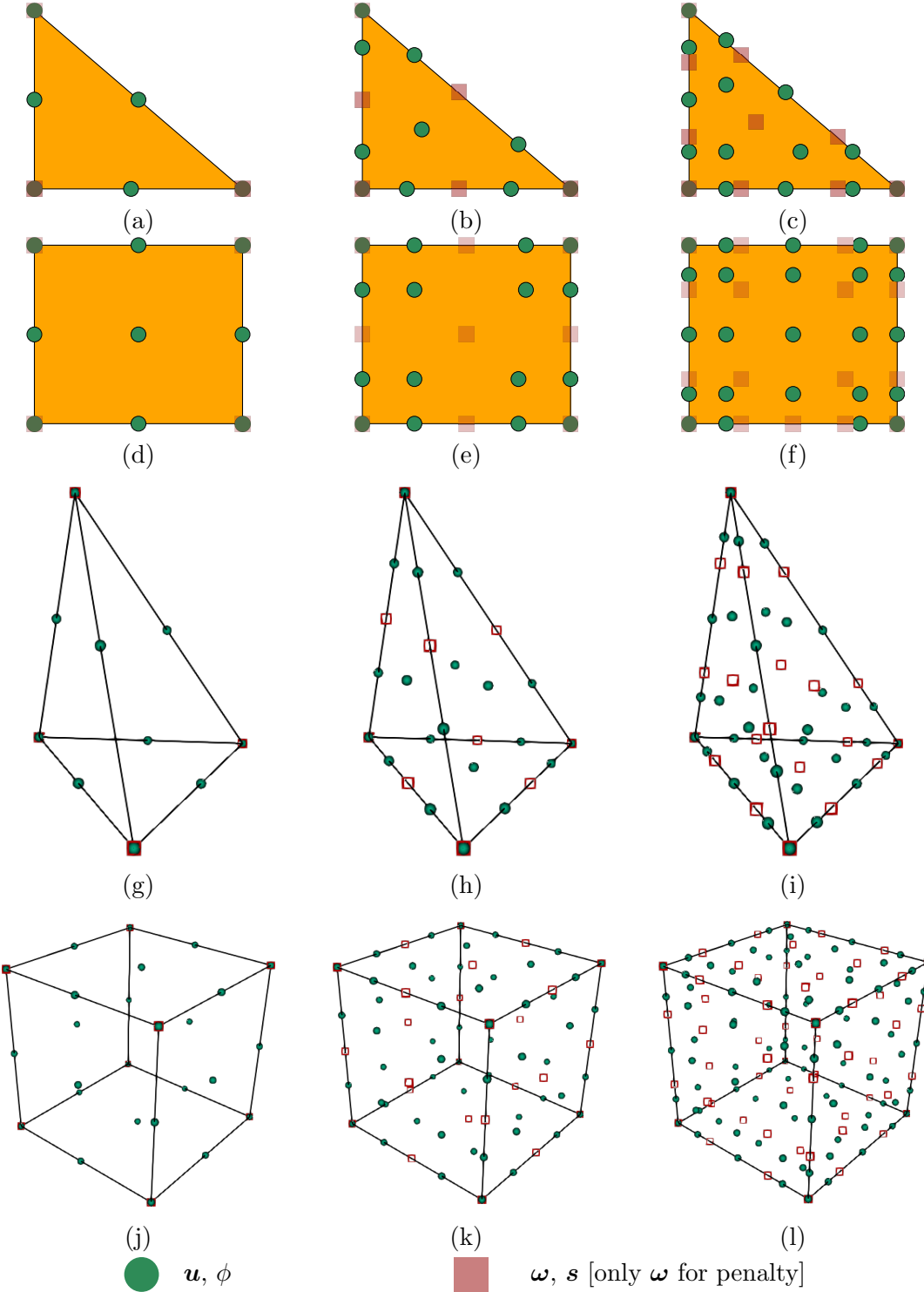


Figure 8.4: A non-exhaustive list of the developed mixed finite elements for triangles: (a) P2-P2-P1<sup>D</sup>-P1<sup>D</sup>/P2-P2-P1<sup>D</sup>, (b) P3-P3-P2<sup>D</sup>-P2<sup>D</sup>/P3-P3-P2<sup>D</sup>, (c) P4-P4-P3<sup>D</sup>-P3<sup>D</sup>/P4-P4-P3<sup>D</sup>; quadrilaterals: (d) Q2-Q1<sup>D</sup>-Q1<sup>D</sup>/Q2-Q1<sup>D</sup>, (e) Q3-Q3-Q2<sup>D</sup>-Q2<sup>D</sup>/Q3-Q3-Q2<sup>D</sup>, (f) Q4-Q4-Q3<sup>D</sup>-Q3<sup>D</sup>/Q4-Q4-Q3<sup>D</sup>; tetrahedra: (g) P2-P2-P1<sup>D</sup>-P1<sup>D</sup>/P2-P2-P1<sup>D</sup>, (h) P3-P3-P2<sup>D</sup>-P2<sup>D</sup>/P3-P3-P2<sup>D</sup>, (i) P4-P4-P3<sup>D</sup>-P3<sup>D</sup>/P4-P4-P3<sup>D</sup> and hexahedra: (j) Q2-Q2-Q1<sup>D</sup>-Q1<sup>D</sup>/Q2-Q2-Q1<sup>D</sup>, (k) Q3-Q3-Q2<sup>D</sup>-Q2<sup>D</sup>/Q3-Q3-Q2<sup>D</sup>, (l) Q4-Q4-Q3<sup>D</sup>-Q3<sup>D</sup>/Q4-Q4-Q3<sup>D</sup>. The developed framework encompasses P<sub>n</sub>-P<sub>n</sub>-P<sub>n-1</sub><sup>D</sup>-P<sub>n-1</sub><sup>D</sup>, P<sub>n</sub>-P<sub>n</sub>-P<sub>n-1</sub><sup>D</sup>, Q<sub>n</sub>-Q<sub>n</sub>-Q<sub>n-1</sub><sup>D</sup>-Q<sub>n-1</sub><sup>D</sup>, Q<sub>n</sub>-Q<sub>n</sub>-Q<sub>n-1</sub><sup>D</sup> for any interpolation degree n.

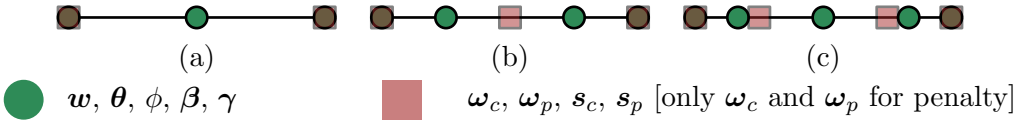


Figure 8.5: A non-exhaustive list of the developed mixed finite elements for one-dimensional beam elements: (a) P2-P2-P2-P2-P2-P1<sup>D</sup>-P1<sup>D</sup>-P1<sup>D</sup>/P2-P2-P2-P2-P2-P1<sup>D</sup>-P1<sup>D</sup>, (b) P3-P3-P3-P3-P3-P2<sup>D</sup>-P2<sup>D</sup>-P2<sup>D</sup>/P3-P3-P3-P3-P3-P2<sup>D</sup>-P2<sup>D</sup>, (c) P4-P4-P4-P4-P4-P3<sup>D</sup>-P3<sup>D</sup>-P3<sup>D</sup>/P4-P4-P4-P4-P4-P3<sup>D</sup>-P3<sup>D</sup>. The developed framework encompasses P<sub>n</sub>-P<sub>n</sub>-P<sub>n</sub>-P<sub>n</sub>-P<sub>n</sub>-P<sub>n-1</sub>-P<sub>n-1</sub>-P<sub>n-1</sub>-P<sub>n-1</sub><sup>D</sup>, P<sub>n</sub>-P<sub>n</sub>-P<sub>n</sub>-P<sub>n</sub>-P<sub>n</sub>-P<sub>n-1</sub>-P<sub>n-1</sub><sup>D</sup> for any interpolation degree n.

## 8.7 Numerical experiments

### 8.7.1 A detailed comparison of couple stress based and strain gradient based flexoelectric models: vanishing volumetric strain gradients, the presence of reverse coupling modes and material characterisation for BaTiO<sub>3</sub>

The objective of this first study is to quantitatively compare the present couple stress based flexoelectric model with the standard strain gradient based flexoelectric models in terms of their effectiveness in predicting size-dependent electric polarisation produced from non-uniform strain distribution. The study primarily focusses on BaTiO<sub>3</sub> whose piezoelectric and flexoelectric material properties are known from [24] and [201], respectively as

Elastic constants	Dielectric constants	Piezoelectric constants	Flexoelectric constants
C <sub>11</sub> = 275 GPa	ε <sub>11</sub> = 12.5 nC/Vm	e <sub>31</sub> = -2.7 C/m <sup>2</sup>	f <sub>11</sub> = 0.15 nC/m
C <sub>12</sub> = 179 GPa	ε <sub>33</sub> = 14.4 nC/Vm	e <sub>33</sub> = 3.65 C/m <sup>2</sup>	f̄ <sub>12</sub> = 100 nC/m
C <sub>13</sub> = 152 GPa		e <sub>15</sub> = 21.3 C/m <sup>2</sup>	f̄ <sub>44</sub> = -1.9 nC/m
C <sub>33</sub> = 165 GPa			
C <sub>44</sub> = 54 GPa			

Table 8.1: Material constants for BaTiO<sub>3</sub>

where these constitutive tensors can be spherically parametrised to form the so-called indicator surfaces of BaTiO<sub>3</sub>, as shown in Figure 8.6. Indicator surface is a convenient way to visualise the major axes of material symmetry as can be clearly seen in the case of piezoelectric tensor in Figure 8.6c. As an essential part of the comparison, this parametrisation is also used later to compare the flexoelectric tensors of couple stress based and standard strain gradient based models.

For the purpose of clarity, let us consider only the flexoelectric coupling mechanisms under both (couple stress and standard strain gradient) theories, in a two dimensional setting. The point of departure, is the flexoelectric enthalpy of the system which under standard strain gradient theories is given in terms of the gradient of strains  $\bar{\chi} = \nabla^{sym}\nabla^{sym}\mathbf{u}$  and the electric field  $\mathbf{E}$  as

$$\Psi_{sg}(\mathbf{E}, \bar{\chi}) = -\mathbf{E} \cdot \bar{\mathbf{f}} : \bar{\chi} = -E_i f_{ijkl} \bar{\chi}_{jkl}, \quad (8.113)$$

where  $\bar{\mathbf{f}}$  is the fourth order flexoelectric tensor with one symmetry i.e.  $\bar{f}_{ijkl} = \bar{f}_{ikjl}$  and in the general three-dimensional case can be characterised with 54 material constants, as shown in Figure 8.7a (for the case of BaTiO<sub>3</sub>). Under a two-dimensional setting, only 12 material constants are required to fully characterise the flexoelectric tensor. The strain gradient tensor  $\bar{\chi}$  and the flexoelectric tensor under Voigt notations can be written as [3, 222]

$$\bar{\chi} = \nabla^{sym}\nabla^{sym}\mathbf{u} = \left[ \frac{\partial^2 u_x}{\partial x^2}, \frac{\partial^2 u_y}{\partial y \partial x}, \frac{\partial^2 u_x}{\partial y \partial x} + \frac{\partial^2 u_y}{\partial x^2}, \frac{\partial^2 u_x}{\partial x \partial y}, \frac{\partial^2 u_y}{\partial y^2}, \frac{\partial^2 u_x}{\partial y^2} + \frac{\partial^2 u_y}{\partial x \partial y} \right]^T, \quad (8.114)$$

$$\bar{\mathbf{f}} = \begin{bmatrix} \bar{f}_{11} & \bar{f}_{12} & 0 & 0 & 0 & \bar{f}_{44} \\ 0 & 0 & \bar{f}_{44} & \bar{f}_{12} & \bar{f}_{11} & 0 \end{bmatrix}, \quad (8.115)$$

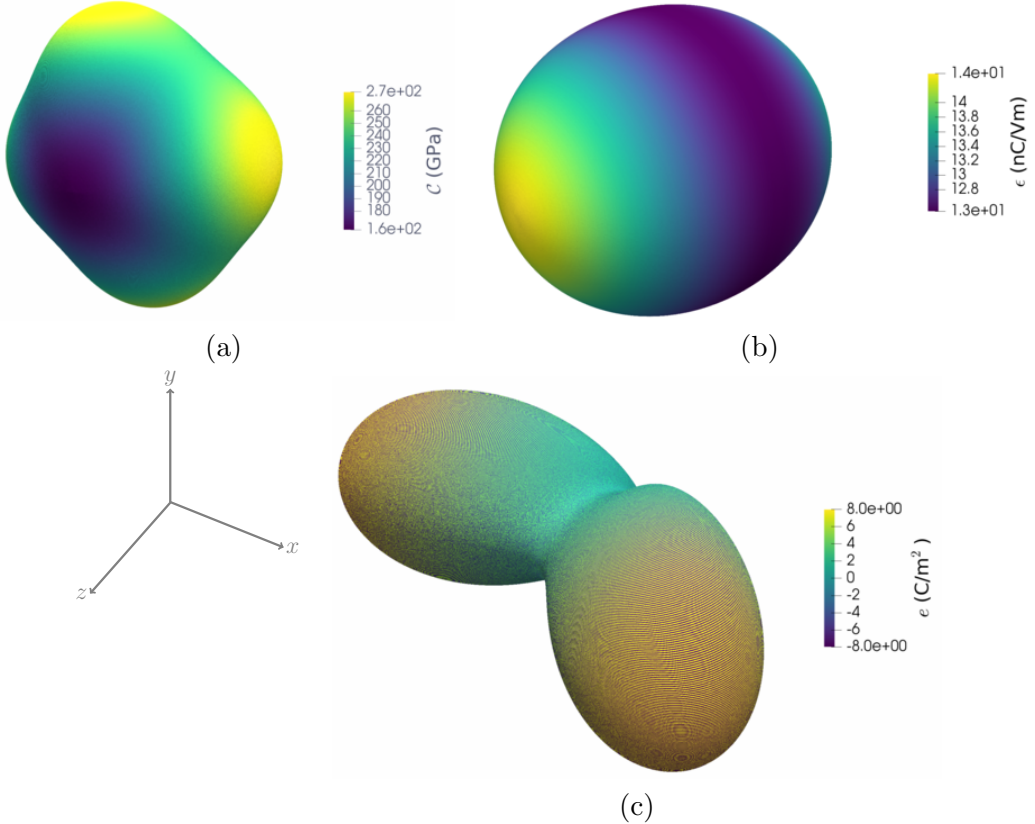


Figure 8.6: Indicatory surfaces of BaTiO<sub>3</sub> constitutive tensors namely, a) the elasticity tensor  $\mathcal{C}$ , b) the dielectric tensor  $\epsilon$  and, c) the piezoelectric tensor  $e$

where (8.114) is the so-called mean or engineering strain gradients, wherein the multiplication factor ( $\frac{1}{4}$ ) is omitted for simplicity. This in general implies that the produced electric displacement must take the form

$$\mathbf{D}_{sg} = -\frac{\partial \Psi_{sg}}{\partial \mathbf{E}} = \begin{bmatrix} \bar{f}_{11} \frac{\partial^2 u_x}{\partial x^2} + \bar{f}_{12} \frac{\partial^2 u_y}{\partial y \partial x} + \bar{f}_{44} \left( \frac{\partial^2 u_x}{\partial y^2} + \frac{\partial^2 u_y}{\partial x \partial y} \right) \\ \bar{f}_{11} \frac{\partial^2 u_y}{\partial y^2} + \bar{f}_{12} \frac{\partial^2 u_x}{\partial x \partial y} + \bar{f}_{44} \left( \frac{\partial^2 u_x}{\partial y \partial x} + \frac{\partial^2 u_y}{\partial x^2} \right) \end{bmatrix}. \quad (8.116)$$

On the other hand, in the case of couple stress based flexoelectric model, as presented earlier the flexoelectric enthalpy can be written as

$$\Psi_{cs}(\mathbf{E}, \boldsymbol{\chi}) = -\mathbf{E} \cdot \mathbf{f} \cdot \boldsymbol{\chi} = -E_i f_{ij} \chi_j, \quad (8.117)$$

where  $\mathbf{f}$  is the second order flexoelectric tensor with no general symmetries. It is characterised by 9 constants in the three-dimensional case and 4 constants in the two-dimensional case. The explicit forms of  $\boldsymbol{\chi}$  and  $\mathbf{f}$  are given as

$$\boldsymbol{\chi} = \nabla \times \nabla \times \mathbf{u} = \left[ \frac{\partial^2 u_y}{\partial y \partial x} - \frac{\partial^2 u_x}{\partial y^2}, \frac{\partial^2 u_x}{\partial x \partial y} - \frac{\partial^2 u_y}{\partial x^2} \right]^T, \quad (8.118)$$

$$\mathbf{f} = \begin{bmatrix} f_{11} & f_{12} \\ f_{21} & f_{22} \end{bmatrix}, \quad (8.119)$$

where  $\boldsymbol{\chi}$  is the mean or engineering curvature vector presented earlier, wherein the multiplication factor ( $\frac{1}{4}$ ) is omitted for simplicity. Note that no correspondence is established between the tensors  $\mathbf{f}$  and  $\bar{\mathbf{f}}$  yet. This in general implies that the produced electric displacement must take the form

$$\mathbf{D}_{cs} = -\frac{\partial \Psi_{cs}}{\partial \mathbf{E}} = \begin{bmatrix} f_{11} \left( \frac{\partial^2 u_y}{\partial y \partial x} - \frac{\partial^2 u_x}{\partial y^2} \right) + f_{12} \left( \frac{\partial^2 u_x}{\partial x \partial y} - \frac{\partial^2 u_y}{\partial x^2} \right) \\ f_{21} \left( \frac{\partial^2 u_y}{\partial y \partial x} - \frac{\partial^2 u_x}{\partial y^2} \right) + f_{22} \left( \frac{\partial^2 u_x}{\partial x \partial y} - \frac{\partial^2 u_y}{\partial x^2} \right) \end{bmatrix}. \quad (8.120)$$

Comparing  $\mathbf{D}_{sg}$  in (8.116) and  $\mathbf{D}_{cs}$  in (8.120), one can observe that, in the case of couple stress flexoelectric theory, the variation of volumetric strains (volumetric strain gradients namely the components  $\frac{\partial^2 u_x}{\partial x^2}$  and  $\frac{\partial^2 u_y}{\partial y^2}$ ) do not generate electric polarisation, as they are fundamentally non-existent. This is true for all variants of couple stress theories (i.e. classical, modified, conformal and skew-symmetric couple stress theories) as the spherical part of strain always vanishes. In other words, the  $\bar{f}_{11}$  coupling mode cannot be characterised under this theory. In the case of BaTiO<sub>3</sub>, we observe that  $\bar{f}_{11}$  parameter corresponds to the weakest coupling mode which can be up to three orders of magnitude smaller than the flexural mode and can be neglected even in the case of standard strain gradient flexoelectricity. Moreover, it can be noticed that, if present, the  $f_{12}$  and  $f_{21}$  give rise to a completely reversed coupling mode in comparison to strain gradient theory. Further comparison of (8.116) and (8.120) for BaTiO<sub>3</sub> constants shown in Table 8.1, reveals that the flexoelectric coupling modes is in fact dominant in  $\bar{f}_{12}$  and one can consequently write

$$\mathbf{D}_{sg} \approx \begin{bmatrix} \bar{f}_{12} \frac{\partial^2 u_y}{\partial y \partial x} \\ \bar{f}_{12} \frac{\partial^2 u_x}{\partial x \partial y} \end{bmatrix}. \quad (8.121)$$

If we were to establish a correspondence between  $\mathbf{f}$  and  $\bar{\mathbf{f}}$ , then the most plausible relationship would be to assume  $f_{11} = f_{22} = \bar{f}_{12}$  and  $f_{12} = f_{21} = 0$  in which case we can write

$$\mathbf{f} \approx \bar{f}_{12} \mathbf{I} = \begin{bmatrix} \bar{f}_{12} & 0 \\ 0 & \bar{f}_{12} \end{bmatrix}, \quad \mathbf{D}_{cs} \approx \begin{bmatrix} \bar{f}_{12} \left( \frac{\partial^2 u_y}{\partial y \partial x} - \frac{\partial^2 u_x}{\partial x \partial y} \right) \\ \bar{f}_{12} \left( \frac{\partial^2 u_x}{\partial x \partial y} - \frac{\partial^2 u_y}{\partial y \partial x} \right) \end{bmatrix}. \quad (8.122)$$

Equation (8.122) establishes the closest possible algebraic relationships between flexoelectric constants of couple stress based and strain gradient based flexoelectric theories, without the need for a nonlinear optimisation process to characterise the constants of one theory with respect to the other. The need for this optimisation can also be negated by noting the significant discrepancies present between atomistic simulations and experimental observations in determining flexoelectric constants [193, 201, 338], as result of which most authors assume the flexural constant  $\bar{f}_{12}$  in the wide range of 1nC/m-100μC/m. Under this setting, the indicatory surfaces of flexoelectric tensors  $\bar{\mathbf{f}}$  and  $\mathbf{f}$  can be represented as shown in Figure 8.7 where the

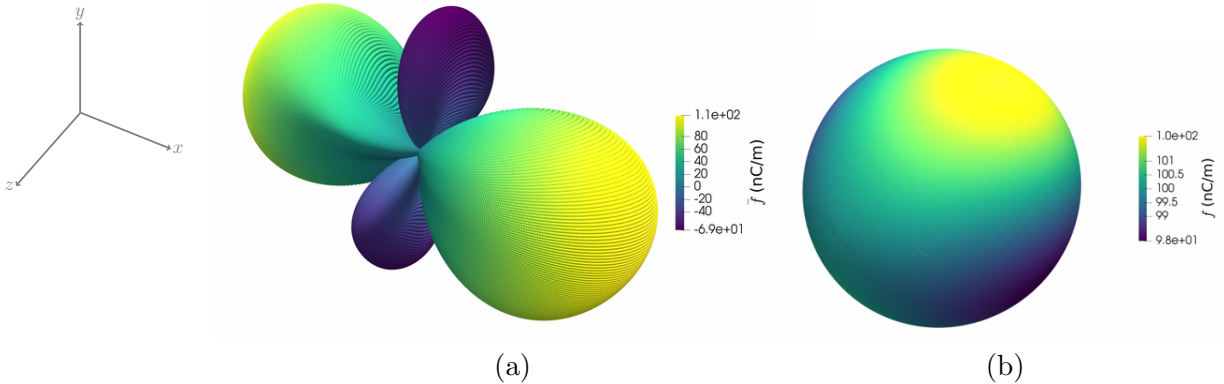


Figure 8.7: Indicatory surface of BaTiO<sub>3</sub> flexoelectric constitutive tensor under, a) standard strain gradient based flexoelectric theory (i.e.  $\bar{\mathbf{f}}$ ), b) couple stress based flexoelectric theory (i.e.  $\mathbf{f}$ )

axes of symmetry for both tensors can be clearly seen. Figure 8.7, once again confirms that characterising the flexoelectric constants of  $\mathbf{f}$  with respect to  $\bar{\mathbf{f}}$  is in general impractical owing to the fact that the tensors belong to two different vector spaces.

In what follows, we consider simplified cases of flexoelectric coupling of nano-specimen under different coupling modes with various boundary conditions and present simple analytical solutions in order to quantify the electromechanical coupling efficiency of couple stress based

and standard strain gradient based flexoelectric theories. The analytical solutions are designed such that the specimen will experience a non-uniform strain distribution, assumed to enough to break the inversion symmetry of BaTiO<sub>3</sub> to produce electric polarisation. While inspired by simple analytical solutions of beams these studies are performed at a continuum level.

### Case 1. Simply supported nanobeam under uniformly distributed load

As a first case, let us consider a nanobeam shown in Figure 8.8. Under the action of uniformly distributed load the beam undergoes bending and as a result, a non-uniform distribution of strains across the cross section of the beam is observed. A simple analytical solution for

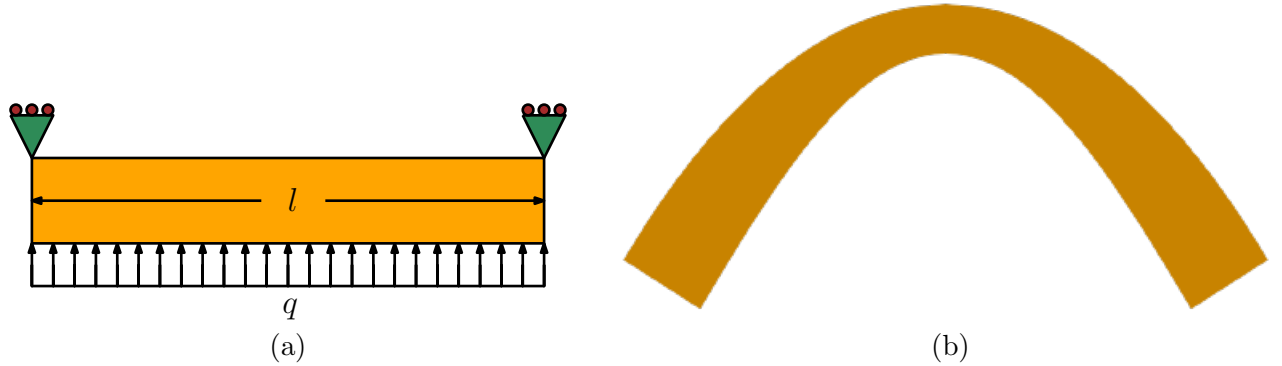


Figure 8.8: Original and deformed shape of nanobeam

the bending of the nanobeam shown in Figure 8.8b can be simply computed using the beam kinematics presented in (8.44), as

$$u_x = -\alpha(l^3 - 6lx^2 + 4x^3)y, \quad (8.123a)$$

$$u_y = \beta(l^3x - 2lx^3 + x^4) + \gamma x(l - x), \quad (8.123b)$$

where the parameters  $\alpha = 1.25 \times 10^{20}$ ,  $\beta = 1.25 \times 10^{20}$  and  $\gamma = 1330$  are chosen for convenience. This in fact corresponds to a load of  $100\mu\text{N}/\text{m}$ .  $l$  denotes the length of the beam which is chosen to be  $10\text{nm}$  and the thickness of the beam is retained as  $t = 1\text{nm}$ . The material constants of BaTiO<sub>3</sub> shown in Table 8.1 are chosen for the study. The electric displacement vectors  $\mathbf{D}_{sg}$  and  $\mathbf{D}_{cs}$  can now be computed using equations (8.116) and (8.120), respectively.

Figure 8.9 compares the generated electric displacement of the couple stress model computed using (8.122) with that of the standard strain gradient model computed using (8.116) (i.e. the fully coupled electric displacement vector), along the length of the beam (i.e. for all  $x$  such that  $y$  coincides with the neutral axis). The figures also compares the electric displacements generated with the standard strain gradient model ignoring the  $\bar{f}_{11}$  parameter which is not present in the couple stress model. Notice that when  $\bar{f}_{11}$  parameter is discarded both couple stress and strain gradient models generate the same (zero) electric displacement component  $D_x$ , in this case. The electric displacement  $D_x$  is zero in the latter two cases, due to the fact the corresponding second derivatives vanish. This generated electric displacement is extremely small owing the fact that  $\bar{f}_{11}$  is significantly weaker in BaTiO<sub>3</sub>. On the other hand, extremely high electric displacement  $D_y$  is generated. Under this coupling mode, it can be observed that the couple stress model generates approximately twice the amount of electric displacement as compared to the strain gradient model and the contribution of  $\bar{f}_{11}$  and  $\bar{f}_{44}$  parameters while present are small enough, that they can be neglected. However, the profile of generated electric displacement along the beam is in general similar for both models.

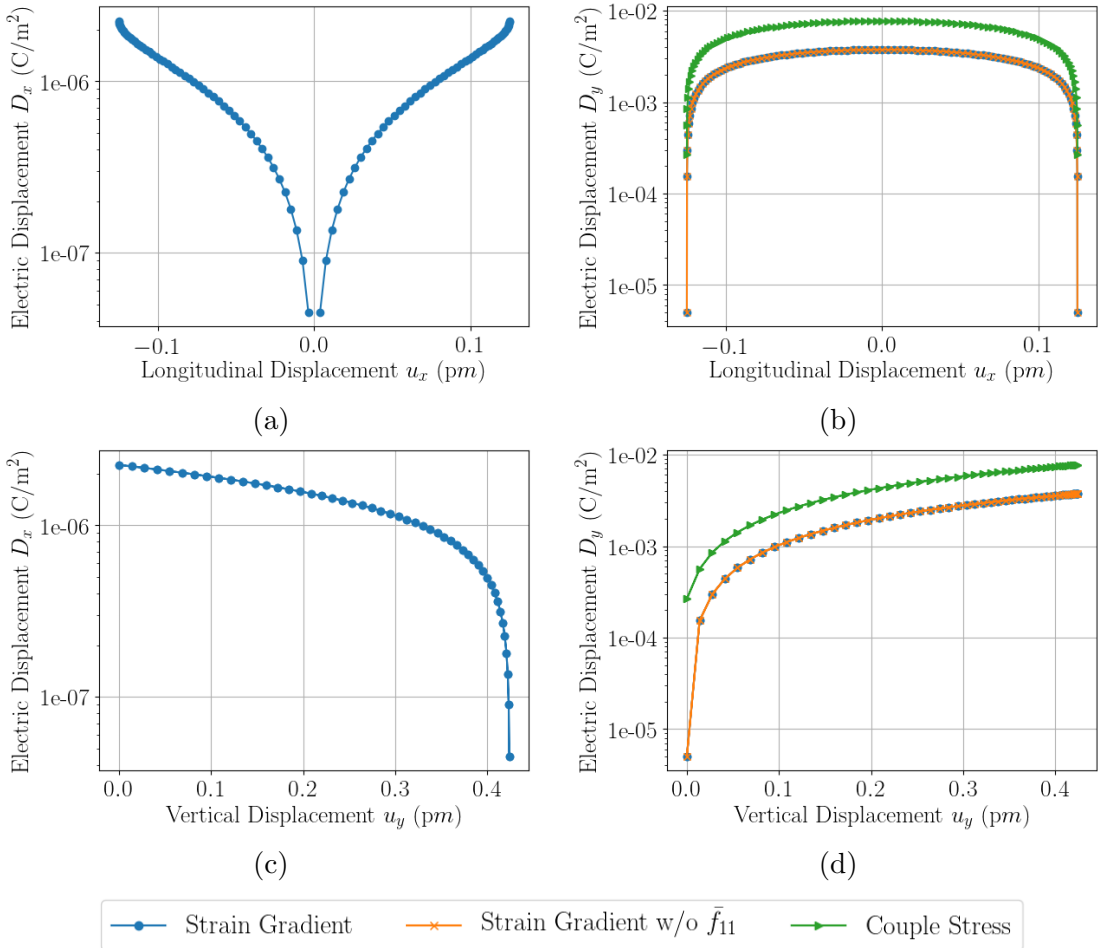


Figure 8.9: Comparison of couple stress based and strain gradient based flexoelectric models for the case of (8.123), when material constants are fitted according to (8.122)

### Cantilever nanobeam undergoing bending and complex cross sectional thinning

Let us next consider a nanobeam undergoing complex cross sectional thinning and bending, as shown in Figure 8.10. The analytical formula describing this morphology is given by

$$u_x = -\alpha(3l^2x - 3lx^2 + x^3)y, \quad (8.124a)$$

$$u_y = \beta(3l^2x^2 - 4lx^3 + x^4) + \gamma x(2l - x), \quad (8.124b)$$

where the parameter  $\alpha = 5.21 \times 10^{18}$  is now chosen. Under this setting, the beam experiences nonuniform distribution of strains across the cross section and along the length and as a result the flexoelectric coupling mechanism is more complex now. Note that the form of loading  $q$  must be coordinate dependent and not generally uniform, in order to produce the aforementioned analytical formula.

Figure 8.11 compares the generated electric displacement of the couple stress model with that of the standard strain gradient model with and without consideration of the  $\bar{f}_{11}$  coupling modes. A similar conclusion can be drawn in this case in that, when  $\bar{f}_{11}$  parameter is discarded both couple stress and strain gradient models generate the same (zero) electric displacement component  $D_x$ , which is negligible regardless. However an extremely high electric displacement  $D_y$  is generated with the couple stress model, which in this case is up to two orders higher than that of strain gradient model. This is due to the strong presence of second derivatives (curvature effect) in the couple stress model, which gives rise to extremely high bending coupling mode. However, the profile of generated electric displacement is in general similar for both models.

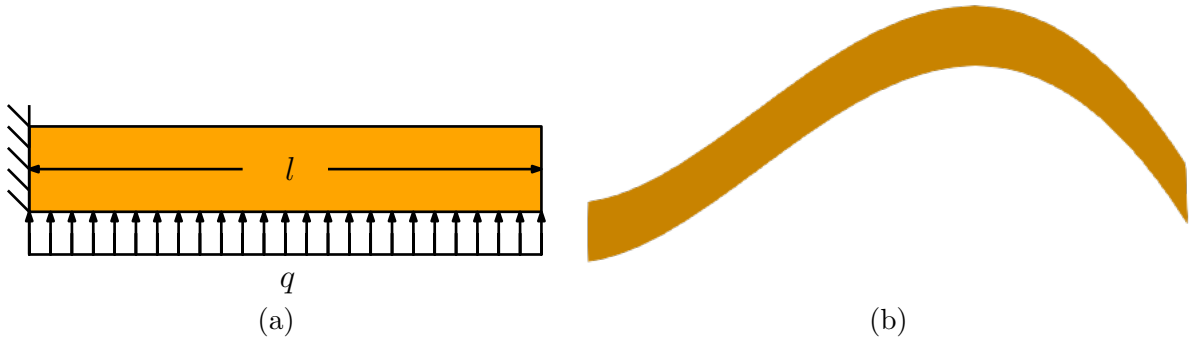


Figure 8.10: Original and deformed shape of nanobeam

### Cantilever nanobeam undergoing extension and thinning

The third and final case considers an even more complex deformation scenario under extension to ensure that there are no vanishing component in the strain gradient tensor/curvature vector. This study also considers the extension coupling mechanism in flexoelectricity. To this effect a nanobeam undergoing complex cross sectional thinning and extension is considered, as shown in Figure 8.12. The analytical formula describing this morphology is given by

$$u_x = \alpha x^2 \left(y - \frac{l}{20}\right)^2, \quad (8.125a)$$

$$u_y = \beta \sqrt{x + 2l} \left(y - \frac{l}{20}\right)^3, \quad (8.125b)$$

where the parameters  $\alpha = 5 \times 10^{21}$  and  $\beta = 1.5 \times 10^{19}$  are chosen. Under this setting, the beam experiences nonuniform distribution of strains across the cross section and along the length giving rise to electric polarisation.

Figure 8.13 compares the generated electric displacement of the couple stress model with that of the standard strain gradient model with and without consideration of the  $\bar{f}_{11}$  constant. As expected in this case the electric displacement component  $D_x$  is more pronounced compared to  $D_y$ , unlike the previous cases. The couple stress model generates up to an order of magnitude higher electric polarisation under this coupling mode and the profile of electric displacement is also very different from that of strain gradient model. The polarisation in the vertical  $y$  direction remains weak and  $\bar{f}_{11}$  parameter is discarded both couple stress and strain gradient models generate the same electric displacement component  $D_y$ . In general, although non-intuitive, it can be observed that in the case of extension the parameter  $\bar{f}_{11}$  plays no significant role.

From the analysis of three flexoelectric coupling cases in this section it can be concluded that, for both couple stress and strain gradient theories the bending/shear coupling mode is typically activated by the action of transverse electric field and the extension coupling mode is activated by the action of electric field aligned in parallel to the axis of extension. Under both these coupling modes the driving parameter is the flexoelectric constant  $\bar{f}_{12}$ . This in contrast to piezoelectricity where different modes of coupling are typically driven by different material constants. If the same flexoelectric constant is chosen to simulate strain gradient and couple stress theory, the couple stress model will in general produce a higher electric polarisation that in some cases could be up to two orders of magnitude higher. It must be believed that for most problems of practical relevance analysed under such settings the couple stress flexoelectric model in general will produce a higher electric polarisation. It is also worth noting that, simplified analytical solutions of strain gradient flexoelectricity overestimate the flexoelectric response in comparison to fully three-dimensional computational simulation as noted by [4, 3]. In the later sections we will see if this is the case for couple stress based flexoelectric models.

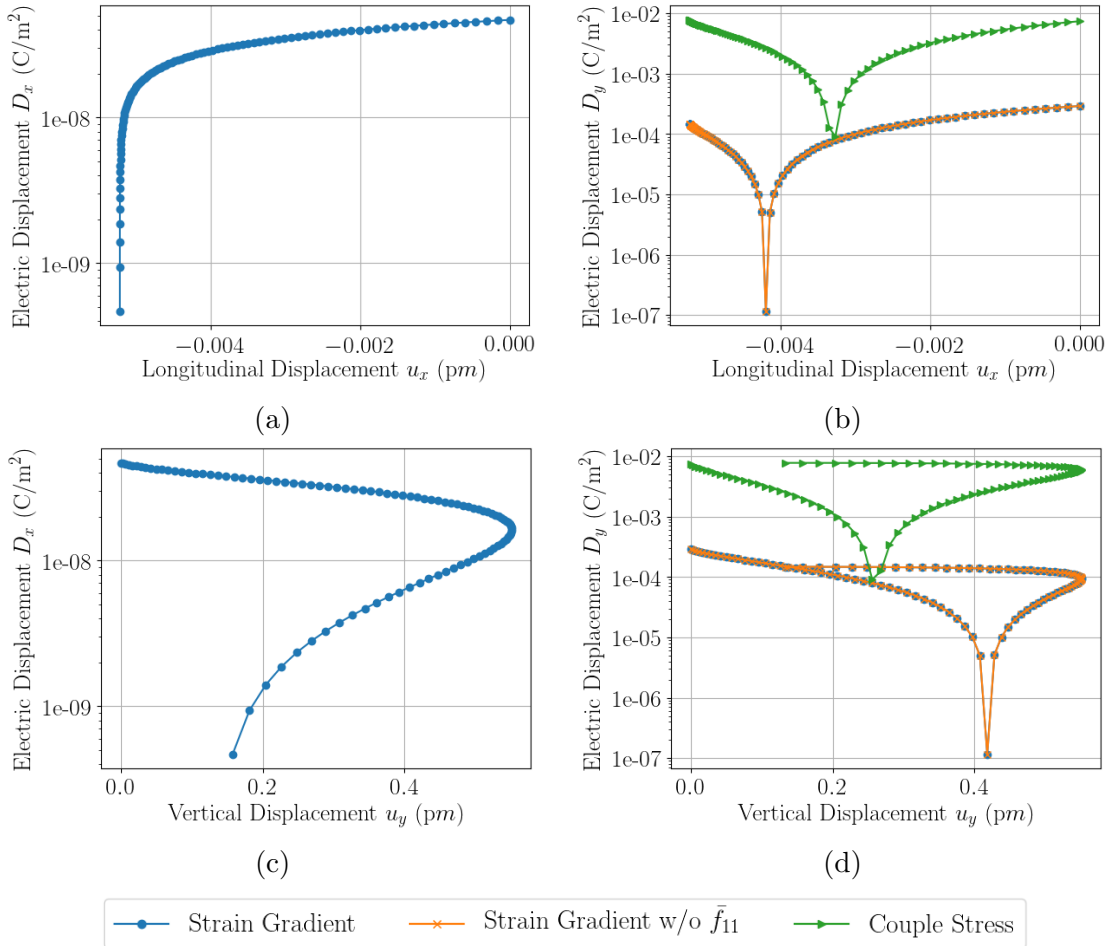


Figure 8.11: Comparison of couple stress based and strain gradient based flexoelectric models for the case of (8.124), when material constants are fitted according to (8.122)

### 8.7.2 Benchmark example: Convergence studies and further quantification of curvature-induced electromechanical coupling efficiency

In this section, the electromechanical coupling efficiency of the couple stress flexoelectric formulation is investigated using all the developed finite element techniques. The study albeit simple in nature, tests both the convergence properties of the finite element schemes and the quantification of flexoelectric based electric polarisation using the skew-symmetric couple stress theory. The problem involves mechanically loading a cantilever beam and monitoring the generated electric polarisation using the electromechanical coupling efficiency as a measure, as shown in Figure 8.14. This problem is analysed under strain gradient elasticity by [222] and an analytical solution for the Electromechanical Coupling Efficiency (ECF) is given in [195] as

$$k_a^{eff} = \frac{\varpi}{1 + \varpi} \sqrt{\frac{\epsilon}{E} \left( e^2 + 12 \left( \frac{f}{h} \right)^2 \right)}, \quad (8.126)$$



Figure 8.12: Original and deformed shape of nanobeam

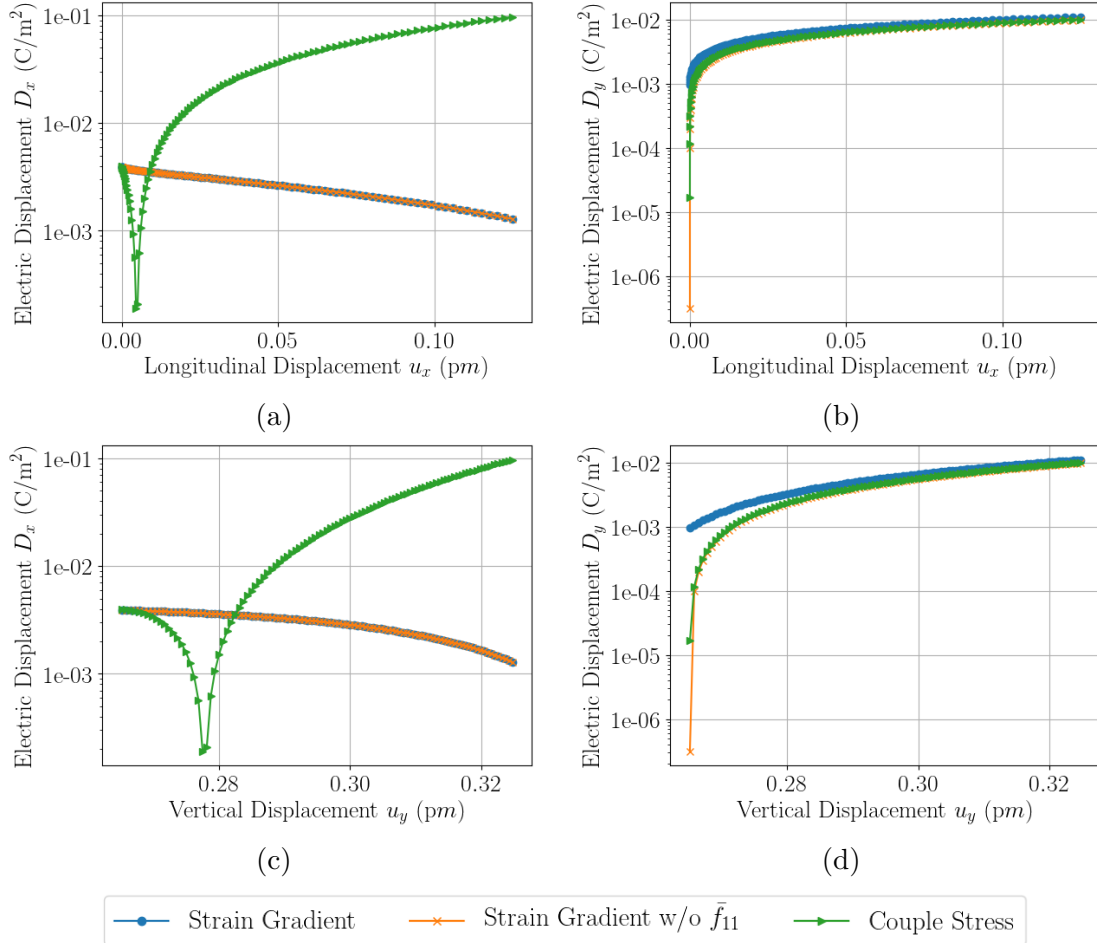


Figure 8.13: Comparison of couple stress based and strain gradient based flexoelectric models for the case of (8.125), when material constants are fitted according to (8.122)

where  $\varpi$  is the electrical susceptibility of the material (where  $\varpi = 1408$  for the case of BaTiO<sub>3</sub>),  $E$  the Young's modulus and  $\epsilon$ ,  $e$  and  $f$  the dielectric, piezoelectric and flexoelectric coupling coefficients of the material, respectively.  $L$  and  $h$  represent the length and the height of the beam, respectively; see also Figure 8.14. In the context of finite elements, the electromechanical conversion efficiency can be computed as the norm of the ratio of electrical energy to mechanical energy i.e.

$$\frac{1}{k_n^{eff}^2} = \left\| \frac{W_{mech}}{W_{elect}} \right\|$$

However, given that the analytical solution for this problem was derived from the strain gradient model, for convergence studies, we choose to work with a reference solution obtained from an extremely fine discretisation. For the purpose of convergence studies, once again BaTiO<sub>3</sub> is chosen with material properties listed in Table 8.1 by neglecting the piezoelectric effects i.e. setting  $e_{31} = e_{33} = e_{15} = e = 0$ . Only  $\bar{f}_{12}$  effect is considered i.e.  $f = \bar{f}_{12}$ . The length of the beam is kept at  $0.8\mu m$  and the aspect ratio of the beam is varied from 10 to 50, while a constant load of  $F = 100\mu N$  is applied on the free end of the beam.

First a series of convergence studies are performed by using the quadratic mixed finite elements i.e. P2-P2-P1<sup>D</sup>-P1<sup>D</sup>/P2-P2-P1<sup>D</sup> and Q2-Q2-Q1<sup>D</sup>-Q1<sup>D</sup>/Q2-Q2-Q1<sup>D</sup> elements in a two-dimensional setting by successively refining the meshes, i.e. by performing the so-called  $h$ -refinement. To this end, two set of meshes are chosen namely a triangular mesh and a quadrilateral mesh, as shown in Figure 8.15 and the ECF is computed using the mixed finite elements and compared to the reference solution. The convergence properties of the mixed finite elements for the three variational formulations namely the penalty formulation, the Lagrange

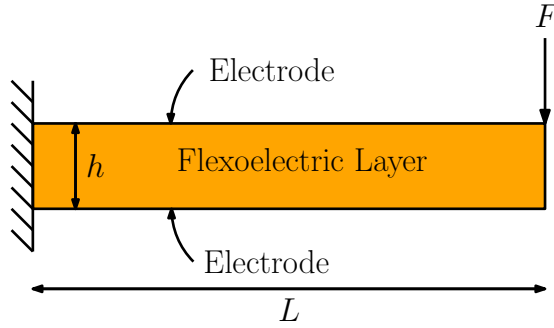


Figure 8.14: Cantilever beam chosen for convergence study of the developed finite element discretisation techniques

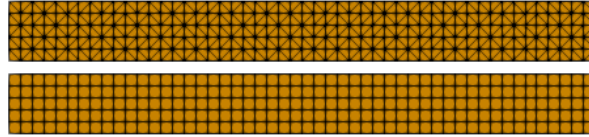


Figure 8.15: Triangular and quadrilateral meshes (only aspect ratio 10 shown here) chosen for convergence study of the developed finite element discretisation techniques. Both meshes possess the same number of nodes

multiplier formulation and the augmented Lagrangian formulation is subsequently studied, by choosing the penalty parameter to coincide with the Cosserat modulus  $\kappa = \mu l_s^2 = 5 \times 10^{-7}$  GPa, where  $l_s = 1\text{nm}$  is the length scale parameter. The chosen value of  $l_s$  is well within the range of the thickness chosen for epitaxial ferroelectric thin films.

Figure 8.16 shows the  $h$ -convergence results of the different finite element discretisation techniques for penalty, Lagrange multiplier and augmented Lagrangian formulations for triangular and quadrilateral meshes, when the quadratic interpolation is used for displacements i.e. P2-P2-P1<sup>D</sup>-P1<sup>D</sup>/P2-P2-P1<sup>D</sup> and Q2-Q2-Q1<sup>D</sup>-Q1<sup>D</sup>/Q2-Q2-Q1<sup>D</sup> discretisations. It can be observed that the expected rate of convergence for electromechanical energy is achieved for all formulations with both triangular and quadrilateral elements [296]. Expectedly, the Lagrange multiplier approach performs the best, while the error incurred using the penalty approach is the highest. The augmented Lagrangian approach converges at the same rate, but the error incurred lies in between the penalty and the Lagrange multiplier approach. As the aspect ratio of the beam increases the incurred error typically increases. The performance of triangular and quadrilateral elements in general similar due the fact that both meshes have the same number of nodes and the triangular mesh is generated by a symmetric tessellation of the quadrilateral mesh. It should be noted that, since the couple stress theory imposes a constraint on the rotation part of the displacement gradients, bending locking becomes an apparent issue. The use of high order mixed finite elements in general resolves such bending problems [253].

Having confirmed the convergence of the quadratic mixed finite element for the two-dimensional case for triangular and quadrilateral meshes, the same problem is then analysed by fixing the refinement level ( $h$ ) and successively increasing the order of finite element interpolation functions i.e. by performing the so-called  $p$ -refinement. In this context, we refer to  $p$  or  $q$  as the highest polynomial degree used for any variable (i.e. displacements and electric potential). This allows us to study the performance of higher order mixed finite elements shown in Figure 8.4. To this end, two three-dimensional meshes are considered namely a tetrahedral mesh and hexahedral mesh, as shown in Figure 8.17.

Figure 8.18 shows the  $p$ -convergence results of the different finite element discretisation techniques for penalty, Lagrange multiplier and augmented Lagrangian formulations for triangular and quadrilateral meshes for aspect ratio 10. Once again, the expected rate of convergence for electromechanical energy is achieved for all formulations with both tetrahedral and hexa-

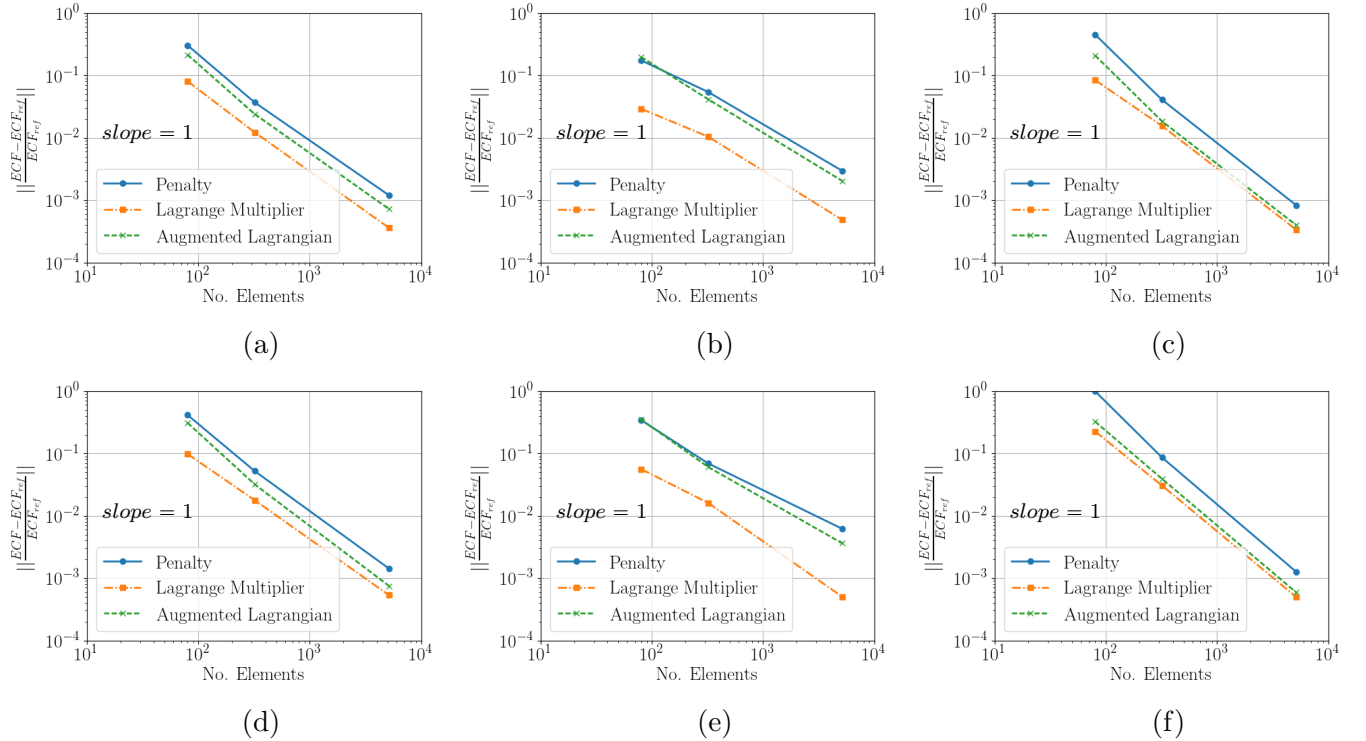


Figure 8.16: Convergence of error in Electromechanical Coupling Efficiency (ECF) for different finite element discretisation techniques on triangular elements, a) aspect ratio 10, b) aspect ratio 25, c) aspect ratio 50, and quadrilateral elements, d) aspect ratio 10, e) aspect ratio 25, f) aspect ratio 50

hedral elements [296]. The Lagrange multiplier approach performs the best, followed by the augmented Lagrangian approach and the penalty, respectively. The performance of tetrahedral and hexahedral elements in general similar due the fact that both meshes have the same number of nodes and the tetrahedral mesh is generated by further tessellation of the hexahedral mesh. Note that this study confirms the rate of convergence for different choices of polynomial functional spaces for mixed finite elements up to  $p = q = 6$ , confirming their suitability for discretising the three aforementioned couple stress variational formulation.

### 8.7.3 Nanocompression of a flexoelectric conical pyramid

In this section, the nanocompression of a complex flexoelectric conical pyramid is chosen for finite element analysis. The objective is to examine the capability of the developed finite element framework in accurately predicting the flexoelectric response when the geometrical representation of the problem is complex and when an analytical solution cannot be obtained.

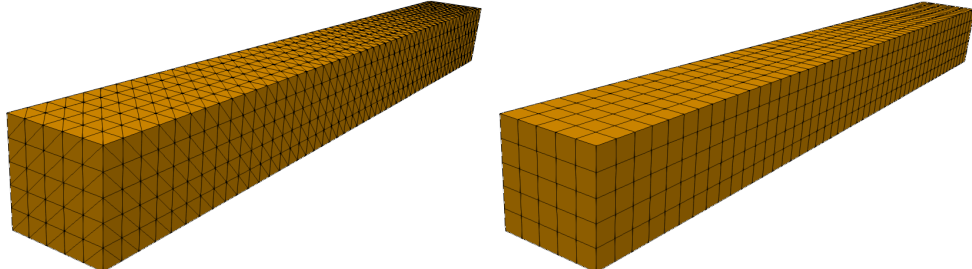


Figure 8.17: Tetrahedral and hexahedral meshes (only aspect ratio 10 shown here) chosen for convergence study of the developed finite element discretisation techniques. Both meshes possess the same number of nodes

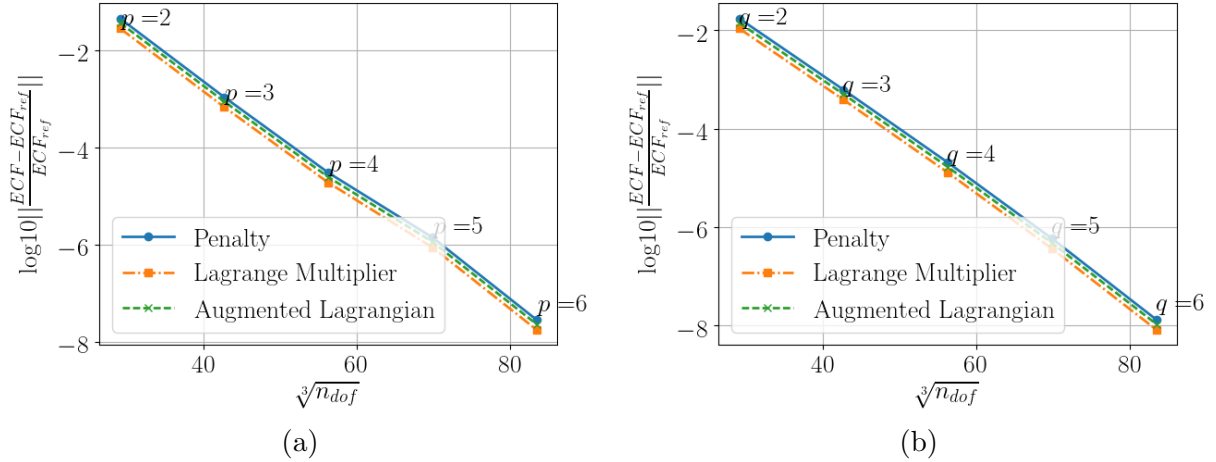


Figure 8.18: Convergence of error in Electromechanical Coupling Efficiency (ECF) for different finite element discretisation techniques on tetrahedral and hexahedral elements for aspect ratio 10

The analysis of flexoelectric pyramidal structures have been carried by many other authors in the past as the differential thickness along the height of the pyramid produces a significant flexoelectric response [4, 3, 108, 70]. Furthermore, flexoelectric material constants are also typically experimentally characterised through either nanoindentation or bending experiments, using similar geometries. [4] has analysed the problem of nanocompression of the flexoelectric pyramid in depth showing that simplified solutions can in general overestimate the flexoelectric response and relying on computational methodologies can help provide better insight in the design of such flexoelectric transducers.

To this end, a rather more complex flexoelectric conical pyramid is chosen for our study. The additional complexity of the problem emanates from the fact that the edges and facets of the pyramid are not straight sided but are rather described through NURBS functions. The geometry and the three-dimensional curved  $p = 4$  tetrahedral mesh of the flexoelectric structure is shown in Figure 8.19. To represent the geometry of the problem accurately, we employ the high order curvilinear finite elements recently developed by [253] which uses a posteriori mesh morphing technique presented in [254] to represent the CAD boundaries of the flexoelectric structure accurately (notice the curved elements representing the circle in the top conical frustum) without requiring a change in the mixed finite element functional spaces presented in section 8.6. The mixed interpolation nature of the flexoelectric variables and the use of high performance data parallel tensor contraction framework for coupled electromechanical problems developed by the authors [251], make the developed finite element techniques a viable candidate for solving extremely large scale problems on complicated geometries.

Once again, we choose the Barium Titanate as the flexoelectric material of choice by neglecting the piezoelectric effect and only considering  $\bar{f}_{12}$  flexoelectric constant. A compressive load of 3MPa is applied as pressure on the circle in top conical frustum and the base of the plate-like support is mechanically fixed. The system has an open circuit configuration in that, only zero electric potential is applied at the base of the plate-like support. The problem consists of approximately 3.4M degrees of freedom excluding the condensed variables and approximately another 2.8M degrees of freedom are condensed out during each run of the analysis. The Lagrange multiplier formulation is used for this analysis and the simulation is performed dynamically using the Newmark's beta method with the density of the Barium Titanate given as  $\rho = 6.02 \text{ g/cm}^3$ . The total load is applied over a period of 30 seconds at a rate of 0.1mPa/sec.

Figure 8.21 summarises various representative results of the analysis. First, a mesh refinement study has been performed to ensure that the results of the analysis are accurate. As can be observed the electromechanical coupling efficiency asymptotically approaches towards a reference solution with mesh refinement, confirming the stable approximation property of the

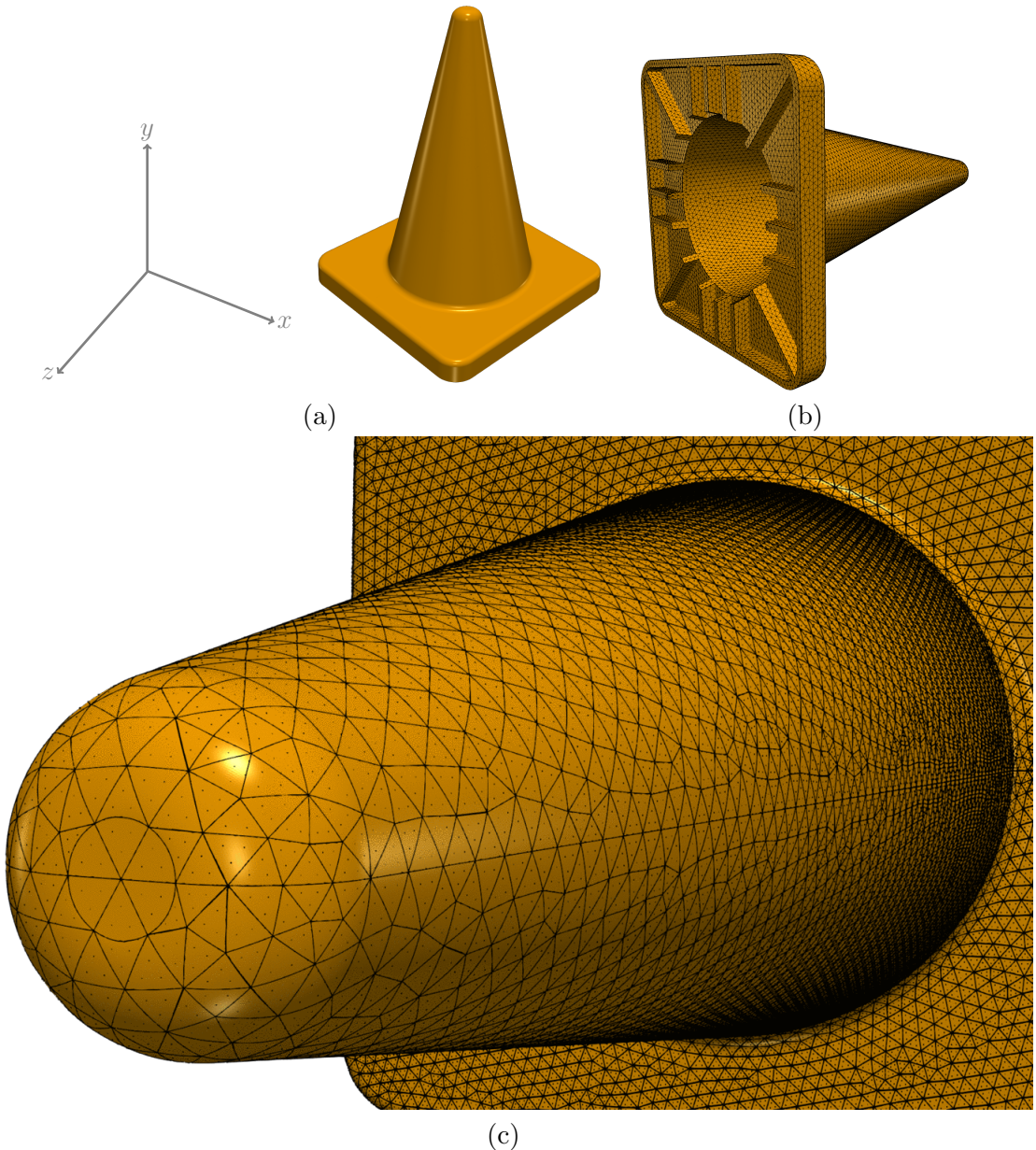


Figure 8.19: Geometry and quartic ( $p = 4$ ) order curved mesh of the flexoelectric conical pyramid. The conical pyramid is being held by a plate-like support of size  $100 \times 100\mu\text{m}^2$  and the total height of the pyramid is  $130\mu\text{m}$ . The thickness of pyramid is  $150\text{nm}$  throughout the structure. The circle in top conical frustum represents the region where the compressive load is applied

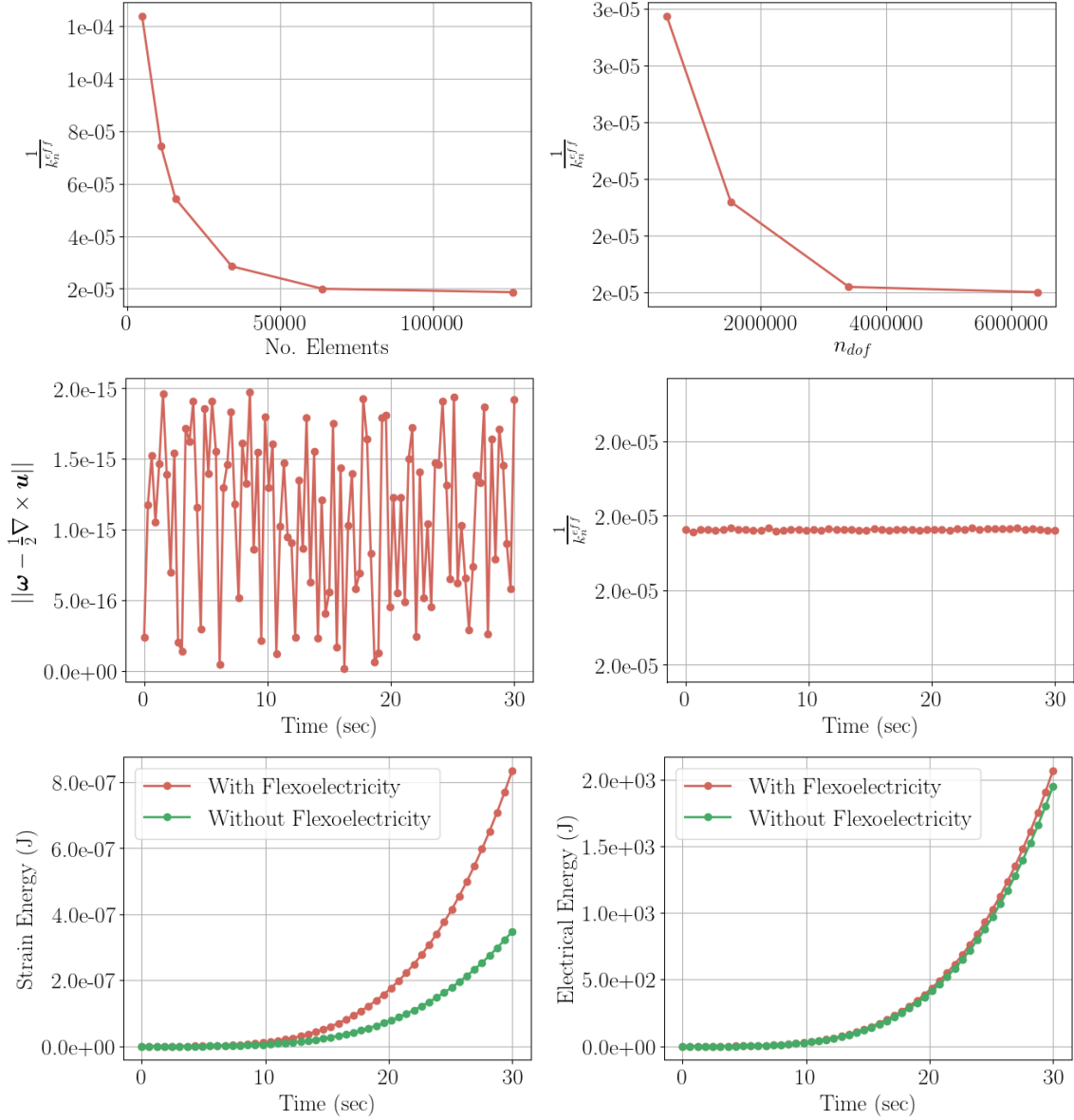


Figure 8.20: Various representative results of the analysis on conical pyramid, a) convergence of the solution with mesh refinement, b) satisfaction of couple stress constraint, c) evolution of strain energy with and without consideration of flexoelectricity characterising evolution of normalised effective stiffness, d) evolution of electrical energy and, e) evolution of effective electromechanical coupling coefficient, f) evolution of normalized effective stiffness

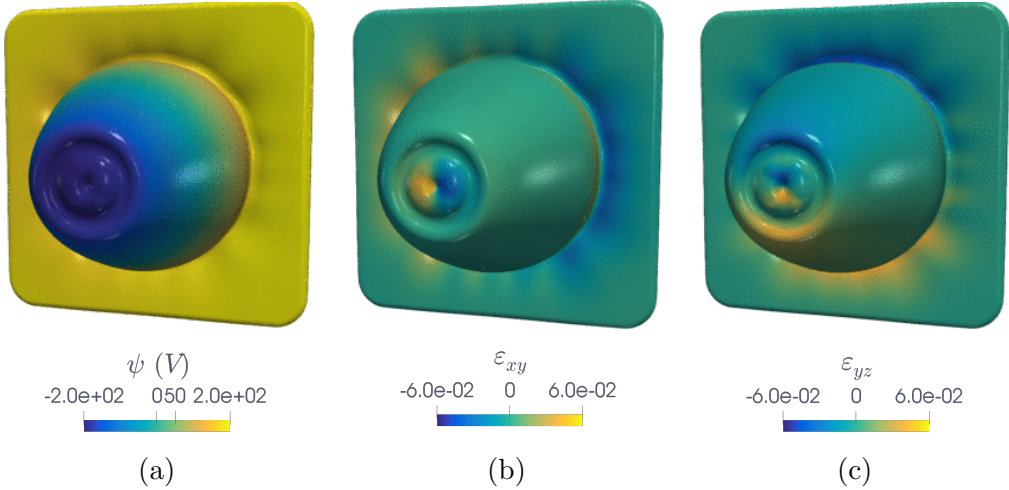


Figure 8.21: The final deformed conical pyramid configuration showing, a) electric potential  $\psi$ , b) strain component  $\varepsilon_{xy}$  and b) strain component  $\varepsilon_{yz}$ . 355M cells have been used to process a detailed resolution of the results. Deformations (not magnitudes) are magnified by a factor of 10 for aesthetics and clarity

developed finite element scheme. All the analyses are performed using the second finest mesh corresponding to Figure 8.21a, where the number of elements in the computational mesh is kept fixed at 63794. Keeping the mesh size fixed a  $p$  refinement is then carried out from  $p = 2$  to  $p = 5$  respectively as shown in Figure 8.21b. It can be observed that under  $p$ -refinement the convergence is much quicker and at  $p = 3$  the reference solution is already obtained. As mentioned before, further analysis of the flexoelectric pyramid are however performed with keeping the polynomial refinement fixed at  $p = 4$ . Figure 8.21c shows the satisfaction of the couple stress constraint throughout the dynamic simulation time. As can be observed the constraint is numerically satisfied for the whole duration of the simulation. Finally, Figure 8.21d shows the effective electromechanical coupling efficiency (ECF) throughout the simulation time. Due to the linear nature of the problem, a constant ECF is obtained for the whole duration of simulation.

A common way to characterise size-dependent effect in flexoelectric theory is to measure the normalised effective piezoelectric constant. For complex problems such as the current one the approximate analytical solution for this constant reported in [195] cannot be used and the more generic formula given below should be used

$$\bar{e} = \frac{\int_{\Omega} \mathbf{E}_c \cdot \boldsymbol{\epsilon} \mathbf{E}_c}{\int_{\Omega} \mathbf{E}_e \cdot \boldsymbol{\epsilon} \mathbf{E}_e}, \quad (8.127)$$

where  $\mathbf{E}_c$  represents the electric field when both piezoelectricity and flexoelectricity are present and  $\mathbf{E}_e$  represents the electric field when flexoelectricity is ignored. It is also established phenomenon that flexoelectricity modifies the inherent mechanical properties specially the bending modulus of the material [279, 163]. The normalised effective stiffness of the system can be computed similarly as

$$\bar{Y} = \frac{\int_{\Omega} \boldsymbol{\epsilon}_c : \mathbb{C} : \boldsymbol{\epsilon}_c}{\int_{\Omega} \boldsymbol{\epsilon}_m : \mathbb{C} : \boldsymbol{\epsilon}_m}, \quad (8.128)$$

where  $\boldsymbol{\epsilon}_c$  represents the small strain tensor when flexoelectricity is present and  $\boldsymbol{\epsilon}_m$  represents the small strain tensor when flexoelectricity is ignored. Figure 8.21e shows the evolution of strain energy of the system with and without consideration of flexoelectricity characterising normalised effective stiffness of the system. We notice a rather constant normalised effective stiffness in the range of  $2.2 \pm 0.2$  for the conical pyramid throughout the dynamic simulation due to the linear nature of the problem. Interestingly, the standard strain gradient models

also produce a similar normalised effective stiffness [4]. Similarly, Figure 8.21f shows the evolution of electrical energy with and without consideration of flexoelectricity characterising the normalised effective piezoelectric constant of the system. Note that all the piezoelectric material constants listed in Table 8.1 are now activated and deformation of the system is much more complex now as all coupling modes are active. A modest 4-6% increase in electrical energy is observed when flexoelectricity is activated. This is in contrast with respect to the results presented in [4, 3, 222, 108] wherein the flexoelectric constant is assumed to be more than an order of magnitude higher than its actual value used here.

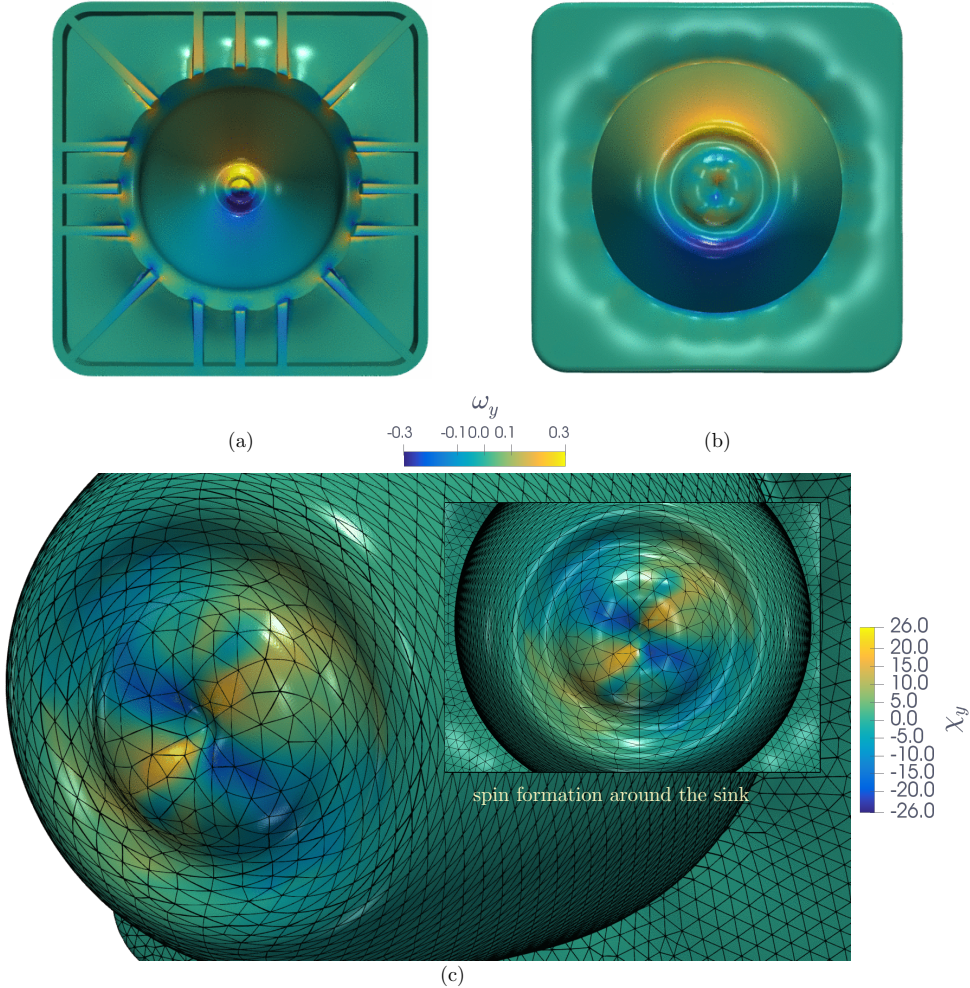


Figure 8.22: The final deformed conical pyramid configuration showing, a,b) axial vorticity vector component  $\omega_y$  and, c) axial curvature vector component  $\chi_y$ . The curvature forms a spin around the deformed sink. 355M cells have been used to process a detailed resolution of the results. Deformations (not magnitudes) are magnified by a factor of 10 for aesthetics and clarity

Figure 8.21 shows the final deformed configuration of the conical pyramid for  $p = 4$  tetrahedral elements with an extremely detailed resolution wherein the results are extrapolated over 355M cells using high order finite element interpolation functions. It can be observed that both electric potential (primary variable) and strain components (derived variables) are well resolved at this level of detail. The deformation initially starts at the circular region in the top frustum of the pyramid. As the compressive pressure is increased the frustum is pushed inwards and the pyramid experiences necking right around the frustum. With further compression, a completely dished and grooved region starts to form around the frustum while the region immediately around the circle where the load is applied starts to bulge outwards. As shown in Figure 8.22 the base of the pyramid is severely pushed towards the plate support. Figure 8.22 further shows strain gradient measures, namely the vorticity vector and the curvature vector

component. Interestingly, it can be observed in Figure 8.22c that the curvature evolves as a spin around the generated sink and starts to disperse near the grooved region. This is because the certain of the sink ( $y$ -axis) corresponds to the axis of rotation.

From the analyses performed in this section it can be concluded that, advanced computational tools help resolve the problem of flexoelectricity to an unprecedented detail beyond the realm of approximate closed form solutions. Certainly, the inclusion of anisotropy, necking and vortex formation is too complex to be handled otherwise. The implementation underpinning of the current framework based on an extremely efficient and highly parallelised framework of [251] ensures efficiency and reliability of the developed finite element results. Given that the normalised effective piezoelectric constant shows only a 4-6% increase due to flexoelectricity for this problem, we can assume that the computational model given its accuracy has modest estimations in comparison to analytical solutions (if available), an issue also present in standard strain gradient models [4]. However, as mentioned before, the major discrepancy in results of normalised effective piezoelectric constants between the current study and those of [4, 3] is due to an order of magnitude higher flexoelectric constant chosen by the latter authors.

## 8.8 Conclusion

In this manuscript, a family of numerical models for the phenomenological linear flexoelectric theory for continua and their particularisation to the case of three-dimensional beams based on a skew-symmetric couple stress theory is presented. In contrast to the traditional flexoelectric models based on standard strain gradient wherein coupling between electric polarisation and strain gradients is assumed, we postulate an electric enthalpy in terms of linear invariants of curvature and electric field. This is achieved by introducing the axial curvature vector as a strain gradient measure. We have shown that the implication of this assumption is many-fold. Firstly, for isotropic (non-piezoelectric) materials it allows constructing flexoelectric energies without breaking material symmetry. Secondly, nonuniform distribution of volumetric part of strains (volumetric strain gradients) do not generate electric polarisation, as confirmed by experimental evidence to be the case for some important classes of flexoelectric materials. In this regard, the current flexoelectric model can be considered as a more restrictive case of strain gradient theories. Thirdly, a state of plane strain generates out of plane deformation through strain gradient effects. Finally, extension and shear coupling modes cannot be characterised individually as they contribute to the generation of electric polarisation as a whole.

For the case of three-dimensional beams, we have shown that the skew-symmetric couple stress model in general, generate stresses spanned over the cross section rather than aligned with the longitudinal axis of the beam and as a result special care must be taken to integrate them over the cross section.

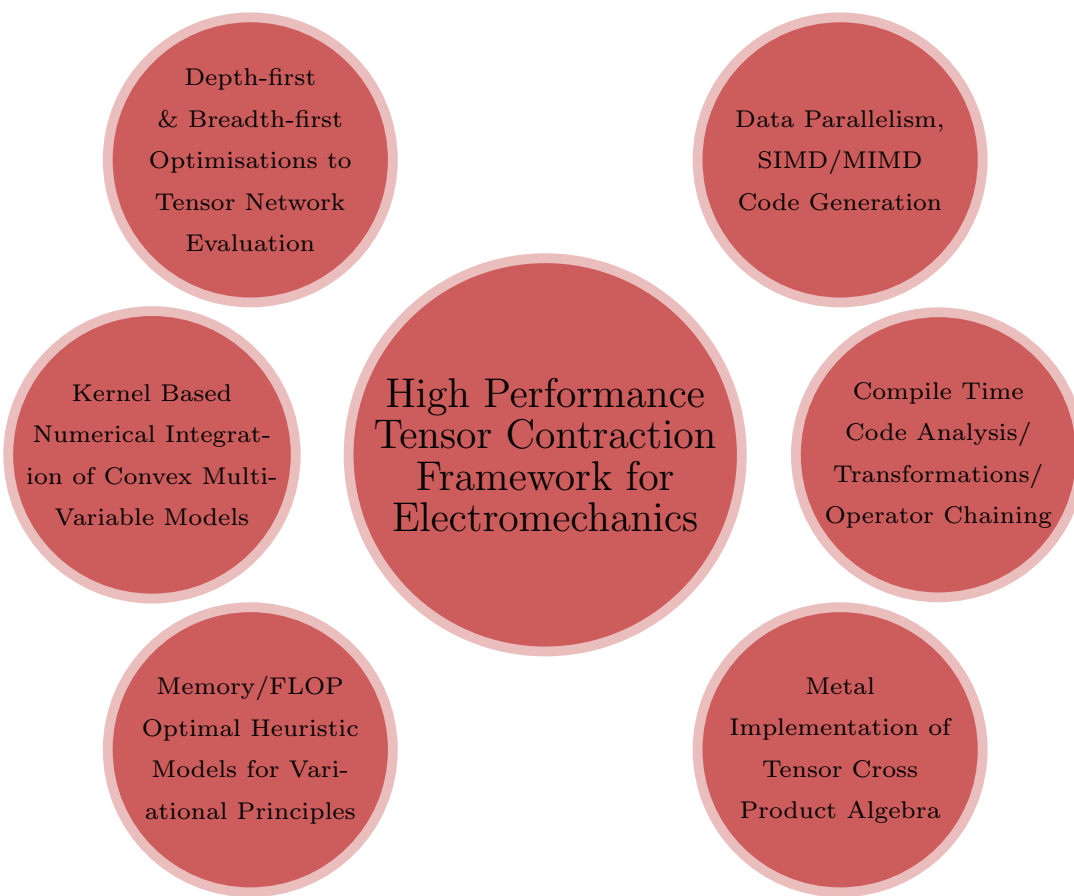
Four distinct variational principles are presented for both continuum and beam models namely, a displacement-potential formulation, a penalty formulation, a Lagrange-multiplier formulation and an augmented Lagrangian formulation. The three latter formulations facilitate incorporation of strain gradient measures in to a standard finite element scheme while maintaining the  $C^0$  continuity. To this end, the efficacy of high order finite elements along with the computational efficiency of mixed finite elements have been utilised to develop a series of low and high order mixed finite element schemes for couple stress based flexoelectricity. Numerical results of finite element discretisations for the three latter variational formulations are first benchmarked against available closed form solutions in regards where good agreements was found between the reference and numerical results. Furthermore, a detailed comparison of the developed couple stress based flexoelectric model with the standard strain gradient flexoelectric models has been performed for the case of Barium Titanate where a myriad of simple analytical solutions have been proposed in order to quantitatively describe the similarities and dissimilarities in effective electromechanical coupling under these two theories. It is observed that, if the same experimental flexoelectric constants are fitted in to both theories, the current couple stress theory in general, reports stronger electromechanical conversion efficiency. This is mainly

due to the fact that, most flexoelectric problems involve bending and flexural deformation and, as a result, the axial curvature vector responsible for generating electric polarisation is much more pronounced in these cases. Finally, nanocompression of a complex flexoelectric conical pyramid for which analytical solution cannot be established has been numerically studied at an unprecedented level of detail to pinpoint the robustness and computational scalability of the framework. Under this experiment, the structure experiences necking and the curvature effect forms a vortex around the generated sink in the frustum. The geometry and the nature of the deformation certainly implies that studying flexoelectricity in these structures is not feasible without resorting to computational tools. In our setting, the problem is resolved using high order curvilinear finite elements by relying on a highly parallelised framework previously developed by the authors. We observe a modest normalised effective piezoelectric coefficient for this study while the normalised effective stiffness of the system reported by the couple stress model is similar to the ones reported by standard strain gradient models.



# Part 3:

## A High Performance Tensor Contraction Framework for Electromechanics



# Chapter 9

## Numerical Implementation of Coupled Electromechanics through a Data Parallel Tensor Contraction Framework

### 9.1 Introduction

This chapter presents aspects of implementation of a new high performance tensor contraction framework for the numerical analysis of polyconvex elasticity and convex multi-variable electro-elasticity problems on streaming architectures. In addition to explicit SIMD instructions and smart expression templates, the framework introduces domain specific constructs for the tensor cross product and its associated algebra. The two key ingredients of the presented expression template engine are as follows. First, the capability to mathematically transform complex chains of operations to simpler equivalent expressions, while potentially avoiding routes with higher levels of computational complexity and, second, to perform a compile time depth-first or breadth-first search to find the optimal contraction indices of a large tensor network in order to minimise the number of floating point operations. For optimisations of tensor contraction such as loop transformation, loop fusion and data locality optimisations, the framework relies heavily on compile time technologies rather than source-to-source translation or JIT techniques. Every aspect of the framework is examined through relevant performance benchmarks, including the impact of data parallelism on the performance of isomorphic and nonisomorphic tensor products, the FLOP and memory I/O optimality in the evaluation of tensor networks, the compilation cost and memory footprint of the framework and the performance of tensor cross product kernels. The framework is then applied to finite element analysis of coupled electromechanical problems to assess the speed-ups achieved in kernel-based numerical integration of complex electroelastic energy functionals. In this context, domain-aware expression templates combined with SIMD instructions are shown to provide a significant speed-up over the classical low-level style programming techniques.

It should be noted that much of the work in this chapter is based on the authors work on tensor contraction presented in [251]. The chapter is organised as follows. In section 9.2, the interface design of the framework is discussed, by starting from the explicit SIMD vector types, the tensor class, the smart expression template engine and finally a convenient interface for tensor contraction operations using indicial notation. This is followed by a discussion on data alignment and compile time loop transformation optimisations in subsection 9.2.6. In section 9.3, a series of numerical examples are provided. These include fundamental performance benchmarks for data parallel isomorphic and nonisomorphic tensor products of tensor pairs in single and double precisions, the memory vs FLOP tradeoff in evaluation of large tensor networks, and their eventual compilation costs. Finally, finite element examples pertaining to the numerical integration of complex constitutive models are presented in section 9.4 illustrating

the importance of data parallelism and domain aware expression templates.

## 9.2 Interface design principle for tensorial operations

In the next subsections, the multiple stages of designing a tensor contraction framework using modern C++ features are presented, with the point of departure being the explicit SIMD vector types. It is assumed that the reader is familiar with the fundamental concepts of generic and generative programming in the context of scientific computing [49, 10, 58, 134, 133, 116]. For computational terminologies used in the chapter, the reader can refer to D.1 and for the actual implementation details, to Fastor’s official repository, <https://github.com/romeric/Fastor>.

### 9.2.1 Data parallelism through SIMD vector types

To facilitate vector based instruction scheduling for tensorial operations, the first step is to implement explicit SIMD vector types. In the current setting, using C++ polymorphism, a set of SIMD vector types are implemented which encompass vector-enabled X86 CPU architectures from SSE to SSE4.2 and AVX to AVX2. While this is an in-built extension to the current framework, further CPU architectures such as AVX-512, MIC, Neon, AltiVec and potentially GPU support can be included by relying on the Vc library [162]. The API for the in-built extensions are kept close to that of Vc, so that in the eventual case of changing backends, a simple change of namespace should suffice. Nevertheless, in the current iteration, the framework is capable of performing vector operations on SSE2-SSE4.2/AVX-AVX2 architectures. For a full implementation of SIMD vector types and further ABI considerations, the reader can refer to [162, 94, 161].

### 9.2.2 The abstract tensor class

The point of departure for the implementation of a tensor framework is a base or an abstract tensor type. Utilising the Curiously Recurring Template Pattern (CRTP) idiom [313, 116], a straightforward implementation of the `AbstractTensor` is shown in Listing 9.1.

Listing 9.1: A canonical implementation of abstract tensor type

```
template<class Derived, FASTOR_INDEX Rank>
class AbstractTensor {
public:
    static constexpr FASTOR_INDEX Dimension = Rank;
    AbstractTensor() = default;
    FASTOR_INLINE const Derived& self() const {
        return *static_cast<const Derived*>(this);
    }
};
```

In this context, the `AbstractTensor` facilitates static binding of all derived classes to the base class, avoiding the late binding mechanism [314, 58, 209, 10], which is a key step for a successful implementation of the expression templates (notice the presence of member function `self`) [133, 134]. Additionally, note that the seemingly unnecessary template parameter, the rank of the tensor is also passed for instantiation of the `AbstractTensor`.

### 9.2.3 The tensor class

The implementation of the tensor class then follows a rather classical approach. A canonical implementation of the tensor class, removing the bounds checking and further trivial details is shown in Listing 9.2, where the key ingredients of the class can be summarised as follows. First, a set of data members are defined, namely the order or spatial dimension of the tensor (`Dimension`), the total size of the tensor to be allocated in the memory (`Size`) and the stride necessary for vector instructions (`Stride`).<sup>1</sup>

---

<sup>1</sup>Note that in Listing 9.2, it is assumed that data is appropriately aligned by the vector (register) size, the size of the tensor is a multiple of the vector stride and that no padding is necessary.

Listing 9.2: A canonical implementation of the tensor class

```

template<typename T, FASTOR_INDEX ... Rest>
class Tensor: public AbstractTensor<Tensor<T,Rest...>, sizeof...(Rest)> {
private:
    typedef T scalar_type;
    T FASTOR_ALIGN _data[product<Rest...>::value];
public:
    static constexpr FASTOR_INDEX Dimension = sizeof...(Rest);
    static constexpr FASTOR_INDEX Size = product<Rest...>::value;
    static constexpr FASTOR_INDEX Stride = stride_finder<T>::value;

    template<typename Derived, FASTOR_INDEX Rank>
    FASTOR_INLINE Tensor<T,Rest...>& operator=(const AbstractTensor<Derived,Rank>& expr)
    {
        const Derived &src = expr.self();
        for (FASTOR_INDEX i = 0; i < Size; i+=Stride) {
            src.template evaluate<T>(i).store(&_data[i]);
        }
        return *this;
    }

    FASTOR_INLINE SIMDVector<T> evaluate(FASTOR_INDEX i) const {
        SIMDVector<T> out;
        out.load(&_data[i]);
        return out;
    }

    template<FASTOR_INDEX I, FASTOR_INDEX J, FASTOR_INDEX K>
    FASTOR_INLINE Tensor(const UnaryTraceOp<BinaryMatMulOp<Tensor<T,I,J>,
        UnaryTransposeOp<Tensor<T,K,J>>>&a) {
        _doublecontract<T,I,K>(a.expr.lhs.data(), a.expr.rhs.expr.data());
    }
}

```

In this context, the first member function (the copy assignment operator) is responsible for static binding of any complex expression that performs element-wise operations on the tensors, to the tensor class. Note that in contrast to the classical expression templates, in the current implementation shown in Listing 9.2, the expression is evaluated for one SIMD vector, instead of one scalar at a time, as can be seen in the implementation of the member function `evaluate`. It is also necessary for all the expressions (such as `UnaryOps` and `BinaryOps`) to provide an `evaluate` member function. Listing 9.2 represents a simple example of blending expression templates and SIMD instructions (also refer to [134], for a similar implementation) for a truly multi-dimensional tensor algebra framework.

#### 9.2.4 Smart expression templates: Operation minimisation through mathematical transformation

Once the tensor class is defined, what remains is the implementation of a high level interface for tensor algebraic operations. However, efficient execution of these operations does not only depend on how each individual operation/subroutine is implemented, but also on the pattern these operations are evaluated (in situations when they operate jointly on tensors). The fundamental idea of expression templates is to treat complex chain of operations as a single expression and the decision to when (how soon or late) this expression should be evaluated is called the *evaluation policy*, which typically depends on the nature and complexity of the operators involved in the expression [116]. For instance, in Listing 9.2 the evaluation of an expression is bound to the assignment operator (`operator=`). The evaluation policy can be also overwritten at any given time by invoking the `evaluate` function explicitly.

As a common practice in implementing expression templates, all element-wise and level 1 BLAS expressions inherit from the `AbstractTensor` to facilitate delayed evaluation of chained operations, as can be seen in the copy assignment operator in Listing 9.2.

Fastor implements operator chaining for beyond level 1 BLAS routines through template specialisation(s) of the copy and move constructors. The idea behind chaining certain operators of level 2/3 BLAS type routines is essentially to be able to mathematically transform them

to simpler expressions before evaluating them. This leads to the interesting notion of smart expression templates that facilitate exploitation of complexity reducing algorithms through mathematical equivalence and that can be viewed as more of domain specific semantics, built on top of a generic tensor algebra library.

For instance, the last member function (copy constructor) in Listing 9.2, provides an example of smart expression template in Fastor, where the tensor expression  $\text{tr}(\mathbf{AB}^T)$  is dispatched to  $\mathbf{A} : \mathbf{B} = A_{ij}B_{ij}$ . This indeed reduces the computational complexity of the problem from  $O(n^3)$  for matrix matrix multiplication,  $O(n^2)$  for transpose and  $O(n)$  for trace, to  $O(n^2)$  for double contraction. Furthermore, vector implementation of double contraction is trivial. In the context of tensor algebra, such operations frequently occur and Fastor implements copy and move constructors for a series of such type of operations. Once again, note that expressions such as `BinaryMatMulOp`, `UnaryTransposeOp` and `UnaryTraceOp` are evaluated immediately if they act individually on a tensor. A canonical implementation of a smart expression (`UnaryTransposeOp`) is shown in Listing 9.3 (notice the second overload of the member function `evaluate`).

Listing 9.3: A canonical implementation of transpose operator

```
template<typename Expr>
struct UnaryTransposeOp {
    UnaryTransposeOp(const Expr& expr) : expr(expr) {}

    template<typename U>
    FASTOR_INLINE U evaluate(FASTOR_INDEX i, FASTOR_INDEX j) const {
        return expr(j,i);
    }

    const Expr &expr;
};

template<typename Expr>
FASTOR_INLINE UnaryTransposeOp<Expr> transpose(const Expr &expr) {
    return UnaryTransposeOp<Expr>(expr);
}
```

### 9.2.5 Smart expression templates: Operation minimisation through compile time depth-first constructive approach

While exploiting low-flop algorithms through mathematical transformation may be sufficient for named operators (such as `UnaryTraceOp`, `UnaryDetOp` etc), when the tensorial operations are expressed in indicial notation (i.e. when no named operators are present), a generalisation of the approach presented in subsection 9.2.4, is to perform a graph optimisation technique to find the optimal contraction indices of the tensor network. This leads to the more generic operation minimisation technique implemented in Fastor, the so-called depth-first constructive approach, defined in D.1.

For the purpose of illustrating specific features and a possible function signature for tensor contraction through indicial notation, a prototypical implementation of the (`einsum`) function, between three arbitrary order tensors is presented in Listing 9.4, without the use of expression templates.<sup>2</sup>

Listing 9.4: Overloaded implementation of Einstein summation for three tensor singlets of arbitrary order

```
template<typename Index_I, typename Index_J, typename Index_K,
         template<typename, FASTOR_INDEX... Rest0> class Tensor0,
         template<typename, FASTOR_INDEX... Rest1> class Tensor1,
         template<typename, FASTOR_INDEX... Rest2> class Tensor2,
         typename T, FASTOR_INDEX... Rest0, FASTOR_INDEX... Rest1, FASTOR_INDEX... Rest2,
```

<sup>2</sup>In the presence of expression templates, overloading the `einsum` function to account for more (or less) than three tensors is not necessary, as a single tensor expression can take care of all possible overloads. For instance, the `ContractionType` in Listing 9.4 could as well be an expression instead of the resulting tensor and then its evaluation could be bound to a copy assignment operator similar to the one presented in Listing 9.2.

```

        typename std::enable_if<sizeof...(Rest0)==Index_I::NoIndices &&
                               sizeof...(Rest1)==Index_J::NoIndices &&
                               sizeof...(Rest2)==Index_K::NoIndices, bool>::type=0 >
FASTOR_INLINE typename ContractionType<Index_I, Index_J, Index_K, Tensor<T, Rest0...>, Tensor
<T, Rest1...>, Tensor<T, Rest2...>>::type einsum(const Tensor0<T, Rest0...> &a, const
Tensor1<T, Rest1...> &b, const Tensor2<T, Rest2...> &c) {
// perform compile time depth-first search
// if necessary call the by-pair (two tensor) overload
// if not, set up the contraction loop nest (Cartesian product)
// perform loop transformation and SIMD vectorisation
// perform isomorphic/noisomorphic tensor product
}

```

Notice how the static nature of the tensors facilitates resolving the indices of the `einsum` function at compile time. With an optimising compiler this leads to no extra register allocation for the indices. This is in contrast with most of the existing tensor algebra frameworks that allocate tensors dynamically. In Listing 9.4, `Index` is simply a template structure (`struct`) of integral constants with one compile time (`constexpr`) data member, the `NoIndices` which accounts for the number of template parameters passed to it. Furthermore, note that the return type of `einsum` is computed at compile time through the `ContractionType` meta-function and the right amount of stack memory is allocated beforehand, which is also in contrast with the C/Fortran static arrays. A few representative examples of how the tensor objects are called and the above `einsum` function can be applied, are presented in Listing 9.5.

Listing 9.5: An example of `Tensor` instantiation and contraction of  $A_{ijk}B_{ijlm}C_{klmnpq}$

```

enum {I,J,K,L,M,N,P,Q};
Tensor<double,2,3,4> A; Tensor<double,2,3,5,6> B; Tensor<double,4,5,6,8,4,3> C;
// fill/populate A,B and C explicitly
A.random(); B.range(2); C.fill(42.42);
// perform tensor contraction
auto d = einsum<Index<I,J,K>, Index<I,J,L,M>, Index<K,L,M,N,P,Q>>(A,B,C);
// d is deduced as Tensor<double,8,4,3> and 96*sizeof(double)=768B is statically
allocated.

```

### 9.2.6 Data alignment and compile time construction of contraction loop nests

From a computational point of view, vector or data parallel implementation of tensor contraction requires careful attention to memory alignment. In a generic tensor contraction procedure, since arbitrary indices are allowed to contract, computations along strides leading to non-contiguous and unaligned memory access patterns and cache misses become the fundamental bottleneck. To solve this issue, some libraries designed for large dynamically allocated arrays, allow computations on general strides [312], while there are alternative frameworks that work with strict alignment and further data padding for the purpose of vectorisation [133]. Due to the strong focus of this framework on data parallelism and further due to stack allocation, the tensors are always aligned in the memory by the largest SIMD vector size that the processor is capable of i.e. 16B alignment for SSE and 32B alignment for AVX and so on, as shown in Listing 9.2 (i.e. `FASTOR_ALIGN`). However, strided data access is intrinsic to the nature of tensor contraction [287, 81], and as will be discussed shortly, Fastor employs cost-effective broadcasting vectorisation in such cases. With this decision on data alignment, Fastor classifies tensor operations into three categories, namely isomorphic tensor products (outer products), non-isomorphic tensor products (tensor contraction), and tensor permutation, as defined in D.1.

Once the decision on memory alignment is fixed, a variable number of nested `for` loops need to be set up depending on the contraction indices of the tensors appearing in the network. Since the `Tensor` objects presented in Listing 9.2 are static, Fastor uses this information to set up the contraction loop nest at compile time by generating the Cartesian product of iteration spaces of tensors. This can be typically achieved using recursive template instantiation. To illustrate this, consider the isomorphic tensor product of singleton  $[D]_{ijk} = [\mathbf{a}]_i[\mathbf{B}]_{jk}$ , where  $\mathbf{a}$  is a first order tensor of size 2 and  $\mathbf{B}$  is a second order tensor of  $2 \times 3$ . The loop transformation

procedure for this singleton is shown in Figure 9.1. Figure 9.1 is a simple example of loop

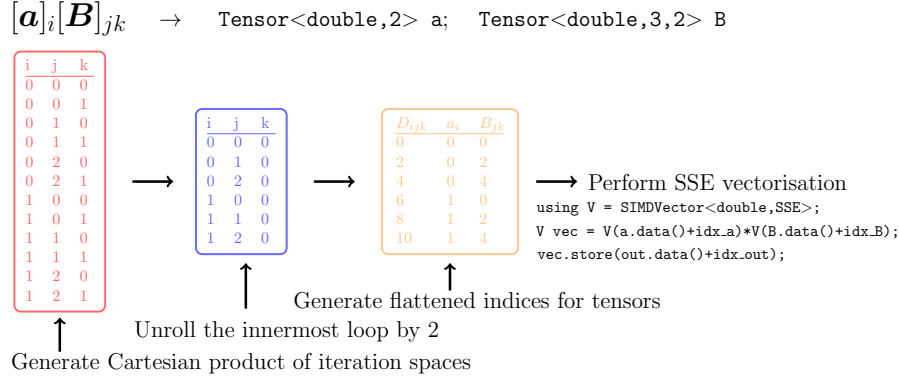


Figure 9.1: Loop transformation optimisation for the contraction loop nest of singleton  $[D]_{ijk} = [a]_i[B]_{jk}$

transformation through compile time code generation. Note that, this approach is a generalisation of an efficient matrix-matrix multiplication implementation using SIMD vector types proposed as a language extension to the C++ standard committee [161]. Once performed, this type of loop transformation can facilitate other compile time optimisation opportunities, such as distinguishing loop-invariant code, subsequent hoisting and more importantly studying the vectorisability nature of the nest. In the context of vectorisability, a Cartesian product (contraction loop nest) can be classified as fully vectorisable, partially vectorisable or broadcast-vectorisable (refer to D.1 for definitions). While partial vectorisability implies that the final remainder operations that do not fit in the vectorised loop nest during tensor contraction procedures should be treated in a scalar fashion, broadcast-vectorisable means employing multiple cost-effective broadcast vector instructions, for computing tensor contraction on strides. This definition of vectorisability allows for an implementation strategy that enables explicit vectorisation in floating point as well as in memory load and store operations. To elaborate this vectorisation procedure, a schematic representation of a broadcast-vectorisable tensor pair is shown in Figure 9.2 for the nonisomorphic tensor product  $[C]_{im} = [A]_{ijkl}[B]_{mkl}$ .

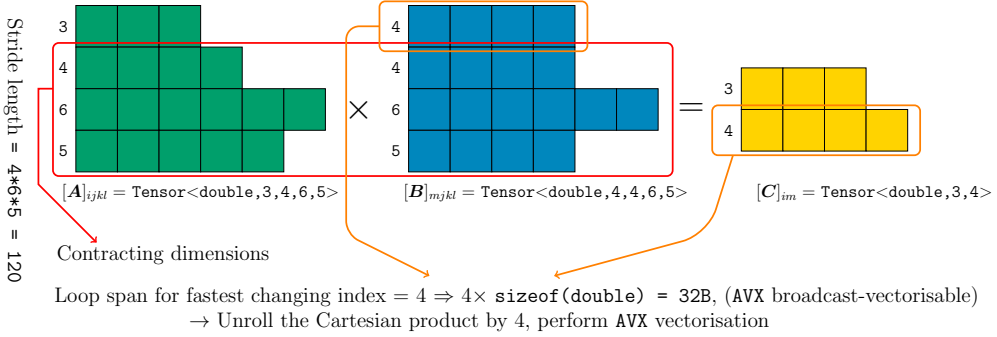


Figure 9.2: AVX vectorisation of the nonisomorphic tensor product of singleton  $[C]_{im} = [A]_{ijkl}[B]_{mkl}$  on strides (cells represent tensor's dimensions not the register width).

Notice that, in Figure 9.2  $m$  is the fastest changing index of the nest  $ijklm$ , and the memory access for tensor  $B$  requires broadcasting intrinsics [178] of the tensor into AVX registers (as opposed to aligned loading) by an `offset=120`, while the floating point and memory I/O operations on tensors  $A$  and  $C$  remain fully AVX vectorisable.

Finally, having performed loop transformation (Figure 9.1) and SIMD vectorisation (Figure 9.2), the third optimisation step is to perform loop fusion. Loop fusion is a direct consequence of operator chaining applied on tensor networks. At its current iteration, Fastor tries to obey the ISO C standard on strict aliasing rules. This implies that, if a network comprising of

many singletons is to be evaluated, the contraction of each singleton is evaluated individually into temporaries and the loop fusion is then applied at the top level, in order to avoid chaining of singletons of different complexity and hence memory aliasing. To elaborate this, consider the evaluation of the tensor network  $[G]_{jkl} = [A]_{ijk}[B]_{il} + \rho \text{tr}(\mathbf{I})[c]_k[D]_{jl} + \sqrt{[E]_{jkl}}$ , where  $\rho$  is a constant coefficient,  $\mathbf{I}$  is the second order identity tensor in  $\mathbb{R}^{3 \times 3}$  and  $\mathbf{c}$ ,  $\mathbf{D}$  and  $\{\mathbf{A}, \mathbf{B}, \mathbf{E}, \mathbf{G}\}$  are first, second and third order tensors of arbitrary size, respectively. The loop fusion procedure applied on this network is shown in Figure 9.3. In Figure 9.3,  $\rho$  being a constant and

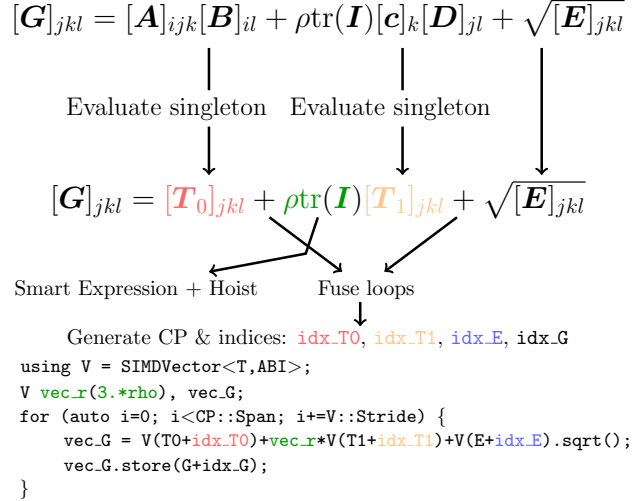


Figure 9.3: Loop fusion for the evaluation of the network  $[G]_{jkl} = [A]_{ijk}[B]_{il} + \rho \text{tr}(\mathbf{I})[c]_k[D]_{jl} + \sqrt{[E]_{jkl}}$

$\text{tr}(\mathbf{I})$  a Fastor smart expression, are hoisted out of the loop during the evaluation of singleton  $[T1]_{jkl} = [c]_k[D]_{jl}$ . After evaluation of all singletons, the Cartesian product (CP) is computed and a single vectorised loop is set up to compute  $\mathbf{G}$ . The cost of creating these temporaries is evaluated in subsection 9.3.2 in the context of compile time operation minimisation. The future endeavour for extending Fastor is to explore batched evaluations of intermediate singletons in a multi-threaded environment as also recently presented in the context of GPGPU in [1].

It is worth mentioning that, generating the Cartesian product of the iteration space and the indices of the tensor network metaprogrammatically can lead to dramatic increase in compilation time. Depending on the level of optimisation required, each individual step described above can be performed either at compile time or run time, by issuing the `-DCONTRACT_OPT` to the compiler. These optimisation steps and further compilation aspects of tensor contraction in Fastor are studied in more detail in subsection 9.3.3.

### 9.3 Benchmark examples

In this section, a series of fundamental benchmarks are presented to highlight further aspects of the tensor contraction framework. In particular, the benchmarks presented in the next few subsections examine the following aspects of the framework:

1. Impact of SIMD vectorisation on the performance of tensor contraction of arbitrary order tensors
2. Impact of operation minimisation on tensor contraction and the associated memory vs FLOPs tradeoff for various cache hierarchies
3. Compilation aspects of the framework and the impact of aggressive loop transformation

All the numerical examples are run on Intel(R) Xeon(R) CPU E5-2650 v2 @2.60GHz processor running Ubuntu 16.04. The processor has three cache levels namely, an 8 way associative

private 32KB L1 data cache (and 32KB L1 instruction cache), an 8 way associative private 256KB L2 cache and a 20 way associative shared 20MB L3 cache, in addition to a 32GB DDR3 (1866 MHz) RAM. Furthermore, it supports SSE to SSE 4.2 and AVX, but not AVX2 or FMA instructions. The following three compilers are used for the benchmarks namely, GCC 6.2.0, Clang 3.9.0 and ICC 17.0.1. If the compiler and Fastor’s optimisation level are not specified, GCC and `-DCONTRACT_OPT` should be assumed, respectively. All the reported CPU run-times are measured by taking the average of one million calls, unless the benchmark took a considerably long time finish, in which case the number of calls were lowered by a factor of 10. Furthermore, in the SIMD tensor contraction benchmark presented in the next subsection, the performance was measured by turning off the turbo mode (although similar performance traits were observed under the turbo mode). The raw data, pre-built binaries and Python scripts for visualisation, for all the numerical examples presented in the chapter are accessible through <https://github.com/romeric/LogfilesFastor>.

### 9.3.1 Impact of SIMD vectorisation on the performance of tensor contraction of arbitrary order tensors

As a starting point, it is important to verify that the tensor contraction framework achieves predicted speed-ups from explicit SIMD vectorisation and that no significant overhead is introduced by the underlying layers of abstractions. To this end, the present benchmark attempts to analyse the speed-ups achieved in FLOP and memory I/O over the scalar code (in the sense of [162], it is a combination of arithmetic and memory I/O benchmark, but rather in the context of tensor contraction). Here, scalar code refers to a variant of the implementation where no explicit vectorisation has been performed and the compiler auto-vectoriser is purposely turned off. This is important in order to assess if the framework achieves the theoretical maximum of SSE/AVX FLOPs and (read/write) bytes per cycle.

In the present benchmark, the interest is in the run-time performance of SIMD vectorised tensor contraction of tensor pairs, hence, operation minimisation is not performed. Furthermore, both vector and scalar variants are based on the same contraction loop nest and are both compiled with “`-O3 -mavx`” options. Furthermore, for the purpose of benchmarking, it was necessary to ensure that the scalar code was not vectorised by passing `-fno-tree-vectorize` to GCC, `-fno-vectorize` to Clang and `-no-vec` to ICC and carefully examining the generated assembly codes. The internal level of optimisation utilised for these benchmarks correspond to the default option `-DCONTRACT_OPT=0`. This optimisation level is indeed equivalent to writing the contraction loop nest explicitly as multiple nested for loops and relying on the compiler for further optimisations. This is indeed also important in order to completely isolate and measure the performance of SIMD vectorisation. Fastor’s further internal optimisation levels are studied in subsection 9.3.3.

Figure 9.4 presents the speed-ups gained from SIMD vectorisation over the scalar code, for isomorphic tensor products of arbitrary order tensors. These include outer products of the following pairs  $[A]_{ij}[B]_{kl}$ ,  $[A]_{ijk}[B]_{lmn}$ ,  $[A]_{ijkl}[B]_{mnpq}$ ,  $[A]_{ijklm}[B]_{npqrs}$ ,  $[A]_{ijklmn}[B]_{pqrsu}$  and  $[A]_{ijklmnpq}[B]_{rstuvwxyz}$ , where the size of tensors  $A$  and  $B$  are kept identical. Furthermore, to assess the performance of SIMD vectorisation, the last dimension of the tensors are chosen to be a multiple of SSE (4 for single precision and 2 for double precision) and/or AVX (8 for single precision and 4 for double precision) registers. It should be emphasised that, Figure 9.4 benchmarks are relative to the scalar code and essentially show the speed-up in load and store (bytes transferred per cycle) as well as floating point operations (only multiplication in case of outer product). While for arithmetic operations optimal speed-ups can be achieved, the memory I/O strongly depend on the size of the tensor. In the benchmarks presented in this section, the smallest tensor size resulting from the outer product is  $288B = 0.0087890625 \times L1$  cache and the largest tensor size is  $1MB = 4 \times L2$  cache.

Next, the performance of nonisomorphic tensor contraction of pairs of arbitrary order tensors are analysed against the scalar code, with the analysis parameters and the compiler options remaining the same as before. However, in contrast to the case of outer product of tensors,

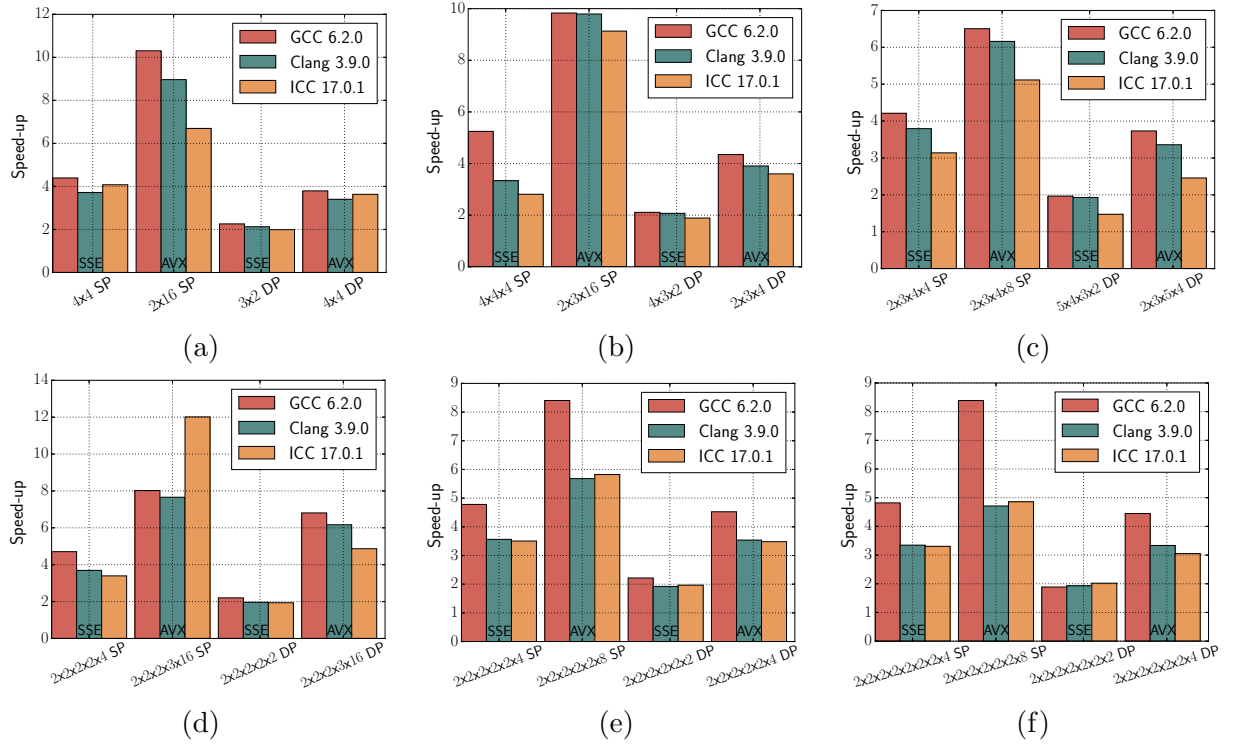


Figure 9.4: Speed-ups achieved by SIMD vectorisation in performing outer product of tensors of single precision (SP) and double precision (DP) floating point over the scalar version with tensors of order (a) 2 ( $[A]_{ij} [B]_{kl}$ ), (b) 3 ( $[A]_{ijk} [B]_{lmn}$ ), (c) 4 ( $[A]_{ijkl} [B]_{mnop}$ ), (d) 5 ( $[A]_{ijklm} [B]_{nopqr}$ ), (e) 6 ( $[A]_{ijklmn} [B]_{opqrst}$ ) and, (f) 8 ( $[A]_{ijklmno} [B]_{pqrsuvwxyz}$ ). Since the order and dimension of the tensors in outer product are kept the same, a  $4 \times 4$  for instance, essentially implies  $[A]_{4 \times 4} \otimes [B]_{4 \times 4}$ .

the number of loops to be set up/merged depend on the number of contracting indices (see Figure 9.2) and the floating point operations performed are multiplication followed by addition. Figure 9.5 shows the speed-up achieved in tensor contraction of pairs of tensors using SIMD vector types over the scalar code. For this benchmark all tensors fit in to L1 cache.

As can be observed, in both isomorphic (outer product) and nonisomorphic tensor product benchmarks, optimal speed-ups are achieved with SSE (4X for SP and 2X for DP) as well as AVX (8X for SP and 4X for DP) vectorisation over the scalar variant. Certainly, for the isomorphic tensor products where tensors do not fit in L1 cache Figure 9.4(e,f), a more noticeable degradation in speed-up is observed. The variations in speed-up with different tensor sizes can be explained by carefully studying the assembly code generated by the compilers. In that, since tensor objects in Fastor are static, an optimising compiler may generate different intrinsics for different tensor sizes, which may be optimal for some but not the other. As a particular example, consider the case of AVX vectorisable double precision tensor products in Figure 9.4 and Figure 9.5, for whom the three compilers used for this benchmark generate the following different intrinsics for the innermost loop:

1. **GCC 6.2.0** generates one additional move (`movslq`), one add (`addq`) and one shift and rotate instruction (`salq`) and emits aligned load and store instructions for all tensors.
2. **Clang 3.9.0** generates the most compact code with no additional instructions, but changes the aligned load instruction for tensor  $A$  to a broadcast (`vbroadcastsd`), and emits aligned store instructions.
3. **ICC 17.0.1** generates two additional move (`movslq`) and two shift and rotate instructions (`shlq`), changes the aligned load instruction for tensor  $A$  to a broadcast (`vbroadcastsd`)

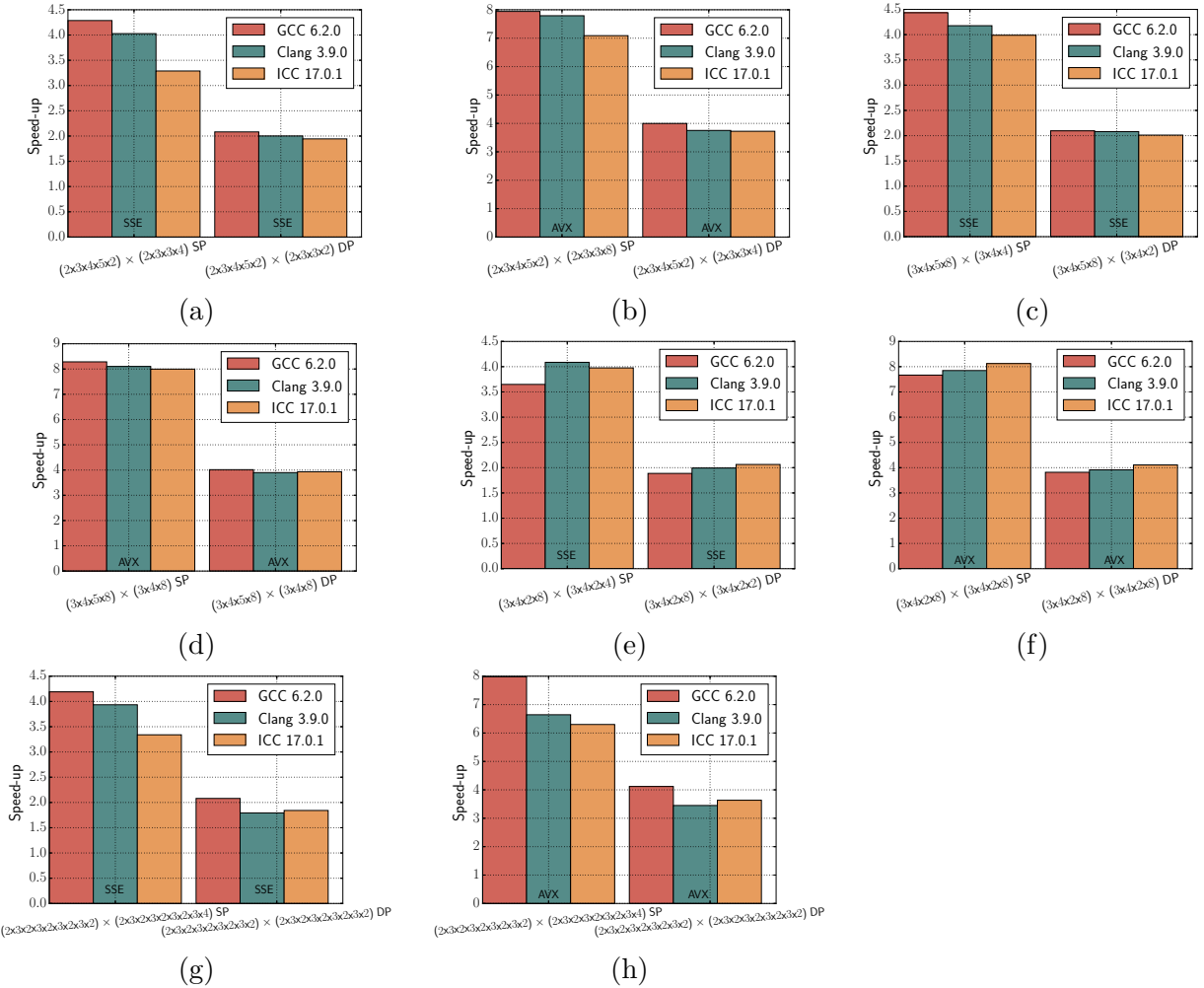


Figure 9.5: Speed-ups achieved by SIMD vectorisation in performing tensor contraction on pairs of tensors of single precision (SP) and double precision (DP) floating point over the scalar version with (a) single index contraction ( $[A]_{ijklm}[B]_{njop}$ ) using SSE, (b) single index contraction ( $[A]_{ijklm}[B]_{njop}$ ) using AVX, (c) two index contraction ( $[A]_{ijkl}[B]_{ijm}$ ) using SSE, (d) two index contraction ( $[A]_{ijkl}[B]_{ijm}$ ) using AVX, (e) three index contraction ( $[A]_{ijkl}[B]_{ijkm}$ ) using SSE, (f) three index contraction ( $[A]_{ijkl}[B]_{ijkm}$ ) using AVX, (g) 8 index contraction ( $[A]_{ijklmnopq}[B]_{ijklmnopr}$ ) using SSE and, (h) 8 index contraction ( $[A]_{ijklmnopq}[B]_{ijklmnopr}$ ) using AVX. x-labels represent the actual dimensions of the tensors.

and emits an unaligned store instruction (`vmovupd`) for the output tensor. This explains the slight drop in speed-up observed with ICC in certain cases.

It is important to clarify this aspect through inspecting the generated intrinsics, since the vectorisation approach followed by Fastor is through explicit SIMD vector types, which at times, is known to be sensitive to compiler's mis-compilation [162, 116].

### 9.3.2 The depth-first search approach and memory vs FLOPs tradeoff

As defined in D.1, the depth-first search is an operation minimisation technique for tensor contraction over complex networks that performs by-pair tensor contraction in the network. This essentially leads to the creation of multiple intermediate temporaries and hence can be perceived as a performance bottleneck. An alternative methodology to this is to evaluate the whole tensor network at once, without performing a depth-first algorithm. On the other hand, if the tensors are statically allocated (like in Fastor) and the temporaries created by the depth-first search fit in CPU cache, the operation minimisation may instead prove to be more cache

optimal, by virtue of increasing the spatial locality. In this section, a fundamental benchmark is manufactured that compares the run-time performance of the by-pair (termed here as FLOP optimal) tensor contraction algorithm against the single expression evaluation (termed here as memory-saving) algorithm. Note that, these benchmarks do not include the performance of the depth-first search approach in finding the optimal sequence of tensor contraction. As the depth-first search algorithm itself is performed metaprogrammatically, no run-time code is generated for it. The compilation time and further performance aspects of the depth-first search are studied in subsection 9.3.3.

To be able to compare the performance of the two aforementioned approaches, a three tensor singleton ( $[\mathbf{D}]_{kmn} = [\mathbf{A}]_{ijk}[\mathbf{B}]_{ijl}[\mathbf{C}]_{mnl}$ ) is chosen first. The cost of contracting this network through a single evaluation is  $3\xi_i\xi_j\xi_k\xi_l\xi_m\xi_n$ , where  $\xi_a$  denotes the iteration space of index  $a$  and the 3 stands for 2 multiplications and one addition. A fixed sequence for by-pair tensor contraction is then chosen, namely  $[\mathbf{T}]_{kl} = [\mathbf{A}]_{ijk}[\mathbf{B}]_{ijl} \Rightarrow [\mathbf{D}]_{kmn} = [\mathbf{T}]_{kl}[\mathbf{C}]_{mnl}$ , where  $\mathbf{T}$  represents the temporary. The total cost of the contraction over the network is now  $2(\xi_i\xi_j\xi_k\xi_l + \xi_k\xi_l\xi_m\xi_n)$ , where 2 stands for one multiplication and one addition.

Note that depending on the iteration space of tensors the above sequence may not always correspond to the most optimal one. Nonetheless, an attempt is made to keep the above sequence optimal either by manually choosing the sizes of tensors  $\mathbf{A}$ ,  $\mathbf{B}$ ,  $\mathbf{C}$  or through the compiler flag `-DFASTOR_KEEP_DP_FIXED`. The sizes of the tensors are then successively increased in such a way that the memory requirement for the intermediate temporary  $\mathbf{D}$  ranges from fitting into L1 cache to four times the size of L3 cache. Certainly, as the dimensions increase, the number of floating point operations also increase. The assessment is then based on how much reduction in FLOP count is necessary to outweigh the cost of allocation of the temporary i.e. for a temporary fitting into a given cache, what should be the approximate **reduced FLOP count**, where

$$\begin{aligned}\text{reduced FLOP count} &= \text{cost}_{\text{MemOpt}} - \text{cost}_{\text{FLOPOpt}} \\ &= 3(\xi_i\xi_j\xi_k\xi_l\xi_m\xi_n) - 2(\xi_i\xi_j\xi_k\xi_l + \xi_k\xi_l\xi_m\xi_n).\end{aligned}$$

Figure 9.6 shows the speed-up of FLOP optimal contraction over the memory-saving contraction scheme, while keeping the temporary size to fit into a fixed cache and successively increasing the iteration space in order to increase the **reduced FLOP count**. Hence, every bar in Figure 9.6, compares the two schemes for a fixed data size and fixed **reduced FLOP count**. While the contraction loop nest certainly differs, it is made sure that both algorithms are equally vectorised (in particular, using AVX intrinsics), in order to fully isolate the aspect of SIMD vectorisation from operation minimisation. Hence, depending on the vectorisation, the reduction in FLOP count should be divided by the vector size (which is not done here for the purpose of clarity).

As can be observed in Figure 9.6, for tensor networks fitting L1 cache, even a reduction of 100-1000 FLOPs through the depth-first scheme can be beneficial. For L2 cache a saving of  $10^3$  or more in FLOPs is needed to actually outweigh the single expression evaluation scheme. Similarly, for L3 cache, a reduction of  $10^6$  and for tensor networks not fitting in any cache, a reduction of  $(10^7)$  in floating point operations is required for the by-pair tensor contraction scheme to be beneficial. Certainly, as the saving in FLOP increases for a given cache size, orders of magnitude performance can be gained over the memory-saving approach.

The same benchmark is then repeated with a different tensor network, namely the four tensor singleton  $[\mathbf{E}]_{lo} = [\mathbf{A}]_{ijk}[\mathbf{B}]_{ijl}[\mathbf{C}]_{mnk}[\mathbf{D}]_{mno}$ , where the performance of contracting this network through a single expression evaluation (with cost  $4\xi_i\xi_j\xi_k\xi_l\xi_m\xi_n\xi_o$ ) is compared with the by-pair approach for the sequence  $[\mathbf{T}_0]_{kl} = [\mathbf{A}]_{ijk}[\mathbf{B}]_{ijl}; [\mathbf{T}_1]_{ko} = [\mathbf{C}]_{mnk}[\mathbf{D}]_{mno} \Rightarrow [\mathbf{E}]_{lo} = [\mathbf{T}_0]_{kl}[\mathbf{T}_1]_{ko}$  requiring the creation of two temporaries now (with a total cost of  $2(\xi_i\xi_j\xi_k\xi_l + \xi_m\xi_n\xi_k\xi_o + \xi_k\xi_l\xi_o)$ ), hence

$$\begin{aligned}\text{reduced FLOP count} &= \text{cost}_{\text{MemOpt}} - \text{cost}_{\text{FLOPOpt}} \\ &= 4(\xi_i\xi_j\xi_k\xi_l\xi_m\xi_n\xi_o) - 2(\xi_i\xi_j\xi_k\xi_l + \xi_m\xi_n\xi_k\xi_o + \xi_k\xi_l\xi_o).\end{aligned}$$

Figure 9.7 shows the speed-up of FLOP optimal contraction over memory-saving contraction

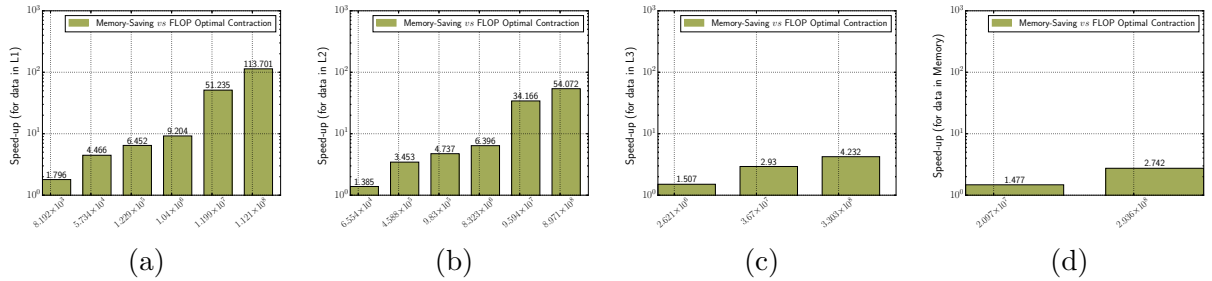


Figure 9.6: Speed-up achieved for contraction of three tensor singletons ( $[A]_{ijk}[B]_{ijl}[C]_{mnl}$ ) using by-pair contraction over single expression evaluation for tensor sizes that fit a) L1 cache (size of temporary created  $16\text{KB}=0.5 \times \text{L1 cache}$ ), b) L2 cache (size of temporary created  $128\text{KB}=0.5 \times \text{L2 cache}$ ), c) L3 cache (size of temporary created  $10\text{MB}=0.5 \times \text{L3 cache}$ ) and, d) main memory (size of temporary created  $80\text{MB}=4 \times \text{L3 cache}$ ).  $x$ -labels indicate the number of FLOPs saved/reduced by utilising by-pair (FLOP optimal) contraction and numbers on top of bars show the corresponding speed-up.

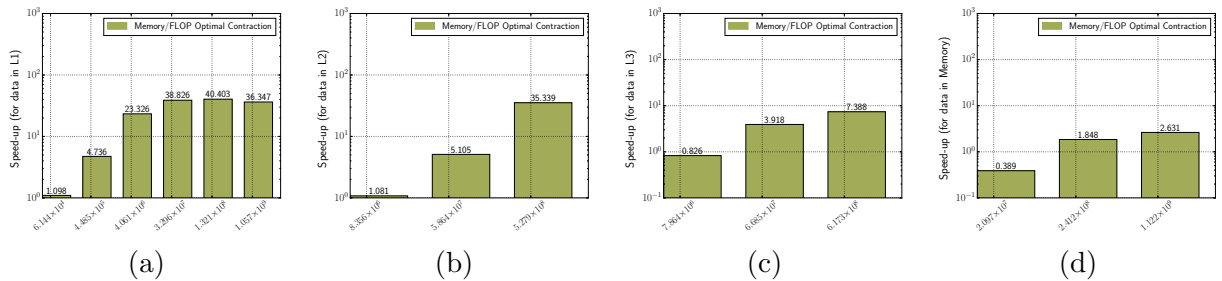


Figure 9.7: Speed-up achieved for contraction of four tensor singletons ( $[A]_{ijk}[B]_{ijl}[C]_{mnk}[D]_{mno}$ ) using by-pair contraction over single expression evaluation for tensor sizes that fit a) L1 cache (size of temporary created  $16\text{KB}=0.5 \times \text{L1 cache}$ ), b) L2 cache (size of temporary created  $128\text{KB}=0.5 \times \text{L2 cache}$ ), c) L3 cache (size of temporary created  $10\text{MB}=0.5 \times \text{L3 cache}$ ) and, d) main memory (size of temporary created  $80\text{MB}=4 \times \text{L3 cache}$ ).  $x$ -labels indicate the number of FLOPs saved/reduced by utilising by-pair (FLOP optimal) contraction and numbers on top of bars show the corresponding speed-up.

scheme, while keeping the sizes of the temporaries to fit into fixed cache and successively increasing the iteration space in order to increase the **reduced FLOP count**.

Certainly, the performance is now affected by the creation of two temporaries. For tensor networks fitting L1 cache a reduction of  $10^4$  in FLOPs, for tensor networks fitting L2 cache a reduction of  $10^6$  in FLOPs, for tensor networks fitting L3 cache a reduction of  $10^7$  in FLOPs and for tensor networks not fitting in any cache a reduction of  $> 10^8$  in FLOP count is required for the by-pair tensor contraction scheme to outperform the single expression evaluation scheme.

One can correlate these numbers to the latency of data fetch (from different caches) of the architecture. For the L1 cache of the tested Intel Xeon processor, the ratio of bytes read/written (4 cycle latency) to floating point operation (5 cycles `mul` + 3 cycles `add`) per each iteration of contraction loop nest is going to be small enough (refer to [178] for various cache latencies). Hence, for tensors fitting in L1 cache, even minimal savings in FLOPs can be beneficial.

Note that, due to the design of the current tensor contraction framework, all temporaries are allocated on the stack. Different (and perhaps more in favour of the memory-saving approach) performance traits should be expected for dynamic and heap allocated tensors. Since the reduction in FLOP count is correlated to the size of tensors, it may not always be apparent to choose one scheme over the other, and that leads to the idea of a heuristic cost model [180, 188]. It is worth mentioning that, these benchmarks essentially relate the correlation of fixed memory allocations to the sequence (evaluation pattern) of operation minimisation. In cases where the sequence is not fixed, the operation minimisation may prove to be even more beneficial [6].

### 9.3.3 Compilation aspects of operation minimisation and further compile time tensor contraction optimisations

As described in subsection 9.2.6, generating the Cartesian product of iteration space and further the indices of tensors metaprogrammatically can lead to an increase in compilation time. In this subsection, compilation aspects of Fastor are studied under two settings. First, the different optimisation levels available in Fastor for tensor contraction (supplied as compiler flag `-DCONTRACT_OPT`) are studied. These optimisation levels essentially relate to the construction of contraction loop nests (i.e. the Cartesian products) and loop transformation optimisations described in subsection 9.2.6 which are in fact not related to operation minimisation. Second, the compilation aspects of operation minimisation is studied and compared to the compilation aspects of single expression evaluation scheme. The latter study is indeed related to the benchmarks described in previous subsection on runtime performance of the two schemes.

As Fastor can compute the Cartesian product of contraction loop nest either at compile time or at runtime, this leads to the following three optimisation levels

1. `-DCONTRACT_OPT=0` [default]: The Cartesian product is computed at runtime. This is equivalent to explicitly writing the contraction loop nest and relying on the compiler to optimise it.
2. `-DCONTRACT_OPT=1`: The Cartesian product is computed at compile time and stored in variadic template containers, but the indices of tensors are computed at runtime. In that, the cost of indexing and memory access is still present at run time.
3. `-DCONTRACT_OPT=2`: The Cartesian product and the indices of tensors are computed at compile time and stored in variadic template containers. This is an extreme level of optimisation which completely eliminates dynamic memory I/O (at least in theory) and mandates that only floating point arithmetics should be performed at run time.

Note that, irrespective of the optimisation levels described above, Fastor will always have enough information to perform loop unrolling and vectorisation, as the information regarding the iteration space of tensors and the microprocessor family are available at compile time.

To study the various aspects of the above optimisation levels, a singleton comprising of one 7th order tensor  $\mathbf{A}$  and one 8th order tensor  $\mathbf{B}$  is considered. The singleton is then contracted such that the nonisomorphic vector space is successively increased. These correspond to 7 index contraction  $[\mathbf{A}]_{ijklmno}[\mathbf{B}]_{ijklmnp}$ , 6 index contraction  $[\mathbf{A}]_{ijklmno}[\mathbf{B}]_{ijklmnpr}$ , 5 index contraction  $[\mathbf{A}]_{ijklmno}[\mathbf{B}]_{ijklmprs}$ , 4 index contraction  $[\mathbf{A}]_{ijklmno}[\mathbf{B}]_{ijklprst}$ , 3 index contraction  $[\mathbf{A}]_{ijklmno}[\mathbf{B}]_{ijkpqrst}$ , 2 index contraction  $[\mathbf{A}]_{ijklmno}[\mathbf{B}]_{ijprstuv}$  and finally one index contraction  $[\mathbf{A}]_{ijklmno}[\mathbf{B}]_{iprstuvwxyz}$ , respectively. The dimensions of the tensors are chosen such that each of the aforementioned multi-index contractions correspond to a Cartesian product with dimensions  $2^8 \times 8$ ,  $2^9 \times 9$ ,  $2^{10} \times 10$ ,  $2^{11} \times 11$ ,  $2^{12} \times 12$ ,  $2^{13} \times 13$  and  $2^{14} \times 14$ , respectively. In fact, these dimensions range from small to large, in order to assess the compilation times for all kinds of feasible applications. Four aspects of these optimisation levels are then studied namely, the compilation time, memory footprint, generated binary size and the eventual execution time of each. All the benchmarks are run with double precision AVX vectorisable nests with compiler flags as “`-O3 -mavx`”. Although various compiler flags could be used to optimise for generated binary sizes and sanitise memory footprint, they would lead to extensive parametric studies, which is not the purpose here. The goal here is, to study Fastor’s internal optimisation schemes with realistic compiler flags (also in order to be consistent with the other benchmarks). The only two additional flags used are `-Wstack-usage` for GCC and `-fconstexpr-steps=16000000` for Clang.

From Figure 9.8 (shown as raw data), the first observation is that `-DCONTRACT_OPT=0` has the compilation time and memory footprint of a typical application in C++, with all the compilers. The second observation is that for `-DCONTRACT_OPT=2`, GCC compilation time and memory usage (8.2GB memory footprint) increases exponentially for 5 index contraction (i.e.

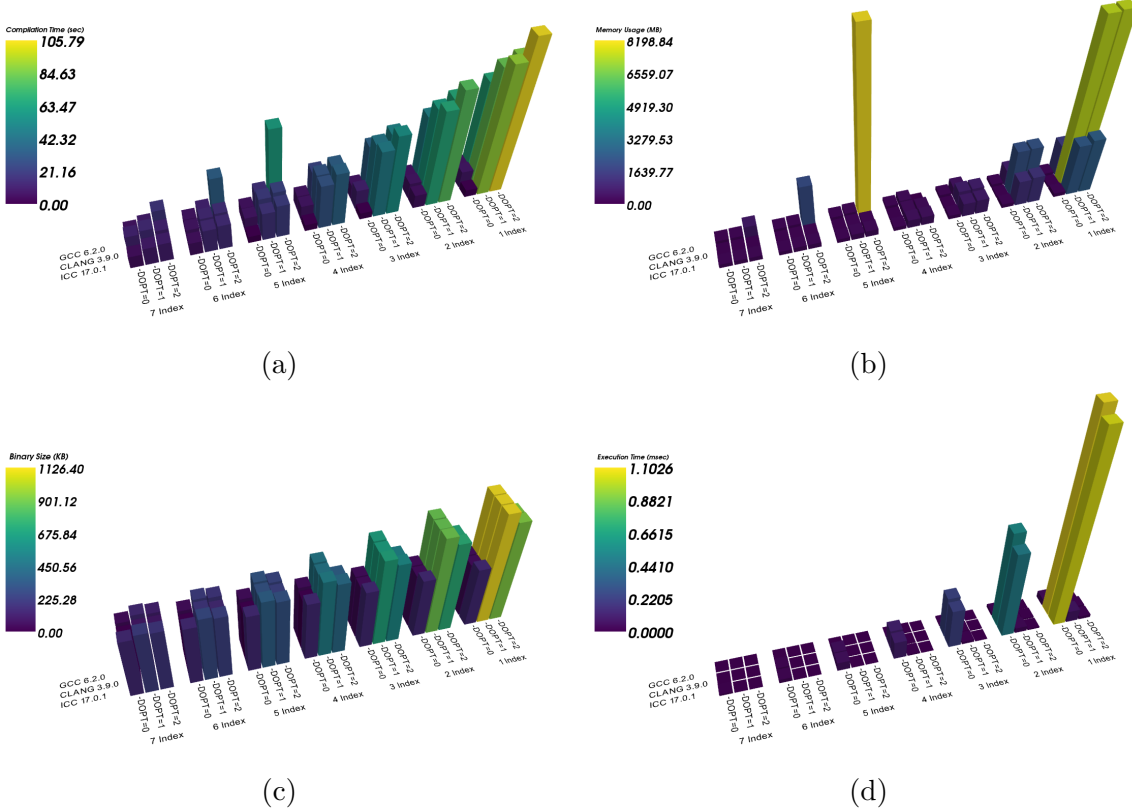


Figure 9.8: Compilation aspects of different optimisation levels for multi-index tensor contraction of singletons (Lower is better). a) compilation time (wall time), b) memory footprint, c) size of binaries generated, and d) eventual execution time (wall time). Contraction indices correspond to: (7 index) →  $[A]_{ijklmno}[B]_{ijklmnop}$  (span  $2^8 \times 8$ ), (6 index) →  $[A]_{ijklmno}[B]_{ijklmnpr}$  (span  $2^9 \times 9$ ), (5 index) →  $[A]_{ijklmno}[B]_{ijklmprs}$  (span  $2^{10} \times 10$ ), (4 index) →  $[A]_{ijklmno}[B]_{ijklprst}$  (span  $2^{11} \times 11$ ), (3 index) →  $[A]_{ijklmno}[B]_{ijkprstu}$  (span  $2^{12} \times 12$ ), (2 index) →  $[A]_{ijklmno}[B]_{ijprstuv}$  (span  $2^{13} \times 13$ ) and (1 index) →  $[A]_{ijklmno}[B]_{iprstuvwxyz}$  (span  $2^{14} \times 14$ ), respectively. Note that data for GCC 6.2.0 for 4 index contraction and lower is not available for optimisation level -DOPT=2, due to stall and excessive memory footprint. -DOPT is used as a shorter alias for -DCONTRACT\_OPT.

for the span  $2^{10} \times 10$ ) and eventually consumes all the available memory and stalls for 4 index contraction (i.e. for the span  $2^{11} \times 11$ ). Further build profiling reveals that unlike ICC and Clang, GCC stores up all large variadic templates and static arrays on the stack in order to perform global optimisation for fixed indices, but does not optimise the memory I/O. A deeper insight can be gained through a comparison of different optimisation levels presented in Table 9.1 and Table 9.2. As can be observed, the memory usage and compile time increases quadratically for Clang starting from 4 index contraction, under the two latter optimisation levels. ICC shows the least memory footprint (up to  $\approx 2\text{GB}$ ) for both higher optimisation levels and GCC and Clang show the shortest compilation time for -DCONTRACT\_OPT=1 and -DCONTRACT\_OPT=2, respectively. The size of generated binaries are all comparable for all compiler for a fixed optimisation level. Clang generates a slightly more compact code compared to the other two compilers for -DCONTRACT\_OPT=0 and ICC generates the most compact code for the other two optimisation levels.

These results impact the run time accordingly. GCC compiled codes, show no significant improvement in run time since the stack size is increased but memory I/O is still present. However, at the cost of high memory usage and compilation time, ICC and Clang completely optimise away the run time memory I/O and generate codes with -DCONTRACT\_OPT=2 which is more than

80X faster than that of `-DCONTRACT_OPT=0` and nearly up to 5X faster than `-DCONTRACT_OPT=1` (see Figure 9.8d). Note that, these performance gains come on top of the benchmarks presented in subsection 9.3.1 for vectorisation (as here all the generated codes are AVX vectorised). However, as can be seen from the raw data in Figure 9.8, for `-DCONTRACT_OPT=0`, GCC emits fully aligned memory load and store instructions which perform slightly faster than their counterparts from the other compilers (as also explained in subsection 9.3.1).

It should be mentioned that `-DCONTRACT_OPT=1,2` correspond to optimisation levels that neither a compiler would be willing to perform nor are they available in any vendor specific libraries, such as BLAS. In fact, their implementation, require building a compile time virtual engine to perform numerical analysis on template parameters (analogous to a numerical analysis software that performs computations on arrays at runtime). Certainly, the complexity involved in developing a metaprogramming engine of such sort is tremendous and the benchmarks in Figure 9.8 reflect that. For instance, at `-DCONTRACT_OPT=2`, Fastor performs sorting, concatenation, reshaping and many more operation of  $O((n \log(n))$  on `std::integer_sequences` (C++14) with potentially  $n > 1000$ . This shows that the metaprogramming engine in Fastor extends much beyond expression templates and operator chaining.

The motivation behind implementing these optimisations, is due to the domain specific nature of Fastor to primarily optimise tensor contractions in finite element computations where extremely large tensors rarely occur, and for which the compilation time could remain in seconds and the memory footprint would be in the range of a few 100 megabytes at most. Note that, a more in-depth analysis of template instantiation and compile time profiling is beyond the scope of this study. For such diagnostic studies (carried out using the LLVM based Templight [247, 238]), the interested reader can refer to <https://github.com/romeric/LogfilesFastor> for more details.

$\downarrow \setminus \rightarrow$	Compilation Time			Memory Usage			Binary Size			Execution Time		
	GCC	Clang	ICC	GCC	Clang	ICC	GCC	Clang	ICC	GCC	Clang	ICC
7 Index	1.127	1.112	1.189	1.084	1.116	1.103	0.274	0.353	0.315	0.7	0.669	7.388
6 Index	1.253	1.34	1.395	1.18	1.29	1.241	0.347	0.511	0.383	1.038	17.352	12.565
5 Index	1.564	1.745	2.016	1.384	1.751	1.539	0.495	0.746	0.516	1.239	22.809	17.058
4 Index	2.082	2.64	3.423	1.836	3.064	2.195	0.813	1.253	0.832	1.004	27.694	16.102
3 Index	3.34	4.214	7.033	2.686	7.261	3.638	1.542	2.428	1.501	1.012	28.171	15.837
2 Index	6.212	10.086	13.435	4.748	21.449	6.767	3.111	4.88	2.905	0.938	30.133	17.053
1 Index	12.78	23.506	44.008	9.296	72.99	13.52	6.935	11.006	6.277	0.778	22.376	15.942

Table 9.1: Compilation aspects & run time performance of `-DCONTRRACT_OPT=1` normalised with respect to `-DCONTRRACT_OPT=0`

$\downarrow \setminus \rightarrow$	Compilation Time			Memory Usage			Binary Size			Execution Time		
	GCC	Clang	ICC	GCC	Clang	ICC	GCC	Clang	ICC	GCC	Clang	ICC
7 Index	1.639	0.995	1.243	3.688	1.122	1.117	0.249	0.353	0.293	0.763	0.765	11.984
6 Index	3.247	1.444	1.487	12.618	1.304	1.269	0.322	0.432	0.338	1.458	25.055	25.361
5 Index	10.583	1.981	2.363	50.688	1.778	1.593	0.396	0.589	0.427	2.329	44.861	46.86
4 Index	-	3.236	4.61	-	3.13	2.307	-	0.9	0.607	-	66.444	67.764
3 Index	-	5.316	10.439	-	7.378	3.847	-	1.528	0.986	-	82.122	80.098
2 Index	-	12.54	22.455	-	21.7	7.185	-	2.811	1.721	-	73.247	73.02
1 Index	-	28.31	83.96	-	73.481	14.369	-	5.589	3.277	-	65.373	62.965

Table 9.2: Compilation aspects & run time performance of `-DCONTRRACT_OPT=2` normalised with respect to `-DCONTRRACT_OPT=0`

Next, the compilation aspect of operation minimisation is studied. For this benchmark, the cost of compilation over the single expression evaluation scheme (when depth-first search is

not performed) is studied. However, unlike the benchmarks conducted in subsection 9.3.2, the interest here is not in the runtime performance of the operation minimisation, hence, studying cache heirarchies and creation of intermediate temporaries are not pursued. Instead the two compilation aspect namely, compilation time and compiler's memory footprint is studied as a function of the Cartesian product (iteration space of nests) and reported in Table 9.3-Table 9.5 as the number of FLOPS saved/reduced, since these two parameters (iteration span and number of FLOPS saved) are correlated. All the benchmarks are run by resorting back to the default optimisation level i.e. `-DCONTRACT_OPT=0`, as operation minimisation is an orthogonal matter to loop transformation optimisations. Analogous to the benchmarks presented in subsection 9.3.2, a three tensor singleton  $[A]_{ijk}[B]_{ijl}[C]_{mnl}$ , a four tensor singleton  $[A]_{ijk}[B]_{ijl}[C]_{mnl}[D]_{no}$  and a five tensor singleton  $[A]_{ijk}[B]_{ijl}[C]_{mnl}[D]_{no}[E]_p$  are chosen and their sizes are successively increased. Table 9.3, Table 9.4 and Table 9.5 show the compilation time and memory

Saved FLOPs	Compilation Time			Memory Usage		
	GCC	Clang	ICC	GCC	Clang	ICC
44544	1.307	1.307	1.325	1.07	1.07	1.076
89088	1.331	1.255	1.32	1.063	1.249	1.075
178176	1.288	1.712	1.289	1.062	1.726	1.077
356352	1.29	1.331	1.385	1.074	1.063	1.078
712704	1.34	1.252	1.283	1.062	1.242	1.078
1425408	1.295	1.705	1.323	1.07	1.729	1.078
2850816	1.294	1.288	1.364	1.067	1.062	1.079

Table 9.3: Compilation cost of operation minimisation **normalised** with respect to single expression evaluation for 3 tensor singleton

usage operation minimisation scheme over the single expression scheme for each of the aforementioned singleton. As can be observed from the results, the compilation time is not related to the sizes of the tensors but rather to the number of tensors (or operators) appearing in the whole tensor network. This is a fairly certain issue as the depth-first search is recursive in nature<sup>3</sup>. In that, the compilation time and memory footprint of four and five tensor singletons are around 30% and 80-100% more than those of single expression evaluations. However, in terms of raw timings, the highest compilation time for operation minimisation has been 2.25 seconds (with ICC) which corresponds to a FLOP reduction of 41566208. The conclusion drawn from these results is that, a compile time depth-first search is fundamentally low-cost if the number of tensors in the network are small. At the cost increasing the compile time by merely a few seconds million to billions of runtime operations can be saved.

Saved FLOPs	Compilation Time			Memory Usage		
	GCC	Clang	ICC	GCC	Clang	ICC
256512	1.255	1.281	1.78	1.27	1.271	1.294
513024	1.26	1.758	1.584	1.261	1.731	1.292
1026048	1.256	1.282	1.359	1.26	1.054	1.296
2052096	1.31	1.318	1.459	1.262	1.259	1.295
4104192	1.268	1.716	1.512	1.258	1.731	1.295
8208384	1.263	1.314	1.427	1.265	1.047	1.296
16416768	1.281	1.244	1.438	1.268	1.249	1.299

Table 9.4: Compilation cost of operation minimisation **normalised** with respect to single expression evaluation for 4 tensor singleton

## 9.4 Applications & Real-world experimentation: Kernel-based numerical integration of nonlinear materials

In this section, numerical examples pertaining to the application of the current tensor contraction library in an embedded finite element framework are presented, specifically, in numerical

<sup>3</sup>The cost of depth-first search through Fastor's meta-engine is at most  $n!$ , where  $n$  is the number of tensors appearing in the network.

Saved FLOPs	Compilation Time			Memory Usage		
	GCC	Clang	ICC	GCC	Clang	ICC
649472	1.745	1.778	2.293	1.758	1.759	1.822
1298944	1.727	1.32	2.288	1.753	1.052	1.823
2597888	1.724	1.263	2.188	1.745	1.242	1.827
5195776	1.716	1.747	2.311	1.763	1.749	1.829
10391552	1.778	1.277	2.205	1.756	1.046	1.828
20783104	1.724	1.256	2.274	1.752	1.246	1.827
41566208	1.745	1.712	2.314	1.756	1.738	1.828

Table 9.5: Compilation cost of operation minimisation **normalised** with respect to single expression evaluation for 5 tensor singleton

integration of work-conjugates and Hessian of some polyconvex hyperelastic and multi-variable convex electroelastic energy functionals presented in chapter 2 and chapter 4. The objective of these examples are to examine the speed-ups gained in numerical integration (or the so-called local assembly) of complex energy functionals using the framework’s data parallelism, smart expression templates and additional domain specific features (benchmarked in the previous sections). In order to gain insights into each of the aformationed optimisation steps, the Fastor’s implementation is benchmarked against three different individual implementations, namely

1. **Explicitly-vectorised Implementation [Variant 1]:** This implementation benefits from Fastor’s explicit vectorisation but uses classical operator overloading. Comparison against this implementation will measure solely the benefit of operator chaining of expression templates for finite element local assembly procedures.
2. **Auto-vectorised Implementation [Variant 2]:** This implementation does not benefit from Fastor’s explicit vectorisation and this is left to the compiler’s auto-vectoriser. The implementation also uses classical operator overloading. Comparison against this implementation will measure the impact of explicit SIMD vectorisation and operator chaining for finite element local assembly procedures.
3. **Classical Implementation [Variant 3]:** This implementation does not benefit from Fastor’s explicit vectorisation and operator chaining. Furthermore, unlike variants 2 and 3, this implementation uses a classical implementation of the tensor cross product. Comparison against this implementation will measure the impact of explicit SIMD vectorisation, operator chaining and optimised tensor cross product kernels for finite element local assembly procedures. Note that this implementation only holds for three-dimensional problems, as the tensor cross product is a three-dimensional operator.

Note that while the backend implementations for each implementation differs, they are all similar in terms of API, functions’ signatures, data structures used and the local assembly contraction loop nest (in fact, all implementations are fundamentally based on Listing 9.6). Furthermore, all variants are compiled with identical compiler flags. An attempt is made to keep the other implementations as close to a realistic implementation as possible, in that the calls to functions such as determinant, inverse, transpose and cofactor used within the quadrature loop nest (as shown in Listing 9.6) are kept the same for all the implementations i.e. they are all call optimised in-built routines. This is true for most implementations, where such calls are dispatched to either vendor BLAS or optimised in-built subroutines. The only exception is that for the third variant of the implementation, the `cross` function in Listing 9.6 uses a classical implementation as its implementation is not available in say, BLAS. It is worth mentioning that, in the current tensor contraction framework, the optimised implementation of the tensor cross products involves complete manual loop unrolling, explicit AVX vectorisation, zero elimination and restructuring of the data for super-scalar execution. The technique of eliminating zeros from the computation is a rather common practice in generating domain specific kernels [230, 326].

To this effect, three energy functionals are chosen, one purely mechanical (the Mooney-Rivlin model described in subsection 2.4.3) and two electro-mechanical, one ideal dielectric

described in subsection 4.2.5 and the other a regularised convex multi-variable model described in (6.8). The assessment is then to perform finite element analyses based on displacement-based formulation for mechanical problems and displacement-potential based formulation for electromechanical problems with high order triangles and tetrahedral elements and monitor the speed-ups achieved for local assembly. The quadrature loop nest is set up in the most classical fashion, in that it includes iteration over the quadrature points and test and trial spaces [180, 11, 181, 230, 188]. However, the last two loops (over test and trial spaces) are removed in favour of the abstraction provided by Fastor's `Tensor` class.

Consequently, in line with the theme of this framework, explicit tensorial operations involving computation of the following quantities are carried out within every quadrature point: a) the Jacobian of the isoparametric mapping ( $\nabla_{\mathbf{X}} \xi$ ) (as described in [30] b) the material gradient of the displacements ( $\nabla_0 \mathbf{u}$ ), c) the variables in the extended kinematic set  $\mathcal{V}$ , d) the set of work-conjugates and subsequently the first Piola-Kirchhoff stress tensor and the electric field vector and finally e) the Hessian of the internal energy.

It should be clear that, the utmost efficiency of the approach taken here for local assembly is not the objective of these benchmarks. The benchmarks rather showcase the usage of the framework in explicit finite element programming through seemingly hidden domain aware expressions, which plays a key role in kernel-based numerical integration shown in Listing 9.6.

Listing 9.6: The structure of the quadrature loop nest

```
for (auto g=0; g<n_gauss; ++g) {
    // Compute Jacobian of isoparametric mapping
    auto ParentGradientX = matmul(GradBases, LagrangeElemCoords);
    // Compute material gradient
    auto MaterialGradient = matmul(inverse(ParentGradientX), GradBases);
    // Compute the deformation gradient tensor
    auto F = matmul(MaterialGradient, EulerElemCoords);
    // Compute the cofactor of deformation gradient tensor
    auto H = cofactor(F);
    // Compute the Jacobian of deformation gradient tensor
    auto J = determinant(F);
    // Compute work-conjugates
    // Sigma_F, Sigma_H, Sigma_J, Sigma_D0 and Sigma_d
    // Compute the first Piola-Kirchhoff stress tensor
    auto P = Sigma_F + cross(Sigma_H, F) + Sigma_J * H;
    // Compute the electric field/displacement
    // EO, DO
    // Compute the Hessian components
    // WFF, WFH, WFJ, WFDO, WFD, WHH, WHJ, ... Wdd
    // Compute the Hessian of the energy W
    // H_W ...
}
```

In the current setting, kernel-based computation is a consequence of expression templates combined with the C++11 `auto` keyword, in that, specific quantities within a quadrature loop nest can be lumped as a single expression and a single kernel can be launched for it. To illustrate this, consider the evaluation of the deformation gradient tensor  $F$  in Listing 9.6. Computing this quantity requires computation of `ParentGradientX` and `MaterialGradient` first. However, note that the automatic type deduction via `auto` does not force these quantities to bind to an object and as a result their computation is postponed and their automatic type is chained and carried over to the next line. Now, by the time the computation of  $F$  is requested, three `matmul` and one `inverse` functions are chained together, see Listing 9.6. A canonical and rather schematic representation of how the type of  $F$  is detected in Fastor can be represented as in Listing 9.7.

Listing 9.7: A single expression for computing the deformation gradient tensor

```
BinaryMatMulOp<BinaryMatMulOp<UnaryInvOp<BinaryMatMulOp<GradBases, LagrangeElemCoords>, GradBases>, EulerElemCoords>
```

The evaluation policy in Fastor, detects that an efficient implementation for this chained expression is available that does not require as many memory load and store operations. Hence, it statically dispatches the expression for  $F$  to a bespoke kernel. In particular, the evaluation

of this kernel involves SIMD optimised matrix multiplications for on-cache tensors. It is worth mentioning that, chaining multiple operations of level 3 BLAS as shown in Listing 9.7, is a fundamentally rare feature for generic tensor algebra libraries. Fastor leverages from this by virtue of being domain specific. Similarly, for computing the first Piola-Kirchhoff stress tensor, Fastor detects the following expression, shown in Listing 9.8.

Listing 9.8: A single expression for computing the Piola-Kirchhoff stress tensor

```
BinaryAddOp<Sigma_F, BinaryAddOp<BinaryCrossOp<Sigma_H,F>, BinaryMulOp<Sigma_J,H>>>
```

Evaluation of this expression requires a single transparent loop within the quadrature loop nest, which also gives rise to a myriad of other optimisation possibilities other than vectorisation, as shown in Figure 9.3. The same concept is applied for the computation of other variables such as electric field and the Hessian.<sup>4</sup>

Based on our initial set up explained at the start of the section, synthetic finite element examples are manufactured based on two meshes, one triangular mesh and one tetrahedral mesh, respectively, as shown in Figure 9.10. Moreover, careful attention is paid to the assembly code generated by the compilers. However, for the purpose of brevity, only the results from the Intel compiler with “`-O3 -xHost`”, are presented here. All the benchmarks in this section are carried out with double precision floating point. For high order elements, nodal Lagrange basis functions with optimal nodal placements [254, 323] are chosen, to guarantee the stability and  $p$ -convergence property of the basis functions. These correspond to Fekete point nodal distribution for triangles and Warburton nodes for tetrahedra. Furthermore, the optimal quadrature scheme for triangles and tetrahedra presented in [323] is employed.

Table 9.6 and Table 9.7 show the speed-ups achieved using Fastor over the other implementations for the triangular mesh and the tetrahedral mesh, respectively. As can be observed

$p$	Mooney-Rivlin Model		Electroelastic Model 1		Electroelastic Model 2	
	Explicit SIMD	Auto-Vectoriser	Explicit SIMD	Auto-Vectoriser	Explicit SIMD	Auto-Vectoriser
$p = 1$	1.32	1.598	1.734	1.135	2.168	1.661
$p = 2$	1.226	1.758	1.645	1.336	1.982	1.77
$p = 3$	1.177	1.924	1.497	1.528	1.856	1.912
$p = 4$	1.132	2.064	1.485	1.747	1.723	1.972
$p = 5$	1.145	2.095	1.366	1.667	1.595	1.928
$p = 6$	1.089	2.085	1.334	1.93	1.517	2.202

Table 9.6: Speed-ups achieved in numerical integration using Fastor over other implementations for the 2D triangular mesh

$p$	Mooney-Rivlin Model			Electroelastic Model 1			Electroelastic Model 2		
	Explicit SIMD	Auto-Vectoriser	Classic	Explicit SIMD	Auto-Vectoriser	Classic	Explicit SIMD	Auto-Vectoriser	Classic
$p = 1$	1.462	2.226	5.514	1.928	2.51	4.63	1.591	2.054	3.004
$p = 2$	1.964	3.52	6.711	1.957	3.358	5.181	1.7	1.978	3.208
$p = 3$	1.183	3.321	6.277	1.582	3.341	5.815	1.643	2.813	4.294
$p = 4$	1.506	4.89	7.557	1.401	3.674	5.367	1.505	3.021	4.26
$p = 5$	1.604	6.114	8.313	1.362	4.063	5.397	1.485	3.474	4.44
$p = 6$	2.009	5.96	7.382	1.247	4.171	5.034	1.267	3.214	3.971

Table 9.7: Speed-ups achieved in numerical integration using Fastor over other implementations for the 3D tetrahedral mesh

from Table 9.6 (corresponding to the two-dimensional case with triangular mesh), for Mooney-Rivlin model, where the constitutive law is simpler and the number of operators to chain within the quadrature nest is small, most of the performance comes from SIMD vectorisation. However, for the two electroelastic models, where the constitutive law is significantly complex and the number of operators to chain are large, up to 85% of the performance of Fastor comes from operator chaining; see Figure 9.9(a,b,c) for a visual representation.

<sup>4</sup>In fact, as a part of the smart expression template engine for a domain specific tensor contraction framework, it is possible to decessively change the evaluation policies of the expressions (as described in subsection 9.2.4) such that specific quantities of interest can be computed as a single kernel. This facilitates locality of reference which has a significant importance in SIMD and GPU computing.

A counter-intuitive finding from Figure 9.9 is that, at high polynomial degrees, the effect of explicit vectorisation is more pronounced than operator chaining. However, by studying the quadrature nest shown in Listing 9.6, one can observe that most of the tensors within the nest are small (of size  $d \times d$  where the  $d = 2, 3$  is the spatial dimension of the problem). In the absence of operator chaining and at low polynomial degrees, Fastor attempts to generate vectorised code for every operator individually by strictly aligning the operands pointers at 16B or 32B boundaries, depending on the vectorisation level. This is too strict of a requirement, that eventually forces the compiler to insert further paddings in order to avoid cache spills. This destroys the data locality and hence impacts the run time. However, as seen in Table 9.6, if the decision of vectorisation is left to the auto-vectoriser, the compiler tries to be much more conservative about vectorisation. Alternatively if the operators are chained and then vectorised as a single expression, the combined benefit of both paradigms (vectorisation and operator-chaining) can be harnessed. The conclusion drawn from this observation is that, operator chaining is essential for maintaining data locality in the quadrature nest.

At high polynomial degrees, most of the simulation time is consumed in computing the deformation gradient tensor  $\mathbf{F}$ , which mainly involves the three `matmul` functions in Listing 9.6. Despite being a Fastor smart expression (as explained earlier), the cost of matrix-matrix multiplications is certainly going to dominate the computation time as the sizes of `GradBases`, `LagrangeElemCoords` and `EulerElemCoords` are much bigger compared to the rest of the variables within the quadrature loop. Operator chaining effect, while present is going to be a fraction of the cost of `matmuls` between larger tensors. Accelerating the local matrix-matrix multiplication kernels within the quadrature loop is also studied in [326].

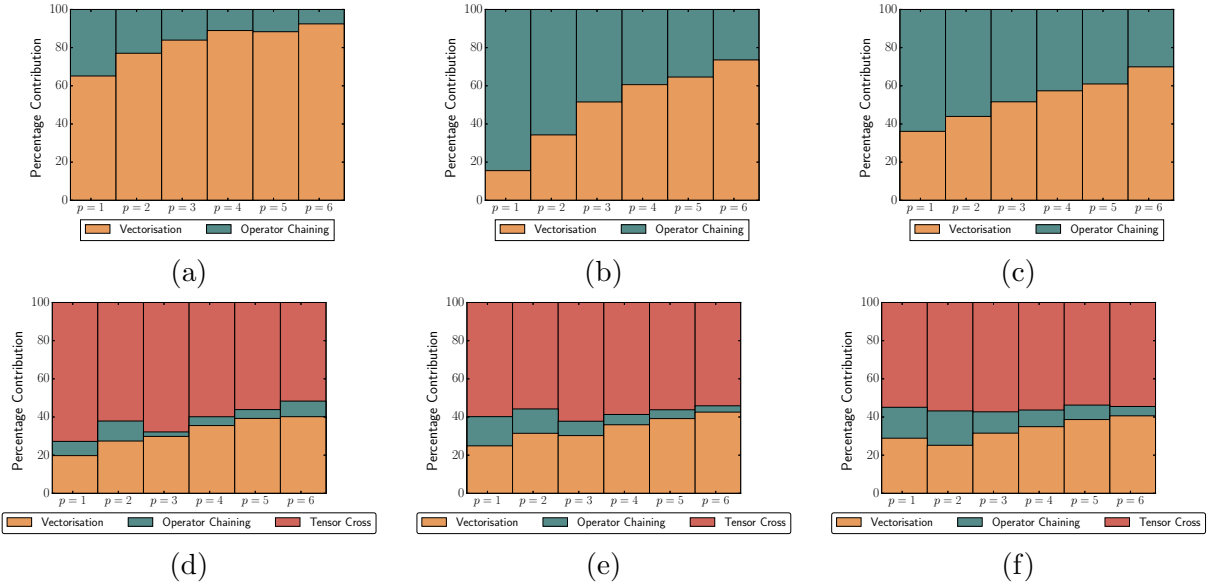


Figure 9.9: Contribution percentile of different optimisations for numerical integration using Fastor; (a), (b), (c) for triangular mesh and (d), (e), (f) for tetrahedral mesh.

For the three-dimensional problems (tetrahedral mesh), similar performance traits can be observed as shown in Table 9.7 and Figure 9.9(d,e,f). However, here the effect of zero-elimination using the bespoke tensor cross product kernels comes into play. Note that, straightforward implementation of the tensor cross product is  $d^6$  in computational complexity and  $d^4$  in memory access, implying that it is dimension dependent and independent of the polynomial degree. As a result, a rather constant speed-up is observed using the optimised tensor cross product kernels. It is worth mentioning that, while a different approach to performing numerical integration could be employed, the aforementioned results can be used as indicative numbers, of what is possible by relying on explicit tensor manipulations.

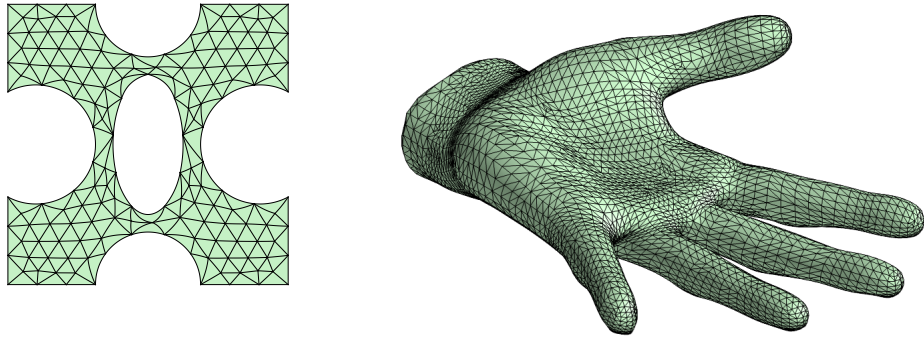


Figure 9.10: Meshes used for finite element benchmarks, a) A curved mechanical component [254] and b) Artificial hand used for simulating electrostriction [233].

#### 9.4.1 Kernel-based data parallel code generation for electromechanics on curvilinear meshes

Having studied the  $h$  and  $p$  convergence properties of the computational framework and its performance with respect to mixed variational principles in earlier chapters, the objective of this example is to present some implementation details of the framework. The present high order curvilinear finite element framework is tied and closely developed on top of **Fastor** library [251]. Fastor (<https://github.com/romeric/Fastor>) is an open source (MIT licensed) C++ based generic tensor contraction library that can perform heavy numerical computations such as mathematical/algorithmic transformations and graph optimisations at compile time using a powerful in-built expression template engine. The transformed algorithms are then used by Fastor to generate data parallel (SIMD-vectorised) code for modern CPU and potentially GPU architectures. Recently, it has been shown in [251] that Fastor is able to generate carefully crafted data parallel code (SSE-SSE4.2, AVX-AVX2-AVX512, FMA) for the local assembly of low and high order finite elements for a series of convex multi-variable electro-elastic models, exhibiting manyfold performance improvement over hand-written C code. As described earlier, since convex multi-variable electro-elasticity models require Legendre transformation through a Newton-Raphson scheme per quadrature point to find the appropriate constitutive tensors, local assembly of the finite elements become a critical hotspot for performance optimisations (see [254, 251] for performance benchmarks). In fact, if the solver time is discarded, for complicated material models it can be shown that, 80% of the computational time is spent in local assembly (numerical integration) of the finite element matrices.

To this effect, a problem is manufactured where the performance of the current framework (using Fastor) is studied and compared to the equivalent hand-optimised C code. This problem pertains only performance studies of numerical integration of work-conjugates (4.31), Hessian (4.36) and the subsequent quadrature point Newton-Raphson required for the Legendre transform (4.61), during local assembly (also see Algorithm 1). A set of similar benchmark problems has been presented in the author's previous work on Fastor [251], where explicit code snippets for the aforementioned set of operations are presented. The interested reader is advised to consult Poya et. al. [251] and Fastor's repository, for a series of such performance studies, as for the purpose of brevity, complete implementation details of the problem are not presented here.

This performance study considers both curved hexahedral and tetrahedral meshes. The geometry considered for the problem is that of an electromechanical component shown in Figure 9.11 together with curved meshes. For the purpose of benchmark, refined meshes are chosen such that distortion qualities are all almost unity.

Note that the tetrahedral and hexahedral meshes do not have the same number of nodes. The relevant information regarding the meshes is listed in Table 9.8. The geometry essentially consists of two plates connected through an extruded arc/fillet (in the  $z$  direction). No

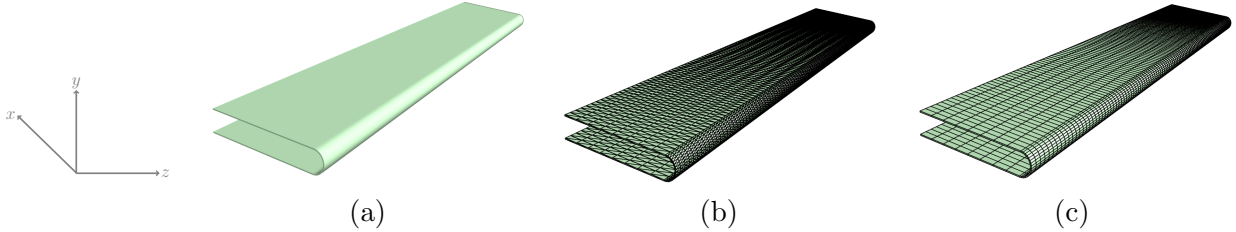


Figure 9.11: a) CAD geometry, b) curved tetrahedral mesh and, c) curved hexahedral mesh for electromechanical component with 1m thickness, 20m height ( $y$ -axis), 100m width ( $x$ -axis) and 500m length ( $z$ -axis)

boundary conditions have been applied on the arc part of the geometry. The electromechanical component is mechanically fixed at one longitudinal end and two different electric voltages are applied across the thickness of the top and bottom plates, namely  $4.5 \times 10^7 V$  for the top plate and  $8.1 \times 10^7 V$  for the bottom plate. The problem exhibits massive snap-back behaviour as the different applied voltages make the component bend initially but after the point of electromechanical instability the difference in displacements in both plates causes the component to deform in the opposite direction.

Mesh (N. Elements)	$p/q = 2$	$p/q = 3$	$p/q = 4$	$p/q = 5$	$p/q = 6$	$p/q = 7$	$p/q = 8$
Tetrahedral (43200)	367196	1223568	2689668	5082200	8366140	12921312	18777812
Hexahedral (7200)	351276	1048144	2322900	4348344	7297276	11342496	16656804

Table 9.8: Degrees of freedom associated with each polynomial degree for tetrahedral and curvilinear meshes

To study the performance of numerical integration, the stabilised convex multi-variable model (6.8) is chosen with material properties listed in Table 6.1. The problem is then analysed under the aforementioned boundary conditions and the performance of numerical integration of work-conjugates  $\Sigma_V$  (4.31), Hessian and constitutive tensors of the internal energy  $\mathcal{C}$ ,  $\mathcal{Q}$ ,  $\theta$  (4.37) and the quadrature point Newton-Raphson required for the Legendre transform (4.61) to obtain the constitutive tensors of Helmholtz energy  $\mathcal{C}_\Phi$ ,  $\mathcal{Q}_\Phi$ ,  $\theta_\Phi$  are monitored under three different compilation flags. These correspond to the same code compiled with `-O3 -march=native` but with auto-vectorisation turned off (i.e. `-fno-tree-vectorize` for gcc, `-fno-vectorize` for LLVM's clang and `-no-vec` for Intel's ICC), same code compiled with `-O3 -march=native` where the compiler is permitted to auto-vectorise the code and Fastor transformed code compiled with `-O3 -march=native`. All performance measurements have been recorded on a single core of Intel(R) Xeon(R) CPU E5-2650 v2 @2.60GHz with AVX instruction sets, 20MB private L1-cache and 32GB memory, running Ubuntu 16.04 and GCC-7, LLVM's Clang 4.0 and ICC 17.0.3 are used to compile all the codes. To keep the comparison fair, careful attention is paid to the compilers generated assembly code.

Figure 9.12 shows the relative speed of the code (with and without auto-vectorisation) in comparison to Fastor's generated code with all the three aforementioned compilers. Since with every polynomial enrichment the quadrature order has to be increased accordingly, as a result the computational cost of numerical integration increases almost cubically for all the cases (for three-dimensional problems). Nevertheless, Fastor's data parallelism falling into the category of latency hiding techniques, hides much of this computational complexity. For both hexahedra and tetrahedra, Fastor's SIMD vectorised code shows consistently nearly 2X speed-up over compilers auto-vectorised code on an AVX capable processor and 3-3.5X speed up over non-vectorised (but well-optimised) code. It can also be seen from the figures, that unlike Fastor, auto-vectorisation is compiler specific and in some cases the code may not benefit from it, specifically with Intel's ICC in this case, Figure 9.12(e,f). On the other hand, Fastor is extremely less sensitive to the compiler (and optimisations) used. This is potentially the ultimate speed-up achievable for non-trivial codes using data parallelism on AVX architectures

over non-vectorised codes (ideal speed-up is 4X for double precision). For complex algorithms, such as numerical integration of convex multi-variable electro-elastic models, compile time code transformation and graph search optimisation are necessary to be able to achieve this performance. One again, these aspects of Fastor library are presented and benchmarked in detail in [251].

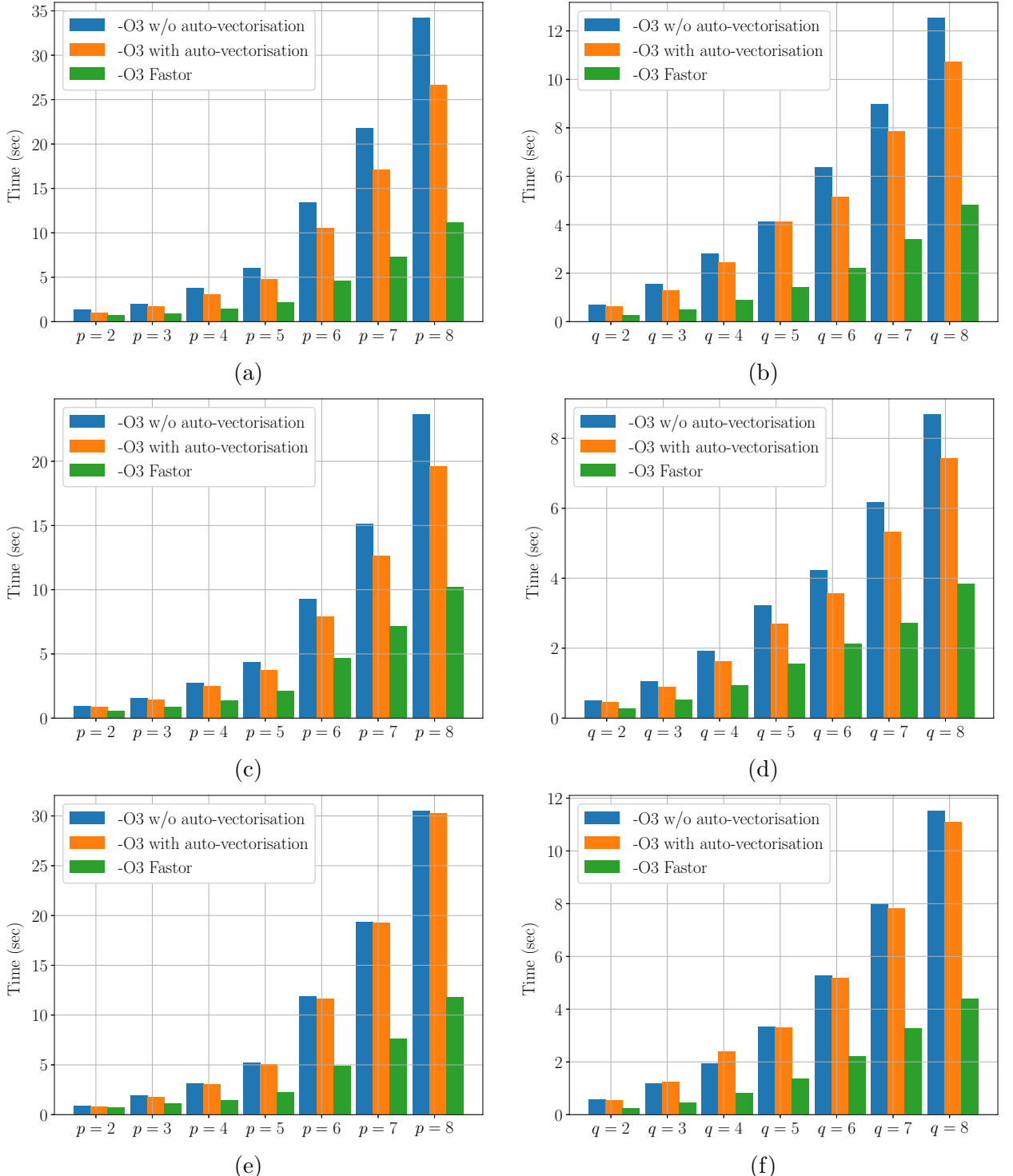


Figure 9.12: Speed-up achieved by compile time algorithmic transformation and data parallelism for numerical integration of work-conjugates and Hessian of convex multi-variable electro-elastic model (6.8) with high order curved tetrahedral and hexahedral meshes with compilers a,b) GCC, c,d) LLVM's Clang and, e,f) Intel's ICC

Finally, Figure 9.13 shows the evolution of voltage induced hydrostatic pressure  $p_{hyd}$  at

different loading stages, for  $q = 3$  hexahedral mesh. Notice the massive snap-back behaviour of system and butterfly shape it occupies at the final deformed configuration.

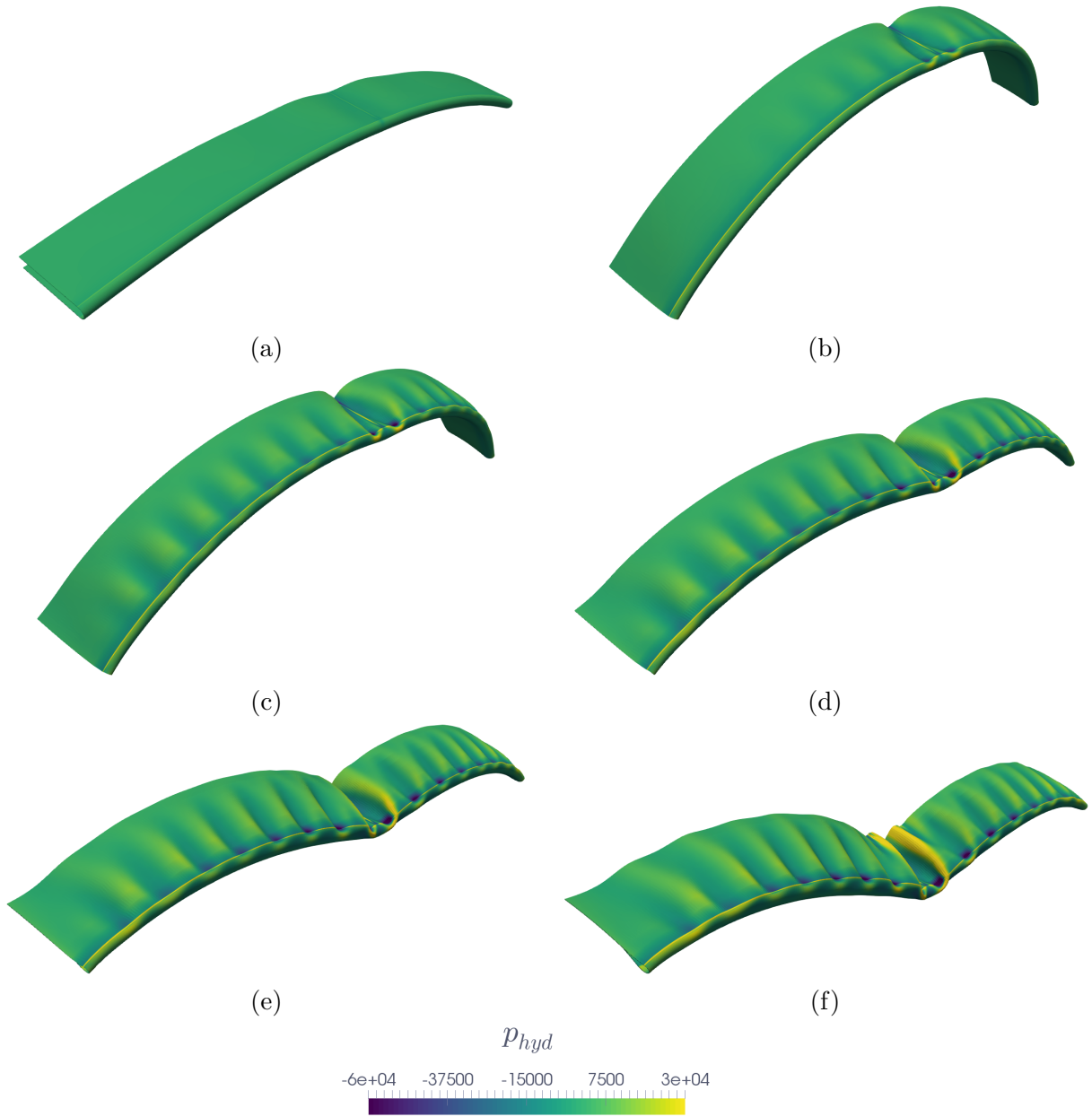


Figure 9.13: Evolution of voltage induced hydrostatic pressure  $p_{hyd}$  in electromechanical component with accumulated load factor  $\Lambda$  being a)  $\Lambda = 0.416$  b)  $\Lambda = 0.806$ , c)  $\Lambda = 0.889$ , d)  $\Lambda = 0.944$ , e)  $\Lambda = 0.972$  and, f)  $\Lambda = 1.0$ . Note that in the figures shown, the electromechanical component is mirrored along the  $z$ -axis

## 9.5 Conclusions

A domain specific data parallel tensor contraction framework for numerical analysis of coupled and multi-physics applications is presented. The framework encompasses tensor contraction of isomorphic and nonisomorphic tensor networks by relying on explicit vectorisation using SIMD vector types. Furthermore, the in-built smart expression template engine performs compile time operation minimisation technique using mathematical transformation for named chained operators and depth-first or breadth-first constructive approach for un-named operators on

tensor networks. The framework utilises heavy compile technologies to perform aggressive loop optimisation, which in certain cases can completely eliminate the run time memory I/O. Benchmark examples presented show optimal SIMD speed-ups for contraction of arbitrary order tensors on a recent Intel processor using three different compilers. Finally, finite element examples involving kernel-based numerical integration of complex convex multi-variable energy functional are carried out in two and three dimensions, where all the features of the current tensor contraction framework are utilised, in particular, the effect of operator chaining and launching vectorised kernels, is shown to be paramount. In this context, numerical examples presented, confirm significant speed-ups over the classical approaches.



## **Concluding Remarks & Future Outlook**

# Chapter 10

# Concluding Remarks & Future Outlook

## 10.1 Concluding Remarks

The work presented in this thesis, deals with three fundamental issues pertaining to the computational modelling of coupled electromechanical system. Firstly, the problem of accurate geometrical representation is considered. Recent advances in isogeometric BSplines and TSpline analysis, NURBS-enhanced methods and subdivision surfaces make it possible to embed finite element technology into a CAD description and glue computer aided design and finite element analysis tightly. However, in this process the bigger portion of the numerical analysis based on standard finite element is left out of consideration. Development of these technologies in the recent past have happened in parallel to the high order finite element methods instead and their seems to have been little effort in combining legacy finite elements with an adequately accurate geometrical design. In this thesis, an approach to accurately represent the geometry in standard finite elements is presented. To this end, the problem of generating curvilinear meshes which are required for high order finite element analysis is undertaken. As a matter of consequence, a curvilinear high order mesh generator for high order finite elements is developed using a metric controlled polyconvex mechanics analogy and using the finite element itself. The use of polyconvex elasticity to deform meshes with planar faces to curve faces seems to provide good quality high order volume meshes due to the fact that the fundamental distortion measures of deformation are already encoded in the definition of polyconvex elastic material model. The convergence properties of the finite element scheme on these meshes is shown to be dependent on these fundamental metrics, namely the edge distortion metric, face distortion metric and volume distortion metric. A series of  $h$  and  $p$  convergence studies have been carried out for Poisson type problems, elasticity problems and electroelasticity problems on these meshes using different continuum mechanics analogies, different polyconvex and non-polyconvex material models with isotropic, anisotropic and boundary layer meshes. The scalability of the platform is shown through the generation of high order curved computational meshes with millions of nodes.

Putting the technique into practice, the second part of the thesis deals with the development of a curvilinear finite element technique for four classes of coupling in electromechanics. The first class is the large deformation large electric field electromechanics, typically suitable for modelling massive deformations observed in Electro-Active Polymers (EAPs) and in particular Dielectric Elastomers (DEs). The recently developed convex multi-variable electro-elasticity is employed to model the large deformation characteristics of DEs and through exhaustive numerical simulations, massive deformations, instabilities in the form wrinkling, snap-through and pull-in instabilities are shown to be captured extremely well using the curvilinear high order displacement potential technique for convex multi-variable electro-elasticity.

The second class of electromechanics discussed is linearised electrostriction with nonlinear electrostatic response. The point of departure for modelling linearised electrostriction once

again lies in the convex multi-variable energies which are consistently linearised and particularised for the case of small strains. A staggered scheme is developed to solve the nonlinear equations of electrostatics which is then coupled incrementally (non-iteratively) with the equations of elasticity providing significantly superior performance to the fully monolithic approach. Through numerical examples it is shown that the method is capable of capturing excessively large displacements as long as the strains remain small. Once again the curvilinear high order finite element scheme is utilised for this staggered approach.

The third class of electromechanics discussed is the most well established linear piezoelectricity. Due to the physical applications of this class in simplified settings and structurally reduced models a new variational and computational framework is introduced for the analysis of three dimensional linear piezoelectric beams using  $hp$ -finite elements is presented. The framework is suitable for static, modal and dynamic scenarios; it is not restricted to either actuation or energy harvesting applications and, moreover, it can cope with any anisotropy or electric polarisation orientation. Derived from first principles, namely the fundamental equations of continuum piezoelectricity, a new set of beam balance equations is presented based on a Taylor series expansion for the displacement and electric potential across the cross section of the beam. The coupled nature of the piezoelectric phenomenon at a beam level arises via a series of mechanical (and electrical counterparts) stress and strain cross sectional area resultants. To benchmark the numerical algorithm, and in order to aid prospective researchers, a new closed-form solution is presented for the case of cantilever type systems subjected to end tip mechanical/electrical loads. Finally, some numerical aspects of the  $hp$ -discretisation are investigated including the exponential convergence of the  $hp$ -refinements and the consideration of linear or quadratic electric potential expansions across the cross section of the beam.

Immediately following the linear piezoelectricity is the fourth class of electromechanics discussed on size dependent linear piezoelectricity or better known as flexoelectricity. Once again, an effort is made to develop a family of numerical models for the phenomenological linear flexoelectric theory for continua and their particularisation to the case of three-dimensional beams based on a skew-symmetric couple stress theory. In contrast to the traditional flexoelectric models based on standard strain gradient wherein coupling between electric polarisation and strain gradients is assumed, we postulate an electric enthalpy in terms of linear invariants of curvature and electric field. This is achieved by introducing the axial curvature vector as a strain gradient measure. We have shown that the implication of this assumption is many-fold. Firstly, for isotropic (non-piezoelectric) materials it allows constructing flexoelectric energies without breaking material symmetry. Secondly, nonuniform distribution of volumetric part of strains (volumetric strain gradients) do not generate electric polarisation, as confirmed by experimental evidence to be the case for some important classes of flexoelectric materials. In this regard, the current flexoelectric model can be considered as a more restrictive case of strain gradient theories. Thirdly, a state of plane strain generates out of plane deformation through strain gradient effects. Finally, extension and shear coupling modes cannot be characterised individually as they contribute to the generation of electric polarisation as a whole. For the case of three-dimensional beams, we have shown that the skew-symmetric couple stress model in general, generate stresses spanned over the cross section rather than aligned with the longitudinal axis of the beam and as a result special care must be taken to integrate them over the cross section. Four distinct variational principles are presented for both continuum and beam models namely, a displacement-potential formulation, a penalty formulation, a Lagrange-multiplier formulation and an augmented Lagrangian formulation. The three later formulations facilitate incorporation of strain gradient measures in to a standard finite element scheme while maintaining the  $C^0$  continuity. To this end, the efficacy of high order finite elements along with the computational efficiency of mixed finite elements have been utilised to develop a series of low and high order mixed finite element schemes for couple stress based flexoelectricity. Numerical results of finite element discretisations for the three latter variational formulations are first benchmarked against available closed form solutions in regards where good agreements was found between the reference and numerical results. Furthermore, a detailed comparison of

the developed couple stress based flexoelectric model with the standard strain gradient flexoelectric models has been performed for the case of Barium Titanate where a myriad of simple analytical solutions have been proposed in order to quantitatively describe the similarities and dissimilarities in effective electromechanical coupling under these two theories. It is observed that, if the same experimental flexoelectric constants are fitted in to both theories, the current couple stress theory in general, reports stronger electromechanical conversion efficiency. This is mainly due to the fact that, most flexoelectric problems involve bending and flexural deformation and, as a result, the axial curvature vector responsible for generating electric polarisation is much more pronounced in these cases.

The final and third part of the thesis deals with the high performance implementation of electromechanics using a generic domain-aware tensor contraction framework. In order to have a unified base for developing high performance kernels for all classes of electromechanics discussed, a new high performance tensor contraction framework for the numerical analysis of coupled electromechanics on streaming architectures is presented. In addition to explicit SIMD instructions and smart expression templates, the framework introduces domain specific constructs for the tensor cross product and its associated algebra. The two key ingredients of the presented expression template engine are as follows. First, the capability to mathematically transform complex chains of operations to simpler equivalent expressions, while potentially avoiding routes with higher levels of computational complexity and, second, to perform a compile time depth-first or breadth-first search to find the optimal contraction indices of a large tensor network in order to minimise the number of floating point operations. For optimisations of tensor contraction such as loop transformation, loop fusion and data locality optimisations, the framework relies heavily on compile time technologies rather than source-to-source translation or JIT techniques. Every aspect of the framework is examined through relevant performance benchmarks, including the impact of data parallelism on the performance of isomorphic and nonisomorphic tensor products, the FLOP and memory I/O optimality in the evaluation of tensor networks, the compilation cost and memory footprint of the framework and the performance of tensor cross product kernels. The framework is then applied to finite element analysis of coupled electro-mechanical problems to assess the speed-ups achieved in kernel-based numerical integration of complex electroelastic energy functionals. In this context, domain-aware expression templates combined with SIMD instructions are shown to provide a significant speed-up over the classical low-level style programming techniques.

## 10.2 Future Outlook

In line with the theme of this work, we will once again divide our future outlook in further development of the platform presented in the thesis into three parts

- 1. High order curvilinear mesh generation:** The multi-level curvilinear mesh deformation technique discussed in the thesis despite being able to generate extremely good quality meshes is not designed to enforce the fundamental metrics in either a strong or weak form on to the meshes. It is merely designed to employ these metrics using a poly-convex definition of the internal energy. We are certain that for complicated geometries a two-step strategy should be employed in such a way that the first step would consist of deforming the mesh using the solid mechanics analogy and in the second step a mesh enhancement procedure would be undertaken once again using the solid mechanics analogy. However, in the second step the metrics would be enforced weakly using a mixed variational principles guaranteeing the fulfilment of the desired qualities.
- 2. Fluid-structure interaction for electromechanics:** Dielectric elastomers have a promising future in biomedical applications, where they have already been suggested as reliable actuators capable of pumping blood and hence, act as an artificial heart. Immersed or boundary fitted methodologies are reliable numerical techniques for the simulation of these fluid structure interaction scenarios. Alternatively, considering the

effect of vacuum through a FEM-BEM coupling is also an interesting notion that needs to be explored.

3. **Automatic code generation for electromechanics:** High performance computing in the field material science has witnessed a significant growth in the last decade. Automatic code generation from a variational formulation description could be a driving force for building high performance kernels for modelling of materials. The tensor contraction framework described in this thesis, at the moment can only study the topological structure of tensors and can emit extremely efficient data and instruction parallel low-level code from it. Future work in this regard would be focussed on automatically generating code directly from the description of a convex multi-variable electroelastic energy. Other forms of automatic parallelisation would be also explored with an eye to leave minimal to no effort for user intervention.



# Appendices

## Appendix A

# Coefficients of the closed-form solution for piezoelectric beam

The coefficients used in the analytical solution presented in section 7.6 are as follows

$$\begin{aligned}
b_1 &:= \frac{a_2 a_6}{a_1} + a_7, & b_2 &:= \frac{a_3 a_6}{a_1} + a_8, \\
c_1 &:= a_{13} + \frac{a_3 a_{11}}{a_1}, & c_2 &:= a_8 + \frac{a_3 a_6}{a_1}, \\
c_3 &:= a_{10} + \frac{a_5 a_9}{a_4}, & c_4 &:= \frac{a_9}{a_4} - \frac{a_{11}}{a_1} + \frac{a_6 c_1}{a_1 c_2}, \\
b_3 &:= -\frac{c_4}{c_3}, & b_4 &:= \frac{c_1}{c_2 c_3}, \\
b_5 &:= a_{12} - \frac{b_1 c_1}{c_2} + \frac{a_2 a_{11}}{a_1}, & b_6 &:= \frac{a_{11}}{a_1} - \frac{a_6 c_1}{a_1 c_2}, \\
b_7 &:= \frac{c_1}{c_2}, & b_8 &:= \frac{1}{2} \left( \frac{a_{14} a_6}{a_1} + a_{16} \right), \\
b_9 &:= \frac{a_{17}}{2} + \frac{b_8 c_1}{c_2} - \frac{a_{11} a_{14}}{2 a_1}, & k &:= \sqrt{\frac{b_5}{c_3}}, \\
c_5 &:= \frac{1}{2} \left( a_{20} + \frac{a_3 a_{18}}{a_1} \right), & c_6 &:= \frac{b_8 c_5}{c_2} - \frac{a_{21}}{4} - \frac{a_{14} a_{18}}{4 a_1}, \\
k_1 &:= \sqrt{\frac{a_{24}}{c_6}}, & c_7 &:= \frac{a_{19}}{2} - \frac{c_5 b_1}{b_2} + \frac{a_2 a_{18}}{2 a_1}, \\
c_8 &:= \frac{a_{21}}{4} - \frac{b_8 c_5}{b_2} + \frac{a_{14} a_{18}}{4 a_1}, & c_9 &:= \frac{a_{18}}{2 a_1} - \frac{a_6 c_5}{a_1 b_2}, \\
m_1 &:= \frac{c_7 - a_{23}}{c_8}, & m_2 &:= \bar{Q}^m \frac{c_9}{c_8} + \bar{Q}^e \frac{c_5}{b_2 c_8} - \beta|_{x=l} \frac{c_7}{c_8},
\end{aligned}$$

## Appendix B

# Couple stress theories and constitutive laws for linear flexoelectricity

### B.1 The indeterminate couple stress theory and its relation to the classical Cosserat theory

The theory in this section is a reiteration of the classical couple stress model briefly discussed here for the convenience of the reader. In classical linear elasticity due to symmetry of strains ( $\boldsymbol{\varepsilon}$ ) an isotropic material is fully described with only two strain invariants. However, when the strain tensor is non-symmetric ( $\tilde{\boldsymbol{\varepsilon}}$ ), at least three invariants are needed to describe an isotropic solid. Hence, the free energy takes the form, [227, 136]

$$\begin{aligned} W^{iso}(\tilde{\boldsymbol{\varepsilon}}, \tilde{\boldsymbol{\chi}}) &= W_{\tilde{\boldsymbol{\varepsilon}}}^{iso}(\tilde{\boldsymbol{\varepsilon}}) + W_{\tilde{\boldsymbol{\chi}}}^{iso}(\tilde{\boldsymbol{\chi}}) \\ &= \frac{\mu + \mu_c}{2} \tilde{\boldsymbol{\varepsilon}} : \tilde{\boldsymbol{\varepsilon}} + \frac{\mu - \mu_c}{2} \tilde{\boldsymbol{\varepsilon}} : \tilde{\boldsymbol{\varepsilon}}^T + \frac{\lambda}{2} (\text{tr} \tilde{\boldsymbol{\varepsilon}})^2 \\ &\quad + \frac{\zeta + \eta}{2} \tilde{\boldsymbol{\chi}} : \tilde{\boldsymbol{\chi}} + \frac{\zeta - \eta}{2} \tilde{\boldsymbol{\chi}} : \tilde{\boldsymbol{\chi}}^T + \frac{\alpha}{2} (\text{tr} \tilde{\boldsymbol{\chi}})^2, \end{aligned} \quad (\text{B.1})$$

where  $\mu$  and  $\lambda$  are Lamé constants and  $\mu_c, \zeta, \eta$  and  $\alpha$  are four additional material parameters known as Cosserat constants. The constant  $\mu_c$  is called the Cosserat's coupled modulus. If we additively decompose  $\nabla \mathbf{u}$  and  $\nabla \boldsymbol{\omega}$  into their symmetric and skew-symmetric parts

$$\nabla \mathbf{u} = \nabla^{sym} \mathbf{u} + \nabla^{skew} \mathbf{u}, \quad \nabla \boldsymbol{\omega} = \nabla^{sym} \boldsymbol{\omega} + \nabla^{skew} \boldsymbol{\omega}, \quad (\text{B.2})$$

and substitute in (B.1), we obtain

$$\begin{aligned} W_{ce}^{iso}(\tilde{\boldsymbol{\varepsilon}}, \tilde{\boldsymbol{\chi}}) &= \mu \|\nabla^{sym} \mathbf{u}\|^2 + \mu_c \|\hat{\boldsymbol{\omega}} - \nabla^{skew} \mathbf{u}\|^2 + \frac{\lambda}{2} \|\nabla \cdot \mathbf{u}\|^2 \\ &\quad + \zeta \|\nabla^{sym} \boldsymbol{\omega}\|^2 + \eta \|\nabla^{skew} \boldsymbol{\omega}\|^2 + \frac{\alpha}{2} \|\nabla \cdot \boldsymbol{\omega}\|^2. \end{aligned} \quad (\text{B.3})$$

At the limit when the Cosserat couple modulus  $\mu_c \mapsto \infty$ , the effect of microstructure would be too rigid to be incorporated in the strain energy  $W_{\tilde{\boldsymbol{\varepsilon}}}^{iso}(\tilde{\boldsymbol{\varepsilon}})$  and one can constrain the rotations as

$$\hat{\boldsymbol{\omega}} - \nabla^{skew} \mathbf{u} = \mathbf{0} \quad \Rightarrow \quad \boldsymbol{\omega} = \frac{1}{2} \nabla \times \mathbf{u}, \quad (\text{B.4})$$

which renders

$$\nabla \cdot \boldsymbol{\omega} = \frac{1}{2} \nabla \cdot (\nabla \times \mathbf{u}) = 0, \quad (\text{B.5})$$

leaving the parameter  $\alpha$  indeterminate. Also called the *Cosserat theory of constrained rotations*, this model was first introduced by [215], discussed in [305], and elaborated lucidly by [154]; hence it is also referred to as the Mindlin-Toupin-Koiter theory. The strain and curvature tensors now become

$$\tilde{\boldsymbol{\varepsilon}} = \nabla \mathbf{u} - \nabla^{skew} \mathbf{u} = \nabla^{sym} \mathbf{u} = \boldsymbol{\varepsilon}, \quad (\text{B.6})$$

$$\tilde{\boldsymbol{\chi}} = \nabla \boldsymbol{\omega} = \frac{1}{2} \nabla (\nabla \times \mathbf{u}) \quad (\text{B.7})$$

Hence, in couple stress theory, the strain tensor is symmetric and the curvature tensor as seen in (B.5) is solenoidal. Also note that in the modified couple stress theory [330], the curvature tensor is symmetric, meaning that the parameter  $\eta$  in (B.1) also vanishes and the curvature energy considered is then the *weakest* possible in [227, 137] sense.

## B.2 Constitutive equations for isotropic and anisotropic couple stress flexoelectric materials

In this section, the constitutive equations for isotropic and anisotropic couple stress based linear flexoelectric material models are presented, based on [117]. For the anisotropic case the constitutive equations are given both in terms of the curvature vector and its dual, Table B.1. Note that the following relationships exist between material tensors and their duals

Description	Isotropic	Anisotropic
Enthalpy	$\Psi^{iso}(\varepsilon_{ij}, \chi_i, E_i) = \mu \varepsilon_{ij} \varepsilon_{ij} + \frac{\lambda}{2} \varepsilon_{kk} \varepsilon_{ll} + 8\eta \chi_i \chi_i - 4\bar{f} \chi_i E_i - \frac{1}{2} \epsilon_{ij} E_i E_j$	$\Psi^{anis}(\varepsilon_{ij}, \hat{\chi}_{ij}, E_i) = \frac{1}{2} \mathcal{C}_{ijkl} \varepsilon_{ij} \varepsilon_{kl} + \frac{1}{2} \hat{\mathcal{B}}_{ijkl} \hat{\chi}_{ij} \hat{\chi}_{kl} + \hat{\mathcal{D}}_{ijkl} \varepsilon_{ij} \hat{\chi}_{kl} - e_{ijk} E_i \varepsilon_{jk} - \hat{f}_{ijk} E_i \hat{\chi}_{jk} - \frac{1}{2} \epsilon_{ij} E_i E_j$ or $\Psi^{*anis}(\varepsilon_{ij}, \chi_i, E_i) = \frac{1}{2} \mathcal{C}_{ijkl} \varepsilon_{ij} \varepsilon_{kl} + \frac{1}{2} \mathcal{B}_{ij} \chi_i \chi_j - \mathcal{D}_{ijk} \varepsilon_{ij} \chi_k - e_{ijk} E_i \varepsilon_{jk} - f_{ij} \chi_i E_j - \frac{1}{2} \epsilon_{ij} E_i E_j$
Force stress	$\sigma_{ij} = 2\mu \varepsilon_{ij} + \lambda \varepsilon_{kk} \delta_{ij}$	$\sigma_{ij} = \mathcal{C}_{ijkl} \varepsilon_{kl} + \hat{\mathcal{D}}_{ijkl} \hat{\chi}_{kl} - e_{kij} E_k$ or $\sigma_{ij} = \mathcal{C}_{ijkl} \varepsilon_{kl} + \mathcal{D}_{ijk} \chi_k - e_{kij} E_k$
Couple stress	$\mu_i = 8\eta \chi_i - 2\bar{f} E_i$	$\hat{\mu}_{ij} = \hat{\mathcal{B}}_{ijkl} \hat{\chi}_{kl} + \hat{\mathcal{D}}_{kl} \varepsilon_{kl} - \hat{f}_{ijk} E_k$ or $\mu_i = \frac{1}{2} (\mathcal{B}_{ij} \chi_j + \mathcal{D}_{jki} \varepsilon_{jk} - f_{ji} E_j)$
Electric Displacement	$D_i = \epsilon E_i + 4\bar{f} \chi_i$	$D_i = \epsilon_{ij} E_j + e_{ijk} \varepsilon_{jk} + f_{ijk} \hat{\chi}_{jk}$ , or $D_i = \epsilon_{ij} E_j + e_{ijk} \varepsilon_{jk} + \hat{f}_{ij} \chi_j$

Table B.1: Constitutive equations for isotropic and anisotropic couple stress based linear flexoelectric materials

$$\begin{aligned} \hat{\mathcal{B}}_{ijkl} &= \frac{1}{4} \xi_{ijm} \xi_{klm} \mathcal{B}_{mn}, & \mathcal{B}_{mn} &= \xi_{ijm} \xi_{klm} \hat{\mathcal{B}}_{ijkl}, \\ \hat{\mathcal{D}}_{ijkl} &= \frac{1}{2} \xi_{mlk} \mathcal{D}_{ilm}, & \mathcal{D}_{ilm} &= \xi_{lkm} \hat{\mathcal{D}}_{ijkl}, \\ \hat{f}_{ijk} &= \frac{1}{2} f_{il} \xi_{kjl}, & f_{il} &= \hat{f}_{ijk} \xi_{kjl}, \end{aligned}$$

with the following restrictions on material tensors

$$\begin{aligned} \mathcal{C}_{ijkl} &= \mathcal{C}_{klij} = \mathcal{C}_{jikl}, & \hat{\mathcal{B}}_{ijkl} &= \hat{\mathcal{B}}_{klij} = -\hat{\mathcal{B}}_{jikl}, & \hat{\mathcal{D}}_{ijkl} &= \hat{\mathcal{D}}_{jikl} = -\hat{\mathcal{D}}_{iklj}, \\ e_{ijk} &= e_{ikj}, & \hat{f}_{ijk} &= -\hat{f}_{ikj}, & \epsilon_{ij} &= \epsilon_{ji}, \end{aligned}$$

or equivalently in their vector form

$$\begin{aligned}\mathcal{B}_{ij} &= \mathcal{B}_{ji}, \\ \mathcal{D}_{ijk} &= \mathcal{D}_{jik}.\end{aligned}$$

Note that in general there is no restriction on flexoelectric tensor  $\mathbf{f}$  and for the most general case, there are 78 distinct material parameters. For isotropic materials, the number of distinct component reduces to 4 material constants and one characteristic length scale. These are the two Lamé constants ( $\lambda, \mu$ ), one permittivity coefficient ( $\epsilon$ ), one flexoelectric coefficient ( $\bar{f}$ ) and the curvature coefficient  $\eta$  is related to  $\mu$  through the characteristic length scale  $l_s$ , such that

$$\mathcal{B}_{ij} = 16\eta\delta_{ij}, \quad \eta = \mu l_s^2, \quad f_{ij} = \bar{f} \delta_{ij}, \quad \epsilon_{ij} = \epsilon \delta_{ij}.$$

## Appendix C

# Boundary conditions, process design and rendering of curvilinear elements

In this section, the issue of applying boundary conditions, post processing and rendering of curvilinear finite element is discussed. Unlike standard finite elements where the boundary conditions are always applied on an a planar mesh approximating the CAD geometry and wherein only the vertices of the mesh are exactly placed on CAD, in curvilinear finite elements it is possible to reconstruct an interpolated surface using the finite element interpolation functions and have a much more accurate representation of the actual CAD boundaries. Particularly, with the developed curved finite element technique it is possible to interact with the CAD model at different stages of the analysis and be able to identify the right topological surfaces to apply the boundary conditions on. Most finite element packages lack a standard interface for applying boundary conditions on the actual model boundaries and instead tend to work on the discretised mesh, which make their scope limited to simple geometries. Figure C.1 shows how the user can apply Dirichlet and/or Neumann boundary condition on a specified region of a CAD model in **Florence**.

In general if the linear mesh and the CAD model are supplied externally from different sources, identifying the right topological surfaces for applying boundary conditions become a time consuming process as an associativity has to be established between the two (smooth and discrete representations). The sub-package of **Florence** for processing curvilinear meshes namely **PostMesh** has multiple algorithms to identify the right CAD surfaces that mesh faces lie on. In general, these algorithms can be categorised as:

1. Axis-aligned bounding box algorithm
2. Projection algorithm
3. Surface-to-surface minimisation algorithm

The axis aligned bounding box technique is fast way to identify mesh faces lying on CAD surfaces, by creating exact bounds for each topological surface. Mesh faces lying on the topological surface will always remain within the box. The projection algorithm is the most standard way of building associativity between smooth and discrete surfaces but suffers from  $O(n^2)$  computational complexity. The surface-to-surface minimisation algorithm is an extremely sophisticated procedure to build the associativity by either reconstructing a smooth representation of the discrete surfaces or by discretising the smooth topology into discrete mesh faces. The interested readers and users can read more about the topic on the **PostMesh** webpage.

Once the surfaces have been identified and reconstructed using the desired curved FEM interpolation degree, further processing of each individual mesh face is necessary to find basic properties of the discrete mesh such as unit normals, mean, Gaussian and principal curvatures etc. This is necessary for applying boundary conditions on curved faces and is done using an

internal tessellation strategy. This tessellation is performed in the isoparametric coordinate using the same FE interpolation degree that is used for geometry and analysis and the transformed to physical space. Figure C.2 shows how unit normals can be computed (necessary for applying pressure type boundary conditions) on a curvilinear  $p = 9$  mesh.

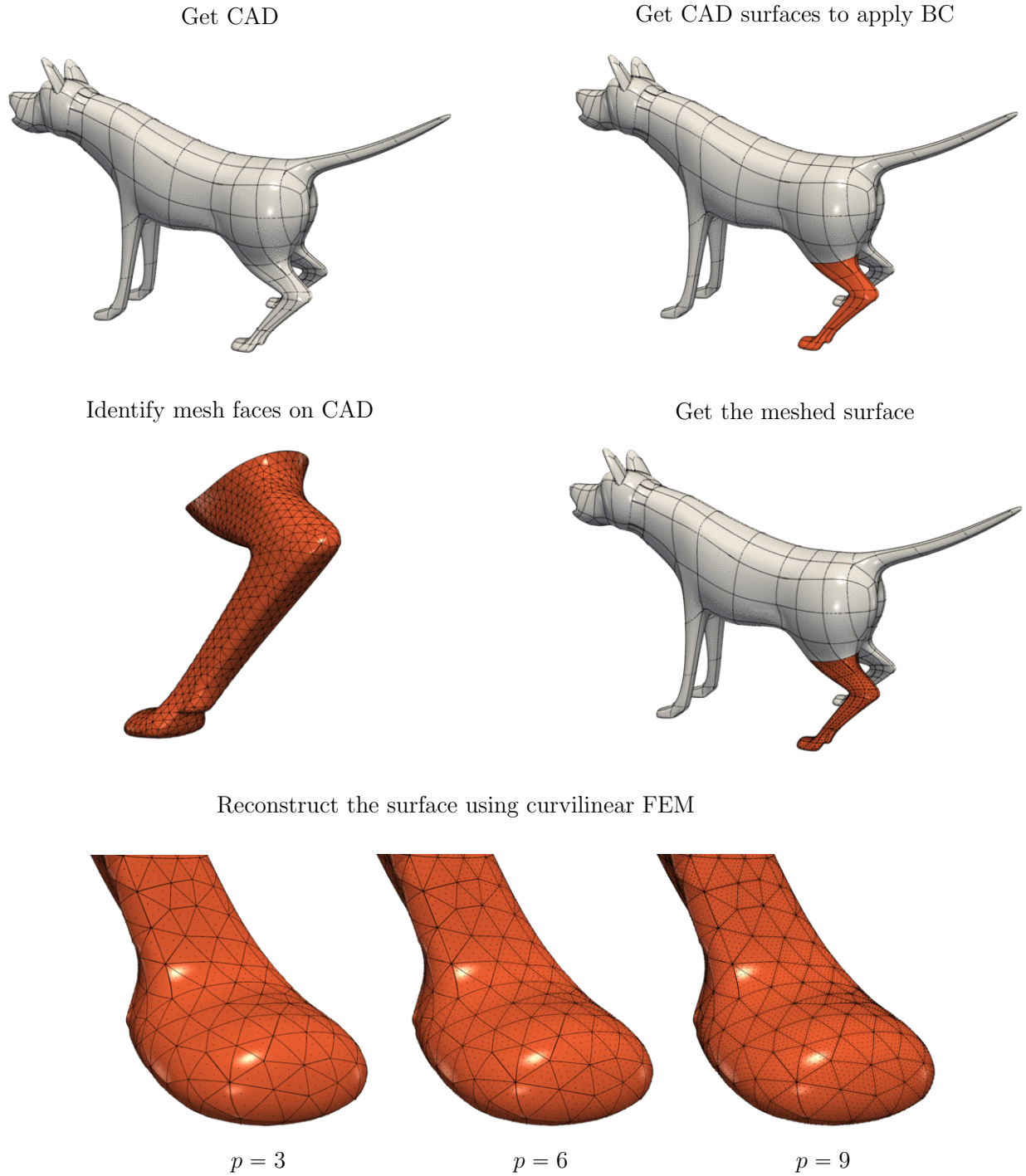


Figure C.1: Procedure to identify associativity between smooth and discrete topologies and reconstruct the smooth topology using curvilinear FEM

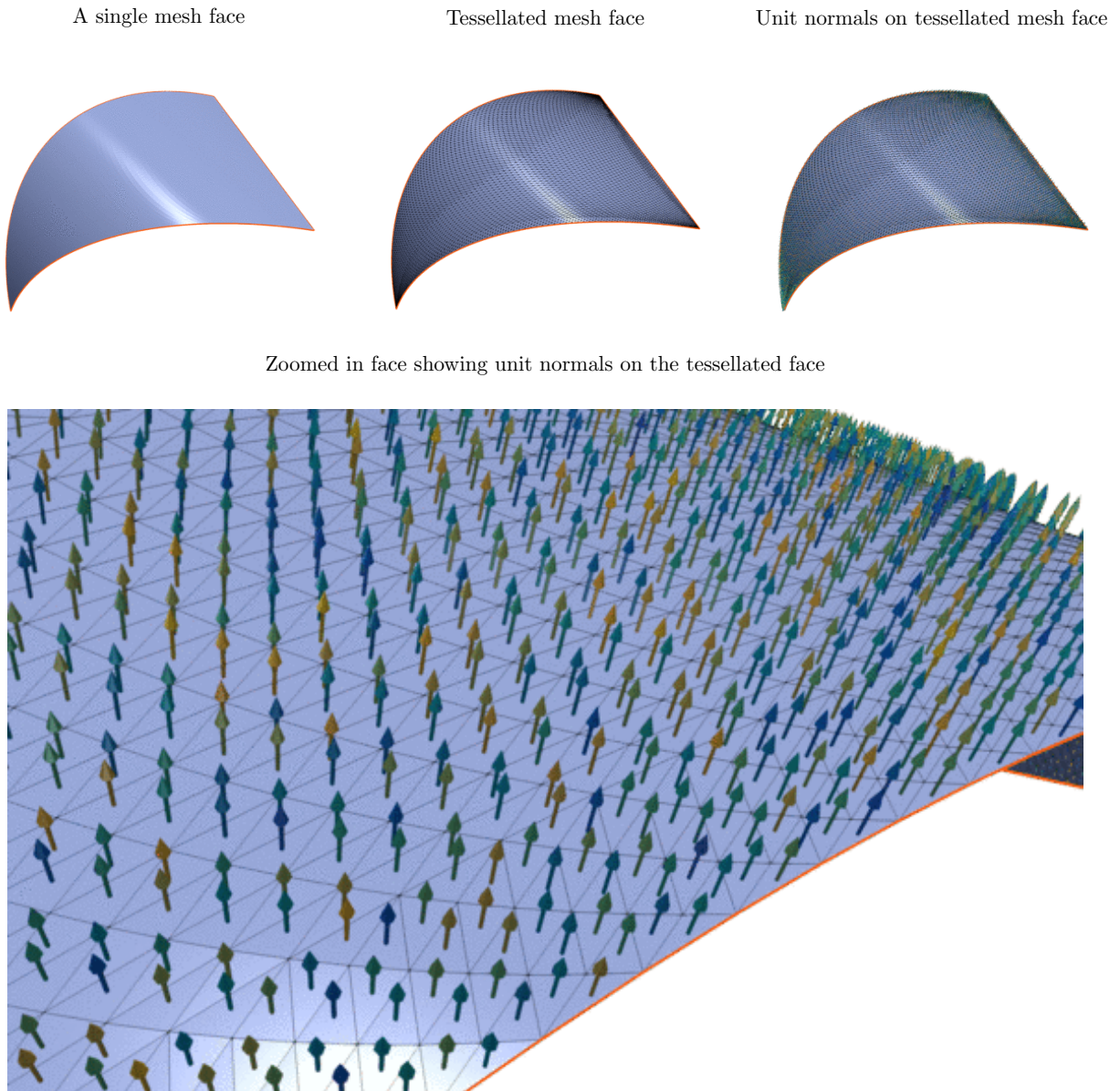


Figure C.2: Finding unit normals on a single curved mesh face

## Appendix D

# Computational terminologies, idioms and relationships in tensor networks' theory

### D.1 Computational aspects of tensor contraction

In this section, some common computational terminologies used in the context of tensor contraction are defined.

**Definition 1** *Tensor network:* A complex network of tensors comprising of two or more tensors, multiplied and summed over a set of indices, for instance  $\mathcal{A}_{ijk}\mathcal{B}_{lmj} + \mathcal{C}_{ijl}\mathcal{D}_j\mathcal{E}_m + \dots$ .

**Definition 2** *Singleton:* A singleton or a single term tensor network is a single sub-expression of (Definition 1), for instance  $\mathcal{A}_{ijk}\mathcal{B}_{lmj}$ .

**Definition 3** *Isomorphic tensor product (outer product):* Given a tensor pair  $\mathbf{A}$  and  $\mathbf{B}$  belonging to vector spaces  $\mathbf{\Xi}$  and  $\mathbf{\Eta}$ , respectively, their product is said to be isomorphic, if and only if there are no contracting indices between the two, i.e. if isomorphism exists between the vector space of the product  $\mathbf{\Upsilon}$  and the product of the vector spaces  $\mathbf{\Xi} \otimes \mathbf{\Eta}$ .

**Definition 4** *Nonisomorphic tensor product (tensor contraction):* Given a tensor pair  $\mathbf{A}$  and  $\mathbf{B}$  belonging to vector spaces  $\mathbf{\Xi}$  and  $\mathbf{\Eta}$ , respectively, their product is said to be nonisomorphic, if at least there is one common index between the two i.e. if no isomorphism exists between the vector space of the product  $\mathbf{\Upsilon}$  and the product of the vector spaces  $\mathbf{\Xi} \otimes \mathbf{\Eta}$ .

**Definition 5** *Named operator:* An operation performed on a tensor, a pair or a network is said to be named, if there is a specific name for the function signature, for instance, `gemm`, `matmul`, `rotg`, `transpose`, `trace`.

**Definition 6** *Un-named operator:* An operation performed on a tensor, a pair or a network is said to be un-named, if it is expressed through indicial notation and there is no in-built or standardised BLAS or LAPACK name it. For instance,  $\mathcal{A}_{iiii}$  is an un-named reduction operation.

**Definition 7** *Contraction loop nest:* A variable number of nested for loop iterating over the space of tensor dimensions.

**Definition 8** *Fully vectorisable contraction loop nest:* A loop nest is said to be fully vectorisable if and only if a) the span (iteration space) of the fastest changing index in the Cartesian product is a multiple of SIMD vector size and b) the index is not a contraction index.

**Definition 9** *Partially vectorisable contraction loop nest:* A loop nest is said to be partially vectorisable if and only if a) the span (iteration space) of the fastest changing index in the Cartesian product is not a multiple of SIMD vector size but nevertheless greater than it and b) the index is not a contraction index.

## APPENDIX D. TENSOR NETWORK THEORY

**Definition 10** *Broadcast-vectorisable contraction loop nest:* A loop nest is said to be broadcast-vectorisable if a) the span (iteration space) of the fastest changing index in the Cartesian product is a multiple of or greater than SIMD vector size b) the index is a contraction index. Double contraction is a special case of broadcast-vectorisable contraction loop nests.

**Definition 11** *Depth-first constructive search:* A compile-time graph search to find the order in which pairs of tensors need be contracted so that the contraction over all tensor network incurs minimum floating point operations. The by-pair nature of tensor network evaluation leads to multiple intermediate temporaries which introduces a memory vs FLOP tradeoff.

# Bibliography

- [1] ABDELFATTAH, A., BABOULIN, M., DOBREV, V., DONGARRA, J., EARL, C., FALCONU, J., HAIDAR, A., KARLIN, I., KOLEV, T., MASLIAH, I., AND TOMOV, S. High-performance tensor contractions for GPUs. *Procedia Computer Science 80* (2016), 108 – 118. International Conference on Computational Science 2016, ICCS 2016, 6-8 June 2016, San Diego, California, USA.
- [2] ABDELKEFI, A., NAJAR, F., H., N. A., AND AYED, S. B. An energy harvester using piezoelectric cantilever beams undergoing coupled bending-torsion vibrations. *Smart Materials and Structures 20*, 11 (2011), 115007.
- [3] ABDOLLAHI, A., MILLÁN, D., PECO, C., ARROYO, M., AND ARIAS, I. Revisiting pyramid compression to quantify flexoelectricity: A three-dimensional simulation study. *Physical Review B 91* (2015), 104103.
- [4] ABDOLLAHI, A., PECO, C., MILLAN, D., ARROYO, M., AND ARIAS, I. Computational evaluation of the flexoelectric effect in dielectric solids. *Journal of Applied Physics 116* (2014), 093502.
- [5] ABGRALL, R., DOBRZYNISKI, C., AND FROEHLY, A. A method for computing curved meshes via the linear elasticity analogy, application to fluid dynamics problems. *International Journal for Numerical Methods in Fluids 76*, 4 (2014), 246–266.
- [6] ACAR, E., HARRISON, R. J., OLKEN, F., ALTER, O., HELAL, M., OMBERG, L., BADER, B., KENNEDY, A., PARK, H., BAI, Z., KIM, D., PLEMMONS, R., BEYLKIN, G., KOLDA, T., RAGNARSSON, S., DELATHAUWER, L., LANGOU, J., PONNAPALLI, S. P., DHILLON, I., LIM, L., RAMANUJAM, J. R., DING, C., MAHONEY, M., RAYNOLDS, J., ELDEN, L., MARTIN, C., REGALIA, P., DRINEAS, P., MOHLENKAMP, M., FALOUTSOS, C., MORTON, J., SAVAS, B., FRIEDLAND, S., MULLIN, L., AND LOAN, C. V. Future directions in tensor-based computation and modeling. In *NSF Workshop Report* (VA, USA, February 2009).
- [7] ADHIKARI, S., FRISWELL, M., AND INMAN, D. J. Piezoelectric energy harvesting from broadband random vibrations. *Smart materials and Structures 18*, 11 (2009).
- [8] AINSWORTH, M. Dispersive and dissipative behaviour of high order discontinuous Galerkin finite element methods. *Journal of Computational Physics 198*, 1 (2004), 106–130.
- [9] ALDRAIHEM, O. J., AND KHDEIR, A. A. Smart beams with extension and thickness-shear piezoelectric actuators. *Smart Materials and Structures 9*, 1 (2000), 1–9.
- [10] ALEXANDRESCU, A. *Modern C++ Design: Generic Programming and Design Patterns Applied*. Addison-Wesley, 2001.
- [11] ALNÆS, M. S., LOGG, A., ØLGAARD, K. B., ROGNES, M. E., AND WELLS, G. N. Unified Form Language: A domain-specific language for weak formulations of partial differential equations. *ACM Trans Math Software 40*, 2 (2014), 9:1–9:37.

- [12] AMESTOY, P. R., DUFF, I. S., L'EXCELLENT, J.-Y., AND KOSTER, J. A fully asynchronous multifrontal solver using distributed dynamic scheduling. *SIAM Journal on Matrix Analysis and Applications* 23, 1 (2001), 15–41.
- [13] ANTON, S. R., AND SODANO, H. A. A review of power harvesting using piezoelectric materials (2003-2006). *Smart Materials and Structures* 16, 3 (2007), R1.
- [14] BAGWELL, S., LEDGER, P. D., GIL, A. J., MALLETT, M., AND KRUIP, M. A linearised  $hp$ -finite element framework for acousto-magneto-mechanical coupling in axisymmetric MRI scanners. *International Journal for Numerical Methods in Engineering* (2017), DOI: <http://dx.doi.org/10.1002/nme.5559>.
- [15] BAILLARGEON, B. P., AND VEL, S. S. Active Vibration Suppression of Sandwich Beams using Piezoelectric Shear Actuators: Experiments and Numerical Simulations. *Smart Materials and Structures* 16, 6 (2005), 517–530.
- [16] BALL, J. Convexity conditions and existence theorems in nonlinear elasticity. *Archive for Rational Mechanics and Analysis* 63, 4 (1976), 337–403.
- [17] BALL, J. M. Energy-minimising configurations in nonlinear elasticity. In *Proceedings of the International Congress of Mathematicians* (Warsaw, August 1983).
- [18] BASSI, F., AND REBAY, S. High-order accurate discontinuous finite element solution of the 2D Euler equations. *Journal of Computational Physics* 138, 2 (1997), 251–285.
- [19] BAUER, S., DETTMER, W. G., D. PERIĆ, D., AND SCHÄFER, M. Micropolar hyperelasticity: constitutive model, consistent linearization and simulation of 3D scale effects. *Computational Mechanics* 50 (2012), 383–396.
- [20] BAZILEVS, Y., CALO, V., COTTERELL, J., EVANS, J., HUGHES, T., LIPTON, S., SCOTT, M., AND SEDERBERG, T. Isogeometric analysis using t-splines. *Computer Methods in Applied Mechanics and Engineering* 199, 5 (2010), 229 – 263. Computational Geometry and Analysis.
- [21] BENJEDDOU, A. Advances in piezoelectric finite element modeling of adaptive structural elements: a survey. *Computers and Structures* 76, 1-3 (2000), 347–363.
- [22] BENJEDDOU, A., TRINIDADE, M. A., AND OHAYON, R. A unified beam finite element model for extension and shear piezoelectric actuation mechanisms. *Intelligent Material Systems and Structures* 8, 12 (1997), 1012–1025.
- [23] BÉRIOT, H., GABARD, G., AND PERREY-DEBAIN, E. Analysis of high-order finite elements for convected wave propagation. *International journal for numerical methods in engineering* 96, 11 (2013), 665–688.
- [24] BERLINCOURT, D., AND JAFFE, H. Elastic and piezoelectric coefficients of single-crystal barium titanate. *Phys. Rev.* 111 (Jul 1958), 143–148.
- [25] BERTOLDI, K., AND GEI, M. Instabilities in multilayered soft dielectrics. *Journal of the Mechanics and Physics of Solids* 59, 1 (2011), 18 – 42.
- [26] BONET, J., AND BURTON, A. A simple orthotropic, transversely isotropic hyperelastic constitutive equation for large strain computations. *Computer Methods in Applied Mechanics and Engineering* 162, 14 (1998), 151 – 164.
- [27] BONET, J., GIL, A. J., LEE, C. H., AGUIRRE, M., AND ORTIGOSA, R. A first order hyperbolic framework for large strain computational solid dynamics. Part I: Total Lagrangian isothermal elasticity. *Computer Methods in Applied Mechanics and Engineering* 283 (2015), 689–732.

## BIBLIOGRAPHY

- [28] BONET, J., GIL, A. J., AND ORTIGOSA, R. A computational framework for polyconvex large strain elasticity. *Computer Methods in Applied Mechanics and Engineering* 283 (2015), 1061–1094.
- [29] BONET, J., GIL, A. J., AND ORTIGOSA, R. On a tensor cross product based formulation of large strain solid mechanics. *International Journal of Solids and Structures* doi:10.1016/j.ijsolstr.2015.12.030 (2015).
- [30] BONET, J., GIL, A. J., AND WOOD, R. D. *Nonlinear Solid Mechanics for Finite Element Analysis: Statics*, 3rd ed. Cambridge University Press, Cambridge, UK, 2016.
- [31] BONET, J., AND WOOD, R. D. *Nonlinear Continuum Mechanics for Finite Element Analysis*, second ed. Cambridge University Press, Cambridge, UK, 2008.
- [32] BRAUN, M. *Linear Elasticity with Couple Stresses*. In *Mechanics of Microstructured Solids 2* 50 (2010), 1–8.
- [33] BREWER, M., DIACHIN, L., KNUPP, P., LEURENT, T., AND MELANDER, D. The mesquite mesh quality improvement toolkit. In *Proceedings of the 12th International Meshing Roundtable* (2003), Sandia National Laboratories, pp. 239–250.
- [34] BREZZI, F. On the existence, uniqueness and approximation of saddle-point problems arising from Lagrange multiplier. *Revue francaise d'automatique, informatique, recherche opérationnelle, Analyse numérique* 8 (1974), 129–151.
- [35] BRISCOE, J., AND DUNN, S. Piezoelectric nanogenerators a review of nanostructured piezoelectric energy harvesters. *Nano Energy* 14, Supplement C (2015), 15 – 29. Special issue on the 2nd International Conference on Nanogenerators and Piezotronics (NGPT 2014).
- [36] BRÜNAHL, J., AND GRISHIN, A. M. Piezoelectric shear mode drop-on-demand inkjet actuator. *Sensors and Actuators A: Physical* 101, 3 (2002), 371 – 382.
- [37] BUSTAMANTE, R., A., D., AND OGDEN, R. W. Nonlinear electroelastostatics: a variational framework. *Zeitschrift fur angewandte Mathematik und Physik* 60 (2009), 154–177.
- [38] BUSTAMANTE, R., AND MERODIO, J. On simple constitutive restrictions for transversely isotropic nonlinearly elastic materials and isotropic magneto-sensitive elastomers. *Journal of Engineering Mathematics* 68, 1 (2009), 15–26.
- [39] BUTZ, A., KLINKEL, S., AND WAGNER, W. A geometrically and materially non-linear piezoelectric three-dimensional-beam finite element formulation including warping effects. *International Journal for Numerical Methods in Engineering* 76, 5 (2008), 601–635.
- [40] CALVIN, J. A., AND VALEEV, E. F. Task-based algorithm for matrix multiplication: A step towards block-sparse tensor computing.
- [41] CATALAN, G., NOHEDA, B., MCANENEY, J., SINNAMON, L. J., AND GREGG, J. M. Strain gradients in epitaxial ferroelectrics. *Physical Review B* 72 (2005), 020102(R).
- [42] CHAKRAVARTY, S., HADJESFANDIARI, A. R., AND DARGUSH, G. F. A penalty-based finite element framework for couple stress elasticity. *Finite Element in Analysis & Design* 130, C (2017), 65–79.
- [43] CHAPELLE, D., AND BATHE, K. The inf-sup test. *Computers & Structures* 47, 4 (1993), 537 – 545.
- [44] CHEN, J. *Micropolar theory of flexoelectricity*. *Journal of Advanced Mathematics and Applications* 1 (2012), 269–274.

## BIBLIOGRAPHY

- [45] CHEN, M.-H., COCKBURN, B., AND REITICH, F. High-order RKDG methods for computational electromagnetics. *Journal of Computational Physics* 22-23, 22-23 (2005), 205–226.
- [46] CHI-CHUNG, L., SADAYAPPAN, P., AND WENGER, R. On optimizing a class of multi-dimensional loops with reduction for parallel execution. *Parallel Processing Letters* 07, 02 (1997), 157–168.
- [47] CHILTON, L., AND SURI, M. *On the selection of a locking-free hp element for elasticity problems*. *International Journal for Numerical Methods in Engineering* 40 (1997), 2045–2062.
- [48] CIARLET, P. G., AND MARDARE, C. Existence theorems in intrinsic nonlinear elasticity. *Journal de Mathématiques Pures et Appliquées* 94, 3 (2010), 229 – 243.
- [49] CIRAK, F., AND CUMMINGS, J. C. Generic programming techniques for parallelizing and extending procedural finite element programs. *Engineering with Computers* 24, 1 (2008), 1–16.
- [50] CIRAK, F., ORTIZ, M., AND SCHRDER, P. Subdivision surfaces: a new paradigm for thin-shell finite-element analysis. *International Journal for Numerical Methods in Engineering* 47, 12 (2000), 2039–2072.
- [51] CIRAK, F., SCOTT, M. J., ANTONSSON, E. K., ORTIZ, M., AND SCHRÖDER, P. Integrated modeling, finite-element analysis, and engineering design for thin-shell structures using subdivision. *Computer-Aided Design* 34, 2 (2002), 137 – 148.
- [52] COCIORVA, D., WILKINS, J., BAUMGARTNER, G., SADAYAPPAN, P., RAMANUJAM, J., NOOIJEN, M., BERNHOLDT, D., AND HARRISON, R. *Towards Automatic Synthesis of High-Performance Codes for Electronic Structure Calculations: Data Locality Optimization*. Springer Berlin Heidelberg, Berlin, Heidelberg, 2001, pp. 237–248.
- [53] COCKBURN, B., LI, F., AND SHU, C.-W. Locally divergence-free discontinuous Galerkin methods for the Maxwell equations. *Journal of Computational Physics* 194 (2004), 588–610.
- [54] CORMEN, T. H., LEISERSON, C. E., RIVEST, R. L., AND STEIN, C. *Introduction to Algorithms*, 3rd ed. MIT Press, 2009.
- [55] COSSERAT, E., AND COSSERAT, F. Théorie des corps déformables. *Librairie Scientifique A. Hermann et Fils Paris* (1909).
- [56] CRISFIELD, M. A. *Nonlinear Finite Element Analysis of Solids and Structures: Essentials*. John Wiley & Sons, Chichester, West Sussex, United Kingdom, 1996.
- [57] CURIEL SOSA, J., AND GIL, A. J. *Analysis of a continuum-based beam element in the framework of explicit-FEM*. *Finite Elements in Analysis and Design* 45, 8-9 (2009), 583 – 591.
- [58] CZARNECKI, K., EISENECKER, U., GLÜCK, R., VANDEVOORDE, D., AND VELDHUIZEN, T. *Generic Programming: International Seminar on Generic Programming Dagstuhl Castle, Germany, April 27–May 1, 1998 Selected Papers*. Springer Berlin Heidelberg, Berlin, Heidelberg, 2000, ch. Generative Programming and Active Libraries, pp. 25–39.
- [59] DAGUM, L., AND MENON, R. OpenMP: An industry standard API for shared-memory programming. *Computational Science & Engineering, IEEE* 5, 1 (1998), 46–55.
- [60] DANOWSKI, C., GRAVEMEIER, V., YOSHIHARA, L., AND WALL, W. A. A monolithic computational approach to thermo-structure interaction. *International Journal for Numerical Methods in Engineering* 95, 13 (2013), 1053–1078.

## BIBLIOGRAPHY

- [61] DARRALL, B. T., DARGUSH, G. F., AND HADJESFANDIARI, A. R. Finite element Lagrange multiplier formulation for size-dependent skew-symmetric couple-stress planar elasticity. *Acta Mechanica* 255 (2014), 195–212.
- [62] DARRALL, B. T., HADJESFANDIARI, A. R., AND DARGUSH, G. F. Size-dependent piezoelectricity: A 2D finite element formulation for electric field-mean curvature coupling in dielectrics. *European Journal of Mechanics A/Solids* 49 (2015), 308–320.
- [63] DAVIES, R. W., MORGAN, K., AND HASSAN, O. A high order hybrid finite element method applied to the solution of electromagnetic wave scattering problems in the time domain. *Computational Mechanics* 44, 3 (2009), 321–331.
- [64] DAVIS, T. A. Algorithm 832: UMFPACK V4.3—an unsymmetric-pattern multifrontal method. *ACM Transactions on Mathematical Software* 30, 2 (2004), 196–199.
- [65] DE BOER, R. *Vektor- und Tensorrechnung für Ingenieure*. Springer, 1982.
- [66] DE BORST, R., CRISFIELD, M. A., REMMERS, J. J. C., AND VERHOOSSEL, C. V. *Nonlinear Finite Element Analysis of Solids and Structures*, second ed. John Wiley & Sons, Chichester, West Sussex, United Kingdom, 2012.
- [67] DE BORST, R., AND SLUYS, L. J. Localisation in a Cosserat continuum under static and dynamic loading conditions. *Computer Methods in Applied Mechanics and Engineering* 90 (1991), 805–827.
- [68] DE SOUZA NETO E. A., PERIĆ, D., AND OWEN, D. R. J. *Computational Methods for Plasticity: Theory and Applications*, first ed. John Wiley & Sons, Chichester, West Sussex, United Kingdom, 2008.
- [69] DEMKOWICZ, L. *Computing with hp-Adaptive Finite Elements: Volume 1: One and Two Dimensional Elliptic and Maxwell Problems*. Chapman and Hall, Boca Raton FL, USA, 2007.
- [70] DENG, F., DENG, Q., AND SHEN, S. A three-dimensional mixed finite element for flexoelectricity. *Journal of Applied Mechanics* 85, 3 (2018), 031009.
- [71] DENG, G., AND DARGUSH, G. F. Mixed Lagrangian formulation for size-dependent couple stress elastodynamic and natural frequency analyses. *International Journal for Numerical Methods in Engineering* 109, 6 (2017), 809–836.
- [72] DENG, Q., KAMMOUN, M., ERTURK, A., AND SHARMA, P. Nanoscale flexoelectric energy harvesting. *International Journal of Solids and Structures* 51 (2014), 3218–3225.
- [73] DENG, Q., LIU, L. P., AND SHARMA, P. Flexoelectricity in soft materials and biological membranes. *Journal of the Mechanics of Physics of Solids* 62 (2014), 209–227.
- [74] DEY, S., O’BARA, R. M., AND SHEPHARD, M. S. Curvilinear mesh generation in 3D. In *8th International Meshing Roundtable* (1999), Sandia National Laboratories.
- [75] DEY, S., O’BARA, R. M., AND SHEPHARD, M. S. Towards curvilinear meshing in 3D: the case of quadratic simplices. *Computer-Aided Design* 33, 3 (2001), 199 – 209.
- [76] DEY, S., SHEPHARD, M. S., AND FLAHERTY, J. E. Geometry representation issues associated with  $p$ -version finite element computations. *Computer Methods in Applied Mechanics and Engineering* 150, 1-4 (Dec. 1997), 39–55.
- [77] DOMINEK, A. K., AND SHAMANSKI, H. T. The almond test body. The Ohio State University ElectroScience Laboratory, Department of Electrical Engineering Report 721929-9, NASA Langley Research Center, 1990.

## BIBLIOGRAPHY

- [78] DORFMANN, A. L., AND OGDEN, R. W. *Nonlinear Theory of Electroelastic and Magnetoelastic Interactions*. Springer, Dordrecht, Heidelberg, London, New York, 2014.
- [79] DUMITRICA, T., LANDIS, C. M., AND YAKOBSON, B. I. Curvature-induced polarization in carbon nanoshells. *Chemical Physics Letters* 360 (2002), 182–188.
- [80] DU TOIT, N. E., WARDLE, B. L., AND KIM, S. G. Design considerations for MEMS-scale piezoelectric mechanical vibration energy harvesters. *Integrated Ferroelectrics* 16 (2005), 121–160.
- [81] EPIFANOVSKY, E., WORMIT, M., KU, T., LANDAU, A., ZUEV, D., KHISTYAEV, K., MANOHAR, P., KALIMAN, I., DREUW, A., AND KRYLOV, A. I. New implementation of high-level correlated methods using a general block tensor library for high-performance electronic structure calculations. *Journal of Computational Chemistry* 34, 26 (2013), 2293–2309.
- [82] ERICKSEN, J. L., AND TRUESDELL, C. Exact theory of stress and strain in rods and shells. *Archive for Rational Mechanics and Analysis* 1 (1958), 295–323.
- [83] ERINGEN, A. C. Linear theory of micropolar elasticity. *Indiana University Mathematics Journal* 15 (1966), 909–923.
- [84] ERINGEN, A. C. Theory of Micropolar Elasticity. *Technical Report No. 1 Princeton University* (1967), 1–152.
- [85] ERINGEN, A. C. Linear theory of nonlocal elasticity and dispersion of plane waves. *International Journal of Engineering Science* 10 (1972), 425–435.
- [86] ERINGEN, A. C. Nonlocal polar elastic continua. *International Journal of Engineering Science* 10 (1972), 1–16.
- [87] ERINGEN, A. C. On differential equations of nonlocal elasticity and solutions of screw dislocation and surface waves. *Journal of Applied Physics* 54 (1983), 4703.
- [88] ERINGEN, A. C. Theory of micropolar elasticity. In: *Microcontinuum Field Theories* Springer, Dordrecht, Heidelberg, London, New York (1999), 101–248.
- [89] ERINGEN, A. C., AND MAUGIN, G. A. *Electrodynamics of Continua I: Foundations and Solid Media*. Springer, Dordrecht, Heidelberg, London, New York, 1990.
- [90] ERTURK, A. *Electromechanical Modeling of Piezoelectric Energy Harvesters*. PhD thesis, Virginia Polytechnic Institute and State University, 2009.
- [91] ERTURK, A., AND INMAN, D. J. Issues in mathematical modeling of piezoelectric energy harvesters. *Smart Materials and Structures* 17 (2008), 065016.
- [92] ERTURK, A., AND INMAN, D. J. *Piezoelectric Energy Harvesting*, first ed. John Wiley & Sons Inc., Chichester, England, 2011.
- [93] EVENBLY, G., AND PFEIFER, R. N. C. Improving the efficiency of variational tensor network algorithms. *Phys. Rev. B* 89 (Jun 2014), 245118.
- [94] FOG, A. *VCL: C++ Vector Class Library*, 1.22 ed. Agner Fog, GNU Public License, 2016.
- [95] FORTUNATO, M., AND PERSSON, P.-O. High-order unstructured curved mesh generation using the winslow equations. *Journal of Computational Physics* 307 (2016), 1 – 14.

## BIBLIOGRAPHY

- [96] FRIGO, M., HALPERN, P., LEISERSON, C. E., AND LEWIN-BERLIN, S. Reducers and other Cilk++ hyperobjects. In *Proceedings of the Twenty-first Annual Symposium on Parallelism in Algorithms and Architectures* (New York, NY, USA, 2009), SPAA 2009, ACM, pp. 79–90.
- [97] FUKADA, E., SESSLER, G. M., WEST, J. E., BERRAISSEUL, A., AND GÜNTHER, P. Bending piezoelectricity in monomorph polymer films. *Journal of Applied Physics* 62 (1987), 3643.
- [98] GANAPATHI, M., PATEL, B. P., AND TOURATIER, M. Refined finite element for piezoelectric laminated composite beams. *Smart Materials and Structures* 13, 4 (2004), N57.
- [99] GARG, N., AND HAN, C.-S. Axisymmetric couple stress elasticity and its finite element formulation with penalty terms. *Archive of Applied Mechanics* 85, 5 (May 2015), 587–600.
- [100] GARGALLO-PEIRÓ, A., ROCA, X., PERAIRE, J., AND SARRATE, J. Distortion and quality measures for validating and generating high-order tetrahedral meshes. *Engineering with Computers* (2014), 1–15.
- [101] GARGALLO-PEIRÓ, A., ROCA, X., PERAIRE, J., AND SARRATE, J. A distortion measure to validate and generate curved high-order meshes on cad surfaces with independence of parameterization. *International Journal for Numerical Methods in Engineering* (2015), To Appear. nme.5162.
- [102] GARGALLO-PEIRÓ, A., ROCA, X., PERAIRE, J., AND SARRATE, J. Optimization of a regularized distortion measure to generate curved high-order unstructured tetrahedral meshes. *International Journal for Numerical Methods in Engineering* 103, 5 (2015), 342–363.
- [103] GEE, M. W., KÜTTLER, U., AND WALL, W. A. Truly monolithic algebraic multigrid for fluid-structure interaction. *International Journal for Numerical Methods in Engineering* 85, 8 (2011), 987–1016.
- [104] GEORGIADIS, H. G., AND VELGAKI, E. G. High-frequency Rayleigh waves in materials with micro-structure and couple-stress effects. *International Journal of Solids and Structures* 40 (2003), 2501–2520.
- [105] GEUZAIN, C., JOHNEN, A., LAMBRECHTS, J., REMACLE, J.-F., AND TOULORGE, T. The generation of valid curvilinear meshes. In *IDIHOM: Industrialization of High-Order Methods-A Top-Down Approach*. Springer, 2015, pp. 15–39.
- [106] GEUZAIN, C., AND REMACLE, J.-F. Gmsh: A 3-d finite element mesh generator with built-in pre- and post-processing facilities. *International Journal for Numerical Methods in Engineering* 79, 11 (2009), 1309–1331.
- [107] GHARBI, M., SUN, Z., SHARMA, P., WHITE, K., AND S., E.-B. Flexoelectric properties of ferroelectrics and the nanoindentation size-effect. *International Journal of Solids and Structures* 48 (2011), 249–256.
- [108] GHASEMI, H., PARK, H. S., AND RABEZUK, T. A level-set based IGA formulation for topology optimization of flexoelectric materials. *Computer Methods in Applied Mechanics and Engineering* 313 (2017), 239 – 258.
- [109] GHIBA, I.-D., NEFF, P., MADEO, A., AND MÜNCH, I. A variant of the linear isotropic indeterminate couple-stress model with symmetric local force-stress, symmetric nonlocal force-stress, symmetric couple-stresses and orthogonal boundary conditions. *Mathematics and Mechanics of Solids* 22, 6 (2017), 1221–1266.

## BIBLIOGRAPHY

- [110] GIL, A. J., ADHIKARI, S., SCARPA, F., AND BONET, J. The formation of wrinkles in single-layer graphene sheets under nanoindentation. *Journal of Physics: Condensed Matter* 22, 14 (2010), 145302.
- [111] GIL, A. J., AND LEDGER, P. D. A coupled *hp*-finite element scheme for the solution of two-dimensional electrostrictive materials. *International Journal for Numerical Methods in Engineering* 91, 11 (2012), 1158–1183.
- [112] GIL, A. J., LEE, C. H., BONET, J., AND ORTIGOSA, R. A first order hyperbolic framework for large strain computational solid dynamics. Part II: Total Lagrangian compressible, nearly incompressible and truly incompressible elasticity. *Computer Methods in Applied Mechanics and Engineering* 300 (2016), 146–181.
- [113] GIL, A. J., AND ORTIGOSA, R. A new framework for large strain electromechanics based on convex multi-variable strain energies: Variational formulation and material characterisation. *Computer Methods in Applied Mechanics and Engineering* 302 (2016), 293 – 328.
- [114] GIL, A. J., ORTIGOSA, R., AND LEE, C. H. A computational framework for large strain nearly and truly incompressible electromechanics based on convex multi-variable strain energies. *Computer Methods in Applied Mechanics and Engineering* 310 (2016), 297 – 334.
- [115] GOLUB, G. H., AND VAN LOAN, C. F. *Matrix Computations*, 4th ed. Johns Hopkins Studies in Mathematical Sciences, Baltimore, USA, 2012.
- [116] GUENNEBAUD, G., AND JACOB, B. Eigen v3. <http://eigen.tuxfamily.org>, 2010.
- [117] HADJESFANDIARI, A. R. Size-dependent piezoelectricity. *International Journal of Solids and Structures* 50 (2013), 2781–2791.
- [118] HADJESFANDIARI, A. R., AND DARGUSH, G. F. Couple stress theory for solids. *International Journal of Solids and Structures* 48 (2011), 2496–2510.
- [119] HARTONO, A., SIBIRYAKOV, A., NOOIJEN, M., BAUMGARTNER, G., BERNHOLDT, D. E., HIRATA, S., LAM, C.-C., ITZER, R. M., RAMANUJAM, J., AND SADAYAPPAN, P. *Automated Operation Minimization of Tensor Contraction Expressions in Electronic Structure Calculations*. Springer Berlin Heidelberg, Berlin, Heidelberg, 2005, pp. 155–164.
- [120] HEINECKE, A., HENRY, G., HUTCHINSON, M., AND PABST, H. LIBXSMM: Accelerating small matrix multiplications by runtime code generation. In *Proceedings of the International Conference for High Performance Computing, Networking, Storage and Analysis* (Piscataway, NJ, USA, 2016), SC ’16, IEEE Press, pp. 84:1–84:11.
- [121] HENRY, A. S., PARK, G., AND DANIEL, J. I. Estimation of electric charge output for piezoelectric energy harvesting. *Strain* 40, 2 (2004), 49–58.
- [122] HESTHAVEN, J. S., AND WARBURTON, T. Nodal high-order methods on unstructured grids I. time-domain solution of Maxwell’s equations. *Journal of Computational Physics* 181, 1 (2002), 186–221.
- [123] HESTHAVEN, J. S., AND WARBURTON, T. *Nodal discontinuous Galerkin methods: algorithms, analysis, and applications*. Springer Science & Business Media, 2007.
- [124] HIGHAM, N. J., AND TISSEUR, F. A block algorithm for matrix 1-norm estimation, with an application to 1-norm pseudospectra. *SIAM Journal on Matrix Analysis and Applications* 21 (2000), 1185–1201.

## BIBLIOGRAPHY

- [125] HIRATA, S. Tensor Contraction Engine: Abstraction and automated parallel implementation of configuration-interaction, coupled-cluster, and many-body perturbation theories. *The Journal of Physical Chemistry A* 107, 46 (2003), 9887–9897.
- [126] HJELMSTAD, K. D. *Fundamentals of Structural Mechanics*. International series in civil engineering and engineering mechanics. Springer Inc., New York, 2005.
- [127] HOLZAPFEL, G. A. *Nonlinear Solid Mechanics: A Continuum Approach for Engineering*. Wiley, 2000.
- [128] HUERTA, A., ANGELOSKI, A., ROCA, X., AND PERAIRE, J. Efficiency of high-order elements for continuous and discontinuous galerkin methods. *International Journal for Numerical Methods in Engineering* 96, 9 (2013), 529–560.
- [129] HUGHES, T., COTTRELL, J., AND BAZILEVS, Y. Isogeometric analysis: Cad, finite elements, nurbs, exact geometry and mesh refinement. *Computer Methods in Applied Mechanics and Engineering* 194, 39 (2005), 4135 – 4195.
- [130] HUGHES, T. J. R. *The Finite Element Method, Linear Static and Dynamic Analysis*. Prentice-Hall, Englewood Cliffs, New Jersey, 1987.
- [131] HUGHES, T. J. R. *The Finite Element Method: Linear Static and Dynamic Finite Element Analysis*. Prentice Hall Inc., Englewood Cliffs, New Jersey, 1987.
- [132] HUYNH, H., WANG, Z. J., AND VINCENT, P. High-order methods for computational fluid dynamics: a brief review of compact differential formulations on unstructured grids. *Computers & Fluids* 98 (2014), 209–220.
- [133] IGLBERGER, K., HAGER, G., TREIBIG, J., AND RDE, U. Expression Templates Revisited: A performance analysis of current methodologies. *SIAM Journal on Scientific Computing* 34, 2 (2012), C42–C69.
- [134] PROGSCH, Y. I., AND ADELMANN, A. A new vectorization technique for expression templates in C++. *American Journal of Undergraduate Research* 10, 4 (2012).
- [135] JEON, Y. B., SOOD, R., H., J. J., AND KIM, S. G. MEMS power generator with transverse mode thin film PZT. *Sensors and Actuators* 122, 1 (2005), 16–22.
- [136] JEONG, J., AND NEFF, P. Existence, uniqueness and stability in linear Cosserat elasticity for weakest curvature conditions. *Mathematics and Mechanics of Solids* 15 (2010), 78–95.
- [137] JEONG, J., RAMÉZANI, H., MUNCH, I., AND NEFF, P. A numerical study for linear isotropic Cosserat elasticity with conformally invariant curvature. *ZAMM - Zeitschrift für Angewandte Mathematik und Mechanik* 89 (2009), 552–569.
- [138] JEREMIĆ, B., RUNESSON, K., AND STURE, S. Object-oriented approach to hyperelasticity. *Engineering with Computers* 15, 1 (1999), 2–11.
- [139] JEREMIĆ, B., AND STURE, S. Tensor objects in finite element programming. *International Journal for Numerical Methods in Engineering* 41, 1 (1998), 113–126.
- [140] JI, X., CAI, W., AND ZHANG, P. High-order DGTD methods for dispersive Maxwell's equations and modelling of silver nanowire coupling. *International Journal for Numerical Methods in Engineering* 69 (2007), 308–325.
- [141] JIANGA, X., HUANGA, W., AND ZHANGB, S. Flexoelectric nano-generator: Materials, structures and devices. *Nano Energy* 2 (2013), 1079–1092.

## BIBLIOGRAPHY

- [142] JIN, D., LEDGER, P. D., AND GIL, A. J. An *hp*-fem framework for the simulation of electrostrictive and magnetostrictive materials. *Computers and Structures* 133 (2014), 131–148.
- [143] JOHN, V., AND MATTHIES, G. Higher-order finite element discretizations in a benchmark problem for incompressible flows. *International Journal for Numerical Methods in Fluids* 37, 8 (2001), 885–903.
- [144] JOHNSON, A. A., AND TEZDUYAR, T. E. Mesh update strategies in parallel finite element computations of flow problems with moving boundaries and interfaces. *Computer Methods in Applied Mechanics and Engineering* 119, 1–2 (1994), 73–94.
- [145] JOHNSON, C. *Numerical Solution of Partial Differential Equations by the Finite Element Method*. Dover Publications Inc., Mineola, New York, USA, 2009.
- [146] KABAKIAN, A. V., SHANKAR, V., AND HALL, W. F. Unstructured grid-based discontinuous Galerkin method for broadband electromagnetic simulations. *Journal of Scientific Computing* 20, 3 (2004), 405–431.
- [147] KALININ, S. V., AND MEUNIER, V. Electronic flexoelectricity in low-dimensional systems. *Physical Review B* 77 (2008), 033403.
- [148] KARNIADAKIS, G. E., AND SHERWIN, S. J. *Spectral/hp Element Methods for CFD*. Oxford University Press, Oxford, England, 1999.
- [149] KARNIADAKIS, G. E., AND SHERWIN, S. J. *Spectral/hp element methods for computational fluid dynamics*, 2nd. ed. Oxford University Press, 2004.
- [150] KIRBY, R. C., KNEPLEY, M., LOGG, A., AND SCOTT, L. R. Optimizing the evaluation of finite element matrices. *SIAM Journal on Scientific Computing* 27, 3 (2005), 741–758.
- [151] KIRBY, R. C., LOGG, A., SCOTT, L. R., AND TERREL, A. R. Topological optimization of the evaluation of finite element matrices. *SIAM Journal on Scientific Computing* 28, 1 (2006), 224–240.
- [152] KLINKEL, S., LEGNER, D., AND WAGNER, W. Advanced finite element formulations for modeling thin piezoelectric structures. *PAMM: Proceedings in Applied Mathematics and Mechanics* 11 (2011), 31–34.
- [153] KLINKEL, S., AND WAGNER, W. A piezoelectric solid shell element based on a mixed variational formulation for geometrically linear and nonlinear applications. *Computers and Structures* 86, 1-2 (2007), 38–46.
- [154] KOITER, W. T. Couple-stresses in the theory of elasticity: I and II. *Proc. Ned. Akad. Wetenschap B* 67 (1964), 17–44.
- [155] KOK, S. L., WHITE, N. M., AND HARRIS, N. R. Free-standing thick-film piezoelectric device. *Electronics Letters* 44, 4 (2008), 280–281.
- [156] KOK, S. L., WHITE, N. M., AND HARRIS, N. R. A free-standing, thick-film piezoelectric energy harvester. *Proceedings of IEEE Sensors* (26-29 October 2008), 589–592.
- [157] KOK, S. L., WHITE, N. M., AND HARRIS, N. R. Fabrication and characterization of free-standing thick-film piezoelectric cantilevers for energy harvesting. *Measurement in Science and Technology* 20, 12 (2009), 124010.
- [158] KOK, S. L., WHITE, N. M., AND HARRIS, N. R. Free-standing thick-film piezoelectric multimorph cantilevers for energy harvesting. *IEEE International Ultrasonics Symposium* (20-23 September 2009), 1977–1980.

## BIBLIOGRAPHY

- [159] KÖNIG, M., BUSCH, K., AND NIEGEMANN, J. The discontinuous Galerkin time-domain method for Maxwell's equations with anisotropic materials. *Photonics Nanostruct.* 8 (2010), 303–309.
- [160] KOUTSAWA, Y., GAETANO, G., AND BELOUETTAR, S. Hierarchical FEM modelling of piezo-electric beam structures. *Composite Structures* 95 (2013), 705–718.
- [161] KRETZ, M. Data-parallel vector types & operations. *ISO/IEC C++ Standards Committee Paper* (2016).
- [162] KRETZ, M., AND LINDENSTRUTH, V. Vc: A C++ library for explicit vectorization. *Software: Practice and Experience* 42, 11 (2012), 1409–1430.
- [163] KRICHEN, S., AND SHARMA, P. Flexoelectricity: A perspective on an unusual electromechanical coupling. *Journal of Applied Mechanics* 83, 3 (2016), 030801.
- [164] KRIVODONOVÁ, L., AND BERGER, M. High-order accurate implementation of solid wall boundary conditions in curved geometries. *Journal of Computational Physics* 211, 2 (Jan. 2006), 492–512.
- [165] KROLL, N. The ADIGMA project. In *ADIGMA – A European initiative on the development of adaptive higher-order variational methods for aerospace applications*, N. Kroll, H. Bieler, H. Deconinck, V. Couaillier, H. van der Ven, and K. Sørensen, Eds., vol. 113 of *Notes on Numerical Fluid Mechanics and Multidisciplinary Design*. Springer, 2010, ch. 1, pp. 1–9.
- [166] KUSHNIR, U., AND RABINOVITCH, O. Nonlinear ferro-electro-elastic beam theory. *International Journal of Solids and Structures* 46, 11-12 (2009), 2397–2406.
- [167] KWON, Y.-R., AND LEE, B.-C. A mixed element based on lagrange multiplier method for modified couple stress theory. *Computational Mechanics* 59, 1 (2017), 117–128.
- [168] LAKES, R. Experimental methods for study of Cosserat elastic solids and other generalized continua. In *Continuum Models for Materials with Micro-structure* (1995), 1–22.
- [169] LAM, C.-C., RAUBER, T., BAUMGARTNER, G., COCIORVA, D., AND SADAYAPPAN, P. Memory-optimal evaluation of expression trees involving large objects. *Computer Languages, Systems and Structures* 37, 2 (2011), 63 – 75.
- [170] LAM, D. C. C., YANG, F., CHONG, A. C. M., WANG, J., AND TONG, P. Experiments and theory in strain gradient elasticity. *Journal of the Mechanics and Physics of Solids* 51 (2003), 1477–1508.
- [171] LANDAU, L. D., AND LIFSHITZ, E. M. *Electrodynamics of Continuous Media*. Pergamon, Oxford, 1960.
- [172] LANDMANN, B., KESSLER, M., WAGNER, S., AND KRÄMER, E. A parallel, high-order discontinuous Galerkin code for laminar and turbulent flows. *Computers & Fluids* 37, 4 (2008), 427–438.
- [173] LANDRY, W. Implementing a high performance tensor library. *Sci. Program.* 11, 4 (Dec. 2003), 273–290.
- [174] LARWOOD, B. G., WEATHERILL, N. P., HASSAN, O., AND MORGAN, K. Domain decomposition approach for parallel unstructured mesh generation. *International Journal for Numerical Methods in Engineering* 58, 2 (2003), 177–188.
- [175] LEDGER, P. D., GIL, A. J., POYA, R., KRUIP, M., WILKINSON, I., AND BAGWELL, S. Solution of an industrially relevant coupled magnetomechanical problem set on an axisymmetric domain. *Applied Mathematical Modelling* 40, 3 (2016), 1959 – 1971.

## BIBLIOGRAPHY

- [176] LEDGER, P. D., MORGAN, K., AND HASSAN, O. Frequency and time domain electromagnetic scattering simulations employing higher order edge elements. *Computer Methods in Applied Mechanics and Engineering* 194, 2-5 (2005), 105–125.
- [177] LEJEUNE, E., JAVILI, A., AND LINDER, C. An algorithmic approach to multi-layer wrinkling. *Extreme Mechanics Letters* 7 (2016), 10 – 17. Mechanics in Extreme Manufacturing.
- [178] LEVINTHAL, D. Performance Analysis Guide for Intel Core<sup>TM</sup> i7 Processor and Intel Xeon<sup>TM</sup> 5500 processors, 2009.
- [179] LIMACHEA, A., AND ROJAS FREDINI, P. A tensor library for scientific computing. In *Mecanica Computacional* (San Luis, Argentina, November 2008), vol. XXVII, pp. 2907–2925.
- [180] LOGG, A., MARDAL, K.-A., AND WELLS, G. N., Eds. *Automated Solution of Differential Equations by the Finite Element Method*, vol. 84 of *Lecture Notes in Computational Science and Engineering*. Springer, 2012.
- [181] LOGG, A., AND WELLS, G. N. DOLFIN: Automated finite element computing. *ACM Trans Math Software* 37, 2 (2010), 20:1–20:28.
- [182] LÖHNER, R. A parallel advancing front grid generation scheme. *International Journal for Numerical Methods in Engineering* 51, 6 (2001), 663–678.
- [183] LU, Q., GAO, X., KRISHNAMOORTHY, S., BAUMGARTNER, G., RAMANUJAM, J., AND SADAYAPPAN, P. Empirical performance model-driven data layout optimization and library call selection for tensor contraction expressions. *J. Parallel Distrib. Comput.* 72, 3 (Mar. 2012), 338–352.
- [184] LU, T., ZHANG, P. W., AND CAI, W. Discontinuous Galerkin methods for dispersive and lossy Maxwell’s equations and PML boundary conditions. *Journal of Computational Physics* 200, 2 (2004), 549–580.
- [185] LUO, H., BAUM, J. D., AND LÖHNER, R. A fast,  $p$ -multigrid Discontinuous Galerkin method for compressible flows at all speeds. In *Proceedings of the 44th AIAA Aerospace Sciences Meeting and Exhibit* (Reno, Nevada, January 2006), AIAA.
- [186] LUO, X.-J., SHEPHARD, M. S., AND REMACLE, J.-F. The influence of geometric approximation on the accuracy of higher order methods. In *8th International Conference on Numerical Grid Generation in Computational Field Simulations* (2002).
- [187] LUO, X.-J., SHEPHARD, M. S., REMACLE, J.-F., O’BARA, R. M., BEALL, M. W., SZABÓ, B., AND ACTIS, R.  $p$ -version mesh generation issues. In *11th International Meshing Roundtable* (2002), Sandia National Laboratories, pp. 343–354.
- [188] LUPORINI, F., VARBANESCU, A. L., RATHGEBER, F., BERCEA, G., RAMANUJAM, J., HAM, D. A., AND KELLY, P. H. J. COFFEE: an optimizing compiler for finite element local assembly. *CoRR abs/1407.0904* (2014).
- [189] MA, H. M., GAO, X.-L., AND REDDY, J. N. [A microstructure-dependent Timoshenko beam model based on a modified couple stress theory](#). *Journal of the Mechanics and Physics of Solids* 56 (2008), 3379–3391.
- [190] MA, W., AND CROSS, L. E. [Large flexoelectric polarization in ceramic lead magnesium niobate](#). *Applied Physics Letters* 79 (2001), 4420.
- [191] MA, W., AND CROSS, L. E. [Flexoelectric polarization of barium strontium titanate in the paraelectric state](#). *Applied Physics Letters* 81 (2002), 3440.

## BIBLIOGRAPHY

- [192] MA, W., AND CROSS, L. E. Flexoelectric effect in ceramic lead zirconate titanate. *Applied Physics Letters* 86 (2005), 072905.
- [193] MA, W., AND CROSS, L. E. Flexoelectricity of barium titanate. *Applied Physics Letters* 88 (2006), 232902.
- [194] MADEO, A., GHIBA, I.-D., NEFF, P., AND MÜNCH, I. A new view on boundary conditions in the griolikoitermindlintonupin indeterminate couple stress model. *European Journal of Mechanics - A/Solids* 59 (2016), 294 – 322.
- [195] MAJDOUB, M. S., SHARMA, P., AND CAGIN, T. Enhanced size-dependent piezoelectricity and elasticity in nanostructures due to the flexoelectric effect. *Physical Review B* 77 (2008), 125424.
- [196] MAJDOUB, M. S., SHARMA, P., AND CAGIN, T. Erratum: Enhanced size-dependent piezoelectricity and elasticity in nanostructures due to the flexoelectric effect. *Physical Review B* 79 (2009), 119904.
- [197] MÄKIPELTO, J. Exact geometry description with unstructured triangular meshes for shape optimization. In *Proceedings of the 6th Word Congress of Structural and Multidisciplinary Optimization* (Brasil, 2005).
- [198] MAO, G., HUANG, X., DIAB, M., LIU, J., AND QU, S. Controlling wrinkles on the surface of a dielectric elastomer balloon. *Extreme Mechanics Letters* 9 (2016), 139 – 146.
- [199] MAO, S., AND PUROHIT, P. K. Insights into flexoelectric solids from strain-gradient elasticity. *ASME - Journal of Applied Mechanics* 81 (2014), 081004.
- [200] MARANGANTI, R., SHARMA, N. D., AND SHARMA, P. Electromechanical coupling in nonpiezoelectric materials due to nanoscale nonlocal size effects: Greens function solutions and embedded inclusions. *Physical Review B* 74 (2006), 014110.
- [201] MARANGANTI, R., AND SHARMA, P. Atomistic determination of flexoelectric properties of crystalline dielectrics. *Physical Review B* 80 (2009), 054109.
- [202] MARSDEN, J. E., AND HUGHES, T. J. R. *Mathematical Foundations of Elasticity*. Dover Civil and Mechanical Engineering, 1994.
- [203] MATSUZAKI, K., AND EMOTO, K. *Implementation and Application of Functional Languages: 21st International Symposium, IFL 2009, South Orange, NJ, USA, September 23-25, 2009, Revised Selected Papers*. Springer Berlin Heidelberg, Berlin, Heidelberg, 2010, ch. Implementing Fusion-Equipped Parallel Skeletons by Expression Templates, pp. 72–89.
- [204] MCRAE, A. T. T., BERCEA, G.-T., MITCHELL, L., HAM, D. A., AND COTTER, C. J. Automated generation and symbolic manipulation of tensor product finite elements. *Submitted to SIAM Journal on Scientific Computing* (2014).
- [205] MEIER, C., POPP, A., AND WALL, W. A. An objective 3D large deformation finite element formulation for geometrically exact curved Kirchhoff rods. *Computer Methods in Applied Mechanics and Engineering* 278 (2014), 445 – 478.
- [206] MEIER, C., POPP, A., AND WALL, W. A. A locking-free finite element formulation and reduced models for geometrically exact Kirchhoff rods. *Computer Methods in Applied Mechanics and Engineering* 290 (2015), 314 – 341.
- [207] MERODIO, J., AND OGDEN, R. Instabilities and loss of ellipticity in fiber-reinforced compressible non-linearly elastic solids under plane deformation. *International Journal of Solids and Structures* 40, 18 (2003), 4707 – 4727.

- [208] MERODIO, J., AND OGDEN, R. A note on strong ellipticity for transversely isotropic linearly elastic solids. *Quarterly Journal of Mechanics and Applied Mathematics* 56, 4 (2003), 589–591.
- [209] MEYERS, S. *Effective Modern C++*. O'Reilly Media, 2014.
- [210] MIEHE, C., VALLICOTTI, D., AND ZH, D. Computational structural and material stability analysis in finite electro-elasto-statics of electro-active materials. *International Journal for Numerical Methods in Engineering* 102, 10 (2015), 1605–1637. nme.4855.
- [211] MINDLIN, R. D. Micro-structure in linear elasticity. *Archive for Rational Mechanics and Analysis* 16 (1964), 51–78.
- [212] MINDLIN, R. D. Second gradient of strain and surface-tension in linear elasticity. *International Journal of Solids and Structures* 1 (1965), 417–438.
- [213] MINDLIN, R. D. Polarization gradient in elastic dielectrics. *International Journal of Solids and Structures* 4 (1968), 637–642.
- [214] MINDLIN, R. D., AND ESHEL, N. N. On first strain-gradient theories in linear elasticity. *International Journal of Solids and Structures* 4 (1968), 109–124.
- [215] MINDLIN, R. D., AND TIERSTEN, H. F. Effects of couple-stresses in linear elasticity. *Archive for Rational Mechanics and Analysis* 11 (1962), 415–488.
- [216] MOSLER, J. A novel variational algorithmic formulation for wrinkling at finite strains based on energy minimization: Application to mesh adaption. *Computer Methods in Applied Mechanics and Engineering* 197, 9 (2008), 1131 – 1146.
- [217] MOSLER, J., AND CIRAK, F. A variational formulation for finite deformation wrinkling analysis of inelastic membranes. *Computer Methods in Applied Mechanics and Engineering* 198, 27 (2009), 2087 – 2098.
- [218] MOXEY, D., EKELSCHOT, D., KESKIN, U., SHERWIN, S., AND PEIRÓ, J. A thermo-elastic analogy for high-order curvilinear meshing with control of mesh validity and quality. *Procedia Engineering* 82, 0 (2014), 127 – 135. 23rd International Meshing Roundtable (IMR23).
- [219] MOXEY, D., GREEN, M., SHERWIN, S., AND PEIRÓ, J. An isoparametric approach to high-order curvilinear boundary-layer meshing. *Computer Methods in Applied Mechanics and Engineering* 283 (2015), 636 – 650.
- [220] MÜNCH, I., AND NEFF, P. Rotational invariance conditions in elasticity, gradient elasticity and its connection to isotropy. *Mathematics and Mechanics of Solids* 23, 1 (2018), 3–42.
- [221] MÜNCH, I., NEFF, P., MADEO, A., AND GHIBA, I. The modified indeterminate couple stress model: Why yang etal.'s arguments motivating a symmetric couple stress tensor contain a gap and why the couple stress tensor may be chosen symmetric nevertheless. *ZAMM - Journal of Applied Mathematics and Mechanics / Zeitschrift fr Angewandte Mathematik und Mechanik* 97, 12 (2017), 1524–1554.
- [222] NANAKUMAR, S., ZHUANG, X., PARK, H. S., AND RABCZUK, T. Topology optimization of flexoelectric structures. *Journal of the Mechanics and Physics of Solids* 105 (2017), 217 – 234.
- [223] NAUMANN, D., EVANS, B., WALTON, S., AND HASSAN, O. A novel implementation of computational aerodynamic shape optimisation using modified cuckoo search. *Applied Mathematical Modelling To Appear* (2015), –.

## BIBLIOGRAPHY

- [224] NEFF, P. A finite-strain elasticplastic cosserat theory for polycrystals with grain rotations. *International Journal of Engineering Science* 44, 8 (2006), 574 – 594.
- [225] NEFF, P. The Cosserat couple modulus for continuous solids is zero viz the linearized Cauchy-stress tensor is symmetric. *ZAMM - Zeitschrift für Angewandte Mathematik und Mechanik* 86 (2006), 892–912.
- [226] NEFF, P., AND FOREST, S. A geometrically exact micromorphic model for elastic metallic foams accounting for affine microstructure. modelling, existence of minimizers, identification of moduli and computational results. *Journal of Elasticity* 87, 2 (Jun 2007), 239–276.
- [227] NEFF, P., AND JEONG, J. A new paradigm: the linear isotropic Cosserat model with conformally invariant curvature energy. *ZAMM - Zeitschrift für Angewandte Mathematik und Mechanik* 89 (2009), 107–122.
- [228] NEFF, P., MÜNCH, I., GHIBA, I.-D., AND MADEO, A. On some fundamental misunderstandings in the indeterminate couple stress model. a comment on recent papers of A.R. Hadjesfandiari and G.F. Dargush. *International Journal of Solids and Structures* 81 (2016), 233 – 243.
- [229] NOWACKI, W. *Theory of Assymmetric Elasticity*, second ed. Pergamon Press and PWN, Warsaw, Oxford, New York, Toronto, Sydney, Paris, Frankfurt, 1986.
- [230] ØLGAARD, K. B., AND WELLS, G. N. Optimisations for quadrature representations of finite element tensors through automated code generation. *ACM Trans Math Software* 37, 1 (2010), 8:1–8:23.
- [231] OPENMP ARCHITECTURE REVIEW BOARD. OpenMP application program interface version 4.0, July 2013.
- [232] ORTIGOSA, R., AND GIL, A. J. A new framework for large strain electromechanics based on convex multi-variable strain energies: Conservation laws, hyperbolicity and extension to electro-magneto-mechanics. *Computer Methods in Applied Mechanics and Engineering* 309 (2016), 202 – 242.
- [233] ORTIGOSA, R., AND GIL, A. J. A new framework for large strain electromechanics based on convex multi-variable strain energies: Finite element discretisation and computational implementation. *Computer Methods in Applied Mechanics and Engineering* 302 (2016), 329 – 360.
- [234] ORTIGOSA, R., AND GIL, A. J. A computational framework for incompressible electromechanics based on convex multi-variable strain energies for geometrically exact shell theory. *Computer Methods in Applied Mechanics and Engineering* 317 (2017), 792 – 816.
- [235] ORTIGOSA, R., GIL, A. J., BONET, J., AND HESCH, C. A computational framework for polyconvex large strain elasticity for geometrically exact beam theory. *Computational Mechanics* 57, 2 (2016), 277–303.
- [236] PARK, S. K., AND GAO, X.-L. Bernoulli-Euler beam model based on a modified couple stress theory. *Journal of Micromechanics and Microengineering* 16 (2006), 2355.
- [237] PARK, S. K., AND GAO, X.-L. Variational formulation of a modified couple stress theory and its application to a simple shear problem. *Zeitschrift für angewandte Mathematik und Physik* 59 (2008), 904–917.
- [238] PATAKI, N. Testing by C++ template metaprograms. *Acta Univ. Sapientiae* 2, 2 (2010), 154–167.

## BIBLIOGRAPHY

- [239] PEARCE, D. H., HOOLEY, A., AND BUTTON, T. W. On piezoelectric super-helix actuators. *Sensors and Actuators A: Physical* 100, 2-3 (2002), 281–286.
- [240] PELTERET, J.-P., DAVYDOV, D., McBRIDE, A., VU, D. K., AND STEINMANN, P. Computational electro-elasticity and magneto-elasticity for quasi-incompressible media immersed in free space. *International Journal for Numerical Methods in Engineering* (2016), DOI: <http://dx.doi.org/10.1002/nme.5254>.
- [241] PÉREZ-APARICIO, J. L., PALMA, R., AND TAYLOR, R. L. Multiphysics and thermodynamic formulations for equilibrium and non-equilibrium interactions: Non-linear finite elements applied to multi-coupled active materials. *Archives of Computational Methods in Engineering* (2015), 1–49.
- [242] PERSSON, P.-O., AND PERAIRE, J. Curved mesh generation and mesh refinement using lagrangian solid mechanics. In *Proceedings of the 47th AIAA Aerospace Sciences Meeting and Exhibit* (2009), AIAA.
- [243] PERSSON, P.-O., AND STRANG, G. A simple mesh generator in MATLAB. *SIAM Review* 46, 2 (2004), 329–345.
- [244] PETROV, A. G. Electricity and mechanics of biomembrane systems: Flexoelectricity in living membranes. *Analytica Chimica Acta* 568, 1 (2006), 70 – 83. Molecular Electronics and Analytical Chemistry.
- [245] PFEIFER, R. N. C., HAEGEMAN, J., AND VERSTRAETE, F. Faster identification of optimal contraction sequences for tensor networks. *Phys. Rev. E* 90 (Sep 2014), 033315.
- [246] PLANTE, J.-S., AND DUBOWSKY, S. Large-scale failure modes of dielectric elastomer actuators. *International Journal of Solids and Structures* 43, 25 (2006), 7727 – 7751.
- [247] PORKOLÁB, Z., MIHALICZA, J., PATAKI, N., AND SIPOS, Á. Analysis of profiling techniques for C++ template metaprograms. *Ann. Univ. Sci. Budapest. Sect. Comput.* 30 (2009), 97116.
- [248] POYA, R. FEAPB: Finite Element Analysis of Piezoelectric Beams. <https://github.com/romeric/FEAPB>, 2013.
- [249] POYA, R. Higher Order Finite Elements for Energy Harvesting Piezoelectric Beams. Master’s thesis, Swansea University, Swansea, UK, 2013.
- [250] POYA, R., GIL, A. J., AND LEDGER, P. D. A computational framework for the analysis of linear piezoelectric beams using *hp*-FEM. *Computers and Structures* 152 (2015), 155–172.
- [251] POYA, R., GIL, A. J., AND ORTIGOSA, R. A high performance data parallel tensor contraction framework: Application to coupled electro-mechanics. *Computer Physics Communications* 216 (2017), 35 – 52.
- [252] POYA, R., GIL, A. J., ORTIGOSA, R., AND PALMA, R. On a family of numerical models for couple stress based flexoelectricity of continua and beams. *Journal of the Mechanics and Physics of Solids Under Review* (2018).
- [253] POYA, R., GIL, A. J., ORTIGOSA, R., SEVILLA, R., BONET, J., AND WALL, W. A. A curvilinear high order finite element framework for electromechanics: From linearised electro-elasticity to massively deformable dielectric elastomers. *Computer Methods in Applied Mechanics and Engineering* 329 (2018), 75 – 117.
- [254] POYA, R., SEVILLA, R., AND GIL, A. J. A unified approach for a posteriori high-order curved mesh generation using solid mechanics. *Computational Mechanics* 58, 3 (2016), 457–490.

## BIBLIOGRAPHY

- [255] PRUDHOMME, CHRISTOPHE, CHABANNES, VINCENT, DOYEUX, VINCENT, ISMAIL, MOURAD, SAMAKE, ABDOULAYE, AND PENA, GONCALO. Feel++ : A computational framework for galerkin methods and advanced numerical methods. *ESAIM: Proc.* 38 (2012), 429–455.
- [256] RATHGEBER, F., HAM, D. A., MITCHELL, L., LANGE, M., LUPORINI, F., MCRAE, A. T. T., BERCEA, G.-T., MARKALL, G. R., AND KELLY, P. H. J. Firedrake: automating the finite element method by composing abstractions. *Submitted to ACM TOMS* (2015).
- [257] REDDY, J. N. *An Introduction to the Finite Element Method*, third ed. McGraw-Hill, New York, 2006.
- [258] REDDY, J. N. Microstructure-dependent couple stress theories of functionally graded beams. *Journal of the Mechanics and Physics of Solids* 59 (2011), 2382–2399.
- [259] REDDY, J. N., AND EL-BORGI, S. Eringen nonlocal theories of beams accounting for moderate rotations. *International Journal of Engineering Science* 82 (2014), 159–187.
- [260] REIF, J. H. Depth-first search is inherently sequential. *Information Processing Letters* 20, 5 (1985), 229 – 234.
- [261] REMACLE, J.-F., LAMBRECHTS, J., SENY, B., MARCHANDISE, E., JOHNEN, A., AND GEUZAINET, C. Blossom-quad: A non-uniform quadrilateral mesh generator using a minimum-cost perfect-matching algorithm. *International Journal for Numerical Methods in Engineering* 89, 9 (2012), 1102–1119.
- [262] RINALDI, C., AND BRENNER, H. Body versus surface forces in continuum mechanics: is the maxwell stress tensor a physically objective cauchy stress? *Physical Review E* 65 (2002), 036615.
- [263] RIVARD, M., LALIBERTÉ, M., BERTRAND-GRENIER, A., HARNAGEA, C., PFEFFER, C. P., VALLIÈRES, M., ST-PIERRE, Y., PIGNOLET, A., KHAKANI, M. A. E., AND LÉGARÉ, F. The structural origin of second harmonic generation in fascia. *Biomed. Opt. Express* 2, 1 (Jan 2011), 26–36.
- [264] ROUNDY, S., AND WRIGHT, P. K. A piezoelectric vibration based generator for wireless electronics. *Smart Materials and Structures* 13, 5 (2004), 1131–1142.
- [265] RUIZ-GIRONS, E., ROCA, X., AND SARRATE, J. High-order mesh curving by distortion minimization with boundary nodes free to slide on a 3d cad representation. *Computer-Aided Design* 72, Supplement C (2016), 52 – 64. 23rd International Meshing Roundtable Special Issue: Advances in Mesh Generation.
- [266] RUSSELL, S. J., AND NORVIG, P. *Artificial Intelligence: A Modern Approach*, 3rd ed. Prentice Hall, 2009.
- [267] SARRATE, J., AND HUERTA, A. Efficient unstructured quadrilateral mesh generation. *International Journal for Numerical Methods in Engineering* 49, 10 (2000), 1327–1350.
- [268] SARRATE, J., AND HUERTA, A. An improved algorithm to smooth graded quadrilateral meshes preserving the prescribed element size. *Communications in Numerical Methods in Engineering* 17, 2 (2001), 89–99.
- [269] SCHRÖDER, J., AND GROSS, D. Invariant formulation of the electromechanical enthalpy function of transversely isotropic piezoelectric materials. *Archive of Applied Mechanics* 73 (2004), 533–552.
- [270] SCHRÖDER, J., NEFF, P., AND EBBING, V. Anisotropic polyconvex energies on the basis of crystallographic motivated structural tensors. *Journal of the Mechanics and Physics of Solids* 56, 12 (2008), 3486 – 3506.

- [271] SCHRÖDER, J., WRIGGERS, P., AND BALZANI, D. A new mixed finite element based on different approximations of the minors of deformation tensors. *Computer Methods in Applied Mechanics and Engineering* 200, 4952 (2011), 3583 – 3600.
- [272] SEVILLA, R., FERNÁNDEZ-MÉNDEZ, S., AND HUERTA, A. NURBS-enhanced finite element method (NEFEM). *International Journal for Numerical Methods in Engineering* 76, 1 (2008), 56–83.
- [273] SEVILLA, R., FERNÁNDEZ-MÉNDEZ, S., AND HUERTA, A. Comparison of high-order curved finite elements. *International Journal for Numerical Methods in Engineering* 87, 8 (2011), 719–734.
- [274] SEVILLA, R., FERNÁNDEZ-MÉNDEZ, S., AND HUERTA, A. NURBS-Enhanced Finite Element Method (NEFEM): a seamless bridge between CAD and FEM. *Archives of Computational Methods in Engineering* 18, 4 (2011), 441–484.
- [275] SEVILLA, R., HASSAN, O., AND MORGAN, K. An analysis of the performance of a high-order stabilised finite element method for simulating compressible flows. *Computer Methods in Applied Mechanics and Engineering* 253 (2013), 15–27.
- [276] SEVILLA, R., HASSAN, O., AND MORGAN, K. The use of hybrid meshes to improve the efficiency of a discontinuous galerkin method for the solution of maxwells equations. *Computers & Structures* 137, 0 (2014), 2 – 13.
- [277] SEVILLA, R., REES, L., AND HASSAN, O. The generation of triangular meshes for NURBS-enhanced FEM. *International Journal for Numerical Methods in Engineering* 108, 8 (2016), 941–968. nme.5247.
- [278] SHARMA, N. D., LANDIS, C. M., AND SHARMA, P. [Piezoelectric thin-film superlattices without using piezoelectric materials](#). *Journal of Applied Physics* 108 (2010), 024304.
- [279] SHARMA, N. D., MARANGANTI, R., AND SHARMA, P. [On the possibility of piezoelectric nanocomposites without using piezoelectric materials](#). *Journal of the Mechanics and Physics of Solids* 55 (2007), 2328–2350.
- [280] SHEPHARD, M. S., FLAHERTY, J. E., JANSEN, K. E., LI, X., LUO, X., CHEVAUGEON, N., REMACLE, J.-F., BEALL, M. W., AND O'BARA, R. M. Adaptive mesh generation for curved domains. *Applied Numerical Mathematics* 52, 2-3 (2005), 251 – 271.
- [281] SHERWIN, S. J., AND PEIRÓ, J. Mesh generation in curvilinear domains using high-order elements. *International Journal for Numerical Methods in Engineering* 53, 1 (2002), 207–223.
- [282] SIMO, J., FOX, D., AND HUGHES, T. Formulations of finite elasticity with independent rotations. *Computer Methods in Applied Mechanics and Engineering* 95, 2 (1992), 277 – 288.
- [283] ŞİŞMEK, M., AND REDDY, J. N. [Bending and vibration of functionally graded microbeams using a new higher order beam theory and the modified couple stress theory](#). *International Journal of Engineering Science* 64 (2012), 37–53.
- [284] ŞİŞMEK, M., AND REDDY, J. N. [A unified higher order beam theory for buckling of a functionally graded microbeam embedded in elastic medium using modified couple stress theory](#). *Composite Structures* 101 (2013), 47–58.
- [285] SOLIN, P., AND SEGETH, K. *Higher-Order Finite Element Methods*. Chapman & Hall, 2003.

## BIBLIOGRAPHY

- [286] SOLOMONIK, E., AND HOEFLER, T. Sparse Tensor Algebra as a Parallel Programming Model. *ArXiv e-prints* (Nov. 2015).
- [287] SOLOMONIK, E., MATTHEWS, D., HAMMOND, J. R., STANTON, J. F., AND DEMMEL, J. A massively parallel tensor contraction framework for coupled-cluster computations. *Journal of Parallel and Distributed Computing* 74, 12 (2014), 3176 – 3190. Domain-Specific Languages and High-Level Frameworks for High-Performance Computing.
- [288] SRINIVASA, A. R., AND REDDY, J. N. A model for a constrained, finitely deforming, elastic solid with rotation gradient dependent strain energy, and its specialization to von Krmn plates and beams. *Journal of the Mechanics and Physics of Solids* 61 (2013), 873–885.
- [289] STEIN, K., TEZDUYAR, T. E., AND BENNEY, R. Mesh moving techniques for fluid-structure interactions with large displacements. *Journal of Applied Mechanics* 70, 1 (2003), 58–63.
- [290] STEINMANN, P. A micropolar theory of finite deformation and finite rotation multiplicative elastoplasticity. *International Journal of Solids and Structures* 31, 8 (1994), 1063 – 1084.
- [291] STEINMANN, P., AND STEIN, E. A unifying treatise of variational principles for two types of micropolar continua. *Acta Mechanica* 121, 1 (1997), 215–232.
- [292] STONE, J. E., GOHARA, D., AND SHI, G. OpenCL: A parallel programming standard for heterogeneous computing systems. *IEEE Des. Test* 12, 3 (May 2010), 66–73.
- [293] STÜBEN, K. A review of algebraic multigrid. *Journal of Computational and Applied Mathematics* 128, 1 (2001), 281 – 309. Numerical Analysis 2000. Vol. VII: Partial Differential Equations.
- [294] SUDEEP, K. L., BONET, J., PERAIRE, J., AND CASALS, L. A variationally consistent fractional time-step integration method for incompressible and nearly incompressible Lagrangian dynamics. *International Journal for Numerical Methods in Engineering* 63 (2005), 1371–1395.
- [295] SURI, M. Analytical and computational assessment of locking in the *hp* finite element method. *Computer Methods in Applied Mechanics and Engineering* 133 (1996), 347–371.
- [296] SZABÓ, B., AND BABUŠKA, I. *Finite Element Analysis*. John Wiley and Sons Inc., New York, 1991.
- [297] TABESH, A., AND FRÉCHETTE, L. G. An improved small-deflection electromechanical model for piezoelectric bending beam actuators and energy harvesters. *Journal of Micromechanics and Microengineering* 18 (2008), 104009.
- [298] TAGANTSEV, A. K. Piezoelectricity and flexoelectricity in crystalline dielectrics. *Physical Review B* 34 (1986), 5883.
- [299] TAKAYOSHI, I. Bending piezoelectricity in polytetrafluoroethylene. *Japanese Journal of Applied Physics* 13 (1974), 197.
- [300] TAUPIN, V., CAPOLUNGO, L., FRESSENGEAS, C., DAS, A., AND UPADHYAY, M. J. A theory of disclination and dislocation fields for grain boundary plasticity. In *Advanced Structured Materials: Generalized Continua as Models for Materials* 22 (2013), 303–320.
- [301] TEZDUYAR, T., ALIABADI, S., BEHR, M., JOHNSON, A., AND MITTAL, S. Parallel finite-element computation of 3D flows. *Computer* 26, 10 (1993), 27–36.

- [302] THOMPSON, E. G., AND HAQUE, M. I. A high order finite element for completely incompressible creeping flow. *International Journal for Numerical Methods in Engineering* 6, 3 (1973), 315–321.
- [303] TOULORGE, T., AND DESMET, W. Curved boundary treatments for the discontinuous Galerkin method applied to aeroacoustic propagation. *AIAA journal* 48, 2 (2010), 479–489.
- [304] TOULORGE, T., GEUZAIN, C., REMACLE, J.-F., AND LAMBRECHTS, J. Robust untangling of curvilinear meshes. *Journal of Computational Physics* 254 (2013), 8–26.
- [305] TOUPIN, R. A. *Elastic materials with couple-stresses*. *Archive for Rational Mechanics and Analysis* 11 (1962), 385–414.
- [306] TOUPIN, R. A. *Theories of elasticity with couple-stress*. *Archive for Rational Mechanics and Analysis* 17 (1964), 85–112.
- [307] TRINDADE, M., BENJEDDOU, A., AND OHAYON, R. Finite element modelling of hybrid activepassive vibration damping of multilayer piezoelectric sandwich beams-part I: Formulation. *International Journal for Numerical Methods in Engineering* 51, 7 (2001), 835–854.
- [308] TRINDADE, M., BENJEDDOU, A., AND OHAYON, R. Finite element modelling of hybrid activepassive vibration damping of multilayer piezoelectric sandwich beams-part II: System analysis. *International Journal for Numerical Methods in Engineering* 51, 7 (2001), 855–864.
- [309] TSIATAS, G. C. A new Kirchhoff plate model based on a modified couple stress theory. *International Journal of Solids and Structures* 46 (2009), 2757–2764.
- [310] UPADHYAY, M. J., CAPOLUNGO, L., TAUPIN, V., AND FRESSENGEAS, C. Elastic constitutive laws for incompatible crystalline media: the contributions of dislocations, disclinations and G-disclinations. *Philosophical Magazine* 93 (2013), 794–832.
- [311] ŠISTEK, J., AND CIRAK, F. Parallel iterative solution of the incompressible navier-stokes equations with application to rotating wings. *Computers & Fluids* 122 (2015), 165 – 183.
- [312] VAN ZEE, F. G., AND VAN DE GEIJN, R. A. BLIS: A framework for rapidly instantiating BLAS functionality. *ACM Transactions on Mathematical Software* 41, 3 (2015), 14:1–14:33.
- [313] VELDHUIZEN, T. Expression templates. *C++ Report* 7 (1995), 26–31.
- [314] VELDHUIZEN, T. L. *Computing in Object-Oriented Parallel Environments: Second International Symposium, ISCOPE 98 Santa Fe, NM, USA, December 8–11, 1998 Proceedings*. Springer Berlin Heidelberg, Berlin, Heidelberg, 1998, ch. Arrays in Blitz++, pp. 223–230.
- [315] VERMA, C. S., AND TAUTGES, T. *Jaal: Engineering a High Quality All-Quadrilateral Mesh Generator*. Springer Berlin Heidelberg, Berlin, Heidelberg, 2012, pp. 511–530.
- [316] VERTECHY, R., FRISOLI, A., BERGAMASCO, M., CARPI, F., FREDIANI, G., AND ROSSI, D. D. Modeling and experimental validation of buckling dielectric elastomer actuators. *Smart Materials and Structures* 21, 9 (2012), 094005.
- [317] VINCENT, P. E., AND JAMESON, A. Facilitating the adoption of unstructured high-order methods amongst a wider community of fluid dynamicists. *Math. Model. Nat. Phenom.* 6, 3 (2011), 97–140.
- [318] VU, D. K., AND STEINMANN, P. Nonlinear electro- and magneto-elastostatics: Material and spatial settings. *International Journal of Solids and Structures* 44 (2007), 7891–7905.

## BIBLIOGRAPHY

- [319] VU, D. K., STEINMANN, P., AND POSSART, G. Numerical modelling of non-linear electroelasticity. *International Journal for Numerical Methods in Engineering* 70 (2007), 685–704.
- [320] WANG, Z., FIDKOWSKI, K., ABGRALL, R., BASSI, F., CARAENI, D., CARY, A., DECONINCK, H., HARTMANN, R., HILLEWAERT, K., HUYNH, H., ET AL. High-order CFD methods: current status and perspective. *International Journal for Numerical Methods in Fluids* 72, 8 (2013), 811–845.
- [321] WELLS, G., SLUYS, L., AND DE BORST, R. A  $p$ -adaptive scheme for overcoming volumetric locking during plastic flow. *Computer Methods in Applied Mechanics and Engineering* 191, 2930 (2002), 3153 – 3164.
- [322] WITHERDEN, F., FARRINGTON, A., AND VINCENT, P. PyFR: An open source framework for solving advection-diffusion type problems on streaming architectures using the flux reconstruction approach. *Computer Physics Communications* 185, 11 (2014), 3028 – 3040.
- [323] WITHERDEN, F., AND VINCENT, P. On the identification of symmetric quadrature rules for finite element methods. *Computers & Mathematics with Applications* 69, 10 (2015), 1232 – 1241.
- [324] WOO, A. C., WANG, H. T. G., AND SCHUB, M. J. Benchmark radar targets for the validation of computational electromagnetics programs. *IEEE Transactions on Antennas and Propagation* 35, 1 (1993), 84–89.
- [325] WOOSTER, W. A. *Tensors and Group Theory for the Physical Properties of Crystals*. Clarendon Press, Oxford, England, 1973.
- [326] WOZNIAK, B. D., WITHERDEN, F. D., RUSSELL, F. P., VINCENT, P. E., AND KELLY, P. H. GiMMiK - Generating bespoke matrix multiplication kernels for accelerators: Application to high-order computational fluid dynamics. *Computer Physics Communications* 202 (2016), 12 – 22.
- [327] WRIGGERS, P. *Nonlinear Finite Element Methods*, 3rd ed. Springer, Berlin Heidelberg, 2008.
- [328] XIE, Z. Q., SEVILLA, R., HASSAN, O., AND MORGAN, K. The generation of arbitrary order curved meshes for 3D finite element analysis. *Computational Mechanics* 51, 3 (2013), 361–374.
- [329] XUE, D., AND DEMKOWICZ, L. Control of geometry induced error in  $hp$  finite element (FE) simulations. I. Evaluation of FE error for curvilinear geometries. *International Journal of Numerical Analysis and Modeling* 2, 3 (2005), 283–300.
- [330] YANG, F., CHONG, A. C. M., LAM, D. C. C., AND TONG, P. *Couple stress based strain gradient theory for elasticity*. *International Journal of Solids and Structures* 39 (2002), 2731–2743.
- [331] YANG, J. *Special Topics in the Theory of Piezoelectricity*. Springer Inc., Dordrecht, Heidelberg, London, New York, 2009.
- [332] YUDIN, P. V., AND TAGANTSEV, A. K. *Fundamentals of flexoelectricity in solids*. *Nanotechnology* 24 (2013), 432001.
- [333] ZELISKO, M., HANLUMYUANG, Y., YANG, S., LIU, Y., LEI, C., LI, J., AJAYAN, P. M., AND SHARMA, P. *Anomalous piezoelectricity in two-dimensional graphene nitride nanosheets*. *Nature Communications* 5 (2014), 4284.

## BIBLIOGRAPHY

- [334] ZHANG, X. D., AND SUN, C. T. Formulation of an adaptive sandwich beam. *Smart Materials and Structures* 5, 6 (1996), 814.
- [335] ZHOU, J., HONG, W., ZHAO, X., ZHANG, Z., AND SUO, Z. Propagation of instability in dielectric elastomers. *International Journal of Solids and Structures* 45, 13 (2008), 3739 – 3750. Special Issue Honoring K.C. Hwang.
- [336] ZHU, J., KOLLOSCHE, M., LU, T., KOFOD, G., AND SUO, Z. Two types of transitions to wrinkles in dielectric elastomers. *Soft Matter* 8 (2012), 8840–8846.
- [337] ZUBKO, P., CATALAN, G., BUCKLEY, A., WELCHE, P. R. L., AND SCOTT, J. F. Strain-gradient-induced polarization in SrTiO<sub>3</sub> single crystals. *Physical Review Letters* 99 (2007), 167601.
- [338] ZUBKO, P., CATALAN, G., AND TAGANTSEV, A. K. Flexoelectric Effect in Solids. *Annual Review of Materials Research* 43 (2013), 387–421.

